Multi-ligand Functionalised, Atomically Precise Gold Nanoclusters for Antibacterial and Anticancer Applications

Zeyang Pang

Main Supervisors: Dr Dejian Zhou

Dr Xingyu Jiang

Submitted in accordance with the requirements for the degree of Doctor of Philosophy

School of Chemistry, University of Leeds

September 2022

The candidate confirms that the work submitted is his/her own, except where work that has formed part of jointly authored publications has been included. The contribution of the candidate and the other authors to this work has been explicitly indicated below. The candidate confirms that appropriate credit has been given within the thesis where reference has been made to the work of others.

Chapter 4 is based on work from the following jointly-authored publication: Zeyang Pang, Qizhen Li, Yuexiao Jia, Weixiao Yan, Jie Qi, Yuan Guo, Fupin Hu, Dejian Zhou, and Xingyu Jiang, "Controlling the pyridinium–zwitterionic ligand ratio on atomically precise gold nanoclusters allowing for eradicating Gram-positive drug-resistant bacteria and retaining biocompatibility." *Chem. Sci.*, 2021, **12**(44), 14871–14882.

Author contributions:

Zeyang Pang (the candidate): conceived this study, performed all the experiments, wrote the manuscript, and analysed the data except those clarified below.

Qizhen Li: provided TEM images and related analysis.

Jie Qi: provided TEM images and related analysis.

Yuexiao Jia: contributed to some of the bacterial experiments.

Yuan Guo: contributed to some of the bacterial experiments.

Weixiao Yan: carried out animal experiments.

Fupin Hu: contributed MDR bacteria strains.

Dejian Zhou: conceived ideas, supervised the whole experiment, and funded the project.

Xingyu Jiang: co-supervised the whole experiment and funded the project.

Chapter 7 is based on just accepted work from the following jointly-authored publication: Zeyang Pang, Weixiao Yan, Jie Yang, Qizhen Li, Yuan Guo, Dejian Zhou, and Xingyu Jiang, "Multifunctional gold nanoclusters for effective targeting, near-infrared fluorescence imaging, diagnosis, and treatment of cancer lymphatic metastasis." *ACS NANO*, 2022. DOI: 10.1021/acsnano.2c03752 (in press).

Author contributions:

Zeyang Pang (the candidate): designed and performed all the experiments and data

analyses except those stated below.

Weixiao Yan: helped with the animal experiments.

Jie Yang: wrote the software for the automatic recognition of mouse body outline and lower-body lymph nodes.

Qizhen Li: performed TEM imaging

Yuan Guo: performed some relevant work that is not included in this paper and provided help in designing the experiments.

Dejian Zhou: supervised the whole experiment and funded the project.

Xingyu Jiang: co-supervised the whole experiment and funded the project.

Acknowledgements

First and foremost, I would like to offer my gratitude to my supervisor Prof. Dejian Zhou. Of the many things I've learned from him, his approach to experimental rigour and passion for science have influenced me the most. I would like to sincerely thank him for his patient academic guidance and his advice and help with my future career planning.

I also want to thank my co-supervisor, Prof. Xingyu Jiang. I appreciate him for choosing me for his research group, for his continuous encouragement in my studies, for his selfless support with my research funding, and for taking care of my life in Shenzhen. From him, I learned the quality of scientific persistence and the self-confidence of a researcher. Notably, I also want to acknowledge both the University of Leeds and the Southern University of Science and Technology for offering me the scholarship and living expenses of this joint programme.

Thanks to my labmates and friends, who provided emotional encouragement and facilitated my PhD adventure, especially James Hooper, Dr Darshita Budhadev (University of Leeds), Nan Zong, Weixiao Yan, Dr Yangzhouyun Xie, Dr Yi Liu, Dr Ning Ren, Qinghong Hou, Zhuowei Feng, Xuedong Wang, Qizhen Li, and Leni Zhong (SUSTech). They not only help me academically and in life, affirm my progress, but also keep me positive every day.

Finally, I would like to extend my deepest gratitude to my family members: mum, dad, and other family members for their unwavering support throughout the whole PhD adventure. I could not have done it without your understanding and encouragement. Very special thanks to you!

Abstract

Ultrasmall gold nanoclusters (GNCs) are clusters of Au atoms with an overall diameter of less than 2 nm. This material possesses many outstanding properties due to its small size, including bright near-infrared (NIR) fluorescence, catalytic activity, unique *in vivo* distribution patterns, and two-photon properties. Thus, GNCs were applied as a powerful, versatile nanomaterial in broad biomedical areas, including bioimaging, drug delivery, disease treatment, and immunotherapy. However, most examples reported so far are a mixture of GNCs with varying numbers of gold atoms, which limited their druggability and potential for clinical application. Atomically precise GNCs can greatly improve the quality control as they are highly efficient molecules. However, synthesising atomically precise GNCs is still challenging, and most examples were capped with a single type of ligand, making it difficult to tune surface properties to meet the need of specific biomedical applications. My work focuses on developing a novel method for synthesising dual- and/or multi-functional ligand-capped, atomically precise GNCs through controlling the ligand feed ratios, which allows fine-tuning of the stability and bio-compatibility of GNCs for specific biomedical applications. Notably, I have demonstrated the feasibility and positive outcomes of this approach in two categories of disease models: antibacterial and anticancer. Below I am going to give a detailed introduction on both points.

Infections caused by multidrug-resistant (MDR) bacteria are an increasing global healthcare concern. Among Gram-positive MDR bacteria, the prevalence of methicillin-resistant *Staphylococcus aureus* (MRSA) and methicillin-resistant *Staphylococcus epidermidis* (MRSE) makes bacterial infections more difficult to deal with. Their widespread distribution increases the likelihood of pathogenicity, and their ability to transmit genes inter- and intra-species greatly contributes to the development of drug resistance. MRSA and MRSE mainly cause infections in the skin, mucous membranes, and soft tissues. Specifically, with the increase of contact lens users, the proportions of

bacterial keratitis (corneal infections) caused by MRSA or MRSE are increasing yearly and have become one of the most significant causes of blindness, seriously affecting patients' quality of life. I firstly developed a dual-ligand-functionalised $Au_{25}(SR_1)_x(SR_2)_{18-x}$-type GNC and determined its antibacterial activity against MDR bacterial strains. The pyridinium ligand (SR_1) provided bactericidal potency, and the zwitterionic ligand (SR_2) enhanced the stability and biocompatibility. By optimising the ligand ratio, this GNC could effectively kill MDR Gram-positive bacteria *via* multiple antibacterial actions, including inducing bacterial aggregation, disrupting bacterial membrane integrity and potential, and generating ROS. Moreover, combining the optimised GNC with common antibiotics could significantly enhance the antibacterial activity against MDR bacteria both in *in vitro* and animal models of skin infections. Furthermore, the fluorescence of the GNC at the second near-infrared (NIR-II) biological window allowed for monitoring its biodistribution and body clearance, which confirmed that the GNCs had good renal clearance and biocompatibility (Chapter 4).

Based on previous studies on dual-ligand antibacterial GNCs, I further replaced the pyridinium ligand with a non-antibacterial mercaptan fragrance molecule (SR_1), which was used together with thiolated zwitterionic ligands (SR_2) to synthesize dual-ligand antibacterial $Au_{25}(SR_1)_x(SR_2)_{18-x}$ GNCs. Surprisingly, although neither ligand had antibacterial capacity, this dual-ligand GNC exhibited prominent antibacterial capacity, with the minimum inhibitory concentration (MIC) as low as 2 μg mL^{-1} against MRSA, comparable to many last-resort antibiotics. More unexpectedly, unlike common antibiotics, the treatment of this GNC did not cause cell rupture but slowly killed MRSA by binding with the cell membrane, causing dissipation of membrane potential and disrupting respiration pathways, thereby minimizing the possibility of inflammatory responses in the body. Compared with vancomycin, the treatment of GNC improved the transparency of the mice's cornea and accelerated the healing of corneal surface wounds in the bacterial keratitis model. This work thus greatly increased the breadth of screening of antibacterial molecules to combat the bacterial MDR problem (Chapter 5).

My second research direction focuses on applying NIR fluorescent dual-/multi-ligand-capped GNCs for the theranostics of tumour lymphatic metastasis. Developing effective

lymph-node (LN) targeting and imaging probes is crucial for the early detection and diagnosis of tumour metastasis to improve patient survival. Most current clinical LN imaging probes are based on small organic dyes (*e.g.,* indocyanine green) or radioactive ^{99m}Tc-complexes, which often suffer from limitations, such as rapid photobleaching, poor signal contrast, and potential biosafety issues. Moreover, these probes cannot easily incorporate therapeutic functions to achieve more beneficial theranostics without affecting their LN-targeting ability. Herein, I have developed dual/multiligand-capped GNCs for specific targeting, NIR fluorescence imaging, diagnosis, and treatment of LN cancer metastasis in *in vivo* mouse models. By optimizing surface ligand coating, I have prepared $Au_{25}(SR_1)_n(SR_2)_{18-n}$-type GNCs, which display highly effective LN targeting, excellent stability and biocompatibility, and optimal body-retention time. Moreover, they can provide continuous NIR fluorescence imaging of LNs for >3 h from a single dose, making them well-suited for fluorescence-guided surgery. Importantly, I have further incorporated methotrexate, a chemotherapeutic drug, into the GNCs without affecting their LN-targeting ability. Consequently, they can significantly improve the efficiency of methotrexate delivery to target LNs, achieving excellent therapeutic efficacy with up to 4-fold lower hepatotoxicity. Thus, this GNC is a highly effective and safe theranostic nanomedicine against cancer lymphatic metastasis (Chapter 7).

Table of Contents

List of Tables

List of Figures

List of Abbreviations

ACQ	Aggregation-caused Quenching
AIE	Aggregation-induced Emission
ALP	Alkaline Phosphatase
ALT	Alanine Aminotransferase
AMP	Antimicrobial Peptides
AMR	Antimicrobial Resistant/ Antimicrobial Resistance
AST	Aspartate Aminotransferase
ATP	Adenosine Triphosphate
BK	Bacterial Keratitis
B-S	Brust-Schiffrin
B. s	*Bacillus subtilis*
BSA	Bovine Serum Albumin
CD	Cyclodextrin
CDC	Center for Disease Control and Prevention
CDI	1,1'-Carbonyldiimidazole
COVID-19	Corona Virus Disease 2019
CPC	Cetylpyridinium Chloride
CT	X-ray Computer Tomography
Cys	Cysteine
Cystm	Cysteamine
DAB	3,3'-Diaminobenzidine Tetrahydrochloride
Dap	Daptomycin
DAPI	4',6-Diamidino-2-phenylindole
DAPT	4,6-Diamino-2-pyrimidinethiol
DCM	Dichloromethane
DDAB	Didodecyldimethylammonium Bromide

DHLA	Dihydrolipoic Acid
DLS	Dynamic Light Scattering
DMEM	Dulbecco's Modified Eagle Medium
DMF	Dimethyl Formaldehyde
DSAC-TEM	Double Spherical Aberration Corrected Transmission Electron Microscope
DSPC	1,2-distearoyl-sn-glycero-3-phosphocholine
E. c	*Escherichia coli*
E. f	*Enterococcus faecalis*
ECM	Extracellular Matrix
EDC	1-(3-Dimethylaminopropyl)-3-ethylcarbodiimide hydrochloride
EDS	Energy Dispersive Spectroscopy
ESI	Electrospray Ionization
F.P.	Footpad Injection
FAO	Food and Agriculture Organization of the United Nations
FBS	Fetal Bovine Serum
FDA	Food and Drug Administration
FEMA	Flavour and Extract Manufacturers Association of the United States
FITC	Fluorescein Isothiocyanate
G^-	Gram-negative
G^+	Gram-positive
GC	Glycol Chitosan
GNCs	Gold Nanoclusters
GNPs	Gold Particles
GP	General Polarization
Gra	Gramicidin
GSH	Glutathione
H&E	Hematoxylin and Eosin
His	Histidine
HPLC	High-performance Liquid Chromatography

HRP	Horseradish Peroxidase
HUVEC	Human Umbilical Vein Endothelial Cell
I.V.	Intravenous Injection
IACUC	Institutional Animal Care and Use Committee
ICG	Indocyanine Green
IM	Inner Membrane
ITC	Isothermal Titration Calorimetry
K. p	*Klebsiella pneumoniae*
LA	Lipoic Acid
LCMS	Liquid Chromatography-Mass Spectroscopy
LN	Lymph Node
LNP	Lipid Nanoparticle
LPS	Lipopolysaccharides
LTA	Lipoteichoic acid
MALDI-Tof MS	Matrix-assisted Laser Desorption Ionization Time-of-flight Mass Spectrometry
MBC	Minimum Bactericidal Concentration
MDR	Multi-drug Resistant/ Multi-drug Resistance
MDRSP	Multidrug-resistant *Streptococcus pneumoniae*
MDR-TB	Multidrug-resistant *Mycobacterium tuberculosis*
MetH	Mercaptoethanol
MHA	Mercaptohexanoic Acid
MIC	Minimal Inhibition Concentration
MOA	Mercaptooctanoic Acid
MPA	Mercaptopropionic Acid
MRAB	Multidrug-resistant *Acinetobacter bauman*
MRI	Magnetic Resolution Imaging
MRL	Magnetic Resonance Lymphography
MRSA	Methicillin-resistant *Staphylococcus aureus*
MRSE	Methicillin-resistant *Staphylococcus epidermidis*
MS	Mass Spectroscopy

MTU	5-Methyl-2-Thiouracil
MTX	Methotrexate
MUA	Mercaptoundecanoic Acid
MUTAB	(11-mercaptoundecyl)-N, N, N-trimethylammonium bromide
NBT	Nitro-blue Tetrazolium
NDM-1	New Delhi metallo-beta-lactamase-1
NIR	Near Infrared
NMR	Nuclear Magnetic Resonance
NP	Nanoparticles
ODD	Ocular Drug Delivery
OM	Outer Membrane
OVA	Ovalbumin
P. a	*Pseudomonas aeruginosa*
PA	Photoacoustic
PAGE	Polyacrylamide Gel Electrophoresis
PBS	Phosphate Buffer Saline
PDT	Photodynamic Therapy
PEG	Poly ethylene glycol
PEI	Polyethyleneimine
PET	Positron Emission Computed Tomography
PG	Phosphatidylglycerol
PI	Propidium Iodide
p-MBA	p-mercaptobenzoic Acid
PP	Periplasmic Space
PTT	Photothermal Therapy
PVP	Polyvinylpyrrolidone
QA	Quaternary Ammonium
QD	Quantum Dot
QY	Quantum Yield
RND	Resistance-Nodulation-Cell Division

RNS	Reactive Nitrogen Species
ROS	Reactive Oxygen Species
S. a	*Staphylococcus aureus*
S. e	*Staphylococcus epidermidis*
S. h	*Staphylococcus hemolyticus*
S. p	*Streptococcus pneumoniae*
SCS	Subcapsular Sinus
SPDP	n-Succinimidyl-3-(2-pyridyldithiol) propionate
SPECT	Single Photon Emission Computed Tomography
SPR	Surface Plasmon Resonance
SRB	Sulforhodamine B
TA	Teichoic Acid
TBO	Toluidine Blue O
TBST	Tris-HCl buffer saline + Tween 20
TDT	Tetra(ethylene glycol) Dithiol
TEM	Transmission Electron Microscopy
THF	Tetrahydrofuran
TP	Two-photon
TPA	Two-photon Absorption
TPE	Tetraphenyl Ethylene
TPF	Two-photon Fluorescence
UCNPs	Upconverting Nanoparticles
UV–Vis	UV–Visible Spectroscopy
Van	Vancomycin
VRE	Vancomycin-resistant *Enterococci*
VRSA	Vancomycin-resistant *Staphylococcus aureus*
WHO	World Health Organization
WTA	Wall teichoic acid
ZW	Zwitterion/ Zwitterionic

Part I

General Introduction to Gold Nanomaterials and Summary of Experimental Methods and Materials

Chapter 1
A brief introduction to the development of GNPs and GNCs

1.1 The development of gold nanomaterials, from GNPs to atomically precise GNCs in antibacterial applications

Gold nanomaterials hold many unique characteristics, including high chemical inertness that renders them a long lifespan within the body (over 6 months in primary human fibroblast cells)[1], as well as easy surface modification due to versatile coordination chemistry with many groups like thiol, amine, selenol, carbene, and phosphine groups.[2] Moreover, its shape and size can be easily tuned during synthesis and further modified with different functional surface ligands for a wide range of different applications.[3] Thus, gold nanomaterials were chosen to be the perfect carrier in my research. Common gold nanomaterials consist of gold nanoparticles (GNPs), gold nanoclusters (GNCs), gold nanorods, etc.[4] A brief introduction to the recent development of these gold nanomaterials will be given below.

1.1.1 History of the application of Au-based compound in biomedicine

Gold, as one of the earliest metals utilised by humans, has been mined and smelted for over 4000 years. Due to its chemical inertness, it is relatively easy to obtain metallic gold compared with other active metals. Thus, the easy application of gold has facilitated a long history of research on it. In around 25-year A.C. in China, a book *Zhou Yi Can Tong Qi* already recorded that "*the nature of gold is immortal, so it is a treasure for all things, and the magician eats it to live a long life*," indicating that people in that time has already linked gold to medical use. In the 7th century A.C., due to the development of alchemy, the application of gold chloride or chloroauric acid was common. Lately, gold compounds have been gradually applied in treating various

diseases, which gradually developed the so-called chrysotherapy.[5] For example, chloroauric acid solutions were still used to treat syphilis as late as the 19th century.[6] With the development of modern medicine, the application of gold compounds is more prudent and precise. The chemical valence state of gold could vary from -1 to +5, and the most common ones are +1 and +3, and most gold complexes have gold in these two valences.[7] For example, potassium gold cyanide ($K[Au(CN)_2]$), an Au(I) compound discovered in 1890, was applied for the treatment of tuberculosis due to its ability to inhibit bacteria growth (refer to **Figure 1.1.1** for molecular structures). Since the 1920s, gold thiolates (sodium aurothiomalate and aurothioglucose) have been used in treating rheumatoid arthritis. These gold-containing compounds have abilities to modulate the host immune response.[8] Many of these gold-based drugs (tetra-acetylglucose gold and auranofin [tetra-O-acetyl-β-D-(glucopyranosyl)thio-(triethyl phosphine) gold(I)]) are still active in treating rheumatoid arthritis today .[9] Besides, some gold compounds also display medical application potentials in treating cancer, for example, $Na_3Au(S_2O_3)_2{\cdot}2H_2O$ or aurothio propanesulfonate .[10] Therefore, the gold element has played a pivotal role in the development of ancient and modern medicines.

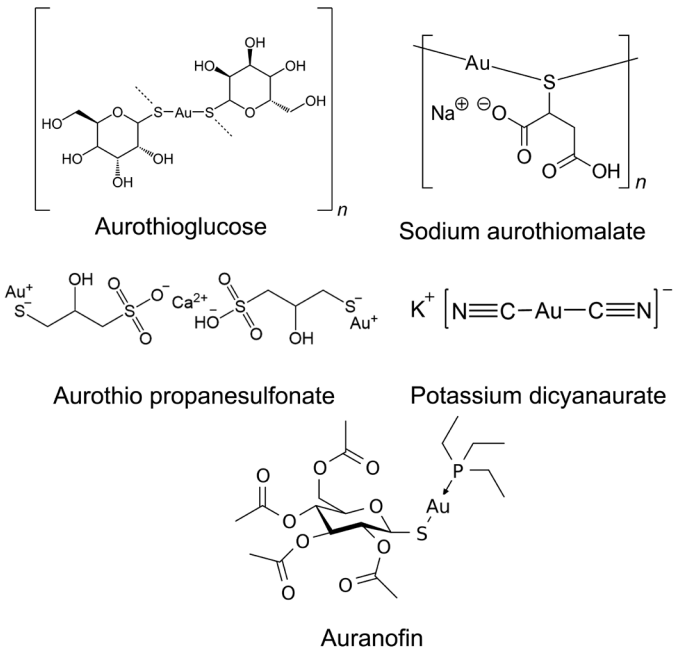

Figure 1.1.1 Chemical structures of the above-mentioned Au-based small molecular

compounds and drugs. Most of these drugs are applied for the treatment of rheumatoid arthritis and cancer.

1.1.2 Development history of GNPs

Although the rise of the concept of nanomaterials has only been around 66 years in history, the application of gold nanomaterials can be dated back to ancient India. For example, in the 1st century AD, ancient *Ayurveda* physicians already knew to use *swarna bhasma* or "gold ash," which is now known as a type of primitive GNP (> 60-nm) prepared with mechanical comminution. This GNP can be mixed with food and taken orally to treat a series of physical ailments.[11] Although the inner mechanism and reason for its actions were not clearly studied due to the limitation of era and techniques, this still represents a meaningful step forward for human beings to harness the power of nanomaterials for the treatment of diseases. Moreover, the gold-silver alloy NPs, discovered in the 4th century, were doped into the famous Lycurgus cup, which is now displayed in the British Museum. The addition of ~30 nm NPs gave this glass cup unique optical properties, allowing it to display different colours in different light directions (scattering-transmission-dichroism) [12] (**Figure 1.1.2**).

Figure 1.1.2 The Lycurgus cup is made of dichroic glass and presents differently coloured in front-lit (green) and back-lit (red) due to differences in the type of reflected and transmitted light caused by the Au-Ag alloy NPs in the glass.[12] (Copied from the ACS

Publishing Group)

In modern concepts, GNPs refer to round gold spheres with a diameter of about 1 to a few hundred nm. The first person who did systemic research on the optical properties of GNPs was Michael Faraday. He observed that, with the reduction of particle size, the colour of GNPs is no longer metallic yellow but ruby red or violet-ruby [13], and now I know that this dark red colour is due to the GNPs can strongly absorb the lights in the blue and green region due to the local surface plasmon resonance but reflect red light. Surface plasmon resonance (SPR) is one of the many unique properties of GNP that is widely used in all fields of detection and treatment.[14] The mechanism is, firstly, a certain angle of incident light would pass the surface of the material and cause an electronic wave inside. The GNPs influenced will change the shape of the electron cloud and form a new plasmon wave inside the atom. If half wavelength of incident light is bigger than the diameter of GNPs, and the frequency of them can have resonance, then the reflected light would get extremely weak, and NPs can absorb most of the light energy (**Figure 1.1.3**). This is also the prerequisite for the photothermic and photodynamic effects of GNPs.

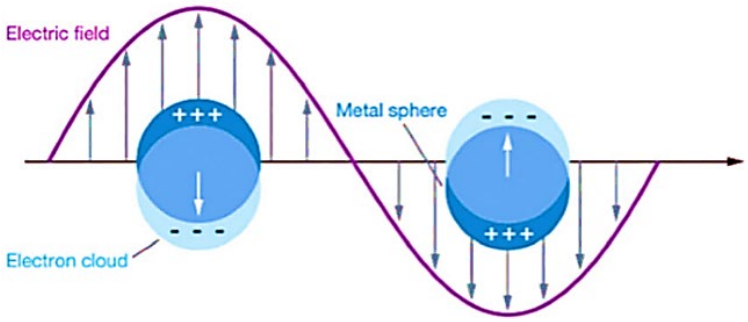

Figure 1.1.3 Schematic of the SPR property of GNP. The resonant absorption of light with a specific wavelength by the electron cloud change on the surface of GNP can explain the reason why GNP solution usually exhibits characteristic ruby colour.[14] (Copied from the RSC Publishing Group)

In addition, the reduction in the size of GNP to the nanoscale has granted it many other

unique properties, including electrochemical reactivities, catalytic activity, optical properties, and even quantum properties.[6] After 170 years of development after Faraday's study, GNP has become one of the most studied gold nanomaterials with expansive applications in bio-detection and bio-sensing, drug delivery and disease treatment, chemical catalysis, as well as molecular electronics. The special gold-thiol (Au-S) bond that is as robust as the Au-Au bond constitutes the basis of the surface modification of common GNPs and other gold nanomaterials. Taking advantage of the high affinity yet dynamic of this covalent bond (almost non-polar), the surface modification of gold nanomaterials is simple and straightforward, which also grants an easy cap change process to suit the application environments. Due to the valence of gold atoms on the surface of GNPs being normally +1, they are in a straight line with the attached two thiol groups and form a self-assembled monolayer that wraps the Au(0) kernel inside.[7] As the size gradually decreases, the conformation gradually changes and forms GNCs, which have different crystal forms, and will be discussed in the next section. In addition, other functional groups, including phosphine or amine, are also used for the surface capping of various gold nanomaterials.

1.1.3 Introduction to the synthetic methods of GNPs

The methods to synthesise GNPs can be generally divided into top-down and bottom-up two main categories (**Figure 1.1.4**). The mechanical grinding and calcining method to prepare *swarna bhasma* is a primitive top-down method by breaking down bulky gold into nanometre-scale particles by destroying its crystal structure to reduce its size.[15] Others include chemical ligand etching to break up large particles or mechanical methods, including ball milling, plastic deformation, and laser ablation.[16] However, precise control of the size of acquired GNPs is a great challenge for these top-down methods.

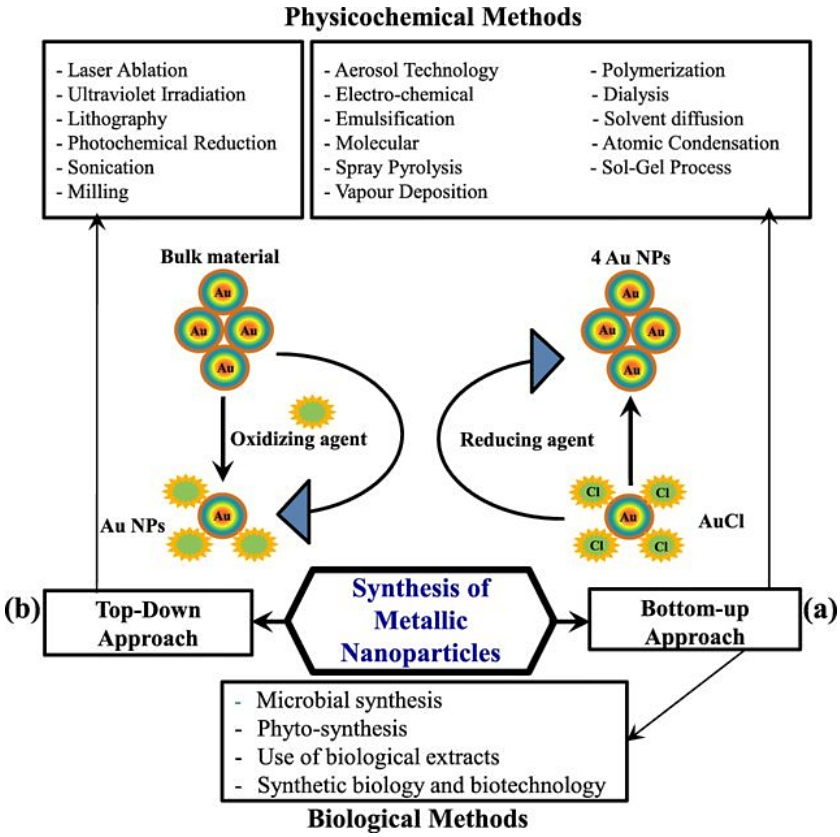

Figure 1.1.4 Typical physicochemical or biological methods for the synthesis of GNPs. The synthetic method of GNPs could be simply divided into top-down (starting from bulky materials) or bottom-up (starting from molecules) two main categories.[17] (Copied from the Springer Publishing Group)

Comparatively, a bottom-up method is much easier for size control. One of the most widely used methods is the addition of reducing agents to control the reduction of gold salts to yield GNPs, which is the foundation of many GNP synthetic methods. For example, using trisodium citrate to reduce the chloroauric acid solution is widely used to prepare poly-dispersed GNPs. By tuning the gold salt to the reducer ratio, GNPs of different sizes can be readily prepared.[18] Moreover, precise control of synthetic environments, such as the solution pH, can further reduce the GNP size dispersity.[6] In addition, the Brust-Schiffrin method was developed for the synthesis of GNPs in 1994. This is a two-phase GNP synthesis method aided by a phase transfer agent, *e.g.,* tetraoctylammonium bromide (TOAB). The gold salt, *e.g.,* $[Au(Cl_4)]^-$, is transferred from the aqueous phase to the organic phase by the added tetraoctylammonium. Then the

organothiol ligand is introduced, and finally, an excess reducing agent, *e.g.,* sodium borohydride, is added to reduce the gold salt to metallic gold and subsequently capped with the thiol ligand to form GNPs (**Figure 1.1.5**).[3] The obtained GNPs typically have high size uniformity, and the whole synthesis process is not very complicated. Various subsequent optimisations have made the size of the GNPs synthesised by the Brust-Schiffrin method more uniform, which also laid the foundation for the subsequent synthesis of various atomically precise GNPs and GNCs.

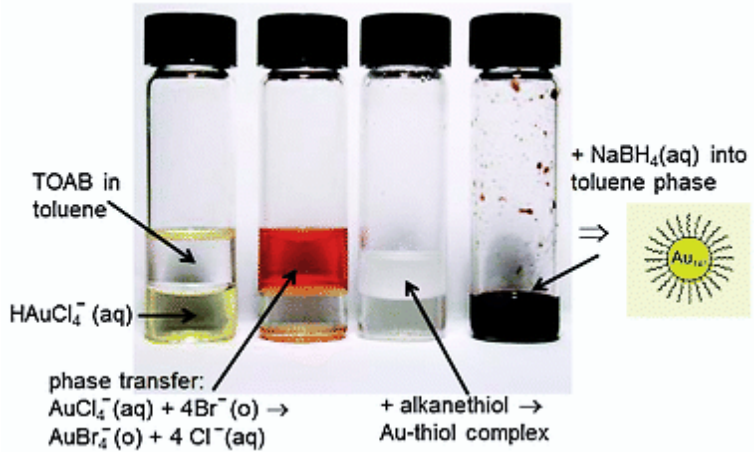

Figure 1.1.5 Flow diagram of the Brust-Schiffrin method. The Au^{3+} ion was first transferred to the organic phase with TOAB and then reacted with the alkanethiol ligands to form the turbid Au-thiol complexes. After that, the addition of $NaBH_4$ solution further reduced the complexes to monodispersed GNPs.[19] (Copied from the RSC Publishing Group)

During the Brust-Schiffrin method synthesis, the application of the surfactant—TOAB helps the transfer of Au^{3+} ions in different phases. During the synthesis of GNPs, the important role played by surfactants is not limited to this. The high surface energy, as well as inter-particle forces, could destabilize the GNPs to cluster and form aggregates. Those GNPs with smaller sizes have a higher tendency to aggregate. Thus, surfactants are applied to reduce the surface energy and provide steric hindrance between GNPs to stop aggregation. Several surfactants have been shown to provide the GNPs with outstanding stability, solubility, and even adjust the dispersity of yielded GNPs. For

example, Triton X-100 was used in the synthesis of 5 to 20 nm GNPs *via* a seeded growth method, where the size of yielded GNPs could be controlled by the Triton concentration.[20] Many ionic liquids, including those containing imidazolium and quaternary ammonium groups, were also used as a stabiliser as well as a reducing agent in GNP synthesis due to their ability to provide electrical charges to increase the dispersion and stability of the resulting GNPs (Figure 1.1.6).[21–23] Besides, a tetrazolium-based ionic liquid can also act as a novel solvent for the preparation of high-quality GNPs.[24]

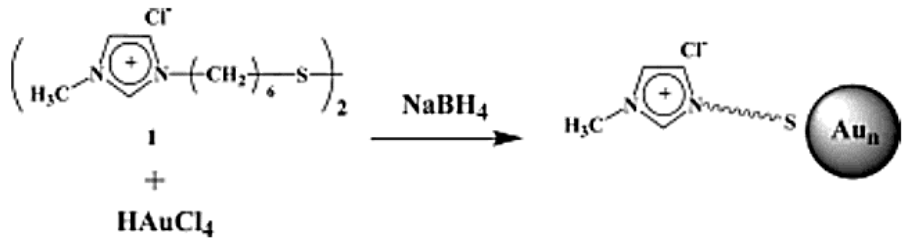

Figure 1.1.6 Scheme of the synthesis of imidazolium ligand-capped GNP. The capping of the cation ligand on the surface of GNP could provide the electrostatic repulsion between NPs, which counteracts the strong aggregation tendency between GNPs.[22] (Copied from the ACS Publishing Group)

Macromolecules, including linear polymers or dendrimers, were also applied for the synthesis of GNPs. For instance, polyethylene glycol (PEG) is one of the most widely used materials. Other biomolecules or bio-derived macromolecules, such as nucleic acid, proteins, chitosan, starch, and dextran, are also applied for capping GNPs [25] [26], which has several advantages: 1) the gold ions could be sequestered within the polymers, and subsequent reduction could happen in a stoichiometric way to enable the precise control of the particle size and uniform dispersity. 2) These macromolecules could provide steric stabilisation to prevent single GNPs from coming together to form aggregations. Taking the PEG as an example, due to the rich hydrogen bond donors and acceptors, a long PEG chain could effectively recruit a large number of water molecules

through extensive hydrogen bonding and form a hydration layer on the GNP surface.[27] This not only can act as a substantial physical barrier to prevent GNP aggregation but also block the non-specific adsorption of proteins on such PEGylated GNP surface.[28] **3)** For the property of these macromolecules themselves, their exposed groups can further tune the solubility and stability of the as-synthesised GNPs to suit their application environments. **4)** The shape or molecular weight of these macromolecules to gold can also control the size of prepared GNCs. For example, polyvinyl pyrrolidone (PVP) was used as the capping ligand to synthesise GNPs and ethylene glycol as the reducer. By controlling the molecular weight (or viscosity) of PVP, different sizes of GNPs can be synthesised.[29] In the following chapter, I will give a detailed discussion on the influence of different types of ligands on the synthesis of antibacterial GNPs.

The synthesis of GNPs has been extensively studied. Other methods for the synthesis of GNPs include electrochemical synthesis[30–32], photochemical synthesis[33–38], radiosynthesis[39–44], and biosynthesis[45–47]. Since it is not the focus of my thesis, I will not go deeper into the synthesis of GNPs in this paper.

1.2 Synthesis, properties, and applications of GNCs

The research and development of GNPs, as a bright star of gold nanomaterials, have bloomed with brilliant results for nearly a century. With the development of new characterization methods, such as electron microscopy and mass spectrometry, people have gradually expanded the scale of research objects down to the atomic and even sub-atomic levels. Normally, rather small GNPs, with sizes of ≤2 nm and consisting of up to ~300 Au atoms, are named as GNCs. As an extension of GNP, research in GNC is a step further in the precision of both synthesis and application of zero-dimensional nanomaterials. Compared to their larger GNP counterparts, the research on GNCs is more in-depth because their chemical and physical properties can be more precisely controlled by the number of Au atoms in each GNC. Driven by today's technology, one

can delve deeper into the mechanisms of these properties to better utilize GNCs. Compared with the GNPs, the ratio of gold to the ligand is further reduced in GNCs, which further increases the utilization of Au atoms. In addition, the Thus, GNCs are recently finding more applications in the theranostic applications in a variety of diseases (Figure 1.2.1).[48]

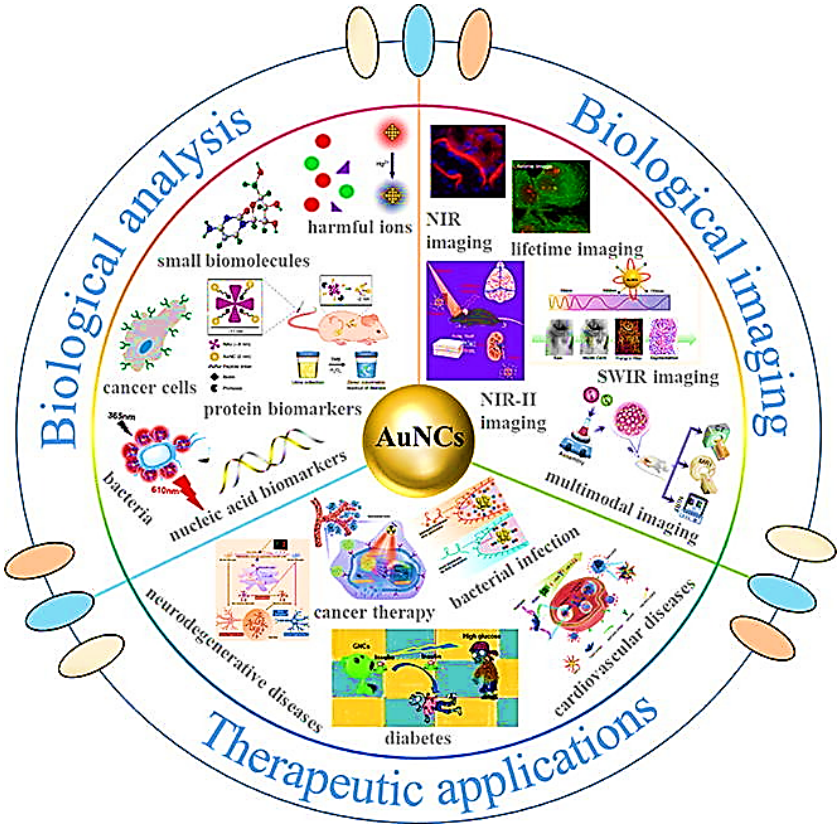

Figure 1.2.1 GNCs capped with various ligands serve as novel multifunctional tools in many fields of bioimaging and disease therapy.[48] (Copied from the Elsevier Group)

1.2.1 Development of early phosphonium ligand-capped GNCs

Unlike GNPs, the synthesis of GNC requires more precise control of the number of Au atoms in each particle, and the demonstration of successful GNC synthesis is highly dependent on the development of microscopic characterization. Thus, the development of GNC is closely related to the breakthroughs in its synthetic method. I have summarized the timeline of GNC development in Figure 1.2.2, where the important breakthroughs are labelled in red. Basically, for a successful atomically

precise GNC synthesis, the following points need to be considered: 1) the selection of applicable ligands, 2) the selection of adequate reducing agents, 3) time, including the stirring and ageing time, 4) the selection of reaction conditions, such as temperature, pH, stirring speed, and additional reaction conditions (laser power, ultrasonic power, current intensity, etc.), and 5) the gold to ligand ratios.[49]

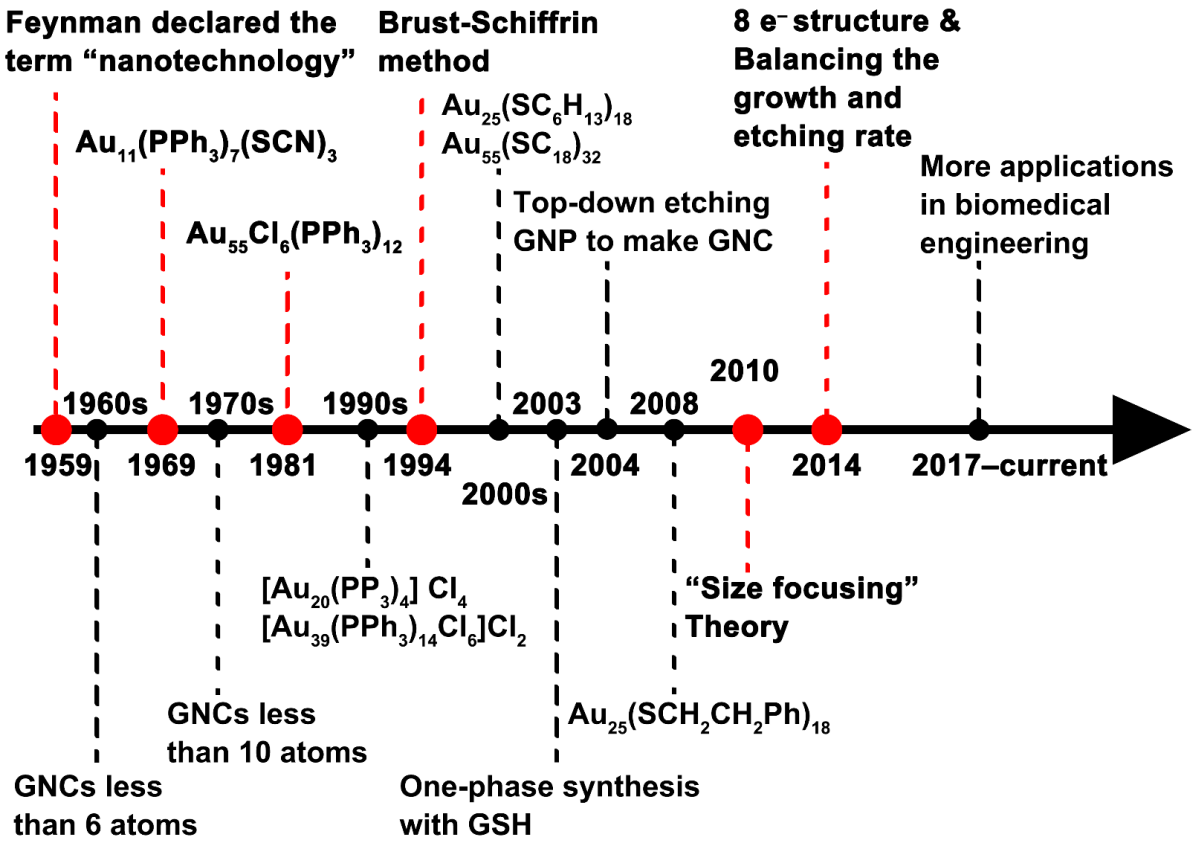

Figure 1.2.2 Timeline showing the development history of GNCs.[50] Many important time points that promote the development of GNCs are labelled in red.

Restricted by technological development, GNCs were discovered and synthesised much later than GNPs. Well after 1959, when physicist Feynman declared the arrival of nanotechnology, then GNCs were just beginning to develop.[13] The earliest record of the preparation of atomically precise GNCs with less than six Au atoms capped by 1,2 bis(diphenylphosphino)ethane was reported by L. Naldini and F. Cariati in the 1960s, which was called noble metal quantum clusters at that time. By the reaction of

chlorotriphenylphosphine gold(I) with sodium borohydride in ethanol, a GNC was formed as a red solution.[51] A few years later, the same group determined the GNC as $Au_{11}(PPh_3)_7(SCN)_3$ *via* X-ray diffraction[52] and revealed an incomplete icosahedron structure with ten Au atoms surrounding a central Au atom. In subsequent years, this group continuously reported a few more gold quantum clusters capped with tris-para substituted phenyl phosphine, tris-p-tolyl phosphine, and triphenylphosphine. These GNCs were synthesized by adding $NaBH_4$ to an ethanol solution of Au-ligand complexes which produced brown-coloured precipitates. After purification and recrystallization, dark red crystals suitable for X-ray structural determination were obtained.[53] During this period, research on GNC has made great progress, and more GNCs with Au atom numbers less than ten were synthesized, building a bridge between atoms and nanoparticles. In 1981, the Au_{13} NC was discovered and determined to have a standard icosahedral structure, which laid a theoretical foundation for the subsequent development of GNC geometry.[54] In the same year, Schmid's group presented the epoch-making multi-shell GNC—$Au_{55}Cl_6(PPh_3)_{12}$ through reduction of $(C_6H_5)_3PAuCl$ with B_2H_6 in benzol, which is also known as a member of the full-shell NCs.[55 56] (**Figure 1.2.3**) Due to its self-assembly nature and unique electronic properties, this GNC was widely studied as nanoelectronics, DNA delivery vehicle and antitumour reagent.[57 58] Due to the difficulty in characterization, the GNCs with higher numbers of Au atoms, *e.g.,* $[Au_{20}$(tris[2-(diphenylphosphino)ethyl]phosphine$)_4]$ Cl_4 and $[Au_{39}(PPh_3)_{14}Cl_6]Cl_2$, have not been reported until the 1990s.[59] However, the capping of these GNCs is highly restricted to hydrophobic groups like phosphine and lacks other types of ligand modifications.

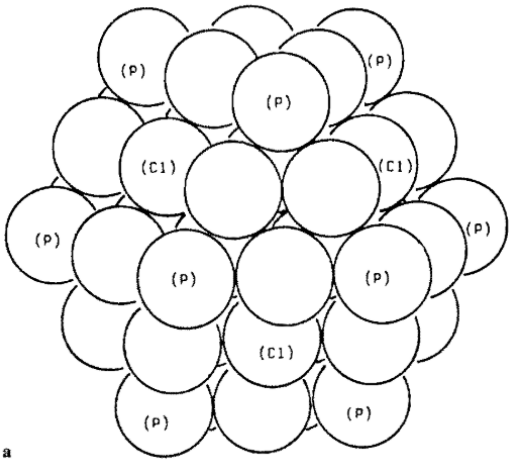

Figure 1.2.3 The Au atoms of the kernel of $Au_{55}[PPh_3]_{12}Cl_6$ arrange in a cuboctahedral shape so that there are no excess Au atoms.[60] (Copied from the Springer Publishing Group)

1.2.2 B-S method and subsequent improvements enable more thiol ligand-capped GNCs

In 1994, the development of the Brust-Schiffrin (B-S) method for the preparation of thiolated GNPs also brought light to the synthesis of thiolated GNCs. The reduction in structural constraints enables a wider variety of thiolated ligands to be used in the synthesis of GNCs. As I have introduced in the last section, this two-phase GNP synthetic method utilizes surfactants, organic thiol ligands, and reducing agents to give a high-yield synthesis of GNPs. For GNCs, using alkyl thiols of different lengths, both $Au_{25}(SC_6H_{13})_{18}$ and $Au_{55}(SC_{18})_{32}$ can be synthesised. Zhu et al., in 2008, reported the improved B-S method for GNC synthesis where alkylthiol (RSH) reduction of Au(III) into Au(I): SR was performed at a low temperature (0 °C) to impose a kinetic control of the reaction. The formed small-aggregate intermediates controlled by temperature and stirring rate were then reduced by $NaBH_4$ to generate $Au_{25}(SCH_2CH_2Ph)_{18}$ in high yield.[61] Interestingly, Jin et al. found that during the synthesis, a few specific GNCs were found to be more stable than others, for example, Au_{25}, Au_{38}, Au_{102}, and Au_{144}. They proposed a "size-focusing" methodology that could partially explain the underlying mechanism (Figure 1.2.4).[62]

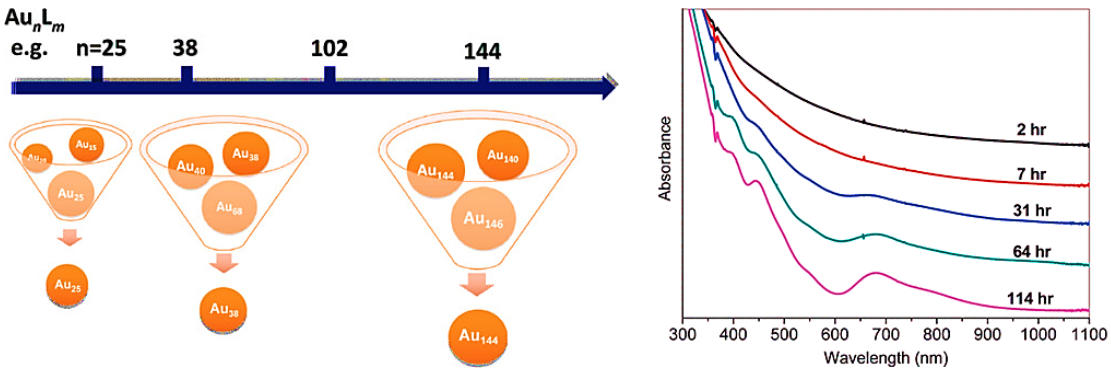

Figure 1.2.4 Although GNC intermediates containing various numbers of Au atoms are rapidly formed during the reduction process, they eventually form several classes of stable forms with specific numbers of Au atoms.[62] (Copied from the ACS Publishing Group)

However, the B-S method still has problems with using toxic low-polarity solvents like toluene. To improve the B-S method, the two-phase solvent was replaced with a one-

phase polar solvent (like methanol), and further control of the reaction conditions could generate GNCs with good dispersity. To further enhance the stability of the GNCs in the aqueous phase, glutathione was applied to replace the alkyl thiol. In 2003, Negishi et al. proposed the synthesis of ultrasmall (~1 nm) glutathione-protected GNCs in methanol under low temperatures. Specifically, GSH was added to the 0 ^{o}C methanol solution of $HAuCl_4$, and $NaBH_4$ was introduced with vigorous stirring for the preparation of GNCs with varying Au numbers. Then they used the polyacrylamide gel electrophoresis (PAGE) for the purification and separation of GNCs with different atomic numbers.[63] Besides, THF was also used as the solvent for the synthesis.[64] Subsequently, the reaction system gradually changed from the organic to the aqueous phase.

Xie's group has done many works in precise control of GNCs' size and formula. The formation of GNCs is a dynamic equilibrium procedure that includes the formation of Au(0) core from gold trivalent ions or the complex staple motifs [Au(I)-SR] as well as the etching of the surface Au atoms by free deprotonated thiol ligands. As the purification of GNCs is difficult, high precision synthesis is a better approach to making atomically precise GNCs. The method to produce GNCs was concluded to be "natural selection".[65] Under certain environments, the most "adaptable" or "stable" GNCs would compose the majority of the final product.[66] Thus, the provision of a suitable environment is the most important part of the $Au_{25}(SR)_{18}$ synthesis. Using NaOH to strongly basify the pH of the solution was found to be a good method. Here, the addition of NaOH could prevent hydrolysis of sodium borohydride as well as deprotonate thiol groups. Therefore, the synthesized GNCs have a narrower size distribution and a relatively higher yield of target GNCs compared to that without NaOH addition (**Figure 1.2.5**).[67] Methods of controlling the concentration of [Au(I)-SR] intermediates were also published. It was found that low temperature and slow stirring before adjusting the pH can boost the formation of $Au_{25}(SR)_{18}$.[61]

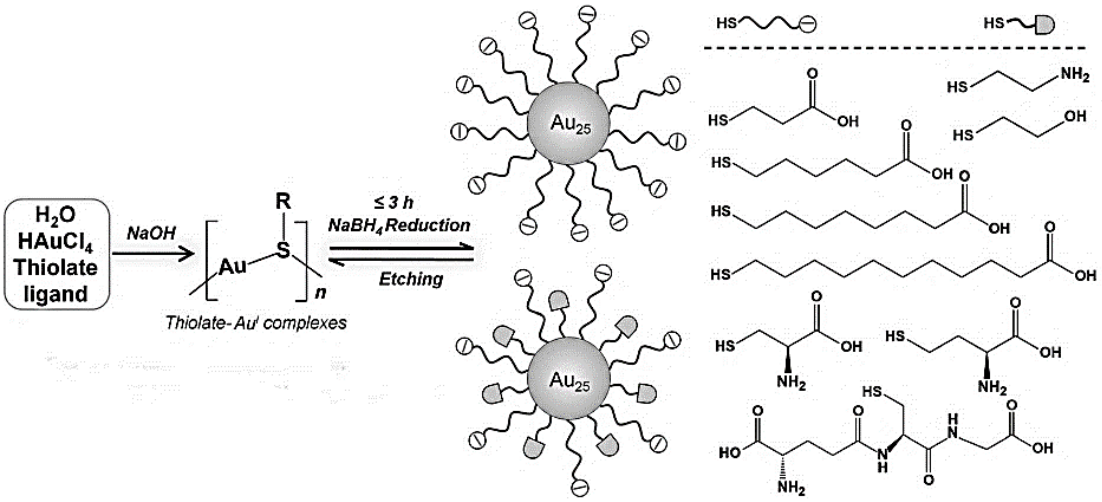

Figure 1.2.5 Schematic of the formation mechanism of $Au_{25}(SR)_{18}$ NC with a controlled amount of NaOH. The concentrations of NaOH and $NaBH_4$ control the balance between the reduction of the Au(I)-SR complex and the etching of deprotonated thiol ligands. This dynamic equilibrium has enabled the preparation of a high yield of monodispersed $Au_{25}(SR)_{18}$ NC [67]. (Copied from the Wiley Publishing Group)

During this time, a series of small and highly fluorescent gold compounds capped with either thiol ligands or thiol-containing macromolecules such as proteins or dendrimers were also characterised as GNCs because they showed a small size (~2 nm) under the electron microscope observation. Although it is difficult to characterize such GNCs using MS to determine their exact chemical formulas (due to the product uncertainty), the number of Au atoms in these GNCs could be analysed by subtracting the mass of the ligand molecule from the synthesized product to deduce the mass of the gold kernel.[68] For example, compared with atomically precise GNCs, their fluorescence is usually higher, and the fluorescence quantum yield (QY) is also in the range of ~5% to 56%.[69] In addition, instead of showing fluorescence wavelengths in the NIR region, like atomically precise GNCs, their fluorescence can vary from blue to red depending on the preparation method and capping ligands. Although their structures are not clearly defined, they were developed along with the atomically precise GNCs introduced earlier. I will distinguish them in the following introductions (by not mentioning their

specific molecular formula).

1.2.3 Other synthetic methods of atomically precise GNCs

Besides the methods introduced above, other novel methods were also applied for the synthesis of GNCs.

1.2.3.1 Top-down methods

During the early twenty-first century, similar to GNPs, the top-down synthesis of GNCs has also been proposed, which mainly uses the etching effect of thiol ligands to etch larger GNPs to generate ultra-small GNCs. For example, in 2004, Jin et al. used dodecyl thiol in octyl ether to etch 6-nm GNPs for the preparation of GNCs. The process was observed with a decrease in the characteristic absorption peak at 520 nm and an increase in the peak at 305 nm. The GNCs were then classified as mostly $Au_3(SC_{12}H_{25})_3$.[70] In 2007, Duan et al. reported using PEI as the etching ligand for the preparation of fluorescent GNCs containing ~8 Au atoms.[71] In 2008, Lin et al. used didodecyldimethylammonium bromide (DDAB) to etch GNPs in a toluene-water two-phase system and formed a light-yellow solution in toluene. After further treatment with dihydrolipoic acid (DHLA), it formed a brightly fluorescent GNC solution in water. This is a modified method to that reported in 2003 by Jana et al.[72] These GNCs are around 1.56 nm in size, and through 1-(3-Dimethylaminopropyl)-3-ethyl carbodiimide hydrochloride (EDC) chemistry, the GNCs can be further linked to biomacromolecules for cell bioimaging, biomarker detection, and other potential application.[73] (**Figure 1.2.6**) In another study, microwave-assisted etching of a ruby-red GNP solution was applied for the preparation of GNCs capped with non-thiolated 1,3,5-triaza-7-phosphaadamantane or L-glutamine and successfully produced colourless blue light-emitting GNCs. The GNCs are predicted to be mainly ligand-stabilized GNC containing more than 5 Au atoms through spectrum comparison. Both GNCs are highly water-soluble and with high biomedical application prospects.[74]

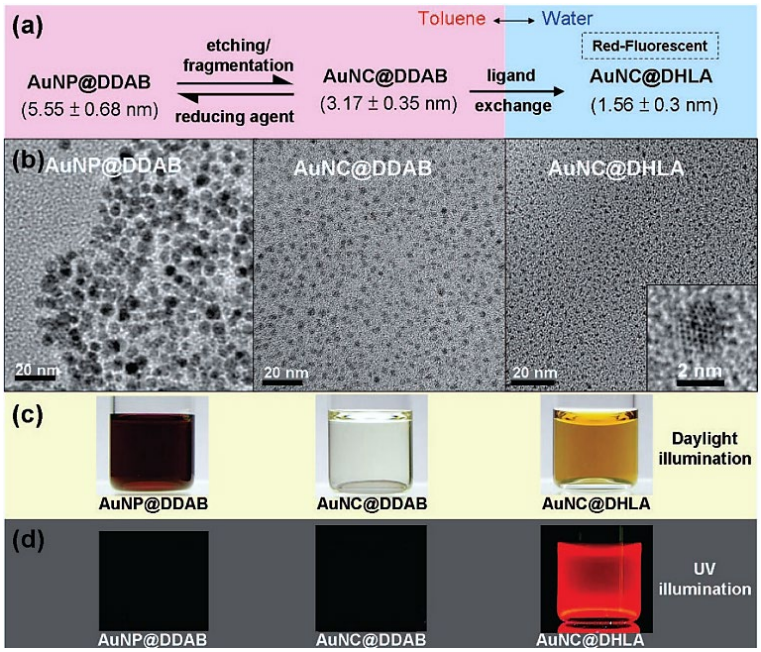

Figure 1.2.6 Highly fluorescent DHLA-capped GNC was prepared by etching the GNPs with excess DDAB ligands. Through phase transfer, the acquired DHLA-GNC with uniform size was collected in the aqueous phase. Upon UV light radiation, the GNC gave out red fluorescence at 700 nm with QY around 1–3%.[73] (Copied from the ACS Publishing Group)

1.2.3.2 Using slow-reducers to control the distribution of GNCs

CO, as a moderate reductant, can also be used to make $Au_{25}(SR)_{18}$-type GNCs.[75] Scale-up preparation of up to ~200 mg atomically precise $Au_{25}(SR)_{18}$ NCs in a single batch synthesis can be achieved by simply introducing CO into a Au(I)-ligand complex solution containing relevant thiol ligands (such as Cys), which is in stark contrast to a few mg of product per batch in common methods. In addition, the end time of the reaction can be determined by performing spectrophotometric measurements, making the reaction highly controllable (**Figure 1.2.7**).

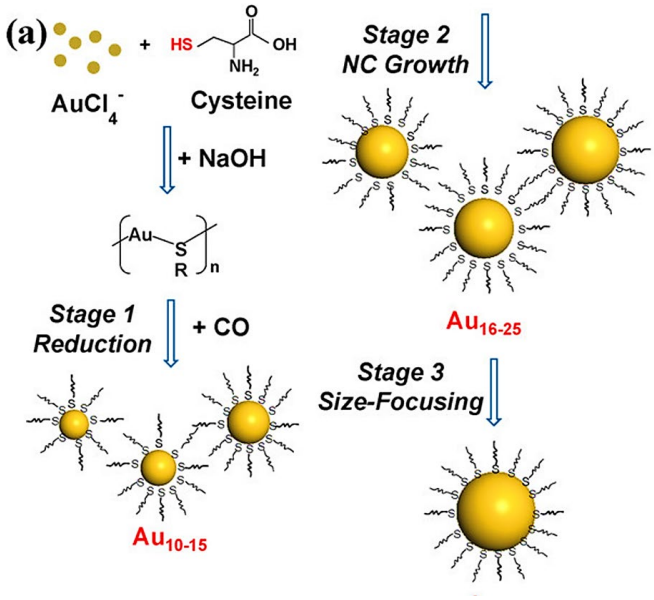

Figure 1.2.7 Mechanism of the formation of atomically precise $Au_{25}(Cys)_{18}$ NC with the addition of CO as a slow reducer compared with $NaBH_4$. The reaction was separated into reduction→growth→size-focusing three stages.[75] (Copied from the ACS Publishing Group)

1.2.3.3 Electromagnetic wave-assisted synthesis

Compared with the widely used chemical reduction method, the photoreduction of GNC is less common due to the difficulty in controlling the size dispersity of synthesized GNCs. Zhang et al. have used UV light (365 nm) for the synthesis of poly (methacrylic acid) functionalized with pentaerythritol tetrakis 3-mercapto propionate for the synthesis of water-soluble GNCs. Through MALDI-TOF analysis, $[Au_5S_9]^-$, $[Au_5S_{10}]^-$, $[Au_6S_{10}]^-$, $[Au_6S_{11}]^-$, and $[Au_6S_{12}]^-$ have been distinguished from the product.[76]

The microwave irradiation synthetic method, like in the synthesis of GNPs, has the advantages of an easily accessible microwave source, less chemical waste, fast and stable heating process, controllable reaction, *etc.,* so it is widely used in the synthesis of GNCs. For example, Liu et al. applied the commonly used antibacterial enzyme—lysozyme for the synthesis of fluorescent GNCs (**Figure 1.2.8**). With a greatly reduced reaction time to minutes compared with chemical methods, the fluorescence wavelength was shifted to ~690 nm in the red-light range and is suitable for dual-

modality imaging with the NIR fluorescence and X-ray computed tomography.[77] In another study, garlic extractions were used for ligand modification of microwave-assisted bovine serum albumin (BSA)-capped GNCs. In only 10 mins, the G-BSA-GNC could be synthesized and applied in the rapid detection of lead ions.[78]

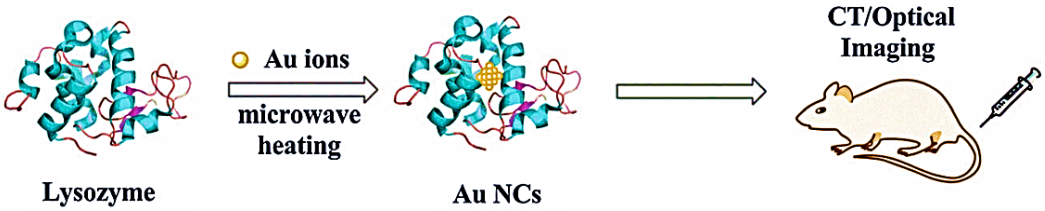

Figure 1.2.8 By microwave-assisted synthesis, the fluorescent GNCs capped with lysozyme were synthesized for the (CT/Optical) dual-modality imaging of tumours *in vivo*.[77] (Copied from the MDPI Publishing Group)

In addition, ultrasonic synthesis was combined with the microwave method to prepare orange-red fluorescent GNC. This GNC with a high QY (over 7%) can be developed for visualizing latent fingermarks with high potential in crime investigation.[79]

1.2.3.4 Biosynthesis of GNCs

As a characteristic of tumour cells, a highly reducing microenvironment within solid tumour tissue has been widely used for molecular response, drug release, and synergistic cancer therapy.[80] This is mainly because many reducing compounds, including glutathione and NAD(P)H, are abundant in the tumour cells. However, accompanied by a highly reducing environment, the relative level of oxidating materials, including reactive oxygen species (ROS) and reactive nitrogen species (RNS), are also higher than in normal cells. In previous studies, people have utilized the tumour cell microenvironment and prepared GNCs *in situ*. The mechanism was attributed to the reducibility of both peroxide and glutamate. Thus, GNCs tend to be selective in tumour environments due to different redox environments. Taking advantage of this property, papers have been focusing on the *in-situ* synthesis of GNCs in tumours for bioimaging,

detection, and chemotherapeutic therapy of GNCs.[81 82] However, West et al. reported the successful *in situ* synthesis of fluorescent GNCs ($\lambda_{EX}/\lambda_{EM}$: 540 nm/590 nm) in non-tumourigenic microglial cells and broadened the potential applications of this method (Figure 1.2.9). Where protein-stabilized GNCs with a particle size of approximately 2 nm were prepared, glutamate was shown to be essential for GNC biosynthesis. This transition from cancer cells to non-cancer cells further broadens the biological application situations of GNCs.[83] Besides mammalian cells, bacteria could also be used for the synthesis of GNCs. Using green fluorescent protein-expressing *E. coli*, orange-luminescent (580 nm) GNCs of ~2 nm size were synthesized on the bacteria envelope. In this case, mercaptopentanoic acid was added as the capping ligand, and the reaction only needed 5-min co-incubation of bacteria and chloroauric acid solution under 37 °C to get highly fluorescent GNCs. Other bacterial strains, including *Bacillus cereus* and *Enterococcus faecalis,* could also be used to make GNCs.[84–87]

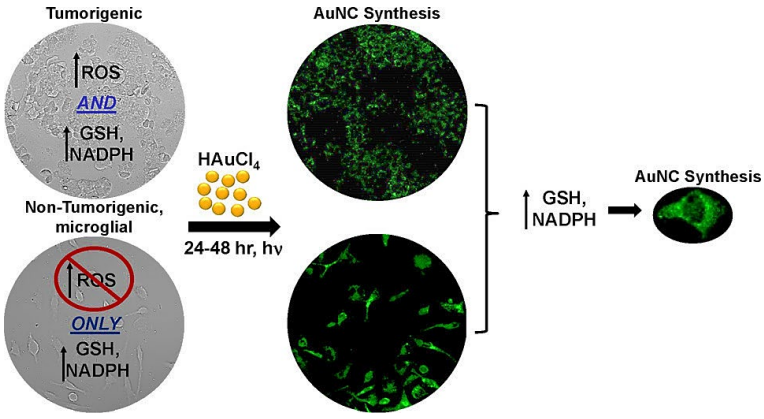

Figure 1.2.9 In addition to tumourigenic cells, the non-tumourigenic microglial cells with no excess ROS generation could also be used for the preparation of GNCs with high fluorescence for cell imaging.[83] (Copied from the ACS Publishing Group)

1.2.4 Properties of atomically precise GNCs

GNCs share many common characteristics with GNPs, including characteristic UV–vis absorption peaks, unique colour change upon size variations, high catalytic activity, photothermal property, and electrical chemical properties. However, due to their

extremely small size and limited Au atom numbers of Au atoms, electrons are confined, and their energy states become quantized, which gives GNCs some unique properties over GNPs like discrete energy levels, strong photoluminescence, extraordinary catalytic reactivity, etc. In addition, atomically precise GNCs have several unique properties that are unavailable for GNPs, which include quantum effect, surface, and supramolecular properties. I am going to introduce a specific presentation on each property and its underlying mechanism. Some related articles are also introduced to give related research progress.

1.2.4.1 Specific UV–vis absorption

Unique size-dependent optical properties are naturally shared by all gold nanomaterials and can be represented by the various colours they exhibit. There is no exception for GNCs. Each GNC has its unique UV–vis absorption spectrum, and the characteristic absorption peaks can be used for the discrimination of GNC species.[65] However, the causes of the unique UV–vis absorption of GNP and GNC are different. For GNP, its SPR effect induces a strong absorption in the blue-green region of visible light (λ = ~520 nm, ~2.4eV), rendering a ruby-red colour for 15-nm GNPs. Upon aggregation, the bathochromic shift of the SPR peak of GNP turns the solution colour to purple and even blue, depending on the scale of aggregation. However, for GNCs, due to their extremely small sizes, GNCs present a molecular-like transition arising from an efficient quantum effect. The absorption is based on the discrete electronic transition between the HOMO-LUMO band gap, giving rise to the absorption of photons with specific energy and hence specific absorption peaks. Because of the different Au atomic numbers of Au atoms in different-sized GNCs, their band gaps are also different. Thus, each specific GNC exhibits a specific UV–vis absorption spectrum, which is also the fluorescent mechanism of different GNCs.[54] Because of the absorption of specific wavelengths of colour light, the solutions of GNCs show different colours. For example, Yu et al. reported the synthesis of $Au_{25}(Cys)_{18}$ GNC in water through the reduction of carbon

monoxide. With the extension of the reaction time, the colour of the reaction solution gradually changes from colourless to dark brown, indicating the gradual formation of $Au_{25}(Cys)_{18}$ NCs from the Au-SR complex (**Figure 1.2.10**).

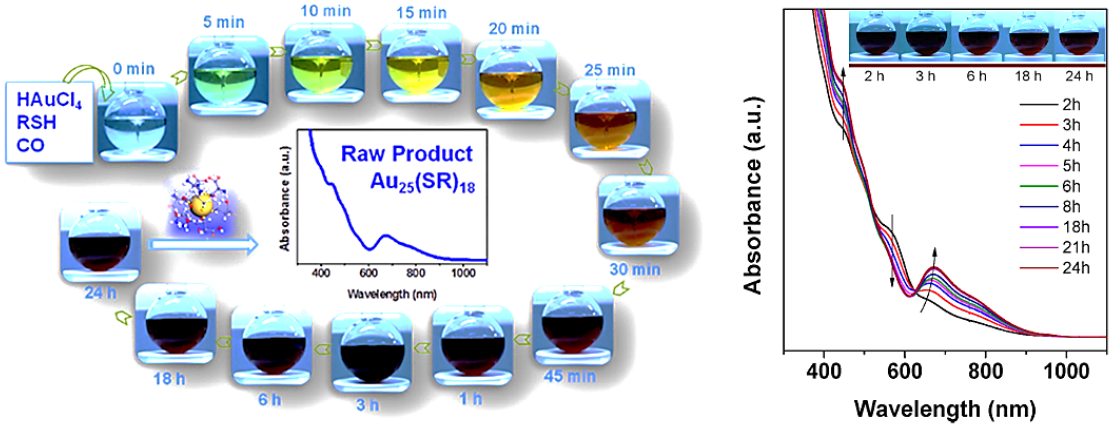

Figure 1.2.10 The solution colour changed from colourless to dark brown within 24 h (left), and the corresponding UV–vis spectra shifted of the $Au_{25}(SR)_{18}$ GNC.[75] (Copied from the ACS Publishing Group)

According to the ESI-MS analysis, the Au atomic number of Au atoms in the GNC was found to gradually increase from 10-15 to 16-25 and finally to 25, accompanied by a significant colour change.[75] Besides, combined with the XRD and DFT calculations, the absorption energies were attributed to the characteristic absorption peaks on the UV–vis spectrum. Taking $Au_{25}(SR)_{18}$ as an example, the three distinct peaks at 1.8, 2.75, and 3.1 eV were attributed to the HOMO→LUMO (*sp→sp*) transition, *sp→sp* + *d→sp*, and *d→sp* transition, respectively (**Figure 1.2.11**).[88] Taking advantage of the unique UV–vis absorption of GNCs, the UV–vis spectrum of GNCs can be used to determine their purity, which in turn directs the GNC synthesis. For example, by monitoring the UV–vis spectrum, the optimized reaction time for Au_{25} GNC synthesis could be determined [89].

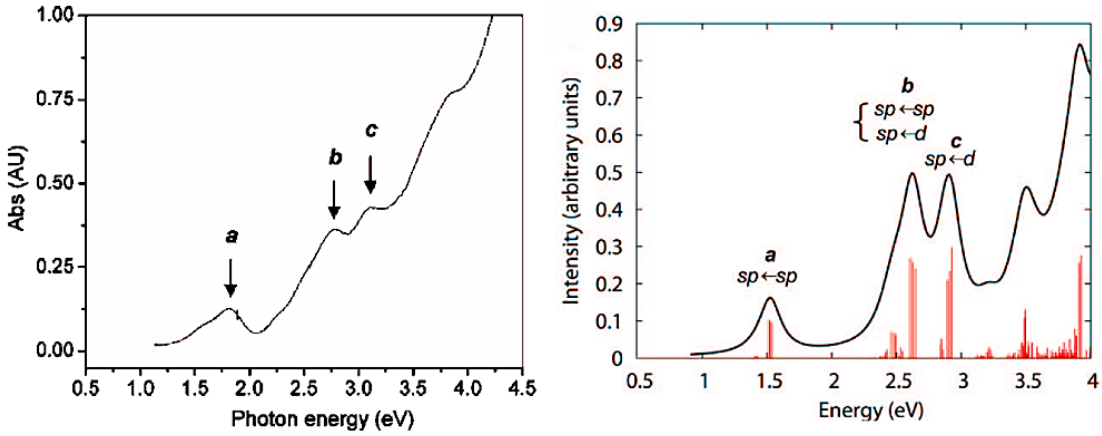

Figure 1.2.11 The peak position of the UV–vis spectrum of $Au_{25}(SR)_{18}$ GNC and the correspondence with electron orbital transitions.[88] (Copied from the ACS Publishing Group)

In addition to the Au atomic number, the oxidation state of Au_{25} NC is another factor that influences its UV–vis fluorescence. There have been reports that the colour of Au_{25} NC shifted from brown to greenish-brown, with the overall charge of Au_{25} NC changed from –1 to 0. The corresponding characteristic peak change in the UV–vis spectrum can be observed in **Figure 1.2.12**.[65]

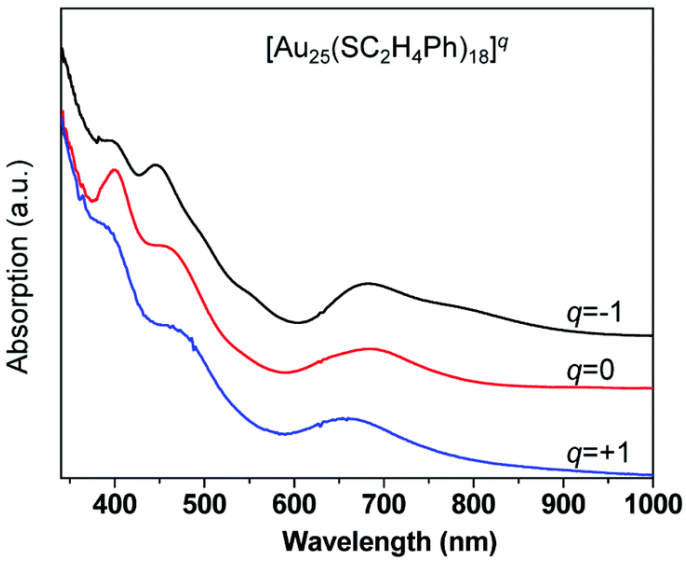

Figure 1.2.12 UV–vis spectra of phenylethane thiolate-protected $Au_{25}(SR)_{18}$ of different charge states.[65] (Copied from the RSC Publishing Group)

1.2.4.2 Photoluminescence properties

As a 0-D material, the size of GNC is extremely small (~2 nm) and approaches the Fermi wavelength of the electron. Thus, the quantum scale effect is more significant on it. As introduced above, the photoluminescence of GNC could be explained by the molecular orbitals and the HOMO→LUMO electronic transitions. For bulk Au, the excited electrons quickly undergo a nonradiative relaxation to the ground state without photon emission due to the continuous band. However, due to the discrete band structure in GNCs, after electron excitation, the radiation transitions between adjacent (LUMO→HOMO) bands could generate either visible or NIR fluorescence.[90] The Jellium model is normally used for illustrating the relationship between the number of Au atoms and the wavelength of photoluminescence. This model treats the lattice background formed by positive ions as a homogeneous gel-like medium, and the uniform electron gas evenly mixes with it so that the whole system is electrically neutral (which is called self-consistent). However, there is a dipole layer forming on the metal surface, and the energy gap is equal to $\sim E_f/N^{1/3}$ [54] (Figure 1.2.13).

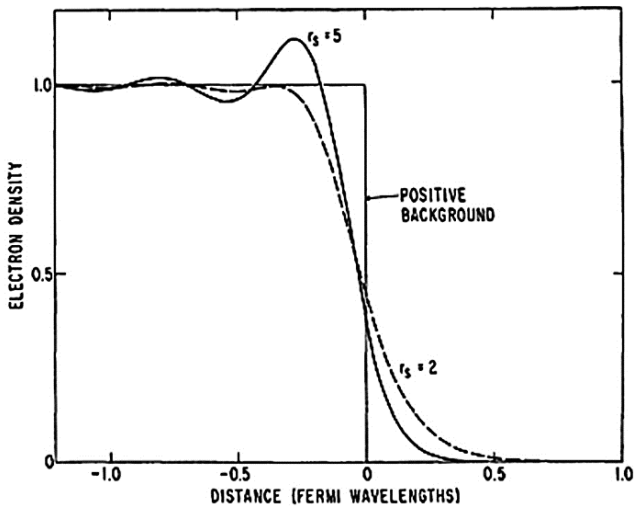

Figure 1.2.13 Mechanism of jellium model: a dipole layer forms on the surface of the metal border. Make the energy gap inversely proportional to the number of constituent atoms.[54] (Copied from the RSC Publishing Group)

Based on this theory, ultrasmall GNCs could give out not only high-energy fluorescence but also extremely high QY. For example, in 2003, Zheng et al. reported the Au_8 GNCs prepared with poly(amino dopamine) dendrimers.[91] Upon 380 nm UV light irradiation, this GNC could emit blue light (λ = 450 nm) with a QY as high as ~40%. In addition to the structural changes, many methods were applied for the preparation of highly luminescent GNCs through ligand design.

1) By **changing the capping ligand**, highly fluorescent GNCs could be acquired. Aldeek et al. prepared the PEGylated, zwitterionic ligand-capped GNCs *via* a one-pot reaction which gave out a red to NIR fluorescence with 10-14% QY with good photostability.[92] Using macromolecules such as protein as the template, many ultrabright GNCs could be prepared. Xie et al. reported the synthesis of BSA-capped GNCs through a novel one-pot method where BSA acted as both the stabilising and reducing reagent, which gave a good QY as high as 6% at ~640 nm (**Figure 1.2.14**).[68]

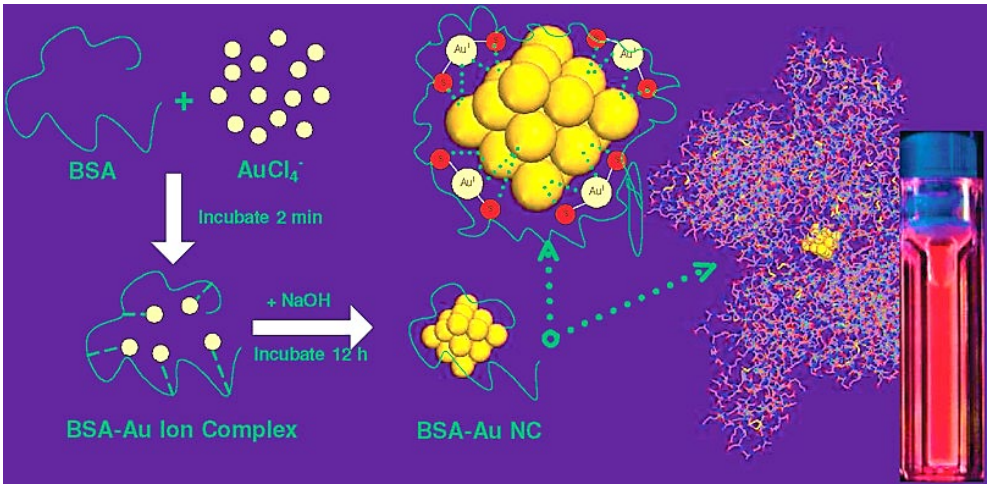

Figure 1.2.14 Using BSA as both scaffold, reducer and capping ligand, highly fluorescent BSA-capped GNC could be synthesized with a one-pot hydrothermal method.[68] (Copied from the ACS Publishing Group)

Through MS confirmation, the GNCs are generally Au_{25}. Chen et al. reported the blue-emitting Au_8 NC capped by lysozyme type VI with a high QY (~56%).[93] The GNCs prepared with natural proteins are summarized in a review by Guo et al., and the QYs of

most of the GNCs prepared with enzymes and other proteins are around 6%, which is quite high. In addition, the emission wavelengths are concentrated in the blue to orange-red ranges of the spectrum, and the latter is dominant.[69]

2) By doping **other metal atoms** into the Au kernel, the fluorescent QY could be enhanced. For instance, Liu et al. increased the NIR fluorescence of $Au_{25}(SG)_{18}$ by replacing one Au atom with Er/Ag/Cu/Zn atom (**Figure 1.2.15**).[94] Using this method, the utmost boost appeared in Cu doping, where the QY increased to 5.2 times that of the original value. Wang et al. reported the doping of less than 13 Ag atoms into the Au_{25} NC. By the reaction of Au_{11} clusters with alkanethiosilvers, $Ag_{13}Au_{12}$ was prepared, and the QY was dramatically increased 200-fold to ~40%.[95]

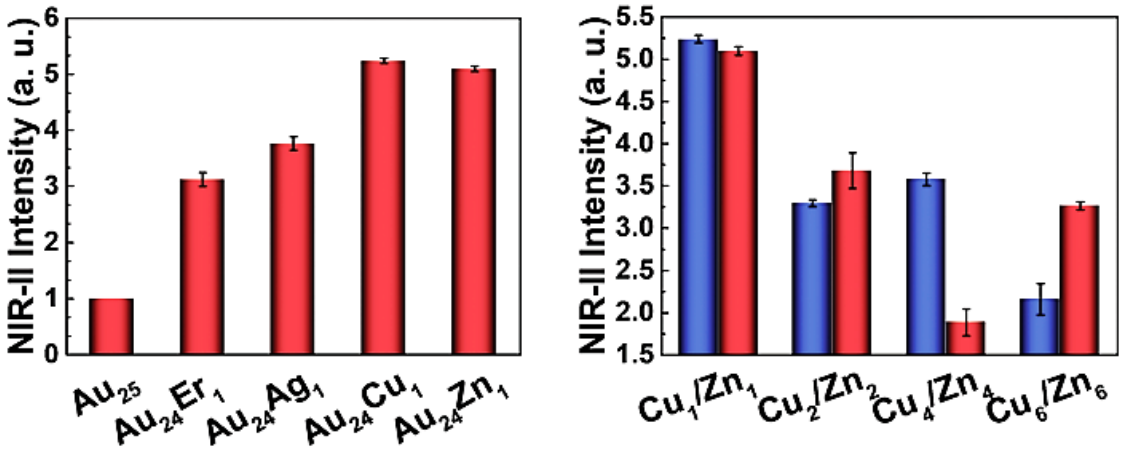

Figure 1.2.15 NIR-II fluorescence comparison of different Er/Ag/Cu/Zn atoms doped in the Au_{25} kernel. The incorporation of 1 Cu/Zn into the Au_{25} kernel has increased the fluorescence to 5-fold of the original fluorescence. On the contrary, with the doping atom increased to 2/4/6, the fluorescence generally showed a decreasing trend.[94] (Copied from the Wiley Publishing Group)

3) In 2012, Luo et al. discovered the **aggregation-induced emission** (AIE) property of Au(I)-ligand complexes. This property could be used for the preparation of highly fluorescent GNC in an aggregate state. The controllable solvent-induced aggregation of the complex and the generation of Au(0) core resulted in a high QY of around 15%.[96]

However, the aggregation method can have an adverse impact on the GNC size uniformity and potential applications. How to control the aggregation and apply it to prepare uniform GNCs is an issue that needs to be discussed. Liu et al. reported the synthesis and AIE properties of thiobarbituric acid-modified GNCs. This GNC has a low fluorescence under normal conditions and forms a loose network structure. However, the addition of zinc ions could induce the self-assembly into a bowknot-like structure, where the fluorescence greatly improved. Thus, the system could be used for the detection of zinc ions.[97] In another study, the GSH-capped GNCs were self-assembled into 120 nm NPs upon adding positively charged poly(allylamine hydrochloride) (PAH). Through aggregation, the QY was greatly enhanced from 7% to 25%. Having the ability to respond to pH changes, the Au-GSH-PAH complex was applied for enhanced delivery of peptides and antibodies. In addition to GSH, the zwitterionic ligand could also be used as an alternative for the preparation of this GNC assembly.[98]

4) The rigidification of the capping ligand was also used to enhance the fluorescence QY of the GNCs. Pyo et al., in 2015, reported a method that could enhance the fluorescence QY of $Au_{22}(SG)_{18}$ to 60% by "rigidifying the surface ligand."[99] In other words, through further addition of bulky surfactant-like molecules (for example, tetraoctylammonium ligand), the GNCs were bonded and phase-transferred to toluene, which could also be considered as another type of "aggregation." Through this strategy, the QY has increased ~8 times the original value (Figure 1.2.16).[99] However, the QY fell back to the original value upon redispersion into the aqueous phase.

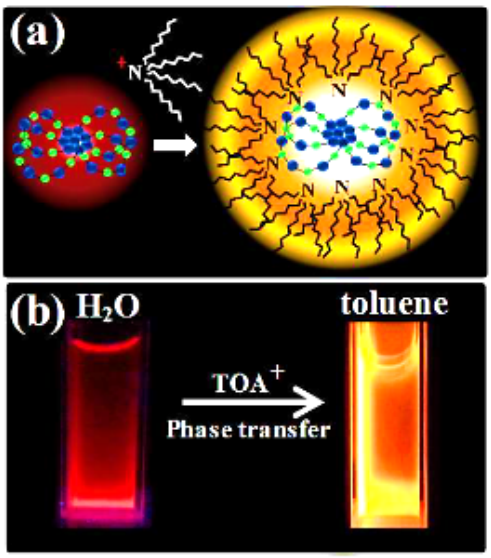

Figure 1.2.16 Through surface rigidification by surfactant molecules induced phase transfer, the fluorescence of GNC is significantly enhanced.[99] (Copied from the Wiley Publishing Group)

Deng et al. put forward a new strategy called "Host-Guest recognition" for the synthesis of water-soluble GNCs with ultrahigh QY. 6-aza-2-thiothymine (ATT) was firstly used for the preparation of ~2 nm ATT-GNCs with orange light emission (peaking at ~560 nm). They subsequently added arginine (Arg) into the GNCs and found no obvious changes in the GNC size. However, the fluorescence was blue-shifted to green (λ_{EM} ~530 nm) with a high QY of 65%. This phenomenon was assigned to interactions between ATT and the guanidine group of Arg that rigidified the ATT capping ligand. As a result, the intramolecular vibrations and rotations are greatly suppressed, leading to greatly reduced nonradiative relaxation of excited states. [100] Other methods to improve the fluorescence QY are also abundant, including change of the GNC valence or adding light-harvesting ligands (**Figure 1.2.17**).[90] Due to space limitations, I will not go into details here.

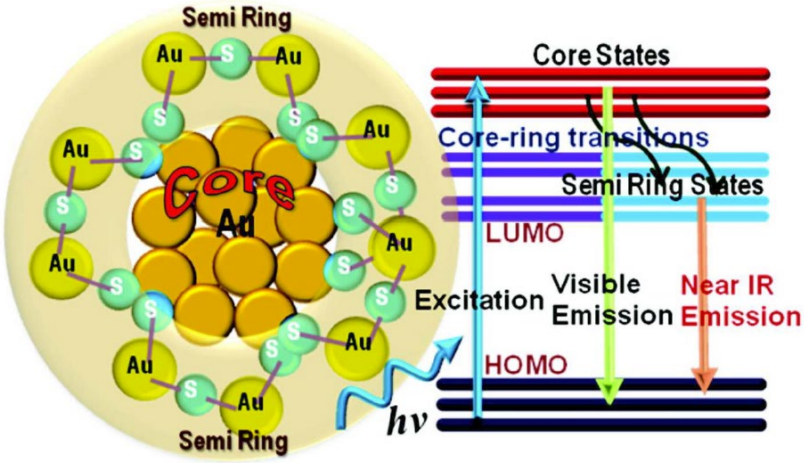

Figure 1.2.17 The electronic states and transitions are responsible for the dual emission of Au_{25} NCs. Through adjusting the oxidation of GNC, the quantum yield could be effectively enhanced.[90] (Copied from the Wiley Publishing Group)

Many advantages, including long Stokes shift, long lifetime, good photostability, and biocompatibility, make GNC an attractive candidate for bioimaging and biosensing.[101] However, most NIR-emitting GNCs capped with small molecular thiolate-ligands have a rather low QY of around 1%. Last year, Li et al. reported two brightly NIR fluorescent GNCs, Au_{21}(1-admantanethiolate)$_{15}$ and $Au_{38}S_2$(1-admantanethiolate)$_{20}$, whose QYs reached as high as 15%.[102] They revealed two underlying mechanisms that govern the large Stokes shift and long photoluminescence lifetime of the GNCs. One is that the absorption coefficient of the band-edge transition is low. Thus, the intrinsic radiative decays are slow in GNCs compared with other NIR fluorophores. The other is the GNCs' excited-state processes are normally complex, including rich structure–relaxation /transformation processes, which could increase the Stokes shift. They then proved the application of the surface "lock rings" and the surface "lock atoms" could reduce nonradiative decay and further improve the QY of GNC. The NIR fluorescence of GNCs in the Bio-NIR II Window (the second bio-near-infrared window, 1000–1700 nm) is cherished. The related content will be introduced in Chapter 6 of this thesis.

1.2.4.3 Optical nonlinearity

As a novel nanomaterial with a quantum-scale effect, the optical nonlinearity of GNC (including two-photon absorption (TPA) and two-photon fluorescence (TPF)) is an attractive character that is widely studied. This is mainly due to the source of two-photon excitation is usually in the NIR region, which exhibits much weaker tissue absorption and scattering than the visible region, and hence offers better penetration depth.[103] Thus, TPA and TPF are favoured in bioimaging and biosensing. Normally, the electron transfer from the ground state to a higher energy electronic state by simultaneous absorption of two photons with the same or different energy is called TPA, while the subsequent radiative relaxation to emit a specific photon is called TPF. The study of the TPA effect of GNC was started in 2008 by Ramakrishna et al., who showed that the Au_{25} cluster is a good TPA absorber with a high cross-section at 1290 nm (NIR-II region). The corresponding TPF peaked at ~800 nm (NIR-I region). They also observed that the TPA cross-section increased with the increasing Au atomic number from Au_{25} to Au_{309} in GNCs (**Figure 1.2.18**).[104]

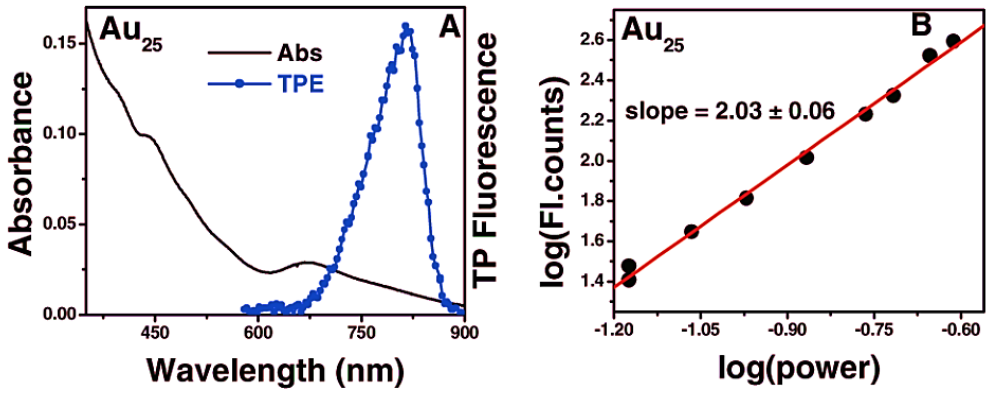

Figure 1.2.18 UV-vis absorption spectrum and TPF spectrum of Au_{25} NC under 1290 nm excitation (left). The fluorescence has a significant power dependency, indicating the nature of the two-photon process.[104] (Copied from the ACS Publishing Group)

Knoppe et al. measured the influence of ligand type as well as the Au atom number on the TPF property of different GNCs. They found that the TPF was obvious in $Au_{25}[(capt)_{18}]^{-}$ (capt = Captopril) but not in $Au_{25}(SCH_2CH_2Ph)_{18}$, which was ascribed to

the higher QY of the former. Besides, the $Au_{38}(SCH_2CH_2Ph)_{24}$ NC demonstrated a high TPF under an 800 nm laser irradiation, but not for $Au_{25}(SCH_2CH_2Ph)_{18}$. The difference was attributed to the centre of inversion in the Au_{25} NC.[105] In addition, Banska et al. reported that the two-photon circular dichroism of $Au_{25}[(capt)_{18}]^-$ was about two orders of magnitude higher than the one-photon one, which is also a unique property of the GNC optical nonlinearity.[106] These studies are followed by many related studies using GNC as the imaging reagent in bioimaging applications.[107] A brief introduction to the applications will be specifically elaborated in **Chapter 6**.

1.2.4.4 Supramolecular property

With the advances of both single-crystal XRD and HRTEM, I can now determine the exact formulas of GNCs containing Au atom numbers as high as 279.[57] Although there are many types of GNCs with various combinations of Au atoms and ligands initially in the synthesis, through the control of the ambient environment, most of them are gradually converted into $Au_{25}(SR)_{18}$ and $Au_{38}(SR)_{24}$, most likely due to their higher thermodynamic stability.[7] The possibility to quantify reactions also caters to the atom economy principles. Among all the GNCs, $Au_{25}(SR)_{18}$ (SR = thiolate ligand) is one of the most extensively studied.[61] It has many specific UV–vis absorbance peaks, including very significant characteristic peaks at around 440 nm and 670 nm that are essential to determine the relative $Au_{25}(SR)_{18}$ purity, as I have introduced in **Figure 1.2.12** previously.[67]

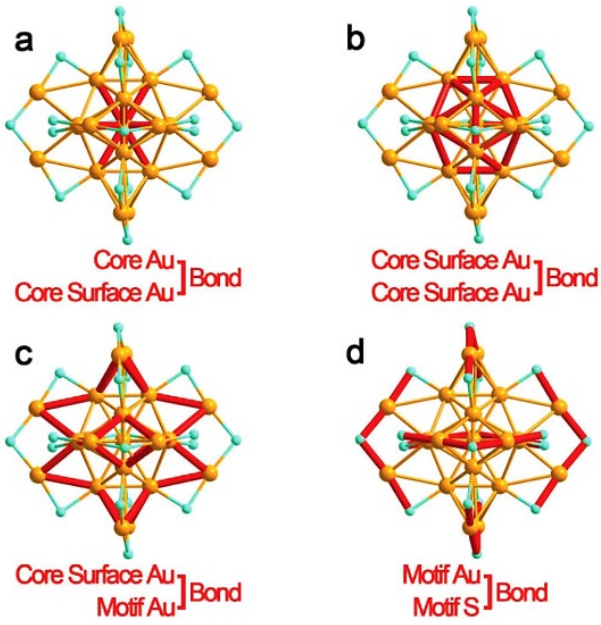

Figure 1.2.19 Three-dimensional structure of $Au_{25}(SR)_{18}$ GNC, yellow balls represent gold atoms, and cyan balls represent thiolate ligands.[108] (Copied from the RSC Publishing Group)

In 2008, Heaven et al. firstly reported the synthesis and crystal structure of $Au_{25}(SCH_2CH_2Ph)_{18}$.[109] One month later, Zhu et al. also reported the same research outcome, which showed a clear deciphering of the UV–vis spectrum.[88] Learning from the former studies, $Au_{25}(SR)_{18}$ has a structure of a centred Au_{13} icosahedral kernel and six dimeric "staple" motifs composed of "-SR-Au-SR-Au-SR-" patterns surrounding the compacted Au_{13} core.[65] This high symmetry of structure ensures excellent thermodynamic stability, allowing it to withstand the etching of excess thiolate ligands (**Figure 1.2.19**).[110] Due to its high stability and easy preparation in high yield with excellent purity, $Au_{25}(SR)_{18}$ type nanoclusters were widely used in antimicrobial[111], catalytic[112], and drug delivery[113] applications.

In 2010, Qian et al. reported the specific crystal structure of $Au_{38}(SC_2H_4Ph)_{24}$ NC. This uniquely stable GNC is composed of an Au_{23} core, which is a face-fused bi-icosahedral, surrounded by three groups "-SR-Au-SR-" on the equator and three groups of "-SR-Au-SR-Au-SR-" on two poles of the polygon core. (**Figure 1.2.20**) These capping staple

motifs link to the central gold core through short Au-Au bonds. The three "-SR-Au-SR-" monomeric staples in the equatorial part bridge the two Au6 corrugated planes while the "-SR-Au-SR-Au-SR-" dimeric staples formed the tri-blade fan configuration with the bottom fan rotates ~60° relative to the top fan (**Figure 1.2.21**).[114]

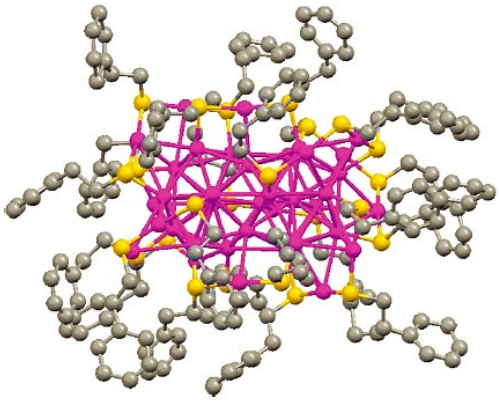

Figure 1.2.20 The three-dimensional structure of $Au_{38}(SC_2H_4Ph)_{24}$ NC. Pink balls represent Au atoms, yellow balls represent thiolate ligands, and grey balls represent other atoms on the ligand.[114] (Copied from the ACS Publishing Group)

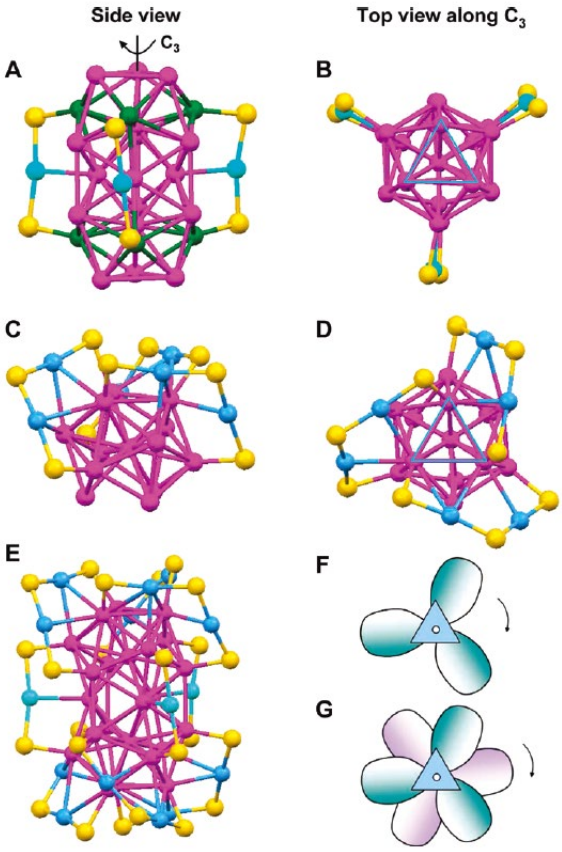

Figure 1.2.21 In the structure of the staple motifs of $Au_{38}(SC_2H_4Ph)_{24}$ NC, pink represents the Au atoms in the Au_{23} kernel, and blue represents the Au atoms on the capping. Yellow represents the ligand molecules. The shape is similar to the fan blade.[114] (Copied from the ACS Publishing Group)

Earlier than this, in 2007, the crystal structure of $Au_{102}(MBA)_{44}$ was reported in *Science*. This GNC has a core of 49-atom, forming five-twinned face-centred cubic or hexagonal close-packed crystallites. Two "caps" consisted of 20 atoms, each symmetrical distribution at the poles. The rest 13 atoms formed a band with no apparent symmetry on the equator.[115] In addition, the "staple" motif is also seen in this GNC species (**Figure 1.2.22**).

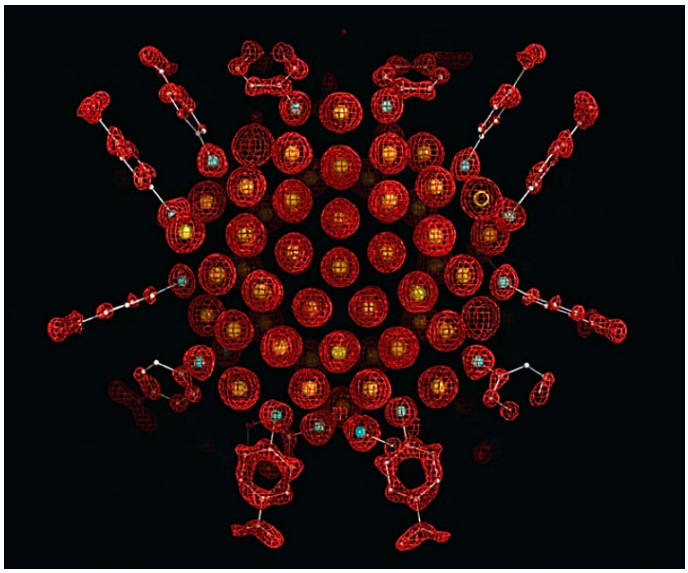

Figure 1.2.22 The XRD crystal structure of the $Au_{102}(MBA)_{44}$ GNC. (Gold atoms in yellow, sulfur in cyan, carbon in grey, and oxygen in red).[115] (Copied from the Science Publishing Group)

1.2.4.5 Isomerization (stereoisomerism)

Similar to molecules, atomically precise GNCs can exit in different isomers. The GNCs with the same chemical formula can have different molecular configurations and optical properties, depending on different synthetic conditions, ageing conditions, or coordination environments.[116] However, stereoisomerism was late-discovered. It was not until 2015 did the isomers of Au_{38T} were confirmed by Tian et al. with single-crystal XRD (*T* is short for the first author). Compared with the classic Au_{38} structure with a bi-icosahedral core, the Au_{23} kernel was replaced by one Au_{13} icosahedral and one Au_{12} cap composed of three tetrahedra. The core is surrounded by 2× "-SR-Au-SR-Au-SR-Au-SR-", 3× "-SR-Au-SR-Au-SR-", and 3× "-SR-Au-SR" (**Figure 1.2.23**).

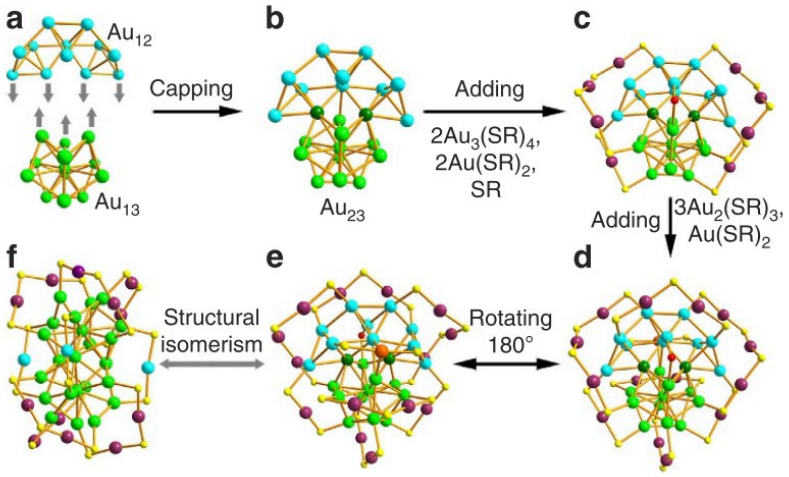

Figure 1.2.23 Structural anatomy of the isomer of Au_{38} NC.[117] (Copied from the Nature Publishing Group)

The optical and catalytic activities of the two isomers are largely different. By elevating the temperature to 50 °C, the asymmetric and less stable Au_{38T} isomer could transform into the more stable and symmetric traditional Au_{38} species.[117]

Following on from this work, the stereoisomerism of $Au_{28}(SR)_{20}$ NC was also observed in 2015. Interestingly, the isomerization was found to be ligand-induced and thermally reversible.[118] Intermolecular interactions could also assist the isomerization of GNCs. Cao et al. recently reported a facial modification of negatively charged $[Au_{25}(p\text{-MBA})_{18}]^-$ NC's configuration in water. By coupling and decoupling positively charged surfactant, CTA^+ (cetyltrimethylammonium cations) in water, the two isomers could be transformed reversibly. The two isomers are distinctly different in electronic structures as well as optical properties. This work confirmed the possibility of influencing the atomic packing of the Au kernel by controlling the surface ligand capping rigidity (**Figure 1.2.24**).[119]

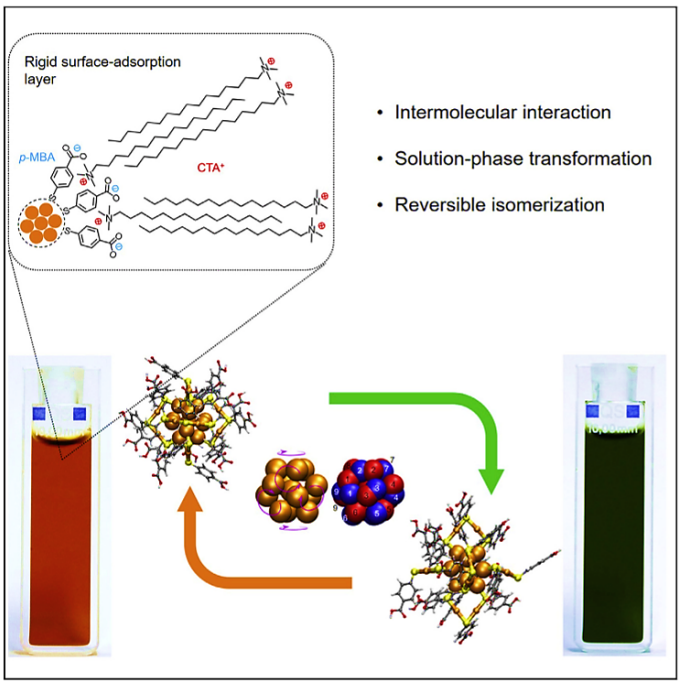

Figure 1.2.24 Through surface rigidification induced by the incorporation of cationic surfactant molecules, the kernel configuration of $Au_{28}(SR)_{20}$ NC could be shifted reversely within two isomers, resulting in the colour change of the solution.[119] (Copied from the Elsevier Publishing Group)

In addition to thiolated GNCs, the isomerization of GNC also exists in other ligand-capped GNCs. Guan et al. firstly reported the isomerization of alkynyl-protected $Au_{23}(C{\equiv}CBu^t)_{15}$ NC-1 and -2 with different optical properties. Although their chemical structures are totally the same, the HOMO-LUMO transition of NC-2 is allowed while in NC-1 is forbidden, leading to a totally different UV–vis spectrum. In addition, the transformation of unstable NC-2 to stable NC-1 could be achieved with a change in solvent condition.[120]

1.2.4.6 Chirality

The chirality is a molecule that cannot fully superimpose its mirror image. As a special isomerization, chirality is also a fascinating supramolecular character of GNC. As early as 2007, chirality was observed in the Au kernel of the $Au_{102}(MBA)_{44}$ NC with two enantiomers in the crystal structure.[115] In GNCs, the chirality mainly comes from four

aspects: **1)** Protein or ligand with chiral structure. **2)** The arrangement of ligands on the GNC surface. **3)** The inherent chirality of the Au core, and **4)** the isomerism in the bridging Au-S staple motifs.[121] Applying chiral ligands as capping is a common method of preparing chiral GNCs. For instance, Ueno et al. applied enantiopure (*R*)-/(*S*)-mercapto succinic acid (MSA) to prepare corresponding enantiomeric ligand-modified GNCs. They have observed that the chiroptical property depends on the solution pH, with acidity could enhance the optical isomerism.[122] Dolamic et al. reported the first enantio-separation of $Au_{38}(SCH_2CH_2Ph)_{24}$ NC and reported the left-handed enantiomer has a large anisotropy factor. In addition, the ligand structure has a minor influence on its chiroptical properties.[123] In addition, the staple motif consisting of repeating "-SR-Au-SR-" unit could also contribute to the chirality of GNC by adopting *cis* and *trans* geometries. Due to sp^3 hybridization, the S atom has a tetrahedral coordination geometry and can be the stereogenic centre for the monomeric unit. However, the configuration of the di- and trimeric Au-SR complex could be complex (**Figure 1.2.25**).[121]

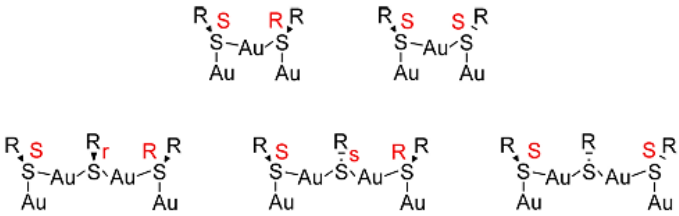

Figure 1.2.25 Schematic showing the chiral structure of di- and trimeric Au-SR complexes.[121] (Copied from the ACS Publishing Group)

1.2.4.7 Catalytic activity

The macroscopic gold material is known for its chemical and catalytic inertness. However, when the size of gold is reduced to a few tens atoms, the catalytic activity of GNCs is greatly improved.[124] Due to the greatly reduced size to ~1.5 nm, the surface-to-volume ratio, or to say, the surface energy of GNCs, is greatly improved. This is called the surface effect of quantum-sized materials. Thus, many unique properties that are

different from bulky material could gradually appear. In addition, the core-shell structure and nonmetallic electronic properties have also contributed to their high catalytic activity.[59] GNC as a catalyst has been widely used in many aspects of chemical synthesis, including CO oxidation, sulfoxidation, semi hydrogenation of alkynes to alkenes, C–C Coupling reactions, photocatalysis, photoelectrochemical water splitting, photovoltaics, etc.[107] Due to the wider scope involved and less correlation with the content of this study. I won't go into details here. However, the photocatalytic activity of GNC is worth discussing, which is an extremely important phenomenon in the biological field and is closely related to its nanotoxicity. Kawasaki et al. in 2014 reported the generation of singlet oxygen through photocatalytic of $[Au_{25}(SR)_{18}]^-$ NC (SR=phenylethanethiolate/captopril). They have found that Au_{25} NC, upon visible or NIR light irradiation (532, 650, and 808 nm), could automatically generate abundant singlet oxygen, but it was not obvious for Au_{38}. As the optical gap of $Au_{25}(SR)_{18}$ clusters is larger than the energy required to convert triplet oxygen into singlet oxygen, excited $Au_{25}(SR)_{18}$ clusters can efficiently transfer energy to triplet oxygen to convert it into singlet oxygen. In addition, the abundant surface sites also facilitate catalysis. The produced ROS were applied in the cancer cell treatment and the oxidation of organic sulfide (**Figure 1.2.26**).[125]

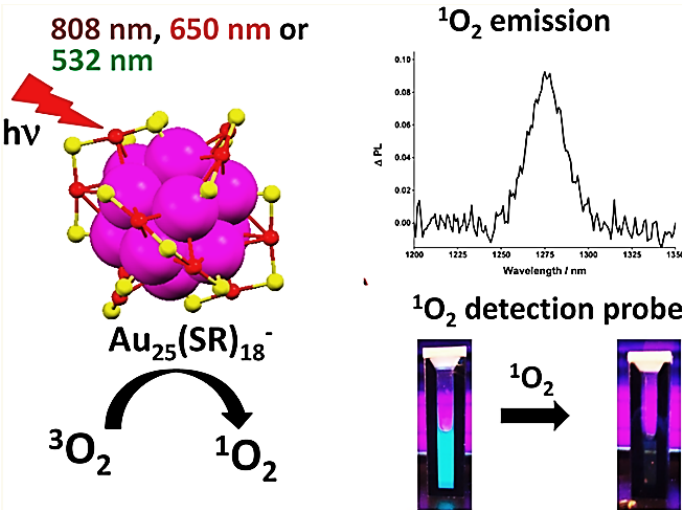

Figure 1.2.26 Upon laser irradiation, the Au_{25} NC could effectively produce singlet

oxygen, which could be used for biomedical or chemical applications.[125] (Copied from the ACS Publishing Group)

Matulionyte et al. reported the comparison of ROS generating ability of BSA- and 2-(N-morpholino) ethanesulfonic acid (MES)-capped GNCs and found the ligand bulkiness has a significant influence on its ROS generating ability and nanotoxicity. MES-capped GNC (0.25 M) has induced an increase in ROS generation by 89.2% in the cancer cell line, in contrast to a negligible increase for BSA-GNC. This difference may come from the exposure of surface catalytic sites for short ligand capped GNCs.[126]

1.3 Stage Summary

Based on the reading of the above pieces of literature, I have acquired a thorough understanding of the developing history, synthetic methods, and important physiochemical properties of gold nanomaterials. GNP, as a type of ancient gold material with thousands of years of using history, has found its excellent application prospects since the late 20th century. The notable B-S method further makes it possible to control the size of synthesized GNPs, thus highly increasing its scope of application *in vitro* and *in vivo*. Significantly, further restrictions on the size of GNPs produced GNCs with sizes approaching the quantum scale while greatly altering their characters. Due to the unique optical properties of GNCs, they have found growing applications in fields related to biomedical engineering. Moreover, because of its specific crystal structure, various synthetic methods inherited from the B-S method enable the control of its size to achieve an atomically precise level, thereby ensuring its relative stability between batches, which is extremely important for the application prospects of nanomaterials. This has also become a focus of my PhD research. From these studies, I have not only adopted the basic synthetic and characterization methods of $Au_{25}(SR)_{18}$ NCs, which is the cornerstone of my PhD study; but also learnt various properties of synthesised GNCs and exploited them in antibacterial and antitumour applications (*e.g.,* specific UV-vis absorption spectra, near-infrared fluorescence, catalytic ROS generation, and

specific organ accumulation patterns).

However, through reading these papers, I have also found a few challenges in the current applications of GNCs in biomedical applications. For example, although many methods are raised for the synthesis of atomically precise GNCs, high yield preparation, especially for water-soluble atomically precise GNCs, is still hard to achieve. In addition, for atomically precise GNCs, the QY is always lower (than those macromolecule-encapsulated GNC complexes with no specific chemical configurations) for more than ten times, which has limited the application as an effective probe *in vivo*. Last but not least, most of the water-soluble atomically precise GNCs nowadays are prepared with a single type of ligand, like Cys or GSH, which has restricted their applications adaptation for specific disease types or certain application environments.

To solve these problems, I have incorporated dual or multiple ligands as capping ligands for the preparation of water-soluble, atomically precise GNCs to broaden their biomedical application prospects. By adjusting the ligand capping ratios, I could tune the properties of these GNCs to achieve selective organ targeting or balance their antimicrobial ability and biosafety. In the following chapters, I will give a detailed introduction to my projects.

1.4 References

1 A. Balfourier, N. Luciani, G. Wang, G. Lelong, O. Ersen, A. Khelfa, D. Alloyeau, F. Gazeau and F. Carn, *Proc. Natl. Acad. Sci. U. S. A.*, 2020, **117**, 103–113.

2 R. W. Y. Man, C. H. Li, M. W. A. MacLean, O. V. Zenkina, M. T. Zamora, L. N. Saunders, A. Rousina-Webb, M. Nambo and C. M. Crudden, *J. Am. Chem. Soc.*, 2018, **140**, 1576–1579.

3 P. Zhao, N. Li and D. Astruc, *Coord. Chem. Rev.*, 2013, **257**, 638–665.

4 X. Yang, M. Yang, B. Pang, M. Vara and Y. Xia, *Chem. Rev.*, 2015, **115**, 10410–

10488.

5 R. Eisler, *Inflamm. Res.*, 2003, **52**, 487–501.

6 R. Sardar, A. M. Funston, P. Mulvaney and R. W. Murray, *Langmuir*, 2009, **25**, 13840–13851.

7 H. Häkkinen, *Nat. Chem.*, 2012, **4**, 443–455.

8 G. Faa, C. Gerosa, D. Fanni, J. I. Lachowicz and V. M. Nurchi, *Curr. Med. Chem.*, 2017, **25**, 75–84.

9 S. P. Fricker, *Gold Bull.*, 1996, **29**, 53–60.

10 S. Yue, M. Luo, H. Liu and S. Wei, *Front. Chem.*, 2020, **8**, 543.

11 D. Beaudet, S. Badilescu, K. Kuruvinashetti, A. Sohrabi Kashani, D. Jaunky, S. Ouellette, A. Piekny and M. Packirisamy, *Sci. Rep.*, 2017, **7**, 1–12.

12 P. Mulvaney, *ACS Nano*, 2015, **9**, 2215–2217.

13 R. R. Arvizo, S. Bhattacharyya, R. A. Kudgus, K. Giri, R. Bhattacharya and P. Mukherjee, *Chem. Soc. Rev.*, 2012, **41**, 2943.

14 S. S. Yi, X. B. Zhang, B. R. Wulan, J. M. Yan and Q. Jiang, *Energy Environ. Sci.*, 2018, **11**, 3128–3156.

15 M. R. Rashidian Vaziri, A. Omidvar, B. Jaleh and N. Partovi Shabestari, *Opt. Mater. (Amst).*, 2017, **64**, 413–420.

16 N. Z. A. Naharuddin, A. R. Sadrolhosseini, M. H. Abu Bakar, N. Tamchek and M. A. Mahdi, *Opt. Mater. Express*, 2020, **10**, 323.

17 F. Ahmad, N. Ashraf, T. Ashraf, R. Bin Zhou and D. C. Yin, *Appl. Microbiol. Biotechnol.*, 2019, **103**, 2913–2935.

18 R. Herizchi, E. Abbasi, M. Milani and A. Akbarzadeh, *Artif. Cells, Nanomedicine Biotechnol.*, 2016, **44**, 596–602.

19 L. M. Liz-Marzán, *Chem. Commun.*, 2013, **49**, 16–18.

20 T. K. Sau, A. Pal, N. R. Jana, Z. L. Wang and T. Pal, *J. Nanoparticle Res.*, 2001, **3**, 257–261.

21 N. Bhawawet, J. B. Essner, J. L. Atwood and G. A. Baker, *Chem. Commun.*, 2018, **54**, 7523–7526.

22 H. Itoh, K. Naka and Y. Chujo, *J. Am. Chem. Soc.*, 2004, **126**, 3026–3027.

23 W. Huang, S. Chen, Y. Liu, H. Fu and G. Wu, *Nanotechnology*, 2011, **22**, 025602.

24 P. Singh, K. Kumari, A. Katyal, R. Kalra and R. Chandra, *Spectrochim. Acta - Part A Mol. Biomol. Spectrosc.*, 2009, **73**, 218–220.

25 M. Huang, E. Xiong, Y. Wang, M. Hu, H. Yue, T. Tian, D. Zhu, H. Liu and X. Zhou, *Nat. Commun.*, 2022, **13**, 1–14.

26 N. T. K. Thanh and L. A. W. Green, *Nano Today*, 2010, **5**, 213–230.

27 S. Chen, L. Li, C. Zhao and J. Zheng, *Polymer (Guildf).*, 2010, **51**, 5283–5293.

28 J. Shaoyi and C. Zhiqiang, *Adv. Mater.*, 2009, **22**, 920–932.

29 R. Seoudi, *Phys. B Condens. Matter*, 2008, **403**, 4236–4240.

30 C.-J. Huang, P.-H. Chiu, Y.-H. Wang, K.-L. Chen, J.-J. Linn and C.-F. Yang, *J. Electrochem. Soc.*, 2006, **153**, D193.

31 I. Saldan, O. Dobrovetska, L. Sus, O. Makota, O. Pereviznyk, O. Kuntyi and O. Reshetnyak, *J. Solid State Electrochem.*, 2018, **22**, 637–656.

32 H. Ma, B. Yin, S. Wang, Y. Jiao, W. Pan, S. Huang, S. Chen and F. Meng, *ChemPhysChem*, 2004, **5**, 68–75.

33 M. Alle, B. reddy G, T. H. Kim, S. H. Park, S. H. Lee and J. C. Kim, *Carbohydr. Polym.*, 2020, **229**, 115511.

34 J. Hussein, M. E. El-Naggar, M. M. G. Fouda, S. I. Othman, A. A. Allam, E. H. Nadwa, E. K. Rashwan and O. M. Hendawy, *J. Clust. Sci.*, 2021, **32**, 423–435.

35 T. Thanayutsiri, P. Patrojanasophon, P. Opanasopit, T. Ngawhirunpat, S. Plianwong and T. Rojanarata, *Carbohydr. Polym.*, 2020, **250**, 116983.

36 M. Amina, N. M. Al Musayeib, N. A. Alarfaj, M. F. El-Tohamy and G. A. Al-Hamoud, *Nanomaterials*, 2020, **10**, 1–20.

37 S. K. Seol, D. Kim, S. Jung and Y. Hwu, *Mater. Chem. Phys.*, 2011, **131**, 331–335.

38 P. R. Teixeira, M. S. C. Santos, A. L. G. Silva, S. N. Báo, R. B. Azevedo, M. J. A. Sales and L. G. Paterno, *Colloids Surfaces B Biointerfaces*, 2016, **148**, 317–323.

39 K. D. N. Vo, C. Kowandy, L. Dupont, X. Coqueret and N. Q. Hien, *Radiat. Phys. Chem.*, 2014, **94**, 84–87.

40 N. Hanžić, T. Jurkin, A. Maksimović and M. Gotić, *Radiat. Phys. Chem.*, 2015, **106**, 77–82.

41 A. Akhavan, H. R. Kalhor, M. Z. Kassaee, N. Sheikh and M. Hassanlou, *Chem. Eng. J.*, 2010, **159**, 230–235.

42 Y. C. Yang, C. H. Wang, Y. K. Hwu and J. H. Je, *Mater. Chem. Phys.*, 2006, **100**, 72–76.

43 B. Akar, K. Pushpavanam, E. Narayanan, K. Rege and J. J. Heys, *Biomed. Phys. Eng. Express*, 2018, **4**, 065011.

44 L. F. De Freitas, G. H. C. Varca, J. G. D. S. Batista and A. B. Lugão, *Nanomaterials*, 2018, **8**, 939.

45 C. N. Lunardi, M. P. F. Barros, M. L. Rodrigues and A. J. Gomes, *Gold Bull.*, 2018, **51**, 131–137.

46 I. Hammami, N. M. Alabdallah, A. Al jomaa and M. kamoun, *J. King Saud Univ. - Sci.*, 2021, **33**, 101560.

47 S. A. Akintelu, S. C. Olugbeko and A. S. Folorunso, *Int. Nano Lett.*, 2020, **10**, 237–248.

48 Y. Zheng, J. Wu, H. Jiang and X. Wang, *Coord. Chem. Rev.*, 2020, **431**, 213689.

49 N. Goswami, Q. Yao, T. Chen and J. Xie, *Coord. Chem. Rev.*, 2016, **329**, 1–15.

50 I. M. Khan, S. Niazi, L. Yue, Y. Zhang, I. Pasha, M. K. Iqbal Khan, W. Akhtar, A. Mohsin, M. F. J. Chughati and Z. Wang, *Talanta*, 2022, **241**, 123228.

51 L. Malatesta, L. Naldini, G. Simonetta and F. Cariati, *Chem. Commun.*, 1965, 212–213.

52 M. McPartlin, R. Mason and L. Malatesta, *J. Chem. Soc. D Chem. Commun.*, 1969,

334.

53 F. Cariati and L. Naldini, *Inorganica Chim. Acta*, 1971, **5**, 172–174.

54 P. Khandelwal and P. Poddar, *J. Mater. Chem. B*, 2017, **5**, 9055–9084.

55 G. Schmid, R. Pfeil, R. Boese, F. Bandermann, S. Meyer, G. H. M. Calis and J. W. A. van der Velden, *Chem. Ber.*, 1981, **114**, 3634–3642.

56 W. Vogel, B. Rosner and B. Tesche, *J. Phys. Chem.*, 1993, **97**, 11611–11616.

57 S. Kenzler and A. Schnepf, *Chem. Sci.*, 2021, **12**, 3116–3129.

58 Günter Schmid, *Chem. Soc. Rev*., 2008, **37**, 1909-1930.

59 I. Chakraborty and T. Pradeep, *Chem. Rev.*, 2017, **117**, 8208–8271.

60 K. Fauth, U. Kreibig and G. Schmid, *Zeitschrift für Phys. D Atoms, Mol. Clust.*, 1989, **12**, 515–520.

61 M. Zhu, E. Lanni, N. Garg, M. E. Bier and R. Jin, *J. Am. Chem. Soc.*, 2008, **130**, 1138–1139.

62 R. Jin, H. Qian, Z. Wu, Y. Zhu, M. Zhu, A. Mohanty and N. Garg, *J. Phys. Chem. Lett.*, 2010, **1**, 2903–2910.

63 Y. Negishi, K. Nobusada and T. Tsukuda, *J. Am. Chem. Soc.*, 2005, **127**, 5261–5270.

64 Z. Wu, J. Suhan and R. Jin, *J. Mater. Chem.*, 2009, **19**, 622–626.

65 R. Jin, *Nanoscale*, 2015, **7**, 1549–1565.

66 A. C. Dharmaratne, T. Krick and A. Dass, *J. Am. Chem. Soc.*, 2009, **131**, 13604–13605.

67 X. Yuan, B. Zhang, Z. Luo, Q. Yao, D. T. Leong, N. Yan and J. Xie, *Angew. Chemie - Int. Ed.*, 2014, **53**, 4623–4627.

68 J. Xie, Y. Zheng and J. Y. Ying, *J. Am. Chem. Soc.*, 2009, **131**, 888–889.

69 Y. Guo, H. T. N. N. Amunyela, Y. Cheng, Y. Xie, H. Yu, W. Yao, H. W. Li and H. Qian, *Food Chem.*, 2021, **335**, 127657.

70 R. Jin, S. Egusa and N. F. Scherer, *J. Am. Chem. Soc.*, 2004, **126**, 9900–9901.

71 H. Duan and S. Nie, *J. Am. Chem. Soc.*, 2007, **129**, 2412–2413.

72 N. R. Jana and X. Peng, *J. Am. Chem. Soc.*, 2003, **125**, 14280–14281.

73 C. A. J. Lin, T. Y. Yang, C. H. Lee, S. H. Huang, R. A. Sperling, M. Zanella, J. K. Li, J. L. Shen, H. H. Wang, H. I. Yeh, W. J. Parak and W. H. Chang, *ACS Nano*, 2009, **3**, 395–401.

74 C. Helmbrecht, D. Lützenkirchen-Hecht and W. Frank, *Nanoscale*, 2015, **7**, 4978–4983.

75 Y. Yu, Z. Luo, Y. Yu, J. Y. Lee and J. Xie, *ACS Nano*, 2012, **6**, 7920–7927.

76 H. Zhang, X. Huang, L. Li, G. Zhang, I. Hussain, Z. Li and B. Tan, *Chem. Commun.*, 2012, **48**, 567–569.

77 Y. Liu, G. F. Tian, X. W. He, W. Y. Li and Y. K. Zhang, *J. Mater. Chem. B*, 2016, **4**, 1276–1283.

78 L. Ryavanaki, H. Tsai and C. B. Fuh, *Nanomaterials*, 2020, **10**, 94.

79 R. Huang, H. Chen and Z. Xia, *Bull. Chem. Soc. Jpn.*, 2017, **90**, 754–759.

80 X. Zhang, X. Chen, Y. W. Jiang, N. Ma, L. Y. Xia, X. Cheng, H. R. Jia, P. Liu, N. Gu, Z. Chen and F. G. Wu, *ACS Appl. Mater. Interfaces*, 2018, **10**, 10601–10606.

81 J. Wang, G. Zhang, Q. Li, H. Jiang, C. Liu, C. Amatore and X. Wang, *Sci. Rep.*, 2013, **3**, 1–6.

82 W. Mi, S. Tang, S. Guo, H. Li and N. Shao, *Chinese Chem. Lett.*, 2022, **33**, 1331–1336.

83 A. L. West, N. M. Schaeublin, M. H. Griep, E. I. Maurer-Gardner, D. P. Cole, A. M. Fakner, S. M. Hussain and S. P. Karna, *ACS Appl. Mater. Interfaces*, 2016, **8**, 21221–21227.

84 U. Goswami, S. Basu, A. Paul, S. S. Ghosh and A. Chattopadhyay, *J. Mater. Chem. C*, 2017, **5**, 12360–12364.

85 R. Antoine, *Nanomaterials*, 2020, **10**, 15–17.

86 S. Basu, A. Paul and R. Antoine, *Nanomaterials*, 2022, **12**, 62.

87 J. Gil-Rubio and J. Vicente, *Chem. - A Eur. J.*, 2018, **24**, 2018.

88 M. Zhu, C. M. Aikens, F. J. Hollander, G. C. Schatz and R. Jin, *J. Am. Chem. Soc.*, 2008, **130**, 5883–5885.

89 X. Yuan, N. Goswami, I. Mathews, Y. Yu and J. Xie, *Nano Res.*, 2015, **8**, 3488–3495.

90 A. Cantelli, G. Guidetti, J. Manzi, V. Caponetti and M. Montalti, *Eur. J. Inorg. Chem.*, 2017, **2017**, 5068–5084.

91 J. Zheng, J. T. Petty and R. M. Dickson, *J. Am. Chem. Soc.*, 2003, **125**, 7780–7781.

92 F. Aldeek, M. A. H. Muhammed, G. Palui, N. Zhan and H. Mattoussi, *ACS Nano*, 2013, **7**, 2509–2521.

93 T. H. Chen and W. L. Tseng, *Small*, 2012, **8**, 1912–1919.

94 H. Liu, G. Hong, Z. Luo, J. Chen, J. Chang, M. Gong, H. He, J. Yang, X. Yuan, L. Li, X. Mu, J. Wang, W. Mi, J. Luo, J. Xie and X. Zhang, *Adv. Mater.*, 2019, **31**, 1901015.

95 S. Wang, X. Meng, A. Das, T. Li, Y. Song, T. Cao, X. Zhu, M. Zhu and R. Jin, *Angew. Chemie*, 2014, **126**, 2408–2412.

96 Z. Luo, X. Yuan, Y. Yu, Q. Zhang, D. T. Leong, J. Y. Lee and J. Xie, *J. Am. Chem. Soc.*, 2012, **134**, 16662–16670.

97 J. Liu, J. Feng, Y. Yu, L. Xu, Q. Liu, H. Zhang, J. Shen and W. Qi, *J. Phys. Chem. C*, 2020, **124**, 23844–23851.

98 A. Yahia-Ammar, D. Sierra, F. Mérola, N. Hildebrandt and X. Le Guével, *ACS Nano*, 2016, **10**, 2591–2599.

99 K. Pyo, V. D. Thanthirige, K. Kwak, P. Pandurangan, G. Ramakrishna and D. Lee, *J. Am. Chem. Soc.*, 2015, **137**, 8244–8250.

100 H. H. Deng, X. Q. Shi, F. F. Wang, H. P. Peng, A. L. Liu, X. H. Xia and W. Chen, *Chem. Mater.*, 2017, **29**, 1362–1369.

101 M. Zhou, T. Higaki, G. Hu, M. Y. Sfeir, Y. Chen, D. Jiang and R. Jin, *Science (80-.).*, 2019, **364**, 279–282.

102 Q. Li, C. J. Zeman, G. C. Schatz and X. W. Gu, *ACS Nano*, 2021, **15**, 16095–16105.

103 Kenry, Y. Duan and B. Liu, *Adv. Mater.*, 2018, **30**, 1802394.

104 G. Ramakrishna, O. Varnavski, J. Kim, D. Lee and T. Goodson, *J. Am. Chem. Soc.*, 2008, **130**, 5032–5033.

105 S. Knoppe, M. Vanbel, S. Van Cleuvenbergen, L. Vanpraet, T. Bürgi and T. Verbiest, *J. Phys. Chem. C*, 2015, **119**, 6221–6226.

106 J. Olesiak-Banska, M. Waszkielewicz and M. Samoc, *Phys. Chem. Chem. Phys.*, 2018, **20**, 24523–24526.

107 R. Jin, C. Zeng, M. Zhou and Y. Chen, *Chem. Rev.*, 2016, **116**, 10346–10413.

108 X. Kang, H. Chong and M. Zhu, *Nanoscale*, 2018, **10**, 10758–10834.

109 A. Dass, A. Stevenson, G. R. Dubay, J. B. Tracy, R. W. Murray, D. U. V and N. Carolina, *J. Am. Chem. Soc.*, 2008, **130**, 5940–5946.

110 Y. Shichibu, Y. Negishi, H. Tsunoyama, M. Kanehara, T. Teranishi and T. Tsukuda, *Small*, 2007, **3**, 835–839.

111 K. Zheng, M. I. Setyawati, D. T. Leong and J. Xie, *ACS Nano*, 2017, **11**, 6904–6910.

112 R. R. Nasaruddin, T. Chen, N. Yan and J. Xie, *Coord. Chem. Rev.*, 2018, **368**, 60–79.

113 E. Porret, L. Sancey, A. Martín-Serrano, M. I. Montañez, R. Seeman, A. Yahia-Ammar, H. Okuno, F. Gomez, A. Ariza, N. Hildebrandt, J. B. Fleury, J. L. Coll and X. Le Guével, *Chem. Mater.*, 2017, **29**, 7497–7506.

114 H. Qian, W. T. Eckenhoff, Y. Zhu, T. Pintauer and R. Jin, *J. Am. Chem. Soc.*, 2010, **132**, 8280–8281.

115 P. D. Jadzinsky, G. Calero, C. J. Ackerson, D. A. Bushnell and R. D. Kornberg, *Science*, 2007, **318**, 430–433.

116 W. W. Xu, X. C. Zeng and Y. Gao, *Nanoscale*, 2018, **10**, 9476–9483.

117 S. Tian, Y. Z. Li, M. B. Li, J. Yuan, J. Yang, Z. Wu and R. Jin, *Nat. Commun.*, 2015, **6**, 8667.

118 Y. Chen, C. Liu, Q. Tang, C. Zeng, T. Higaki, A. Das, D. E. Jiang, N. L. Rosi and R. Jin, *J. Am. Chem. Soc.*, 2016, **138**, 1482–1485.

119 Y. Cao, S. Malola, M. F. Matus, T. Chen, Q. Yao, R. Shi, H. Häkkinen and J. Xie, *Chem*, 2021, **7**, 2227–2244.

120 Z. J. Guan, F. Hu, J. J. Li, Z. R. Wen, Y. M. Lin and Q. M. Wang, *J. Am. Chem. Soc.*, 2020, **142**, 2995–3001.

121 S. Knoppe and T. Burgi, *Acc. Chem. Res.*, 2014, **47**, 1318–1326.

122 R. Ueno and H. Yao, *Chem. Lett.*, 2015, **44**, 171–173.

123 I. Dolamic, S. Knoppe, A. Dass and T. Bürgi, *Nat. Commun.*, 2012, **3**, 1–6.

124 R. Jin, *Nanoscale*, 2010, **2**, 343–362.

125 H. Kawasaki, S. Kumar, G. Li, C. Zeng, D. R. Kauffman, J. Yoshimoto, Y. Iwasaki and R. Jin, *Chem. Mater.*, 2014, **26**, 2777–2788.

126 M. Matulionyte, D. Dapkute, L. Budenaite, G. Jarockyte and R. Rotomskis, *Int. J. Mol. Sci.*, 2017, **18**, 1–17.

Chapter 2
Summary of experimental methods, instruments, and materials

2.1 Materials and reagents

Deionized water was prepared by a laboratory water purifier (Milipore Mili-Q). The N_2 flow is provided by the school pipeline. All organic solvents, salts and reagents are purchased from Sigma-Aldrich except for the following: Potassium thioacetate, 6-bromohexanoic acid, 1,1'-carbonyldiimidazole (CDI), N, N-dimethyl-1,3-propanediamine, 1,3-propanesultone, 4-mercapto-4-methyl-2-pentanol (4MMP), gadolinium chloride, and pyridine were purchased from Alfa Aesar. Na_2SO_4 and potassium thioacetate were purchased from Fisher Scientific. 1,12-dibromododecane was purchased from Acros Organics. NaOH and Anhydrous ethanol were purchased from Aladdin. HBr was purchased from Honeywell. Chloroauric acid tetrahydrate and glucose were purchased from Macklin Reagent. Phosphate buffer saline and LB broth powder were purchased from Gibco. CCK-8 reagent was purchased from DOJINDO. Calcein-AM and PI were purchased from Keygen. Fresh pig whole blood and 4% paraformaldehyde solution were purchased from YUANYE. The Reactive Oxygen Detection Kit was purchased from Beyotime. Bacterial ROS (hydroxyl radical) quantitative detection kit (colourimetric), bacterial potassium ion concentration biological enzyme spectrophotometry kit and the GENMED ROS (superoxide anion) quantitative detection kit [colourimetric, nitro-blue tetrazolium (NBT) method] were purchased from GENMED. BBcellProbe™ Colourimetric Cell Membrane Integrity Test Kit was purchased from BestBio. BODIPY™-TR-cadaverine was purchased from J&K Scientific. Laurdan, DiSC3(5), and MycoLight™ Ratiometric Bacterial Membrane Potential Kit were purchased from AAT Bioquest. The bacteria and somatic cell lines

used in this study were purchased from **ATCC**, USA. The ultra-thin copper mesh was purchased from **EMCN**. The ATP level test kit, adhesive glass slides, and the ATPase level test kit were purchased from **Nanjing Jiancheng Bioengineering Institute**. DilC12(3) was purchased from **Enzo Life Sciences**. The 2.5% glutaraldehyde solution was purchased from **Acmec**. 10% povidone-iodine solution was purchased from **ZHONGYIHE**. 2.5% tribromoethanol was acquired from the school animal centre. 0.5% prilocaine hydrochloride eye drop was purchased from the local pharmacy. FAS eyeball fixative solution (G1109) and citric acid antigen retrieval buffer pH=6.0 were purchased from **Servicebio**. AcS-PEG_4-NH_2. HCl was purchased from **Tansh-Tech**. Mercaptoundecylsulfonic acid (MUS) was purchased from **Prochimia Surfaces**. AURION® R-Gent SE-EM silver staining kit and AURION® R-Gent SE-LM silver staining kit were purchased from **Aurion**. Tissue-Tek O.C.T. Compound 4583 was purchased from **SAKURA**. Tris-HCl buffer pH = 7.4 was purchased from **BIO-RAD**. 10% Goat serum solution was purchased from **Boster Bio**. 3-(4,5-Dimethyl-2-thiazolyl)-2,5-diphenyltetrazolium bromide (MTT) was purchased from **Invitrogen**. Anticoagulant test tubes and procoagulant test tubes were purchased from **HARVEYBIO**. Sources of antibodies and test kits are illustrated in the following chapters.

2.2 Experimental Methods

2.2.1 Synthesis of ligands

2.2.1.1 Synthesis and characterisation of C5 ZW Ligand

This synthetic method was mainly acquired from a previous report.[1] According to this protocol, potassium thioacetate was reacted with 6-bromohexanoic acid to introduce a thiol acetate that was later hydrolysed to give a free thiol under essential conditions.

Potassium thioacetate (3.5 g, 31.0 mmol) was mixed with 2.0 g (10.3 mmol) of 6-bromohexanoic acid in dimethylformamide (DMF, 100 mL) at ~0 ^{o}C under N_2 atmosphere. The mixture was left stirring overnight, with the temperature gradually

warmed up to room temperature, producing a dark brown solution. The reaction mixture was rotary evaporated to remove most of the DMF, diluted with DCM (200 mL), and washed three times with acidic water (100 mL × 3) (pH = 2). The organic layer was dried over Na_2SO_4 and evaporated to dryness to give a dark brown crude product **C5-1** in >80% yield (**Figure 2.2.1**).

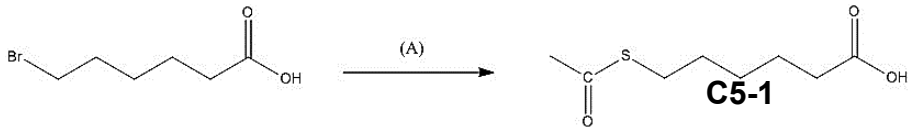

Figure 2.2.1 Scheme of replacement of the bromo group with thioacetate. **(A)** Potassium thioacetate, DMF, and 24 hours.

CDI (1,1'-Carbonyldiimidazole) was used in the second step as the amidation reagent to react with the carboxyl group to form intermediate (acyl imidazole), which subsequently reacted with an amine to form an amide bond.[2]

C5-1 (0.50 g, 2.63 mmol) and CDI (0.64 g, 3.90 mmol) were added in a two-necked round-bottomed flask with a magnetic stirring bar. The flask was purged with N_2 flow, and 10 mL of dry chloroform was added using a syringe. The mixture was left stirring for 1 h, transferred to an addition funnel, and added dropwise to a three-necked flask containing 1.65 mL of N, N-dimethyl-1,3-propanediamine under N_2 at 0 ^{o}C. After stirring overnight, the reaction mixture was washed with saturated $NaHCO_3$ solution (10 mL × 3). The organic layer was dried over Na_2SO_4, and the solvent was evaporated to give a light orange waxy solid (**C5-2**) in ~100% yield, which was directly used in the next step (**Figure 2.2.2**).

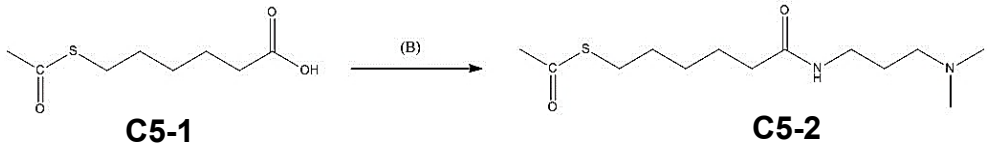

Figure 2.2.2 Amidation step of C5 preparation, producing C5-2. **(B)** CDI, N, N-dimethyl-

1, 3-propanediamine, and dry chloroform.

C5-2 (0.6 g, 2.2 mmol) and 1,3-propanesultone (0.8 g, 6.6 mmol) were added in a two-necked round-bottomed flask equipped with a magnetic stirring bar. 25 mL of dry chloroform was added to the flask, and the mixture was left stirring under N_2 at room temperature for two days. Then chloroform was evaporated to obtain a light orange residue named C5-3. The residue was washed several times with tetrahydrofuran (THF) to remove the excess of unreacted sultone. C5-3 was dried under a vacuum. HPLC is performed with a gradient concentration (10%–90%) of methanol with water (Figure 2.2.3).

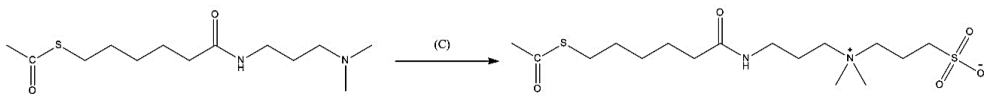

C5-2 C5-3

Figure 2.2.3 Synthetic route to C5 ZW ligand. (C) 1,3-propanesultone and dry $CHCl_3$

To get free thiol, 0.5 g of the ligand was dissolved in 5 mL of methanol. One equivalent of NaOH dissolved in 1 mL of water was injected into the solution, and the mixture was left stirring for 24 h under N_2. The product was neutralized by adding HCl (a few mL of 0.5 M solution). To collect the monothiol-zwitterion ligand, I dried the product under vacuum and re-dispersed it in methanol. The insoluble salts were precipitated out, and the clear supernatant liquid was collected. This process was repeated two times, yielding around 99%; C5-4 is what I need. It is worth saying that the amidation step needs strict time control (overnight) because the alkaline of amine can hydrolyse the thioacetate protection group to give free thiols. It was found that after stirring for two days at 35 ^{o}C, nearly all the thioacetate groups were deprotected and formed a disulfide bond (Figure 2.2.4). The MS and NMR graphs of the C5 ligand are demonstrated in Figure 2.2.5 and Figure 2.2.6.

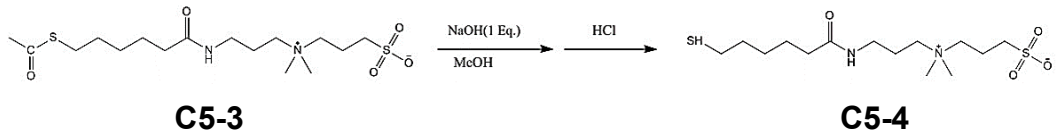

Figure 2.2.4 Deprotection step of the thiol group.

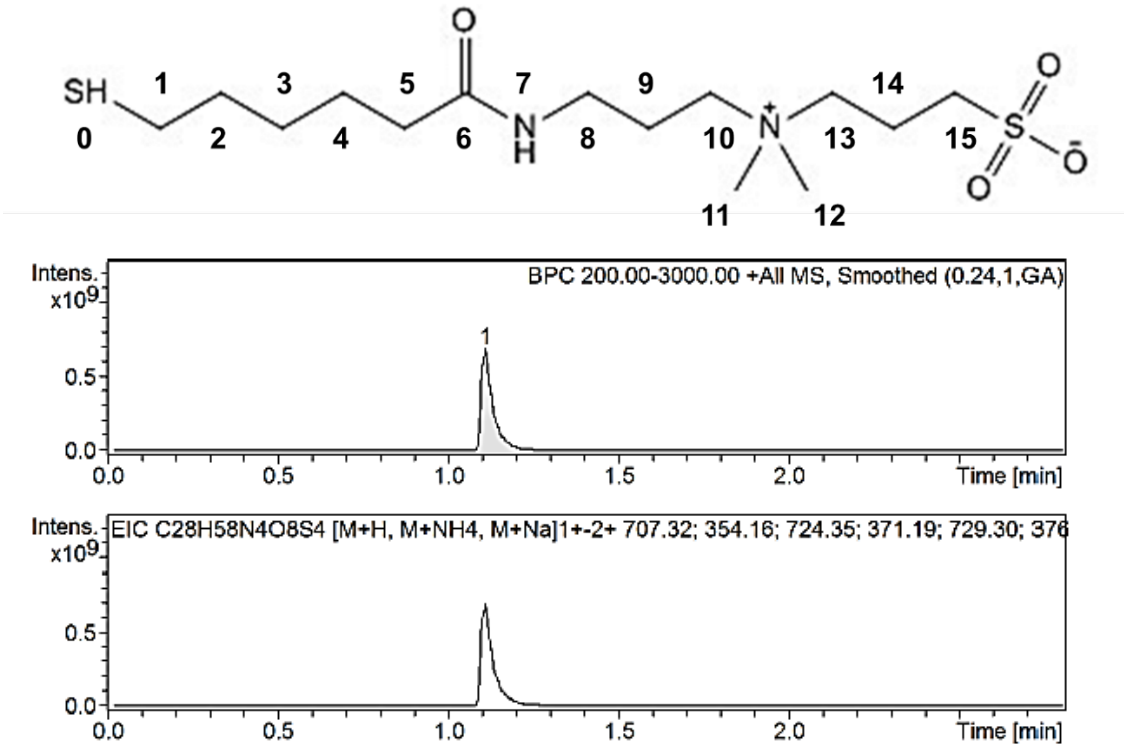

Figure 2.2.5 Mass spectrometry of C5 ZW ligand (dimer). Calcd m/z for $C_{28}H_{58}N_4O_8S_4$ $(M + H)^{1+}$706.86, found 707.32.

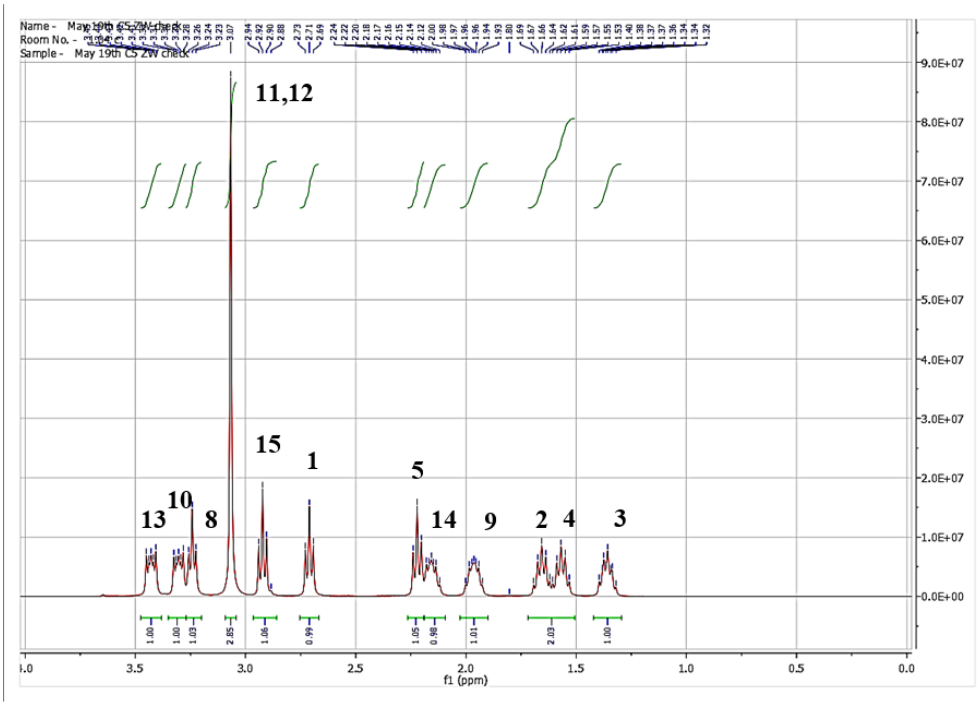

Figure 2.2.6 ^{1}H NMR graph of C5 ZW ligand. ^{1}H-NMR (400 MHz, D_2O): δ 3.45 (t, *J*= 8 Hz, 4H), 3.34 (t, *J*= 8 Hz, 4H), 3.26 (t, *J*= 8 Hz, 4H), 3.07 (s, 12H), 2.92 (t, *J*= 8 Hz, 4H), 2.71 (t, *J*= 8 Hz, 4H), 2.21 (t, *J*= 8 Hz, 4H), 2.14 (p, *J*= 8 Hz 4H),1.96 (p, *J*= 8 Hz 4H),1.66 (p, *J*= 8 Hz 4H), 1.62 (p, *J*= 8 Hz 4H), 1.37 (p, *J*= 8 Hz 4H).

2.2.1.2 Synthesis and characterisation of P12 Ligand

The synthetic method was adopted from a previous paper in our group.[3] 6.9 g of 1,12-dibromododecane (21.02 mmol) in dry THF was added to 1.2 g of potassium thioacetate (10.51 mmol). The mixture was then heated to reflux with stirring for 24 h under N_2 atmosphere. The reaction results in a turbid liquid. The product was then filtered and washed with 20 mL THF. The THF solution was rotary evaporated to obtain a yellowish oil, which was further purified with a silica gel column using 3:1 (v/v) then 2:1 (v/v) hexane/dichloromethane (DCM) as the eluent to give the **P12-1** (2.11 g, 63.7%) as white solid (**Figure 2.2.7**).

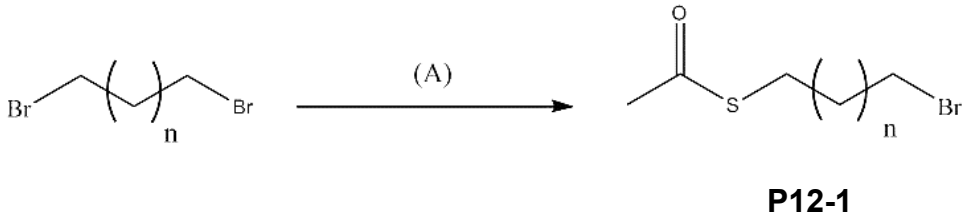

P12-1

Figure 2.2.7 Replacement of bromic group with thioacetate group. **(A)** Potassium thioacetate/Reflux. (n = 10).

To **P12-1** (2.11 g, 6.53 mmol) in 25 mL of THF, was added pyridine (2.15 g, 2.2 mL, 27.2 mmol). After 3-day reflux, the solvent and excess reactant was removed by vacuum distillation. The residue was washed with diethyl ether (2 × 10 mL) and hexane (1 × 10 mL) and dried to obtain an orange sticky oil. The product was further purified with precipitation induced by the addition of diethyl ether to give **P12-2** (2.3 g, 80.15%) as pale brown solid (**Figure 2.2.8**).

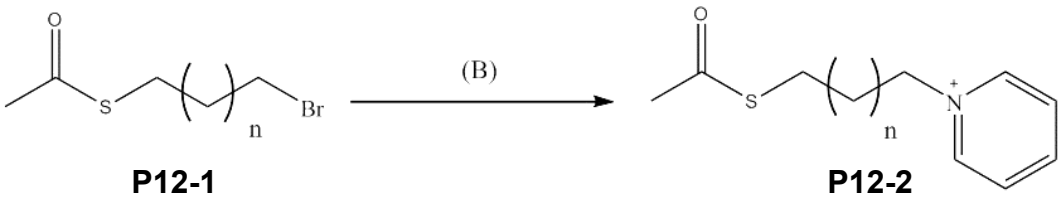

P12-1 **P12-2**

Figure 2.2.8 Mechanism of the addition of pyridine onto the alky chain. **(B)** Pyridine/THF and Reflux. (n = 10).

HBr (5.3 mL, 46.78 mmol) was added to a mixture of MeOH and H_2O (42.0 mL, 50/50 v/v) to prepare the HBr solution. **P12-2** (2.3 g, 7.13 mmol) was dissolved in the HBr solution and then heated to reflux under N_2 atmosphere for 12 h. The product was rotary evaporated and purified with a typical gradient elution HPLC with methanol. **P12-3** (0.745 g, 39.6%) was obtained as light-yellow oil (turned into a white waxy solid at 4 ^oC) (**Figure 2.2.9**). The MS and NMR results were demonstrated in **Figure 2.2.10** and **Figure 2.2.11**.

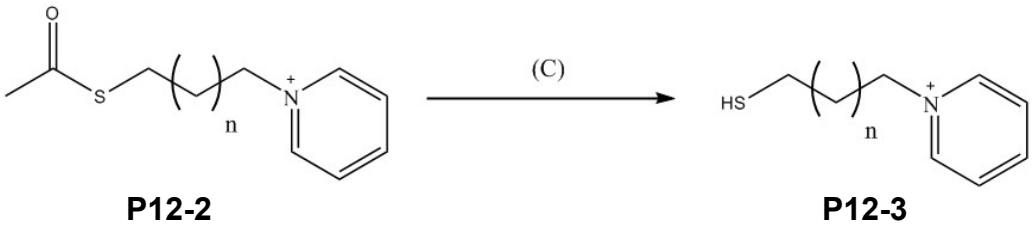

P12-2 **P12-3**

Figure 2.2.9 Deprotection of the thiol group. (C) HBr/Reflux. (n = 10).

The ion exchange procedure is based on a previous report.[4] After receiving the ion exchange resin, deionized water was applied to rinse until the drainage was clear. Ethanol was used to soak the resin for 24 h and was renewed every 8 h. To prevent fragmentation caused by quick expansion, 25% (wt) brine was used for soaking for 12 h until it reached the osmotic balance. The concentration was changed to 10% (wt). The expanded resin can be kept within 10% resin until the next step.

To bring enough chloride ions onto the positively charged scaffold. 4% (v/v) HCl was used to rinse and immerse the resin for 24 hours. After that, the resin was washed with deionized water until there was no detectable colour change in the pH test paper.

The ion exchange was operated in a 20 mm chromatography column. To be specific, the P12 solution was diluted to 5 mL (0.2 M) and then passed through the column. The acquired liquid was put into the column again until the colour did not change. 10 mL water and 10 mL ethanol were applied to wash out all the products. The product was finally dried and lyophilized.

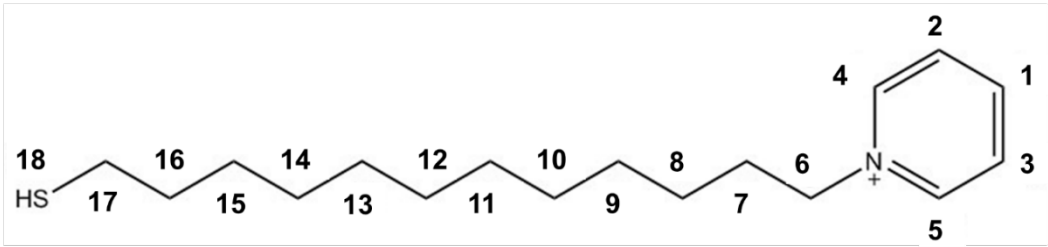

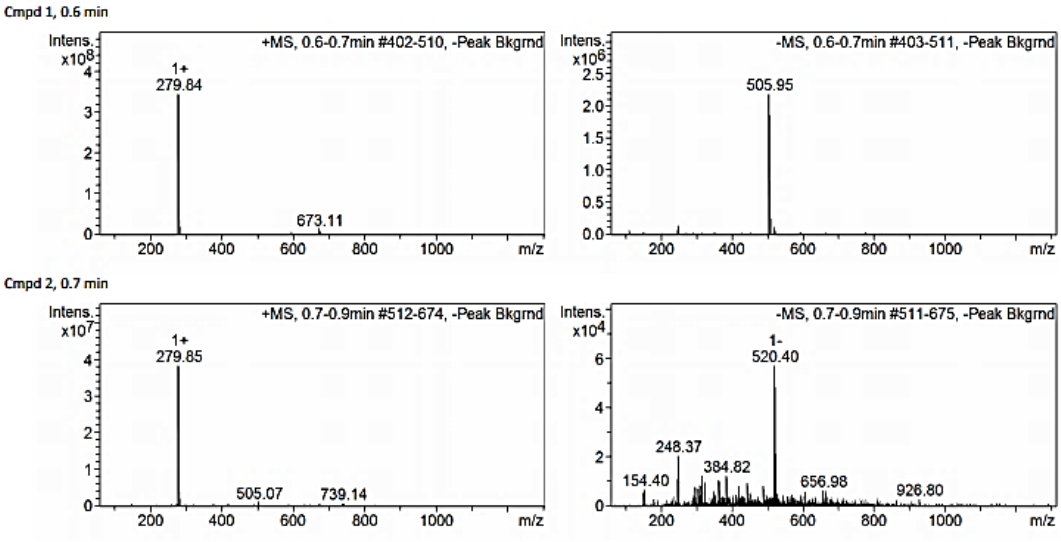

Figure 2.2.10 Mass spectrometry of P12 pyridinium ligand. Calcd m/z for $C_{17}H_{30}NS^+$ $(M\text{-}Br^-)^{1+}$280.22, found 279.84.

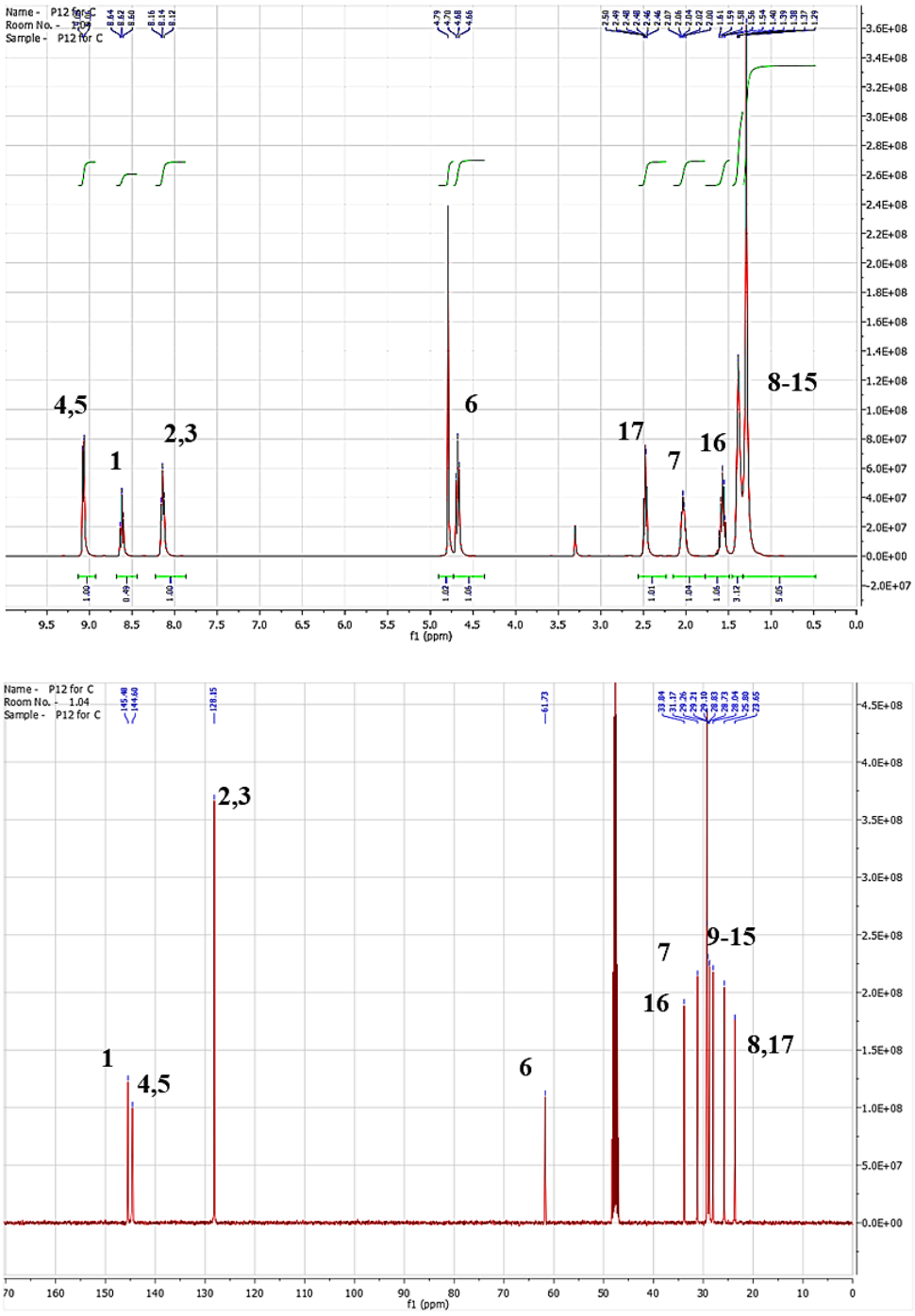

Figure 2.2.11 ^{1}H NMR and ^{13}C NMR graphs of P12 pyridinium ligand. ^{1}H-NMR (400 MHz, CD_3OD): δ 9.01 (d, *J*= 4 Hz, 2H), 8.60 (t, *J*= 8 Hz, 1H), 8.13 (t, *J*= 8 Hz, 2H), 4.63 (t, *J*= 8 Hz, 2H), 2.48 (t, *J*= 8 Hz, 2H), 2.02 (p, *J*= 8 Hz, 2H), 1.58 (p, *J*= 8 Hz, 2H), 1.29-1.39 (m, br, 17H).

2.2.1.3 Synthesis of thiolated methotrexate (HS-MTX)

The synthesis of HS-MTX is based on a previous report with modifications.[5] Step 1: First, methotrexate (MTX) (94.5 mg, 0.21 mmol), 2-(1H-benzotriazol-1-yl)-1,1,3,3-

tetramethyluronium hexafluorophosphate (HBTU) (75.8 mg, 0.20 mmol) and AcS-PEG_4-NH_2. HCl (33.1 mg, 0.11 mmol) were dissolved in 2 mL DMF. Then, N, N'-Diisopropylethylamine (66 µL, 0.4 mmol) was added to the mixture, and the resulting solution was stirred at 25 °C for 12 h. The mixture was purified by semipreparative high-performance liquid chromatography (HPLC) (LC-20AR, SHIMADZU) to yield the target compound as a light-yellow powder (35.2 mg, 43.7%) (**Figure 2.2.12**).

Step 2: NaOH (4.0 mg, 0.1 mmol) was dissolved in 2 mL H_2O, and the compound (35.2 mg, 0.048 mmol) was added. The mixture was stirred at 25 °C for 12 h. The mixture was purified using semipreparative HPLC to yield the target compound (20.1 mg, 60.7%) (**Figure 2.2.13** and **Figure 2.2.14**).

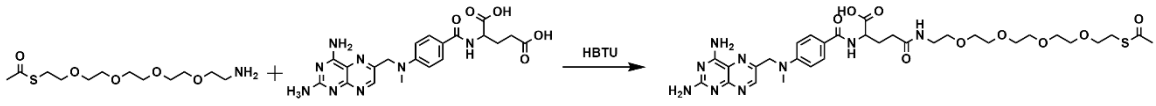

Figure 2.2.12 Experimental route to synthesize acetylthiolated MTX.

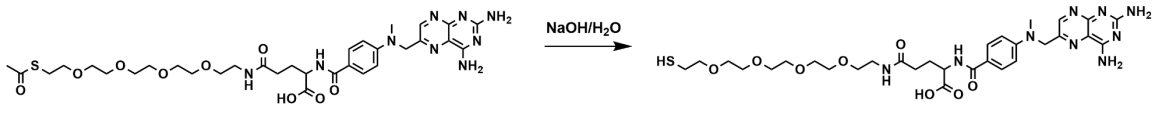

Figure 2.2.13 Experimental route to deacetylate of HS-MTX synthesis.

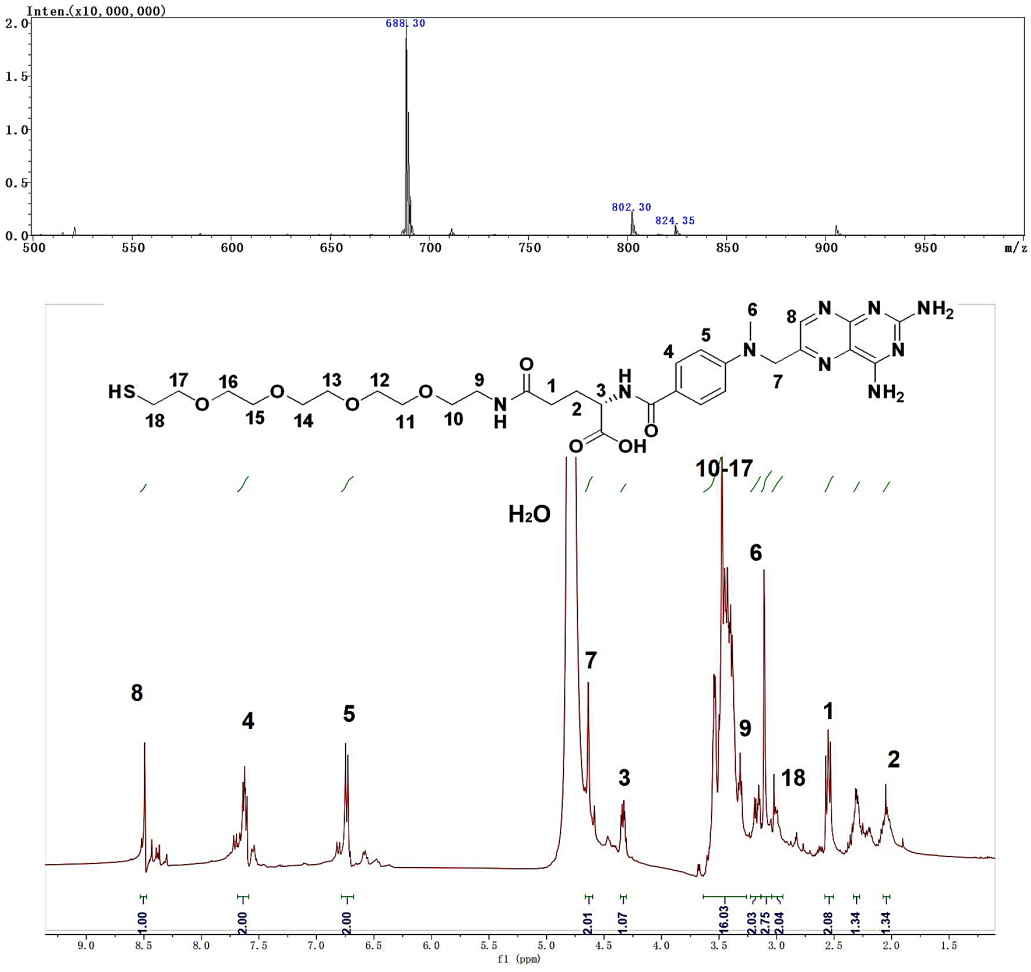

Figure 2.2.14 Mass spectrum of HS-MTX (**LCMS**: calculated for $[C_{30}H_{42}N_9O_8S]^-$ required *m/z* 688.30, found 688.30) and NMR ^1H spectrum of HS-MTX (in D_2O) to confirm the high purity of the product.

2.2.2 Synthesis of dual and multiligand-capped GNCs

2.2.2.1 Synthesis of $Au_{25}(P12)_x(C5)_{18-x}$ NCs

The water-soluble Au_{25} NC synthetic protocol was adopted from the previous report.[6] Briefly, chloroauric acid tetrahydrate (20 mM, 250 µL) was added to the desired C5 & P12 ligand solution (5 mM, 2 mL). The mixture became yellow with some turbidity, which turned to clear upon the addition of NaOH (1 M, 80 µL), followed by 2 mL ethanol. Finally, 12.5 µL $NaBH_4$ (100 mM in 0.2 M NaOH) was added dropwise with vigorous stirring. After 3 h, the product was purified with the 3 kDa-cutoff Amicon®

Ultrafiltration Units and washed with deionized water three times until pH=7.

2.2.2.2 Synthesis of $Au_{25}(4MMP)_x(C5)_{18-x}$ NCs

The $Au_{25}(4MMP)_x(C5)_{18-x}$ NC capped with a single type of ligand was synthesized by mixing chloroauric acid tetrahydrate (20 mM, 250 µL) with 4MMP ligand solution (final concentration 5 mM in 2 mL EtOH), accompanied by the formation of a light-yellow solution. The subsequent addition of NaOH (15 µL, 1 M) turned the solution colourless. Then the mixture of 1 mL ethanol and 1.7 mL H_2O was introduced to keep a final volume of EtOH at 60% (v/v). Finally, 100 µL $NaBH_4$ solution (100 mM in 0.2 M NaOH) was added dropwise with vigorous stirring. The product was purified with 3 kDa cut-off Amicon® Ultrafiltration units after a 3-h reaction and washed with deionized water until the pH of the filtrate reached 7. For dual ligand GNCs, the final concentration for the ligand was kept unchanged, and the amount of NaOH was adjusted through the lowest dosage of both ligands. For example, to synthesize the GNC with 70% 4MMP in feeding, 1400 µL EtOH solution of 5 mM 4MMP was mixed well with 600 µL of 5 mM C5 before mixing with chloroauric acid. The volume of NaOH and EtOH was 15 µL and 60% (v/v), respectively.

2.2.2.3 Synthesis of GNCs capped with different ratios of anionic ligands

The $Au_{25}(SR)_{18}$-type GNC capped with a single type of ligand was synthesized by mixing chloroauric acid tetrahydrate (20 mM, 250 µL) with the solution of each target ligand (final concentration 5 mM, 2 mL). The mixture quickly turned golden yellow. Subsequently, varying amounts of 1M NaOH (*e.g.,* 80, 50, 50, and 15 µL for C5, mercaptoundecanoic acid (MUA), mercaptoundecylphosphonic acid (MUP), and MUS ligand, respectively) were added. Then, ethanol was added to give a final ethanol volume% of 20% for C5, MUA, and MUS, or 10% for MUP (to avoid precipitation). A 25-µL $NaBH_4$ solution (100 mM in 0.2 M NaOH) was added dropwise with vigorous stirring. After reaction for 3 h, the product was purified using 3 k*Da* cut-off Amicon®

Ultrafiltration Units and washed with deionized water until the pH of the filtrate reached 7. For dual-ligand GNCs synthesis, the total ligand concentration was fixed as above, and the amount of NaOH and ethanol was adjusted using the weighted average of both ligands. For MTX-GNC synthesis, the 50% MUA ligand feeding was replaced by 30% MTX and 20% MUA while all other conditions remained the same.

2.2.3 Material Characterizations

2.2.3.1 Electrospray ionization (ESI)-MS spectroscopy characterization of GNC

The ESI-MS analysis was performed by diluting the freshly prepared GNC stock solution with water to achieve a final concentration of ~200 μg mL^{-1}. The samples were injected directly into the atomization system without mobile phase dilution (Q Exactive™ Plus Hybrid Quadrupole-Orbitrap™ Mass Spectrometer, Thermofisher). The acquired MS data were further deconvoluted with *Thermo Scientific Protein Deconvolution* software with an Xtract method. The output mode was MH+ with the S/N threshold set as 8. The resolution at 400 m/z was set to 50000, and the S/N threshold was set to 3. The relative abundance threshold was 5%, and the minimum number of detected charges was set to 2. The overall charge and m/z range were set in terms of the final product condition.

2.2.3.2 UV–visible spectrophotometry analysis of GNCs

The stock solution of GNC was diluted five times to around 200 μg mL^{-1} and added over 2 mL to a quartz cuvette (As one). Then the UV–vis spectrum was analysed with a UV–vis spectrometer (SHIMADZU, UV-2600i) to characterise the absorption curvature. I collected samples every 10 min within the first hour of the dynamic study case. After 1 h, the time interval was increased to 20 min until the end of the reaction.

2.2.3.3 Transmission electron microscope (TEM) analysis of different GNCs

For TEM analysis, the stock solution of GNC was diluted over 10,000-fold to a final concentration of ~0.1 μg mL^{-1} and added 10 μL to the ultra-thin copper mesh. The

copper mesh was then dried overnight and observed with a Titan Themis G2 double spherical aberration-corrected TEM (DSAC-TEM) under HADDF-STEM mode.

2.2.3.4 Fluorescence spectrophotometry analysis of GNCs

The stock solution of GNC was properly diluted to around 200 μg mL^{-1} and added 1 mL to a fluorescence cuvette (Agilent). The cuvette was then sent to a fluorescence spectrometer (HORIBA, iHR320 equipped with an InGaAs detector) with an 808 nm laser source. *Origin 2018* was applied to process the results.

2.2.3.5 Fourier transform infrared absorption spectrometer (FTIR) sample preparation

The GNC solution was lyophilized to a loose brown powder and dried using an infrared dryer to remove the water content. 1–2 mg of the GNC was ground with KBr into a fine powder, transferred to a mould, and pressed into flakes with a hydraulic oil press under 5×10^7 Pa. A Thermo Scientific Nicolet iS5 infrared spectrometer was used to measure the FTIR absorption spectroscopy.

2.2.3.6 Zeta potential analysis

The zeta potential of GNCs was measured using Zetasizer Nano ZS 90 (Malvern Panalytical) equipped with a DTS1070 disposable folded capillary cell. The samples were properly diluted to a light-brown solution (final concentration around 200 μg mL^{-1}) and loaded directly into the equipment.

2.2.4 Antibacterial Tests

Before experiments, all the bacteria species (*Staphylococcus aureus* (S. a), *Escherichia coli* (E. c), *Klebsiella pneumoni*ae (K. p), *Pseudomonas aeruginosa* (P. a), *Staphylococcus epidermidis* (S. e), *Staphylococcus haemolyticus* (S. h), *Enterococcus faecium* (E. f) and their corresponding resistant strains) were selected from single colonies and pre-incubated over 24 h in LB broth. 10 μL bacterial-containing medium was then inoculated

into 1 mL fresh LB broth and incubated for another 6 h. For methicillin-resistant *Staphylococcus epidermidis* (MRSE), its OD_{600} value was around 0.3 and had a concentration of ~7×10^8 CFU mL^{-1}.

2.2.4.1 Calculation of Minimum Inhibitory Concentration (MIC) and Minimum Bactericidal Concentration (MBC)

The antibacterial test was carried out with the broth-dilution method.[7] On a 96-well plate, each well was filled with 100 µL medium, and 100 µL of undiluted GNC was introduced to the first column of wells on the left. After mixing thoroughly, 100 µL solution from the first column was taken out and injected into the second column. This procedure was repeated to dilute the GNC in half each time. I set the very last column as a control group without the GNC. In the end, 10 µL 1000-times diluted bacterial solution was added to each well. After 16 h and 24 h, the antibacterial result was recorded by measuring the OD_{600}.

2.2.4.2 Checkerboard method to measure fractional inhibitory concentration index (FICI)

Similarly, the checkerboard test was carried out with both horizontally and vertically diluting test materials and antibiotics. After 24 h of incubation, I measured the OD_{600} value with a microplate reader. The FIC value that achieves more than 80% inhibition (each equivalent point) was calculated according to the following formula:

$$\Sigma FIC = FIC_A + FIC_B = \frac{C_{A\ combined}}{MIC_{A\ single}} + \frac{C_{B\ combined}}{MIC_{B\ single}}$$

In which the FICI equals the ΣFIC_{MIN}. If the FICI ≤0.5, then there is a synergy of both materials. If 0.5 <FICI ≤1, then there is an additive effect between the two materials.[8] The antibacterial tests of all Gram-positive species were carried out with the same protocol.

2.2.4.3 Time-killing curve

Time-dependent Bacterial Killing Measurement. In each well of the 96-well plate, the GNC and Imp solutions were added to make a final concentration of 16 and 2 μg mL^{-1}, respectively. The final volume was kept at 100 μL per well. Logarithmic phase MRSE stock was diluted 1000 times and then inoculated 10 μL into each well. At predefined time points, the solution was taken out 100 μL, appropriately diluted, and evenly applied on pre-warmed agar plates in triplicates. After 24 h incubation, the colony number on each plate was calculated to get the time-dependent bacterial killing curves.

2.2.4.4 SEM image of antibacterial effect

We cultivated bacteria to the logarithmic period and diluted the solution 100-fold. Then I put coverslips into a 12-well plate and added 1.5 mL bacteria solution to let bacteria stick to the slides for 5 h. After rinsing with PBS buffer, I added GNC solution and antibiotic solution into each well and cultivated for 24 h. After the incubation, bacteria in each well were rinsed again and fixed with a 2.5% glutaraldehyde solution. After 12 h, plankton bacteria and bacteria metabolites were removed with PBS buffer rinse 3 times, 30%, 50%, 70%, 80%, 90%, and 95% ethanol solutions were used for the gradient dehydration for 15 min each. Finally, I added pure ethanol into each well and let the sample dry naturally before SEM imaging (Merlin SEM, ZEISS).

2.2.4.5 Analysis of ROS generation rate and type

The Reactive Oxygen Detection Kit was used to detect ROS levels. The DCFH-DA (2,7-Dichlorodi-hydrofluorescein diacetate) solution was diluted with PBS 1000 times to a 10 μM working solution. The logarithmic phase MRSE was washed with a PBS solution twice, and the proper amount of working solution was added to resuspend the bacteria. The solution was mixed every 3–5 min to make it thoroughly blended. After 30 min, the solution was washed with PBS and mixed with the GNC and antibiotics. The fluorescent readout was carried out after 1 h incubation with 488 nm excitation and 525 nm

emission with a plate reader (Synergy H1, BioTek). The ROS species were detected with the GENMED Bacterial ROS (hydroxyl radical) quantitative detection kit (colourimetric) and the GENMED ROS (superoxide anion) quantitative detection kit [colourimetric, nitro-blue tetrazolium (NBT) method].

2.2.4.6 Membrane Penetration Assay

The membrane integrity was analysed by BBcellProbe™ Colourimetric Cell Membrane Integrity Test Kit. The working solution of membrane integrity staining T12 dye was prepared by diluting the stock solution 50–500 times. Pre-treated MRSE cells within centrifugation tubes were washed with PBS twice, followed by adding the working solution and resuspension of MRSE cells. After 10 min of incubation, the mixture was re-washed with PBS 3 times. The final absorption value was measured with a microplate reader at 620 nm.

2.2.4.7 Analysis of GNC Binding with WTA

The WTA used in the experiments was extracted from *S. a* following a former report.[9] The isothermal titration was performed by adding 1.1 mg mL^{-1} WTA dropwise into the 1.4 mL 200 μg mL^{-1} GNC within the chamber (MicroCal VP-ITC, GE). The total injections were 27 times, with 10 μL each. The titration duration was 20 s and the time spacing was 150 s. The interference was eliminated with the subtraction of pure WTA titration.

To further illustrate the GNC binding with WTA, a competitive fluorescence experiment was conducted by following a former protocol with minor modifications.[10] The working solutions of BODIPY™-TR-cadaverine (10 mM) and WTA (14 μg mL^{-1}) were previously diluted with Tris-buffer (50 mM, pH 7.4). The final concentrations of BODIPY™-TR-cadaverine and WTA were 5 μM and 3.5 μg mL^{-1}, respectively. After 15 min of reaction, the GNC was added, followed by 30 min incubation at 25 °C. The whole procedure was protected from light. The fluorescence was measured using the excitation and emission

wavelengths of 580 nm and 620 nm, respectively.

2.2.4.8 ATP level assay of GNCs compared with antibiotics

The differences in the ATP level of GNC and antibiotics treated groups were analysed with an ATP level kit. The variation of the content of ATP within organisms is related to the energy metabolism change. Normally, the ATP level could reflect cell states and indicate cell apoptosis, necrosis, or poisoned states. The mechanism of this kit is using creatine kinase to catalyse adenosine triphosphate and creatine to generate phosphocreatine, which could be further detected by phosphomolybdic acid colourimetry. All the experiments were conducted according to the kit instruction.

2.2.4.9 ATPase level analysis of GNC compared with antibiotics

The differences in the total ATPase activity of GNC treated groups compared with antibiotics were analysed with a total ATPase kit. The ATPase locates in the cell membrane structure of bacteria cells and is of great significance in material transportation, energy conversion, and information transmission. In addition, during abnormal conditions in the body, the activity of this enzyme will be affected. Thus, the function of this enzyme could indicate the organism's health state. To measure the activity of ATPase, ATP was introduced and reacted with the enzyme. The hydrolysis of ATP would produce inorganic phosphorus as a product, and the activity of ATPase could be analysed by detecting the amount of free phosphorus with phosphomolybdic acid colourimetry.

2.2.4.10 Analysis of membrane fluidity with laurdan

The membrane fluidity was probed with a membrane fluidity-sensitive dye—laurdan. Specifically, the MRSA cells were cultured within LB broth with 0.2% glucose until the OD_{600} reached 0.35. The bacteria were then washed with PBS three times and incubated with 10 μM laurdan (dissolved within 1% (v/v) DMF solution) for 5 mins to facilitate the

staining of the bacteria membrane. Then the MRSA cells were washed again with 0.2% glucose. Subsequently, different antibiotics and GNCs were added to the aliquoted MRSA solution and incubated for 6 hours. The confocal images were taken with a laser scanning confocal microscope (Nikon Confocal A1R, https://www.healthcare.nikon.com/en/lifescience/index.html) with 405 nm laser excitation, and the fluorescence intensity at 460 and 500 nm were recorded. The general polarization (GP) level was calculated with the following equation:

$$GP = \frac{I_{460} - I_{500}}{I_{460} + I_{500}}$$

2.2.4.11 DilC12(3) membrane clusterization study

The membrane clusterization was analysed with a membrane mimicking dye DilC12(3), which binds with the fluid phase regions on the cell membrane.[11] I firstly cultured the MRSA cells overnight and diluted the bacteria solution 200-folds with LB containing 2 μg mL^{-1} DilC12(3), 1.25 mM $CaCl_2$, and 1% (v/v) DMSO. The solution was further cultured until OD_{600} reached 0.3, followed by washing with PBS 4 times. The MRSA cells were then resuspended with the same solution and treated with materials of different groups. After 12 h incubation, the fluorescence was monitored with 549 nm excitation and 565 nm emission.

2.2.4.12 Measurement of K+ change of MRSA after different treatments

The measurement of the K^+ is based on a potassium ion concentration biological enzyme spectrophotometry kit. The kit principle is based on the analysis of the absorption peak change at 340 nm resulting from the conversion of NADH to NAD^+ in the potassium-dependent pyruvate kinase and lactate dehydrogenase systems. The experimental method was all based on the kit instructions.

2.2.4.13 Membrane potential staining with MycoStain It™ Green and DiSC3(5)

The membrane potential intensity could be analysed by a series of polarization-sensitive dyes. Here I applied two types of membrane potential dyes. MycoStain It™ Green is a type of fluorescent sensor that exhibits green fluorescence upon binding with the MRSA bacterial membrane. The fluorescence would shift toward red emission at higher membrane potentials, and the red/green ratio is strongly related to the membrane potential density. The MRSA cells were cultured to around 1×10^6 CFU mL^{-1} and then washed three times with PBS. Then the bacterial suspension was aliquoted 500 µL each into centrifugation tubes and treated with either GNC or antibiotics. Then 5 µL stock solution of MycoStain It™ Green (100×) was added to each centrifugation tube, and the solution was further incubated for half an hour before being observed with a confocal microscope. The fluorescence was analysed with 488 nm excitation and monitored at 510-530 nm for green and 600–660 nm for red.

As a common membrane staining dye, DiSC3(5) demonstrates a fluorescence increase that is in good accordance with the bacteria membrane depolarization. MRSA cells were incubated at 37 ^oC until the OD_{600} value reached 0.3, then were washed three times with HEPES buffer and 5 mM glucose with 3000g centrifugation for 10 mins. The pellet was then resuspended in LB broth with 5 mM glucose, 100 mM KCl and DiSC3(5) with a final concentration of 4 µM. The MRSA solution was kept under 37 ^oC for 4 mins with strict protection from light. Then the MRSA cells were washed three times and incubated with antibiotics or GNCs. After 12-h incubation, the fluorescence image was taken by the confocal microscope under 646 nm excitation and 675 nm emission.

2.2.5 Cell Experiments

2.2.5.1 Cell viability test

After treatment with GNC, the cell viability of HUVECs (ATCC PCS-100-010™) was measured using the 3-(4,5-dimethyl-2-thiazolyl)-2,5-diphenyltetrazolium bromide (MTT)

method and characterized with cell living and death staining. Specifically, the HUVECs were preincubated 5×10^5 mL^{-1} overnight in a 96-well plate. The GNC was added to each well of the 96-well plate, and the plate was further incubated for one day. After that, the working solution containing MTT (5 mg mL^{-1}) was used to replace the original medium. After 4 h, the solution was absorbed by a thick stack of napkins, and purple sediment was dissolved in 150 µL DMSO. The mixture is pumped several times with a pipette and placed on a shaker for 10 mins to dissolve the crystals fully. The absorbance at 570 nm was measured with a microplate reader (Synergy H1, BioTek).

2.2.5.2 Haemolytic assay

The haemolytic study was conducted following a reported method.[16] Fresh pig whole blood was slightly stirred with a glass rod to remove fibrinogen and separated into 2 mL tubes. PBS buffer was added to each tube. After centrifugation at 2500 rpm for 5 min, the supernatant with plasma was discarded, and this procedure was repeated three times until the supernatant was clear. The resulting concentrated red blood cell suspension was diluted to 4% red blood cell suspension. GNCs were diluted to 500 µL to make the desired concentrations and added the same amount of red blood cell suspension. The mixture was incubated in a 37 ^{o}C water bath for 3 h. Triton-X and PBS buffer were used as positive and negative controls. After 3 h, the tubes were centrifugated at 1500 rpm for 15 min. The supernatants were transferred to the wells of a microtiter plate, and the absorbance (*A*) at 540 nm (A_{540}) was measured on a microplate reader. The haemolytic rate (HL) was calculated *via* the equation below:

$$HL = \frac{A_{sample} - A_{negative}}{A_{positive} - A_{negative}} \times 100\%$$

Typically, a 5% haemolytic rate, referred to as HD_5, is the criteria used to compare the toxicity of different materials toward red blood cells.

2.2.5.3 In vitro wound-healing assay

A wound-healing assay was conducted to investigate cell migration and proliferation visually. HuH-7 cells (ATCC PTA-4583™) were inoculated 5×10^5 mL^{-1} into a 24-well plate and cultivated for 16 h to almost cover the bottom of the wells. After cell adhesion, a pipette tip was used to make a straight scratch on the cell layer along the ruler, and each well was washed with PBS thrice. PBS and different concentrations of MTX-GNCs were added to each well, and the plate was incubated and removed after 12, 24 or 36 h incubation for gap width measurement and photograph. The images were processed with *ImageJ*.

2.2.6 Tissue Experiments

2.2.6.1 Preparation of biomaterials for TEM analysis

For tissue sampling, freshly dissected LNs were fixed in 2.5% glutaraldehyde overnight at 4°C. The sample was rinsed twice with PBS for 15 mins each time and then gradiently dehydrated with ethanol solution (including 30%, 50%, 70%, 80%, 90%, and 95%, every 15 mins), and 100% ethanol for 20 mins. Acetone was used as a solvent replacement for 20 mins. The sample was then incubated with a mixture of embedding agent and acetone (V/V = 1/1) for 1 h, V/V = 3/1 for 3 h, and the pure-embedding agent. After maintaining a constant temperature of 70°C overnight, the sample was sliced on the LEICA EM UC7 ultra-thin microtome to obtain 70–90 nm slices. After drying, the sample was captured with cooper film and observed on a biological electron microscope (HT7700, HITACHI).

2.2.6.2 Frozen section

The LN tissue was fixed with a 4% paraformaldehyde solution overnight and then washed and soaked in 20% and 30% sucrose solution, respectively, until it sank to the bottom. After that, the sample was removed and frozen in the embedding agent (Tissue-Tek O.C.T. Compound 4583). The frozen slice was made with a Leica CM1950

cryostat, and the section thickness was 5 μm. The sections were placed onto a glass slide coated with 3-aminopropyltriethoxysilane (APES), naturally dried, and stored at 4 °C.

2.2.6.3 Immunofluorescence staining

The GNC NIR-II fluorescence within sections was monitored directly using a NIR-II microscopic imaging system with 10× magnification *via* 808 nm laser excitation. The laser power was adjusted to 50 mW cm^{-2}.

The gold signal was enhanced with silver staining before immunostaining. The glass slides were treated with AURION® R-Gent SE-LM silver staining kit following the instructions. The incubation time was controlled at ~35 mins under room temperature. The silver staining can be observed with a normal upright biological microscope (DM750, Leica, equipped with an ICC50W camera).

The sections were rinsed with Tris-HCl buffer saline + Tween 20 (TBST) thrice before immunofluorescence staining. The samples were incubated in a 10% goat serum solution for antigen blocking. After removing excess liquid, the primary antibodies were added, and the sections were incubated overnight at 4 °C and rinsed with TBST, followed by the addition of secondary antibodies. After 1 h incubation at room temperature, the sections were rinsed and incubated with ready-to-use DAPI staining solution for 5 mins and rinsed again. The sample was mounted with the anti-quenching agent and was observed using Nikon A1R laser scanning confocal microscope. The SCS macrophage cells were stained using rabbit anti-CD169 antibody (ab183356, Abcam; 1:200) followed by goat anti-rabbit IgG H+L (Alexa Fluor® 647) (ab150079, Abcam; 1:400). The germinal centre was stained with purified rat anti-GL7 antibody (144602, Biolegend; 1:300), followed by goat anti-rat IgG H+L (Alexa Fluor® 555) (ab150158, Abcam; 1:400). For the terminal deoxynucleotidyl transferase-mediated dUTP-biotin nick end labelling (TUNEL) assay, the positive apoptosis cells were characterized with a

TUNEL assay kit (Green fluorescence, Servicebio, G1501) and labelled with fluorescein isothiocyanate (FITC) according to the kit instructions.

For immunohistochemistry assay, the paraffin-embedded sections were sequentially treated in xylene Ⅰ 15 min-xylene Ⅱ 15 min-xylene III 15 min-anhydrous ethanol Ⅰ 5 min-anhydrous ethanol Ⅱ 5 min-85% alcohol 5 min-75% alcohol 5 min and distilled water to rinse. Then the dewaxed sections were placed in an antigen retrieval box filled with citric acid antigen retrieval buffer, heated for 8 mins to boiling, stopped for 8 mins, and turned to medium and low heat for 7 mins. After natural cooling, the slides were placed in PBS (pH = 7.4) and washed 3 times with shaking on a decolorizing shaker, 5 mins each time. The sections were placed in 3% hydrogen peroxide solution, incubated at room temperature for 25 min, and the slides were placed in PBS and washed 3 times with shaking on a decolorizing shaker to block the endogenous peroxidase. After that, 3% BSA was added dropwise to cover the tissues evenly and sealed at room temperature for 30 mins. Then, the blocking solution was gradually removed, and PBS was added with a certain ratio of Anti-Ki67 Rabbit pAb (GB111499, Servicebio; 1:500) to the slices and placed in a humidified box at 4 °C and incubated overnight. The slides were placed in PBS and washed 3 times, 5 mins each time. Horseradish peroxidase (HRP) conjugated goat anti-rabbit IgG (H+L) secondary antibody (GB23303, Servicebio; 1:500) was added to cover the tissue and the slices were incubated at room temperature for 50 mins. The substrate of HRP, 3,3'-diaminobenzidine tetrahydrochloride (DAB), was used for colour development, with a positive signal indicating brown colour. The slides were placed in PBS and washed 3 times with shaking, 5 mins each. A freshly prepared DAB colour developing solution (G1211, Servicebio) was added after the sections were slightly dried, and the colour development time under the microscope was controlled. The sections were rinsed with distilled water to stop the colour development. Subsequently, the slides were counterstained with hematoxylin (G1004, Servicebio) for ~3 mins, rinsed, differentiated for a few seconds with hematoxylin differentiation solution

(G1039, Servicebio), rinsed, blued with hematoxylin blue solution (G1040, Servicebio), and rinsed with running water. The slides were immersed in 75% alcohol 5min—85% alcohol 5min—anhydrous ethanol I 5min—anhydrous ethanol II 5min—n-butanol 5min, and xylene 5min for dehydration and transparency. The slices were mounted with neutral balsam.

For confocal laser microscope imaging, 90 μL of 2 × 10^4 cell suspension was added to each 35 mm glass bottom petri dish, then incubated for 12 h. 10 μL of the test material was inoculated and mixed well with the culture medium, then incubated for 12/24 h. The cells were taken out and stained with an adequate concentration of Calcein-AM and PI for 30 min. The confocal fluorescence images were taken with a 488 nm excitation and 515 (for Calcein-AM)/617 (for PI) nm emission. The cell counting was operated with a Countess™ II Automated Cell Counter (Thermo Fisher) with cell suspension.

2.2.6.4 Pathological analysis

Fixed tissue specimens were cut and trimmed into blocks. The tissue was dehydrated in a gradient alcohol solution, embedded in paraffin, and sliced with a Leica 2235 microtome (https://us.leica-camera.com/) into 4 μm thick sections. For H&E staining, paraffin sections were dewaxed three times, rehydrated with a gradient alcohol solution, rinsed, and stained with hematoxylin dye and eosin dye solution in order. After that, sections were gradient dehydrated again, transparentized with xylene, and sealed with neutral resin glue. The tissue slices were observed with *CaseViewer*.

2.2.6.5 The *in vitro* porcine corneal infection model

The preparation of the porcine infection model has followed the method of Ubani-Ukoma, et al.[12] The fresh pig eyes were purchased from the local slaughterhouse and instantly dissected after the execution. The eyeballs were kept frozen in the refrigerator under –80 ^{o}C until surgery. I firstly used a hole puncher with an 8 mm diameter (TED

PELLA, Rapid-Core) to create wounds that are deep into the stroma on the porcine cornea. The cornea was then separated from the eyeball with a thin scleral ring (for structural support) with conjunctival tissue, iris, and ciliary body completely removed. The corneas were then immersed in 10% povidone-iodine solution for 30 mins for quick sterilization and washed several times before subsequent treatments. For the preparation of the agar cornea model, the sterilized porcine corneas were placed upside-down within an equal-sized silicone mould and filled with melted agar medium. After the agar was solidified, I turned over the agar-filled corneas and placed them within deep agar plates separately. MRSA solution (1×10^4 CFU mL^{-1}) was dropped 1 µL in the centre of the circle wound and infected for 12 hours. Subsequently, GNC and vancomycin were applied to different groups of 2.5 µL every 6 hours, three times. The antibacterial effect was photographed at the end of the treatment. For plate coating, the corneas in each group were cut through the edge of the puncher and immersed in 7 mL PBS-T solution in 15 mL centrifugation tubes. The centrifugation tubes were vortexed 5 times each and shaken upside down 5 times. I then diluted the stock solution to 1×10^4, $1 \times 10^{5,}$ and 1×10^6-fold and evenly spread 100 µL on the new agar plates. The plates were further incubated 24 hours before colony counting.

2.2.7 Animal Experiments

All animal experiments were conducted in compliance with the relevant laws and institutional guidelines and the Institutional Animal Care and Use Committee (IACUC) ethical requirements for animal experiments, with animal experiment welfare and ethical approval (No: TOP-IACUC-2021-0063). The mice were purchased from Charles River and temporarily housed in a barrier facility in the animal centre. Specifically, the temperature was controlled from 20 °C to 26 °C. The relative humidity was between 40% and 70%. The airflow in the cages was controlled at 0.2 m s^{-1}, and the minimum static pressure difference was 10. The animals were fed once a day with water renewed. All the images taken were viewed with *PSLViewer*.

2.2.7.1 The GNC *in vivo* biosafety assay

The biosafety test was performed with evenly-grouped 36 BALBc mice (female, 6 weeks old, SPF grade). Before injection, the test subjects were evenly grouped (n = 4), shaved, and fasted over 12 h. 5 mg kg^{-1} GNC and 1.28 mg kg^{-1} Imp (final concentration) mixed solution was applied 200 µL while 200 µL PBS was applied to the control group through tail vein injection. At different time points, the organs of one group of mice were dissected to characterise the GNC accumulation under the same imaging condition. The fluorescence image was monitored with the NIR animal imager using an 808 nm laser excitation and a 1020 nm emission filter. The power of the laser source is 5 W.

To acquire the Au content in the main organs, the main organs were taken out, thawed, washed with PBS buffer, and ground to slurry with a tissue grinder separately. The masses of the organs were recorded. Aqua regia (3:1 v/v of concentrated HCl and HNO_3) was freshly prepared and added to each vial containing tissue homogenate. After a 12-h incubation, each vial mixture was heated to >100 ^oC until the aqua regia was evaporated and the tissue fully incinerated. The remnant was re-dissolved in water, diluted, and analysed with an inductively coupled plasma-mass spectrometry (ICP-MS, Agilent 7700) to measure the Au content. After 3 days, I collected blood samples of the experiment and control groups, and then did a routine blood test and blood biochemical analysis to confirm the safety of the combination.

2.2.7.2 Skin infection model

The animal test was based on a previous report with modifications.[13] 12 Sprague Dawley rats (female, 8 weeks old, ~250 g) were divided evenly (n = 3). Three whole-sized wounds (*d* = 1.5 cm) were created at the back of each rat, and 150 µL MRSE bacteria solution (~1 × 10^9 CFU mL^{-1}) was spread evenly on the wound. After 1 h infection, 100 µL PBS, 24 µg mL^{-1} Imp solution, 64 µg mL^{-1} GNC solution, and the combination of 24 µg mL^{-1} Imp (~0.12 mg kg^{-1}, final concentration) and 64 µg mL^{-1} GNC

solution (~0.32 mg kg^{-1}, final concentration) were spread on the wounds of each group, respectively. The wound size and wound bacteria number were recorded every three days. On day 6 and day 12, wounds were randomly dissected from rats and fixed with 4% paraformaldehyde solution for the subsequent H&E staining.

2.2.7.3 The *in vivo* corneal infection model

Before the animal experiments, the mice were anaesthetized by peritoneally injecting 2.5% tribromoethanol (12–15 μL g^{-1} Wt) and 0.5% prilocaine hydrochloride eye drop was dropped 5 μL on each eye of the mice to enhance local anaesthesia. The mice were then distributed into 5 groups with 5 individuals in each group. I firstly created 5 groups of W-shaped scratches that are deep to the stroma on the cornea of mice with a BD insulin syringe (BD Biosciences) and infected them with 2 μL MRSA solution (5×10^8 CFU mL^{-1}). After around 24 hours, the keratitis model was built up with obvious opacity on the cornea of both eyes. Then different treatments were applied to different groups with a frequency of three times per day at 6-hour intervals. I photographed the change of opacity size daily with a stereomicroscope (Nikon, SMZ18). After that, a clean swab was applied for the sampling of the eye discharge and suddenly immersed in 1 mL PBS-T. The solution was then spread 200 μL on the agar plate for colony count. On day 4, the mice were sacrificed by neck dislocation, and their eyeballs were taken out and fixed with FAS eyeball fixative solution (G1109). After 24-h fixation, the eyeballs were taken out for the H&E and Gram staining.

2.2.7.4 *In vivo* LN imaging effect comparison

GNCs were administered (100 μL; 1 mg mL^{-1}; ~5 mg kg^{-1}) through the tail vein or hindlimb footpad and detected with a NIR-II animal imager (NIROPTICS, Series III 900/1700) equipped with 808 nm laser irradiation. A 1020 nm long-pass filter (same below) was used for bioimaging and surgical operations. The photos of the supine and prone position were taken separately. The metabolic procedure was checked every two

days. The urine sample was collected every hour post intravenous administration by placing a group of three mice in each metabolic cage.

After three days of administration with 40 mg kg^{-1} MUA-GNC, the mice were sacrificed for blood routine and liver and kidney function tests. The blood samples were collected with anticoagulant or procoagulant test tubes with serum separating gel for each group. The latter ones were centrifuged at 2500 rpm for 15 mins to promote serum separation. The entire blood samples were sent to an animal blood cell analyzer (DF55Vet, DYMIND) for analysis, while the serum samples were sent to a fully automatic bioanalysis machine (MS480, MedicalSystem) for biochemical index analysis.

For the photostability test, the initial ICG concentration was set as ~200 μM, and the fluorescence brightness of the GNC was adjusted to be similar to that of ICG. The photostability comparison was performed by exposing both groups to an 808 nm laser irradiation (20 mW cm^{-2}) or natural light irradiation.

2.2.7.5 Macrophage inhibition model construction

Macrophage inhibition was achieved by dissolving $GdCl_3$ with normal saline to prepare a 4 mg mL^{-1} $GdCl_3$ solution.[14] Three days before the experiment, a 100-μL $GdCl_3$ solution was injected into the hindlimb footpad of mice, and PBS was used as the negative control.

2.2.7.6 Surgical guiding and metastatic LN removal

The tumour-bearing model was constructed by injecting human hepatic carcinoma cell Hep 3B cell suspension (ATCC HB-8064™, 1×10^7 mL^{-1}, 100 μL) on the left hind limb footpad subcutaneously or intraperitoneally. The GNC was injected from the ipsilateral footpad after the tumour diameter had reached ~6 mm, and the LN accumulating effect was monitored for 6 h. The mice were then sacrificed, and abnormal LNs were removed from the body *via* surgery, guided with a NIR imager (25 ms, 20 mW cm^{-2}).

2.2.7.7 *In vivo* LN metastasis treatment

Mice were randomly divided into 5 groups, with 5 mice in each group. The tumour LN metastatic model was constructed by injecting Hep3B cell suspension (ATCC HB-8064™, 1×10^7 mL^{-1}, 100 µL) into the left hind footpad and then incubated for 4 days to construct the LN metastatic model in the ipsilateral popliteal LN of the injection position. Different groups were treated with 100 µL PBS, MUA-GNC, MTX-GNC, or free MTX. Each dose of free MTX, MUA-GNC, or MTX-GNC was 5, 20, 10 (low) or 20 mg kg^{-1} (high), respectively, for these *in vitro* tests. Mice were administered the above dose once every two days, and their body weights were tracked. After 12 days, I anaesthetized the mice for weighing, collected the blood samples, sacrificed them to collect the main organs, and dissected the ipsilateral popliteal LN on the injection site.

2.3 Appendix (Others Contributed Experiments)

2.3.1 Cell culture conditions and toxicology tests

Ocular and somatic cell line culture and testing in Chapter 5 are provided by Ning Ren, Department of biomedical engineering, SUSTech. The following synthetic protocols are provided by her.

2.3.1.1 Cell culture condition

The ARPE-19 cell is a human retinal epithelial cell, and it usually takes around 55 to 65 h for cell division generation. The cells are cultured in Dulbecco's modified eagle medium (DMEM)/F12 with 10% bovine serum albumin (FBS)+1% penicillin and streptomycin (P/S) in a culture medium. The cells are cultured in a cell incubator at 37 ^oC, with 5% CO_2. Cells were passaged three times a week at a ratio of 1:3 per passage.

The human umbilical vein endothelial cells (HUVECs) are cultured under the same culture conditions, with the culture medium changed to the endothelial cell culture medium (ECM) with 5% FBS and 1% P/S. All the other conditions are the same.

2.3.1.2 Cell toxicity test

The cells were pre-digested and concentrated to 5×10^5 $mL^{-1,}$ then added to the 96-well plate with 100 µL per well. The cells were then incubated overnight to make them fully adherent, after which GNCs at different concentrations were added to the system in an amount not exceeding 10% of the total medium volume. The cells were further incubated for 12–24 h. The cell viability was measured with a sulforhodamine B (SRB) test kit. The cell viability is positively correlated with the absorbance value at 515 nm. Other cell viability testing methods are abandoned due to the inhibition of respiratory enzymes by GNCs.

2.3.2 Gram, PAS, Masson, and H&E staining

The staining results demonstrated in Chapter 4, Chapter 5, and Chapter 7 are provided by Ning Ren, SUSTech. The following protocols are provided by her.

2.3.2.1 Paraffin embedding

All the organic solvents used are purchased from Sinopharm, except for the EDTA decalcification fluid purchased from Servicebio (G1105).

The fixed corneas or eyeball tissues were rinsed, then put into the dehydrating basket, and dehydrated in gradient alcohol in the dehydrator. Details as follow: 75% alcohol (2 h); 85% alcohol (2 h); 90% alcohol (1.5 h); 95% alcohol (2 h); anhydrous ethanol I (2 h); anhydrous ethanol II (2 h); phenyl alcohol solution (40 min); xylene I (40 min); xylene II (40 min); 65 ^oC melted paraffin I (0.5 h); melted paraffin II (1 h); 65 ^oC melted paraffin III (2 h 45 min). The wax-soaked tissue was then embedded in the embedding machine. The melted wax was put into the embedding frame first. Before the wax solidifies, tissues were taken out of the dehydration box and put into the embedding frame according to the requirements of the embedding surface. Cooling at –20 ^oC freezing table, the wax block was then removed from the embedding frame and trimmed after

solidification. The trimmed paraffin was blocked on a paraffin microtome for preparing 4 μm-thick sections. Slice was spread and flattened on the spreader machine filled with 40 ^{o}C warm water, and then slides were used to pick up the tissue section. The slides were then sent to a 60 ^{o}C oven to remove the wax and then stored at room temperature.

2.3.2.2 Gram staining process

All the organic solvents used are purchased from Sinopharm, except for the Gram staining solution kit purchased from Servicebio (G1105).

The sections were deparaffinized in sequence in xylene I (20 min)-xylene II (20min)-anhydrous ethanol I (5min)-anhydrous ethanol II (5min)-75% ethyl alcohol (5min), then washed with water to remove extra alcohol and complete the de-paraffin. Gram staining solution A was dropped on the sections to stain for 10 s–30 s. Then the section was washed and shaken to dry. Then added Gram staining solution B for 1 min, washed, and shaken to dry. Aspirate Gram Stain C from one end of the frosted side of the slide to rinse the tissue for differentiation until the Gram Stain C flowing down the slide becomes colourless, washed, and shaken to dry. The sections were then dipped in Gram staining solution D for 1 s and washed, then baked in an oven to dry. The sections were then put into anhydrous ethanol to dehydrate for 1 s, 3 s, and 5 s in sequence. Finally, the sections were immersed into clean xylene for 5 min for transparency and then sealed with neutral balsam. Gram-positive bacteria are stained purple, while Gram-negative bacteria are stained red.

2.3.2.3 H&E staining

The fixed tissue specimen was cut out and put in the embedding box. Then, 70%, 75%, 80%, 95%, and 100% alcohol were used for gradient dehydration, followed by paraffin wax embedding. After embedding, the samples were sectioned with Leica 2235

microtome, with a section thickness of 4 μm. The paraffin sections were dewaxed thrice, 15 mins each, and rehydrated with gradient alcohol (from high to low concentration 100%, 95%, 90%, 80%, 70%, every 2 mins) and put in hematoxylin dye solution for 5 mins, rinsed with running water, and put in 0.5% hydrochloric acid alcohol solution for differentiation for 5 s, rinsed with running water again and put in 1% eosin dye solution for 3 mins. After gradient dehydration again, xylene was added to transparent samples for 20–30 mins. The slices were mounted with resin and scanned with a digital pathology scanner (Pannoramic MIDI, 3D HISTECH).

2.3.2.4 PAS staining

The paraffin-embedded sections were dewaxed according to the above process and stained with a PAS staining kit (G1008, Servicebio). The sections were immersed in PAS staining solution B for 10−15 min, washed with tap water, and distilled water twice. The sections were immersed in PAS staining solution A for 25–30 min with light shielding and rinsed with running water for 5 min. Subsequently, the sections were stained with PAS staining solution C for 30 s, washed with tap water, differentiated with HCl solution, washed with water, blued with ammonia solution, and rinsed with running water. Finally, the sections were dehydrated and mounted with neutral resin. After PAS staining, the glycogen and tissues containing polysaccharides are purple-red, and the cell nucleus is light blue.

2.3.2.5 Masson staining

The paraffin-embedded sections were dewaxed according to the above process and stained with a Masson staining kit (G1006, Servicebio). The slices were immersed in Masson A solution overnight and washed with tap water. Then, the mixed solution of Masson B and C in equal proportion was added onto sections and soaked for 1 min. The slices were washed with tap water, differentiated with 1% hydrochloric acid and alcohol, and washed again, then immersed in Masson D and E solutions for 6 and 1 min

each. The slices were then dipped into Masson F solution for 20–30 s, rinsed and differentiated with 1% glacial acetic acid, and dehydrated in two tanks of absolute ethanol. The slices were placed into the third tank of absolute ethanol for 5 mins, made transparent with xylene for 5 mins, and mounted with neutral balsam.

2.3.3 Biochemical indices tests

The biochemical indices test results (blood routine and liver & kidney indices) demonstrated in **Chapter 4**, **Chapter 5**, and **Chapter 7** were performed by the Laboratory Animal Research Center of SUSTech. The mice's blood was collected according to the experimental needs. Then the blood samples were collected in a vacuum coagulation tube with separation glue (BD Biosciences). The samples were then centrifuged at 5000 rpm, 4 ^{o}C for 10 mins until the serum and blood cells were completely separated. The serum was then collected and sent 300 μL to the biochemical testing room for testing. The samples were then analyzed by an automatic biochemical analyzer (MS-480, NBMEDICAL) for various biochemical indicators, and the results were processed by *Origin2018.*

2.4 References

1 D. Mishra, S. Wang, Z. Jin, E. Lochner and H. Mattoussi, *ChemRxiv*, 2018.

2 G. W. Anderson and R. Paul, *J. Am. Chem. Soc.*, 1958, **80**, 4423.

3 D. Zhou, X. Wang, L. Birch, T. Rayment and C. Abell, *Langmuir*, 2003, **19**, 10557–10562.

4 Y. Ishida, K. Narita, T. Yonezawa and R. L. Whetten, *J. Phys. Chem. Lett.*, 2016, **7**, 3718–3722.

5 C. Fiehn, F. Kratz, G. Sass, U. Müller-Ladner and E. Neumann, *Ann. Rheum. Dis.*, 2008, **67**, 1188.

6 T. Chen, V. Fung, Q. Yao, Z. Luo, D. E. Jiang and J. Xie, *J. Am. Chem. Soc.*, 2018, **140**, 11370–11377.

7 Y. Xie, Y. Liu, J. Yang, Y. Liu, F. Hu, K. Zhu and X. Jiang, *Angew. Chemie - Int. Ed.*, 2018, **57**, 3958–3962.

8 L. A. Barbee, O. O. Soge, K. K. Holmes and M. R. Golden, *J. Antimicrob. Chemother.*, 2014, **69**, 1572–1578.

9 T. C. Meredith, J. G. Swoboda and S. Walker, *J. Bacteriol.*, 2008, **190**, 3046–3056.

10 J. Swain, M. El Khoury, A. Flament, C. Dezanet, F. Briée, P. Van Der Smissen, J. L. Décout and M. P. Mingeot-Leclercq, *Biochim. Biophys. Acta - Biomembr.*, 2019, **1861**, 182998.

11 A. Müller, M. Wenzel, H. Strahl, F. Grein, T. N. V. Saaki, B. Kohl, T. Siersma, J. E. Bandow, H. G. Sahl, T. Schneider and L. W. Hamoen, *Proc. Natl. Acad. Sci. U. S. A.*, 2016, **113**, E7077–E7086.

12 U. Ubani-Ukoma, A. Chauhan, G. Schultz and D. J. Gibson, *MethodsX*, 2020, **7**, 100876.

13 M. Chen, Z. Long, R. Dong, L. Wang, J. Zhang, S. Li, X. Zhao, X. Hou, H. Shao and X. Jiang, *Small*, 2020, **16**, 1–11.

14 Y.-N. Zhang, W. Poon, E. Sefton and W. C. W. Chan, *ACS Nano*, 2020, **14**, 9478–9490.

Part II

Developing Dual-/multi-ligand-functionalised GNCs for Antibacterial Applications

Chapter 3
The application of gold nanocluster-based nanomedicine in the treatment of antimicrobial-resistant pathogens-induced infections

3.1 Introduction

The battle between human and pathogenic bacteria species is a protracted war that started with the discovery of *Penicillin* in 1928.[1] Subsequent discoveries of a series of antibiotics such as *Prontosil* and *Tyrothricin* opened a new era in which people could defend themselves from infections caused by common pathogenic bacteria (**Figure 3.1.1**).[2] However, the ecstasy did not last long because people found bacteria could break the antibiotic defence. The widespread use of antibiotics has produced a high selective pressure on all bacterial species: they must evolve to survive. Otherwise, they will be wiped out. As a result, bacteria that have survived the antibiotic attack may have naturally acquired and accumulated drug-resistant genes, making them highly resistant to antibiotic treatment. In particular, the extensive use of antibiotics in hospitals and animal husbandry has greatly accelerated the development of bacterial resistance.[3] Horizontal transmission of antibiotic-resistant genes on a plasmid from both within- and inter-species have produced increasingly antimicrobial-resistant (AMR) bacteria strains.

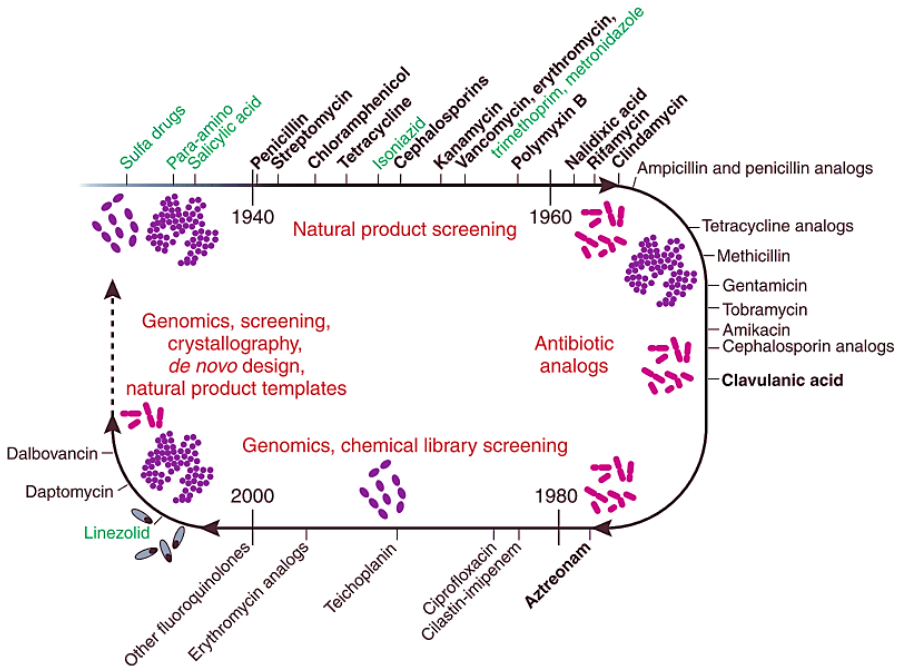

Figure 3.1.1 Chronology of research and development in the field of antibiotics. The discovery of new antibiotics gradually slowed down after 1980 and gradually exhausted after the 21st century.[2] (Copied from the Nature Publishing Group)

To overcome the bacteria resistance problem, people have attempted to increase the scale and depth of natural antibiotic selection. However, as the discovery of new natural antibiotics is getting harder and harder over time, people have started to seek alternative ways, for example, by making modifications or semi-synthesis of existing antibiotic structures, screening microbial fermentations, and using the new-coming genomics, as well as high-throughput screening methods to get the target products.[2] Although these efforts have contributed a lot to the antibacterial discovery, the huge investment of effort and funds has produced only limited/disappointing outputs. Due to the extremely uneven input-output ratio, many pharmaceutical companies have stopped developing new antibiotics, which has caused the antibiotic pipeline to dry up gradually. Meanwhile, the trend of ever-increasing MDR bacterial strains still marches on and begins to cause a big threat to the global healthcare system. Therefore, there is an urgent need to develop novel approaches to combat the bacterial resistance problem to prevent us from returning to the dark ages of the pre-antibiotic era.

Usually, if a bacterium carries multiple resistance genes against antibiotics, I call it an MDR bacterium or superbug.[4] Since the 1960s, people have found a variety of "superbugs," such as Methicillin-resistant *Staphylococcus aureus* (MRSA), Vancomycin-resistant *Enterococci* (VRE), Multidrug-resistant *Streptococcus pneumoniae* (MDRSP), Multidrug-resistant *Mycobacterium tuberculosis* (MDR-TB) and Multidrug-resistant *Acinetobacter baumannii* (MRAB), etc.[5] In 2010, a paper published in *The Lancet* describing a "superbug" containing the New Delhi Metallo-beta-lactamase-1 (NDM-1) raised the word "superbug" again in public opinion and even caused some social panic as this lactamase can disable many commonly used carbapenems and other β-lactam antibiotics.[6] According to the estimate of the US centres for disease control and prevention (CDC), in 2019 alone, antibiotic resistance bacteria caused >2,800,000 cases of infections and >35,000 deaths in the USA (Figure 3.1.2).[7] Moreover, in the USA alone, merely community-associated MRSA infection is estimated to pose $1.4-13.8 billion direct economic cost per year to society, and the cost still keeps on increasing.[8] Therefore, there is an urgent need to develop new drugs that have broad-spectrum antibacterial properties against MDR strains and are also less likely for bacteria to develop resistance.

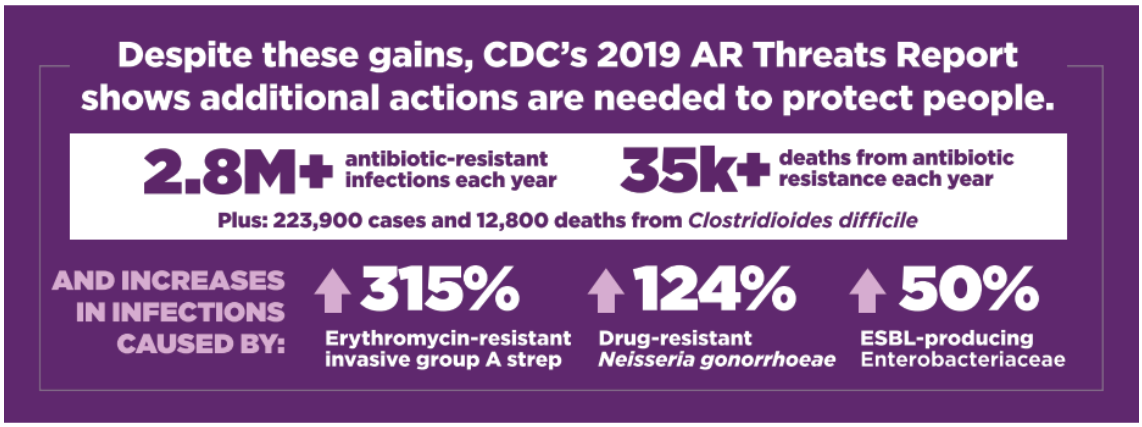

Figure 3.1.2 The impact of bacterial AMR in the USA in 2019, with the emergence of new resistance situations and new AMR strains.[9] (Copied from the Centres for Disease Control and Prevention)

In this chapter, the current global drug resistance situation will be discussed first. Then the development of GNPs for the control of multidrug-resistant pathogens-induced infections will be introduced, including synthesis and surface chemistry for antibacterial applications. Following that, the development of the ultra-small GNC (<2 nm) was briefly summarised. Then, the applications of GNC-based antibacterial nanomaterial, especially for controlling multidrug-resistant infections, will be summarised and discussed.

3.2 From AMR to MDR—The development of global drug resistance

3.2.1 Global development of AMR bacteria in the context of COVID-19

As one of the trickiest international issues, the development of bacterial drug resistance has caused a death toll of around 700,000 per year before the Corona Virus Disease 2019 (COVID-19) pandemic.[10] In another statistical data provided by Antimicrobial Resistance Collaborators, merely in 2019 alone, there were around 4.95 million deaths associated with AMR, and around 1.27 million died directly from AMR-induced infections.[11] This number is just lower than that who died of cardiovascular diseases, making it the second most killer in the world. These shocking data have denounced that bacterial resistance toward antibiotics is no longer an issue that can be ignored, especially when combined with the COVID-19 plague. People with COVID infections are more vulnerable and prone to AMR infections. Thus, combined bacterial and viral infections could cause a higher mortality rate. In addition, lower respiratory tract infections, including thorax infection, caused the greatest burden to the world economy and killed >1.5 million people in 2019. Many organisations, including CDC in the USA and World Health Organization (WHO) have ranked the AMR bacteria according to their trend of resistance, transmissibility, treatability, etc. (Figure 3.2.1).[9 12]

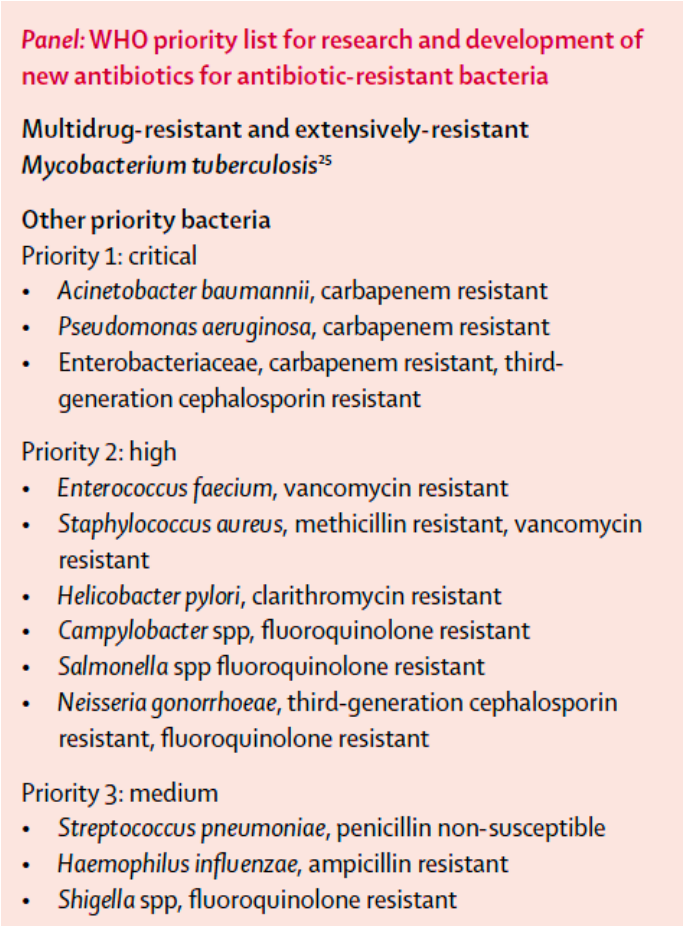

Panel: WHO priority list for research and development of new antibiotics for antibiotic-resistant bacteria

Multidrug-resistant and extensively-resistant *Mycobacterium tuberculosis*[25]

Other priority bacteria

Priority 1: critical

- *Acinetobacter baumannii*, carbapenem resistant
- *Pseudomonas aeruginosa*, carbapenem resistant
- Enterobacteriaceae, carbapenem resistant, third-generation cephalosporin resistant

Priority 2: high

- *Enterococcus faecium*, vancomycin resistant
- *Staphylococcus aureus*, methicillin resistant, vancomycin resistant
- *Helicobacter pylori*, clarithromycin resistant
- *Campylobacter* spp, fluoroquinolone resistant
- *Salmonella* spp fluoroquinolone resistant
- *Neisseria gonorrhoeae*, third-generation cephalosporin resistant, fluoroquinolone resistant

Priority 3: medium

- *Streptococcus pneumoniae*, penicillin non-susceptible
- *Haemophilus influenzae*, ampicillin resistant
- *Shigella* spp, fluoroquinolone resistant

Figure 3.2.1 WHO priority list of MDR bacteria for research and antibiotic development.[12] (Copied from Elsevier Publishing Group)

Although the ranking is varied, six of the most drug-resistant bacteria, including *Escherichia coli* (*E. coli*, *E. c)*, *Staphylococcus aureus* (*S. aureus*, *S. a*), *Klebsiella pneumoniae* (*K. pneumoniae*, *K. p*), *Streptococcus pneumoniae* (*S. pneumoniae*, *S. p*), *Acinetobacter baumannii* (*A. baumannii*, *A. b*), and *Pseudomonas aeruginosa* (*P. aeruginosa*, *P. a*) (collectively caused around 929,000 cases of AMR related deaths in 2019) can all induce lower respiratory tract or lung infections, which has further increased the chances of co-infection.[13]

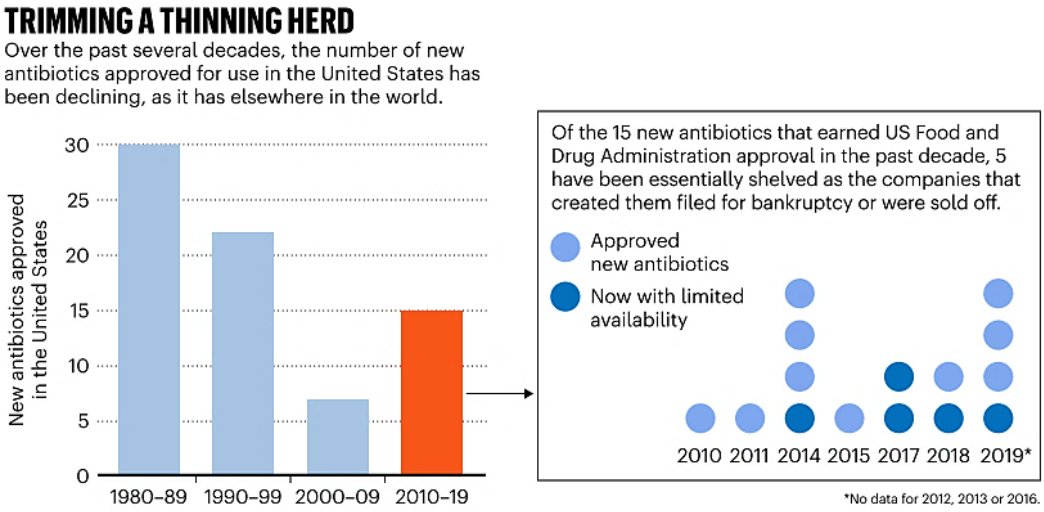

Figure 3.2.2 The number of antibiotics that have been proved for use in the USA is at a low level. In addition, one-third of new antibiotics approved by the FDA over the past decade were discontinued due to poor company management.[10] (Copied from the Nature Publishing Group)

In stark contrast, the development of new antibiotics is fruitless compared with medications for other symptoms. The development pipelines of new antibiotics have broken down for over 20 years, and many new antibiotics are stillborn due to the financial break of the companies. This is because it is an extremely arduous and laborious task to develop a new antibiotic with high efficacy, good pharmacokinetics, and high safety (Figure 3.2.2). In the United States, it typically costs more than $ 1 billion to develop a new antibiotic and get food and drug administration (FDA) approval.[10] For many small companies, this astronomical amount of money is unfordable. In another aspect, compared with many other drugs that must be taken daily, like those to treat hypertension, autoimmune diseases, or antipsychotics, the demand for antibiotics is much lower. It is more commonly used as a reserve drug in the household. In hospitals, the treatment priority for AMR infection is normally lower than cancer because the latter is often more difficult to treat and much more lethal, and the profit of anti-tumour drugs is also much higher, which has led to a huge disparity in investment in cancer drug and antibiotic research. In September 2016, hundreds of antitumour drugs entered clinical trials, compared with only about 40 antibiotics in the

same period.[14] This extreme imbalance between input and output has forced big pharmaceutical companies to give up the development of antibiotics.[12] What's more, once a new antibiotic is put into clinical use, it has entered the countdown to complete failure due to bacteria can develop resistance very rapidly, typically within one or a few years (**Figure 3.2.3**). Limited by a relatively short service life, the application of new antibiotics is very prudent and only applied to life-threatened patients to maintain their efficacy and maximise their availability time, which further decreases the scale of new antibiotics sales. If the current trend of low antibiotic development remains, the estimated global AMR-related deaths could reach 10 million per year by 2050, which is rather alarming.[14]

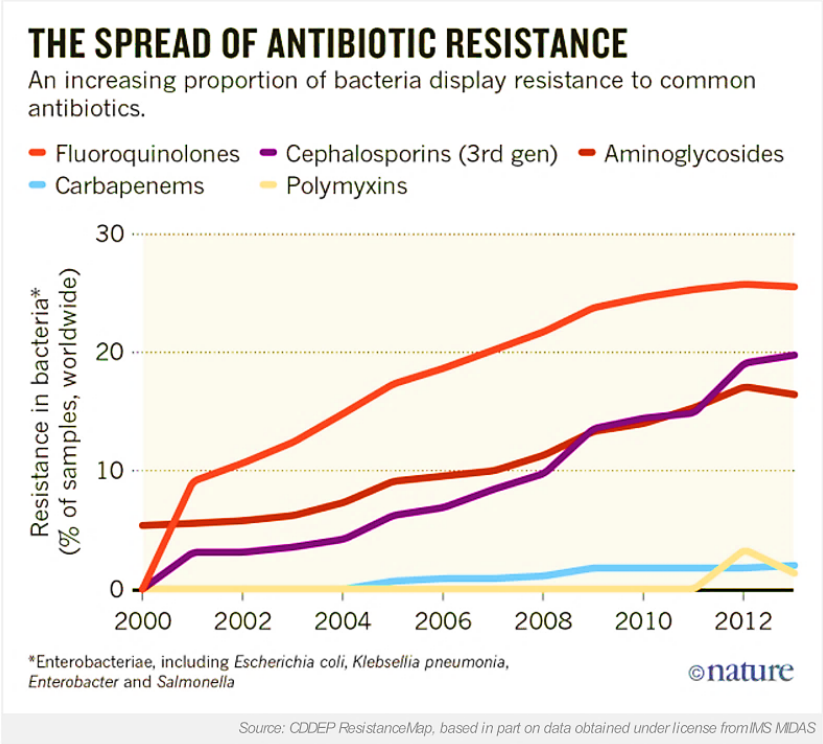

Figure 3.2.3 In recent years, resistance to the last-sorted antibiotics has gradually increased.[15] (Copied from the Nature Publishing Group)

This downturn in new antibiotic research and development has not limited the pace of bacterial resistance growth. The increase in resistance is not only due to the use of antibiotics in medication but also to the misuse of antibiotics in agriculture and animal

husbandry. For example, in the USA, 70%–80% of antibiotics are applied to raising livestock, and in the BRICS countries (Brazil, Russia, India, China, and South Africa), the amount of agricultural antibiotics is expected to double that used in 2010 by 2030.[16] Therefore, the massive use of antimicrobials has posed a high selective pressure on natural microorganisms, and eventually, the resistance of bacteria to some of the last-ditch antibiotics will emerge. For example, the resistance gene *mcr-1* to colistin, the so-called trump card for controlling Gram-negative AMR infections, was observed in bacteria isolated from pigs in China in 2017.[17] Colistin (chemical structure refers to Figure 3.2.4) is a member of polymyxins and has an antibacterial mechanism that is different from that of most common anti-Gram-negative antibiotics. It works by binding to the lipid A moiety of lipopolysaccharide (LPS) through electro statistical interaction, causing the destruction of the outer membrane. The fatty acid moiety of colistin could further penetrate the outer membrane, increasing the permeability of the cytoplasmic membrane, resulting in the spill over of small molecules such as phosphates and nucleosides in the cytoplasm and causing cell dysfunction and death.[18 19] However, due to strong nephrotoxicity, colistin is not a preferred antibiotic for human use and has been generally banned for clinical use since 1980. However, it has a long history of being used as veterinary antibiotics in China and Brazil to treat gastrointestinal infections caused by Gram-negative bacteria in poultry and livestock, which is probably the reason for resistance found in pigs.[20]

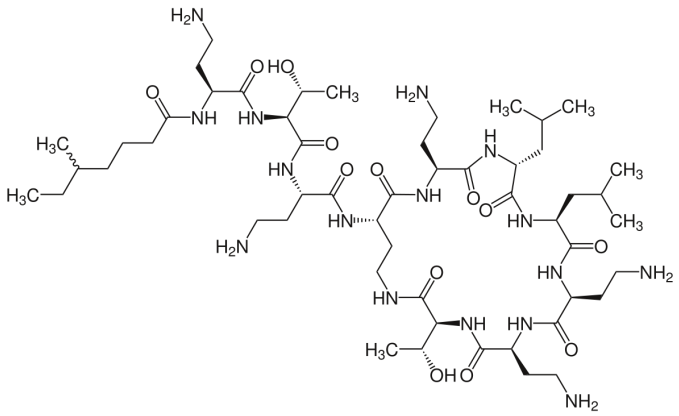

Figure 3.2.4 Molecular structure of colistin. It is a non-ribosomal peptide that binds to

the lipid A in LPS and disrupts the outer membrane of Gram-negative bacteria.[18]

The *mcr-1* gene could guide the synthesis of an enzyme that could modify lipid A and stop the binding of colistin with LPS. Subsequently, this gene was found on the bacteria plasmid and disseminated to Europe and North America. In addition to a trend of global spread, gene transfer between species has also emerged. In China, an investigation has found that the gut flora of one in sixteen people in Guangzhou has this gene, suggesting it can jump inter- and intra-species.[16] Besides colistin, the resistance toward carbapenems, a category of β-lactam antibiotics that has high stability, broad-spectrum antibacterial properties and high potency, is also spreading widely. Although the chemical structures of carbapenems are highly stable and could partly resist the hydrolysis by β-lactamase, its resistance has emerged and gradually become a global healthcare problem.[21] The primary resistant mechanism to carbapenems is the expression of β-lactamase (A, B&D), which is usually encoded by a gene on plasmids. However, other nonenzymatic mechanisms, including the mutations in porin and overexpression of efflux pumps, are also important. In both large and small-scale statistics, the resistance to carbapenems has shown to be relatively high in Gram-negative fermenting bacteria like *P. a*, *A. b*, and *K. p*, but low for non-fermenters (**Figure 3.2.5**). The resistance rate for *A. b* is astonishingly high at 44.8%, and that for *P. a* is around 14.2%. Thus, it is unsurprising that over 80% of carbapenem-resistant infections are caused by *A. b* and *P. a.*[22] In addition, the high molecular stability of some antibiotics allows them to retain within the soil for over hundreds or thousands of years, making soil the cradle of resistance development.

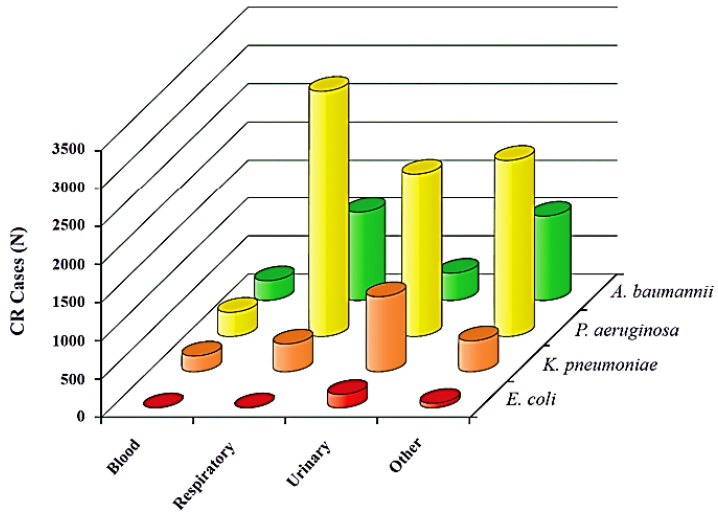

Figure 3.2.5 Statistical results of carbapenem resistance (CR) cases caused by different infection types of *E. c*, *K. p*, *P. a*, and *A. b*. Comparatively, *P. a* has a relatively higher CR infection pathogenicity compared with other species, with a strong ability to induce respiratory and urinary infections.[22] (Copied from the Oxford Academic Publishing Group)

3.2.2 The development of MDR strains and their molecular mechanisms of formation

With the prevalence of AMR strains, the natural gene transfer and exchange between or within the genus has caused the accumulation of multiple resistance genes in the same strain, resulting in the formation of MDR strains. These prevalent resistance genes eventually led to the emergence of multiple MDR species, including *P. a*, *A. b,* and *K. p* with β-lactamases, VRE, MRSA, vancomycin-resistant *S. aureus* (VRSA) and MDR-*Mycobacterium tuberculosis,* which are highly resistant to several classes of commonly used antibiotics. The existence of these MDR bacteria species has imposed a great burden on global health security, especially under the background of COVID-19 prevalence. One of the most lethal MDR pathogens—MRSA, has caused over 100,000 cases of death worldwide in 2019, with the remaining six top lethal MDR pathogens killing 50,000–100,000 people.[23] These MDR pathogens are generally resistant to most of the common clinical antibiotics, including most β-lactams, commonly used macrolides, aminoglycosides, chloramphenicol, quinolones, tetracyclines, and

lincomycin.

The molecular mechanism of the acquired MDR comes from mainly three aspects: 1) the alteration and competition of the antibiotic targets, 2) the destruction or excretion of the antibiotics, and 3) the decreased intake of antibiotics or changes in status. I am going to describe each aspect in detail below.

1) The alteration of targets, including the mutations on the key binding site of antibiotics. One of the most well-known examples is the mutation of the cell wall precursor peptide Lipid II (change from D-Ala-D-Ala to D-Ala-D-Lac or D-Ala-D-Ser, Ala—alanine, Lac—lactate, Ser—serine), thus reducing the hydrogen bond formation of vancomycin with the target, which has greatly reduced the efficiency of vancomycin (Figure 3.2.6).[24] Furthermore, the chemical modification or molecular protection to the binding sites of antibiotics could also induce the same consequence. Another way to reduce the efficiency of antibiotics is to acquire antibiotic-binding proteins from low-sensitive strains through transformation. The subsequent expression of these antibiotic binding proteins could block antibiotics and cause drug resistance. For MDR strains, the combination with either two or all three mechanisms can elevate the resistance to a few categories of antibiotics.

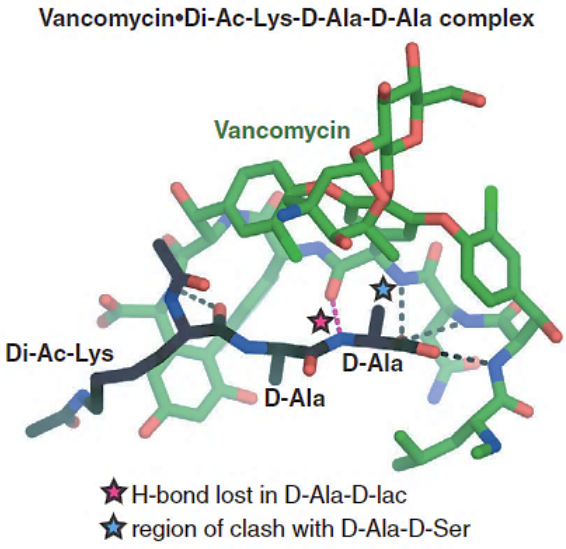

Figure 3.2.6 The molecular simulation experiment results in the effect of replacing alanine with lactate or serine on vancomycin binding. The loss of hydrogen bond was indicated with a pink star (Ala→Lac), and the steric hindrance was labelled with a blue star (Ala→Ser). [24] (Copied from the Wiley Publishing Group)

2) Many MDR organisms could **generate enzymes** to degrade antibiotics. For example, strains including carbapenem-resistant *K. pneumoniae* or carbapenem-resistant *A. b* could secrete carbapenemase that breaks down carbapenem. In addition, the secretion of β-lactamase by bacteria with the NDM-1 gene could further deactivate all types of common and rare antibiotics with β-lactam structure, including penicillins, carbapenems, cephalosporins, monocyclic β-lactams, as well as cephamycins, etc. In addition, another way of MDR development is the overexpression of the efflux pumps, which is normally due to the mutation of the host cell chromosome.[25] In Gram-negative strains particularly, the resistance-nodulation-cell division (RND) efflux pump superfamily is a key factor for their resistance because it is coded by chromosomal DNA and is easy to overexpress.[26] These RND efflux pumps could easily remove most antibiotics from the periplasmic space and develop MDR. In a recent study, the existence of AcrAB-TolC MDR efflux pumps (a type of RND pumps) on Gram-negative bacteria was found to suppress the intracellular concentration of protein-synthesis-inhibitory antibiotics.[27] Moreover, it also facilitates the expression of highly specific

efflux pump proteins acquired through further plasmid conjugation and promotes the acquired drug resistance.

3) The drug resistance of Gram-negative bacteria is generally higher than Gram-positive ones, which is attributed to the natural blockage of the outer membrane that hinders the entry of antibiotics. A further modification of the selectivity of the outer membrane could dramatically increase drug resistance. For example, the presence of porin, a protein channel embedded in the outer membrane that can control the entry of drugs and nutrients, has contributed greatly to the formation of AMR bacteria strains. Any mutation in the number or channel size of the porins on the outer membrane could significantly reduce antibiotic diffusion. In addition, the adaptive resistance induced by porin expression could happen upon exposure to a subinhibitory concentration of antibiotics (Figure 3.2.7).[28] Some bacteria like *P. a* could secrete layers of polysaccharides and biomacromolecules (proteins, DNA, RNA, etc.) that could block the infiltration of antibiotics and increase the settlement of implantations. This kind of biome, together with the biomass secreted, is called the biofilm.[29] Compared with planktonic bacteria, those sessile bacteria within the biofilm are much more difficult to treat, which is possibly due to the physical hindrance of antibiotic transport, the abundance of deactivation enzymes, and/or altered chemical environment.[30] While encountering an adverse environment, bacteria like *A. b* could form persistent colonies and reduce the uptake of antibiotics. Many bacteria will also form L-form bacteria to avoid the attack of antibiotics on the cell wall.

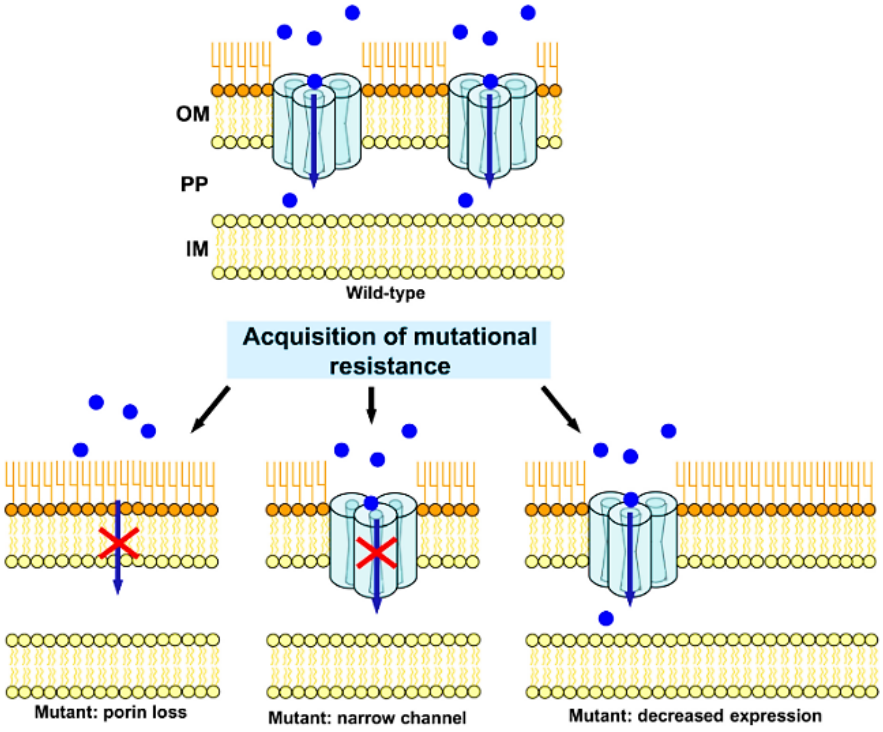

Figure 3.2.7 Possible mechanisms of MDR development related to the porin mutation, including loss, pore narrowing and a decrease in the number of porins.[28] (IM: the inner membrane, OM: the outer membrane, PP: periplasmic space) (Copied from the ASM Publishing Group)

Controlling the global spread of AMR and MDR strains requires cooperation between countries and individuals.[31] In addition to improvements in legal policy, medical education, and public advocacy, the most important thing is to open other sources to treat AMR and MDR bacterial infections. In terms of developing vaccines to control AMR or MDR infections, there is only one vaccine which targets the capsular polysaccharide of *K. p* and is still in developing clinical trials.[32] [33] Other top MDR strains still lack vaccines. In addition, the development of other antibacterial strategies, such as the use of phage to control the MDR infection, can serve as a new way to substitute antibiotics.

With the development of materials in the nano-range, applying nanomaterials to control AMR/MDR infections has raised new hope to fight drug-resistant infections. Raised in 1974, nanotechnology has attracted extensive attention around the world, which is also emerging increasingly frequently in our daily life. At the same time, many

drawbacks of traditional antibiotics, for example, ease of developing resistance and inevitable side effects, have driven people to seek solutions from nanotechnology. Compared to commonly used anti-microbial medicines and antibiotics, nanomaterial-based medicines (nanomedicines) possess many attractive benefits, such as the ability to achieve targeted drug delivery to reduce toxic side effects and the difficulty for bacteria to develop drug resistance and lower manufacturing costs.[34] Besides, nanomedicines also have more stable structures and longer circulation time than conventional antibiotics to exhibit long-lasting pharmaco-kinetic effects. In addition, some nanomaterial can effectively pass through natural biological barriers, like the blood-brain barrier, which has been difficult for some small molecule drugs. According to the main composition, nano-drugs can be divided into inorganic and organic, two main categories. Metallic and metallic oxide nanoparticles (NPs), such as silver[35], zinc oxide, titanium dioxide[36], *etc.,* are one of the most widely researched nanomaterials owing to the ease of size and shape control. Many types of biocompatible metal and metal oxide nanomaterials have been shown to process excellent bactericidal properties at *in vitro* and even *in vivo* levels. However, among all the inorganic nanomaterials, GNP is one of the most valued ones. The synthesis of GNPs, as well as their applications in anti-AMR/MDR bacterial infections, will be introduced in the following sections.

3.3 Activating GNPs as potential anti-AMR/MDR reagents

GNPs, as introduced above, have many handy properties, including strong optical properties like surface plasmon resonance (SPR), photothermic effects, and unique electrochemical activity that are essential to detections and treatments.[37] Due to the inertia, they can act as an excellent carrier to improve system stability.[38] Its high surface-to-volume ratio can increase the loading of either antimicrobial ligands or targeting molecules. Although a GNP does not have bacteria-killing properties itself [39], when applied *in vivo*, the load on its surface can experience a much longer clearance time, which can increase the effective

concentration of antibiotics over those used on their own.[40] Thus, in the treatment of bacterial infections, the GNPs are mainly served as carriers for antibiotics or adjuvants to enhance the antibacterial performance or endow the ability to overcome AMR/MDR (**Figure 3.3.1**). Generally speaking, ligands on the surface of GNPs are critical to their function, and the ligand design and synthesis are the most important part of the whole GNP-making route. Principles of a successful ligand design of GNPs include the appropriate ratio of stable ligands and effective ligands, as well as moderate hydrophilicity to guarantee their stability under the relevant biological environments. The application of ligands on antimicrobial GNPs has three goals: first, to protect ligands that block non-specific adsorption or control the formation of protein corona in plasma to maintain colloidal stability[41]; second, to enable the lethality of bacteria, which mainly comes from the original function of ligands or new capabilities gained by gold-ligand combinations; and third, to play a supporting role, including **1)** acting as an adjuvant to overcome the drug-resistant barrier[42 43], **2)** providing synergistic killing effects[44], **3)** providing responsiveness to the bacterial environment[45] or **4)** acting as targeting ligands to increase the selectivity to pathogens and prevent normal tissue damage.[32] Various types of ligands with different functions could be organically bound to one GNP.[46] It is also possible for a single ligand to achieve multiple functions, including antibacterial and targeting, by, for example, the conversion of environmental responsiveness to antibacterial groups (charge reversal, displacement of protective groups).[47 48] Below, I am going to give a detailed introduction to the ligands of antibacterial GNPs, classified by ligand type, as well as a general table which summarizes the ligand types, particle diameters, and antibacterial effects.

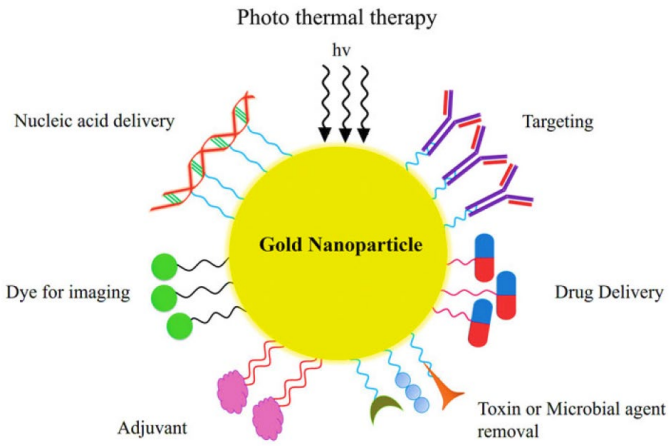

Figure 3.3.1 Methods of functioning GNP as an efficient antimicrobial reagent.[49] (Copied from the Taylor & Francis Publishing Group)

3.3.1 Antimicrobial small molecules as GNP capping ligands

The first big category is small molecular antibacterial materials such as antibiotics[50], antimicrobials, antimicrobial peptides[51], or bacterial growth inhibitors (for example, quorum sensing inhibitors[52]) (**Figure 3.3.2**). In general, connecting to GNPs offers a range of advantages, including an increase in the potency of killing, overcoming drug resistance, providing sites for targeting molecules or adjuvant molecules for co-capping, and increasing retention time or biocompatibility. The multiple binding sites for simultaneous capping of different ligands on the surface of GNPs could avoid the onerous chemical synthesis that possibly damages the efficacy or pharmacokinetic advantages. Taking antibiotics as an example, many antibiotics, including β-lactams[53], aminoglycosides[54], quinolones[55], glycopeptides[56], *etc.,* have been decorated onto the surface of GNPs to control infections and overcome antibiotic resistance. By comparing the MIC value with their free form, capping onto GNPs could significantly reduce the concentration required for bacteria-killing.[57] This is because the whole GNP-antibiotic nanoconjugate can act as a reservoir to significantly increase the half-life of antibiotics.[34 55] The conjugation with GNPs could also improve the stability of antibiotics under elevated temperatures.[4] Moreover, antibiotic resistance could be reversed, which is a viable solution to the global drug resistance problem. Although the mechanism is not very clear, it is speculated that the GNP surface

charge and hydrophobicity could induce the uptake of GNPs or interfere with the normal membrane potential and thus partly counteract the drug resistance. The binding of the whole nano-system with nucleic acids can interfere with normal physiological activities. In addition, due to the catalytic activity of GNPs, they could generate ROS, and these radicals could possibly work additionally to damage bacteria cells.[51] Since there are many articles with similar content, I will not give any further depiction here.[50–57]

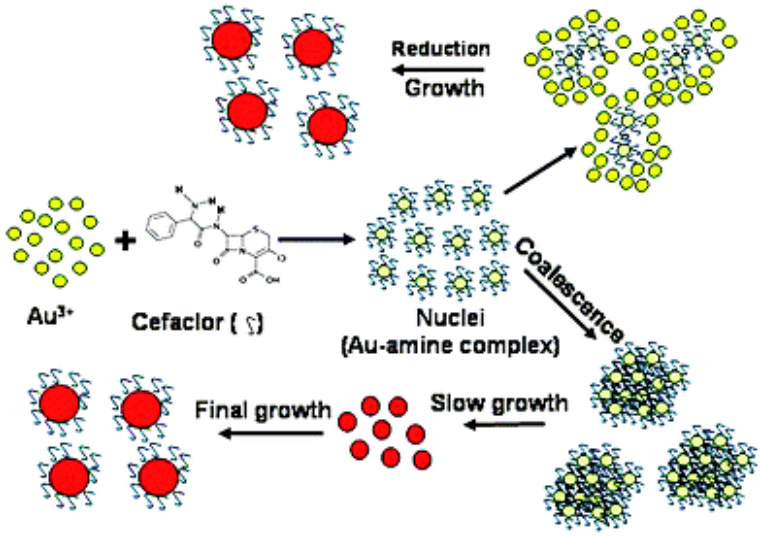

Figure 3.3.2 Possible formation mechanism of antibiotic(Cefaclor)-conjugated GNPs. Compared with the free form of antibiotics, conjugation onto GNP normally enhances their antibacterial property and could possibly serve as the solution to the MDR problem.[50] (Copied from the RSC Publishing Group)

Apart from antibiotics, other kinds of animal-secreted or natural bactericidal small molecules can also be applied in making GNPs, for example, antimicrobial peptides. Due to the easy cysteinylation modification and rich in sulfhydryl, amino, and carboxyl groups, peptides are capable of GNP decoration. Because of the easy degradation and high toxicity of free antimicrobial peptides, conjugation with GNP can also strengthen their effects and selectivity.[58] For example, a 7 nm GNP was decorated with LL-37 antimicrobial peptide for treating skin infection of diabetic wounds. The cationic charge of this GNP was utilised for the co-delivery of plasmids to promote recovery. Both enhanced antibacterial effects and synergistic skin repair were achieved with this system (**Figure 3.3.3**).[59] More importantly, the binding of antimicrobial peptide (VG16KRKP) with GNP was proved to process the ability to

treat intracellular *Salmonella* infections through penetrating cell membrane as well as interacting with bacteria lipopolysaccharide, whereas the application of GNPs or peptides alone did not have this effect.[32]

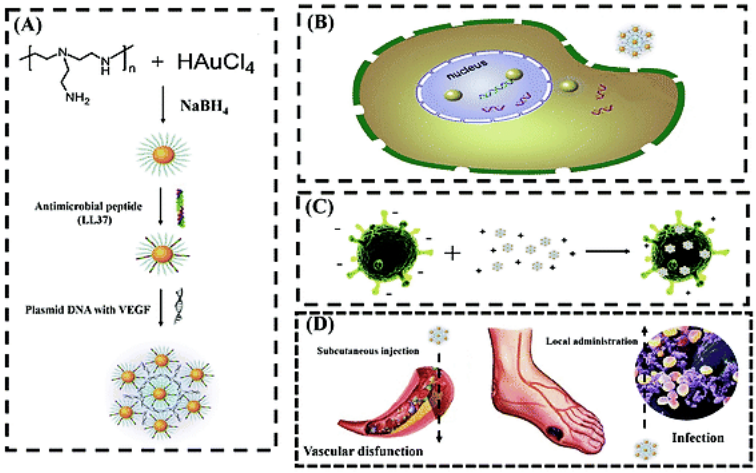

Figure 3.3.3 GNPs capped with PEI were further loaded with LL37 antimicrobial peptide as well as VEGF plasmid DNA for synergistic antibacterial and pro-angiogenesis.[59] (Copied from the RSC Publishing Group)

Biosynthesis is an efficient and safe method for the preparation of GNP. Many soil-oriented production microbial strains that can generate antibiotics, antimicrobial peptides, antimicrobial lipids, inhibitors, interfering proteins, enzymes, and other secondary metabolites can provide natural capping for GNPs during the fermentation process. Applying them for the green synthesis of antibacterial GNP is an attractive method. Elshaer et al. reported the application of *Streptomyces*-isolate S91 for the synthesis of GNPs for combating *P. a*. The prepared 12.2-nm GNP possessed the ability to quench the quorum sensing of bacteria, reducing the virulent factors by inhibiting communication between bacteria.[60] Traditional discovery of antibiotics from microorganisms requires the separation and purification of the antibacterial material from a mixture of metabolites. In contrast, this direct capping could overcome the onerous purification processes and slow down the rate at which resistance develops.

Plants can naturally resist bacterial infections. Thus, plant extract has many active molecules

with bacteriostatic or bactericidal abilities, including flavonoids, phenols, polyphenols, alkaloids, terpenes, organic acid, and other small molecular active antibacterial substances.[61] Using these substances as a capping ligand for GNPs could effectively enhance their bactericidal efficacy. In addition, the synthetic process is normally greener and safer.[62] It was summarised in an extensive review in 2020 that the extracts of all parts of plants (with leaves mentioned relatively more frequently compared with seeds, fruits, flowers, bark, peel, etc.) have been applied for the antibacterial coating of GNPs (**Figure 3.3.4**).[63] The target bacteria also contain common pathogenic Gram-positive bacteria (mostly *S. a*) and Gram-negative bacteria (*P. a*, *E c*, and *K. p*) that have high MDR development, with an average diameter of the inhibition zone as high as 10–20 nm. However, most of these plant extract-derived capped GNPs demonstrate a wide size distribution and non-uniform shape with a relatively large batch-to-batch variation.

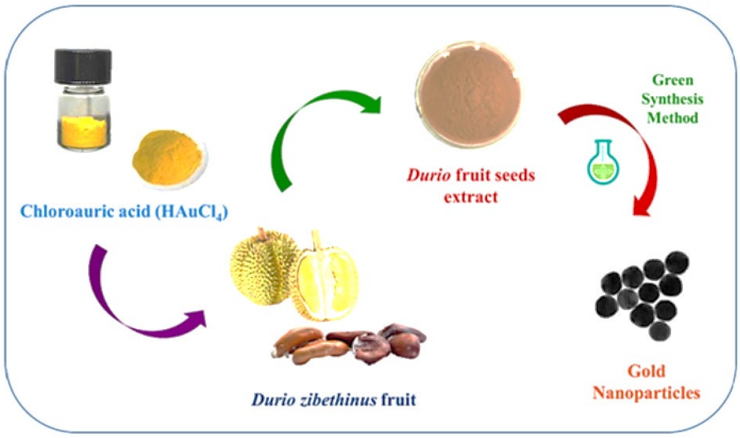

Figure 3.3.4 Mechanism of the synthesis of *Durio zibethinus*-extract-capped GNPs. This GNP has an antibacterial effect on both *Pseudomonas desmolyticum* and *S. a.*[64] (Copied from the Medcrave Publishing Group)

In addition, many antimicrobials could also be used for the capping of the GNP surface. For example, surfactants could serve not only as the stabiliser to prevent GNP aggregation but also as the antibacterial ligand to kill bacteria. Quaternary ammonium ligand, due to the exposed positive charge, could grant the GNPs a high cationic charge on the surface.[65] Alkylated quaternary ammonium could effectively inhibit the Gram-positive bacteria growth

and then induce the membrane rupture, and this ability is strongly related to the optimum carbon chain length. Through Coulomb force interaction, the positive quaternary nitrogen could interact with negatively charged phospholipids of the bacteria cell envelope. Further insertion of the alkyl chain into the phospholipid bilayer could then rupture the bacterial membrane.[66] Li et al. studied the influence of surface chemistry on the antibacterial ability of GNPs by applying different functional groups to replace the side chain of quaternary ammonium (**Figure 3.3.5**). It was observed that the side chain hydrophobicity has a positive relationship with the antibacterial ability of the corresponding GNP. The optimised GNP has a considerable antibacterial effect on 11 clinically isolated Gram-positive and Gram-negative MDR strains, with the toxicity toward mammalian cells greatly reduced. In addition, the generation of resistance toward this GNP was delayed to over 20 generations, indicating bacteria have difficulty in resisting this mechanism.[67] In addition, it was reported in 2016 that by adjusting the quaternary ammonium ligand to carboxylic acid ratio, the antibacterial spectrum of GNP could be tuned in between Gram-positive and negative.[68] Another commonly used surfactant cetyltrimethylammonium bromide was also used to synthesise antibacterial GNPs that could inhibit the growth of pathogenic *E. coli.*[69] The application of biosurfactants in the synthesis of antibacterial GNPs is a new research topic. The synthesis of these biodegradable biosurfactants is usually clean and environmentally friendly, catering to the development trend of GNP synthesis. The application of lipopeptide biosurfactant derived from *Acinetobacter junii* was used for the preparation of 10–17 nm GNPs, which showed a broad-spectrum antibacterial ability to 7 pathogens with low somatic toxicity.[70] Gómez-Graña et al., used the biosurfactants extracted from steep corn liquor for the one-step synthesis of GNPs against *P. a*, *E. c,* and *S. a*. The surfactant produced by non-pathogenic fermentation bacteria made the synthesis process environmentally safe.[71] However, due to the high hemolytic potency of these surfactants, the biosafety of surfactant-capped GNPs should be considered on an equal footing with antimicrobial performance.[72]

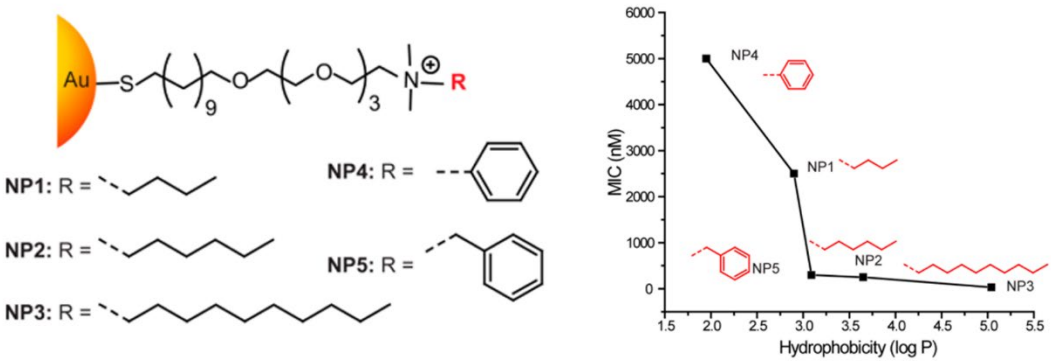

Figure 3.3.5 The antibacterial ability (MIC) of quaternary ammonium ligand-capped GNP was adjusted by changing the R group on the side chain. Comparatively, hydrophobicity is positively correlated with the GNP's antibacterial efficiency.[67] (Copied from the ACS Publishing Group)

3.3.2 Non-antibacterial small molecules exhibit antibacterial properties upon GNP coating

The second main category of ligands consists of small molecules that do not have or have extremely limited antimicrobial viabilities. However, upon the coating on the GNP, the entire nano-system can show strong antimicrobial abilities. Among these, some even have a wide spectrum and indiscriminate bactericidal effect on MDR strains, which provides a superior weapon to defeat superbugs. 4,6-Diamino-2-pyrimidinethiol (DAPT) is one of the most representative reagents reported in 2010.[46] It is an analogue of the tRNA subunit in *E. c* and has a positive charge. However, it shows almost no antibacterial effect against bacteria when applied in free molecular form (**Figure 3.3.6**).

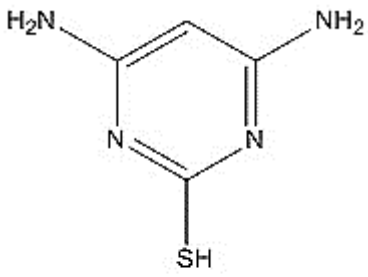

DAPT

Figure 3.3.6 Chemical structure of DAPT. The structure of the aminopyrimidine makes it positively charged, facilitating binding to bacteria.

When conjugated to GNPs, it shows strong antibiotic ability, especially against Gram-negative MDR strains with a MIC value as low as 6 μg mL^{-1} for MDR *E. c* and 18 μg mL^{-1} for MDR *P. a.*[46] From the proteomic research result, Yan et al. deduced that the drug would change membrane potential and inhibit ATP synthase activities by decreasing the ATP level, causing the decline in metabolism, as well as inhibiting the subunit of the ribosome for tRNA binding, indicating a collapse of the biological process.[37] This attack on membrane potential and multi-target interaction can effectively bypass many MDR bacterial resistance mechanisms, making it difficult for bacteria to develop resistance (Figure 3.3.7).[73] Compared with the ROS generating method, this strategy is much safer for tissue cells. Based on this finding, many derivatives that share similar structures have also been proven to have the bactericidal ability.[74] Successful incorporation of bacterial cellulose combined with DAPT anti-infection membrane was developed as a wound dressing and showed potential for *in vitro* and clinical applications.[75] In addition, by simply coating the DAPT-GNPs onto the surface of different substrates, including glass, plastics, silica gel, and ceramics, with facile plasma treatment, these treated surfaces could resist Gram-negative strain colonisation and prevent infections. The GNPs are immobilised on the surface and would not induce worries about entering the human body or causing the potential for drug-resistance development.[76]

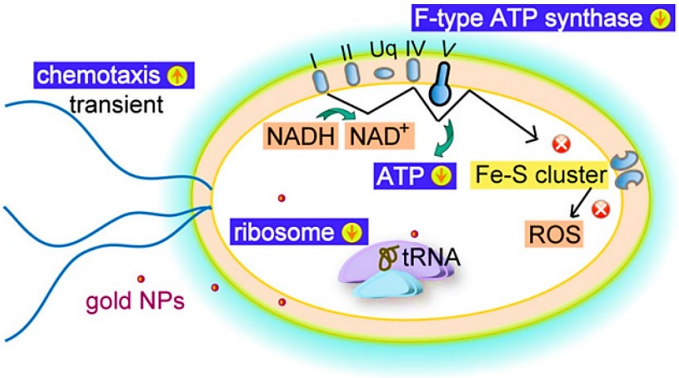

Figure 3.3.7 Antibacterial mechanisms of DAPT-GNP against *E. coli*. Through inhibiting the F-type ATP synthase, the oxidative phosphorylation pathway was down-regulated, resulting in reduced ATP levels. In addition, the ribosomal function was also inhibited, causing a slowdown of the translation process. The influence also includes a transient upregulation of the chemotaxis ability.[73] (Copied from the ELSEVIER Publishing Group)

Despite having a good antibacterial effect on Gram-negative strains, the DAPT-GNP has limited efficiency toward Gram-positive MDR bacteria. Notably, through co-decorating with non-antibiotic drugs (for example, metformin), the antibacterial spectrum could be expanded to Gram-positive strains like MRSA or MDR *E. faecium.*[77]

Besides DAPT, non-antibacterial indole derivatives were also applied as GNP capping for combating MDR Gram-positive infections. The MIC value could be reduced from >128 μg mL^{-1} to 2 μg mL^{-1} against MDR *E. c* strains. After being spun into PLGA sheets by electrospinning, the antibacterial ability of indole-capped GNPs was preserved and demonstrated excellent antimicrobial efficacy in wound healing models (**Table 1**).[78] Other nitrogen-containing heterocyclic small molecules, including imidazole, triazole, benzothiazole, purine, and penicillanic acid, also showed enhanced antibacterial and antibiofilm abilities after coating onto the GNP surface.[79] Besides, the application of pharmaceutical intermediates for the coating of GNPs has also been shown to possess the ability to overcome MDR by inducing bacteria cell envelope damage. These GNPs with high antibacterial activities demonstrated excellent performance in combating the MDR Gram-negative bacteria-induced infections and accelerating the healing process of the full-

thickness wound on the back of rats.[80] In addition, the D-glucosamines, an analogue of the cell wall component—N-acetylglucosamine, -capped GNPs, could interfere with the formation of bacterial cell walls. Due to this working mechanism, this acetylglucosamine-capped GNP has a strong ability to treat Gram-positive bacterial infections and effectively inhibit the growth of MRSA and MRSE in skin infection models.[81] Badwaik et al. have reported the synthesis of 25, 60, and 120 nm GNPs with dextrose with a green method. Dextrose, a non-antimicrobial, was used as both a capping and reducing agent. Dextrose-GNP displayed broad-spectrum antibacterial ability and inhibited the growth of MDR Gram-positive and -negative strains by disrupting the integrity of the cell membrane and causing cell content leakage. Further study revealed that the potency was proportional to the particle size.[82]

Table 1 The MIC comparison of indole derivative small molecules in free form and after decorating onto the GNPs.[78] (Copied from the ACS Publishing Group)

IDs		MIC (μg/mL)		IDs		MIC (μg/mL)	
		Au_IDs	IDs			Au_IDs	IDs
ID	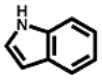	7	>128	5-BI	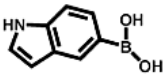	15	>128
W	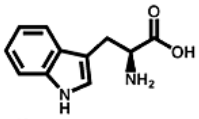	4	>128	5-CLI	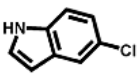	30	>128
4-AI	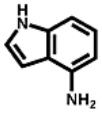	8	>128	IAA	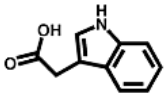	24	>128
5-AI	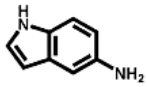	4	>128	5-CNI	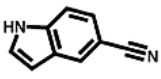	13	>128
6-AI	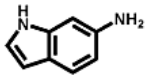	13	>128	4-HI	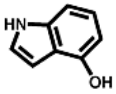	17	>128
7-AI	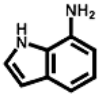	11	>128	3-SI	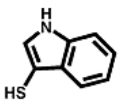	>50	>128

3.3.3 Macromolecules as capping ligand for antibacterial GNPs

The third category is the application of macromolecules, including natural macromolecules and artificial polymers. Natural macromolecules, including antimicrobial enzymes (lysozyme)[83], DNA (aptamer + antibiotics)[84], chitosan[85], lectin[86], polysaccharide[87], and phage[88] have been used for decorating GNPs to achieve a good antibacterial effect (**Figure 3.3.8**). Conjugation with these natural macromolecules could either provide targeting ability or enhance the bactericidal effect toward the MDR pathogens.

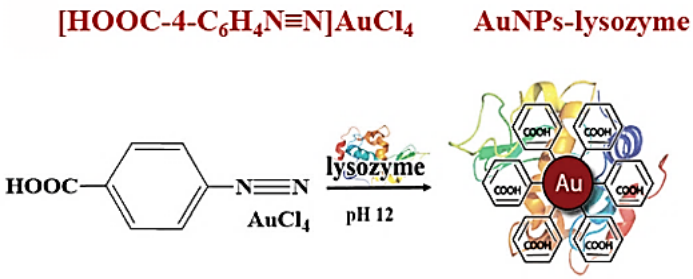

Figure 3.3.8 Fabricating mechanism of lysozyme-decorated GNP. The GNP was applied for combating broad-spectrum MDR bacterial infection, with high selectivity and biosafety.[83] (Copied from the RSC Publishing Group)

In comparison, synthetic polymers of the antibacterial GNP capping are manifold, and the synthetic methods are also various. For instance, in 2015, Boomi et al. used polyvinylpyrrolidone and pristine polyaniline for the direct synthesis of antibacterial GNPs. These 5 nm GNPs could inhibit the growth of both Gram-positive and Gram-negative pathogens.[89] In addition, according to Hareesh et al., polycarbonate-capped GNCs were prepared by gamma-ray-assisted diffusion. Compared with the pure polycarbonate matrix, the GNP-polycarbonate showed a significantly increased inhibition zone, which is attributed to the slow generation of ROS by the small-sized GNPs.[90] Polydopamine is a bionic macromolecule derived from mussel adhesive proteins. It mainly kills bacteria through direct contact-active antibacterial effect, photothermal effect, or ROS generation.[91] As a commonly used antimicrobial coating, polydopamine has also been used for the capping of GNPs. Xu et al., deposited GNPs on polydopamine-coated hydroxyapatite. The PDA@Au-HAp NPs could generate hydroxyl radicals. At a controlled temperature, the combination of photothermal

and photodynamic treatment could kill over 95% of *S. a* as well as *E. c* and increase wound healing pace.[92] Besides linear polymers, dendritic polymers are also applied for the synthesis of GNPs. Polyethyleneimine (PEI), for instance, was combined with PEG for the preparation of GNPs that could suppress the formation of pathogenic biofilm and act as an adjuvant to partial breakthrough resistance.[52] To date, many polymer-capped GNPs are commonly used for antibacterial material delivery (**Figure 3.3.9**).[93] Synthetic polymers are complicated, and further block design can give them multifunctionality. As capping ligands, they could provide GNPs with good stability, antibacterial ability, environmental responsiveness, and stronger binding capacity.

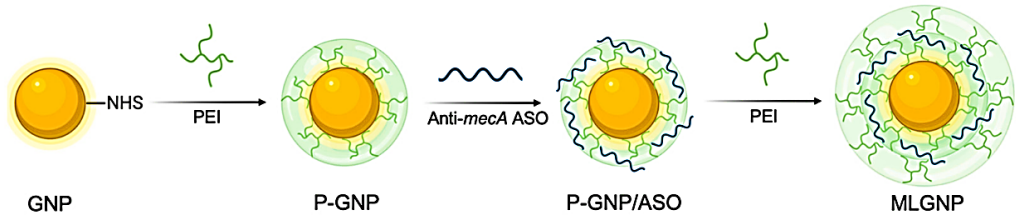

Figure 3.3.9 PEI-conjugated GNP was applied for the delivery of antibacterial antisense nucleotide fragments through electrostatic absorption.[93] (Copied from the ELSEVIER Publishing Group)

3.3.4 Ligands as adjuvants to enhance the physical properties of the GNP

The fourth category is taking advantage of the unique physiochemical properties of GNP (mainly optical effects). Many molecules that can target bacteria or enhance the physical properties of GNP were applied as surface capping to fabricate antibacterial GNPs. The application of additional physical conditions (like laser radiation) could then overcome most of the biological barriers of drug resistance, providing a new resolution to the MDR problem. Generally, due to the SPR effect, GNP has significantly enhanced photothermal and photodynamic effects, which is the basis for both photothermal therapy (PTT) and photodynamic therapy (PDT). The high temperature or ROS they generate under visible light or UV will effectively inactivate bacteria.[94] Modification of targeted molecules on GNPs to selectively bind bacteria and then applying PTT can further reduce the damage to ordinary tissues. Antibiotics or antibodies that could selectively interact with bacteria cells could be

applied as targeting molecules, thus enhancing the selectivity and potency of the GNP photothermal ablation. Moreover, combined with high-resolution photothermic thermolens imaging mode, the detection of bacteria could be achieved simultaneously. For example, anti-protein A antibody was used for the decoration of 10, 20, and 40 nm GNPs to form the "sandwich structure" on the Gram-positive bacteria cell wall. Combined with 420–570 nm focused laser pauses, the overheated GNPs could induce bubble formation in the GNP clustered region, which could then eliminate over 95% of *S. a* in *in vitro* model.[95] Huang et al. reported the synthesis of 808 nm NIR laser-activated vancomycin-capped GNPs for the PTT to not only MDR Gram-positive bacilli (VRE) and cocci (MRSA) but also Gram-negative MDR *A. b* and *E. c*. 5 min irradiation could reduce the total amount of all MDR pathogen species to lower than 0.5%.[96] Besides antibodies or antibiotics, similarly, various antimicrobial peptides have also been applied for the PTT of GNPs (**Figure 3.3.10**).[97] However, due to the local overheating, which is detrimental to normal tissue, the photothermic treatment of bacterial infection is normally restricted to superficial infections and has already found its application in more suitable research fields like cancer treatment.

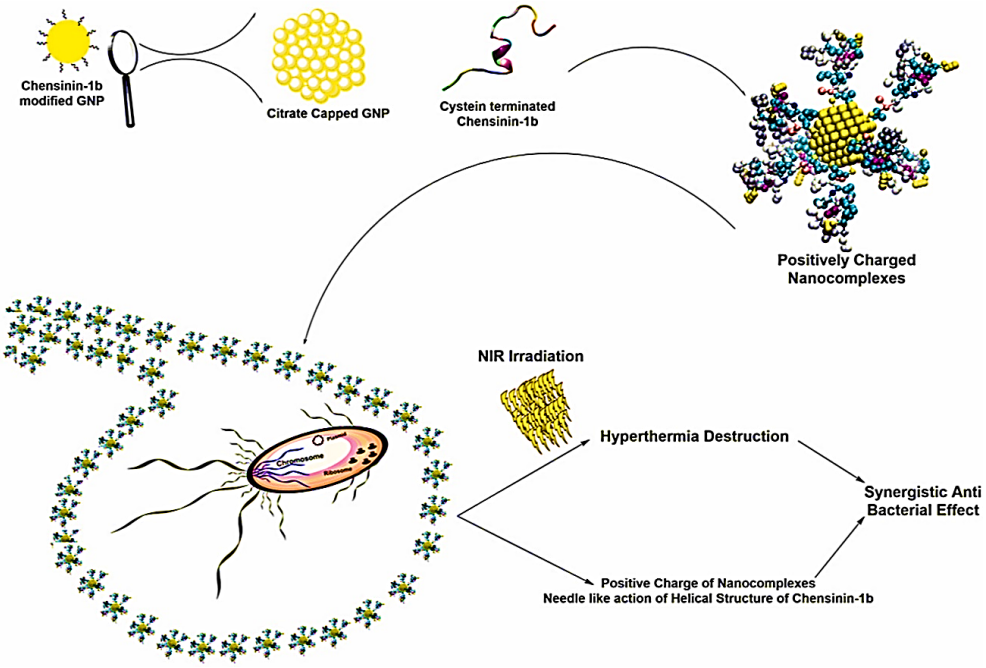

Figure 3.3.10 Synthesis of Chensinin-1b-conjugated GNPs for the photothermal ablation of MDR bacteria. This antimicrobial peptide is derived from frog skin.[97] (Copied from

the ELSEVIER Publishing Group)

Apart from this, the photo-catalyst or photodynamic effect of GNPs can help generate ROS and further destroy the integrity of bacteria cells.[98] This effect is normally enhanced by combining with photosensitive dye molecules, including methylene blue (630 nm) to kill *S. epidermis*[99] and *Streptococcus mutans*[100], toluidine blue O (632 nm) to kill MRSA[101], chlorin e6 (white light) to kill MRSA[102], riboflavin (520 nm) to kill *S. a* and *P. a*[103], and hydroxyaluminum phthalocyanines (650 nm) to kill *S. a*[104] (**Figure 3.3.11**). However, due to the limitation of safe laser power and penetration depth, the photothermal effect induced by GNPs is sometimes not strong enough for treatment, so combining photothermal with photodynamic is an attractive approach. Alvi et al. reported the synthesis of liposomal wrapped GNPs capped with curcumin for the dual-modality treatment of acne induced by *propionibacterium acnes*. Through iontophoresis, the GNP was successfully delivered through the skin and damaged the sebaceous glands to stop infection. By implying sequential irradiation with NIR (photothermal) and blue light (photodynamic), the GNP could well inhibit the growth of bacteria, providing feasibility of this strategy (**Table 2**).[105]

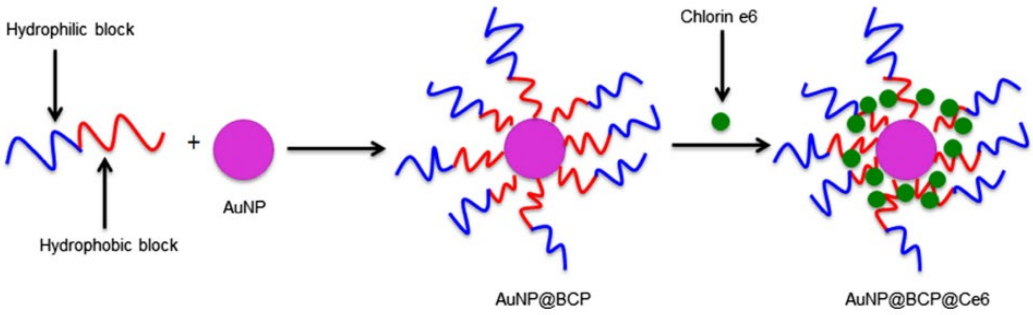

Figure 3.3.11 Synthetic scheme of the amphipathic GNP loaded with hydrophobic photosensitizer (Ce6) for PDT treatment of MRSA.[102] (Copied from the ACS Publishing Group)

Table 2 Summary table of parameters of GNPs mentioned in this section

GNP Size (nm)	Zeta Potential (mV)	Ligand Name & Ligand Type (Ab/nAb/M/Aj)	Bacterial Species (MIC) ($\mu g\ mL^{-1}$)	Ref.
20–30	–31.5	Vanillin (nAb)	*P. a** (Synergy with Meropenem & Trimethoprim)	42
20.1±2.4	–26.1	Citrate (nAb)	Sepsis (Not indicated)	43
30	–	Citrate (nAb)	*Salmonella typhimurium* (2.5) *Salmonella typhi* (5) *Salmonella enteritidis* (2.5) (Synergy with Cefotaxime and Ciprofloxacin)	44
14	–20–+15	HS-C_{10}-COOH HS-C_{10}-N_4^+ (nAb)	*S. a** (Not indicated)	45
3	+18.6 ± 7.3/ +16.1 ± 10.0/ +14.5 ± 9.9/ -48.5 ± 4.5	DAPT/APT/iDAPT/DHPT (nAb)	*E. c**(6) and *P. a**(16/18/24/-)	46
12	+24	HS-$DLL_{90}BLG_{10}$ (Ab)	*S. a**, *S. h*, *B. s* (3.13–12.5)	48
22–52	–	Cefaclor (Ab)	*S. a* (10), *E. c* (100)	50
10–20	–9.39	Apple extract & Trisodium citrate (nAb)	*P. a* (68.56–75.01, IC_{50})	52
27–30	–23	Imipenem (Ab)	*P. a* (21)	53
15	–	Gentamicin (Ab)	*E. c* (7.4)	54
4–5	–	Vancomycin (Ab)	*E. f** (VRE) (2–8)	56

14	–	Ampicillin/Streptomycin/Kanamycin (Ab)	*E. c* (2.453–4.545), *Micrococcus luteus* (1.712–10.493), *S. a* (2.132–16.659)	57
15	+26	Cecropin melittin (Amp) (Ab)	*S. a*, *E. c*, *P. a*, *K. p* (10)	58
7	+36	LL37 peptide (Ab)	*S. a** (1)	59
12.2	–29.7	*Streptomyces* cultivation supernatant (Ab)	*P. a* (9.2–36.9)	60
16–18	–31.2	*Coleus aromaticus* leaf extract (Ab)	*S. e*, *E. c* (Not indicated)	62
2	–	Quaternary ammonium ligand of mercaptopolyethylene glycol (Ab)	*S. a** (64), *E. c** (16), *P. a** (16), *Enterobacter cloacae**(8)	67
2.5±0.6/5.2±0.5/9.5±0.8	–50	HS-$C_{11}H_{22}$-NMe_3^+ HS-$C_{11}H_{22}$-COOH HS-$C_{11}H_{23}$ (Ab)	*E. c*, *A. b*, *S. a*, *E. f*	68
1–22	–	Cetyltrimethylammonium bromide (CTAB) (Ab)	*E. c*	69
10–100	–30.1±1.3	Corn steep liquor extract (Ab)	*E. c*, *P. a*, *S. a* (Not indicated)	71
–	–	DAPT (nAb)	*E. c* (4)	73
<2	–38.6/+12.7/+33.6/+37.6	DAMP/AMP/AHMP/DHMP (nAb)	*E. c**(8–32), *S. a**(2–32), *A. b**(2–64), *K. p**(2–16), *P. a**(4–32), *E. f**(8–128)	74
~3	–	DAPT (nAb)	*E. c** (4), *P. a** (8–16),	75
2	–	DAPT/G/DMB/CPB/CQ/Ach/Mel (nAb)	*E. c**(1–4), *P. a**(4–16), *K. p**(2–4), *A. b**(1–2), *S. a**(8–>64), *S.*	77

			e(16–>64), *Streptococcus suis**(16–64), *E. f**(16–64)	
5.55–10.55	–16.3±2.93/–27.6±1.08	Indole derivatives (nAb)	*E. c**(2–4), *P. a**(4), *K. p**(2–4), *A. b**(4)	78
4.83–7.33	–16.16–+18.71	AMBT/AMP/APA/ATT/MI (nAb)	*E. c**(7.5–16), *S. a**(16–>128),	79
3.5	–27.8±1.1—–23.4±1.4	6-APA/7-ACA/7-ADCA (nAb)	*E. c**(2.5–32), *K. p**(2.5–>64), *P. a*(5–>64)	80
–	–	D-glucosamine (GluN) (nAb)	*S. a**(4), *S. e**(4), *B. s*(4), *E. f*(8), *Listeria monocytogenes*(8)	81
25/60/120	–	Dextrose (nAb)	*E. c*(16×10^{10} mL^{-1}), *S. e*(16×10^{11} mL^{-1}),	82
8±4/18±10	+69.6±0.6	Lysozyme (M)	*E. c**(0.49–1.94), *P. a**(0.97), *K. p*(1.94), *S. a*(15.54), *Salmonella typhimurium*(1.94), *Haemolyticus bacillus*(1.94)	83
14–38	–	Chitosan (M)	*S. a**, *P. a**(Not indicated)	85
15–60	–	Lectin (M)	*E. c**(8), *P. a**, *K. p*, *A. b*, *S. a**(5)	86
20–30	–41—4.16	Exopolysaccharide (EPS)+antibiotics (M)	*K. p*(0.281–1.125), *E. c**(<0.07–1.125), *S. a*(0.562–2.5)	87
20–100	–	Bacteriophage lysate (M)	*E. c*, *P. a*, *K. p*, *Salmonella paratyphi* B, *Proteus vulgaris* (Not indicated)	88

~5	–	Polyvinylpyrrolidone (PVP) & Pristine polyaniline (PANI) (M)	*E. c, Klebsiella, Staphylococcus and Streptococcus*	89
~110	–	Lexan (M)	*E. c*, *S. a* (Not indicated)	90
4.9±0.9	–	Polydopamine (PDA), Hydroxyapatite (Hap) (M)	*E. c*, *S. a* (Not indicated)	92
40	–	Antibody(anti-peptidoglycan) (Aj)	*S. a** (Not indicated)	93
10/20/40	–	Antibody(anti-protein A) (Aj)	*S. a* (Not indicated)	95
–	–	Vancomycin (Aj/Ab)	*S. a**, *E. c*, *Streptococcus pyogenes*, *A. b**, *E. f**	96
54	–	Chensinin (AMP) (Aj)	*P. a*, *S. a*, *A. b*, *E. c*	97
~15	–	Naked GNP	*E. c* (0.5)	98
~13–16	–	PEG-SH, methylene blue (Aj)	*S. e* (Not indicated)	99
28	–	Methylene blue, sucrose (Aj)	*Streptococcus mutans*(78.125–93.75)	100
1.8–2	–	Tiopronin, toluidine blue O (TBO) (Aj)	*S. a**(0.5 μM)	101
~40–100	–34	Poly(NIPAAm-b-styrene), chlorin e6 (Ce6) (Aj)	*S. a**(Not indicated)	102
17±7	–38–0	Pectin, riboflavin (Aj)	*S. a*, *P. a* (50 μM)	103
13–22	–18±3	Cell-free filtrate of *Coriolus versicolor* and hydroxyaluminum phthalocyanines (Aj)	*S. a*(Not indicated)	104
~100–12	+20	Liposomal curcumin	*Propionibacterium*	105

0		(Aj)	*acnes*(200)	

Asterisk (*) indicates corresponding resistant strains.

Ab—antimicrobial small molecules; nAb—non-antimicrobial small molecules; M—macromolecules; Aj—adjuvant or supporting molecules; DAPT/DAMP—4,6-diamino-2-pyrimidinethiol; APT/AMP—4-amino-2-pyrimidinethiol; iDAPT—2,4-diamino-6-pyrimidinethiol; DHPT/DHMP—4,6-dihydroxyl-2-pyrimidinethiol; DLL—D,L-lysine; BLG—γ-benzyl-L-glutamate; AHMP—4-amino-6-hydroxyl-2-mercaptopyrimidine; G—Guanidine; DMB—1,1-dimethylbiguanide; CPB—1-(3-chlorophenyl)biguanide; CQ—chloroquine; Ach—acetylcholine chloride; Mel—melamine; AMBT—6-amino-2-mercaptobenzothiazole; AMP—2-amino-6-mercaptopurine; APA—6-aminopenicillanic acid; ATT—3-amino-1,2,4-triazole-5-thiol; MI—2-mercaptoimidazole

3.4 Recent development of GNC as an antibacterial reagent for controlling AMR and MDR infections

3.4.1 Comparison of properties of GNC and GNP as antibacterial materials

As introduced in the last section, using GNP-based antibacterial materials to target bacterial infections and prevent resistance development is a highly effective strategy. In contrast, due to the short development time, earlier GNCs typically have high hydrophobicity and low bioavailability. These hydrophobic GNCs have been extensively studied in research areas like optics, catalysis, and electromagnetism. However, with the improvement in the synthetic method, the toxic low-polarity solvent was gradually replaced by less toxic high-polarity solvents (aqueous phase). In addition, the capping ligand was also replaced by biosafe or even physiologically derived molecules. Thus, their application in bioimaging and medication has emerged (**Figure 3.4.1**).[106] In terms of antibacterial application, although I have introduced many advantages of GNP, like easy preparation, inertness, and the ability to activate non-antimicrobial molecules, *etc.,* in the section above, the overall antibacterial efficiency of GNP is limited. Below I will compare the properties of GNC and GNP to demonstrate the advantages of GNCs in antibacterial applications.

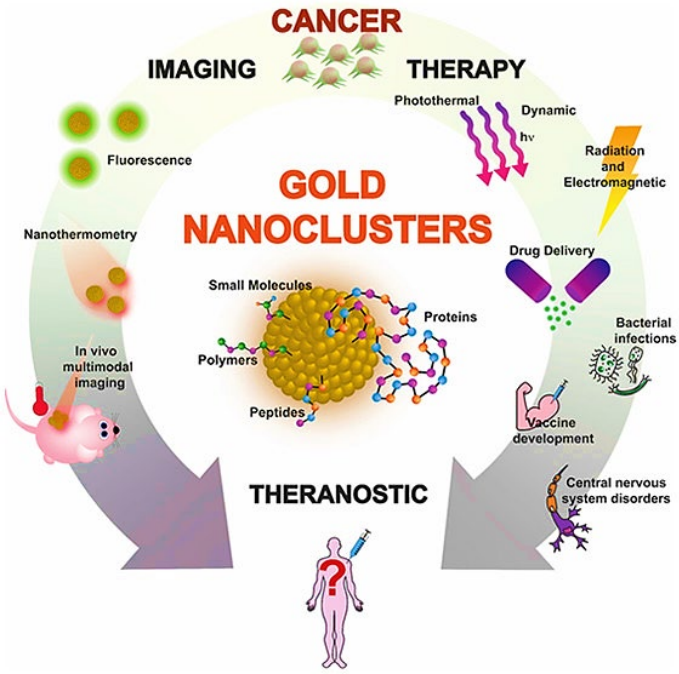

Figure 3.4.1 Schematic demonstrating the biomedical applications of GNCs in each aspect of the theranostics.[106] (Copied from ACS Publishing Group)

3.4.1.1 Size

Because of the relatively big size (usually ~10–100 nm) of GNP compared with bacteria (usually 1-2 µm), the binding and internalisation of GNP are usually limited. In addition, their lower surface-to-volume ratio, compared to GNCs, also makes binding less efficient and causes internal Au(0) atom waste, as these atoms are not linked with any ligand. For *in vivo* application, these GNPs are significantly larger than the renal clearance threshold (5.5 nm), making it difficult to elicit efficient body clearance, resulting in accumulation in the body. Their atomic uncertainty and batch-to-batch variation also limit their drug potential. Comparatively, GNCs not only possess most of the advantages of GNPs but also show virtues in many aspects. In terms of size, GNC is significantly smaller than that of bacteria (over 500 times smaller) and even smaller than the size of peptidoglycan pore (6–60 nm) and pore size of porin (1.2–2 nm) on bacteria membrane[107], as well as the glomerular basement membrane pore size (7–10 nm).[108] Thus, the GNC could not only penetrate the cell envelope but also have a high renal clearance efficiency (**Figure 3.4.2**).

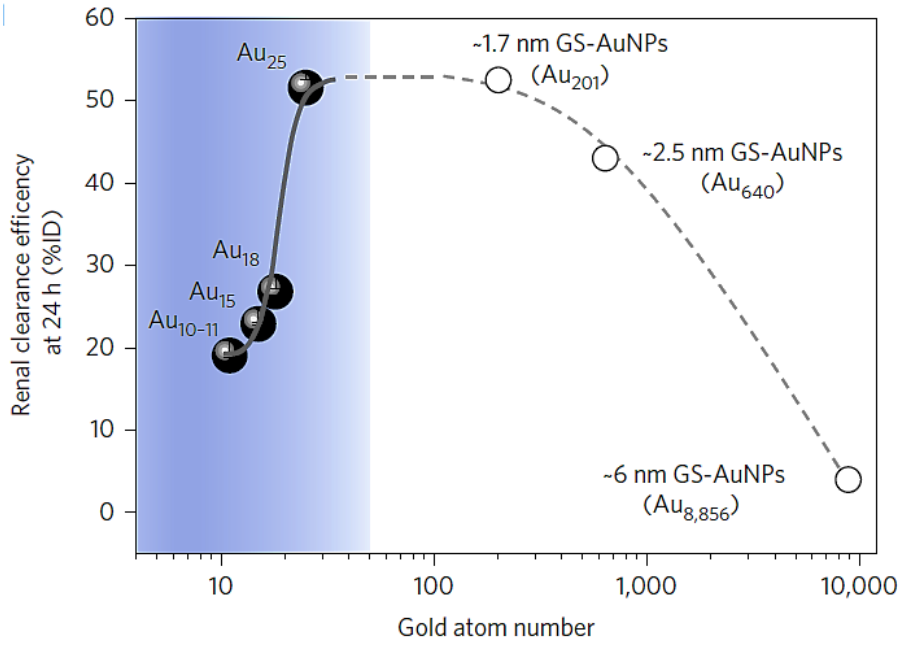

Figure 3.4.2 Relationship between the GNC/GNP size and their renal clearance efficiency. For GNCs, the slight change in the atomic number of its Au kernel significantly influenced the renal clearance property.[108] (Copied from Nature Publishing Group)

3.4.1.2 Binding affinity

The small size greatly enhances the surface energy of GNCs, so the surface ligands are widely exposed, making the binding process easier. Moreover, the Au atoms are highly occupied in the GNC structure, either contributing to the structural stability (in the Au kernel) or providing anchoring for the surface capping ligands. Thus, each Au atom is indispensable to the system's integrity, and there is no atom waste. In terms of druggability, the configuration of a certain species of GNC is defined. Thus, the batch-to-batch difference could be greatly reduced to ensure the reproducibility of GNC-based drugs. Due to its molecule-like property, the binding process and drug interactions are also clearer and could be simulated through calculation.[109]

3.4.1.3 Unique characters

Many unique properties of GNC, including ROS generating ability, high penetration fluorescence, nonlinear optical properties, catalytic ability, and chirality, have all

contributed to its biological application. Many articles have been focusing on the improvement of the antibacterial effect by reducing the size of gold nanomaterials. For example, Xie et al. reported the anti-MDR strategy by reducing the size of antibacterial DAPT-GNPs. They discovered that with the decrease of the GNP size from 14 nm to 3–4 nm, the antibacterial ability appeared merely toward Gram-negative bacteria (MDR-*A. baumannii*/*E. coli*/*K. pneumoniae*) with 4 μg mL^{-1} MIC. Significantly, a further decrease in the GNP size to the GNC range (less than 2 nm) could enable a wide spectrum killing to both MDR Gram-positive and -negative strains. The MICs are as low as 2.5–5 μg mL^{-1}. From GNP to GNC, the antibacterial effect was improved over 60-fold to broad-spectrum bacteria.[110] Similarly, Zheng et al. reported the antibacterial ability of DAPT-GNP with size modulation. The reduction of DAPT-GNP size gradually increased its antibacterial effect, consistent with previous conclusions. However, in the experiments against the development of drug resistance, the 1.8-nm GNC and 8.2-nm GNP showed little elevation in MIC values, but the middle-sized 3.5-nm GNP is not as efficient as the other counterparts. In addition, the drug resistance of *E. coli* toward the GNCs is mechanistically hard to develop (**Figure 3.4.3**).[111] Below, I will review antibacterial GNCs categorised by capped ligand type and then summarise what I have learnt from these strategies. At the end of this chapter, a summary table will be given.

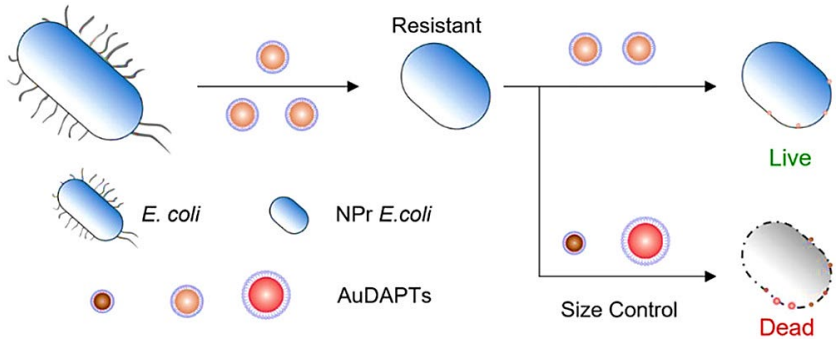

Figure 3.4.3 Influence of the particle size of AuDAPT on their antibacterial ability. Both the small-sized GNC and the 8.2-nm GNP could effectively activate non-antibacterial small molecules and inhibit the growth of E. coli. While the medium-sized GNP shows no obvious antibacterial ability.[111] (Copied from ACS Publishing Group)

3.4.2 Antibacterial material as capping ligand for GNCs

3.4.2.1 Antibiotics

Due to the ultrasmall size of GNC, the internalisation or diffusion of GNCs into a cell is higher than GNPs. Thus, linking antibiotics to GNC could be an effective strategy to improve the overall drug delivery efficiency and partly compensate for the effect of the drug efflux pump.[112] Besides, the synthesis of water-soluble GNCs is facile. Furthermore, by co-conjugating targeting and biocompatible molecules to the GNC, the antibiotics could be directed to bacteria while avoiding no target tissue to further improve compatibility. Thirdly, binding with GNCs could significantly alter the pharmacokinetics of antibiotics, thus possibly prolonging the drug onset time and half-life. Finally, the GNC could generate ROS that could damage macromolecules and interrupt normal physiological activity. Therefore, linking antibiotics to GNCs can have additional or even synergistic antibacterial capabilities compared with free antibiotics.[113]

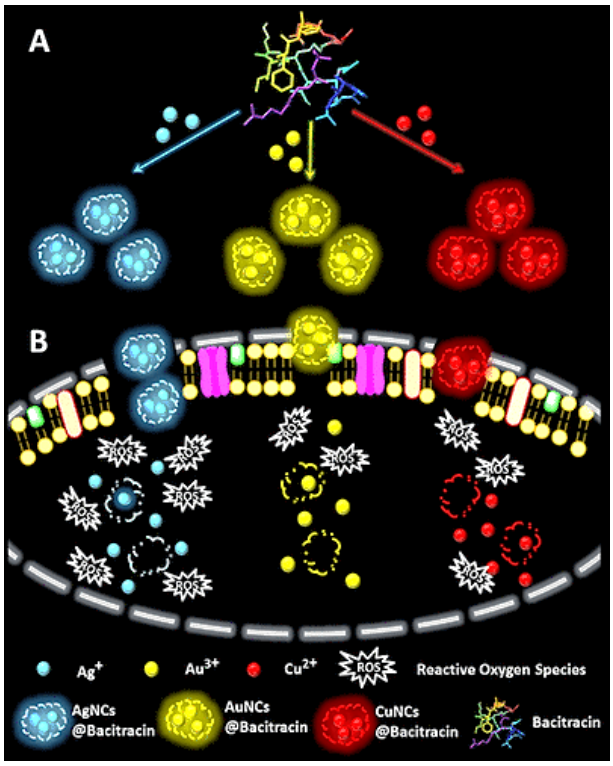

Figure 3.4.4 Differently fluorescent Au/Ag/Cu NCs were applied for the selective antibacterial application after linking with bacitracin.[114] (Copied from ACS Publishing Group)

Wang et al. reported the synthesis of multicolour-emitting Ag, Cu, and Au NCs with one antibiotic—bacitracin and measured their antibacterial effect (Figure 3.4.4). The ~2 nm bacitracin-capped GNCs showed considerable antibacterial ability against *S. a*. A significant increase in the ROS level was observed for the AuNCs@Bacitracin, which could be the reason for its increased antibacterial property.[114] In 2018, Kalita et al. reported the study of decorating ampicillin onto lysozyme-capped GNCs. The co-presence of these two antibacterial reagents could not only reverse the MRSA resistance to ampicillin but also additionally increase the antibacterial efficiency toward MSSA. GNC in this study was applied as an excellent carrier for increasing both the concentration of ampicillin in the foci and the permeation of both antimicrobials. In addition, the GNC was able to interrupt the function of the efflux pump. Together with the bacterial lytic function of lysozyme, the GNC could overcome the drug resistance and cure the MRSA infection in diabetic wound infection.[115] Vancomycin, a member of the glycopeptide antibiotics, is widely applied for the treatment of critical Gram-positive bacteria-induced infections. Using vancomycin (Van) as the template and reducing agent, Liang et al. successfully prepared fluorescent AuNC@Van for antibacterial applications. Notably, the antibacterial spectrum of Van-GNC was shifted toward Gram-negative strains, with an improved inhibitory effect on *E. coli*. This study indicated the ability of GNC to adjust the antimicrobial spectrum of antibiotics.[116]

3.4.2.2 Antimicrobial Peptides (AMPs)

AMP, an emerging type of antimicrobial, has found applications in more and more research areas.[117] Thus, it is a natural combination of GNCs with AMP to create new nanomedicine. For example, Pranantyo et al. wisely engineered AMPs with charge-reversible moieties for the synthesis of pH-response material for selective killing of *E. c*, *P. a*, *S. a*, and *S. e*. Due to the bacterial infection foci is usually in an acidic environment, the anionic citraconyl moieties were applied to neutralise the cationic part of the AMP. Under a normal physiological environment, the GNC is safe for normal tissues. While

encountering a low pH environment, the auto-cleave of the citraconyl moieties would re-expose the primary amine and induce bacteria death (mainly due to the membrane potential depolarisation and ROS generation). In addition, this system could also be used for bacteria detection and imaging (Figure 3.4.5).[118]

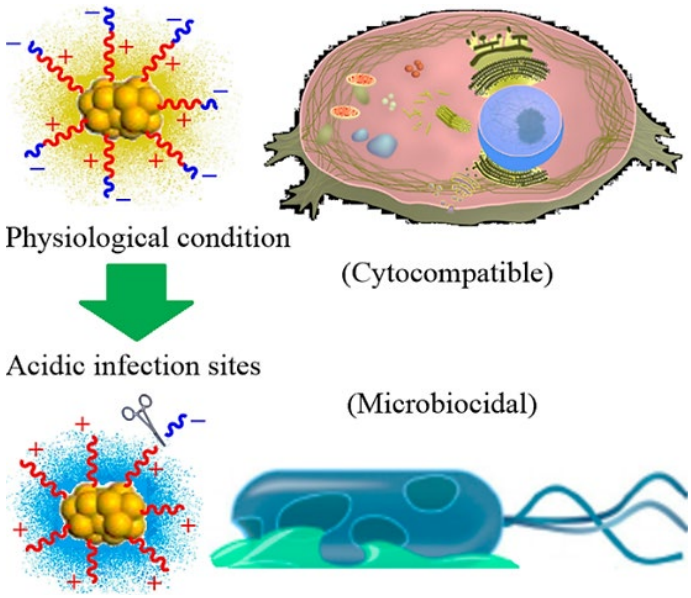

Figure 3.4.5 AMP-capped GNCs with citraconyl moieties can induce group cleavage and charge reverse at acidic sites of infection. The cationic AMP coating could then cause selective bacterial perforation for improved biosafety.[118] (Copied from ACS Publishing Group)

Zhu et al. recently reported a NIR-laser induced in situ formations of GNC for the simultaneous treatment of bacteria and cancer cells. They used a nano-system composed of a photothermal polymer core and AMP (tachyplesin-1) capping. Through irradiation of NIR laser (808 nm), the local photothermal conversion could facilitate the reduction of Au(III) ions to GNCs on the polymer surface to form the core-shell structure [Au(0)NC@ Au(I)AMP]. This AMP-GNC conjugate could act as an antibacterial agent to kill *E. c* cells.[119] In addition to natural peptides, some newly synthesised AMPs were also used to combine with GNCs for property modification and efficacy enhancement. Prada et al. reported the modification of BSA-GNC with two types of new AMP through n-succinimidyl-3-(2-pyridyldithiol) propionate (SPDP) reaction. The 2-nm

GNCs are linked with either NBC2253 or NBC2254 peptides for the enhancement of antibacterial ability. These two peptides have different antibacterial spectrums. NBC2253 has a higher potency to MRSA after decorating onto GNC, while NBC2254 exhibited higher antimicrobial activity on *E. coli.* The biocompatibility of both GNCs is considerably high.[120]

3.4.2.3 Other Antiseptics

Other antiseptics, including surfactants, are also applied in the synthesis of GNCs. Nitrogen-containing cationic surfactants are widely used in the synthesis of antibacterial surfaces due to their high antibacterial effect. In 2018, Xie et al. reported the application of mercaptoundecyl trimethyl quaternary ammonium (QA) as the capping ligand for the synthesis of QA-GNC for treating Gram-positive MDR species-induced infections. Although the QA is highly toxic and thus has low *in vivo* application prospects, the authors wisely used GSH as the capping ligand and reducer to improve biocompatibility while maintaining efficacy. Through adjusting the co-capping ratio of QA and GSH, the QA-GNC demonstrated high antibacterial potency against multiple Gram-positive strains, including MRSA, MRSE, and VRE. The mechanism study revealed that QA-GNC's antibacterial mechanisms include three parts: **1)** disruption of the bacterial cell membrane, **2)** generation of ROS, and **3)** disturbance of intracellular metabolic pathways. Besides, due to the fluorescent property of QA-GNC, it was also used for bacteria fluorescent imaging and counting (**Figure 3.4.6**).[121]

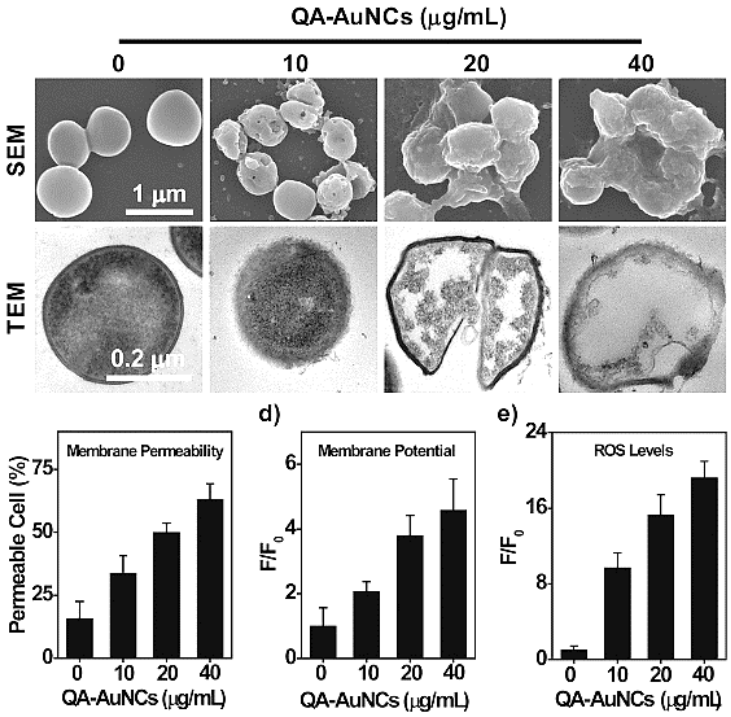

Figure 3.4.6 Antibacterial mechanisms of QA-GNC in different concentrations. The MRSA cell envelope demonstrated significant deformations and perforations, indicating significant membrane-active effects. In addition, dissipation of MRSA membrane potential and increase in ROS level all contributed to the killing of MRSA cells.[121] (Copied from Wiley Publishing Group)

After this work, the QA-GNC was grafted onto orthodontic devices like Invisalign aligners for the treatment of colonised biofilm. Through oxygen plasma treatment, the aligner was immersed in the QA-GNC solution for coating. *Streptococcus mutans* was applied as the model bacterial species, and the bacteria count dropped to 0.01% of the original concentration after treatment. Besides, the QA-GNC coating is highly biocompatible and durable and applicable to other antibacterial surfaces.[29] Coincidentally, in 2020, Li et al. reported the one-pot synthesis of (11-mercaptoundecyl)-N, N, N-trimethylammonium bromide (MUTAB)-capped GNCs with only a change in the anion species. Paying less attention to the ligand type, the authors paid more attention to the antibacterial spectrum of MUTAB-GNC. They found that this GNC is not only effective against Gram-positive bacteria (including VRE) but also effective against Gram-negative and even fungi. In addition to morphological changes,

the author also raised the killing mechanism of inducing oxidative stress and subsequent damage to genetic material (**Figure 3.4.7**).[122]

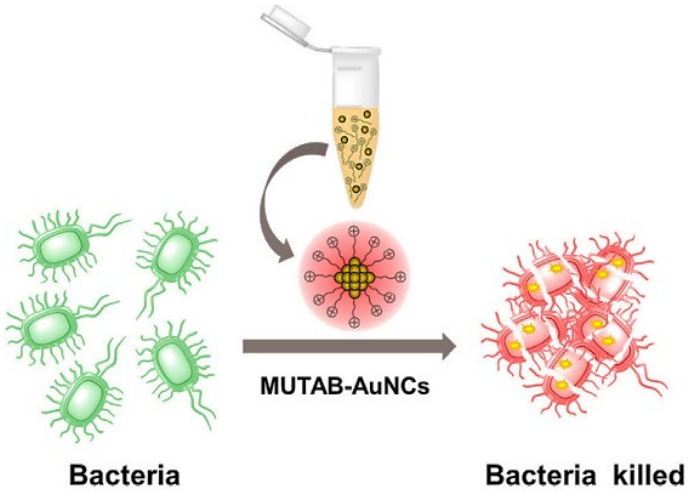

Figure 3.4.7 MUATB-capped, highly positively charged GNC was applied for the treatment of bacteria by inducing cell lysis.[122] (Copied from Elsevier Publishing Group)

Other than QA, benzoic acid is also a long-term-used antibacterial reagent. Thus, the application of *p*-mercaptobenzoic acid (*p*-MBA) as the coating ligand for GNC is another antibacterial strategy. In 2021, Xie's group published two papers on the mechanistic study of antibacterial *p*-MBA-GNC. In one study, they prepared a series of GNCs and GNPs capped with MBA, with sizes from ~1 nm to 5 nm (Au_{25}, Au_{102}, Au_{144}, and two GNPs) to measure the relationship between antibacterial effect and the GNP size. They have found that MBA-GNCs all demonstrated bactericidal potencies, with the smallest Au_{25} being the most toxic to *S. a*. However, by controlling the consistency of the overall mass of all tested materials rather than the Au element, they proved that the antibacterial effect for MBA-GNCs is not linear with their size or, to say, the Au atom number, thus showing a molecular-like behaviour, which is different from previous reports. In addition, the uptakes of two MBA-GNPs by bacteria are also starkly less than MBA-GNCs, which could be the reason for the low efficiency of MBA-GNPs toward *S. a* as well as *E. c* (**Figure 3.4.8**). After getting into bacteria, the GNCs could produce ROS to

oxidise the cell membrane and disrupt the metabolism to kill bacteria.[123] They also tracked the antibacterial process using fluorescent MBA-GNCs. The GNCs were found to first attach to the bacterial membrane, penetrate, and subsequently accumulate inside the bacteria. It then generates ROS as well as causes cell content leakage.[124]

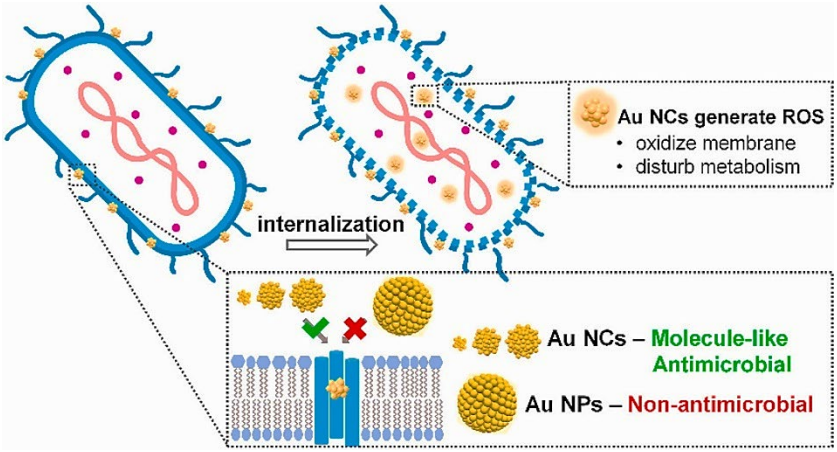

Figure 3.4.8 Benzoic acids have long been used for the treatment of bacterial infections. MBA-capped GNCs and GNPs, due to their different size and property, demonstrated a different pattern in entering the bacteria cell envelope, causing the difference in antibacterial potency.[123] (Copied from Elsevier Publishing Group)

3.4.3 Activating non-antibacterial capping ligands

The second big category is non-antibacterial small molecules. Although the MICs of using these ligands alone are normally high (>2048 μg mL^{-1}), capping onto GNC could effectively convert the whole GNC into a highly potent antibacterial material. As early as 2017, Zheng et al. reported the application of **mercaptohexanoic acid** (MHA)-capped GNCs for the treatment of both Gram-positive and Gram-negative bacteria species. They found that MHA-GNPs of >2 nm are not as effective as MHA-GNCs, due to the surface-to-volume ratio differences. Consequently, the ROS generated by internalised MHA-GNCs could induce a further metabolic imbalance and structural damage in bacteria (**Figure 3.4.9**).[125]

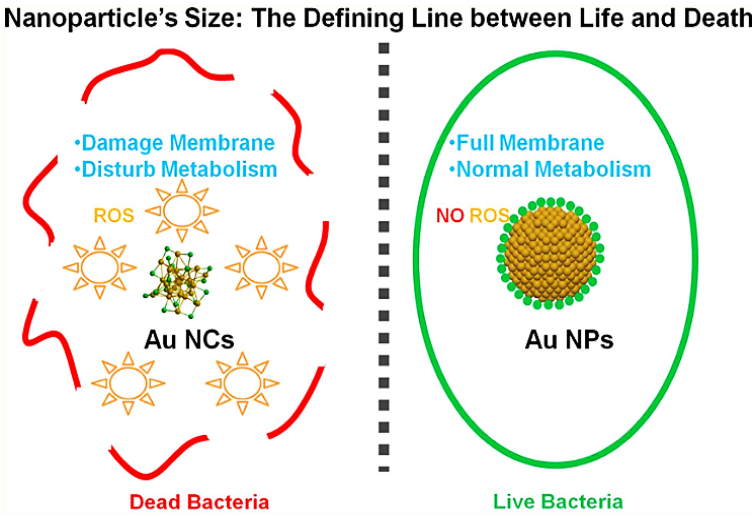

Figure 3.4.9 In contrast to MHA-capped GNP with no antibacterial ability, MHA-capped GNC could significantly lysis bacteria cells by inducing membrane damage as well as metabolic disruption.[125] (Copied from ACS Publishing Group)

Following this work, in 2021, Wang et al. also reported the synthesis of MHA-GNCs that specifically target Gram-negative bacteria species while non-bactericidal to Gram-positive strains. They conducted a series of mechanistic studies as well as transcriptome analysis and concluded the actual antibacterial mechanism of MHA-GNCs is chronological. The GNCs firstly bind with the bacteria cell membrane to damage the membrane integrity and cause cell content leakage. Then the MHA-GNCs would enter the bacteria, generating ROS, causing destruction of genetic material and metabolism disorder. Differential expressions are also observed in the biosynthesis of the bacterial cell wall and cell membrane, oxidative stress and DNA replication and repair.[126]

Strategies for the construction of antimicrobial GNPs, using **N-heterocyclic small molecules** have been previously introduced in the last section (refer to **Figure 3.3.6**). For GNCs, this strategy is also applicable. In 2018, Zheng et al. reported the application of a series of mercaptopyrimidine derivatives for the GNC capping and antibacterial applications. These mercaptopyrimidine derivates are non-antimicrobial themselves. However, the conjugation of these ligands onto GNCs dramatically increased the antibacterial efficiency against Gram-negative MDR strains by >64-fold (for 4,6-

diamino-2-mercaptopyrimidine (DAMP)-capped GNCs) with high biocompatibility to human cells. They also concluded the killing mechanism to be membrane disruption, DNA damage, and ROS generation (**Figure 3.4.10**).[74]

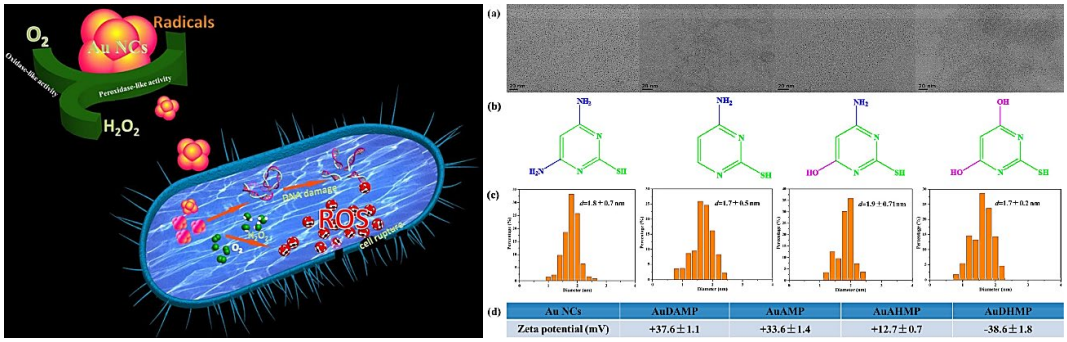

Figure 3.4.10 Capping GNCs with N-heterocyclic small molecules (DAMP/AMP/AHMP/DHMP) without antibacterial ability can activate them as antibacterial GNCs against MDR bacterial infections.[74] (Copied from ACS Publishing Group)

Subsequently, the DAMP-capped GNCs were embedded into antimicrobial fabrics made by electrospinning. Astonishingly, after being spun into nano-fabrics, the antibacterial spectrum was widened to both Gram-positive and -negative strains, including MDR strains. In contrast, the single use of GNC could only treat Gram-negative infections. In wound infection models, this nano-fibrous film demonstrated the ability to accelerate wound healing.[127] With the development of these small molecule-decorated GNCs, many new killing mechanisms were also proposed. Histidine (His), as a common amino acid, could also grant the GNC high antibacterial ability against Gram-negative bacteria. Due to the weak binding between His and Au, the ligand exchange with thiols could then consume the content of reducing mercaptans in the cell, then induce the redox imbalance. The accumulation of excess ROS (probably additive with ROS produced by GNCs) could then induce oxidative stress in MDR *E. coli* and cause cell death.[128] With a similar antibacterial mechanism, 1-vinylimidazole was also capped onto GNCs for the depletion of thiols and causing ROS accumulation.[129]

Macromolecules, including enzymes and proteins, were applied as the capping ligand of GNCs. However, due to the ultrasmall size of GNC, they are usually embedded into these macromolecules rather than exposed, thus may partly influence their interaction with bacteria. Lysozyme—as a natural antimicrobial enzyme that specifically lysis the bacteria cell wall, has been widely used for the preparation of antibacterial GNCs. For example, microwave synthesis of lysozyme-GNC was reported by Chen et al. The modification of GNC greatly increased the antibacterial effect of lysozyme toward MDR species (VRE and Pan-resistant *A. b*) while also providing fluorescence property for bacterial imaging.[130] Zhuang et al. prepared an antibacterial sponge (foam) by adsorbing these cationic lysozyme-GNCs onto an anionic sponge body (Figure 3.4.11). This antibacterial foam inherited the broad-spectrum antibacterial ability of lysozyme-GNCs as well as high biocompatibility and can be used for medical device surface sterilisation.[131]

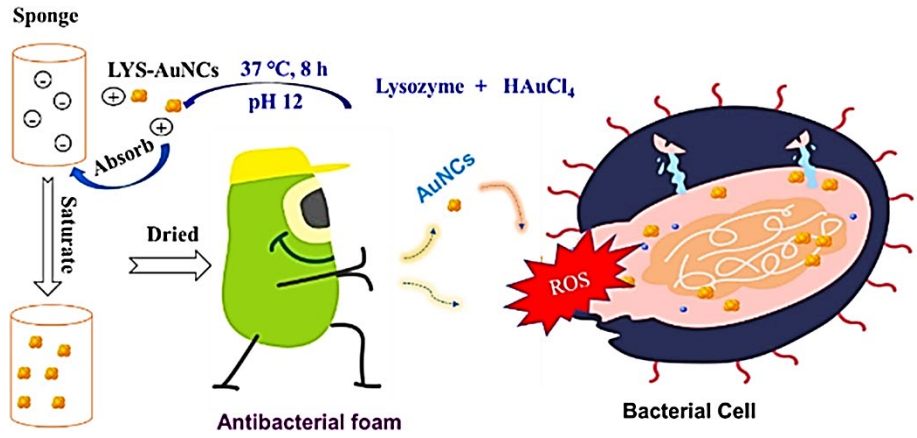

Figure 3.4.11 Lys-GNCs were prepared by applying lysozyme as the capping scaffold. Subsequent electrostatic adsorption of the Lys-GNCs onto an anionic sponge could form antibacterial foam for surface sterilisation through the generation of ROS.[131] (Copied from Future Medicine Publishing Group)

3.4.4 Enhancing GNC's intrinsic properties for antibacterial applications

GNC has many attractive properties, including photothermal and photodynamic properties that can be harnessed for antimicrobial applications. Although ROS

generation (photocatalytic) is well applied in the antibacterial field, other properties of GNC are rarely seen. Xie et al. reported the application of an 808-nm laser to excite DNase-capped GNCs for the photothermal and photodynamic treatment of both Gram-positive and -negative MDR strains. Combining all these antibacterial mechanisms, the GNC demonstrated outstanding ability in removing the biofilms as well as eradicating the settled bacteria.[132] This DNase-GNC was then grafted onto the Invisalign aligners and demonstrated excellent ability in preventing the formation of biofilms from preventing associated inflammatory infections (Figure 3.4.12).

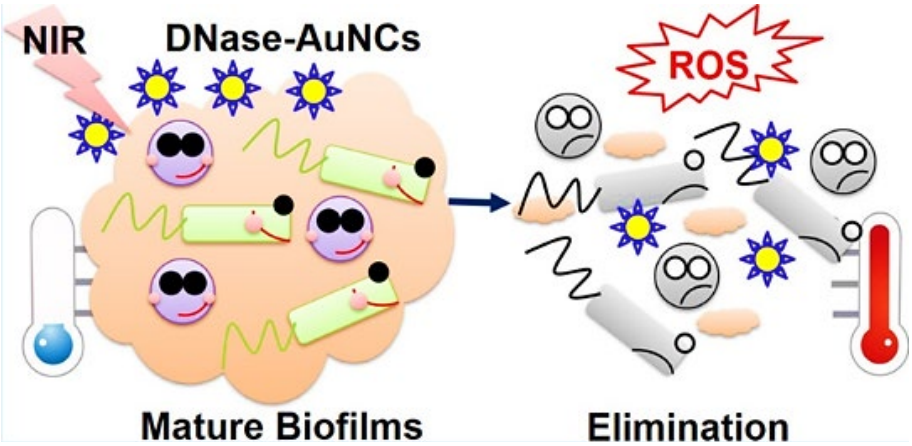

Figure 3.4.12 Through applying the photothermal effect of DNase-GNC, successful removal of the biofilm on dental appliances was achieved.[132] (Copied from ACS Publishing Group)

In another study, highly fluorescent BSA-GNCs (QY~14%) were applied for the synergistic photodynamic killing of *S. a* and MRSA under 660 nm light irradiation, which also achieved high antibacterial potency.[133]

3.4.5 Combining GNC and other materials to enhance antibacterial effects

In addition to direct applications of GNCs for antibacterial purposes, the combinational use of GNCs and polymers or liposomes as a nano-system has gradually been shown in more application scenarios. The binding of GNCs to these multifunctional complexes can overcome the conditional requirement of the ligands for GNCs. In addition, rational

design can increase the efficiency of both components. For instance, Girija et al. proposed the use of nano-aggregates formed by mercaptosuccinic acid (MSA)-capped GNCs and chitosan for the treatment of wound infections. Notably, not only the antibacterial effect but also the biocompatibility of both ligands are synergistically improved after the combination. These nanoaggregates are also more effective in accelerating the healing process of wound infections, proving the feasibility of the strategy.[134]

Apart from this, the synergistic antibacterial property was also observed for the nanocomplex with the conjugation of DAMP-capped GNCs and daptomycin over dosing separately or mechanical mixing, as reported by Zheng et al.[135] In addition to DAMPs, other thiopyrimidines can also be used in preparing nanocomposites. For example, 5-methyl-2-thiouracil (MTU). By adding cationic protamine, both fluorescence and stability of MTU-GNC were improved through "host-guest recognition." MTU-GNC's weak fluorescence was enhanced by 28 folds, making it useful for bacteria imaging. Moreover, this combination has induced a synergistic killing of both *E. c* and MRSA, with >100-fold improved antibacterial potency (**Figure 3.4.13**).[136]

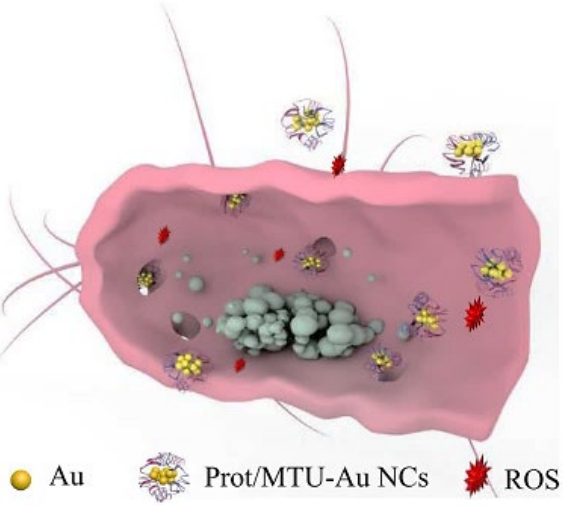

Figure 3.4.13 The Prot/MTU-GNC could synergistically increase the cell envelope permeation as well as ROS generation of *E. coli* to kill bacteria.[136] (Copied from ACS Publishing Group)

Besides polymers, DNA was also applied for the preparation of an antibacterial nanocomplex. In 2014, Setyawati proposed a strategy to use DNA nanopyramid for the deposition of GSH-GNCs and loaded with Actinomycin D. Due to bright fluorescence, GSH-GNC was mainly applied as the fluorescent reporter. The drug-loaded nanopyramid structure could enhance cellular uptake and demonstrate broad-spectrum antimicrobial effects (**Figure 3.4.14**).[137]

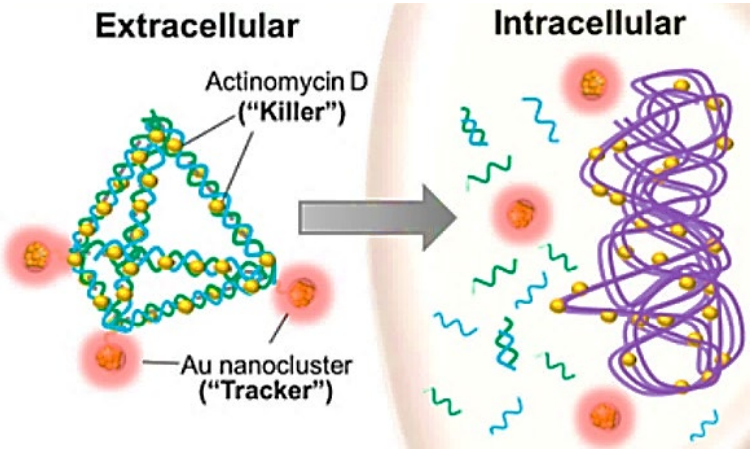

Figure 3.4.14 GNC-decorated DNA nanopyramid was applied for the simultaneous detection and antibacterial treatment of *E. c* and *S. a*. The GNCs were applied as a reporter.[137] (Copied from ACS Publishing Group)

In summary, the application of GNCs in the antibacterial field is a budding research area with a few outcomes. However, there are also some drawbacks, including the chemical structure or crystal structure of the GNC is often ignored, which is unfavourable for application as a nanomedicine. Besides, the ligands are usually limited to a single type and lack the cooperation of two or multiple types of ligands. In addition, the underlying antibacterial mechanism is highly similar but not entirely unveiled. By deepening our understanding of GNCs, I hope that these limitations can be resolved (**Table 3**).

Table 3 Summary of the ligand type, ligand name, and bacterial species mentioned in the above papers.

Ligand Name & Ligand Type	Bacterial Species**	Ref.

4,6-Diamino-2-mercaptopyrimidine (nAb)	*A. b**, *E. c**, *K. p**, *P. a**, *S. a**, *S. e**, *S. p*, *S. h**	110
4,6-Diamino-2-mercaptopyrimidine (nAb)	*E. c**, *P. a**, *A. b**, *K. p** *Salmonella enterica*	111
Ampicillin/Lysozyme (Ab/M)	*S. a** (MRSA)	115
Bacitracin (Ab)	*S. a*	114
Vancomycin (Ab)	*S. a* and *E. c*	116
Citraconyl moieties-decorated CysHHC10 (AMP)	*E. c*, *P. a*, *S. a*, and *S. e*	118
Tachyplesin-1 (AMP)	*E. c*	119
NBC2253/NBC2254 (AMP)	*E. c* and *S. a**	120
Mercaptoundecyl trimethyl quaternary ammonium (S)	*B. s*, *E. f**, *S. a**, *S. e**, *S. h*, *S. p*, and *E. c**	121
Mercaptoundecyl trimethyl quaternary ammonium (S)	*Streptococcus mutans*	29
(11-Mercaptoundecyl) - N,N,N trimethylammonium Bromide (S)	*B. s*, *E. f**, *S. p*, *E. c*, and *P. a*	122
p-Mercaptobenzoic acid (S)	*S. a* and *E. c*	123
p-Mercaptobenzoic acid (S)	*S. a* and *E. c*	124
Mercaptohexanoic acid (nAb)	*S. a*, *S. e*, *B. s*, *E. c*, and *P. a*	125
Mercaptohexanoic acid (nAb)	*E. c*, *A. b*, *S. a*, and *B. s*	126
Mercaptopyrimidines (nAb)	*E. c**, *A. b**, *P. a**, *K. p**, *S. a**, and *E. f**	74
4,6-Diamino-2-mercaptopyrimidine (nAb)	*S. a** and *E. c**	127
Histidine (nAb)	*E. c**, *P. a*, *B. s*, and *S. a**	128
1-Vinylimidazole (nAb)	*S. a*	129
Lysozyme/Ovalbumin (M)	*E. c*, *A. b**, *S. a*, and *E. f**	130
Lysozyme (M)	*S. a* and *E. c*	131
DNase (M)	*S. a**, *S. e**, *E. c**, and *P. a**	132
Bovine serum albumin (M)	*S. a**	133
Mercaptosuccinic acid/ Chitosan (C)	*S. a* and *E. c*	134

4,6-Diamino-2-mercaptopyrimidine/Daptomycin (C)	*S. a**	135
5-Methyl-2-thiouracil/ Protamine (C)	*S. a** and *E. c*	136
Glutathione/DNA plasmid (C)	*S. a* and *E. c*	137

Asterisk (*) indicates corresponding resistant strains.

**: MIC is not included due to the large gap between statistical units and antimicrobial test methods in the literature.

Ab—antimicrobial small molecules; nAb—non-antimicrobial small molecules; M—macromolecules; AMP—antimicrobial peptide; S—surfactant; C—composite.

3.5 Overview of the project (PART II)

The development of bacterial drug resistance is unstoppable. Especially when the drug resistance issue of bacteria encounters the new COVID-19 epidemic.[138 139] Although the discovery of new antibiotics has mostly stalled, the rise of nano-antibiotics, especially GNM-based antibiotics, has brought in a new weapon against bacterial antibiotic resistance. In terms of GNPs, in addition to reversing MDR, the ability to activate non-antibacterial molecules into antimicrobial complexes can be used to build many new antibacterial materials. As the size decreases, GNCs not only have the ability of GNPs but also enhanced ROS generation ability, which makes them a new favourite in the research of antibacterial materials. However, the increased photodynamic and catalytic effects have caused more safety concerns of GNCs for *in vivo* use, which have largely been overlooked. The current GNCs are mostly modified by a single type of ligand, making it difficult to balance the requirement of antibacterial properties and biocompatibility. In addition, the chemical structure of most of the antibacterial GNCs described above is not atomically precise, which could limit their application as viable drugs. In addition, most research has focused on the antibacterial effect of GNCs, and largely ignored their structural characterisation. Therefore, its quality control and batch-to-batch variation can be high, which is unfavourable for druggability.

Consequently, in this part of my project, emphasis will be placed on the modulation of

dual-ligand ratios on atomically precise Au_{25} NC to achieve a balance of antibacterial and biocompatibility. The experiments are focused on zwitterionic ligand-capped NIR-II emitting Au_{25} NCs.[140] This ligand could provide the GNC with high *in vivo* stability as well as biocompatibility (short renal clearance time). The pure zwitterionic ligand-capped GNC has no antimicrobial effect. Two different types of ligands, including pyridinium ligand and small molecular mercapto alcohol, are selected as active molecules.

In the first project, due to the severe toxicity of pyridinium salt, the antibacterial ability and biocompatibility are optimised by adjusting the feeding ratio of pyridinium ligand (zwitterionic ligand as complementary) to 45%. The GNCs could be co-administrated with antibiotics to reverse MDR in drug-resistant Gram-positive bacteria like MRSE. In *in vivo* skin infection model, the GNC+antibiotic group has achieved an excellent treatment for drug-resistant bacterial infections (**Figure 3.5.1**).[109]

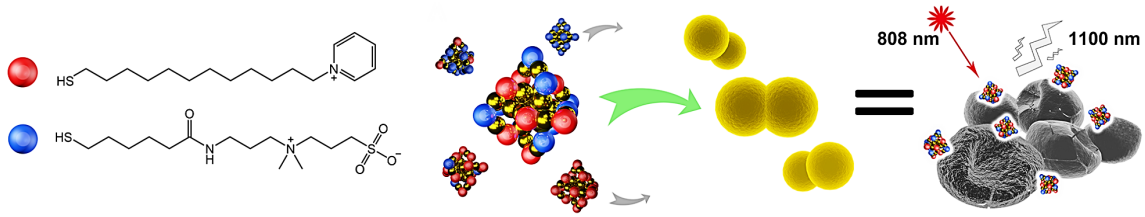

Figure 3.5.1 Fluorescent dual ligand capped Au_{25} NC with a particular ligand feeding ratio can effectively aggregate and then kill multidrug-resistant bacteria while maintaining good biocompatibility.

In the second project, a non-antimicrobial fragrance molecule (4-mercapto-4-methyl-2-pentanol) was co-decorated with zwitterionic ligands onto the GNC surface. By controlling the surface ligand ratio, the antibacterial activity of GNCs was improved by >1024-fold, especially against MRSA, which was more effective than many commonly used ophthalmic antibiotics. In addition, compared with Van, this GNC has achieved better therapeutic effects in both *in vitro* and *in vivo* keratitis models, proving its potential as a novel antibacterial eye drop (**Figure 3.5.2**).

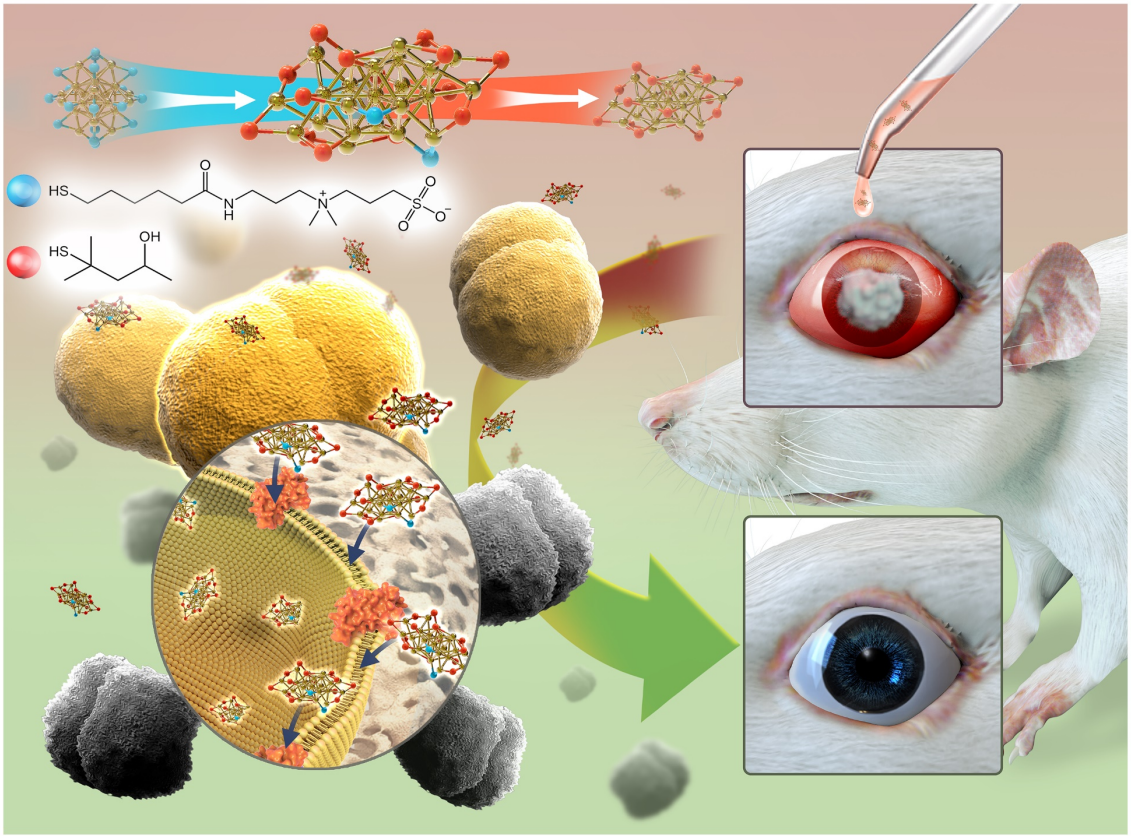

Figure 3.5.2 NIR-II-fluorescent Au_{25} NCs can embed into bacterial cell membranes, resulting in reduced membrane fluidity and consequent instability of the membrane. The consequent K^+ efflux would thus block the energy metabolism of MDR Gram-positive bacteria and lead to death. Its antibacterial mechanism is similar to that of daptomycin used clinically.

3.6 References

1 A. FLEMING, *Br. Med. Bull.*, 2017, **2**, 4–5.

2 P. Fernandes, *Nat. Biotechnol.*, 2006, **24**, 1497–1503.

3 A. Fajardo and J. L. Martínez, *Curr. Opin. Microbiol.*, 2008, **11**, 161–167.

4 B. Saha, J. Bhattacharya, A. Mukherjee, A. K. Ghosh, C. R. Santra, A. K. Dasgupta and P. Karmakar, *Nanoscale Res. Lett.*, 2007, **2**, 614–622.

5 D. Pissuwan, C. H. Cortie, S. M. Valenzuela and M. B. Cortie, *Trends Biotechnol.*, 2010, **28**, 207–213.

6 T. R. Walsh, J. Weeks, D. M. Livermore and M. A. Toleman, *Lancet Infect. Dis.*, 2011, **11**, 355–362.

7 U. . D. of H. and H. Services, *Antibiotic resistance threats in the United States*, 2013.

8 B. Y. Lee, A. Singh, M. Z. David, S. M. Bartsch, R. B. Slayton, S. S. Huang, S. M. Zimmer, M. A. Potter, C. M. Macal, D. S. Lauderdale, L. G. Miller and R. S. Daum, *Clin. Microbiol. Infect.*, 2013, **19**, 528–536.

9 Centers for Disease Control and, *Antibiotic resistance threats in the United States*, Atlanta, Georgia, 2019.

10 M. McKenna, *Nature*, 2020, **584**, 338–341.

11 C. J. Murray, K. S. Ikuta, F. Sharara, L. Swetschinski, G. Robles Aguilar, A. Gray, C. Han, C. Bisignano, P. Rao, E. Wool, S. C. Johnson, A. J. Browne, M. G. Chipeta, F. Fell, S. Hackett, G. Haines-Woodhouse, B. H. Kashef Hamadani, E. A. P. Kumaran, B. McManigal, R. Agarwal, S. Akech, S. Albertson, J. Amuasi, J. Andrews, A. Aravkin, E. Ashley, F. Bailey, S. Baker, B. Basnyat, A. Bekker, R. Bender, A. Bethou, J. Bielicki, S. Boonkasidecha, J. Bukosia, C. Carvalheiro, C. Castañeda-Orjuela, V. Chansamouth, S. Chaurasia, S. Chiurchiù, F. Chowdhury, A. J. Cook, B. Cooper, T. R. Cressey, E. Criollo-Mora, M. Cunningham, S. Darboe, N. P. J. Day, M. De Luca, K. Dokova, A. Dramowski, S. J. Dunachie, T. Eckmanns, D. Eibach, A. Emami, N. Feasey, N. Fisher-Pearson, K. Forrest, D. Garrett, P. Gastmeier, A. Z. Giref, R. C. Greer, V. Gupta, S. Haller, A. Haselbeck, S. I. Hay, M. Holm, S. Hopkins, K. C. Iregbu, J. Jacobs, D. Jarovsky, F. Javanmardi, M. Khorana, N. Kissoon, E. Kobeissi, T. Kostyanev, F. Krapp, R. Krumkamp, A. Kumar, H. H. Kyu, C. Lim, D.

Limmathurotsakul, M. J. Loftus, M. Lunn, J. Ma, N. Mturi, T. Munera-Huertas, P. Musicha, M. M. Mussi-Pinhata, T. Nakamura, R. Nanavati, S. Nangia, P. Newton, C. Ngoun, A. Novotney, D. Nwakanma, C. W. Obiero, A. Olivas-Martinez, P. Olliaro, E. Ooko, E. Ortiz-Brizuela, A. Y. Peleg, C. Perrone, N. Plakkal, A. Ponce-de-Leon, M. Raad, T. Ramdin, A. Riddell, T. Roberts, J. V. Robotham, A. Roca, K. E. Rudd, N. Russell, J. Schnall, J. A. G. Scott, M. Shivamallappa, J. Sifuentes-Osornio, N. Steenkeste, A. J. Stewardson, T. Stoeva, N. Tasak, A. Thaiprakong, G. Thwaites, C. Turner, P. Turner, H. R. van Doorn, S. Velaphi, A. Vongpradith, H. Vu, T. Walsh, S. Waner, T. Wangrangsimakul, T. Wozniak, P. Zheng, B. Sartorius, A. D. Lopez, A. Stergachis, C. Moore, C. Dolecek and M. Naghavi, *Lancet*, 2022, **399**, 629–655.

12 E. Tacconelli, E. Carrara, A. Savoldi, S. Harbarth, M. Mendelson, D. L. Monnet, C. Pulcini, G. Kahlmeter, J. Kluytmans, Y. Carmeli, M. Ouellette, K. Outterson, J. Patel, M. Cavaleri, E. M. Cox, C. R. Houchens, M. L. Grayson, P. Hansen, N. Singh, U. Theuretzbacher, N. Magrini, A. O. Aboderin, S. S. Al-Abri, N. Awang Jalil, N. Benzonana, S. Bhattacharya, A. J. Brink, F. R. Burkert, O. Cars, G. Cornaglia, O. J. Dyar, A. W. Friedrich, A. C. Gales, S. Gandra, C. G. Giske, D. A. Goff, H. Goossens, T. Gottlieb, M. Guzman Blanco, W. Hryniewicz, D. Kattula, T. Jinks, S. S. Kanj, L. Kerr, M. P. Kieny, Y. S. Kim, R. S. Kozlov, J. Labarca, R. Laxminarayan, K. Leder, L. Leibovici, G. Levy-Hara, J. Littman, S. Malhotra-Kumar, V. Manchanda, L. Moja, B. Ndoye, A. Pan, D. L. Paterson, M. Paul, H. Qiu, P. Ramon-Pardo, J. Rodríguez-Baño, M. Sanguinetti, S. Sengupta, M. Sharland, M. Si-Mehand, L. L. Silver, W. Song, M. Steinbakk, J. Thomsen, G. E. Thwaites, J. W. van der Meer, N. Van Kinh, S. Vega, M. V. Villegas, A. Wechsler-Fördös, H. F. L. Wertheim, E. Wesangula, N. Woodford, F. O. Yilmaz and A. Zorzet, *Lancet Infect. Dis.*, 2018, **18**, 318–327.

13 A. Mullard, *Nat. Rev. Drug Discov.*, 2022, 21, 170.

14 Willyard Cassandra, *Nature*, 2017, **543**, 15.

15 S. Reardon, *Nature*, 2015.

16 P. S. Jørgensen, D. Wernli, S. P. Carroll, R. R. Dunn, S. Harbarth, S. A. Levin, A. D. So, M. Schlüter and R. Laxminarayan, *Nature*, 2016, **537**, 159–161.

17 S. Reardon, *Nature*, 2017.

18 M. I. Hutchings and K. R. Duncan, *Cell Host Microbe*, 2022, **30**, 273–274.

19 A. Sabnis, K. L. H. Hagart, A. Klöckner, M. Becce, L. E. Evans, R. C. D. Furniss, D. A.

I. Mavridou, R. Murphy, M. M. Stevens, J. C. Davies, G. J. Larrouy-Maumus, T. B. Clarke and A. M. Edwards, *Elife*, 2021, **10**, 1–26.

20 M. Mendelson, A. Brink, J. Gouws, N. Mbelle, V. Naidoo, T. Pople, N. Schellack, M. van Vuuren, H. Rees, S. Banoo, K. Bokaba, M. Collins, K. Faure, M. Herbst, B. Hoek, R. Lancaster, J. Lotter, M. Modisane, M. Mohlala, E. Mokantla, A. Molatuli, M. Molefe, G. Molewa, K. Mompati, L. Moshiga, S. Munbodh, P. Nkambule, C. Patterson, D. Reddy, A. Sigobondhla, S. Suliman and G. Swan, *Lancet Infect. Dis.*, 2018, **18**, e288–e294.

21 C. Aurilio, P. Sansone, M. Barbarisi, V. Pota, L. G. Giaccari, F. Coppolino, A. Barbarisi, M. B. Passavanti and M. C. Pace, *Antibiotics*, 2022, **11**, 421.

22 P. Nordmann and L. Poirel, *Clin. Infect. Dis.*, 2019, **69**, S521–S528.

23 S. Di Franco, A. Alfieri, M. C. Pace, P. Sansone, V. Pota, C. Fittipaldi, M. Fiore and M. B. Passavanti, *Life*, 2021, **11**, 1–20.

24 P. J. Stogios and A. Savchenko, *Protein Sci.*, 2020, **29**, 654–669.

25 M. N. Alekshun and S. B. Levy, *Cell*, 2007, **128**, 1037–1050.

26 H. Nikaido, *Annu. Rev. Biochem.*, 2009, **78**, 119–146.

27 V. R. Povolo and M. Ackermann, *Science*, 2019, **364**, 737–738.

28 L. Fernández and R. E. W. Hancock, *Clin. Microbiol. Rev.*, 2012, **25**, 661–681.

29 Y. Xie, M. Zhang, W. Zhang, X. Liu, W. Zheng and X. Jiang, *ACS Biomater. Sci. Eng.*, 2020, **6**, 1239–1246.

30 P. S. Stewart and J. W. Costerton, *Lancet*, 2001, **358**, 135–138.

31 D. Chang, L. Sharma, C. S. Dela Cruz and D. Zhang, *Front. Microbiol.*, 2021, **12**, 1–9.

32 R. Chowdhury, H. Ilyas, A. Ghosh, H. Ali, A. Ghorai, A. Midya, N. R. Jana, S. Das and A. Bhunia, *Nanoscale*, 2017, **9**, 14074–14093.

33 G. D. Wright, *Trends Microbiol.*, 2016, **24**, 862–871.

34 A. J. Huh and Y. J. Kwon, *J Control Release*, 2011, **156**, 128–145.

35 S. Mumtaz, V. M. Rotello, S. Z. Hussain, A. Gupta, I. Hussain, I. Javed, Z. Huma and R. Das, *ACS Omega*, 2018, **3**, 16721–16727.

36 L. K. Adams, D. Y. Lyon and P. J. J. Alvarez, *Water Res.*, 2006, **40**, 3527–3532.

37 Y. Zhao and X. Jiang, *Nanoscale*, 2013, **5**, 8340–8350.

38 J. Zhang, L. Mou and X. Jiang, *Chem. Sci.*, 2020, **11**, 923–936.

39 D. N. Williams, S. H. Ehrman and T. R. P. Holoman, *J. Nanobiotechnology*, 2006, **4**, 1–8.

40 P. Ghosh, G. Han, M. De, C. K. Kim and V. M. Rotello, *Adv. Drug Deliv. Rev.*, 2008, **60**, 1307–1315.

41 B. D. Johnston, W. G. Kreyling, C. Pfeiffer, M. Schäffler, H. Sarioglu, S. Ristig, S. Hirn, N. Haberl, S. Thalhammer, S. M. Hauck, M. Semmler-Behnke, M. Epple, J. Hühn, P. Del Pino and W. J. Parak, *Adv. Funct. Mater.*, 2017, **27**, 1–9.

42 S. S. Arya, M. M. Sharma, R. K. Das, J. Rookes, D. Cahill and S. K. Lenka, *Heliyon*, 2019, **5**, e02021.

43 D. Di Bella, J. P. S. Ferreira, R. de N. O. Silva, C. Echem, A. Milan, E. H. Akamine, M. H. Carvalho and S. F. Rodrigues, *J. Nanobiotechnology*, 2021, **19**, 1–15.

44 B. Lee and D. G. Lee, *J. Appl. Microbiol.*, 2019, **127**, 701–712.

45 D. Hu, H. Li, B. Wang, Z. Ye, W. Lei, F. Jia, Q. Jin, K. F. Ren and J. Ji, *ACS Nano*, 2017, **11**, 9330–9339.

46 Y. Zhao, Y. Tian, Y. Cui, W. Liu, W. Ma and X. Jiang, *J. Am. Chem. Soc.*, 2010, **132**, 12349–12356.

47 W. Zhang, Y. Wu, L. Liu, X. Xiao, Z. Cong, N. Shao, Z. Qiao, K. Chen, S. Liu, H. Zhang, Z. Ji, X. Shao, Y. Dai, H. He, J. Xia, J. Fei and R. Liu, *J. Mater. Chem. B*, 2021, **9**, 5092–5101.

48 A. Reznickova, N. Slavikova, Z. Kolska, K. Kolarova, T. Belinova, M. Hubalek Kalbacova, M. Cieslar and V. Svorcik, *Colloids Surfaces A Physicochem. Eng. Asp.*, 2019, **560**, 26–34.

49 S. Bagheri, M. Yasemi, E. Safaie-Qamsari, J. Rashidiani, M. Abkar, M. Hassani, S. A. Mirhosseini and H. Kooshki, *Artif. Cells, Nanomedicine Biotechnol.*, 2018, **46**, 462–471.

50 A. Rai, A. Prabhune and C. C. Perry, *J. Mater. Chem.*, 2010, **20**, 6789–6798.

51 U. Rajchakit and V. Sarojini, *Bioconjug. Chem.*, 2017, **28**, 2673–2686.

52 Q. Yu, J. Li, Y. Zhang, Y. Wang, L. Liu and M. Li, *Sci. Rep.*, 2016, **6**, 26667.

53 A. Amini, M. Kamali, B. Amini and A. Najafi, *J. Phys. D. Appl. Phys.*, 2019, **52**, 065401.

54 G. L. Burygin, B. N. Khlebtsov, A. N. Shantrokha, L. A. Dykman, V. A. Bogatyrev and N. G. Khlebtsov, *Nanoscale Res. Lett.*, 2009, **4**, 794–801.

55 M. Shah, V. Badwaik, Y. Kherde, H. K. Waghwani, T. Modi, Z. P. Aguilar, H. Rodgers, W. Hamilton, T. Marutharaj, C. Webb, M. B. Lawrenz and R. Dakshinamurthy, *Front. Biosci. - Landmark*, 2014, **19**, 1320–1344.

56 H. Gu, P. L. Ho, E. Tong, L. Wang and B. Xu, *Nano Lett.*, 2003, **3**, 1261–1263.

57 B. Saha, J. Bhattacharya, A. Mukherjee, A. K. Ghosh, C. R. Santra, A. K. Dasgupta and P. Karmakar, *Nanoscale Res. Lett.*, 2007, **2**, 614–622.

58 A. Rai, S. Pinto, T. R. Velho, A. F. Ferreira, C. Moita, U. Trivedi, M. Evangelista, M. Comune, K. P. Rumbaugh, P. N. Simões, L. Moita and L. Ferreira, *Biomaterials*, 2016, **85**, 99–110.

59 S. Wang, C. Yan, X. Zhang, D. Shi, L. Chi, G. Luo and J. Deng, *Biomater. Sci.*, 2018, **6**, 2757–2772.

60 S. L. Elshaer and M. I. Shaaban, *Antibiotics*, 2021, **10**, 1461.

61 F. Chassagne, T. Samarakoon, G. Porras, J. T. Lyles, M. Dettweiler, L. Marquez, A. M. Salam, S. Shabih, D. R. Farrokhi and C. L. Quave, *Front. Pharmacol.*, 2021, **11**, 1–29.

62 P. Boomi, R. M. Ganesan, G. Poorani, H. Gurumallesh Prabu, S. Ravikumar and J. Jeyakanthan, *Mater. Sci. Eng. C*, 2019, **99**, 202–210.

63 S. A. Akintelu, S. C. Olugbeko and A. S. Folorunso, *Int. Nano Lett.*, 2020, **10**, 237–248.

64 V. SP, U. bhanu, N. G, H. B, C. C P and C. N, *Int. J. Biosens. Bioelectron.*, 2019, **5**, 150–155.

65 W. Huang, S. Chen, Y. Liu, H. Fu and G. Wu, *Nanotechnology*, 2011, **22**, 025602.

66 S. Buffet-Bataillon, P. Tattevin, M. Bonnaure-Mallet and A. Jolivet-Gougeon, *Int. J. Antimicrob. Agents*, 2012, **39**, 381–389.

67 X. Li, S. M. Robinson, A. Gupta, K. Saha, Z. Jiang, D. F. Moyano, A. Sahar, M. A. Riley and V. M. Rotello, *ACS Nano*, 2014, **8**, 10682–10686.

68 P. P. Pillai, B. Kowalczyk, K. Kandere-Grzybowska, M. Borkowska and B. A. Grzybowski, *Angew. Chemie - Int. Ed.*, 2016, **55**, 8610–8614.

69 A. Azam, F. Ahmed, N. Arshi, M. Chaman and A. H. Naqvi, *Int. J. Theor. Appl. Sci.*, 2009, **1**, 1–4.

70 M. Ohadi, H. Forootanfar, G. Dehghannoudeh, T. Eslaminejad, A. Ameri, M. Shakibaie and A. Najafi, *Bionanoscience*, 2020, **10**, 899–908.

71 S. Gómez-Graña, M. Perez-Ameneiro, X. Vecino, I. Pastoriza-Santos, J. Perez-Juste, J. M. Cruz and A. B. Moldes, *Nanomaterials*, 2017, **7**, 139.

72 P. Walvekar, R. Gannimani, S. Rambharose, C. Mocktar and T. Govender, *Chem. Phys. Lipids*, 2018, **214**, 1–10.

73 Y. Cui, Y. Zhao, Y. Tian, W. Zhang, X. Lü and X. Jiang, *Biomaterials*, 2012, **33**, 2327–2333.

74 Y. Zheng, W. Liu, Z. Qin, Y. Chen, H. Jiang and X. Wang, *Bioconjug. Chem.*, 2018, **29**, 3094–3103.

75 W. Zheng, Y. Tian, J. Shao, R. Huang, Y. Feng, W. Zheng, R. Tang, X. Jiang, P. Wang, Y. Jia, J. Zhang, Y. Li and G. Yang, *Small*, 2017, **13**, 1700130.

76 W. Zheng, Y. Jia, W. Chen, G. Wang, X. Guo and X. Jiang, *ACS Appl. Mater. Interfaces*, 2017, **9**, 21181-21189.

77 Y. Zhao, Z. Chen, Y. Chen, J. Xu, J. Li and X. Jiang, *J. Am. Chem. Soc.*, 2013, **135**, 12940–12943.

78 X. Zhao, Y. Jia, J. Li, R. Dong, J. Zhang, C. Ma, H. Wang, Y. Rui and X. Jiang, *ACS Appl. Mater. Interfaces*, 2018, **10**, 29398–29406.

79 L. Wang, L. Wang, M. Natan, W. Zheng, W. Zheng, W. Zheng, S. Liu, G. Jacobi, I. Perelshtein, A. Gedanken, E. Banin and X. Jiang, *Nanoscale Adv.*, 2020, **2**, 2293–2302.

80 X. Yang, J. Yang, L. Wang, B. Ran, Y. Jia, L. Zhang, G. Yang, H. Shao and X. Jiang, *ACS Nano*, 2017, **11**, 5737–5745.

81 X. Yang, Q. Wei, H. Shao and X. Jiang, *ACS Appl. Mater. Interfaces*, 2019, **11**, 7725–7730.

82 V. D. Badwaik, L. M. Vangala, D. S. Pender, C. B. Willis, Z. P. Aguilar, M. S. Gonzalez, R. Paripelly and R. Dakshinamurthy, *Nanoscale Res. Lett.*, 2012, **7**, 1–11.

83 I. M. Ahmady, M. K. Hameed, A. M. Almehdi, M. Arooj, B. Workie, E. Sahle-Demessie, C. Han and A. A. Mohamed, *Biomater. Sci.*, 2019, **7**, 5016–5026.

84 C. C. Wang, S. M. Wu, H. W. Li and H. T. Chang, *ChemBioChem*, 2016, **17**, 1052–1062.

85 A. Regiel-Futyra, M. Kus-Liśkiewicz, V. Sebastian, S. Irusta, M. Arruebo, G. Stochel and A. Kyzioł, *ACS Appl. Mater. Interfaces*, 2015, **7**, 1087–1099.

86 H. M. Alnashiri, F. M. Aldakheel, A. S. Binshaya, N. S. Alharthi and M. Ahmed, *Adsorpt. Sci. Technol.*, 2022, **2022**, 8187260.

87 Pradeepa, S. M. Vidya, S. Mutalik, K. Udaya Bhat, P. Huilgol and K. Avadhani, *Life Sci.*, 2016, **153**, 171–179.

88 S. S. Ahiwale, A. V. Bankar, S. Tagunde and B. P. Kapadnis, *Indian J. Microbiol.*, 2017, **57**, 188–194.

89 P. Boomi, H. G. Prabu, P. Manisankar and S. Ravikumar, *Appl. Surf. Sci.*, 2014, **300**, 66–72.

90 K. Hareesh, A. V. Deore, S. S. Dahiwale, G. Sanjeev, D. Kanjilal, S. Ojha, N. A. Dhole, K. M. Kodam, V. N. Bhoraskar and S. D. Dhole, *Radiat. Phys. Chem.*, 2015, **112**, 97–103.

91 Y. Fu, L. Yang, J. Zhang, J. Hu, G. Duan, X. Liu, Y. Li and Z. Gu, *Mater. Horizons*, 2021, **8**, 1618–1633.

92 X. Xu, X. Liu, L. Tan, Z. Cui, X. Yang, S. Zhu, Z. Li, X. Yuan, Y. Zheng, K. W. K. Yeung, P. K. Chu and S. Wu, *Acta Biomater.*, 2018, **77**, 352–364.

93 M. J. Beha, J. S. Ryu, Y. S. Kim and H. J. Chung, *Mater. Sci. Eng. C*, 2021, **126**, 112167.

94 N. J. Millenbaugh, J. B. Baskin, M. N. DeSilva, W. R. Elliott and R. D. Glickman, *Int. J. Nanomedicine*, 2015, **10**, 1953–1960.

95 V. P. Zharov, K. E. Mercer, E. N. Galitovskaya and M. S. Smeltzer, *Biophys. J.*, 2006, **90**, 619–627.

96 W. C. Huang, P. J. Tsai and Y. C. Chen, *Nanomedicine*, 2007, **2**, 777–787.

97 A. Zarebkohan, A. Ghafoori, F. Bani, S. H. Rasta, E. Abbasi, R. Salehi and M. Milani, *J. Drug Deliv. Sci. Technol.*, 2021, **66**, 102846.

98 S. M. Lashkari, H. Kariminezhad, N. Safarnezhad and H. Amani, *Gold Bull.*, 2019, **52**, 51–60.

99 H. Kariminezhad, M. Mousapour, S. Khorram and H. Amani, *Arab. J. Sci. Eng.*, 2020, **45**, 71–79.

100 F. Lavaee, M. Motamedifar and G. Rafiee, *Lasers Med. Sci.*, 2022, **37**, 1717–1725.

101 J. Gil-Tomás, S. Tubby, I. P. Parkin, N. Narband, L. Dekker, S. P. Nair, M. Wilson and C. Street, *J. Mater. Chem.*, 2007, **17**, 3739–3746.

102 N. Wijesiri, T. Ozkaya-Ahmadov, P. Wang, J. Zhang, H. Tang, X. Yu, N. Ayres and P. Zhang, *ACS Omega*, 2017, **2**, 5364–5369.

103 M. B. Rivas Aiello, F. Ghilini, J. E. Martínez Porcel, L. Giovanetti, P. L. Schilardi and D. O. Mártire, *Langmuir*, 2020, **36**, 8272–8281.

104 I. Maliszewska, *Molecules*, 2021, **26**, 7378.

105 S. B. Alvi, P. S. Rajalakshmi, A. Jogdand, A. Y. Sanjay, B. Veeresh, R. John and A. K. Rengan, *Biomater. Sci.*, 2021, **9**, 1421–1430.

106 S. M. van de Looij, E. R. Hebels, M. Viola, M. Hembury, S. Oliveira and T. Vermonden, *Bioconjug. Chem.*, 2022, **33**, 4–23.

107 L. Pasquina-Lemonche, J. Burns, R. D. Turner, S. Kumar, R. Tank, N. Mullin, J. S. Wilson, B. Chakrabarti, P. A. Bullough, S. J. Foster and J. K. Hobbs, *Nature*, 2020, **582**, 294–297.

108 B. Du, X. Jiang, A. Das, Q. Zhou, M. Yu, R. Jin and J. Zheng, *Nat. Nanotechnol.*, 2017, **12**, 1096–1102.

109 Z. Pang, Q. Li, Y. Jia, W. Yan, J. Qi, Y. Guo, F. Hu, D. Zhou and X. Jiang, *Chem. Sci.*, 2021, **12**, 14871–14882.

110 Y. Xie, J. Yang, J. Zhang, W. Zheng and X. Jiang, *Angew. Chemie Int. Ed.*, 2020, **59**, 23471–23475.

111 W. Zheng, Y. Jia, Y. Zhao, J. Zhang, Y. Xie, L. Wang, X. Zhao, X. Liu, R. Tang, W. Chen and X. Jiang, *Nano Lett.*, 2021, **21**, 1992–2000.

112 M. A. Escudero-Francos, V. Cepas, P. González-Menéndez, R. Badía-Laíño, M. E. Díaz-García, R. M. Sainz, J. C. Mayo and D. Hevia, *J. Biomed. Nanotechnol.*, 2017, **13**, 167–179.

113 M. Tang, J. Zhang, C. Yang, Y. Zheng and H. Jiang, *Front. Chem.*, 2020, **8**, 1–17.

114 S. Wang, Y. Wang, Y. Peng and X. Yang, *ACS Appl. Mater. Interfaces*, 2019, **11**, 8461–8469.

115 S. Kalita, R. Kandimalla, A. C. Bhowal, J. Kotoky and S. Kundu, *Sci. Rep.*, 2018, **8**, 1–13.

116 J. Liang, H. Xiong, W. Wang, W. Wen, X. Zhang and S. Wang, *Sensors Actuators, B Chem.*, 2018, **255**, 2170–2178.

117 C. Wang, T. Hong, P. Cui, J. Wang and J. Xia, *Adv. Drug Deliv. Rev.*, 2021, **175**, 113818.

118 D. Pranantyo, P. Liu, W. Zhong, E. T. Kang and M. B. Chan-Park, *Biomacromolecules*, 2019, **20**, 2922–2933.

119 S. Zhu, X. Wang, S. Li, L. Liu and L. Li, *ACS Appl. Mater. Interfaces*, 2020, **12**, 11063–11071.

120 Y. A. Prada, F. Guzmán, C. Ortíz, R. Cabanzo, R. Torres and E. Mejía-Ospino, *Protein J.*, 2019, **38**, 506–514.

121 Y. Xie, Y. Liu, J. Yang, Y. Liu, F. Hu, K. Zhu and X. Jiang, *Angew. Chemie - Int. Ed.*, 2018, **57**, 3958–3962.

122 Y. Li, J. Zhen, Q. Tian, C. Shen, L. Zhang, K. Yang and L. Shang, *J. Colloid Interface Sci.*, 2020, **569**, 235–243.

123 K. Zheng, M. I. Setyawati, D. T. Leong and J. Xie, *Bioact. Mater.*, 2021, **6**, 941–950.

124 K. Zheng, M. I. Setyawati, D. T. Leong and J. Xie, *Nano Res.*, 2021, **14**, 1026–1033.

125 K. Zheng, M. I. Setyawati, D. T. Leong and J. Xie, *ACS Nano*, 2017, **11**, 6904–6910.

126 Y. Wang, M. J. Malkmes, C. Jiang, P. Wang, L. Zhu, H. Zhang, Y. Zhang, H. Huang and L. Jiang, *J. Hazard. Mater.*, 2021, **416**, 126236.

127 Y. Xie, Q. Zhang, W. Zheng and X. Jiang, *ACS Appl. Mater. Interfaces*, 2021, **13**, 35306–35314.

128 J. Meng, Y. Gao, W. Li, J. Wang and X. Chen, *Talanta*, 2021, **234**, 122618.

129 F. Gong, R. Peng, Q. Wu, H. Zhang, Y. Luo and Q. Cui, *Colloids Surfaces A Physicochem. Eng. Asp.*, 2022, **641**, 128608.

130 W.-Y. Chen, J. Lin, W.-J. Chen, L. Luo, E. Wei-Guang Diau and Y. Chen, *Nanomedicine*, 2010, **5**, 755–764.

131 P. Zhuang, K. Li, K. Qian, D. Li and X. Mei, *IET Nanobiotechnology*, 2020, **14**, 412–416.

132 Y. Xie, W. Zheng and X. Jiang, *ACS Appl. Mater. Interfaces*, 2020, **12**, 9041–9049.

133 B. Khlebtsov, E. Tuchina, V. Tuchin and N. Khlebtsov, *RSC Adv.*, 2015, **5**, 61639–61649.

134 A. Ravindran Girija, S. Balasubramanian, R. Bright, A. J. Cowin, N. Goswami and K.

Vasilev, *ChemNanoMat*, 2019, **5**, 1176–1181.

135 Y. Zheng, W. Liu, Y. Chen, C. Li, H. Jiang and X. Wang, *J. Colloid Interface Sci.*, 2019, **546**, 1–10.

136 H. Zhu, J. Li, J. Wang and E. Wang, *ACS Appl. Mater. Interfaces*, 2019, **11**, 36831–36838.

137 M. I. Setyawati, R. V. Kutty, C. Y. Tay, X. Yuan, J. Xie and D. T. Leong, *ACS Appl. Mater. Interfaces*, 2014, **6**, 21822–21831.

138 J. Hsu, *BMJ*, 2020, **369**, 1–2.

139 M. Arshad, S. F. Mahmood, M. Khan and R. Hasan, *BMJ*, 2020, **371**, 1–2.

140 D. Shen, M. Henry, V. Trouillet, C. Comby-Zerbino, F. Bertorelle, L. Sancey, R. Antoine, J. L. Coll, V. Josserand and X. Le Guével, *APL Mater.*, 2017, **5**, 053404.

Chapter 4
Controlling pyridinium-zwitterionic ligand ratio on atomically precise gold nanoclusters allowing for eradicating Gram-positive drug-resistant bacteria and retaining biocompatibility

4.1 Introduction

Since the discovery of antibiotics in 1928, the unrestrained global use of antibiotics has imposed a highly selective pressure on all bacterial species, which has accelerated the acquisition and accumulation of drug-resistant genes *via* horizontal transmission.[1] Several multidrug-resistant (MDR) pathogens, or the so-called 'superbugs,' have emerged over the past 50 years.[2,3] Moreover, some drug-resistant bacteria that were previously considered less harmful, like MRSE, have gained much attention due to their role in the development of drug-resistant strains.[4,5] The widespread MRSE inevitably increases the risk of infection and promotes intra- and inter-species horizontal transfer of the MDR gene.[6] MDR-related infections have imposed a significant burden on the world economy and healthcare systems, yet, the development of new antibiotics has largely stalled over the past 20 years.[7] Therefore, there is an urgent need to develop new strategies to address this significant global health problem.

Recently, gold nanomaterials, including GNPs,[8,9,10] gold nanorods (GNRs)[11] and GNCs,[12,13] have emerged as potentially effective antibacterial agents. They can exhibit several antibacterial actions, such as delivering antibiotics, producing ROS and offering photothermal treatments.[14,15] Among these, the sub-2 nm GNCs have a distinct advantage of readily renal clearance, which can greatly reduce the potential long-term toxicity.[16] Recent studies have focused on synthesising atomically precise GNCs[17] to achieve better quality control, which is important for potential clinical approval. Among

all formula-precise GNCs, the $Au_{25}(SR)_{18}$ type GNC is the most widely studied owing to its high stability, low toxicity, feasible preparation and stable near-infrared (NIR) fluorescence,[18] making it a powerful tool for bioimaging, drug delivery and therapy.[19,20] However, most $Au_{25}(SR)_{18}$ GNCs reported so far are capped with a single-type ligand, limiting the ability to tune their biocompatibility and antibacterial potency, as the requirements for the two are often incompatible. Consequently, most antibacterial nanomaterials have only demonstrated effectiveness *in vitro* but not *in vivo*.[12]

Herein, I synthesised a pyridinium-zwitterionic dual-ligand functionalised $Au_{25}(SR_1)_x(SR_2)_{18-x}$ GNC to address MDR bacteria-induced infections, especially MRSE. The pyridinium ligand is derived from cetylpyridinium chloride (CPC), a commercial mouth mucosa aseptic addictive approved by the US Food and Drug Administration, which affords antibacterial ability. However, it suffers poor prospects for *in vivo* applications due to high cytotoxicity.[21,22] The zwitterionic (ZW) ligand was introduced due to its biocompatibility, biosafety, and low biofouling properties.[23,24] Previously, our group and other researchers showed that ZW ligand-coated nanoparticles are highly stable, biocompatible and strongly resist biofouling.[25,26] By adjusting the GNC surface capping pyridinium/ZW ligand ratio, GNCs that displayed low cytotoxicity and excellent antibacterial activity against clinically isolated Gram-positive drug-resistant species were obtained. Besides, I discovered that the combination of this GNC with conventional antibiotics could significantly enhance the bactericidal potency against MRSE, allowing me to overcome MDR bacterial infections at the cellular level and *in vivo* skin infection models. Furthermore, I exploited the stable NIR-II fluorescence of this GNC to directly monitor the *in vivo* biodistribution, revealing that the GNC was efficiently cleared from the body without inducing observable long-term toxic effects. All these results show that the optimised $Au_{25}(SR_1)_x(SR_2)_{18-x}$ GNC is a new generation of multifunctional fluorescent nanomaterial for treating MDR bacterial infections induced by Gram-positive strains.

4.2 Measurement of GNC Antibacterial Ability with different ligand ratios

4.2.1 Synthesis and characterisation of $Au_{25}(SR_1)_x(SR_2)_{18-x}$-type GNCs

In this study, alkyl-thiolated ZW and pyridinium ligands (abbreviated as C5 and P12, hereafter) were synthesised, and their chemical structures were confirmed by NMR and mass spectrometry (MS), respectively (see **Chapter 2**, **Figure 2.2.5**, **Figure 2.2.6**, and **Figure 2.2.10**). GNCs with different surface ligand capping were then prepared by varying the feeding ratios between 100% C5 and 100% P12 ligands. The formation of Au_{25} NC was characterised by a UV–visible spectrum (UV–vis) absorption peak at ~690 nm with a shoulder at ~810 nm.[27] The characteristic absorption peak was blue-shifted from ~730 to ~690 nm during the first 2 h. Then, the spectrum for Au_{25} NC stabilised after 3 h, suggesting that the synthesis of Au_{25} NC was complete (**Figure 4.2.1**).[28] Using this reaction time, I synthesised GNCs with the increasing feeding ratio of P12 (from 0% to 100%). All mixed P12/C5 groups successfully produced the $Au_{25}(P12)_x(C5)_{18-x}$-type GNCs, indicated by obvious absorption peaks at 690 nm (**Figure 4.2.2**).

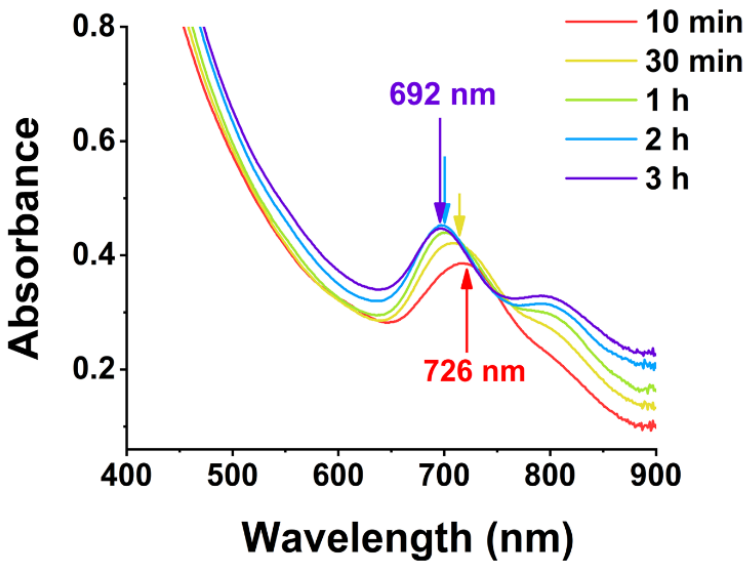

Figure 4.2.1 Time-dependent evolution of the UV–vis spectra of 100% C5-capped GNC (representative species) during the synthesis process.

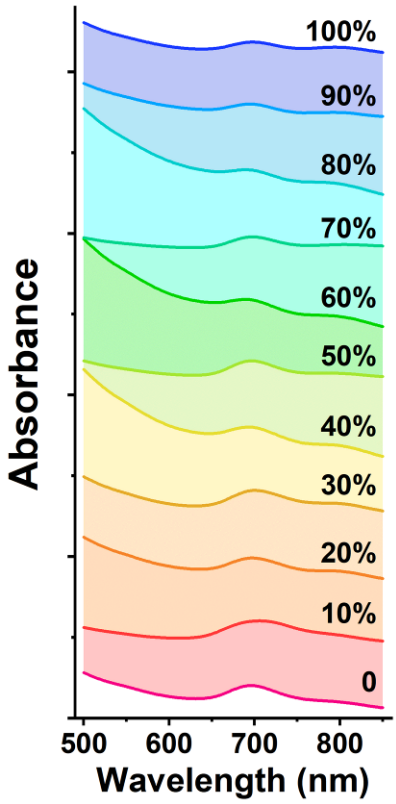

Figure 4.2.2 A collection of UV–vis absorption spectra demonstrating the absorption peaks of $Au_{25}(P12)_x(C5)_{18-x}$ GNCs prepared with different P12 ligand feed ratios. The unanimous peak position has confirmed their structures to be identical.

Under 808 nm laser excitation, the GNCs showed a strong fluorescence peak at ~1100 nm with a shoulder at ~950 nm, regardless of the ligand composition, which is consistent with the previous report (**Figure 4.2.3**).[29] Such fluorescent characteristics are ideal for sensitive fluorescence imaging in the second near-infrared (NIR-II) biological window, which benefits enhanced tissue penetration depth and resolution.[30] Despite having a moderate absolute fluorescence QY (0.54%) compared with small molecular NIR-II emitting dyes, this NIR fluorescence has allowed me to track its localisation *in vitro* and *in vivo*, which will be demonstrated later.[31–33]

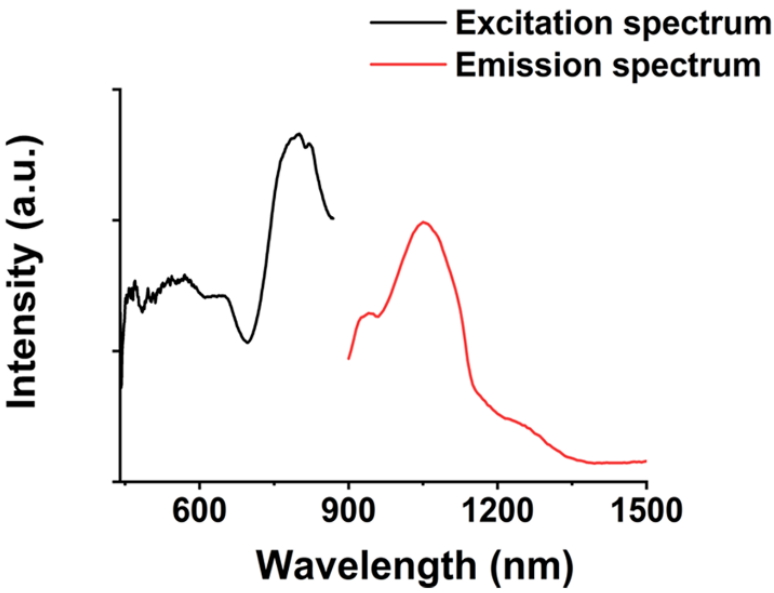

Figure 4.2.3 NIR fluorescence excitation (black line, monitored with λ_{EM} = 1100 nm) and emission (red line, λ_{EX} = 810 nm) spectra of 100% C5-capped GNC.

The GNC size prepared under different ligand feeding ratios was measured by DSAC-TEM analysis, which revealed the GNC granule size to be around 1.2 nm with negligible difference between each different-ligand group (**Figure 4.2.4** and **Table 4**). These results are consistent with the ultra-small size of Au_{25} NCs reported in the literature.[34] The UV–vis spectra, NIR fluorescence spectra and TEM images of GNCs with other P12/C5 composition has no obvious differences with this representative species

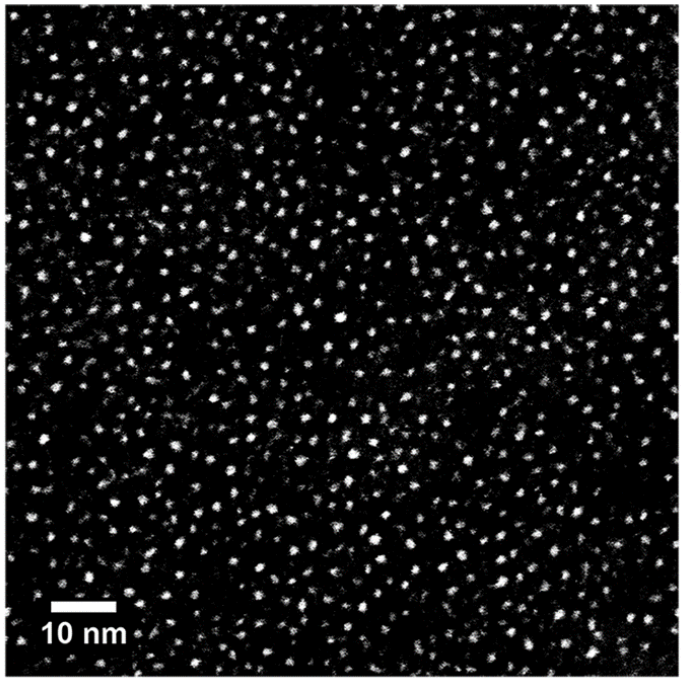

Figure 4.2.4 DSAC-TEM images (scale bar: 10 nm) of 100% C5-capped GNC prepared on an ultra-thin carbon film copper mesh.

Table 4 Characterisation of $Au_{25}(P12)_x(C5)_{18-x}$ GNCs prepared at different P12 feeding ratios.

P12 ratio in feeding (%)	Zeta potential ± SD (mV)	Size ± SD (nm)	Primary product (P12/C5)	Secondary product(s) (P12/C5)	Deconvoluted MW (Da)
0	-4.7 ± 1.1	1.18 ± 0.21	0/18	-	11282
10	8.8 ± 0.6	1.15 ± 0.23	1/17	2/16	11176
20	14.1 ± 2.0	1.21 ± 0.32	1/17	2/16	11167
30	24.1 ± 0.9	1.11 ± 0.41	4/14	5/13	10954
40	36.3 ± 2.3	1.15 ± 0.22	7/11	8/10	10710
45	37.5 ± 1.6	1.19 ± 0.24	8/10	7/11 & 9/9	10708
50	43.3 ± 1.5	1.16 ± 0.23	8/10	7/11 & 9/9	10662
60	49.5 ± 3.1	1.14 ± 0.28	9/9	8/10	10575
70	56.9 ± 3.1	1.15 ± 0.26	11/7	10/8 & 12/6	10466
80	62.5 ± 1.9	1.17 ± 0.17	12/6	11/7	10400

90	66.5 ± 1.0	1.14 ± 0.27	13/5	12/6	10327
100	71.4 ± 1.6	1.18 ± 0.22	18/0	-	9956

In addition, the zeta potential of GNCs prepared under different P12 ligand feeding ratios was measured and summarized in **Table 4**. The zeta potential of GNCs was gradually and progressively shifted from around -5 mV to > +70 mV as the P12 ligand feeding ratio was increased from 0 to 100%, indicating successful incorporation of the P12 ligand onto the GNC surface.

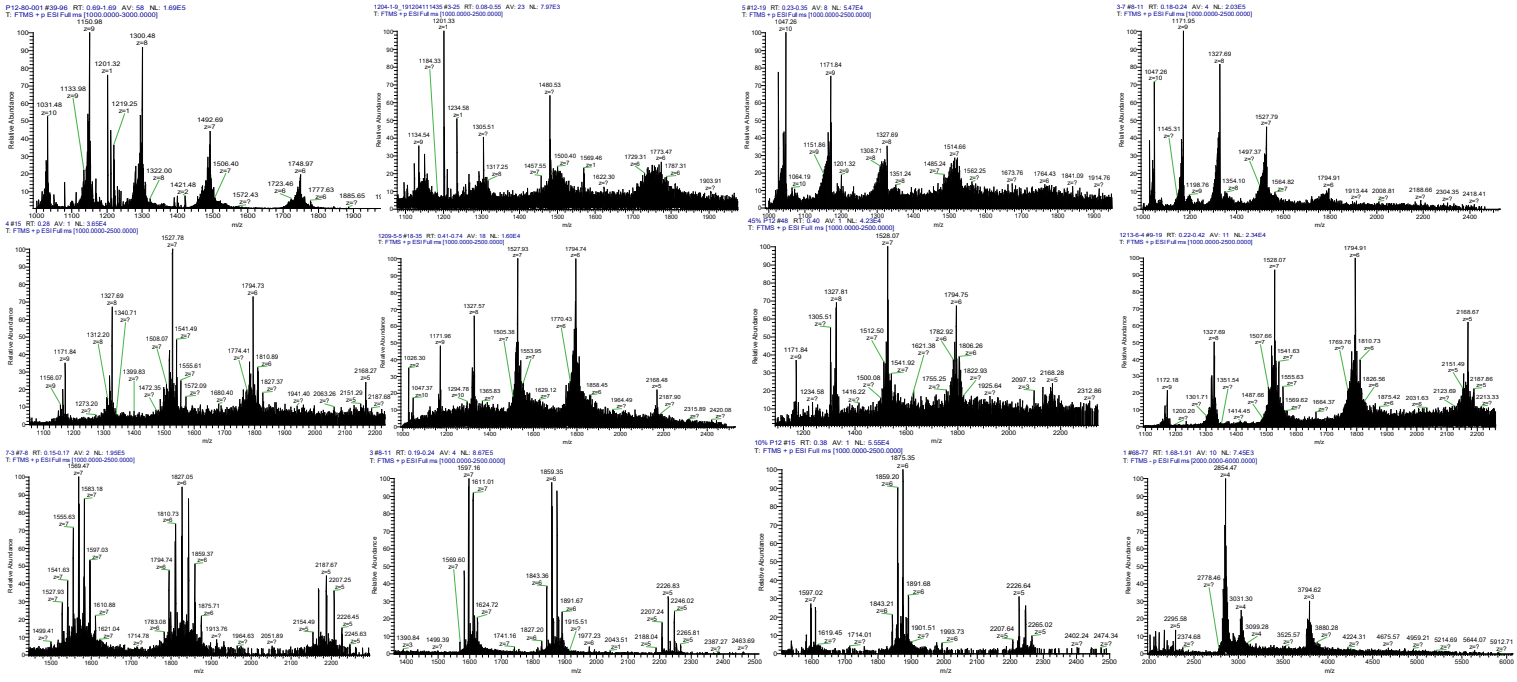

Figure 4.2.5 ESI-MS graphs of GNCs with different P12 ligand feed ratios. (From left to right, top to bottom: 100%, 90%, 80%, 70%, 60%, 50%, 40%, 30%, 20%, 10%, 0%).

The GNCs were further characterised by electrospray ionisation MS (ESI-MS), which yielded the general molecular formula of diverse $Au_{25}(P12)_x(C5)_{18-x}$ (x = 0–18, depending on the P12/C5 feeding ratio). After mass deconvolution, the exact mass of the dominant peaks was matched with the theoretical molecular weight (**Table 4** and **Figure 4.2.5**). The relative abundance of each GNC was derived from its corresponding peak in the MS[35], and the relationship between the GNCs surface ligand composition and corresponding ligand feeding ratio was summarized in **Table 4**. It is apparent that except

for those prepared with 100% P12 or 100% C5, all other GNCs prepared were a mixture of differently formulated $Au_{25}(P12)_x(C5)_{18-x}$ GNCs, which could be explained by the putative forming mechanism of GNCs. Upon adding the dual-ligand solution to chloroauric acid, the thiol groups quickly reduced the trivalent Au(III) ions to Au(I) to form the Au(I)-ligand complexes[36]. Due to the random reduction and combination of Au(I) with different capping ligands, the complex units would have multiple types. The subsequent addition of sodium borohydride to reduce Au(I) for cluster formation and sodium hydroxide (for controlling ligand etching ability) allowed the precisely reduction of some Au(I)-ligand complex to Au(0), forming a stochastic mixture of dual-ligand capped GNCs with a variety of ligand capping ratios[37]. However, controlled mainly by ligand feeding ratio, this synthesis condition could allow for some specific GNCs to be the main product. The relative abundance of each GNC formulation could be derived from the corresponding MS peak intensity.[35]

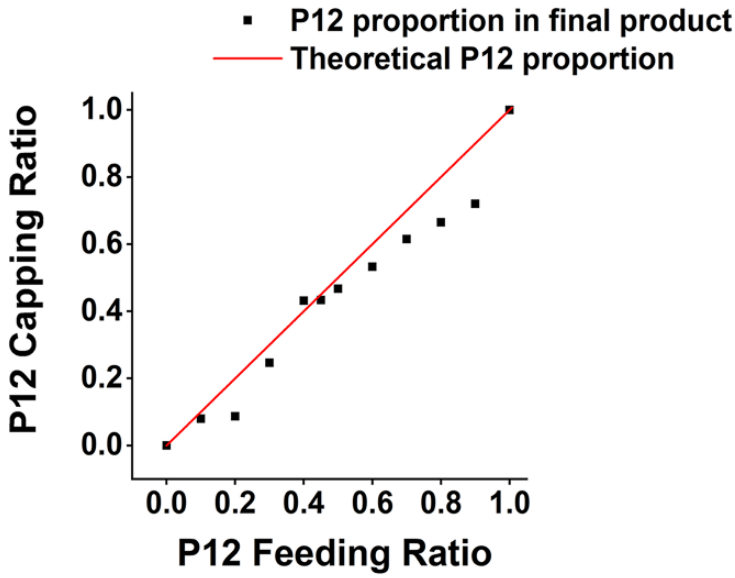

Figure 4.2.6 A plot of the GNC surface P12 capping ratio versus the P12-feeding ratio. The red line indicates the theoretic output, assuming no ligand affinity difference, whereas the black dots represent the actual P12 ratio.

A plot of the average content of P12 in the GNCs against the feed ratio (**Figure 4.2.6**)

revealed that the product line was mostly below the feeding line. Therefore, the C5 ligand appeared to bind more strongly to the gold kernel than P12, possibly because of the lower electrostatic repulsion among the C5 (neutral overall) over P12 (positively charged) ligands. The only exception was observed at a feeding ratio of 40%–45%, where the product composition (mainly $Au_{25}(P12)_8(C5)_{10}$) matched the feeding ratio, suggesting that the products of this ligand ratio were exceptionally stable.

4.2.2 Antibacterial screening

The antibacterial activity of GNCs was assessed using a few common Gram-positive (*S. a* and MRSA) and Gram-negative (*E. c*, *K. p* and *P. a*) species (Table 5 [16 h] and Table 6 [24 h]). The relationship between the antibacterial activity and the P12 ligand feeding ratio (*i.e.* surface positive charge density) of GNCs was interesting: first, the activity increased with the increasing P12 ligand feeding ratio (up to 50%), then there was a slight decrease (from 50% to 70%), and finally it increased again (from 70% to 100%). This trend was totally unexpected; since the antibacterial properties of GNC were mainly derived from the positively charged P12 ligand and not the C5 ligand. I had anticipated the antibacterial activity to be positively correlated with the P12 content (GNC surface positive charge density). The fact that the GNC with a 50% P12-feeding ratio exhibited comparable antibacterial activity to that with 100% P12 ligand suggests that there must be an optimal window to tune the GNC antibacterial properties and biocompatibility.

Table 5 Antibacterial activity of different GNCs against five common pathogens (the colour code represents the antibacterial activity: red for high, yellow for medium, green for low and grey for negligible, and the same below).

P12 ratio in feeding (%)	***MIC (μg mL^{-1} of GNC)**				
	****E. coli***	***K. pneumoniae***	***P. aeruginosa***	*****S. aureus***	***MRSA***
0	>128	>128	>128	>128	>128

10	>128	>128	64	64	128
20	128	128	64	64	64
30	>128	>128	32	64	64
40	128	128	64	32	32
45	32	64	32	8	16
50	32	32	16	8	8
60	64	64	16	32	32
70	64	64	32	16	16
80	64	64	32	16	32
90	32	32	8	16	32
100	32	32	32	8	8

*MIC—Minimum inhibitory concentration

***Escherichia coli, Klebsiella pneumoniae, Pseudomonas aeruginosa* are Gram-negative bacteria.

****Staphylococcus aureus* and Methicillin-resistant *Staphylococcus aureus* (MRSA) are Gram-positive bacteria.

Table 6 24-h antibacterial result of different formulated GNCs toward five common pathogens (the colour scale represents the antibacterial effect: the red stands for high, the yellow stands for medium, the green represents low, and the grey represents negligible).

P12 ratio in feeding (%)	**MIC (μg mL^{-1} of GNC)**				
	E. coli	***K. pneumonia***	***P. aeruginosa***	***S. aureus***	***MRSA***
0	>128	>128	>128	>128	>128
10	>128	>128	128	128	128
20	>128	128	64	128	64
30	>128	>128	64	64	64
40	>128	>128	128	32	64
45	64	128	64	16	32
50	32	64	16	32	16
60	128	128	32	32	32
70	64	64	32	32	32
80	64	64	32	32	32
90	32	64	16	32	32
100	32	64	32	16	16

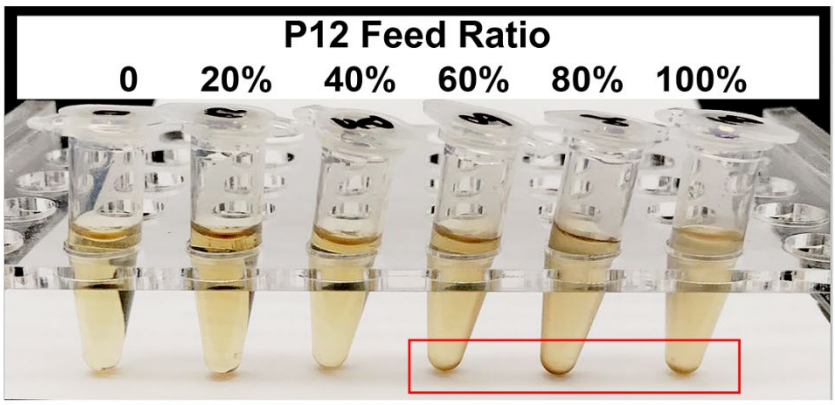

Figure 4.2.7 Photo of GNCs (all 128 μg mL^{-1}) with increasing P12 feed ratio in LB broth. Aggregation was observed for GNCs prepared with ≥60% P12 ligand but not for those prepared with ≤40% P12 ligand (labelled with a red box).

Table 5 and **Table 6** reveal that the GNCs were more potent towards Gram-positive strains than towards Gram-negative ones. This phenomenon can be attributed to the differences in the surface structure between Gram-positive and -negative bacteria. The surface of Gram-positive bacteria is strongly negatively charged;[38] thus, they exhibit a strong electrostatic interaction with cationic materials. For example, wall teichoic acid (WTA), a distinct cell wall component in Gram-positive bacteria, consists of repeating poly(glycerol phosphate) units and a phosphodiester terminus. WTA constitutes the polyanionic network, making the cell envelope highly negatively charged and susceptible to the binding of cationic materials.[39,40] Besides, anionic lipids, such as phosphatidylglycerol (PG) and cardiolipin, constitute ~80% of the total lipids in Gram-positive bacterial membranes, but they only count for ~30% in Gram-negative strains.[41,42] Moreover, negatively charged phospholipids, such as PGs, are present on both sides of bacterial cell membranes rather than only the inside membrane found on mammalian cells. This difference can provide selectivity between mammalian cells and bacteria for some positively changed antibacterial agents.[43] As shown in **Table 5**, the three best-performing GNCs (45%, 50% and 100% P12 feeding ratio) were selected for

further tests using more Gram-positive strains, including *Staphylococcus epidermidis*, *Staphylococcus haemolyticus*, *Enterococcus faecium* and their corresponding drug-resistant strains (MRSE, MDR *S. haemolyticus* and VRE).

Table 7 The antibacterial activity toward Gram-positive bacteria of selected GNCs.

P12 ratio in feeding (%)	MIC (μg mL^{-1} of GNC)							
	S. aureus	*MRSA*	*S. epidermidis*	*MRSE*	*S. haemolyticus*	*MDR S. haemolyticus*	*E. faecium*	*VRE*
45	8	16	8	8	32	32	32	16
50	8	8	8	8	32	32	32	16
100	8	8	4	4	8	8	16	16

Table 7 reveals that although the GNCs with 100% P12 exhibited the best antibacterial potency among the three groups, especially against MRSE, those with 45% and 50% P12 feeding also showed similar activity. These results further affirmed that antibacterial potency is not linearly correlated to the active P12 ligand content. Besides, during antibacterial tests, I observed aggregation of GNCs with ≥60% P12 in feeding in LB culture media, suggesting significant non-specific interactions with negatively charged serum proteins in cell culture media, which could adversely affect their antibacterial potency. This result was consistent with their high positive zeta potentials, allowing them to interact with negatively charged serum proteins *via* electrostatic attractions. This represents a key drawback for such strongly positively-charged GNCs and other nanomaterials, which can greatly limit their applications as antibacterial reagents (**Figure 4.2.7**). Therefore, in synthesising mixed ligand-capped GNCs, I must balance the active/inert ligand (P12/C5 here) ratio and determine their actual antibacterial properties to find out the optimal ligand ratio.

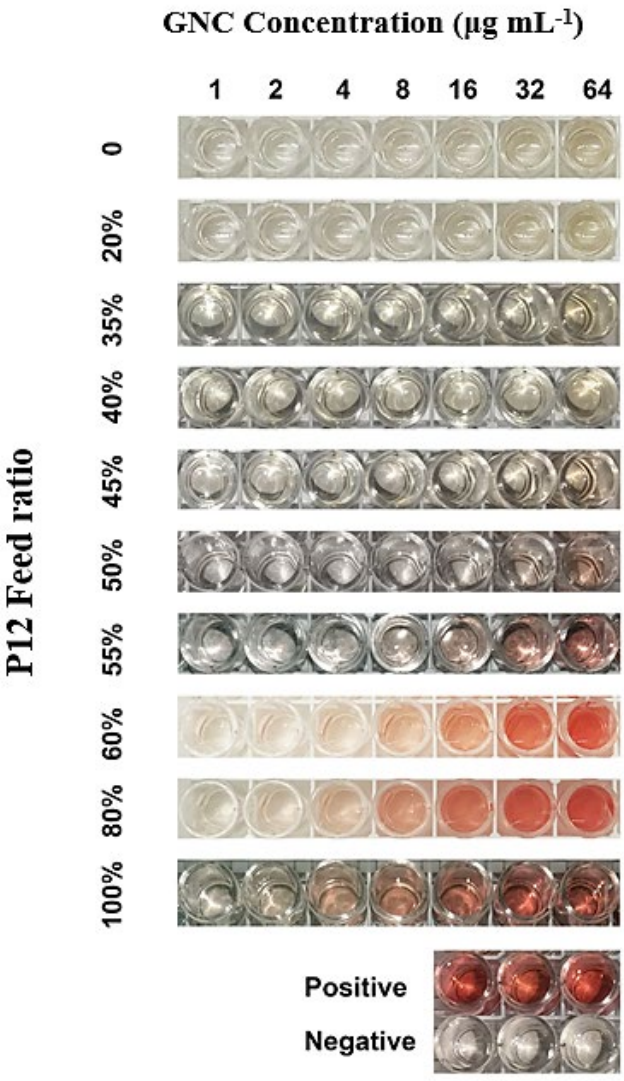

Figure 4.2.8 Haemolytic figures of GNCs with different P12 feed ratios.

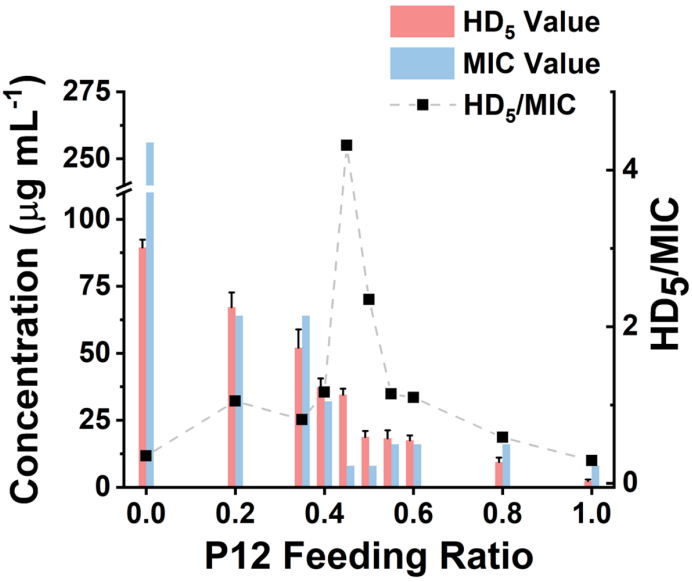

Figure 4.2.9 HD_5/MIC values for dual-ligand GNCs prepared under different P12 feeding ratios. The greater the HD_5/MIC, the higher the biosafety and antibacterial ability of the material. A sudden change in haemolytic potency appears as the feeding ratio approaches 50% (MIC value is from the anti-*S. aureus* result).

4.3 Biocompatibility and Cytotoxicity

4.3.1 Haemolysis test

To determine the optimal ligand ratio, I performed a haemolytic test (**Figure 4.2.8**). The resulting HD_5 (the GNC dose that causes a 5% haemolysis value against the P12 ligand-feeding ratio was calculated to optimise the P12 feeding ratio (**Figure 4.2.9**). The GNC haemolytic efficiency was enhanced (HD_5 reduced) with the increasing P12 ligand content. This result indicated that increasing the ZW ligand ratio could reduce the cytotoxicity of GNCs. The GNC prepared with 45% P12 still maintained a relatively high HD_5 of 34 μg mL^{-1}, about twice that of the GNC prepared with 50% P12, while retaining almost the same MIC. Accordingly, GNCs prepared with >45% P12 could be too cytotoxic, thus unfavourable for *in vivo* applications. To determine the optimal P12 feeding ratio, I plotted the HD_5/MIC ratio versus the P12 feeding ratio to collectively depict the change in biosafety and antibacterial activity of dual ligand GNCs. When the feeding ratio of P12 approached 45%, a sharp peak appeared, indicating GNC prepared

with 45% P12 in feeding has a high antibacterial ability (low MIC) while maintaining low haemolyticity (high HD_5), hence high biosafety, which is important for biomedical applications, especially *in vivo*. This result also highlighted the importance of incorporating a certain proportion of ZW ligand in order to maintain good overall biocompatibility.

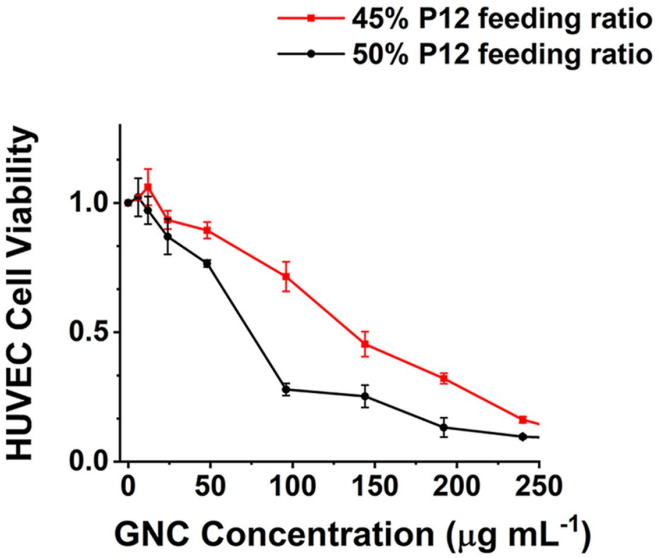

Figure 4.3.1 Comparison of the cytotoxicity of the 45%- and 50%-P12 GNCs toward human umbilical vein endothelial cells (HUVECs) with 24-h incubation.

4.3.2 Cytotoxicity test

We further evaluated the cytotoxicity of GNCs prepared with 45% and 50% P12 ligand feeding toward human umbilical vein endothelial cells (HUVECs). Compared with the 50%-P12 GNC, HUVECs demonstrated a much higher tolerance toward the 45%-P12 GNC (**Figure 4.3.1**), indicating a striking shift in cytotoxicity as the P12 feeding ratio reaches 50%. This result is consistent with the significantly lower HD_5 value for the 50% P12 GNC observed above.

The use of excess cationic P12 ligand on GNC capping can lead to high cytotoxicity, adversely affecting its potential for *in vivo* application. However, too low the P12 ligand content can lead to low antibacterial activity. Thus, the key here is to balance the active/inert ligand ratio to achieve high stability and biocompatibility without

compromising antibacterial potency.

The above results comprehensively proved that GNCs prepared with 45% P12 feeding ligand displayed excellent antibacterial activity, low cytotoxicity, and good stability. Therefore, the 45% P12 ligand-feeding ratio was considered optimal for preparing GNCs (denoted as GNC hereafter) for all the subsequent studies.

4.4 Combinational antibacterial analyses

We considered that, besides the direct killing of bacteria, GNC could sensitise drug-resistant bacteria toward various antibiotics to restore their antibacterial potency.[44] To investigate this potential, I selected MRSE as the model microbe, to which this GNC demonstrated high inhibition. Seven antibiotics used to treat Gram-positive bacterial infections from four main categories: β-lactams (penicillin and carbapenem), glycopeptide, macrolides and tetracycline were tested. The result demonstrated that, except for Van and tetracycline, all the other antibiotics exhibited low efficacy against this bacterial strain, with minimum inhibition concentrations (MICs) value ≥32 μg mL^{-1} (Table 8). The test revealed high drug resistance of this strain of MRSE to several antibiotics.

Table 8 Comparison of MIC values of seven antibiotics used to treat Gram-positive bacterial infections from four main categories: β-lactams, glycopeptide, macrolides, and tetracycline against a clinically isolated strain of MRSE.

Antibiotics	Amp	Oxa	Pen	Imp	Van	Ery	Tet	Azi
MIC (μg mL^{-1})	32	>128	64	64	2	32	≤1	>128

Amp—ampicillin, Oxa—oxacillin, Pen—penicillin, Imp—imipenem, Van—vancomycin, Ery—erythromycin, Tet—tetracycline and Azi—azithromycin.

A checkerboard method was further employed to evaluate the antibacterial properties of GNC and antibiotic combinational therapy.[45,46] Imipenem (Imp), oxacillin (Oxa) and

erythromycin (Ery), representing three classes of antibiotics, were applied with and without the GNC. Then, the fractional inhibitory concentration index (FICI) was calculated after 24 h of incubation. The calculated FICIs show that in joint applications, GNC exhibited the additive antibacterial ability with all three antibiotics, with The FICI values being 1, 0.508, and 0.75 for GNC and Imp, Oxa, and Ery, respectively (**Figure 4.4.1**). Particularly, the Oxa group showed an exciting 128-fold decrease in the antibiotic dosage needed to inhibit bacterial growth compared to the application of the antibiotic alone.

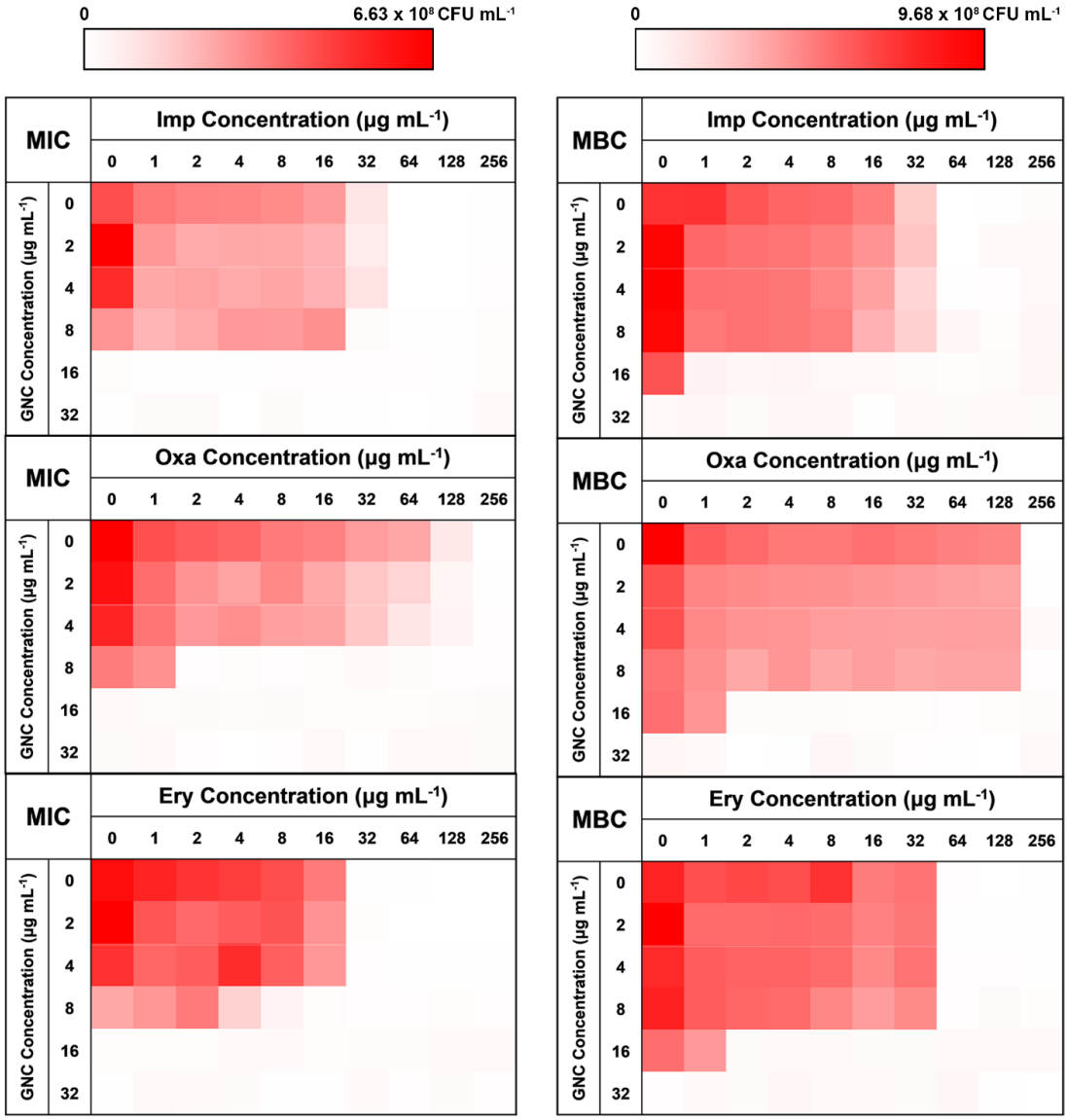

Figure 4.4.1 24-h checkerboard results of the GNC with imipenem (Imp), oxacillin (Oxa), and erythromycin (Ery) (OD_{600} values are given in the colour scale, a darker colour

represents a higher bacteria concentration).

We further prolonged the incubation to 48 h and re-measured FICI for each group (Figure 4.4.1). The FICIs of all three groups were closer to 0.5, indicating the additive effect of GNC and antibiotics was enhanced. Specifically, adding 16 μg mL^{-1} of GNC and 2 μg mL^{-1} of any of the three tested antibiotics could prevent the growth of MRSE. I further took out the bacterial mixture and spread it onto agar plates to check the survival of MRSE completely, and the agar plates remained unstained for the test groups compared with innumerable colonies for PBS control (Figure 4.4.2). The results indicated that GNC had a remarkable ability to re-sensitise MRSE toward several antibiotics. Owing to the higher bactericidal efficiency, Imp was selected as the model antibiotic for further studies.

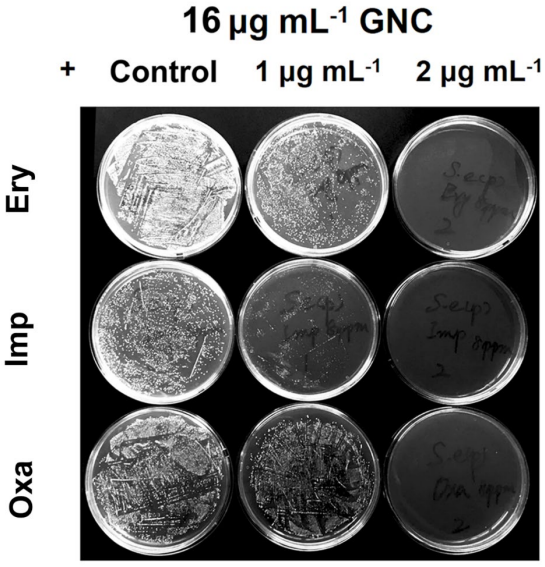

Figure 4.4.2 Undiluted plate-coating results of MRSE colonies after treatment with PBS buffer (control), different concentrations of Ery/Imp/Oxa and 16 μg mL^{-1} GNC to visually display changes in colonies.

The MRSE-killing efficiency of this combination was measured by plotting the time-dependent killing graph (Figure 4.4.3 and Figure 4.4.4). Compared to the PBS control, adding Imp did not significantly inhibit bacterial growth due to inherent high drug

resistance. However, the GNC alone showed considerable bactericidal properties, giving rise to 10^5-fold lower MRSE densities at 24 h. The combined group showed the best results, where the amount of MRSE colony was ~40 and 100-fold lower than that of the GNC-only group at 12 and 24 h, respectively. Impressively, the bacterial count of the GNC+Imp combination group was more than 10^7-fold lower than that of the control group at 24 h, demonstrating an excellent additive potency of the combined GNC and Imp in MRSE killing.

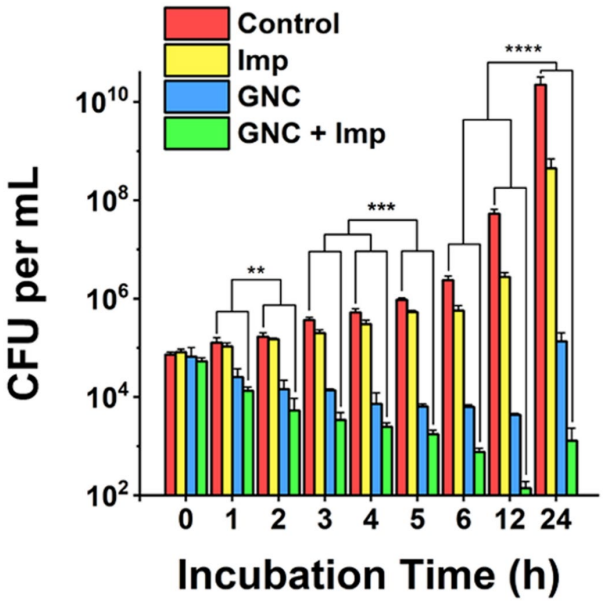

Figure 4.4.3 Time-killing curves demonstrate a superior antibacterial efficiency of the combination of GNC and Imp compared to their separate applications. PBS buffer (control), Imp only (2 μg mL^{-1}), GNC only (16 μg mL^{-1}), and a combination of GNC (16 μg mL^{-1}) and Imp (2 μg mL^{-1}) (n = 3, **: 0.01 <*P* <0.05, ***: *P* <0.01 and ****: *P* <0.001).

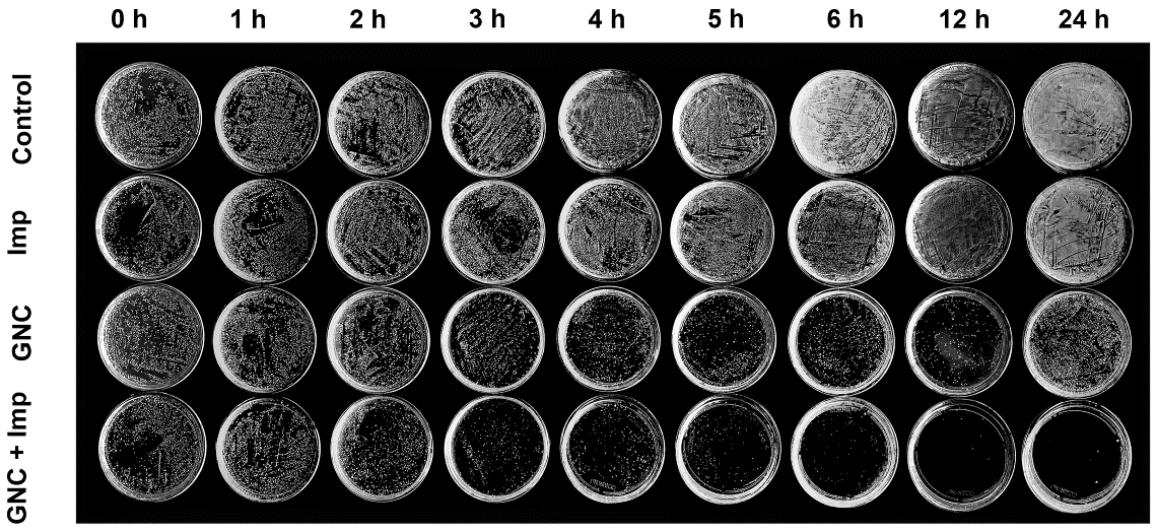

Figure 4.4.4 The undiluted time-dependent bactericidal results of treatments with the PBS buffer (control), Imp only (2 μg mL^{-1}), GNC only (16 μg mL^{-1}), and a combination of GNC (16 μg mL^{-1}) and Imp (2 μg mL^{-1}) to visually display changes in colonies.

4.5 Antibacterial mechanisms

In general, cationic membrane-active molecules can exert several mechanisms to affect bacterial membrane function, for instance, attracting phospholipids to form defects and membrane leakage or perturbing membranes to induce lipid flip-flop.[42] The membrane damage causes detrimental membrane de-polarisation and spillage of cell contents, allowing antibiotics to penetrate the impaired bacterial defence for swift killing.[47] The SEM images of MRSE cells revealed significant morphological differences after each different treatment (**Figure 4.5.1**). For the negative control, all MRSE cells were spherical without apparent broken parts or wrinkles. Almost identical morphologies were observed for the Imp group, suggesting that the treatment with Imp alone did not cause noticeable damage to MRSE cells. In contrast, the GNC-treated group showed significantly altered cell morphologies and collapsed structures. The treated MRSE cells were tightly clustered together on a larger scale. A closer view revealed that the surface was covered with small grooves and wrinkles, indicating viability loss. This phenomenon was even more evident for the combined group (**indicated with red arrows**), where the grooves and wrinkles were deeper with a concave surface, indicating that the GNC+Imp

combination could effectively agglutinate and deform bacterial cells, resulting in efficient bacterial killing.

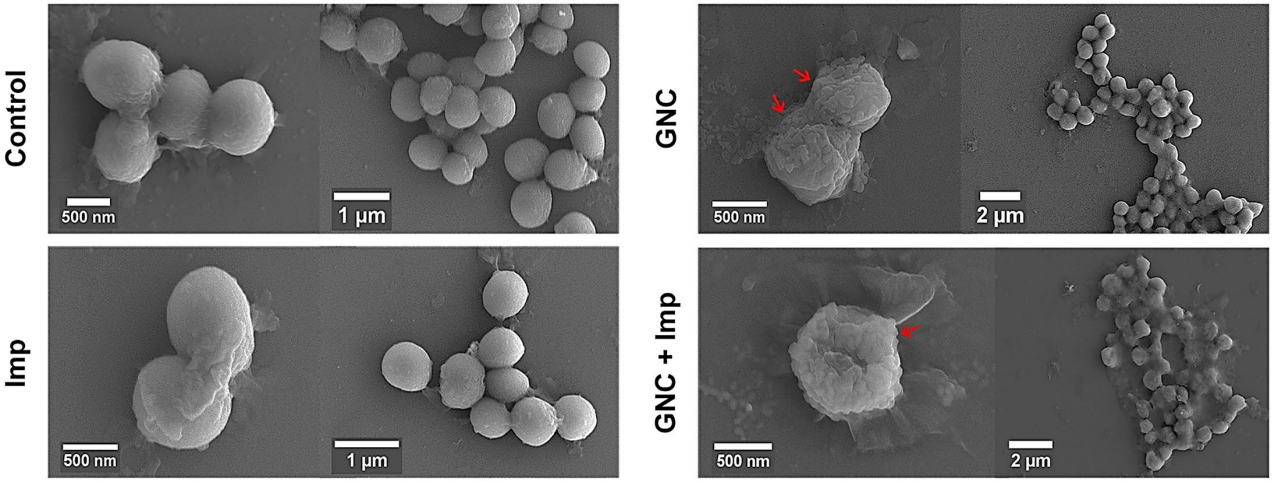

Figure 4.5.1 Typical SEM images of MRSE after a 4-h treatment of PBS buffer (control), 2 μg mL^{-1} Imp, 16 μg mL^{-1} GNC, and a combination of Imp (2 μg mL^{-1}) and GNC (16 μg mL^{-1}).

After treatment with GNC+Imp, the MRSE cells formed irregular clusters, which could hinder migration. This phenomenon was further confirmed by the corresponding NIR fluorescence image of the aggregated MRSE cells (**Figure 4.5.2**). This result indicated that GNCs covered the envelope of MRSE cells, allowing them to aggregate by neutralising their negative surface charges and forming 'bacterial clusters' to limit spread and prolong the interaction.

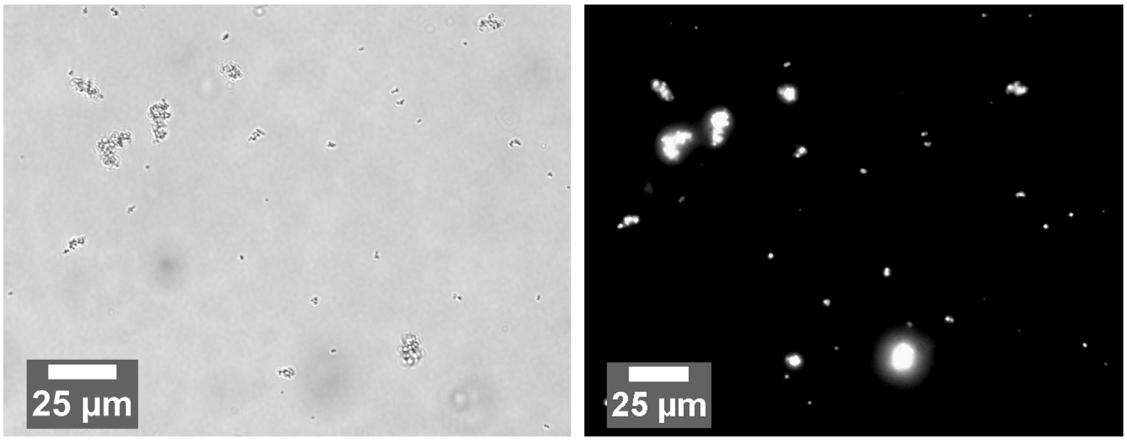

Figure 4.5.2 Bright-field image (left) and the corresponding NIR fluorescence image (right) show that the GNC+Imp treated MRSE bacteria were extensively aggregated.

TEM images (**Figure 4.5.3**) further confirmed the interaction of GNC with MRSE cells, which demonstrated the adhesion and penetration of GNCs within the cell envelope. Compared with the intact shape and apparent division septa for bacterial cells in the control group, the GNC+Imp treated group showed an abnormal cell division phenomenon: uneven division and empty cell walls were observed. Moreover, GNCs were mainly distributed within spaces on the cell envelope, indicating specific binding (**indicated with red arrows**).[48]

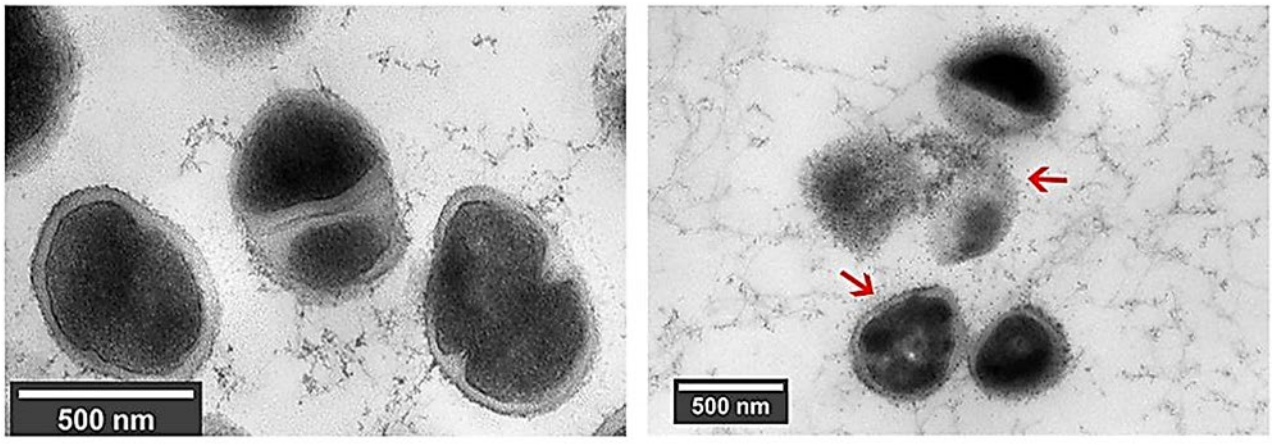

Figure 4.5.3 TEM images of PBS buffer (control group, left) and 16 μg mL^{-1} GNC + 2 μg mL^{-1} Imp-treated MRSE (right).

The antibacterial mechanism of GNC was further investigated. Although GNC binding-

induced bacterial aggregation was already observed, it is still useful to investigate the specific binding target. The high abundance of negatively charged WTA may serve as a binding target for the positively charged GNCs *via* electrostatic interactions. Isothermal titration calorimetry (ITC) was conducted between GNCs and WTA, which revealed a multiple-binding endothermic interaction (Figure 4.5.4), indicating that WTA could initiate bacteria–GNC interactions.[49] To further verify this, a fluorescence competition assay with TR-Cadaverine was carried out. This dye can form a complex with WTA to quench its fluorescence. If GNC can compete with TR-Cadaverine in binding with WTA, adding GNC would result in dye release and fluorescence recovery. Figure 4.5.5 shows that the fluorescence of TR-Cadaverine significantly increased with an increase in GNC concentration and was saturated at ~8 μg mL^{-1}. Further increasing the GNC concentration could quench the dye fluorescence, possibly *via* dynamic quenching at high concentrations.[50] These results confirmed that WTA was a binding target for the GNC.

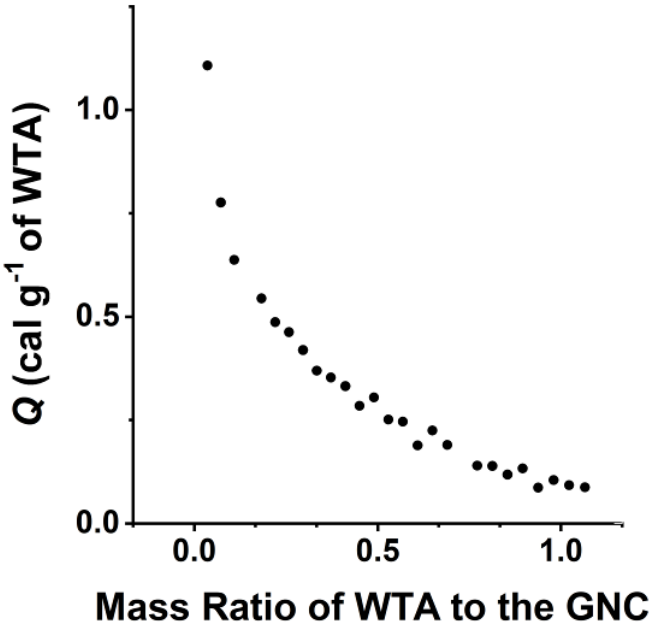

Figure 4.5.4 Isothermal titration calorimetry (ITC) result for specific binding between GNCs and WTA.

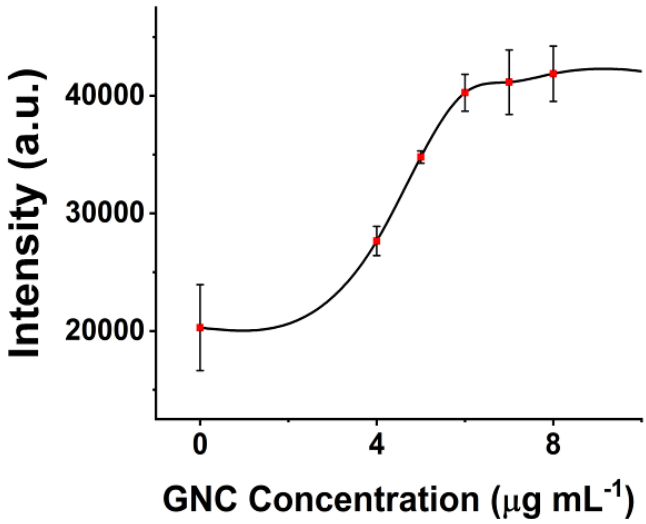

Figure 4.5.5 Plot of fluorescent intensity vs GNC. With an increase in the GNC concentration, the fluorescence emitted by the free TR-cadaverine was enhanced until saturation (n = 4).

Upon binding to the bacterial cell membrane, the positive charges on the GNC could induce membrane potential dissipation and cause cell death. In this study, the membrane potential was determined by measuring the ratio of green to red fluorescence using a fluorescent kit to stain the bacteria, where the green to red fluorescence ratio is linear with the membrane potential dissipation rate (**Figure 4.5.6** and **Figure 4.5.7**). Adding only Imp did not cause a significant upheaval of green fluorescence, indicating that Imp had no apparent effect on the bacterial membrane potential. However, a sharp decrease in the red fluorescence and an increase in green fluorescence were observed for the GNC-treated MRSE cells, suggesting significant membrane potential dissipation. Membrane potential dissipation can severely interfere with normal physiological activities and cause cell death; thus, this result was consistent with the SEM and TEM images. Moreover, clustered bacteria were also observed in the GNC groups, indicating that membrane potential dissipation was related to the GNC-induced bacterial agglomeration.[51]

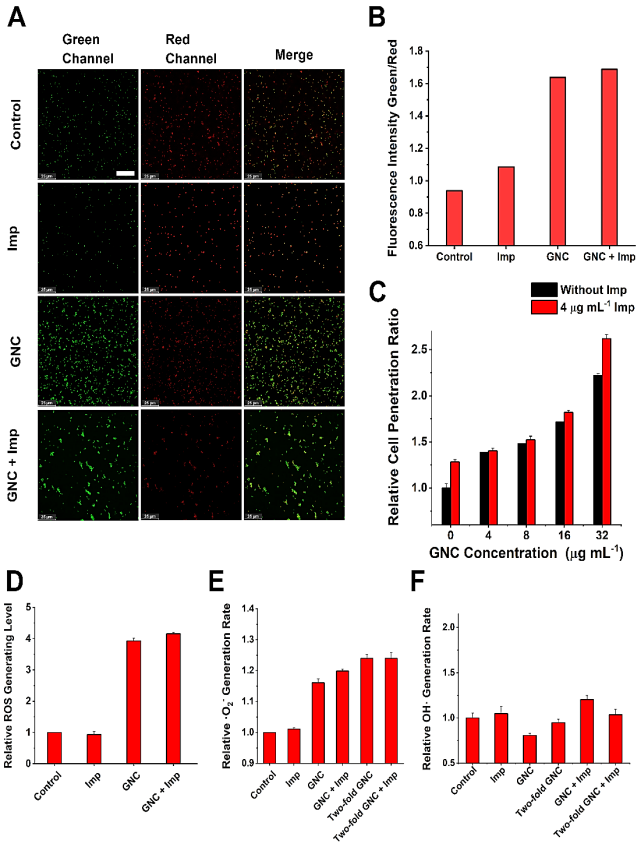

Figure 4.5.6 Membrane potential of MRSE cells after treatment in PBS buffer (control), 4 μg mL^{-1} Imp, 16 μg mL^{-1} GNC, and a combination of Imp (4 μg mL^{-1}) and GNC (16 μg mL^{-1}) (scale bar: 25 μm).

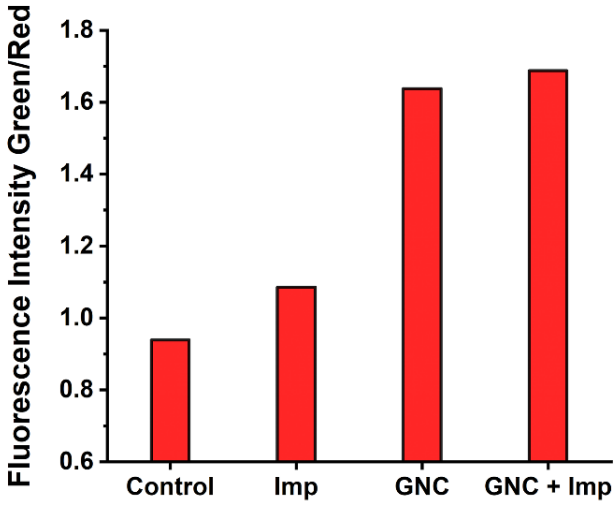

Figure 4.5.7 Comparison of the green-to-red fluorescence intensity ratios in different groups.

Inserting positively charged amphiphilic material has been shown to lysis cell

membranes.[52,53] The collapse of the MRSE cell structure, as observed in the SEM images, indicated that GNC could affect cell envelope completeness. To investigate whether the GNC treatment affected the integrity of cell membranes, I used a cell-integrity analysis kit, in which the dye can penetrate damaged membranes and bind to intracellular proteins. A positive correlation between the GNC concentration and dye incorporation confirmed that GNC could damage the integrity of the cell membrane (Figure 4.5.8). The GNC+Imp combination exhibited even higher membrane permeation than the GNC-only treatment, consistent with the superior bactericidal potency. The antibacterial mechanism of Imp is to inhibit the synthesis of cell walls, thereby bursting the bacterial cells. By damaging bacterial cell membrane, GNC can effectively enhance antibiotics transverse bacterial cell membranes, resulting in additive bactericidal potency.

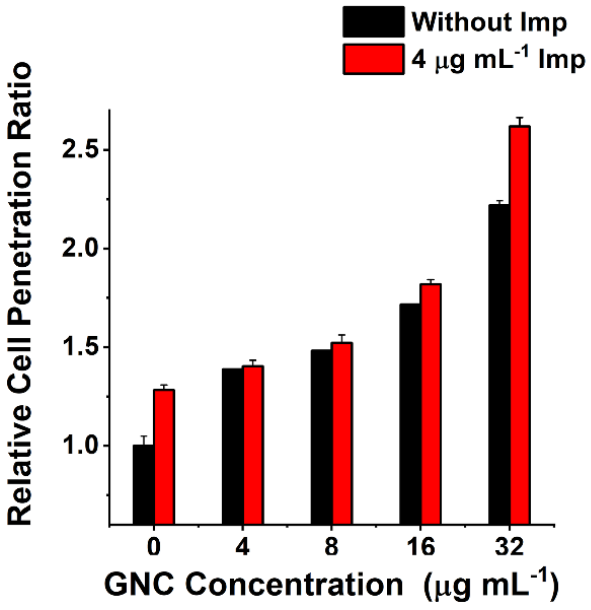

Figure 4.5.8 Comparison of the cell penetration rate at different concentrations of GNC with/without the addition of 4 μg mL^{-1} Imp (n = 4).

GNCs have been shown to generate ROS, which has bactericidal effects.[12] Therefore, I studied ROS generation in all treatments (Figure 4.5.9). Imp alone did not produce significant ROS, whereas GNC exhibited a good ability to generate ROS. Further addition

of Imp did not increase ROS production. Therefore, only GNC is responsible for ROS production in the GNC+Imp combination. To investigate the exact species of ROS responsible here, I used two test kits to detect common ROS species, $\bullet O_2^-$ and •OH (Figure 4.5.10). There was an increase in the production of $\bullet O_2^-$ but not •OH in the GNC treatments (Figure 4.5.11). Hence, $\bullet O_2^-$ was confirmed to be the ROS species generated by the GNC treatment. Its high reactivity can damage cell membranes and other essential biological macromolecules to exert bactericidal effects. Some ROS-generating antibacterial materials have been found to have higher antibacterial activities on Gram-positive over Gram-negative strains, allowing them to be even used as Gram-selective staining reagents[54,55,56]. The ROS generation ability of this GNC may also account for its higher antibacterial effect on Gram-positive species like MRSE or *S. aureus* over Gram-negative ones.

Based on the above experimental results, this GNC exhibits four antibacterial mechanisms. 1) by binding to WTA, the GNC could interact and aggregate bacterial cells to control their spread and initiate subsequent antibacterial steps. 2) Its positive charges can interrupt the bacterial membrane potential, which may interfere with normal bacterial functions by disrupting the functions of some crucial enzymes[57]. 3) Simultaneously, the amphiphilic cationic ligands can disrupt the cell membrane, thus enhancing the permeation of antibiotics and improving their bactericidal effect, which, I believe, is the most important antibacterial mechanism of this GNC.[58] 4) It can effectively generate ROS to damage the bacterial membrane and other vital genetic and cellular molecules. Combining all four bactericidal actions, the combination of GNC and antibiotics can effectively eliminate Gram-positive MDR bacteria like MRSE.

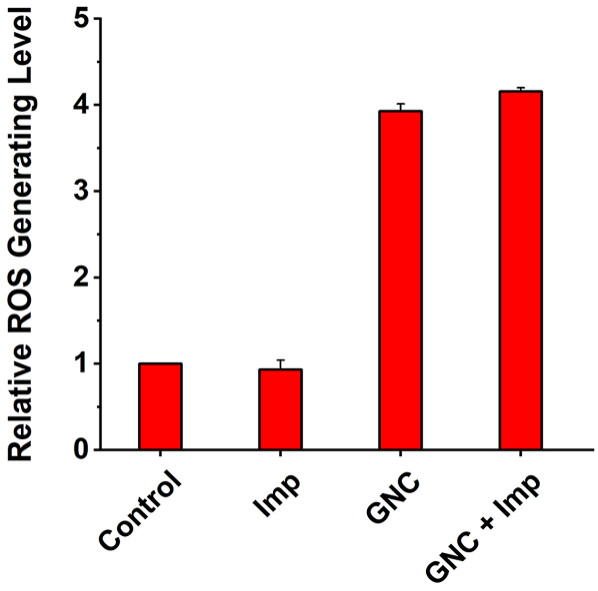

Figure 4.5.9 Total ROS generation rate for the combination group compared with PBS control and individual application (n = 3).

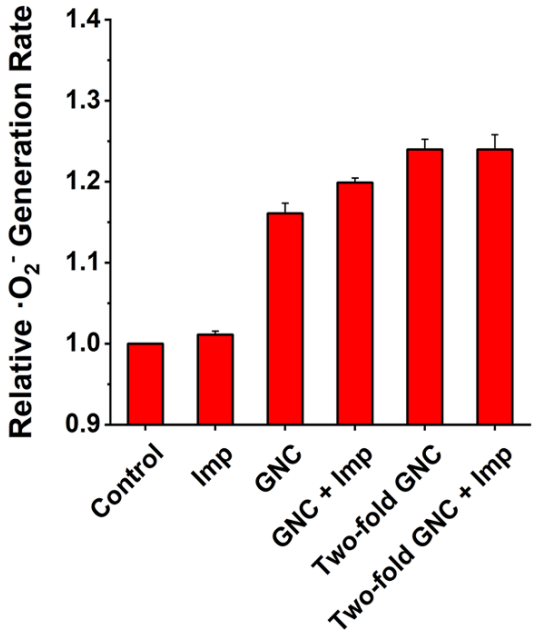

Figure 4.5.10 Superoxide anion generation rate of the combination group, the PBS (control) and single applications (n = 3).

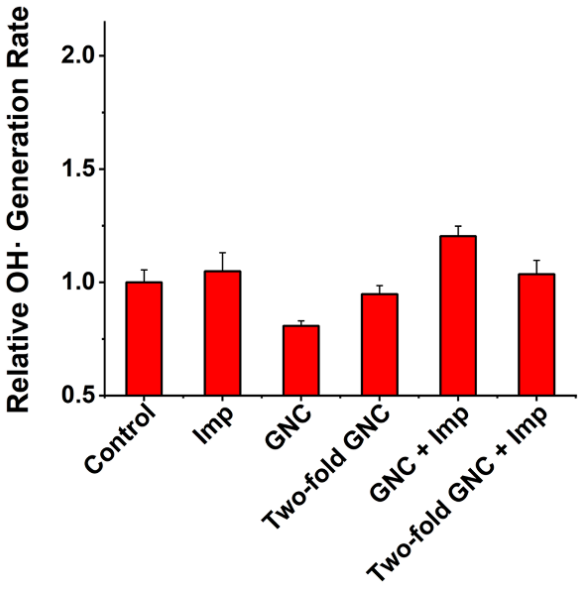

Figure 4.5.11 ROS colourimetric analysis results with the nitro-blue tetrazolium (NBT) method, which demonstrates no correlation between ·OH generation rate and the addition of GNC and Imp (n = 3).

4.6 Stability and cytotoxicity evaluation

The cytotoxicity of combined therapy on somatic (NIH 3T3 and HUVEC) cell lines was investigated by Calcein-AM/propidium iodide staining, where live/dead cells were stained in green/red, respectively. Confocal fluorescence images (**Figure 4.6.1**) reveal that most cells were alive with hardly noticeable numbers of dead cells, suggesting that both cell lines maintained high viability after 24-h incubation with 70 μg mL^{-1} of GNC + 30 μg mL^{-1} Imp. This was further verified by live-cell counting (**Figure 4.6.2**), where the percentage of live cells was above 80%, comparable to that of the controls.

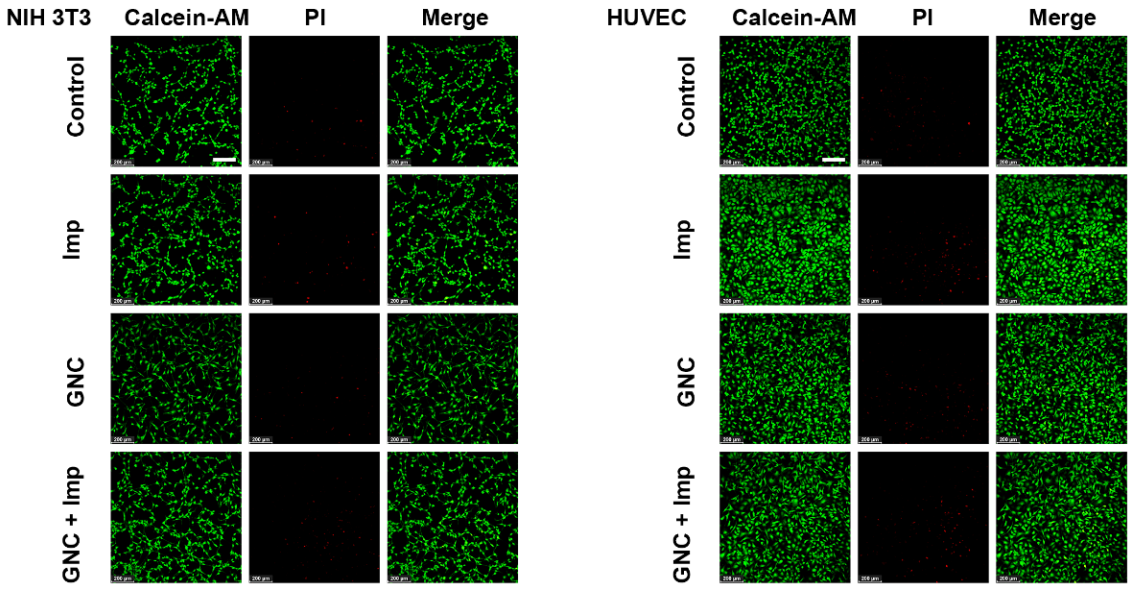

Figure 4.6.1 Confocal fluorescence images of NIH 3T3 and HUVECs after 24 h incubation in PBS, 70 μg mL^{-1} GNC, 30 μg mL^{-1} Imp, and 70 μg mL^{-1} GNC + 30 μg mL^{-1} Imp (scale bar: 200 μm).

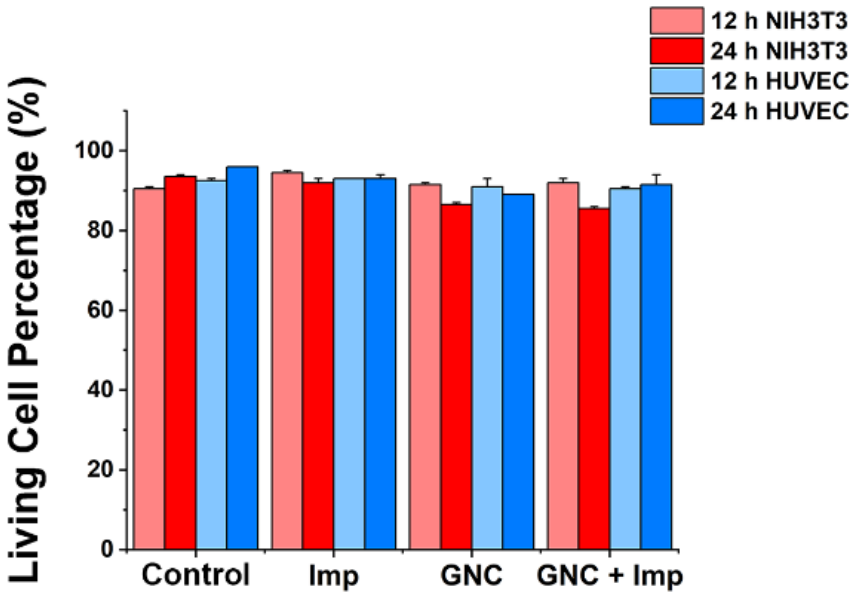

Figure 4.6.2 Cell-counting results reflecting the viability of the two cell lines in 70 μg mL^{-1} GNC and 30 μg mL^{-1} Imp for 12 and 24 h (n = 3).

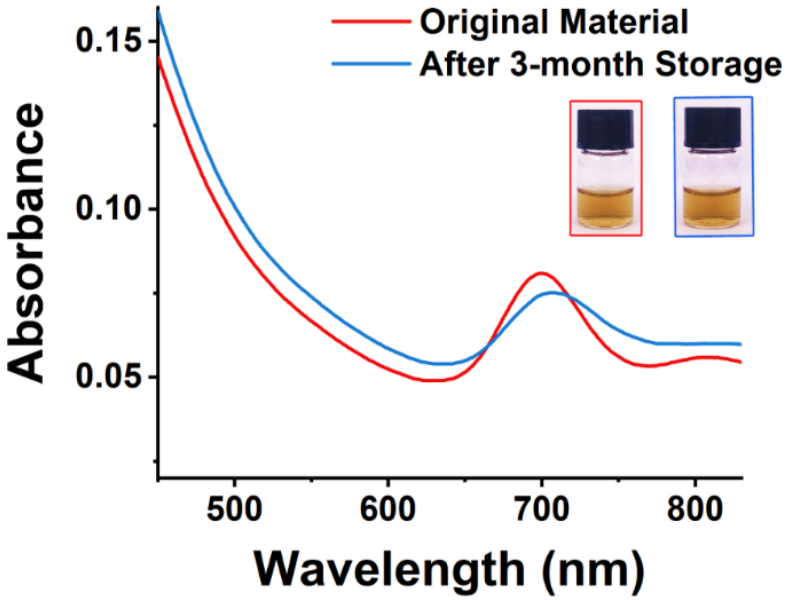

Figure 4.6.3 Comparison of the UV–vis spectrum of the GNC after 3-month storage at 4 ^{o}C. The corresponding physical photos are also displayed. After 3 months, except for a slight red-shift of the characteristic peak position, the overall shape remained unchanged. In addition, the colour and clarity were consistent with the original material, with no precipitation or character changes.

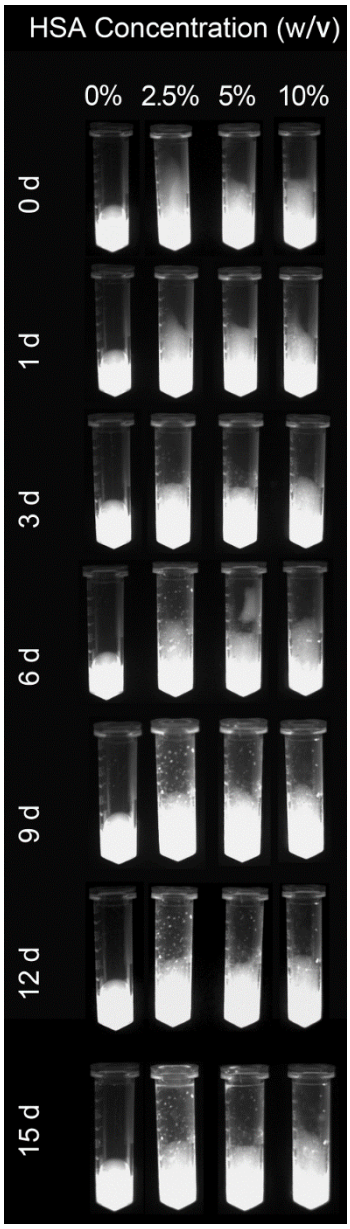

Figure 4.6.4 NIR fluorescence images of the GNC (128 μg mL^{-1}) in PBS solutions containing 0, 2.5%, 5%, and 10% HSA over 15 days. No change in fluorescence intensity was observed.

The stability of nanomaterials in storage is crucial for their potential practical applications. I measured the UV–vis spectrum of freshly prepared GNC solution after 3-month storage at 4 ^{o}C in a normal refrigerator (**Figure 4.6.3**). I did not observe any deformation or emergence of new peaks in the UV–vis spectrum. In addition, there were no changes in the physical appearance, aggregation, or precipitation, confirming the good stability of the GNC.

NIR-II fluorescence is an attractive imaging modality that is well suited for *in vivo* applications. Owing to its attractive NIR fluorescence, GNC can act as fluorescent probes for organ distribution tracking.[59] I evaluated the GNC stability *in vitro* using simulated biological fluids. The GNC fluorescence (128 μg mL^{-1}) was highly stable and showed no observable changes after 15-day incubation in PBS supplemented with up to 10% human serum albumin (HSA, see **Figure 4.6.4**). Thus, its stable NIR fluorescence can be used to directly evaluate the GNC organ distribution with a NIR animal imager using 808-nm laser irradiation (**Figure 4.6.5**). Upon intravenous injection of GNC+Imp, strong NIR fluorescence was observed primarily in the liver, with weak signals in the spleen and kidneys within the first hour, suggesting preferential accumulation in these organs. The NIR fluorescence in the main organs was maintained for 10 h, then it gradually faded away after 24 h and became almost invisible at 96-h post-injection, indicating that most of the GNCs were cleared from the body. The gold contents measured from critical organs harvested at different post-injection times were consistent with the NIR fluorescence results (>80% of the Au contents were cleared after 96 h). These results indicate that the GNC has an adequate body clearance time and is suitable for intravenous administration.

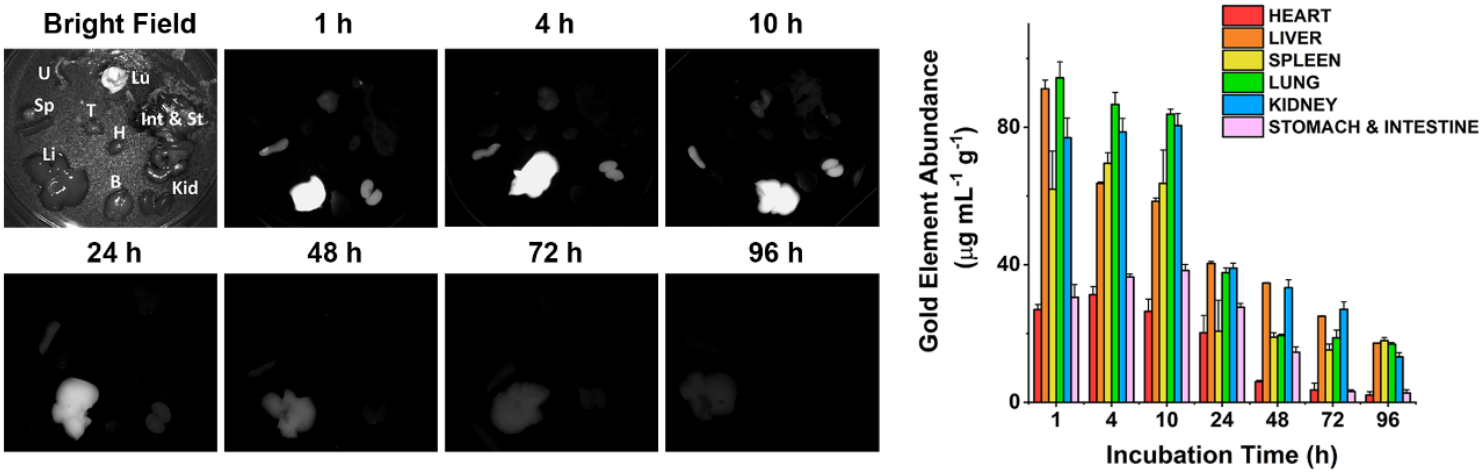

Figure 4.6.5 NIR fluorescence of crucial organs of mice harvested at different time points under bright-field and 808-nm laser radiation and Au content (average weight) in different organs, harvested at different times post-injection (n = 4, B, Brain, H, Heart,

Int & St, Intestine and Stomach, Kid, Kidneys, Li, Liver, Lu, Lungs, Sp, Spleen, T, Thymus and U, Uterus).

4.7 Skin infection model experiments

As a coagulase-negative strain, MRSE can cause soft tissue and skin infections and frequently induces infection in surgical site[5]; thus, I established a skin infection model by creating wounds with the removal of epidermis and dermis on the back of rats and infecting them with MRSE, to which conventional wound treatment methods are difficult to sustain antibacterial ability. Different groups were treated with either PBS control, Imp only, GNC only or GNC+Imp. The effect was monitored by measuring the wound size and bacterial counts after plate coating. Compared with the negative control, the wound healing rate for the rats treated with either Imp or GNC was higher. Notably, the wound healing of the GNC+Imp combinational group was the fastest. The size of the wound was significantly smaller than that of other groups, and the normal skin was almost fully reconstructed in 9 days (Figure 4.7.1). Moreover, the scab size was significantly smaller than other groups, indicating a markedly reduced bacterial infection.

To quantify the clearance of bacteria on the skin wound, I performed plate coating to compare the number of colonies on differently treated wounds (Figure 4.7.2). The MRSE counts of the negative control and Imp groups were slowly reduced over time due to autoimmunity, and the GNC-treated group showed a more significant decrease. Treatment with GNC+Imp resulted in the most rapid reduction of the bacterial population, and by day 12, the bacterial count was >10-fold lower than that of the GNC-only group and almost two orders of magnitude lower than that of the negative control group. This *in vivo* result was consistent with the superior *in vitro* antibacterial potency of GNC+Imp over that of GNC or Imp only. Pathological analyses further confirmed a complete repair of the wound tissue for the GNC+Imp group but not for the negative control and GNC- or Imp-only groups. The reconstruction of well-stratified skin layers

and significantly reduced immune cells indicated the successful removal of the lesions in the GNC+Imp group (Figure 4.7.3).

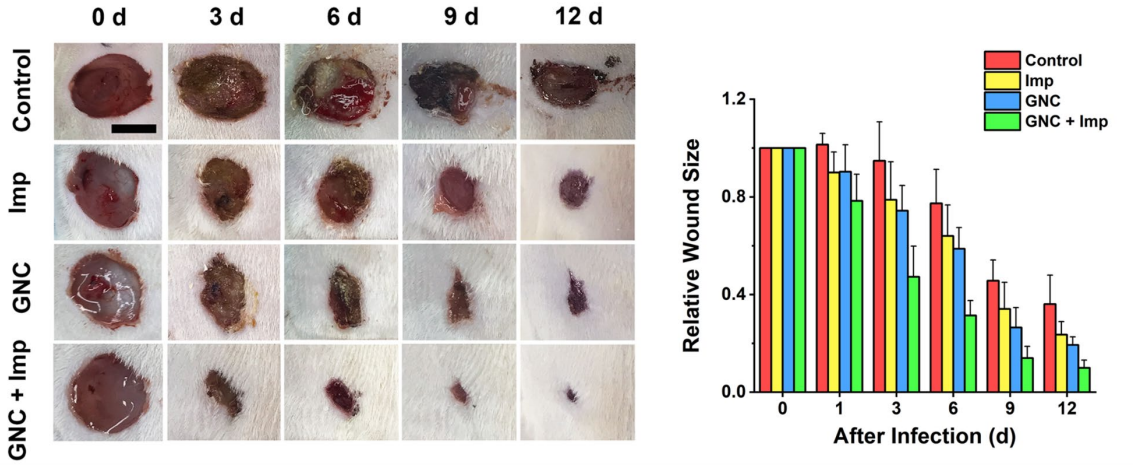

Figure 4.7.1 Representative images of changes in wound size in different groups within 12 days post-treatment and comparison of the relative wound size vs time in different groups: PBS (control), 24 μg mL^{-1} Imp solution, 64 μg mL^{-1} GNC solution, and the combination of 24 μg mL^{-1} Imp (~0.12 mg kg^{-1}, final concentration) and 64 μg mL^{-1} GNC solution (~0.32 mg kg^{-1}, final concentration, same below, n = 3, scale bar: 10 mm).

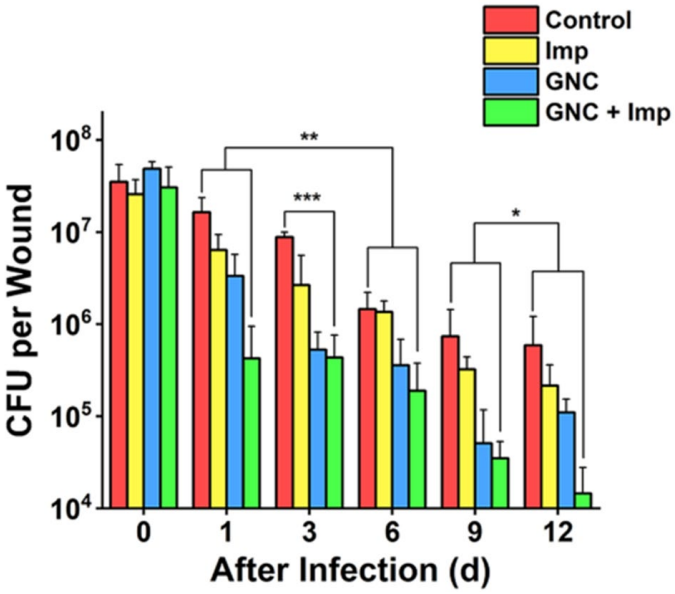

Figure 4.7.2 Plate coating results of the PBS control, single application, and combined therapy groups (n = 3, *: P >0.05, **: 0.01 <P <0.05 and ***: P <0.01).

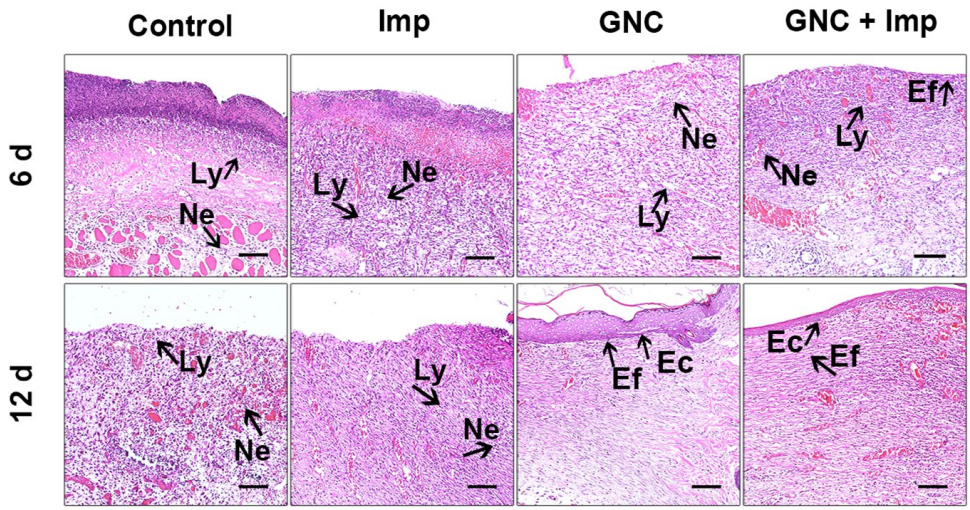

Figure 4.7.3 The hematoxylin-eosin staining graphs in different groups. After 12 days, the epidermis was fully reconstructed in the GNC+Imp group (Ly: lymphocytes; Ne: neutrophil; Ec: epithelial cell and Ef: elongated fibre).

4.8 Conclusions

In this study, I synthesised a series of formula-defined pyridinium-zwitterionic ligand-functionalised $Au_{25}(SR_1)_x(SR_2)_{18-x}$ GNCs as antibacterial nanomaterials. By fine-tuning the feeding ligand ratios, I obtained GNCs that exhibited both excellent antibacterial ability and high stability, successfully addressing a major issue in antibacterial gold nanomaterials development. Besides, the GNCs exert multiple antibacterial mechanisms, giving rise to high potency against Gram-positive MDR bacteria. The optimized GNC can significantly reduce the dosage of antibiotics required to treat MDR bacterial infections, thereby greatly enhancing the efficacy of frontline antibiotics. Compared to other nanomaterials without defined chemical formulas, which could cause difficulties in quality control and mechanism research, these $Au_{25}(SR_1)_x(SR_2)_{18-x}$ GNCs are potentially better suited for medical applications. Moreover, biocompatible Au_{25} GNCs capped with two or more ligands can incorporate more functions, thus widening the scope of its biomedical applications. I envisage that dual/multi-ligand-functionalised GNCs would find broad applications in chemistry, physics, biology, and biomedical sciences.

4.9 References

1 P. Fernandes, *Nat. Biotechnol.*, 2006, **24**, 1497–1503.

2 Willyard Cassandra, *Nature*, 2017, **543**, 15.

3 L. Wang, C. Hu and L. Shao, *Int. J. Nanomedicine*, 2017, **12**, 1227–1249.

4 M. Otto, *Nat. Rev. Microbiol.*, 2009, **7**, 555–567.

5 L. M. Weiner-Lastinger, S. Abner, J. R. Edwards, A. J. Kallen, M. Karlsson, S. S. Magill, D. Pollock, I. See, M. M. Soe, M. S. Walters and M. A. Dudeck, *Infect. Control Hosp. Epidemiol.*, 2020, **41**, 1–18.

6 A. M. Hanssen, G. Kjeldsen and J. U. Ericson Sollid, *Antimicrob. Agents Chemother.*, 2004, **48**, 285–296.

7 Centers for Disease Control and, *Antibiotic resistance threats in the United States*, Atlanta, Georgia, 2019.

8 X. Li, S. M. Robinson, A. Gupta, K. Saha, Z. Jiang, D. F. Moyano, A. Sahar, M. A. Riley and V. M. Rotello, *ACS Nano*, 2014, **8**, 10682–10686.

9 A. Gupta, S. Mumtaz, C. H. Li, I. Hussain and V. M. Rotello, *Chem. Soc. Rev.*, 2019, **48**, 415–427.

10 H. T. T. Duong, N. N. M. Adnan, N. Barraud, J. S. Basuki, S. K. Kutty, K. Jung, N. Kumar, T. P. Davis and C. Boyer, *J. Mater. Chem. B*, 2014, **2**, 5003–5011.

11 K. Ma, Y. Li, Z. Wang, Y. Chen, X. Zhang, C. Chen, H. Yu, J. Huang, Z. Yang, X. Wang and Z. Wang, *ACS Appl. Mater. Interfaces*, 2019, **11**, 29630–29640.

12 K. Zheng, M. I. Setyawati, D. T. Leong and J. Xie, *ACS Nano*, 2017, **11**, 6904–6910.

13 R. R. Nasaruddin, T. Chen, N. Yan and J. Xie, *Coord. Chem. Rev.*, 2018, **368**, 60–79.

14 Y. Xie, Y. Liu, J. Yang, Y. Liu, F. Hu, K. Zhu and X. Jiang, *Angew. Chemie - Int. Ed.*, 2018, **57**, 3958–3962.

15 Y. Xie, W. Zheng and X. Jiang, *ACS Appl. Mater. Interfaces*, 2020, **12**, 9041–9049.

16 M. Yu, J. Xu and J. Zheng, *Angew. Chemie*, 2019, **131**, 4156–4172.

17 R. Jin, *Nanoscale*, 2015, **7**, 1549–1565.

18 X. Kang, H. Chong and M. Zhu, *Nanoscale*, 2018, **10**, 10758–10834.

19 Z. Yu, H. Xiao, X. Zhang, Y. Yang, Y. Yu, H. Chen, X. Meng, W. Ma, M. Yu, Z. Li, C. Li and H. Liu, *ACS Nano*, 2020, **14**, 13536–13547.

20 D. Li, Q. Liu, Q. Qi, H. Shi, E. C. Hsu, W. Chen, W. Yuan, Y. Wu, S. Lin, Y. Zeng, Z. Xiao, L. Xu, Y. Zhang, T. Stoyanova, W. Jia and Z. Cheng, *Small*, 2020, **16**, 1–9.

21 M. Petkovic, K. R. Seddon, L. P. N. Rebelo and C. S. Pereira, *Chem. Soc. Rev.*, 2011, **40**, 1383–1403.

22 P. K. Sreenivasan, V. I. Haraszthy and J. J. Zambon, *Lett. Appl. Microbiol.*, 2013, **56**, 14–20.

23 S. Chen, L. Li, C. Zhao and J. Zheng, *Polymer (Guildf).*, 2010, **51**, 5283–5293.

24 J. Shaoyi and C. Zhiqiang, *Adv. Mater.*, 2009, **22**, 920–932.

25 A. K. Murthy, R. J. Stover, W. G. Hardin, R. Schramm, G. D. Nie, S. Gourisankar, T. M. Truskett, K. V. Sokolov and K. P. Johnston, *J. Am. Chem. Soc.*, 2013, **135**, 7799–7802.

26 Y. Guo, C. Sakonsinsiri, I. Nehlmeier, M. A. Fascione, H. Zhang, W. Wang, S. Pöhlmann, W. B. Turnbull and D. Zhou, *Angew. Chemie*, 2016, **55**, 4738–4742.

27 Z. Luo, V. Nachammai, B. Zhang, N. Yan, D. T. Leong, D. E. Jiang and J. Xie, *J. Am. Chem. Soc.*, 2014, **136**, 10577–10580.

28 R. Jin, H. Qian, Z. Wu, Y. Zhu, M. Zhu, A. Mohanty and N. Garg, *J. Phys. Chem. Lett.*, 2010, **1**, 2903–2910.

29 H. Liu, G. Hong, Z. Luo, J. Chen, J. Chang, M. Gong, H. He, J. Yang, X. Yuan, L. Li, X. Mu, J. Wang, W. Mi, J. Luo, J. Xie and X. D. Zhang, *Adv. Mater.*, 2019, **31**, 1–9.

30 G. Hong, A. L. Antaris and H. Dai, *Nat. Biomed. Eng.*, 2017, **1**, 0010.

31 A. L. Antaris, H. Chen, S. Diao, Z. Ma, Z. Zhang, S. Zhu, J. Wang, A. X. Lozano, Q. Fan, L. Chew, M. Zhu, K. Cheng, X. Hong, H. Dai and Z. Cheng, *Nat. Commun.*, 2017, **8**, 1–11.

32 Y. Sun, M. Ding, X. Zeng, Y. Xiao, H. Wu, H. Zhou, B. Ding, C. Qu, W. Hou, A. G. A. Er-bu, Y. Zhang, Z. Cheng and X. Hong, *Chem. Sci.*, 2017, **8**, 3489–3493.

33 F. Aldeek, M. A. H. Muhammed, G. Palui, N. Zhan and H. Mattoussi, *ACS Nano*, 2013, **7**, 2509–2521.

34 M. Song, G. Zhou, N. Lu, J. Lee, E. Nakouzi, H. Wang and D. Li, *Science*, 2020, **367**, 40–45.

35 Y. Ishida, K. Narita, T. Yonezawa and R. L. Whetten, *J. Phys. Chem. Lett.*, 2016, **7**, 3718–3722.

36 X. Yuan, B. Zhang, Z. Luo, Q. Yao, D. T. Leong, N. Yan and J. Xie, *Angew. Chemie - Int. Ed.*, 2014, **53**, 4623–4627.

37 T. Chen, V. Fung, Q. Yao, Z. Luo, D. E. Jiang and J. Xie, *J. Am. Chem. Soc.*, 2018, **140**, 11370–11377.

38 N. Malanovic and K. Lohner, *Biochim. Biophys. Acta - Biomembr.*, 2016, **1858**, 936–946.

39 L. Pasquina-Lemonche, J. Burns, R. D. Turner, S. Kumar, R. Tank, N. Mullin, J. S. Wilson, B. Chakrabarti, P. A. Bullough, S. J. Foster and J. K. Hobbs, *Nature*, 2020, **582**, 294–297.

40 Z. V. Feng, I. L. Gunsolus, T. A. Qiu, K. R. Hurley, L. H. Nyberg, H. Frew, K. P. Johnson, A. M. Vartanian, L. M. Jacob, S. E. Lohse, M. D. Torelli, R. J. Hamers, C. J. Murphy and C. L. Haynes, *Chem. Sci.*, 2015, **6**, 5186–5196.

41 P. Kumar, J. Kizhakkedathu and S. Straus, *Biomolecules*, 2018, **8**, 4.

42 R. M. R. F. Epand, C. Walker, R. M. R. F. Epand and N. A. Magarvey, *Biochim. Biophys. Acta - Biomembr.*, 2016, **1858**, 980–987.

43 M. Zasloff, *Nature*, 2002, **415**, 389–395.

44 Y. Zhao, Z. Chen, Y. Chen, J. Xu, J. Li and X. Jiang, *J. Am. Chem. Soc.*, 2013, **135**, 12940–12943.

45 M. A. Foxley, S. N. Wright, A. K. Lam, A. W. Friedline, S. J. Strange, M. T. Xiao, E. L. Moen and C. V. Rice, *ACS Med. Chem. Lett.*, 2017, **8**, 1083–1088.

46 J. Campbell, A. Singh, J. Santa Maria, K. Younghoon, S. Brown, J. G. Swoboda, E. Mylonakis, B. J. Wilkinson and S. Walker, *ACS Chem. Biol.*, 2010, **6**, 106–116.

47 N. Zhang and S. Ma, *Eur. J. Med. Chem.*, 2019, **184**, 111743.

48 S. C. Hayden, G. Zhao, K. Saha, R. L. Phillips, X. Li, O. R. Miranda, V. M. Rotello, M. A. El-Sayed, I. Schmidt-Krey and U. H. F. Bunz, *J. Am. Chem. Soc.*, 2012, **134**, 6920–6923.

49 B. Wang, L. Zhang, C. B. Sung and S. Granick, *Proc. Natl. Acad. Sci. U. S. A.*, 2008, **105**, 18171–18175.

50 B. Dubertret, M. Calame and A. J. Libchaber, *Nat. Biotechnol.*, 2001, **19**, 365–370.

51 Z. Huang, Y. Liu, L. Wang, A. Ali, Q. Yao, X. Jiang and Y. Gao, *Biomaterials*, 2020, **253**, 120124.

52 J. N. Pendleton and B. F. Gilmore, *Int. J. Antimicrob. Agents*, 2015, **46**, 131–139.

53 A. Chompoosor, K. Saha, P. S. Ghosh, D. J. Macarthy, O. R. Miranda, Z.-J. Zhu, K. F. Arcaro and V. M. Rotello, *Small*, 2010, **6**, 2246–2249.

54 M. Kang, C. Zhou, S. Wu, B. Yu, Z. Zhang, N. Song, M. M. S. Lee, W. Xu, F. J. Xu, D. Wang, L. Wang and B. Z. Tang, *J. Am. Chem. Soc.*, 2019, **141**, 16781–16789.

55 J. Li, H. Zhou, J. Wang, D. Wang, R. Shen, X. Zhang, P. Jin and X. Liu, *Nanoscale*,

2016, **8**, 11907–11923.

56 R. J. Barnes, R. Molina, J. Xu, P. J. Dobson and I. P. Thompson, *J. Nanoparticle Res.*, 2013, **15**, 1432.

57 Y. Cui, Y. Zhao, Y. Tian, W. Zhang, X. Lü and X. Jiang, *Biomaterials*, 2012, **33**, 2327–2333.

58 M. Godoy-Gallardo, U. Eckhard, L. M. Delgado, Y. J. D. de Roo Puente, M. Hoyos-Nogués, F. J. Gil and R. A. Perez, *Bioact. Mater.*, 2021, **6**, 4470–4490.

59 Y. Kong, J. Chen, H. Fang, G. Heath, Y. Wo, W. Wang, Y. Li, Y. Guo, S. D. Evans, S. Chen and D. Zhou, *Chem. Mater.*, 2016, **28**, 3041–3050.

Chapter 5
Activating non-antibacterial mercaptan fragrance through decorating onto gold nanoclusters for the effective treatment of MRSA-induced bacteria keratitis

5.1 Introduction

Bacterial keratitis (BK), also known as corneal bacterial infection, is a leading cause of monocular blindness[1] and affects around 1.7 million people each year worldwide.[2] BK may occur due to the invasion of opportunistic pathogens following mechanical injuries to the cornea.[3] Even mild BK can cause corneal redness, swelling, and photophobia in patients.[4] If timely and effective treatment is not available, BK could develop severe symptoms, including ulceration, corneal opacity, and eventually blindness, seriously affecting the patient's quality of life.[5] Besides, the cases of BK have increased in recent years due to the boom of contact lens users worldwide.[6] BK is mainly induced by Gram-positive bacteria, especially *Staphylococcus aureus*, which is the leading causative pathogen and is responsible for over 25.2% of total BK cases.[7] Particularly, BK induced by resistant strains, such as methicillin-resistant *Staphylococcus aureus* (MRSA), has worsened this situation because it effectively resists the common ocular antibiotics (fluoroquinolones and aminoglycosides).[8] As a result, the recurrent infection often requires surgical interventions and thus poses a serious threat to the global healthcare system.[2 9]

Gold nanomaterials, especially GNPs and GNCs, have been shown to exhibit great potential in addressing bacterial antibiotic resistance challenges and fighting against multi-drug resistant pathogen infections.[10–12] They can not only act as a delivery vehicle to increase biosafety but also enhance the antibacterial properties of antiseptic

materials.[13] [14] Significantly, they can even have the "Midas Touch" to turn some non-antibacterial molecules into bactericidal materials by decorating multiple such molecules onto their surfaces.[15] [16] Therefore, some molecules that are completely unrelated to antibacterial applications could be used to control the spread of multi-drug-resistant pathogens in conjunction with GNPs, making them a new source to address the multi-drug resistance challenge. Previously, Jiang's group has found that a non-antibiotic molecule—4,6-Diamino-2-pyrimidinethiol could be turned into a potent antibacterial nanomaterial upon capping onto the GNP surface.[17] In addition, other non-antibiotic molecules, including indole derivatives,[18] amines,[19] D/L-cysteine,[20] and zwitterionic molecules,[21] have also been used to cap GNPs and be developed into nano-antibiotics. Compared to small GNPs, the quality of atomically precise GNCs is more controllable, making them highly attractive for biomedical applications.[22] To date, only a few cases of GNCs in combination with limited non-antibacterial molecules for antibacterial applications have been reported.[23–25] Moreover, most cases reported so far are based on GNCs or GNPs capped with a single type of molecule. As a result, it is difficult to tune their biocompatibility and antibacterial potency, which is an important obstacle for practical applications.

Thiol fragrances, an important type of sulfur-containing flavour, have been applied in the fields of condiments, cosmetics, and medication for hundreds of years.[26] Taking advantage of the reductive nature of its thiol group, thiol fragrances have been developed into effective therapeutic agents for anti-corrosion and elimination of carcinogens.[27] [28] [29] Furthermore, because of their relatively high biosafety, natural thiol fragrances can serve as potential drug reservoirs. However, due to the instability of the thiol group under an oxidative environment as well as the high volatility of thiol fragrances, their application in medication still faces an insurmountable obstacle and is easily overlooked. Therefore, I anticipated that by immobilizing these volatile thiols onto GNCs through the Au-S bond, the fragrant molecules could be stabilized. Besides,

capping these thiol fragrances could grant the GNC useful properties for biomedical applications. Combining the complementary properties of GNC with thiol fragrance may allow the development of new gold nanomaterials with outstanding biomedical applications. 4-Mercapto-4-methyl-2-pentanol (denoted as 4MMP hereafter) is a common mercaptan fragrance that has been approved by the Food and Agriculture Organization of the United Nations (FAO)/ World Health Organization (WHO) as well as Flavour and Extract Manufacturers Association of the United States (FEMA) as a compliant food additive.[30 31] 4MMP is produced by grapefruit during maturation and is found as a taste substance in red wine.[32 33 34] In a preliminary selection, I have surprisingly found that capping GNCs with this non-antibacterial 4MMP could inhibit bacteria growth. To the best of my knowledge, there has been no report on the use of any other thiol fragrance molecules in antibacterial applications.

I have recently discovered that capping GNCs with two different functional ligands, one for improving stability while the other for imposing antibacterial potency, is an effective way to afford GNCs with both excellent biocompatibility and antibacterial potency.[14] Herein, I have extended this antibacterial strategy by using 4MMP and a thiolated zwitterionic ligand to synthesize dual-ligand capped antibacterial $Au_{25}(SR)_{18}$-type GNCs (denoted as **4MMP-GNC** hereafter). To my surprise, I have found that GNCs capped with mixed non-antibacterial ligands displayed stronger antibacterial potency than that capped with a single type of ligand. Through optimizing the ligand feed ratio, I have successfully achieved the minimum inhibitory concentration (MIC) as low as 2 μg mL^{-1} against MDR bacteria, such as MRSA. Significantly, this GNC exhibited comparable antibacterial potency with the last-sorted antibiotics against MRSA. More importantly, the dual-ligand-capped GNC could effectively kill MRSA cells without inducing the rupture of the cell membrane and leakage of bacteria cell content and thus may not cause inflammation and overreaction of the immune system, similar to new antibiotics such as daptomycin. In both *in vitro* and the mice keratitis model, this GNC has

displayed outstanding antibacterial potency compared with Van, and does not induce obvious changes to the blood, liver, and kidney function indicators. This work thus demonstrates the immense potential of this dual-ligand GNC as an effective nanomedicine in controlling and treatment of MRSA-induced BK.

5.2 GNC antibacterial ability with different ligand ratios

5.2.1 Characterisation of the GNC size and optical properties

We first characterized the formation of GNCs under different 4MMP feed ratios through UV–visible (UV–vis) spectrophotometry. With the increase of the 4MMP ligand ratio in feeding, the characteristic peak of Au_{23} NC became more prominent at around 580 nm, accompanied by the rapid decrease of the absorption peak of Au_{25} NC at around 700 nm, indicating a shift in the Au kernel configuration with the increasing proportion of 4MMP ligand (**Figure 5.2.1**).

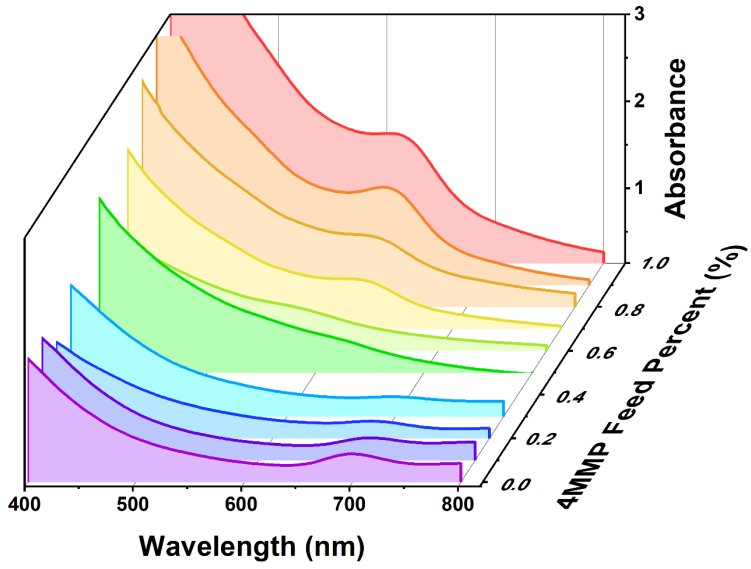

Figure 5.2.1 The UV–vis spectra of GNCs prepared with 0 to 100% 4MMP ratio in feeding.

Besides, the photoluminescence spectroscopy of the GNCs displaced a characteristic excitation peak at ~800 nm and an emission peak at ~1080 nm under 808 nm irradiation

for each group, consistent with the fluorescence characteristics of Au_{25} NCs (**Figure 5.2.2**). This NIR-emitting profile of this GNC can offer deep tissue penetration with high sensitivity and resolution, thereby benefiting *in vivo* fluorescence applications.

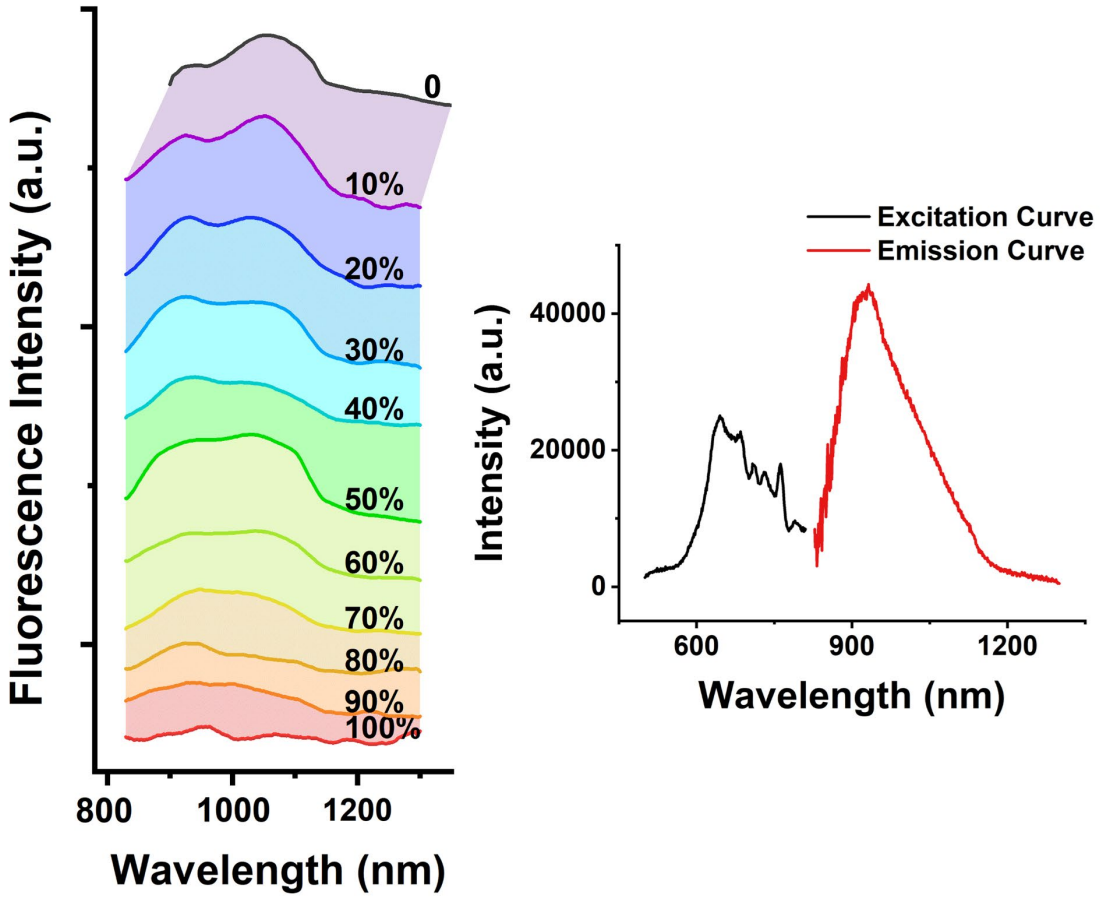

Figure 5.2.2 The NIR fluorescence spectra of GNCs with a 4MMP feed ratio from 0–100% (left) and the typical photoluminescence excitation & emission spectroscopy of dual ligand GNC with 80% 4MMP feed percentage (right).

DSAC-TEM images further confirmed the formation of highly consistent GNCs with an average diameter of around 1.2 nm (**Figure 5.2.3**), which is also in high consistent with the common size of Au_{25} NCs. To work out the exact configuration of GNCs with different ligand feed ratios, I attempted to measure the MWs of different GNCs by ESI-MS and MALDI-TOF. However, due to the difficulty of ionization of the GNCs with high 4MMP ligand capping, I have not successfully acquired high-quality ESI-MS results that could reflect the GNC mass following the changing rule. MALDI-TOF will also be used to

do a further analysis of the GNC mass. The GNCs prepared with different 4MMP and C5 capping ratios were used in antibacterial tests for optimising the ligand feed ratio.

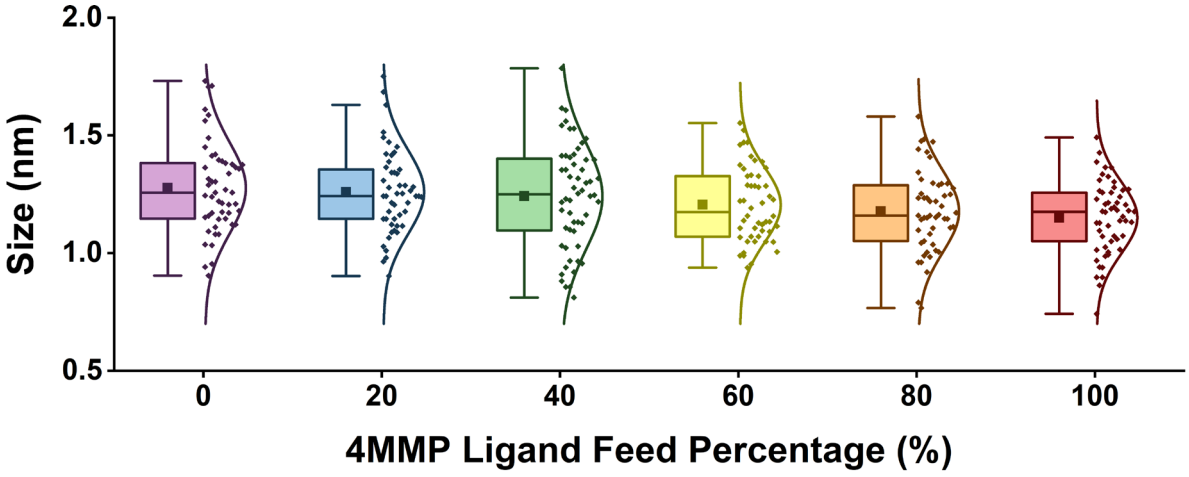

Figure 5.2.3 The statistical results of GNC size with different 4MMP feed percentages. The average diameter of GNCs was measured to be around 1.2 nm, which decreases slightly with the increase of 4MMP ratios.

5.2.2 The antibacterial effect of 4MMP and C5 co-capped GNCs

We then measured the antibacterial effect of GNCs with 0 to 100% 4MMP in feeding, and their MIC and MBC values were given in Table 9 and Table 10. Seven Gram-positive and Gram-negative pathogens were tested, including common dermal and soft tissue pathogens *Staphylococcus*, urinary tract infection, and sepsis pathogens *E. f, E. c,* and *P. a*, as well as pneumonia pathogen *K. p*. The antibacterial effect was displayed by a colour scale, with green indicating low MIC and high antibacterial effect, and red indicating the opposite.

Table 9 MIC values of 4MMP-GNCs prepared with different 4MMP ligand feed percentages toward seven pathogens.

4MMP feed (%)	***S. a****	***S. e****	***S. h****	***E. f****		***E. c****	***P. a****	***K. p****

0	>256	>256	>256	>256	>256	>256	>256
10	>256	>256	>256	>256	>256	>256	>256
20	>256	>256	>256	>256	>256	>256	>256
30	>256	>256	>256	>256	>256	>256	>256
40	16	16	128	256	>256	>256	>256
50	16	16	16	128	128	32	128
60	8	8	16	32	64	32	128
70	4	4	8	8	64	32	128
80	4	4	8	4	128	32	128
90	4	4	8	8	128	64	128
100	16	16	16	32	128	128	128

*Gram-positive strains: *S. a—Staphylococcus aureus*, *S. e—Staphylococcus epidermidis*, *S. h—Staphylococcus hemolyticus*, and *E. f—Enterococcus faecalis.*

**Gram-negative strains: *E. c—Escherichia coli*; *P. a—Pseudomonas aeruginosa*, and *K. p—Klebsiella pneumoniae.*

Table 10 MBC values of 4MMP-GNCs prepared with different 4MMP ligand feed percentages toward seven pathogens.

4MMP feed (%)	***S. a***	***S. e***	***S. h***	***E. f***	***E. c***	***P. a***	***K. p***
0	>256	>256	>256	>256	>256	>256	>256
10	>256	>256	>256	>256	>256	>256	>256
20	>256	>256	>256	>256	>256	>256	>256
30	>256	>256	>256	>256	>256	>256	>256
40	>256	>256	>256	>256	>256	>256	>256
50	32	32	64	256	256	64	256
60	32	32	32	64	256	64	256
70	8	16	16	16	256	64	256
80	8	16	16	16	256	64	256
90	8	8	16	16	256	128	256
100	64	64	128	128	>256	256	256

Horizontally, the antibacterial ability of 4MMP and C5 co-capped GNCs displayed a higher potency toward Gram-positive strains, with a significantly darker green colour in the Gram-positive area than in the Gram-negative area. The vertical comparison further demonstrated that the antibacterial effect of GNC varies with ligand ratio, with the antibacterial efficiency increasing with the incorporation of the 4MMP ligand from 0 to around 60% in feeding. From 70% to 90% 4MMP feed ratio, the antibacterial ability of GNC was maximized and hardly changed, with MIC as low as 4 μg mL^{-1} against *S. a*, *S. e*, and *E. f*. Notably, GNCs capped with 100% 4MMP in feeding demonstrated a significantly lower antibacterial ability compared with the GNCs with 90% 4MMP. These results show that the 4MMP and C5 ligands co-capped GNCs have a relatively higher antibacterial ability toward Gram-positive pathogens. The optimal feed ratio is ~80% 4MMP and 20% C5, where the antibacterial potency of the corresponding GNC was >64-fold better than those prepared with 0% to 40% in feeding. As the problem of drug resistance grows globally, effective reagents that could control the spread of MDR pathogens are highly valued. Therefore, I also tested the corresponding 4MMP-GNC against MDR Gram-positive strains, including MRSA, MRSE, MDR *S. h* and MDR *E. f* (Table 11 & Table 12). Similarly, the GNCs displayed a fluctuated tendency, with antibacterial ability gradually increasing from 0 to 60% and then peaking at around 70%. Astonishingly, the 70% 4MMP-capped GNC demonstrated even higher antibacterial potency against the MDR strains compared with antibiotic-sensitive strains, with the MIC value as low as 2 μg mL^{-1} against MRSA. This result increased the antibacterial effect to 1024-folds and turned a non-antibacterial ligand into an effective antibacterial reagent (Table 13). In contrast, neither free 4MMP nor the C5 ligand showed an obvious antibacterial ability with MIC values >2048 μg mL^{-1} (Table 13). Simply mixing free thiol ligands and chloroauric acid also showed no antibacterial effect. Only if the structures of both GNC and 4MMP ligands are present and follow a certain ratio can the efficient bactericidal effect be achieved. The simple decoration of both ligands onto the surface of the gold kernel of GNC has increased its antibacterial effect to over 512-fold, turning

the non-antibacterial ligands into effective antibacterial reagents. Unless otherwise specified, the 4MMP-GNCs referred to below refer to the GNC prepared under the optimal antibacterial concentration and feeding ratio.

Table 11 MIC values of 4MMP-GNCs toward four MDR pathogens

4MMP feed (%)	MRSA	MRSE	MDR *S. h*	MDR *E. f*
0	>256	>256	>256	>256
10	>256	>256	>256	>256
20	>256	>256	>256	>256
30	16	>256	>256	>256
40	8	256	32	128
50	4	32	16	128
60	4	16	16	32
70	2	4	8	4
80	2	4	8	4
90	2	4	8	8
100	16	16	16	32

Table 12 MBC values of 4MMP-GNCs toward four MDR pathogens

4MMP feed (%)	MRSA	MRSE	MDR *S. h*	MDR *E. f*
0	>256	>256	>256	>256
10	>256	>256	>256	>256
20	>256	>256	>256	>256
30	>256	>256	>256	>256
40	>256	>256	>256	>256
50	16	64	128	>256
60	16	64	64	64
70	8	16	32	16
80	8	16	32	16

90	4	16	64	8
100	32	128	128	128

Table 13 MIC values of each ligand toward different bacterial strains

Ligand	*S. a*	MRSA	*S. e*	MRSE	*S. h*	MDR *S. h*	*E. f*	MDR *E. f*	*E. c*	*K. p*	*P. a*
4MMP	>2048	>2048	>2048	>2048	>2048	>2048	>2048	>2048	>2048	>2048	>2048
C5	>2048	>2048	>2048	>2048	>2048	>2048	>2048	>2048	>2048	>2048	>2048

Table 14 MIC values of this MRSA strain against commonly used ocular antibiotics

Ery	Azi	Kan	Tet	Van	Dap
4	32	>256	64	1	16
Ofx	**Lvx**	**Cln**	**Tob**	**Chl**	
128	64	64	256	8	

*Ery—erythromycin; Azi—azithromycin; Kan—kanamycin; Tet—tetracycline; Van—vancomycin; Dap—daptomycin; Ofx—ofloxacin; Lvx—levofloxacin; Cln—clindamycin; Tob—tobramycin; and Chl—chloramphenicol

The drug-resistant situation of this strain of MRSA toward multiple commonly used ophthalmic antibiotics, including erythromycins, aminoglycosides, tetracyclines, glycopeptide, lipopeptide, quinolones, lincomycins, and chloramphenicol was measured and exhibited (Table 14). Except for Van, Ery, and Dap, this MRSA strain demonstrated high resistance to all other antibiotics tested. Where daptomycin's antibacterial efficacy strongly depends on calcium ion concentration[35] and erythromycin is normally applied in an ointment form, Van is normally the only alternative treatment for MRSA keratitis infection. Compared with these commonly used antibiotics, the MIC value of 4MMP-capped GNC was significantly lower than most of the antibiotics tested. One typical feature of daptomycin is the strong dependence of its antibacterial ability on calcium

ion concentration, with the antibacterial ability greatly increased with the optimum calcium ion concentration (1.25 mM). To measure if the addition of calcium ions would also influence the antibacterial ability of 4MMP-capped GNC, I applied different concentrations of calcium ions and found no obvious influence on its antibacterial ability, indicating good stability and consistent antibacterial effect of 4MMP-capped GNCs (Table 15). Due to an overall negative charge, the electrostatic repulsion between the Gram-positive bacteria cell envelope and the daptomycin molecule could reduce its binding efficiency. Thus, the presence of positively charged calcium ions could change the conformation of the daptomycin molecule and reduce its overall charge density to promote the binding process.[36] However, in terms of the 4MMP-GNC, its capping ligands are electrically neutral alkylated zwitterion and fatty alcohol. Thus, the calcium ion would not be effectively chelated into the GNC to change its overall charge density to influence antibacterial ability. This antibacterial effect is even comparable to many last-resort antibiotics. Thus, I have discovered a useful method that could turn non-antibacterial thiol fragrances into highly effective antibacterial agents.

Table 15 The influence of Ca^{2+} on the MIC of 4MMP-GNC and daptomycin

Ca^{2+} Concentration (mM)	4MMP-GNC	Dap
0	2	16
1.25	2	0.5

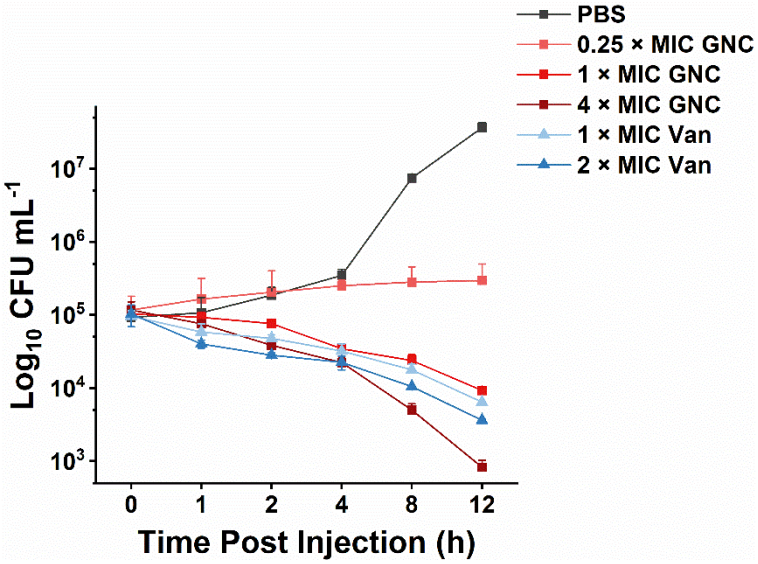

Figure 5.2.4 The time-killing curve of 4MMP-GNC and Van against MRSA under different MIC equivalent doses

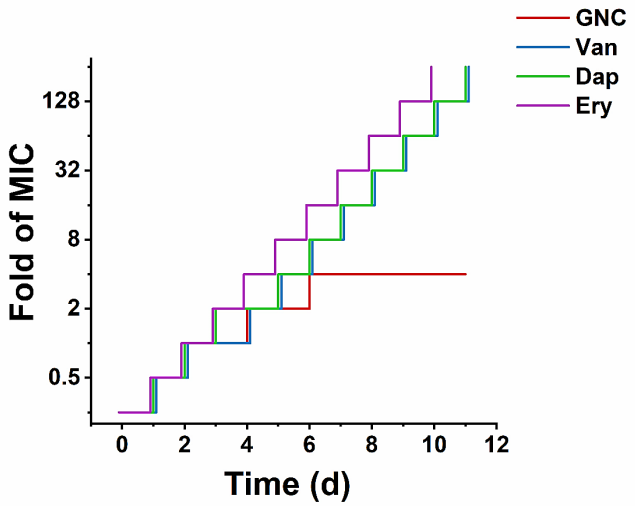

Figure 5.2.5 The resistance evolution curves of MRSA to 4MMP-GNC and several other commonly used antibiotics.

We further measured the time-dependent antibacterial curve (**Figure 5.2.4**). The antibacterial effect of mixed-liganded GNC was comparable with Van. The bacteria amount was reduced to 1% compared with PBS control after 4 hours of treatment at 1 or 2-fold MIC of Van. Different from the initial quick-killing effect of Van, the killing of this GNC was slow but persistent.[37] This effect of slowly inactivating bacteria is significantly different from the mechanism of action of common antibiotics. In addition,

I measured the rate of resistance evolution of MRSA to 4MMP-GNCs compared to other antibiotics (Figure 5.2.5). By day 10, the MICs of all the conventional antibiotics have reached ≥64 folds that of their original MIC values. However, the MIC of 4MMP-GNC remained at 4-fold of the original MIC and did not change since day 6, indicating it can effectively resist bacterial drug resistance evolution. This is possibly due to the complexity of the antibacterial mechanism of GNCs, making it difficult for bacteria to develop resistance.

5.3 Antibacterial mechanisms

SEM images of the untreated and high concentrations of 4MMP-GNC-treated MRSA cells were applied to compare the cell morphology after treatment (Figure 5.3.1). Surprisingly, I did not observe significant morphological changes in MRSA cells, except for some shrinkage compared with that of the PBS control. This phenomenon indicates the viability loss of the treated MRSA cells. In addition, the TEM also indicated no obvious morphological change in MRSA cells in the cell shape and structure. No leakage of cell contents or breaking of the cell envelope was observed even at doses as high as 32-fold of MIC values. However, in many cells in the 4MMP-GNC-treated group, I observed the obvious blebbing of the cell membrane (Figure 5.3.2). Through energy dispersive spectroscopy (EDS) scanning of bacteria-embedded resin sections, I found a wide distribution of Au content on the cell envelope and within the cell content of MRSA. In addition, the Au elements are higher in the cell envelope than within, indicating that GNCs first bind to the MRSA surface and then enter the cells (Figure 5.3.3). The binding of mixed-ligand-capped GNC with MRSA was also confirmed from the NIR-II fluorescence of MRSA cells upon culturing different concentrations of GNCs, followed by washing to remove unbound GNCs, where the NIR-II fluorescence of MRSA cells showed a linear relationship with 4MMP-GNC concentration, demonstrating that GNCs can bind to the bacterial surface or enter into the interior through specific interactions, allowing GNC fluorescence to be preserved on bacteria (Figure 5.3.4).

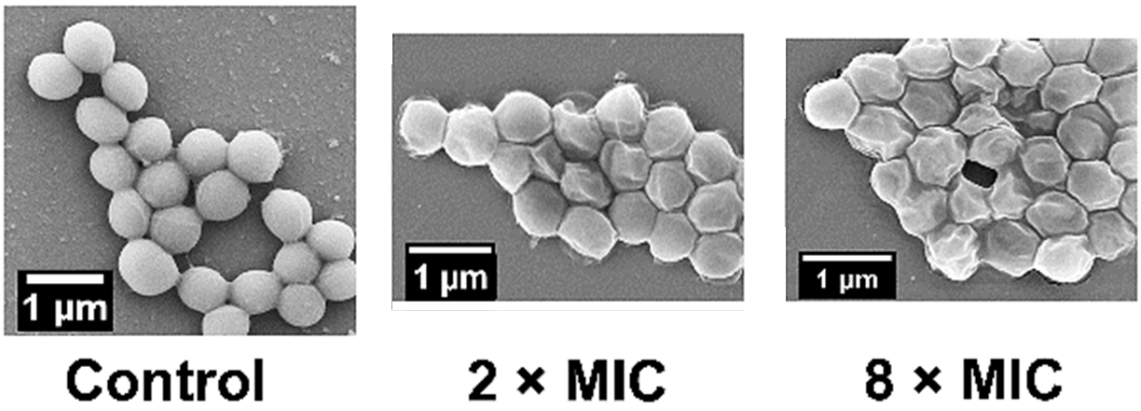

Figure 5.3.1 SEM images of the negative control and 4MMP-GNC treated MRSA.

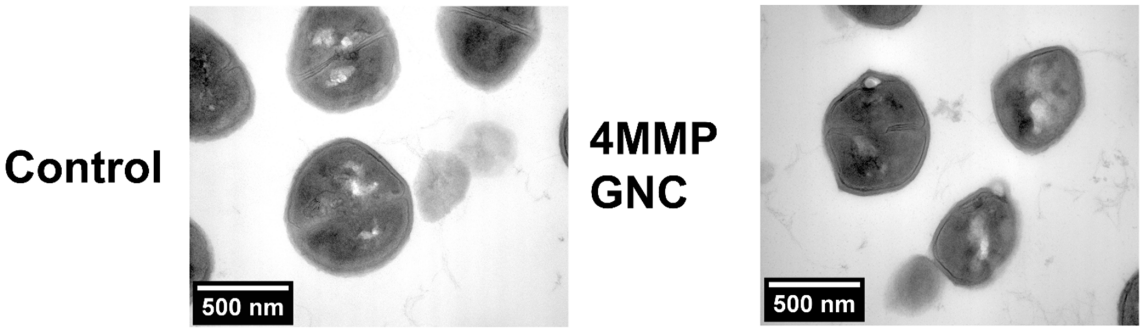

Figure 5.3.2 TEM images of PBS control (left) and 4MMP-GNC (right) treated MRSA.

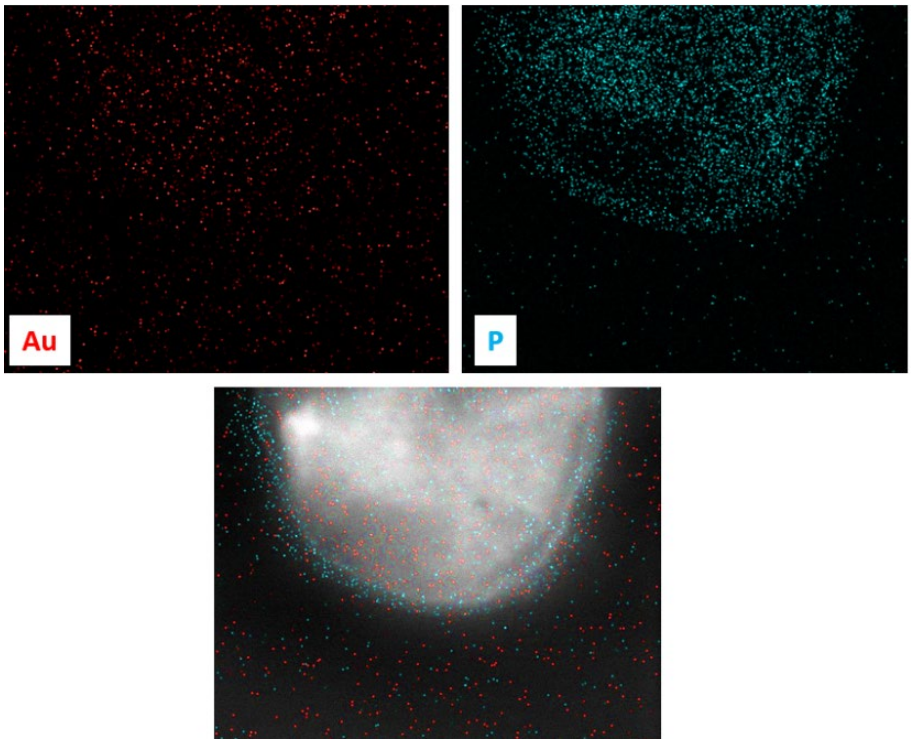

Figure 5.3.3 EDS mapping of Au and P elements on one MRSA cell, where Au

characterizes the presence of GNCs, and P characterizes the presence of bacterial cell envelope.

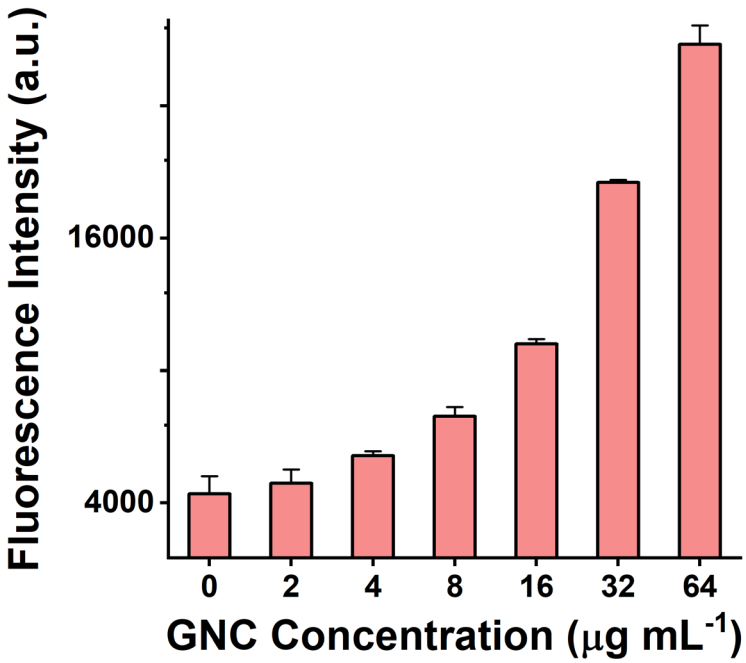

Figure 5.3.4 Relationship between bacterial surface fluorescence and 4MMP-GNC concentrations.

These results indicate that the GNCs have bound with the cell envelope of MRSA. However, based on the SEM and TEM observation, the interaction between GNCs and MRSA does not influence the completeness or cause the bacterial cell membrane lysis like those pyridinium ligand-capped GNCs in the former Chapter (no emergence of empty cell walls). Thus, the antibacterial mechanism of this 4MMP-GNC is different from many antibiotics. While most antibiotics could induce the burst of bacteria cells by directly inhibiting the synthesis of the bacterial cell wall or damaging the integrity of the cell membrane, the antibacterial action of 4MMP-GNC is mild and non-destructive. Several new antibiotics, including daptomycin, could kill bacteria through non-lytic ways[38], which would not induce the spillover of bacterial endotoxin as well as the overreaction of the host immune system to reduce the toxic reaction or excessive damage to the body. This could serve as a relatively safe way to control the spread of pathogens.

As a type of lipopeptide antibiotic, daptomycin was applied to control the critical Gram-positive bacterial infections that were not treatable with those ultimate antibiotics in the conventional sense, like methicillin, including endocarditis or septicemia (**Figure 5.3.5**).[36] Although its antibacterial mechanism is unclear; mainstream concepts treat daptomycin as a class of membrane-active antibiotics. Due to the short length of its lipid tail, daptomycin cannot induce the total rupture or pore formation of the bacteria cell membrane to influence the membrane permeability like antibacterial peptides or surfactants. However, daptomycin could insert its lipid tail into the phospholipid bilayer to influence the stiffness of the phospholipid bilayer as well as the subsequent attachment of crucial proteins that depends on certain membrane curvature and fluidity. Collectively, daptomycin could induce the slow dissipation of normal membrane potential and inhibit the energy metabolism of respiration and production of Adenosine triphosphate (ATP). In addition, it can affect cell wall synthesis. Due to multiple antibacterial mechanisms, the development of bacterial resistance toward daptomycin is much more difficult than toward other common antibiotics. Analogous to daptomycin, I believe that the 4MMP-GNC may have similar antibacterial mechanisms, with the exposed hydroxyl-terminated butanol chains on the GNC surface inserted into the phospholipid bilayer. The binding of GNCs to the cell membrane of MRSA could lead to a series of subsequent membrane potential or membrane integrity changes and finally cause cell death. I first compared the influence on the K^+ concentration, as the membrane instability can cause the efflux of some metal ions, thus undermining the bacterial membrane potential. Gramicidin A and daptomycin were applied as positive controls. Gramicidin A is a linear peptide consisting of 15 amino acids. It has a hydrophobic side chain, and its dimer on the cell membrane can form a transmembrane ionophore channel which selectively transports monovalent cations out of the membrane along the electrochemical gradient, thereby destroying the membrane potential.[37] The result has demonstrated that, similar to both antibiotics, the 4MMP-GNC has the ability to reduce the K^+ concentration in MRSA cells, thus interfering with

normal bacterial cell membrane potential (Figure 5.3.6).

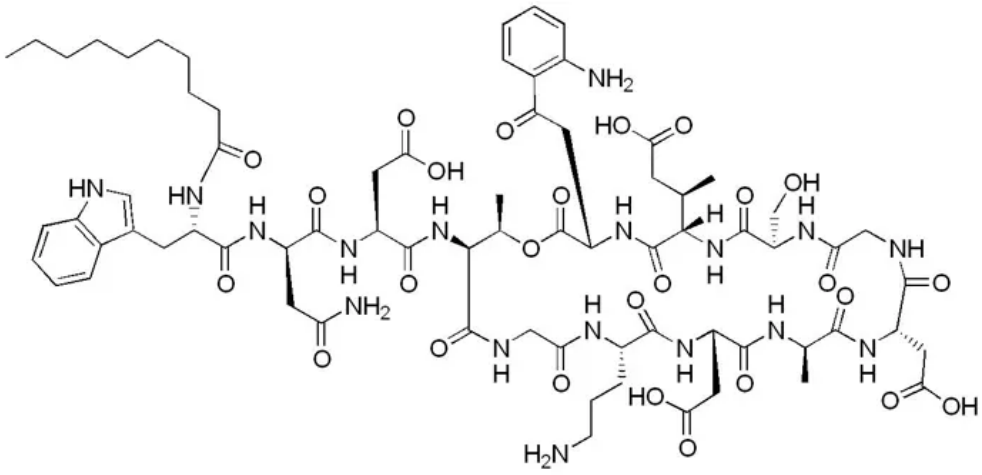

Figure 5.3.5 Chemical structure of daptomycin

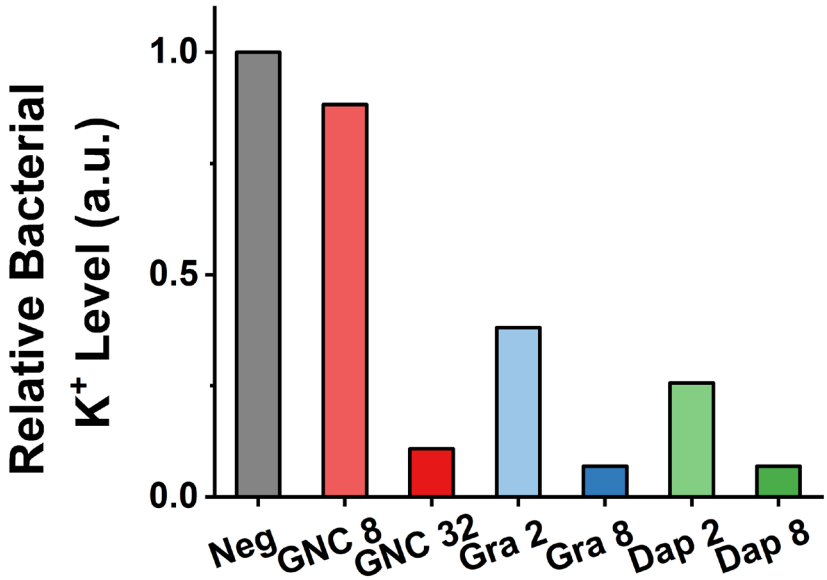

Figure 5.3.6 Comparison of the K^+ level for MRSA treated with different concentrations of 4MMP-GNC, gramicidin (Gra), and daptomycin (Dap).

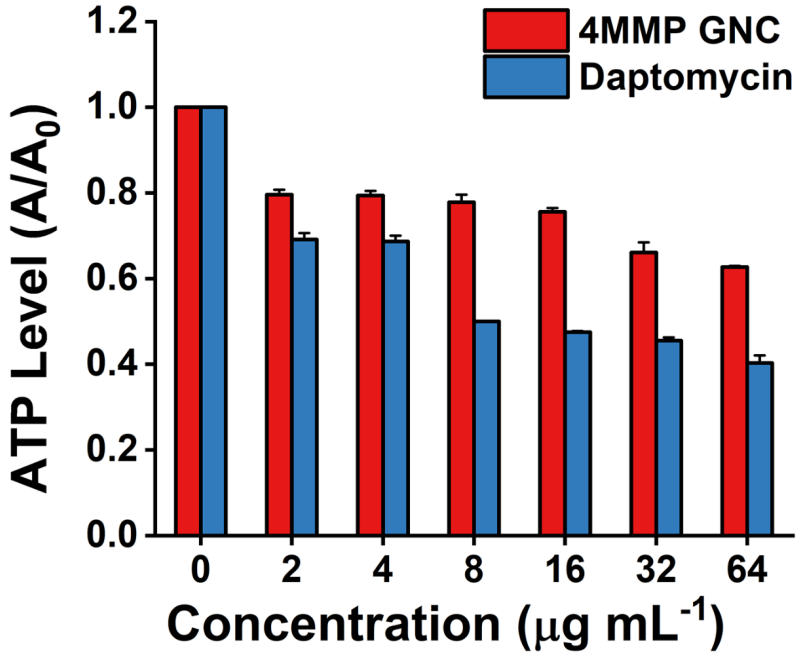

Figure 5.3.7 ATP level of daptomycin and 4MMP-GNC-treated MRSA cells under different dosages.

We then measured the ATP level of MRSA cells treated with 4MMP & C5 mixed-ligand GNCs as well as daptomycin. The result showed that both treatments significantly reduced the ATP level of MRSA, with a clear dosage dependence (**Figure 5.3.7**). For MRSA, the ATP synthesis is highly related to the bacteria cell membrane, with many crucial enzymes located on it. Thus, the influence on bacteria cell membrane would induce a strong interference with bacterial ATP synthesis and could result in the reduction of metabolic activity of bacteria. This influence on the crucial cellular energy currency could downregulate normal physiological activity and could subsequently kill bacteria. In addition, I measured the activity of ATPase in MRSA cells. The ATPases are located either on the cytoplasmic membrane or in the cytoplasm for bacteria (**Figure 5.3.8**). We found that the treatment of daptomycin imposed no influence on the ATPase activity of MRSA as the target of daptomycin is not related to inhibiting the function of a specific enzyme. However, the treatment of 4MMP-GNC had a significant influence on the ATPase activity of MRSA, indicating a direct interference of related enzyme function. In addition, this inhibition of ATPase function is dosage-dependent. In combination with

the SEM images observed, I could conclude that the influence of 4MMP-GNC on ATP and ATPase levels could be the mechanism of killing. Combining the inhibition of ATP synthesis and ATP consumption, this GNC has a comprehensive interference on the metabolic pathways of MRSA.

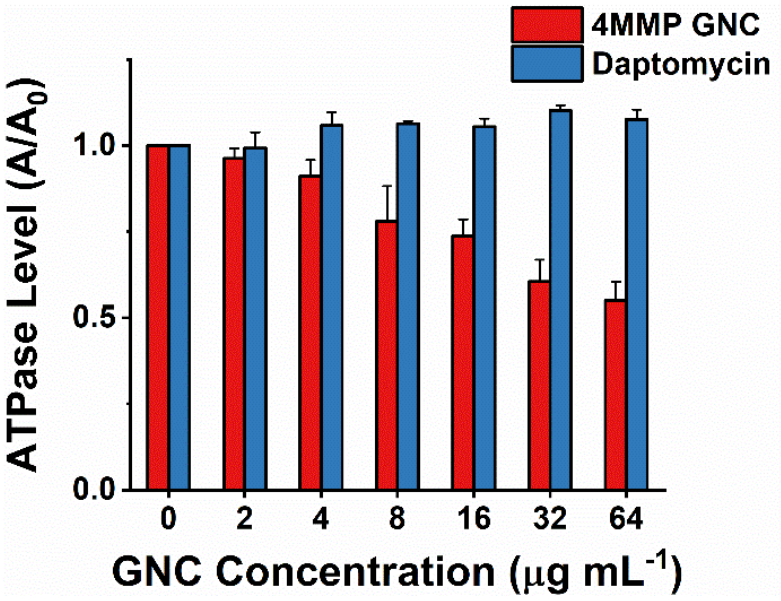

Figure 5.3.8 ATPase level of daptomycin and 4MMP-GNC-treated MRSA cells.

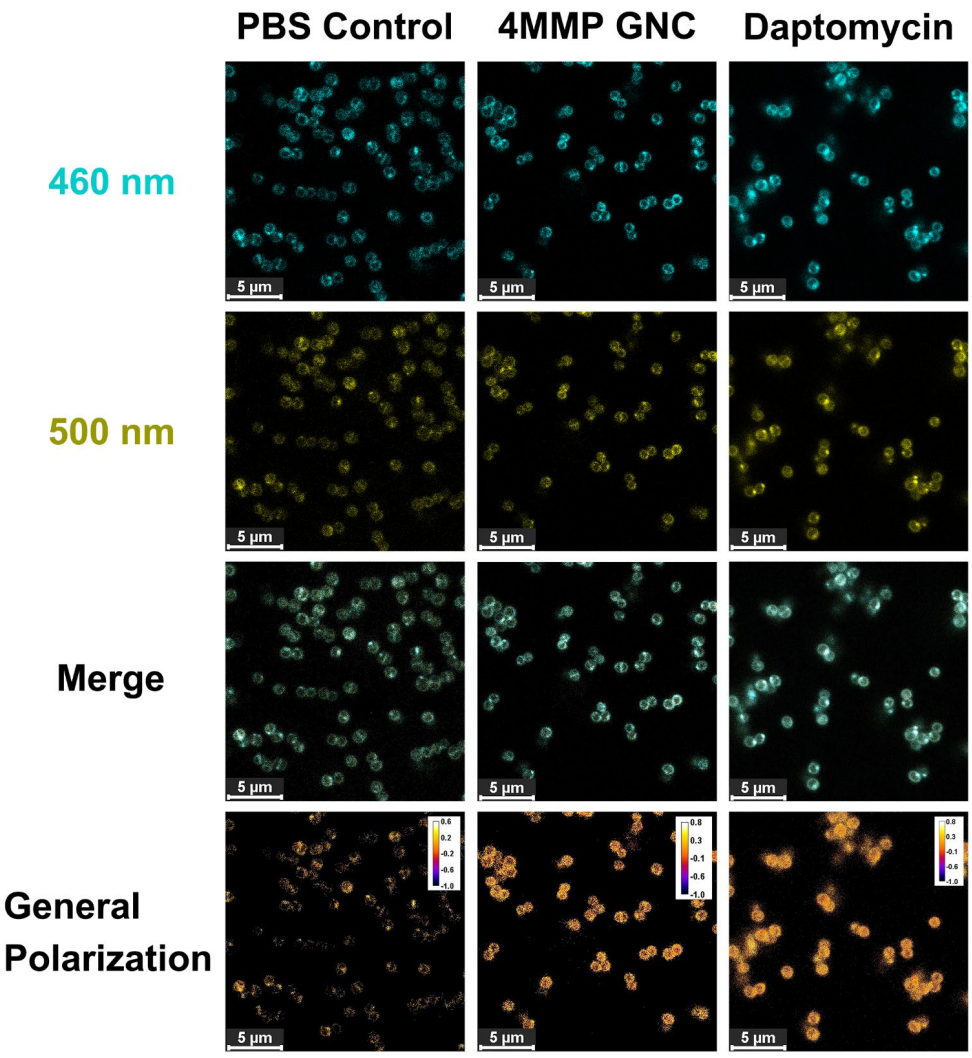

Figure 5.3.9 The laurdan staining result comparison of 4MMP-GNC and daptomycin-treated MRSA. The GP value was calculated according to the calculation formula in the materials and methods part.

The binding of daptomycin could attract phospholipids and influence the membrane fluidity of Gram-positive bacteria to cause rigidification of the phospholipid bilayer.[39] The rigidification of the bacteria membrane could suppress the normal physiological activities of bacteria and then cause cell death. To study if this GNC also could attract phospholipids and cause rigidification of MRSA cell membrane, I applied a membrane fluidity-sensitive dye—laurdan, whose fluorescence is sensitive to the lipid head density (**Figure 5.3.9**). By calculating the general polarization (GP) value, I found that with the addition of daptomycin, the GP value of MRSA has significantly increased compared

with PBS control, indicating the rigidification of MRSA cell membrane upon interacting with daptomycin. Similarly, applying the 4MMP-GNCs also increased the GP and decreased the membrane fluidity. Besides, there were obvious aggregated microdomains and condensed phospholipid areas on the surface of MRSA cell membranes after GNC treatment, which was also observed for daptomycin. Therefore, I conclude that, like daptomycin, the 4MMP-GNC could attract phospholipids to form condensed microdomains and cause the rigidification of the bacteria cell membrane, which could be the antibacterial mechanism.

To further characterize the formation of microdomains on the MRSA cell membrane, a characteristic fluid lipid indicator DilC12(3) was applied for the characterization of fluid lipid region formation. I observed that for both daptomycin and GNC-treated groups, there were DilC12(3) clustered regions (Figure 5.3.10). Thus, for both daptomycin and 4MMP-GNCs, the initial insertion into the cell membrane could further promote the aggregation of phospholipids in the fluid lipid domains and cause the rigidification of the cell membrane to induce MRSA death.

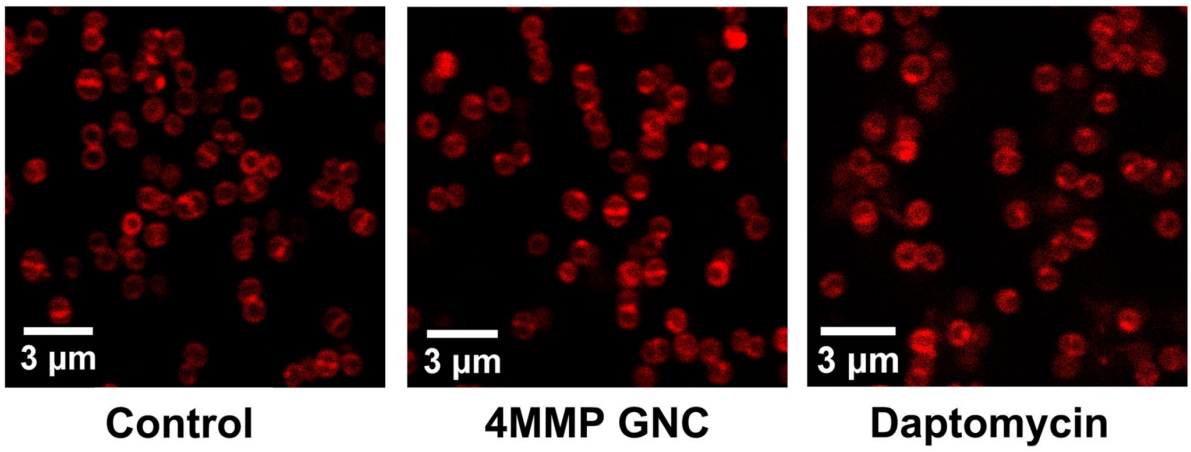

Figure 5.3.10 DilC12(3) staining results of PBS control (left), 4MMP-GNC (middle) and Daptomycin (right). Both 4MMP-GNC and Daptomycin-treated groups showing the existence of phospholipid liquefaction domains (diamond ring-shape) on the bacteria cell membrane.

Previous studies have confirmed that the treatment of peptide antibiotics, including daptomycin, could induce membrane charge dissipation to kill Gram-positive bacteria. To measure if the 4MMP-GNC could also induce the same phenomenon, I applied a membrane potential dye DiSC3(5), whose fluorescence intensity depends on the degree of depolarization of the bacteria cell membrane (**Figure 5.3.11, left**). I observed that the addition of 4MMP-GNC induced a significant increase in the DiSC3(5) fluorescence, which is higher than the same amount of daptomycin, indicating an increase in membrane potential dissipation. To further quantify the membrane potential dissipation rate, MycoLight ratiometric bacterial membrane potential kit was applied to probe the membrane potential dissipation level of MRSA, and the fluorescent images were captured with a laser scanning confocal microscope. As the membrane potential decreases, the red-to-green ratio of fluorescence also decreases accordingly (**Figure 5.3.11, right**). The carbonyl cyanide 3-chlorophenylhydrazone (CCCP), a proton carrier that could induce the increased permeability of the plasma membrane to hydrogen ions to induce membrane potential dissipation, was applied as the positive control. I observed that with the addition of either the GNC or daptomycin, the overall red-to-green ratio showed a clear shift from orange to purple, displaying clear depolarization of the cell membrane. The statistical result also shows a clear decrease in the red-to-green ratio, thereby confirming the dissipation of membrane potential of both daptomycin and GNC-treated groups (**Figure 5.3.12**).

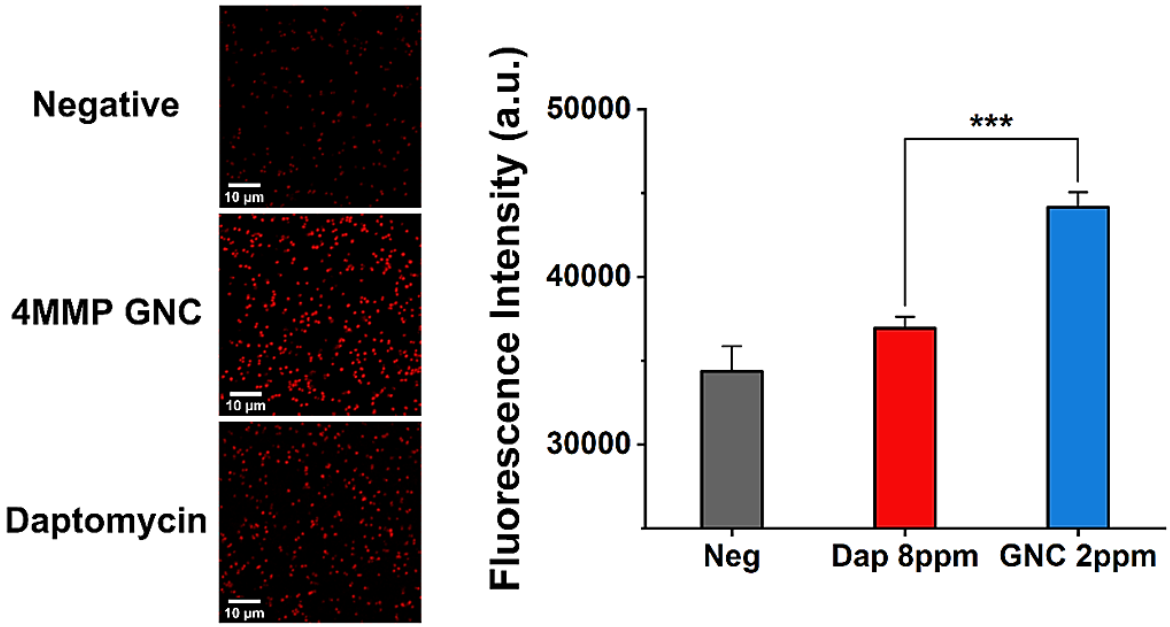

Figure 5.3.11 The MRSA membrane potential images stained with DiSC3(5) and the fluorescence statistical result (***: $P < 0.01$).

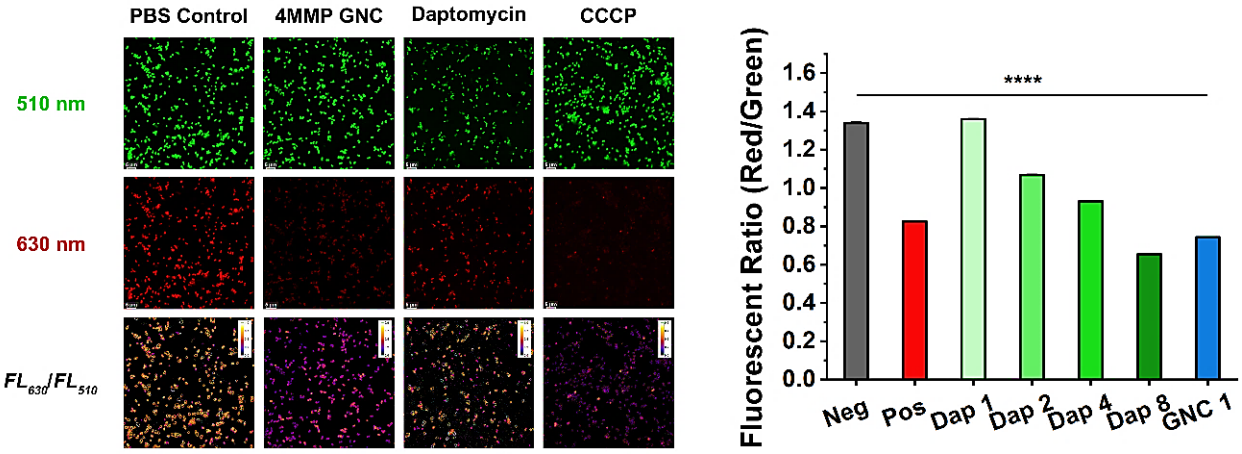

Figure 5.3.12 The MRSA membrane potential results stained with MycoStain It™. The fluorescence ratio could reflect the relative strength of the membrane potential (****: $P < 0.001$).

Based on the above experiments, I concluded that the GNC could bind with the bacterial cell membrane and insert its alkyl chain into the phospholipid bilayer. The binding of GNCs with the bacterial cell membrane could induce a decrease in intracellular K^+ concentration. Moreover, the GNC could attract free phospholipid molecules to form

lipid clusterization and blebbing through hydrophobic interaction and intermolecular forces. Simultaneously, the GNC interferes with the overall metabolism level of MRSA. Furthermore, this interaction could induce membrane potential dissipation and cause cell death.

5.4 Biosafety and biocompatibility analysis of 4MMP-GNC

The biosafety data, as well as biocompatibility of the 4MMP-GNC, was evaluated by Dr Ning Ren, the co-author of this work. She cultured the material with human umbilical vein endothelial cells (HUVECs) for 12 and 24 hours and analyzed the cell viability with an SRB cell viability test kit. Compared with the PBS control, the viability of HUVEC with a high dosage of the 4MMP-GNC treatment was hardly changed (Figure 5.4.1). In addition, a human retinal epithelial cell line ARPE-19 was also used for the analysis of biosafety of the 4MMP-GNC. The cell staining with propidium iodide (PI) and Calcein-AM for dead and living cells, respectively, demonstrated no obvious changes in living cell morphology as well as living cell number compared with the control group, confirming the high biocompatibility of the 4MMP-capped GNCs (Figure 5.4.2).

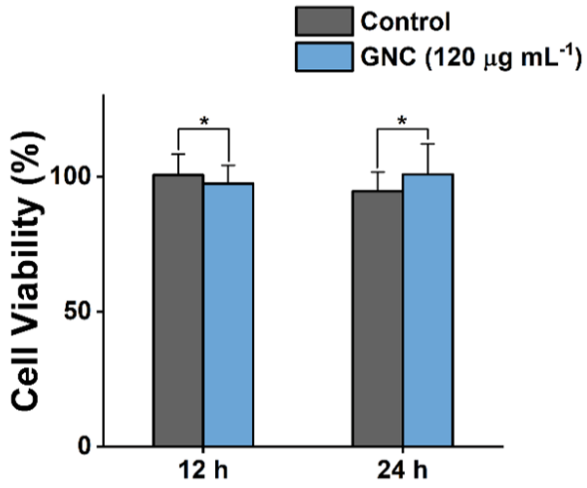

Figure 5.4.1 The cell viability result of HUVEC cultured with PBS as negative control and high-concentration 4MMP-GNC (*: *P* >0.05).

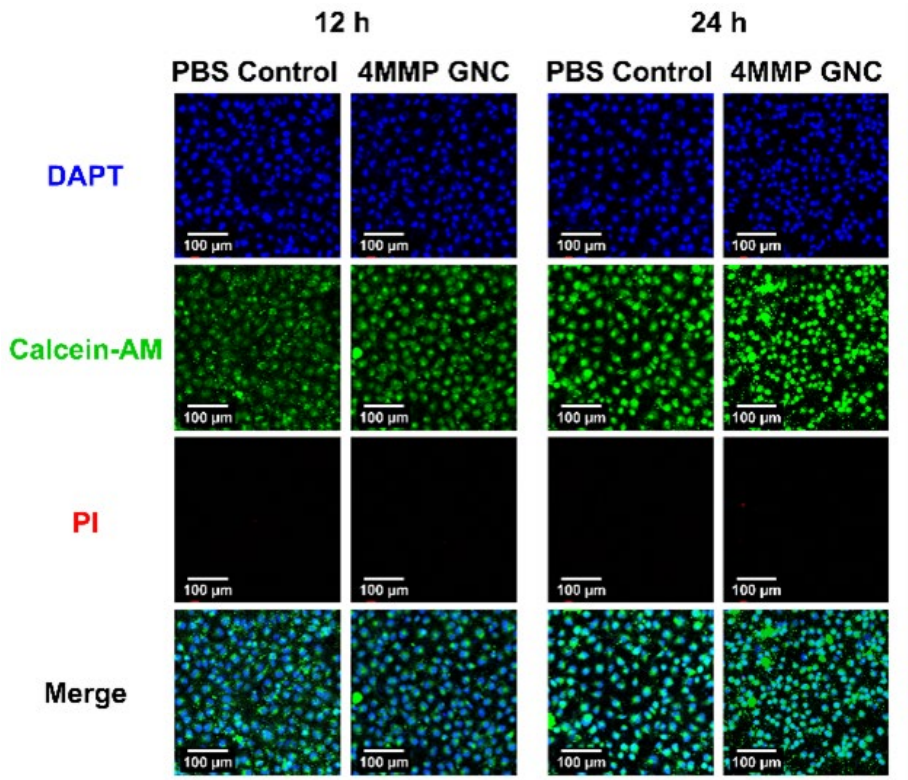

Figure 5.4.2 Live-and-dead staining results of ARPE-19 cells. No increase in cell death (indicated with PI fluorescence) was observed in the 4MMP-GNC-treated group compared with the PBS control.

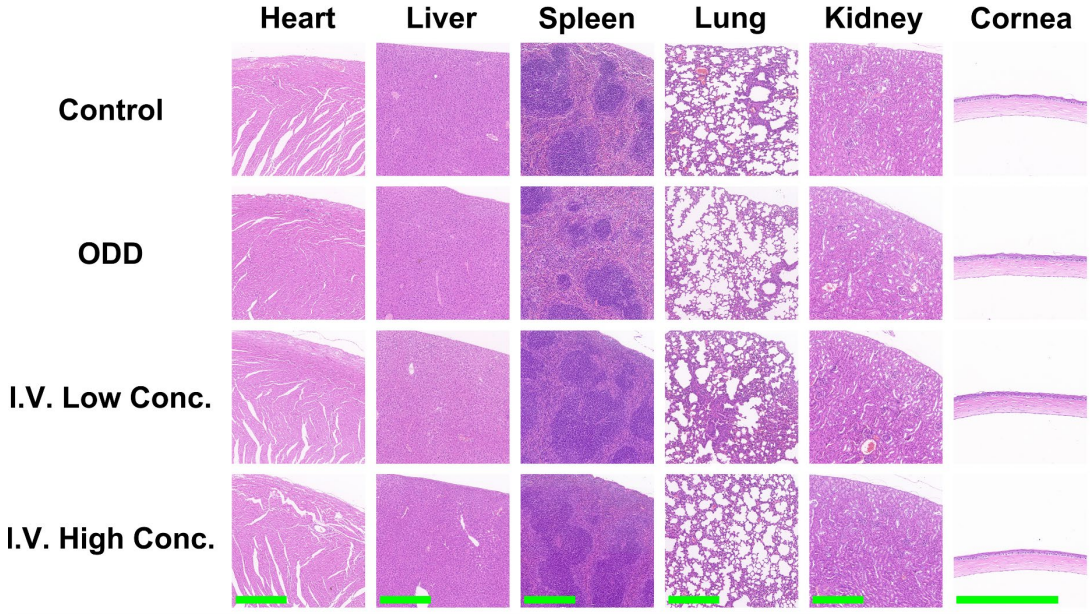

Figure 5.4.3 The H&E staining result of the mice treated with GNCs in different doses and modes of administration (ODD: ocular drug delivery, low concentration: 1.5 mg kg^{-1} Wt, high concentration: 3 mg kg^{-1}, and scale bar: 400 μm).

Dr Ning Ren also measured the organ slices in different groups and found no pathological changes of high concentration (3 mg kg^{-1} Wt) of 4MMP-GNC treatment compared with the negative control, further confirming the high biosafety of this material (**Figure 5.4.3**).

5.5 *In vitro* pig cornea antibacterial model

The antibacterial ability of the 4MMP mixed-ligand-capped GNC was compared with Van, the positive control, for the bacteria-killing effect and keratitis treatment evaluation. The *in vitro* keratitis model building method was summarised in **Chapter 2, Section 2.2.5.3**. Then 1 µL, 1 × 10^4 CFU mL^{-1} of the MRSA cells were inoculated on the wound to mimic the keratitis infection. After 12-h incubation, the wound was treated with PBS as the negative control, Van as the positive control, or the 4MMP-GNC (32 µg mL^{-1}). The treatment was provided three times a day and six hours apart. At the end of the treatment, the porcine cornea was photographed then the infected wound was separated for plate coating to count the MRSA colony numbers in each group. From the graph, I found that for the PBS control group, the keratitis infection was the most severe among all three groups, with the MRSA colonies widely connected to form thick biofilm. In addition, the tentacle-like structure spread to the edge of the scleral tissue through folds, forming a ring on the bottom agar plate, indicating the high viability and proliferation of MRSA. The Van-treated cornea has a reduced biofilm formation in the centre of the wound area as well as less diffusion to the peripheral area. The bacteria ring was also thinner (**Figure 5.5.1**). However, due to the development of drug resistance, even a high concentration of Van could not effectively inhibit the growth of MRSA. In sharp contrast, the GNC-treated group had only separated colony formation, and the biofilm was barely visible. In addition, there was no observable spread of MRSA colonies to the beneath agar plate. The plate coating result also showed a similar result, with the PBS control group having the highest amount of MRSA colonies. The Van group displayed a significantly decreased number of colonies, and the GNC group showed the

least number of MRSA colonies.

By the end of the experiment, the corneas were separated, fixed, and then stained with hematoxylin and eosin (H&E) staining, as well as a Gram staining kit. This part of the data was provided by Dr Ning as well. The negative control group demonstrated an obvious condense of purple spots in the infection foci (Figure 5.5.2). Gram staining further confirmed that the staining is mainly Gram-positive bacteria, *i.e.* MRSA cells. In contrast, the stain of MRSA was less visible for the Van-treated group. While for the GNC-treated group, the stain of MRSA was even less and agreed well with bacteria counting results. All the results confirmed the high efficiency of the 4MMP-GNC in the treatment of MRSA infection in the *in vitro* keratitis model.

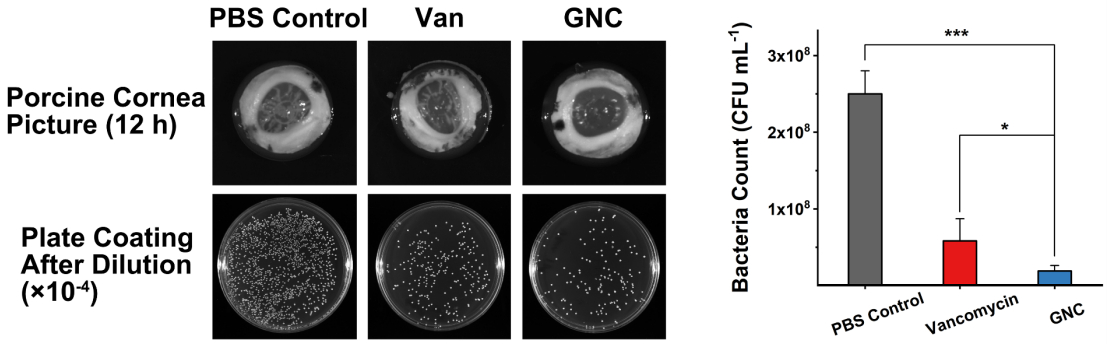

Figure 5.5.1 Optical pictures and plate coating (left), and bacterial counting (right) of MRSA-infected porcine corneas after each treatment (***:P <0.01, *:P >0.05).

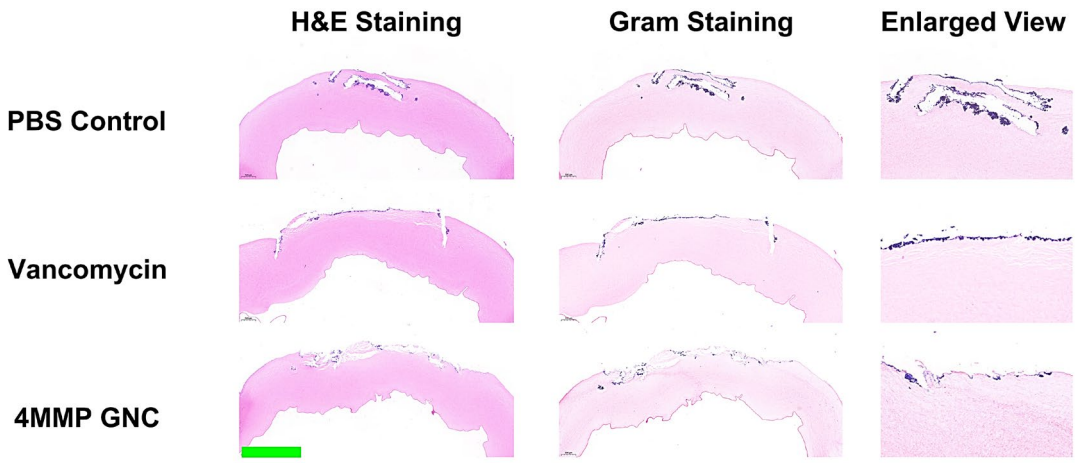

Figure 5.5.2 H&E and Gram staining results of the pig eye cornea after different treatments (scale bar: 2 mm).

5.6 *In vivo* mouse keratitis model

We then applied the 4MMP-GNCs in the *in vivo* murine keratitis model. The model was created by anaesthetizing mice and creating a series of perpendicular "W-shaped" scratches that were deep into the stroma on the cornea of mice with a syringe needle. The wound was then infected with 2 µL, 5 × 10^8 CFU mL^{-1} MRSA bacteria solution for 24-h and then treated with PBS (negative control), Van (positive control), and GNC three times a day, six hours apart for 3 days, respectively. During the treatment period, the infection situation was monitored and photographed each day, and the areas of eye ulceration were measured (**Figure 5.6.1**). Besides, I also collected the swab of eye discharge for colony counting each day (**Figure 5.6.2**). By comparing the area of opaqueness induced by ulceration formation on the cornea, I found that, compared with the PBS control, treatment with Van (30 µg mL^{-1}) reduced the extent of opacity and showed the tendency to cure the ulceration. However, by day 3, the scratch on the cornea was still obvious, accompanied by signs of inflammation. Similarly, the treatment of 16 µg mL^{-1} 4MMP-GNC achieved a comparable effect to Van, with the opaqueness generally cured by day 3, while the injury on the mice cornea was still not fully recovered. In contrast, the treatment with 64 µg mL^{-1} 4MMP-GNC not only significantly reduced the infection induced by MRSA but also accelerated the healing of the wound

on the cornea. By day 3, the corneas were fixed and stained with H&E staining and Gram staining. This data is provided by Dr Ning Ren. From the section scanning, I observed that the PBS-treated group demonstrated a thick and bumpy corneal surface (Figure 5.6.3). A closer view of the corneal section displayed abundant purple stains in the swollen area, indicating severe MRSA infection in this region. Compared with the PBS control, the treatment of Van significantly reduced the degree of infection. However, the thickness of the cornea was still abnormal, possibly due to the foci observed in the eye photographs. In addition, the corneal epithelial cells were disordered, indicating that the wounds were not fully recovered. Likewise, the low GNC group also showed a similar situation. However, the high dosage GNC-treated group showed significantly reduced cornea thickness and well-stratified corneal epithelial cells, indicating a full recovery of the wound on the cornea. This result was further confirmed by the counting of the colony number after plate coating, with the PBS group showing the highest amount of MRSA, the van and low GNC showed a similar result, and the high GNC group showed the lowest amount of MRSA, which is around 100-fold lower than the initial bacterial count, indicating good control of MRSA infection. The statistical result of the ulceration size was consistent with the physical picture observations. From the physical images of the treatment effect of keratitis in mice, I observed the greatly reduced ulcer area and angiogenesis, clear eye anterior chamber, as well as the obviously smooth cornea in the 4MMP-GNC-treated groups (Figure 5.6.4). All the results demonstrated the excellent therapeutic effect of the 4MMP-GNC as a new generation of anti-MDR eye drops.

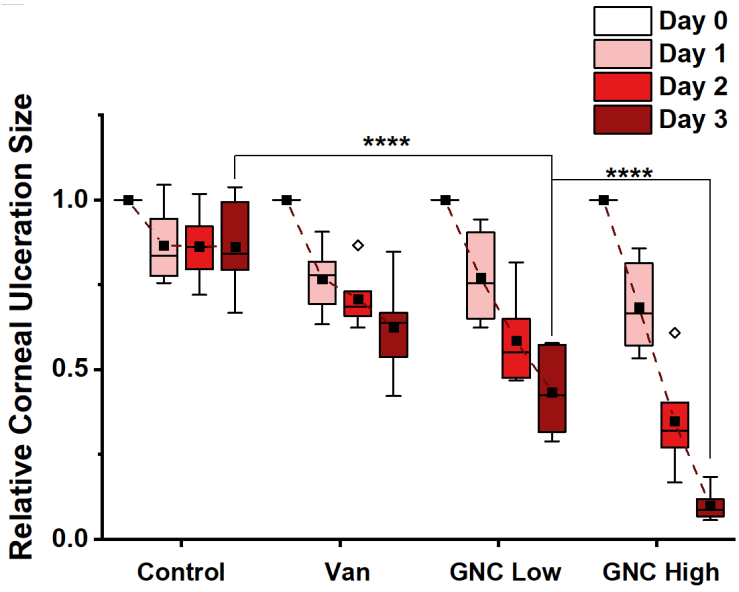

Figure 5.6.1 Statistics on the area of ulcers on the cornea surface (****: p <0.001).

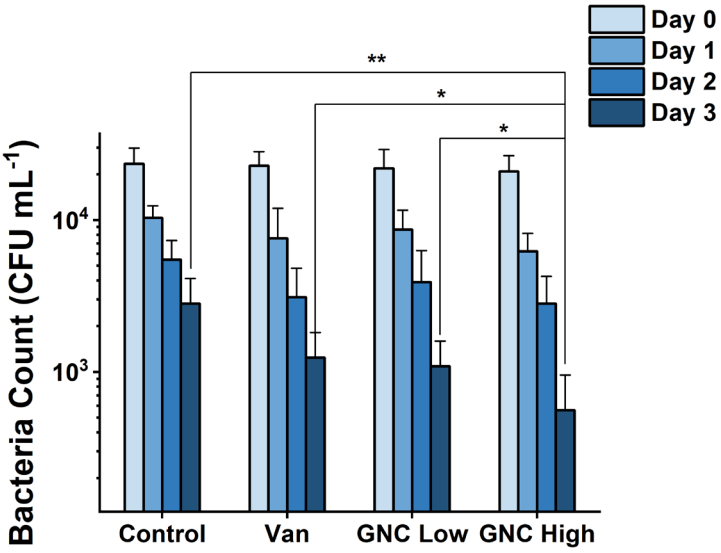

Figure 5.6.2 Comparison of the number of MRSA colony counts acquired in eye discharge (*: p >0.05, **: 0.01< p <0.05).

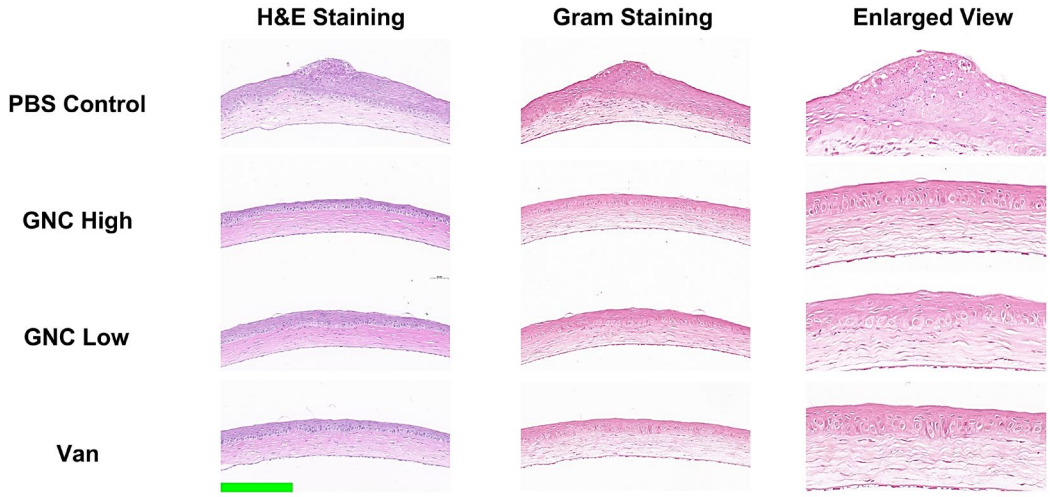

Figure 5.6.3 H&E and Gram staining results of mice corneas treated with PBS, 30 μg mL^{-1} Van, 16 μg mL^{-1} 4MMP-GNC, and 64 μg mL^{-1} 4MMP-GNC, same below (scale bar: 200 μm).

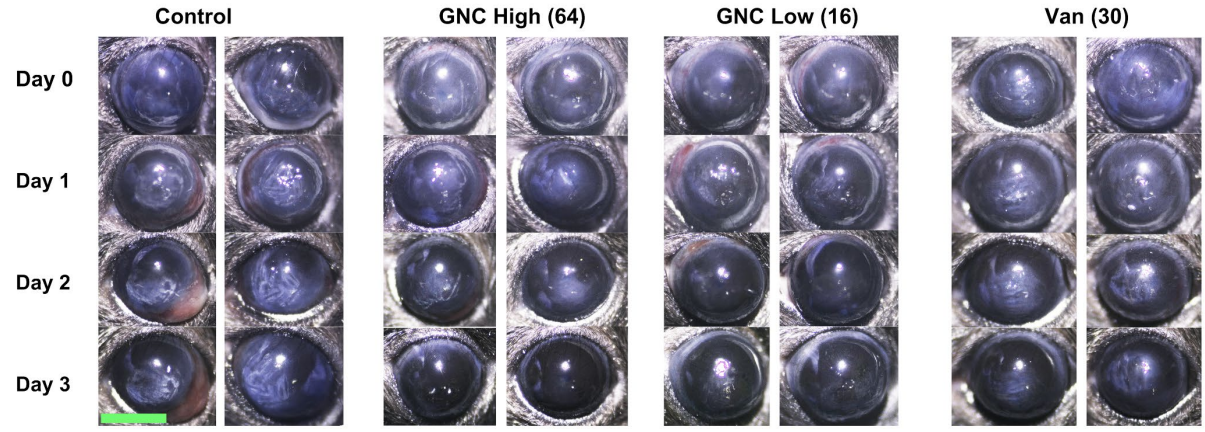

Figure 5.6.4 Physical images of the therapeutic effect in mice keratitis model with different treatments. The area change of the ulceration on the surface of the eyeball can be clearly observed (scale bar: 2mm).

5.7 Conclusions

In summary, I have developed a highly effective therapeutic agent to control MRSA-induced keratitis by capping non-antibacterial 4MMP onto GNCs. After decorating, this non-antibacterial thiol fragrance was turned into a powerful nano-antibiotic with MIC comparable to many last-sorted antibiotics. Surprisingly, I found that treatment with this GNC did not induce the rupture or leakage of bacteria structure but inhibited the

energy metabolism of MRSA and induced the membrane rigidification to kill the bacteria slowly, thus reducing endotoxin release and overreaction of the immune system. In both *in vitro* porcine eye model and *in vivo* keratitis model, the treatment of 4MMP-GNC significantly inhibited the formation of bacteria rings and reduced the bacteria number, as well as alleviated the symptom of corneal ulceration. These results demonstrate that 4MMP-GNC can act as a new generation of therapy for MDR bacteria-induced keratitis.

5.8 References

1 L. J. Luo, T. Y. Lin, C. H. Yao, P. Y. Kuo, M. Matsusaki, S. G. Harroun, C. C. Huang and J. Y. Lai, *J. Colloid Interface Sci.*, 2019, **536**, 112–126.

2 L. Ung, P. J. M. Bispo, S. S. Shanbhag, M. S. Gilmore and J. Chodosh, *Surv. Ophthalmol.*, 2018, **64**, 255–271.

3 Z. Li, J. Jiang, K. Chen, Q. Chen, Q. Zheng, X. Liu, H. Weng, S. Wu and W. Chen, *Nat. Commun.*, 2021, **12**, 3738.

4 Y. Zhang, Y. Yu, G. Li, X. Zhang, Z. Wu and L. Lin, *Biomacromolecules*, 2021, **22**, 2020–2032.

5 J. W. Lee, T. Somerville, S. B. Kaye and V. Romano, *J. Clin. Med.*, 2021, **10**, 758.

6 A. Austin, T. Lietman and J. Rose-Nussbaumer, *Ophthalmology*, 2017, **124**, 1678–1689.

7 V. S. Chang, D. K. Dhaliwal, L. Raju and R. P. Kowalski, *Cornea*, 2015, **34**, 698–703.

8 C. Yu, Y. Gao, Y. Y. Zhang, J. Wang, Y. Y. Zhang, J. Li, X. X. Zhang, Z. Wu and X. X. Zhang, *Biomacromolecules*, 2021, **22**, 3704–3717.

9 A. F. Durrani, S. Atta, A. K. Bhat, A. Mammen, D. Dhaliwal, R. P. Kowalski and V. Jhanji, *Am. J. Ophthalmol.*, 2020, **214**, 119–126.

10 W. Zheng, Y. Jia, Y. Zhao, J. Zhang, Y. Xie, L. Wang, X. Zhao, X. Liu, R. Tang, W. Chen and X. Jiang, *Nano Lett.*, 2021, **21**, 1992–2000.

11 M. Tang, J. Zhang, C. Yang, Y. Zheng and H. Jiang, *Front. Chem.*, 2020, **8**, 1–17.

12 Y. Xie, Y. Liu, J. Yang, Y. Liu, F. Hu, K. Zhu and X. Jiang, *Angew. Chemie - Int. Ed.*, 2018, **57**, 3958–3962.

13 K. Zheng, M. I. Setyawati, D. T. Leong and J. Xie, *ACS Nano*, 2017, **11**, 6904–6910.

14 Z. Pang, Q. Li, Y. Jia, W. Yan, J. Qi, Y. Guo, F. Hu, D. Zhou and X. Jiang, *Chem. Sci.*, 2021, **12**, 14871–14882.

15 Y. Zhao, Z. Chen, Y. Chen, J. Xu, J. Li and X. Jiang, *J. Am. Chem. Soc.*, 2013, **135**, 12940–12943.

16 J. Zhang, L. Mou and X. Jiang, *Chem. Sci.*, 2020, **11**, 923–936.

17 Y. Zhao, Y. Tian, Y. Cui, W. Liu, W. Ma and X. Jiang, *J. Am. Chem. Soc.*, 2010, **132**, 12349–12356.

18 X. Zhao, Y. Jia, J. Li, R. Dong, J. Zhang, C. Ma, H. Wang, Y. Rui and X. Jiang, *ACS Appl. Mater. Interfaces*, 2018, **10**, 29398–29406.

19 X. Yang, J. Yang, L. Wang, B. Ran, Y. Jia, L. Zhang, G. Yang, H. Shao and X. Jiang, *ACS Nano*, 2017, **11**, 5737–5745.

20 Y. Xu, H. Wang, M. Zhang, J. Zhang and W. Yan, *Nanomaterials*, 2021, **11**, 1621.

21 X. Li, S. M. Robinson, A. Gupta, K. Saha, Z. Jiang, D. F. Moyano, A. Sahar, M. A. Riley and V. M. Rotello, *ACS Nano*, 2014, **8**, 10682–10686.

22 R. Jin, *Nanoscale*, 2015, **7**, 1549–1565.

23 T. K. Chang, T. M. Cheng, H. L. Chu, S. H. Tan, J. C. Kuo, P. H. Hsu, C. Y. Su, H. M. Chen, C. M. Lee and T. R. Kuo, *ACS Sustain. Chem. Eng.*, 2019, **7**, 15479–15486.

24 K. Zheng, M. I. Setyawati, D. T. Leong and J. Xie, *Chem. Mater.*, 2018, **30**, 2800–2808.

25 Y. Zheng, W. Liu, Z. Qin, Y. Chen, H. Jiang and X. Wang, *Bioconjug. Chem.*, 2018, **29**, 3094–3103.

26 J. Xie, B. Liao and R.-Y. Tang, *J. Agric. Food Chem.*, 2020, **68**, 12505–12526.

27 B. Tan, S. Zhang, Y. Qiang, W. Li, H. Liu, C. Xu and S. Chen, *J. Mol. Liq.*, 2019, **286**, 110891.

28 Z. Xiong, B. Li, L. Li, X. Peng, Y. Yin and L. Weng, *Toxicol. Environ. Chem.*, 2018, **100**, 47–53.

29 Z. Xiong, B. Li, L. Li, L. Wan, X. Peng and Y. Yin, *Molecules*, 2017, **22**, 1–11.

30 JECFA, 2007, **59**.

31 R. L. Smith, S. M. Cohen, J. Doull, V. J. Feron, J. I. Goodman, L. J. Marnett, P. S. Portoghese, W. J. Waddell, B. M. Wagner and T. B. Adams, *Food Technol.*, 2005, **59**, 24–62.

32 J. Lin, R. L. Rouseff, S. Barros and M. Naim, *J. Agric. Food Chem.*, 2002, **50**, 813–819.

33 I. Blank, *ACS Symp. Ser.*, 2002, **826**, 25–53.

34 R. López, N. Ortín, J. P. Pérez-Trujillo, J. Cacho and V. Ferreira, *J. Agric. Food Chem.*, 2003, **51**, 3419–3425.

35 D. Jung, A. Rozek, M. Okon and R. E. W. Hancock, *Chem. Biol.*, 2004, **11**, 949–957.

36 R. M. Humphries, S. Pollett and G. Sakoulas, *Clin. Microbiol. Rev.*, 2013, **26**, 759–780.

37 A. Müller, M. Wenzel, H. Strahl, F. Grein, T. N. V. Saaki, B. Kohl, T. Siersma, J. E. Bandow, H. G. Sahl, T. Schneider and L. W. Hamoen, *Proc. Natl. Acad. Sci. U. S. A.*, 2016, **113**, E7077–E7086.

38 N. Cotroneo, R. Harris, N. Perlmutter, T. Beveridge and J. A. Silverman, *Antimicrob. Agents Chemother.*, 2008, **52**, 2223–2225.

39 M. T. Lee, W. C. Hung, M. H. Hsieh, H. Chen, Y. Y. Chang and H. W. Huang, *Biophys. J.*, 2017, **113**, 82–90.

Part III

Developing Dual-/multi-ligand-functionalised GNCs for Cancer Metastasis Theranostics

Chapter 6
Introduction to the lymphatic system and application of gold nanomaterial in the lymphatic imaging

6.1 History of lymph node-related research

Lymphatic circulation is a vitally important part of the circulatory system. However, it also intertwines with the other seven systems of the human body and participates in substance transport and homeostasis. It is one of the first systems discovered in the early days of medical cognition. As early as the fifth century BC in ancient Greek, the father of modern medicine and the founder of the humoral theory—Hippocrates, described the discovery of lymphatics and lymph nodes (LNs). He described them as "white blood in nodes" and then coined the term "*chylos*" in the book *Peri Adenon*, which is the first available description of the lymphatic system.[1] Subsequently, many scientists and anatomists, including Aristotle (~4th century, BC), Galen (I–II century), Paul (~ 6th century), and Rufus (I–II century), all gave preliminary anatomical findings on the human or animal lymphatic system and documented their observations in own masterpieces. During this period, the lymphatics, which are nearly colourless, were observed. In addition, axillary, inguinal, and mesenteric nodes, as well as immune organs, including tonsils and thymus, were also described.[2] However, the development and research on the lymphatic system met a long stagnation due to the prohibitions on human body anatomy till the 16th to 17th centuries. The father of modern anatomy—Andreas Vesalius, had called for continued anatomical research using human cadavers, given the vast differences between humans and animals. Therefore, research on the lymphatic system could then continue. During this period, the presence of mesenteric lymphatics and chylous fluid was again demonstrated (by Ambroise Paré and Gabriele Falloppio), and most importantly, the presence of the thoracic duct was firstly proved.[3]

In the 17th–18th century, research on the lymphatic system entered its heyday. Many important findings include the intestinal chylous fluid circulation and lacteals (by Gaspare Aselli and Pierre Gassendi) as well as the thoracic duct with valves and the reservoir of the chyle—cisterna chyli (by Jean Pecquet). The lacteal duct has a milky white colour that contrasts well with muscle, so it was discovered and characterised earlier. However, the contents of the lymphatic vessels are transparent and difficult to distinguish. In addition, the lymphatic vessels of the corpse are more shrivelled and difficult to identify, so it is easy to mistake them for nerves or blood vessels, making them relatively difficult to find. The most exciting outcome is that Thomas Bartholin and Olaus Rudbeck successively separated the non-lacteal lymphatic vessels and named them, and the word "lymphatics" came into existence in 1653. Lately, Francis Glisson described lymphatic circulation, while Frederik Ruysch described the function of the lymphatic valves through inflating the lymphatic vessels with air or mercury sulfide and glycerol. In the early 18th century, Raymond Vieussens and William Hunter gradually completed the function of the lymphatic system, including clarifying its discrete relationship with blood circulation and unifying the functions of the lymphatics and chyle ducts.[3] In the 19th–20th century, the development of research on the lymphatic system became steady. However, the famous Italian anatomist Paolo Mascagni made a huge contribution to the establishment of the human lymphatic system. Through extensive anatomical experiments, he mapped the entire internal lymphatic system of the human body. A series of 19th scientists, including Marie Sappey, Alfred Biesiadecki, Carl Ludwig, Rudolph Heidenhain, and Ernest Henry Starling, supplemented the physical structure and functions of the lymphatic system as well as illustrated the relationship between lymphatic vessels and blood vessels. In the 20th century, the study of the lymphatic system moved to the intraorganic scope. Paul Patek studied the cardiac lymphatic system, while Miltiadès Papamiltiadès did an in-depth study of the lymphatic system in the lungs and genital area. Leonetto Comparini studied the physiological structure of lymphatic vessels and the structure of their musculature. In addition, he

also studied the physiological structure of lymphatic vessels in the liver and did a 3-D reconstruction of its arrangement. In the 21st century, the discovery of the so-called glymphatic system in the central nerve system, including the meninges (discovered in 2015), and brain (discovered in 2017), has once again subverted people's understanding of the lymphatic system.[2]

In general, the functions of the lymphatic system can be summarised in three parts: **1)** the transportation of macromolecules and lipids; **2)** the maintenance of homeostasis (adjusting osmolality and hydrostatic pressure), and **3)** involving in the maturation and transportation of immune cells and participating in body immunity. However, due to not being as visible and fast-moving as blood vessels, research on the lymphatic system has been restricted for a long time and remains mysterious to most people, even after some 2,500 years of research. Compared to the well-known blood circulation system, our knowledge of lymphatics and lymphatic system is far from enough, leading to continuous new discoveries, including the intracerebral lymphatic system, lymphangiogenesis, and lymphosomes.[4] Due to many unsolved problems, the lymphatic system has a high research value. In addition, the lymphatic system is closely related to many diseases that are currently attracting attention, for example, cardiovascular disease,[5] infections and immunity,[6] cancer,[7] and obesity. Therefore, the lymphatic system not only presents an important frontier research area but also offers great potential to address such key human diseases.

Within the lymphatic system, LNs have unique structures. They are circular or oval tissue bodies of 2 mm to 1 cm in size and are arranged in clusters at major confluence sites of lymphatic drainage. They are mainly distributed in the armpit, pelvis, femoral canal, neck, and face, along the descending aorta and inferior vena cava. Due to their relatively big size and close to the surface of the skin, therapeutic diagnosis of LN is the most obvious way to access the lymphatic system. Several methods have been used for the imaging and diagnosis of the LNs, including traditional non-invasive imaging

techniques like palpation, ultrasonic imaging, LN doppler imaging and LN CT imaging, as well as invasive methods like biopsy or intranodal injection of dye to judge the status of LNs. However, most such methods often suffer limitations related to material instability and biosafety. With the development of nanomaterials, new LN theranostic probes which integrate the functions of lymphatic targeting, multimodal imaging, and lymphatic diagnosis, as well as therapeutic delivery, are developed. In addition, the significantly altered retention time has provided these nanoprobes with unparallel advantages compared to traditional imaging probes.[8] The following sections will give a brief introduction to the lymphatic system structure, a few traditional and nanomaterial methods for imaging and diagnosis, and also the use of a gold-based nanomaterial for LN imaging (Figure 6.1.1).

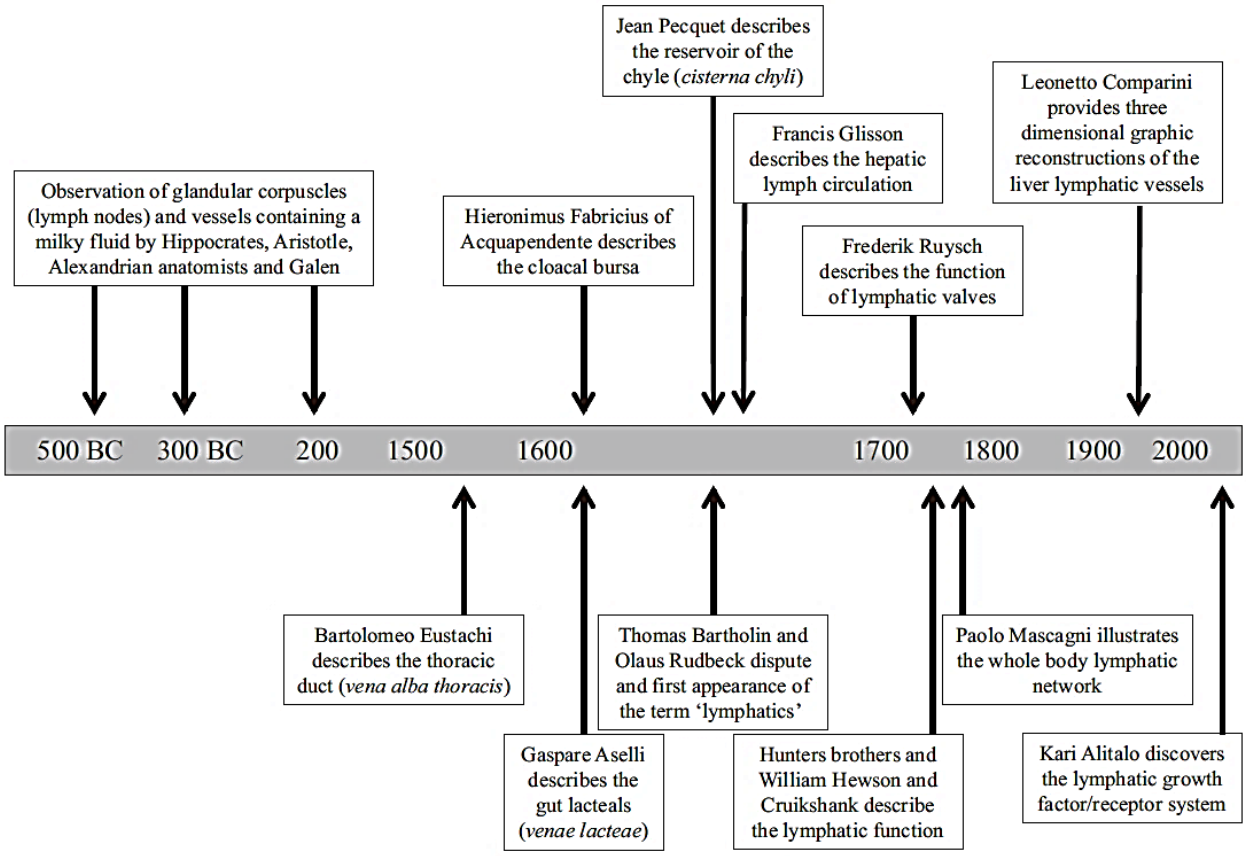

Figure 6.1.1 The timeline and famous anatomists and physicians in the discovery and establishment of the lymphatic system.[4] (Copied from Wiley Publishing Group)

6.2 The lymphatic system and lymph nodes

The lymphatic system is one of the most important defence systems of the human body. It behaves more like intricate slow-moving canals rather than fast-flowing streams like blood circulation. It can be divided into three categories: lymphatics, lymphoid tissues, and lymphoid organs. Lymphatics contain capillaries, lymphatic vessels, trunks, and ducts (Figure 6.2.1). Lymphoid tissues mainly contain diffuse lymphoid tissues and LNs. Lymphoid organs include the thymus, bone marrow, spleen, and tonsils. The lymphatic system is mainly responsible for the body's defence and immunity. 1) It provides sites for lymphocyte production, differentiation, and maturation, which are closely related to cellular immunity and humoral immunity. 2) It can remove foreign bodies, as well as senescent and dead cells from the blood. For example, the spleen, being the biggest lymphoid organ, has the function of destroying ageing and diseased red blood cells for blood renewal. In addition, the LN can filter the lymph and cleanse the antigens and metabolites. 3) It participates in the body's hematopoietic function. 4) Finally, it can partly shunt the blood when its volume is too high. Overall, the lymphatic system is extremely important for the immunity, metabolism, blood renewal, and homeostasis of the organism.[8]

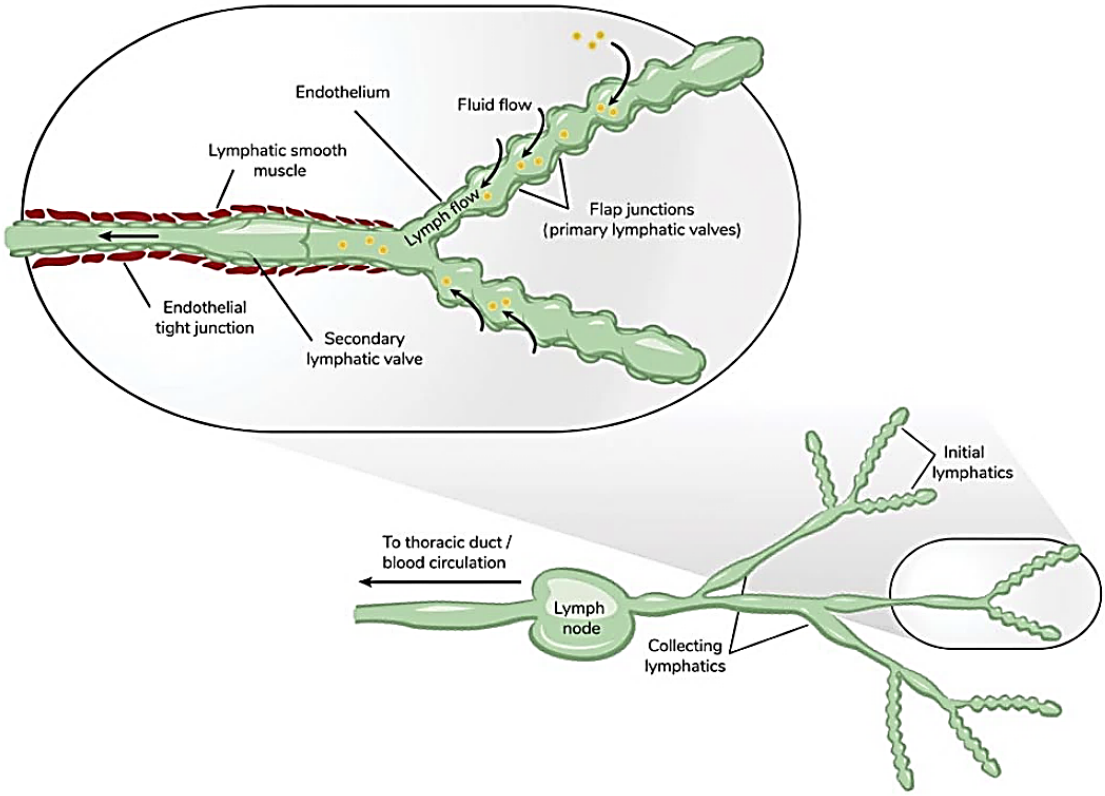

Figure 6.2.1 Structure diagram of initial lymphatics (lymphatic capillaries) and collective lymphatics.[9] (Copied from Thieme Publishing Group)

6.2.1 Lymphatic vessels

The lymphatic system is a one-way flow system, with blind-ended lymphatic vessels open to the interstitial space.[10] From the branch to the main route, it is divided into capillaries, collecting vessels, trunks, and ducts (**Figure 6.2.2**). The lymphatics collect proteins and cell debris in the interstitial spaces, pool it and return it to the blood vessels (left and right venous angle). The lymphatic capillaries, or so-called initial lymphatic vessels, consist of a single layer of endothelial cells with a discontinuous or no basement membrane. The average diameter is ~10–60 µm. Endothelial cells are arranged in imbricate, with an average gap of 500 nm between cells, which are extremely suitable for the diffusion and transport of substances. In addition, there are wide connections of the endothelial cells to the extracellular matrix through the anchoring filaments. Taking advantage of this physiological structure, manual lymph

drainage (MLD) was applied as an effective way to eliminate the oedema of LNs. Within the tissue, lymphatic capillaries gather into clumps and converge into collecting lymphatic vessels, which are surrounded by smooth muscles, collagen, and elastic fibres to generate a persistent, but slow push to drive forward lymph flow (Figure 6.2.3). Besides, a valve structure in the lumen of the collecting lymphatic vessels allows the lymph to flow in one direction. Lymph in the collecting lymphatic vessels can run through many groups of LNs and converge into the trunks, the largest vessels, and finally drain the lymph to ducts and back into the vein. However, the intestinal, hepatic, and lumbar lymphatics drain directly into the cisterna chyli, which is a physiological structure in the thoracic duct.[1 9]

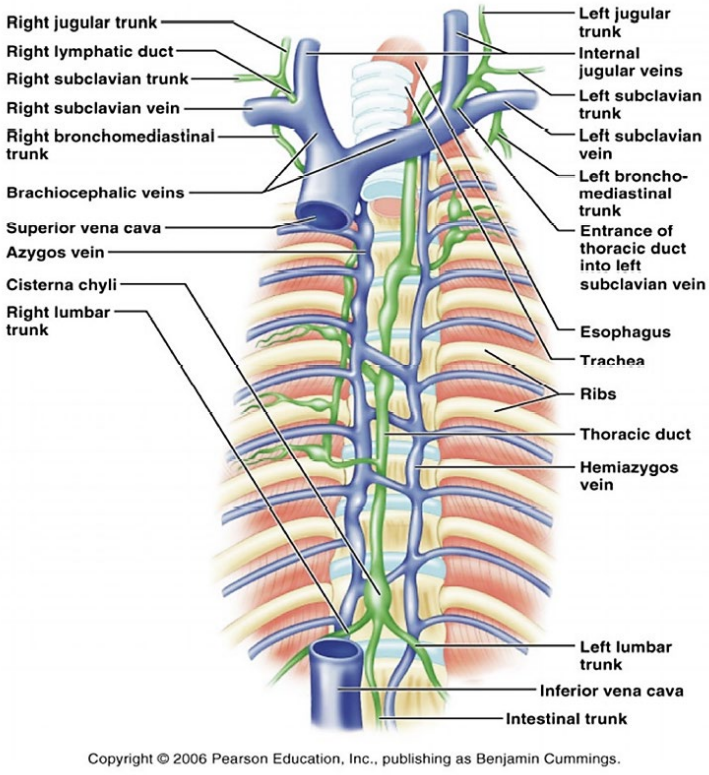

Figure 6.2.2 Diagram of the main lymphatic trunk and the connections between lymphatic ducts and veins.[7] (Copied from Springer Publishing Group)

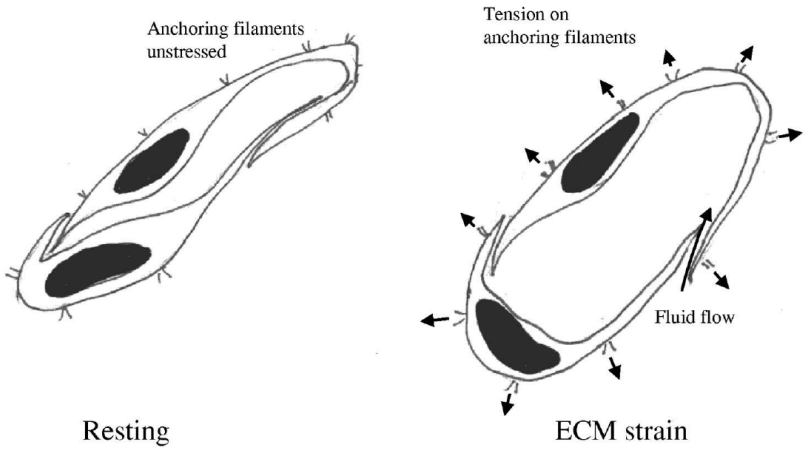

Figure 6.2.3 Schematic of the "tissue pump": the capillary lymphatic vessels are pulled by mechanical force, causing changes in internal pressure, which in turn allows the inflow of interstitial fluid.[12] (Copied from Springer Publishing Group)

6.2.2 Lymph

The content of the lymphatic vessels is called lymph, which is similar in composition and concentration to tissue fluid. The lymph is mainly composed of 5 parts: **1)** cell and cell components (including cell debris and cell lysates); **2)** pathogens; **3)** other protein antigens; **4)** other DNA/RNA antigens and **5)** enzymes.[11] Normally, the lymph is transparent and colourless. However, it is opaque and milky in the intestinal lymphatic system due to the high absorption of fat, called chyle.[9] The objects that can get into the lymph are highly limited by size. Due to the gap between the epithelial cells, only NPs smaller than 500 nm could get access to the lymph. In contrast, the blood flow rate is 100–500 times higher than lymph flow. Thus, although the cell gap of the vascular endothelial cells is only ~10 nm, which is significantly less than that of lymphatic endothelial cells, <10 nm NPs are mainly drained into blood vessels. In addition, the charge and lipophilicity can also contribute to the efficiency of entering the lymph. Through lymph transport, macromolecules, including antigens, could access the lymphoid organs and LNs for antigen presentation and immune stimulation. In addition, the self-antigens could also be transported to maintain the so-called autoimmune tolerance.[11]

6.2.3 Lymph nodes

The LNs are round or oval tissue bodies, usually <0.5 cm in size, with clear boundaries with the surrounding tissue. The LNs usually have some resilience, and the superficial LNs, including those in the neck, armpits, and groins, can be palpated easily. The main function of LN is to filter antigens and other substances in the lymph for antigen presentation. It also plays a crucial role in the maturation of lymphocytes. In addition, a group of special LNs called Peyer's patches also exist in the small intestine and are involved in the immune response. From the capillary lymphatics into the collective lymphatics, the lymph would be filtered by one to a few groups of LNs, with the first-draining LN called the sentinel LNs (SLNs). Due to its lymph filter function, LN could retain nanomaterials and serve as a good target for the delivery of nanomaterials to the lymphatic system. The whole LN tissues are greyish red and are wrapped in a dense layer of connective tissues called a lymphatic capsule. Generally, the LN is kidney-shaped and has one convex and one concave side (hilus). There are usually one to a few afferent lymphatics on the convex side of the LN and one to a few efferent lymphatics on the concave side.[13]

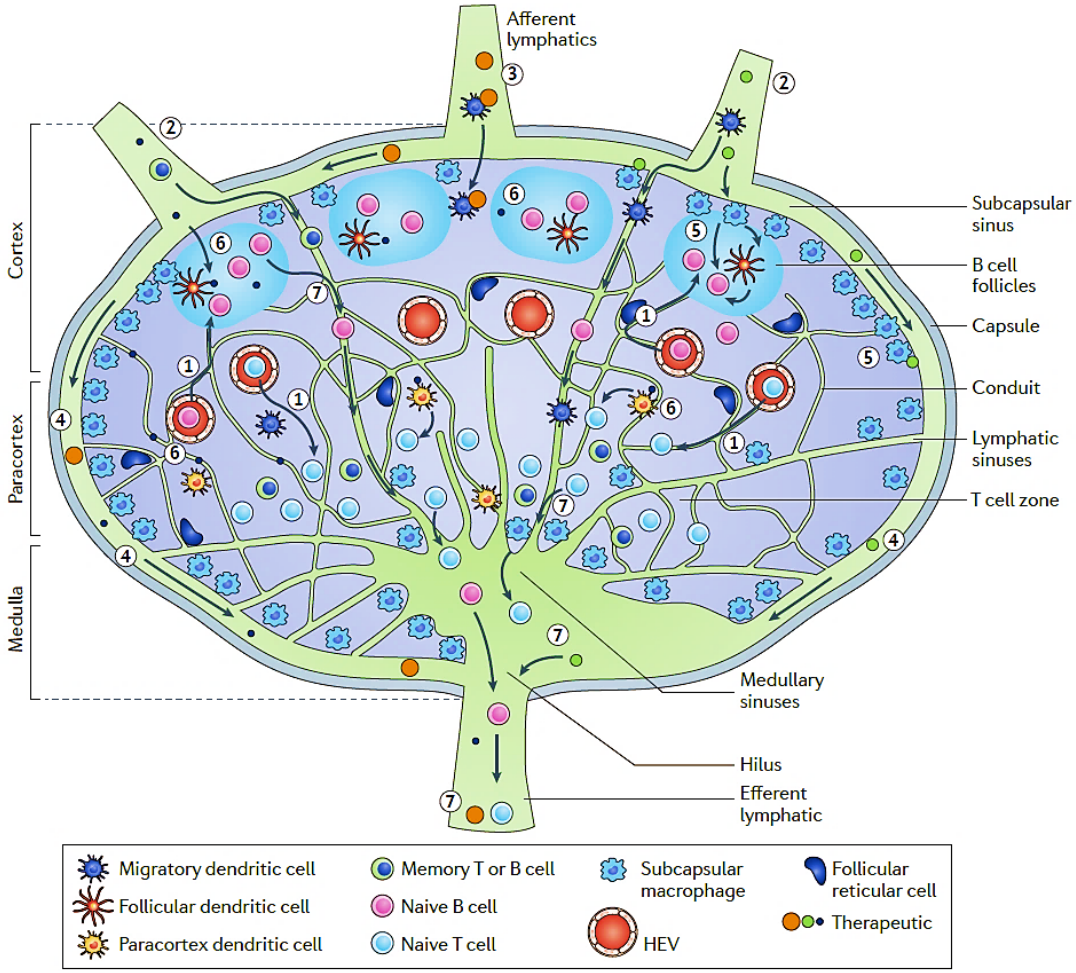

Figure 6.2.4 Schematic diagram showing the structure of the lymph node, the cells inside and their distribution.[16] (Copied from Nature Publishing Group)

From a cross-sectional view, the LN capsule extends inwardly, dividing the LN into multiple sections called lymphatic lobules, and each lobule is connected to one afferent lymphatic (**Figure 6.2.4**). These lobules with relatively big apex and slender cords are closely next to each other. The vessels within the LN, where the internal lymph flows, are called lymphatic sinuses, which surround the lobules.[14] The side of the lobule close to the afferent lymphatic vessels is separated from the lymphatic capsule by the subcapsular sinus, while the other side is connected to the hilus through vascular roots. According to the afferent to efferent lymphatics, LNs can be divided into three layers, namely the nodal cortex, paracortex, and medulla. There are many dense cell bodies distributed in the cortex, forming clusters of B lymphocytes called follicles. These

structures are normally separated by the interfollicular cortex. After receiving the stimuli of antigens, the B lymphocytes contact antigen-presenting dendritic cells directly, then undergo rapid differentiation and training, forming condensed cell clusters called germinal centres. The matured plasma cells then move to the medulla and participate in humoral immunity. In contrast, T lymphocytes travel to the interfollicular cortex and deeper paracortex regions to interact with antigen-presenting dendritic cells without forming similar structures as B lymphocytes.[15] The dendritic cells are generated from the bone marrow. They collect and process pathogens from the blood, then migrate to the peripheral lymphoid organs, and finally get into the paracortex region. They are highly efficient antigen-presenting cells to stimulate the T lymphocytes. In addition, the whole LN is supported by reticular meshwork. The reticular fibres form a system of miniature conduits or pipes that interconnect the sinus and the follicular region.

Other lymphoid organs will not be introduced here due to not being the focus of this study. Understanding the basic structures of the lymphatic system could help us to take advantage of its characteristics to select and modify materials to achieve the effective targeting of the lymphatic system and LNs.

6.3 Current imaging and mapping reagents of the lymphatic system and LNs

The lymphatic system is responsible for the immune defence of the human body, and many diseases can induce significant changes in LNs, like swelling of LNs and changes in texture or even lymphedema. Thus, the LN state is usually utilised to identify and stage diseases, including lymphedema, cancer, chronic inflammation, chylous ascites, and others.[17] In addition, due to the large endothelial cell gap and filtering effect, metastasis of tumours mainly starts with the first draining LNs and then spreads through the lymphatic system. Although palpation is an effective method for superficial LNs diagnosis, it is limited by the detection depth and accuracy. In addition, the

ultrasound LN examination is also limited by the depth of detection. Other invasive methods like lymphatic biopsy or surgical incision of the skin are also highly time-consuming and painful to patients. With the development of medical imaging techniques, the imaging-based examination has gradually become mainstream due to the advantages of non-invasiveness and convenience. Combining with other inspection methods, high accuracy diagnosis of lymphatic diseases and their causes could be achieved. In addition, the most important function of LN imaging is to provide guidance on lymphatic surgery. As lymphatic vessels and LNs are relatively transparent and difficult to see by the eye, preoperative and intraoperative imaging can allow the lesions to be visualised and resected (Figure 6.3.1).

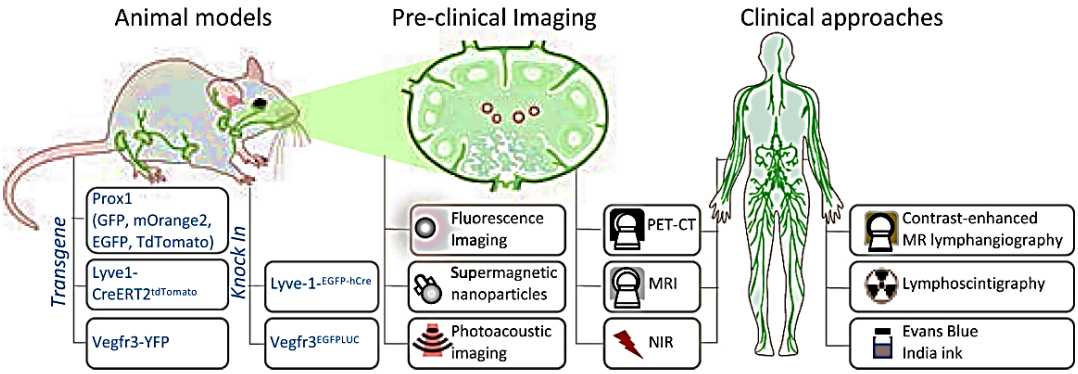

Figure 6.3.1 Commonly used targets and imaging methods in theranostics of LN-related diseases. [Prox1 = Prospero homeobox 1, Lyve1 = lymphatic vessel endothelial hyaluronan receptor 1, Vegfr3 = Vascular endothelial growth factor receptor 3, GFP = Green fluorescence protein, YFP = Yellow fluorescence protein, PET = positron emission tomography, CT = computed tomography, MRI = magnetic resonance imaging, NIR = Near-infrared imaging.][17] (Copied from Elsevier Publishing Group)

The lymphatic imaging techniques can be generally divided into two main categories, radiation-based and non-radiation-based. Here I will compare several lymphatic imaging modalities and find their pros and cons to inspire research on developing new lymphatic imaging materials.

6.3.1 Radiation-based methods

Radiation-based methods are widely used due to the development of radiology and imaging. One of the most ancient lymphatic imaging techniques is **X-ray lymphography**. Methylene blue (blue dye) solution (as the positioning reagent) is firstly injected into the interstitium between fingers or toes to help a rough visual mapping of draining LNs. Subsequently, canulating lipiodol (as the X-ray contrast reagent) in the lymphatic vessels can achieve the purpose of lymphatic imaging by enhancing the X-ray signal (**Figure 6.3.2**). The drawbacks of this method are also obvious. The injection or cannulation is painful and sometimes needs to operate under anaesthesia which is time-consuming.[18]

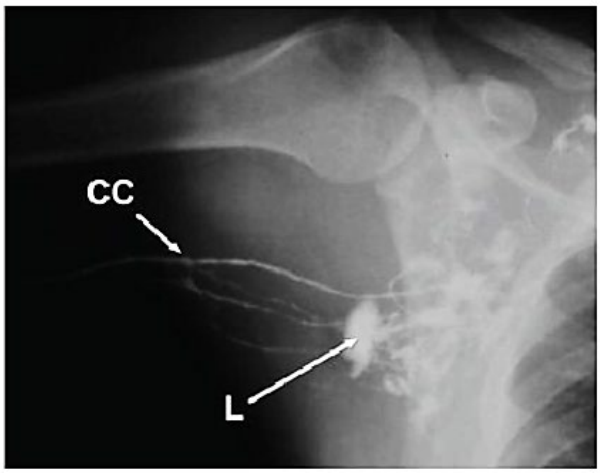

Figure 6.3.2 A typical X-ray lymphography image showing the afferent lymphatic vessels and corresponding LNs. [CC: collector, L: lymph node] [18] (Copied from Elsevier Publishing Group)

As a replacement for X-ray lymphography, **X-ray computer tomography** (CT) was applied for LN imaging. Different from providing a perspective view above, CT could get pictures of layered slices to make positioning more accurate. Thus, CT is therefore widely used for preoperative diagnosis, including spatiotemporal imaging of cancer. However, like X-ray imaging, contrast agents are required to enhance imaging quality. Normally, the contrast agents are water-soluble, high Z atom-containing compounds,

e.g., iodide salts, including sodium and lithium iodide.[19] The current iodide contrast agents are highly water-soluble small iodinated organic molecules, including iopamidol, ioversol, iohexol, and ioxaglate (**Figure 6.3.3**).[20] Although the imaging accuracy is greatly improved, this method still suffers from disadvantages such as injection pain and metabolic problems.

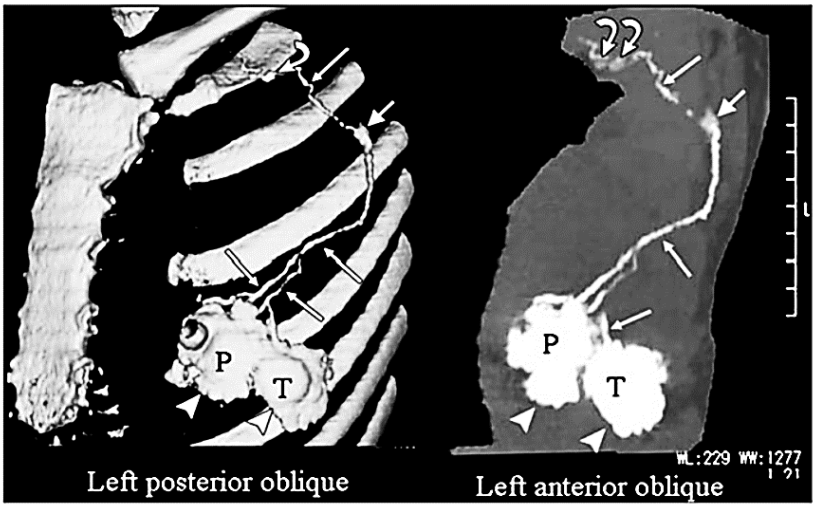

Figure 6.3.3 Typical CT image showing the metastasis of breast tumour through injection of iopamidol.[20] [P = periareolar area, T = tumour site] (Copied from Elsevier Publishing Group)

Lymphoscintigraphy is the most widely recognised method for lymphatic imaging. As a radiological imaging method, it uses a radioactive material that is preinjected into the lymphatic system rather than external radiation used by the former techniques. As a result, the penetration and imaging accuracy are enhanced.[3] Here, lymphatic-specific tracers labelled with Technetium-99 (*e.g.,* ^{99m}Tc-labeled dextran,^{99m}Tc-labeled human serum albumin, or ^{99m}Tc-labeled sulfur colloid) are injected into the interstitium, and subsequently detected from the emitted gamma radiations *in vivo*.[20] Images are acquired every 30 minutes for intraoperative localisation and monitoring of LNs (**Figure 6.3.4**). Lymphoscintigraphy is widely used in all types of abnormal lymphatic detection, including lymphatic function assessment, visualisation of dermal backflow, and SLN mapping. Despite these, its main disadvantage is the difficulty of acquiring detailed

images with high accuracy due to the projection imaging limitations. By combining lymphoscintigraphy with CT, the **single-photon emission computed tomography/CT (SPECT/CT)** could overcome the aforementioned problems where the gamma-ray detector in lymphoscintigraphy is replaced by a group of cameras at different angles. The tomographic reconstruction computer then processes these pictures to 3-D.[17] By combining the two methods, the imaging and localisation accuracy can be further improved for SPECT/CT imaging. However, some problems are still unavoidable, including the need for long-time ionising radiation that can cause health issues to both the patient and the surgeons, as well as the high cost and hence economic burden.[17]

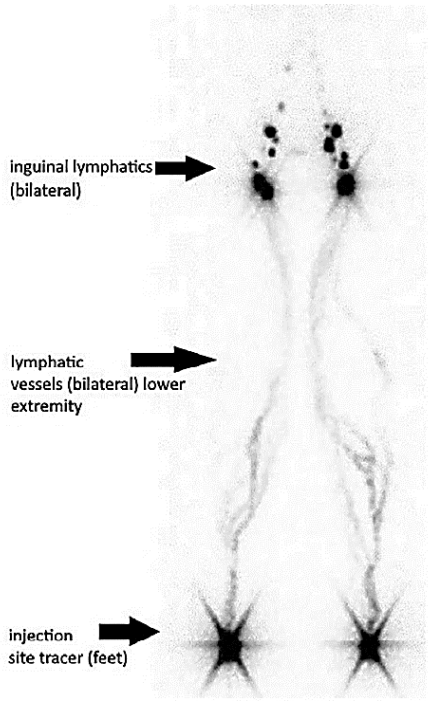

Figure 6.3.4 The typical lymphoscintigraphy image of human lower limbs.[3] (Copied from Wiley Publishing Group)

In general, one big concern for these methods is the effects of radiation on the human body. In addition, due to little difference in density between lymphoid tissue and surrounding tissues, contrast agents generally cannot be avoided to enhance the contrast of lymphoid tissues for better lymphatic imaging results.

6.3.2 Non-radiation-based methods

To avoid ionising radiation damage to the human body, many non-radiation-based techniques are introduced in the mapping of lymphatics and LNs. For example, the magnetic resolution imaging (MRI) technique is highly valued for non-invasive imaging of the lymphatic system. The mechanism of MRI is the excitation of low-energy nuclear spin: through applying a strong permanent magnetic field, the nuclei of protons (hydrogen atoms) experience an alignment in the direction of the magnetic field. Exciting the protons with a pulse of radio waves at the right frequency causes them to resonate and disrupt the magnetic alignment. The excited protons release the absorbed energy in the form of a radio frequency signal. By measuring the spin relaxation processes of protons to the original state (T1 longitudinal or T2 transverse decay), the signal could be converted to a series of volumetric figures. Different tissues with different chemical environments could then be distinguished by comparing the relaxation time and/or the T1/T2 ratio. With the development of magnetic resonance technology, magnetic resonance lymphography (MRL) has become low harm and convenient method for the characterisation of lymphatic system states.[20]

Figure 6.3.5 MRI scanning of rat hind limb with the presence and absence of contrast agents.[18] (Copied from Elsevier Publishing Group)

However, to enhance the signal-to-noise ratio and imaging quality, a contrast agent is essential. For example, Gadolinium-based contrast agents are the most used agents for enhancing the MRL signals (Figure 6.3.5). They are usually low-molecular weight Gd^{3+} complexes containing one water molecule in the inner coordination sphere, *e.g.,* gadolinium-diethylenetriamine pentaacetic acid (Gd-DTPA) or gadoterate meglumine (Gd-DOTA) complexes, or other Gd^{3+} containing polymers and macromolecules containing Gd^{3+}.[19] Ultra-small superparamagnetic particles of iron oxide (USPIO) are also applied as an MRL contrast agent.[17] One main drawback of MRL is the low selectivity of Gd-based contrast agents. To overcome this issue, the dynamic MRL is performed by firstly localising the LN position through ultrasonography. Then the Gd-based contrast agents are injected intranodally to improve the specificity and are normally used for duct observation.[18]

Another widely used non-radiation method is fluorescence mapping. By injecting fluorescent imaging agents (usually in the NIR region) into the interstitium, allowing them to accumulate within the lymphatic system or LN, and then applying a laser to excite these fluorescent agents, we can obtain high-contrast images of the condition of the lymphatic system. A widely used imaging agent for the NIR lymphography is indocyanine green (ICG), a small organic molecule (MW=776.98) with maximum excitation/emission wavelengths of 785/821 nm. It was approved by the FDA in 1959.[21] Due to its relatively high QY, the application concentration is only tens of μg per mL. In addition, through observing with a specific NIR coupled-charged detector (CCD, normally InGaAs detector) during the operation, the NIR images could be observed intraoperatively and provide continuous and live images of the region of interest (ROI). So far, fluorescent lymphography has been applied in many clinical scenarios, including venous lymphatic anastomosis to reduce lymphedema, organ transplant to visualise the lymph flow, and sentinel LN mapping.[18] However, it still suffers several limitations. These fluorophores are generally small organic molecules that are prone to

photobleaching, limiting their lifespan to less than 1 hour. Moreover, its poor hydrophilicity also causes a short half-life. All these necessitate repeated intraoperative injections.[22] In addition, due to the tissue scattering of both the excitation and emission light, the imaging depth is limited to only 20 mm maximum. The observation of fluorescence is highly dependent on the imaging equipment, which is not integrated into the machine, and it is very inconvenient for the surgeons. The prevalence rate of the NIR observation equipment is also quite low. Thus, the fluorescent imaging of the lymphatic system is still limited to specialised hospital settings (Figure 6.3.6).

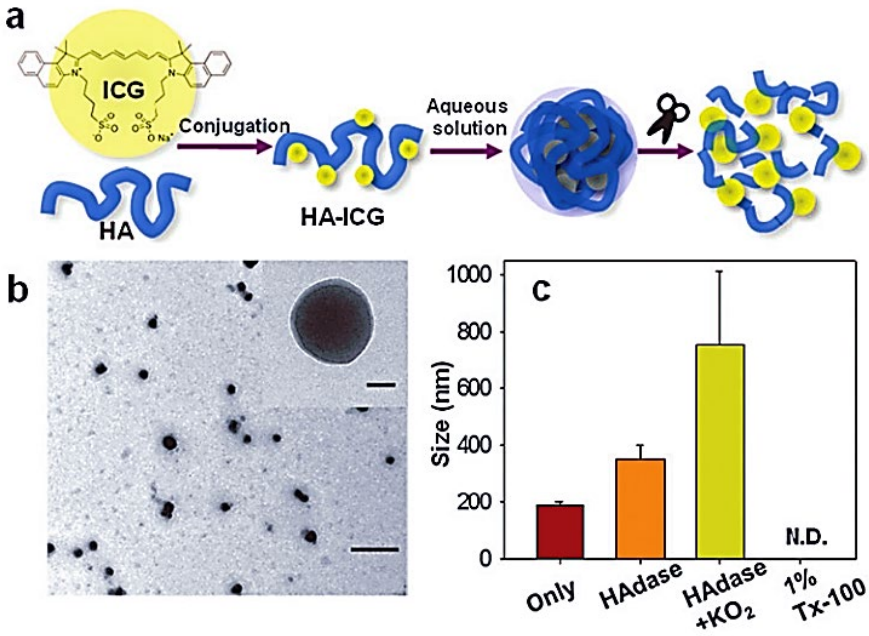

Figure 6.3.6 Considering the disadvantages of a single application of ICG, using hyaluronic acid NPs to encapsulate ICG to enhance its selectivity and photostability was reported.[23] (Copied from RSC Publishing Group)

To avoid these problems, applying nanomaterial to increase the bioavailability of ICG, for example, increasing its *in vivo* half-life or increasing its QY, is an attractive strategy. Kraft et al. applied the liposome [1,2-distearoyl-sn-glycero-3-phosphocholine (DSPC) & 1,2-distearoyl-sn-glycero-3-phosphoethanolamine-N-methoxy-polyethylene glycol-2000 (DSPEmPEG2000)] to encapsulate free ICG to overcome the problems of aqueous instability, aggregation, and easy degradation. They found that encapsulation

significantly altered its pharmacokinetic behaviour *in vivo*. After optimisation, they achieved a higher fluorescence intensity and resolution, as well as more robust fluorescence against the photobleaching than free ICG. As the free ICG has a high affinity to plasma proteins (albumin or lipoproteins etc.) which causes waste, this liposomal ICG has achieved a higher accumulation in the LNs (**Figure 6.3.7**).[24] Coincidentally, Proulx et al. also used another liposomal formulation, [1,2-Oleoyl-sn-glycero-3-phosphocholine (DOPC) and 1,2-distearoyl-sn-glycero-3-phosphoethanolamine-N-[methoxy(polyethylene glycol)-2000] (PEG-DSPE)], to encapsulate the free ICG and achieved a high solubility and fluorescence signal. This material was then used for the quantitative studies of lymphatic function, providing a handy tool for the diagnosis of LN status.[25]

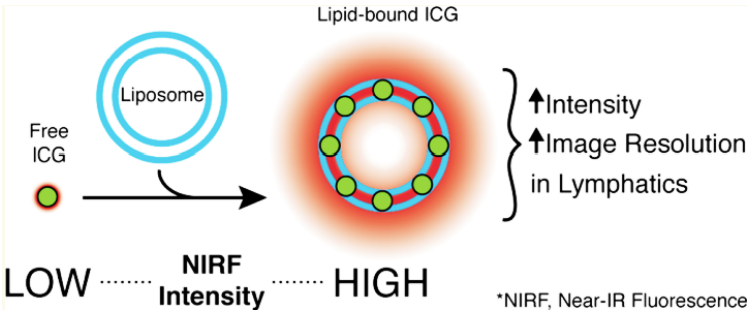

Figure 6.3.7 Schematic of the synthesis route of ICG-doped liposome. The incorporation of ICG molecules with liposomes could grant ICG many advantages, including enhanced fluorescence intensity, higher stability, and deeper imaging depth compared with free ICG.[24] (Copied from ACS Publishing Group)

To develop efficient and inexpensive real-time lymphatic imaging agents for surgical guidance and LN diagnosis, several other nanomaterials are applied.[8] These include **NIR fluorescent quantum dots (QDs)**, which have been applied to imaging living organisms since 2003 and are increasingly used for fluorescence imaging in the NIR region.[26] QDs are colloidal fluorescent semiconductive nanocrystals, where absorption of high-energy photon results in the creation of an electron-hole pair. Thus, QDs have a wide absorption range and higher absorption for high-energy parts of the spectrum, which is

different from small organic dyes. In addition, due to the quantum effects and discrete energy levels, the emission spectrum is strongly dependent on the QD size. Compared with small organic dyes like ICG, QDs often display significantly higher fluorescence QYs, *in vivo* fluorescence stability, and a longer fluorescence lifetime.[27] To further increase the fluorescence QY and prevent surface oxidation, a protected shell of a few atomic layers of a material with a larger band gap is often coated on top of the fluorescent core. As a result, the QY of QDs could be increased to ~100% with greatly enhanced stability. However, biosafety remains to be a major problem for QDs in biomedical research, despite already being used in areas such as tumour detection and LN mapping. In 2003, Kim et al. firstly applied a NIR fluorescent type II QD for the LN mapping of Yorkshire pig. This CdTe(CdSe) core(shell) QD was further coated with a polydentate phosphine coating for the increase in hydrophilicity and biocompatibility. The 15–20-nm QD has a peak emission at ~840 nm in the NIR region, allowing for a maximum tissue penetration of ~1 cm. Intradermal injection of the QD solution into the pig thigh could offer a real-time fluorescence image to help locate the SLN and guide the removal of the LN. The laser power required was relatively low, at only 5 mW/cm^2 and hence safe to use.[28] In addition, Erogbogbo et al. applied Si QDs coated with butenoic acid or a series of di-stearoyl phosphatidylethanolamine (DSPE)-PEG_{2000} ligands with emission at 700–800 nm for the SLN mapping and tumour targeting. Through subcutaneously injecting the QDs into the paw of a mouse, the strong NIR fluorescence was observed in the SLN of mice, allowing for successful identification of at least two LNs (**Figure 6.3.8**).[29]

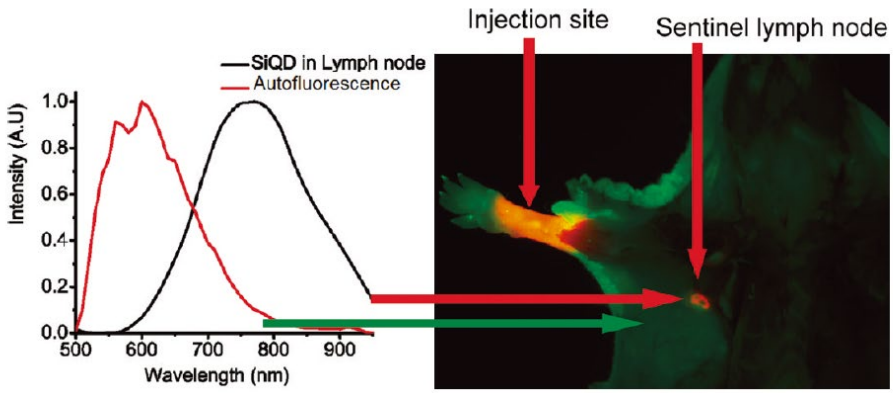

Figure 6.3.8 NIR QDs for SLN imaging. (Left: comparison of the emission spectra of NIR QDs in LNs with the tissue autofluorescence; right: NIR fluorescent image of the SLN imaging with footpad injection of NIR QDs).[29] (Copied from ACS Publishing Group)

In addition, Ballou et al. used 655-nm emitting ZnS-CdSe and 800-nm emitting ZnS-CdSe-CdTe shell-core QDs functionalised with terminal methoxy, carboxy, or amino groups to study the influence of terminal charge on the SLN imaging property. They found that intratumourally injected QDs with different terminal groups were drained directly to the adjacent lymphatics and LNs. Thus, the terminal charged groups have little or no effect on drainage to surrounding LNs.[30] Although using QDs for lymphography has huge advantages, the concerns of biosafety, reproducibility, and reliability have caused a big problem in clinical applications. Notably, most of such QDs contain toxic elements, including Cd or Te, which is the main cause of their *in vivo* safety concern.[26]

Recently, **upconverting nanoparticles (UCNPs)** are also being developed for bioimaging. UCNPs are a group of inorganic crystalline nanomaterials than can convert long-wavelength excitations (normally NIR region) into short-wavelength emissions. The mechanism is the sequential absorption of two or more low-energy photons to excite an electron to a high-energy state, which subsequently relaxes to the ground state and releases a higher-energy photon to achieve the anti-Stokes shift. A typical example of UCNPs includes a $NaYF_4$ nanocrystal matrix containing a combination of upconverting

sensitiser (*e.g.,* Yb^{3+}) and activator (*e.g.,* Eb^{3+} and Tm^{3+}).[31] Due to the excitation light being normally in the NIR region, UCNP imaging can offer deep tissue penetration with reduced scattering. Xia et al. reported dual-modality imaging of LN mapping for small animals. A NIR-to-NIR upconversion $NaYF_4:Yb^{3+},Tm^{3+}@Fe_xO_y$ nanocrystal (core@shell) emits at 800 nm upon excitation at 980 nm. At the same time, the iron oxide nanoshell offers T2-enhanced MR imaging. By combining two imaging modalities, LN localisation, real-time imaging of LNs, and surgical guidance in mice were achieved (**Figure 6.3.9**).[32] Qiu et al. in 2018 also reported the detection of LN metastasis by using a PEGylated $NaGdF_4:Yb,Tm,Ca@NaLuF_4$ core@shell NPs modified with an anti-HER2 monoclonal antibody. The probe could provide targeted imaging (*via* its 804 nm emission) of HER2-positive tumour cells in the popliteal LN metastasis model through intravenous injection. In addition, linking with the antibody also changed its pharmacokinetics *in vivo* and significantly prolonged its half-life in the plasma.[33]

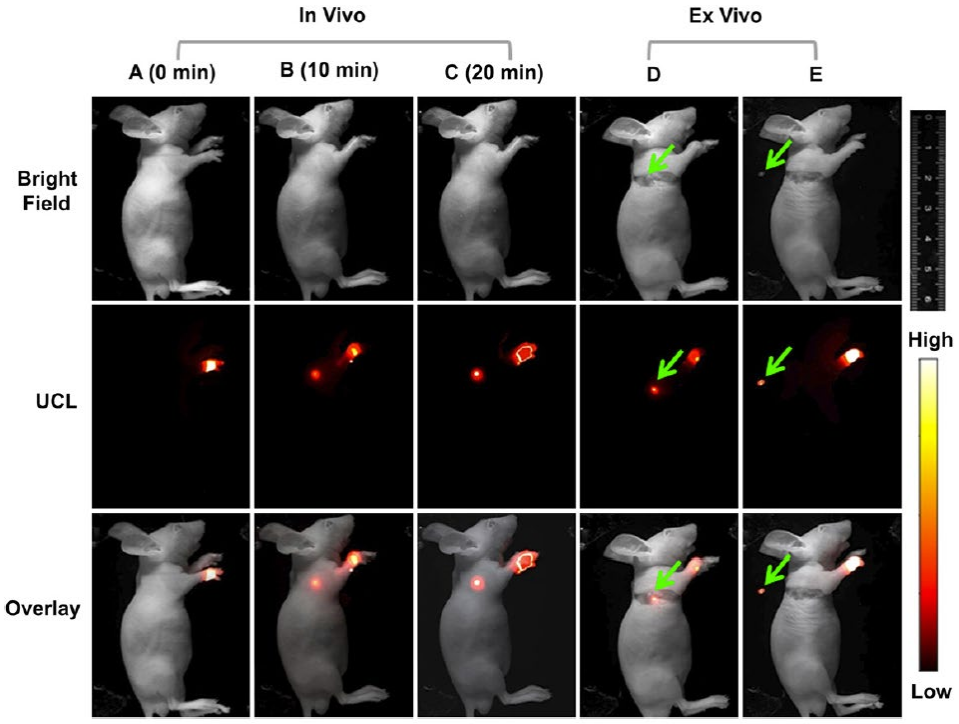

Figure 6.3.9 The combination of NIR imaging and MRI for the dual-modality imaging of mice.[32] (Copied from Elsevier Publishing Group)

Other novel NIR fluorescence small molecules have also been used to synthesise fluorescent nanoprobes.[34] However, due to aromatic structures with moderate hydrophobicity, these molecules tend to aggregate under *in vivo* conditions, leading to significantly quenched fluorescence which can adversely affect their potential applications *in vivo*. This phenomenon is called aggregation-caused quenching (ACQ). However, with the in-depth study of fluorophores, a group of different fluorophores that have opposite properties have been discovered. In 2001, the concept of aggregation-induced emission (AIE) was proposed by Tang et al. to describe a phenomenon where some weakly fluorescent molecules could display significantly enhanced fluorescence upon aggregation upon exposure to poor solvents. This phenomenon is specifically found in molecules with the tetraphenyl ethylene (TPE) basic structure. Many mechanistic explanations for AIE have been proposed, and the most widely accepted one is the restriction of intramolecular motions (rotation, vibration, etc.) that blocks the nonradiative transition pathways, leading to enhanced radiative emission.[35] AIE has served as a strategy for preparing fluorescent NP-based probes for lymphatic system mapping (Figure 6.3.10).

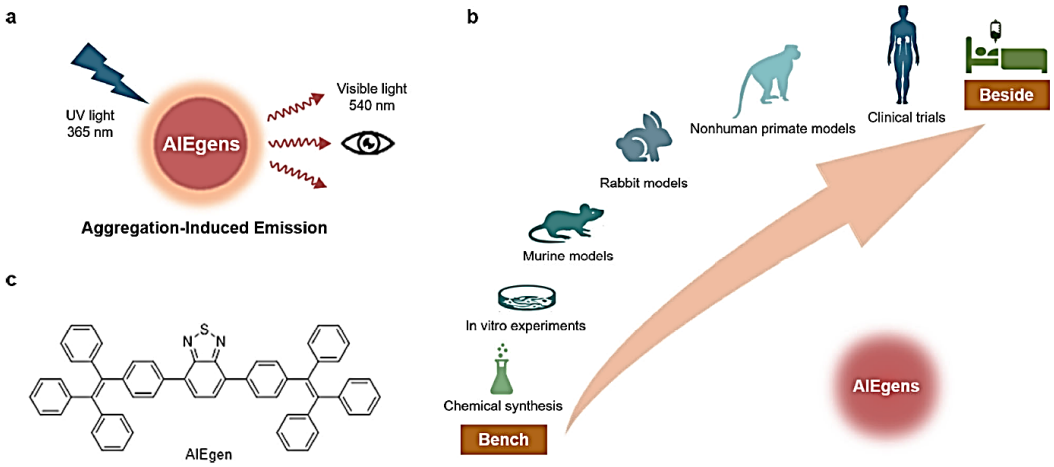

Figure 6.3.10 AIE imaging of LN surgical resection in primates.[36] (Copied from Nature Publishing Group)

Zhong et al. reported the AIEgen-aided imaging-guided surgery in high-ranking

mammals like *rhesus macaque*. AIEgen, a symmetric TPE structure further functionalised with DSPE-PEG_{2000}-folic acid molecules, was used for SLN mapping and imaging-guided surgical removal. The AIEgen had an overall hydrodynamic size of ~20 nm and emitted brightly in the visible range (~540 nm, under UV irradiation), so the surgery could be operated on without the aid of NIR devices. Starting with murine and rabbit models and finally translating to the non-human primate model, the authors have proved the effectiveness of this probe in all kinds of mammalian animals, making it a step closer to application in humans. Moreover, due to the targeting ability of folic acid, this AIEgen probe can be used to observe invisible cancer metastases with a high selectivity relative to normal tissues.[36] However, restricted by the imaging depth, this AIEgen probe can only be used as surgical guidance for superficial LNs. Zhang et al. used another AIEgen based on TPE structure (DPA-TPE-DCM) for the detection of tongue squamous cell carcinoma and subsequent SLN mapping. After PEGylation, the whole particle size was ~127 nm and gave off bright emission at the NIR range (~700 nm) and provided a high signal-to-background ratio of 10.2. After intravenous injection, this AIEgen probe could target the orthotopic tongue squamous cell carcinoma in tumour-bearing mice. The fluorescence in the lesion was significantly higher than in control and could guide the resection of the tumour cells (**Figure 6.3.11**).[37]

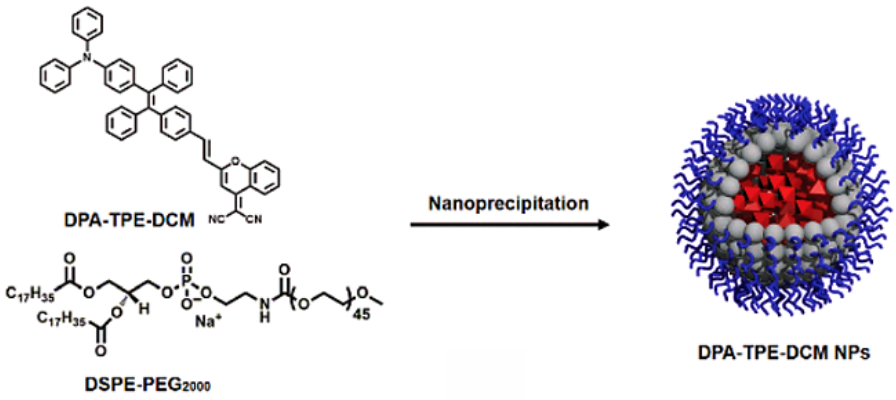

Figure 6.3.11 Development of AIE fluorophore based on the TPE structure. Through co-precipitation with PEGylated phospholipid molecules, the NP displayed good water solubility and tumour accumulation properties, suitable for imaging lymphoid

tumours.[37] (Copied from RSC Publishing Group)

With the development of the NIR fluorescent GNCs, more and more GNC-based nanomaterials are now finding applications in bioimaging and NIR theranostics. The development of GNC-based probes will be introduced in the subsequent sections.

6.4 Nanomaterials for lymphatic system delivery and mapping

To effectively target the lymphatic system, the probe's size, shape, hydrophilicity, and charge must be adjusted to avoid vasculature permeability or retention in the reticuloendothelial system and to increase the uptake by the lymphatic system. Linking targeted molecules for phagocytes or other antigen-presenting cells in peripheral tissues or the LNs could increase access to these components and thus enhance the targeting ability of the lymphatic system (Figure 6.4.1).

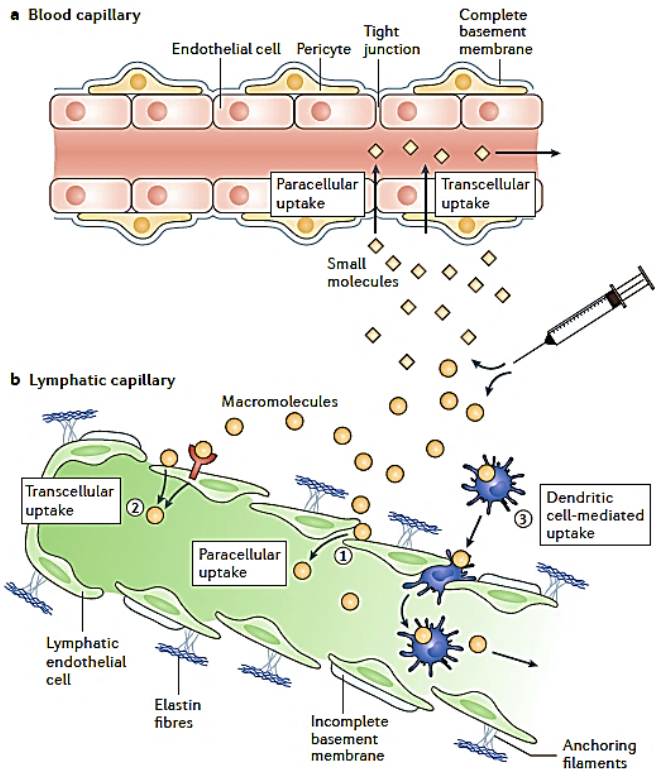

Figure 6.4.1 Pathways of nanomaterials engineered to specifically accumulate in lymphatic vessels. 1) The NPs could be taken up through paracellular pathways, 2) transcellular uptake or 3) immune cell-mediated uptake.[16] (Copied from Nature

Publishing Group)

6.4.1 Nanomaterial size

First, size is one of the most important parameters for lymphatic targeting. Since there is no powerful pumping organ like the heart to provide forward momentum for lymph flow, the flow of lymph depends only on the peristalsis generated by the sequential contraction of lymphatic vessels, and so its flow rate is 100-500 times slower than the blood flow. Thus, small molecules (D_h (hydration diameter) <5 nm or MW <20 kDa) would easily enter blood vessels through the gap of vascular endothelial cells.[18] As the size increases, the proportion of probes entering the blood vessels decreases rapidly, while the proportion entering the lymphatic system gradually increases. However, if the particle size is bigger than the lymphatic endothelial cell gap (normally <500 nm), then the material will likely be trapped in the interstitium and cannot get into the lymphatic system. In addition, for parenteral applications, the interstitium is filled with a large amount of glycosaminoglycan matrix as well as the conduits of water channels. These form a sieve-like structure called the extracellular matrix, with pores of ~100 nm. Any materials that are greater than this size will meet strong obstructions, making it difficult to pass through such gaps. Therefore, nanomaterials with 10 to 100 nm (for proteins, MW >~30 kDa) have optimal accessibility to the lymphatic system (Figure 6.4.2).[38]

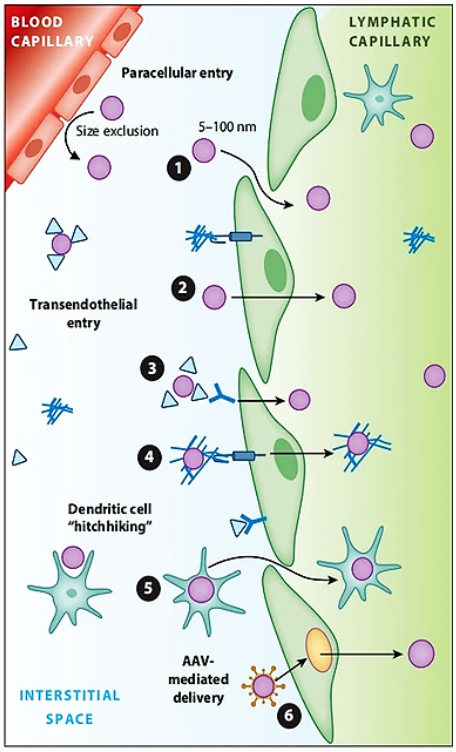

Figure 6.4.2 The cell gap between lymphatic endothelial cells is significantly larger than the vascular endothelial cells, allowing NPs with sizes ranging from 5–100 nm (10–100 nm optimal) to enter the lymphatics.[8] (Copied from BMC Publishing Group)

In addition to passive distribution, the process of crossing lymphatic endothelial cells can also be achieved *via* active transportation. However, the NP size requirement here can vary on the body part as well as the treatment needs. Yang et al. reported the size influence on the LN accessibility and mapping with perylene diimide NPs. NPs of 30, 60, 100 and 200 nm were labelled with [^{64}Cu] as a triple diagnosis and treatment platform offering positron emission tomography, photoacoustic imaging, and photothermal therapy. They observed that the 100-nm NP was the most suitable for LN mapping as its operating time window was suitable for differentiating different LNs. While the 60-nm NP was most suitable for tumour imaging and treatment due to the maximum tumour accumulation efficiency.[39] Zhang et al. reported the influence of size on the NP entry into the lymphatic follicle regions using ovalbumin-conjugated GNPs (OVA-GNPs) ranging from 5 to 100 nm. They found that the follicular dendritic cells, the follicular site-specialised antigen-presenting cells, could quickly remove small-OVA-GNPs (5–15

nm) but retain large OVA-GNPs (50-100 nm) for up to 5 weeks. Thus, the follicular targeting abilities of 50–100-nm OVA-GNPs, including antigen delivery, humoral immune response, antibody production and other aspects, were significantly higher than their smaller-sized counterparts (Figure 6.4.3).[40]

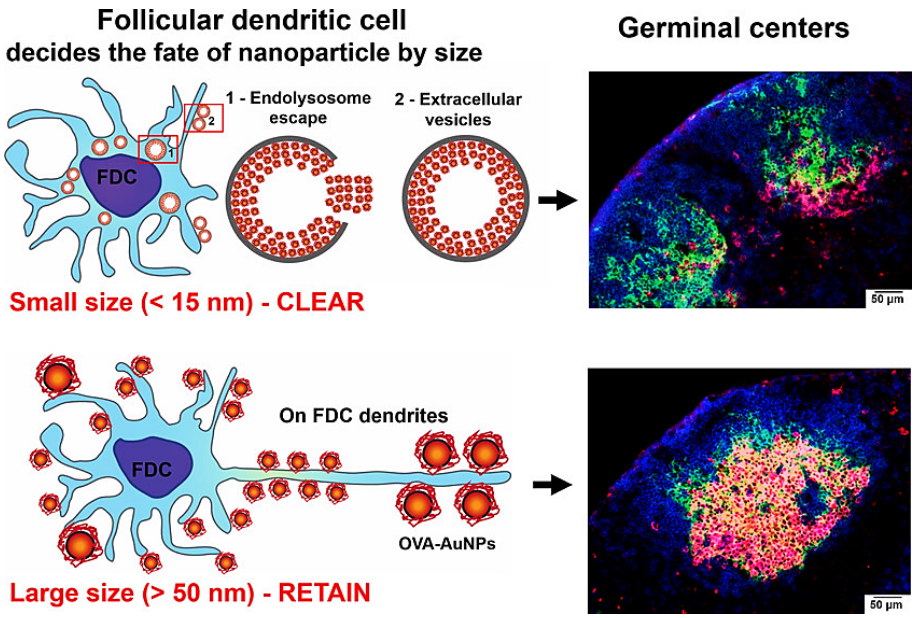

Figure 6.4.3 Compared with small OVA-GNPs with particle diameters lower than 15 nm, the over 50-nm GNPs tend to be trapped in the LNs and are difficult to drain out of the LNs.[40] (Copied from ACS Publishing Group)

Nakamura et al. used the microfluidic platform to prepare a series of pH-sensitive lipid nanoparticles (LNPs) and measured the size (30/100/200 nm) as well as charge (+/–/neutral) influence on their abilities to target the lymphatic system. They found that the 30-nm LNPs were effectively located in the LNs and taken up by the dendritic cells. While for bigger-sized LNPs, this phenomenon was not obvious.[41] Rohner et al. used polystyrene particles and dextran molecules of varied sizes to measure the influence of probe size and rigidity on the LN targeting ability. They found that the accumulation behaviours of macromolecules and polymer particles in the LNs were starkly different. For the dextran, the optimal size was ~30 nm, while for polystyrene spheres, their LN accumulation showed a positive correlation with size.[42]

6.4.2 Nanomaterial shape

The shape of materials also plays a critical role in controlling their lymphatic system entering, although research into this effect is still limited. It is commonly believed that non-spherical NPs impede flow more severely than spherical ones, making it more difficult to pass through lymphatic vessels. Besides, the NP shape can also affect their phagocytic uptake by phagocytes like dendritic cells.[43] Mammadov et al. studied the immunostimulatory ability of rod- and sphere-shaped self-assembled peptides as nano-vaccines. The rod shape structures exhibited a significantly stronger stimulation of the immune processes against intracellular pathogens (*e.g.,* viruses) than the spherical ones and the antigen alone, demonstrating a high uptake or stimulatory efficiency of the rod-shaped stimuli by the dendritic cells. The immune response of rod-shaped nanostructure was >10 fold higher than that of the antigen alone, demonstrating that the dendritic cell phagocytosis and the immune response were selective for rod-shaped materials (**Figure 6.4.4**).[44]

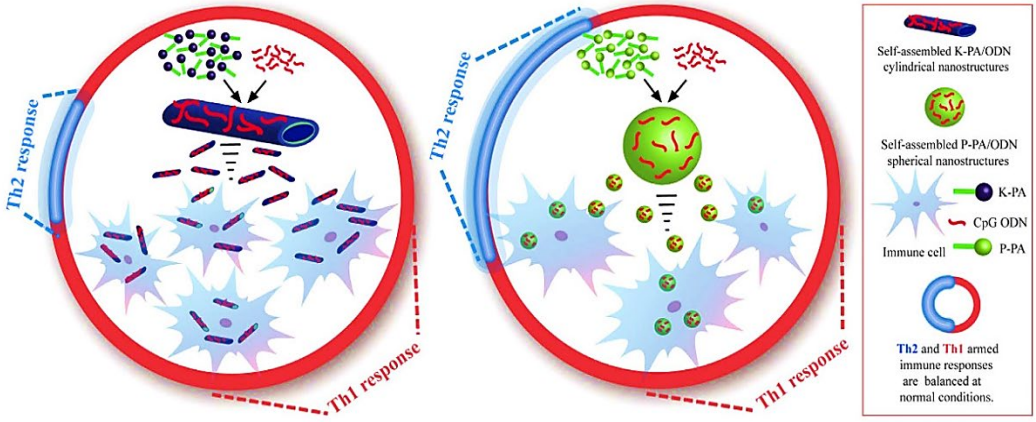

Figure 6.4.4 Comparison of the influence of the shape of the NPs on their internalisation in immune cells. The rod-shaped NPs accumulated more in LN immune cells and have a higher impact on the immune response.[44] (Copied from Nature Publishing Group)

In addition, Agarwal et al. found that a specific nanostructure—nanodiscs, had a higher internalisation rate than nanorods. They used PEG diacrylate-based hydrogel NPs of

varied sizes and shapes (nanorod & nanodisc) for the internalisation tests of mouse bone marrow-derived dendritic cells (BMDCs). The internalisation of nanodisc-shaped hydrogel, especially large- or intermediate-sized ones (with sizes as 325 × 100 nm and 220 × 100 nm [diameter × height]), was significantly higher than the nanorods. Besides, they proposed that conditions such as sedimentation, membrane deformation, surface contact area, and strain energy of membrane deformation are the key parameters that determine this shape selectivity (Figure 6.4.5).[45]

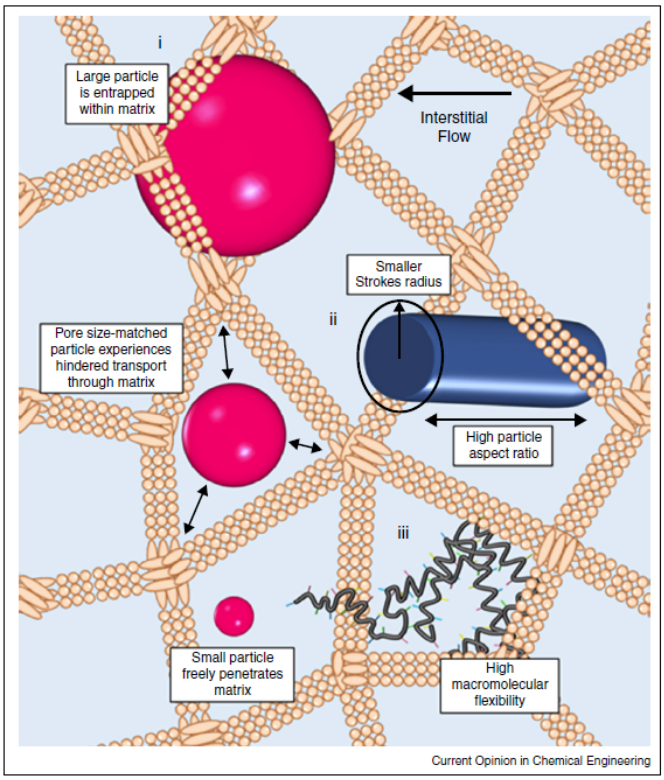

Figure 6.4.5 Size and shape design of nanomaterials that could penetrate the interstitial space. Both size and shape of NPs are important parameters for material design.[38] (Copied from Elsevier Publishing Group)

6.4.3 Nanomaterial charge

The surface charge of NPs also has a significant influence on their localisation in the lymphatic system. Mammalian cell membrane normally carries anionic charges. Nanomaterials with cationic charges thus exhibit strong interactions with cell

membranes that can boost internalisation. However, the interstitium is filled with negatively charged glycosaminoglycans, such as hyaluronic acid (the main component).[18] Therefore, after intramuscular injection, cationic NPs are often adsorbed onto the negatively charged extracellular matrixes and cannot easily enter the lymphatic vessels, while anionic NPs can pass through the interstitial space quickly due to electrostatic repulsion. Besides, the charge density on nanomaterials is important for their stability and interactions with the biological media. Those carrying high surface charges can form strong protein coronas *via* electrostatic attractions, leading to significant changes in size and the ability that may modulate the immune response. In contrast, those carrying low surface charges may aggregate easily due to weak electrostatic stabilisation. Qualitatively speaking, nanomaterials with anionic charges can benefit trans-vascular transport, while those with neutral charges can prolong circulation times.[38] Therefore, the design of effective lymphatic targeting materials needs careful consideration. For example, Nakamura et al. studied the LN targeting ability of differently charged LNPs of ~30 nm in size. After subcutaneous injection, the negatively charged LNP showed a significantly higher ratio (*e.g.,* 23% *vs* 12% or 5% for the neutral or positive LNP) in the LN region, indicating that a negative charge is beneficial for LNs transmission. Besides, the negatively charged LNPs were successfully transported to the T cell-rich paracortex regions.[41]

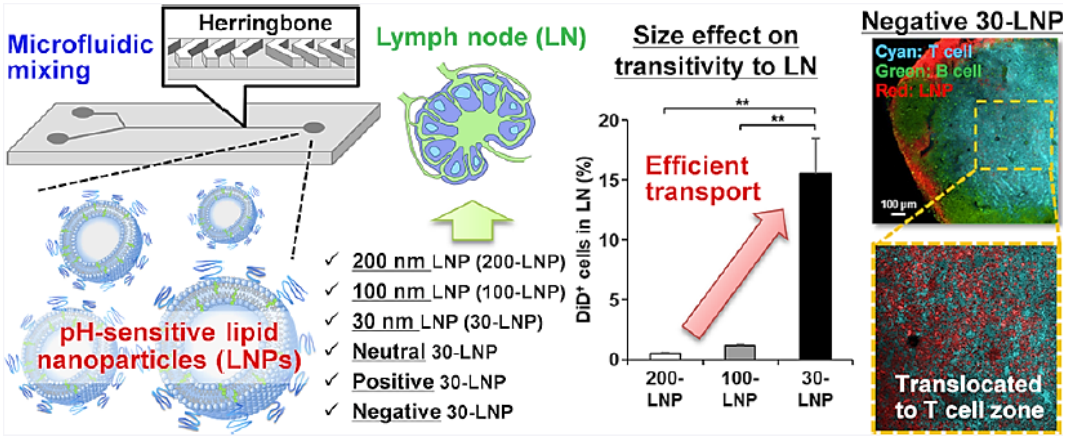

Figure 6.4.6 Compared with large LNPs with 100- or 200-nm diameter, small-sized LNP

(30 nm) has a higher transporting efficiency into the LNs. In addition, the negative charge of LNP further increased the translocation of LNPs into the T cell clustering area.[41] (Copied from ACS Publishing Group)

Fromen et al. reported the surface charge impact on the distribution of ovalbumin (OVA)-functionalised nanohydrogels in the lung lymphatic system. After pulmonary instillation, both the positively and negatively charged nanohydrogels reached the pulmonary draining LNs. The lung dendritic cells demonstrated a high uptake for positively charged hydrogels and increased the expression of chemo-attractants, causing the recruitment of more dendritic cells to the region. While for negatively charged ones, the immune response was significantly reduced.[46] Unfortunately, there were no studies on how the probe surface charge densities affect their lymphatic targeting properties. By varying the surface negatively-charged ligands and the negative to neutral ligand ratios, GNCs carrying a systematically varying negative charge were prepared, and their lymphatic targeting properties were studied and presented in Chapter 7.

6.4.4 Nanomaterial hydrophilicity

Finally, due to the influence of the extracellular matrix, NPs usually move through the interstitium space through the water channels in between the blood capillary and the lymphatic capillary. Thus, hydrophilic NPs move through the interstitium space more effectively than hydrophobic NPs.[47] McCright et al. studied the use of densely PEGylated and nearly charged-neutral polystyrene (PS) NPs to locate the lymphatic system and LNs. Both 40-nm and 100-nm NPs with high densities of PEG graft could pass through the lymphatic endothelial cell layer and enter the LN. Compared with unPEGylated NPs, the LN-targeting efficiency of PEGylated ones was increased 68 folds for 40-nm PS NPs. The PEG density was found to be important for the NP's lymphatic system targeting ability. Halving the PEG grafting density reduced its lymphatic targeting performance by 50%. They also proved that this material was transported *via*

both the micropinocytosis and paracellular transport mechanisms, providing a new idea for lymphatic targeting materials (Figure 6.4.7).[48]

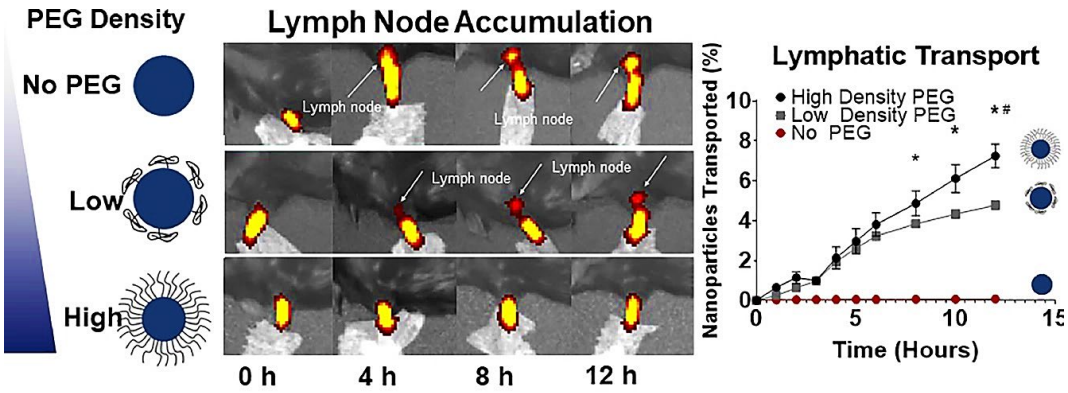

Figure 6.4.7 The Influence of hydrophilic layer density (PEG density) on lymphatic enrichment of materials, with the NPs with the highest PEG density transported more to the LNs.[48] (Copied from Elsevier Publishing Group)

The characteristics of the lymphatic system and the requirements of lymphatic targeting summarised above could provide useful guidance toward the development of effective lymphatic targeting nanomaterials.

6.5 GNP and GNC for lymphatic system theranostics

Gold nanomaterials have been widely used in imaging and drug delivery in different biomedical areas. Typical lymphatic system imaging methods include X-ray and CT for tissue imaging using ionising radiation. Lymphoscintigraphy, positron emission computed tomography (PET), and SPECT with *in vivo* radiation monitoring using radionuclides. Other imaging methods include MRI, PA imaging, photothermography, and fluorescence imaging. The properties of GNPs and GNCs can be perfectly combined with the above imaging methods. The inert nature of gold nanomaterials makes them less toxic and more stable *in vivo* than QDs and other NPs, making them suitable for the delivery of various imaging probes. The high atomic number (high Z atomic) of Au can enhance the scattering of X-rays, therefore increasing the contrast. Although the GNP does not fluoresce, its strong SPR absorption can facilitate photothermal and

photoacoustic (PA) properties for imaging applications. While for GNCs, their newly discovered NIR excitation and emission properties could enable a highly stable, deep penetration and efficient real-time imaging for surgical guidance (Figure 6.5.1).[49]

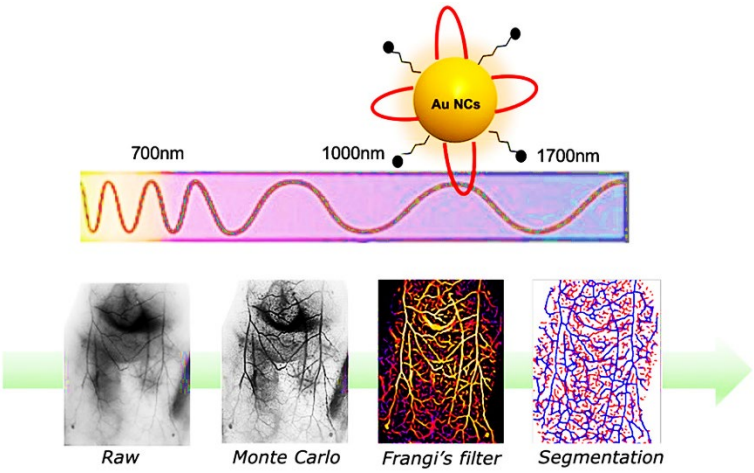

Figure 6.5.1 Applying NIR fluorescence GNC as the imaging probe for blood vessels and lymphatics imaging.[50] (Copied from ACS Publishing Group)

In addition, the enhanced magnetic effect of quantisation GNCs can be used for NMR detection after combining with other magnetic materials. In the following section, I am going to introduce the application of GNPs in the imaging of the lymphatic system, with or without treatment functions. In addition, due to the lack of research in GNC-based lymphatic imaging, I will summarise its prospects.

6.5.1 Functionalised GNP as lymphatic mapping reagents

6.5.1.1 GNP as a CT contrast agent

The detection and image reconstruction of the lymphatic system using CT is a common clinical method. However, due to the low contrast of the lymphoid tissue with surrounding tissues, normally, high-Z element atoms are used to increase the signal-to-background ratio as well as the resolution. As introduced previously, various hypotonic or isotonic iodine-containing contrast agents are used clinically. However, these agents

have several disadvantages, including a short half-life *in vivo*, the possibility of causing allergies, and toxicity to the urinary system.[51] Compared with iodine, the difference in X-ray attenuation between gold (Z = 79) and iodine (Z = 53) becomes significant in the high-energy X-ray region. In addition, the X-ray attenuation of gold is not influenced by the aqueous environment.[51] Thus, gold nanomaterials are attractive alternatives to iodine compounds. GNPs with different biocompatible surface capping were widely applied for lymphatic system X-ray and CT imaging. For instance, Shi et al. applied the G5 PAMAM-mPEG$_{20}$ dendrimer entrapped GNPs for the CT imaging of cervical SLN on the rabbit. The effect was compared with carbon NP mixed with Omnipaque (iohexol). They found this GNP-dendrimer complex had much longer accumulation (72 h vs 15 min) and enhanced Hounsfield units (~230 HU vs ~140 HU) over the conventional method.[52] Another branched polymer, the thiolated polyethyleneimine (PEI), was applied for the coating of GNPs for the imaging of the popliteal LN in the footpad injection model. Compared with a commercial contrast agent (Omnipaque), this ~5 nm GNP complex increased the *in vivo* half-life to 7.8 h with good biocompatibility (**Figure 6.5.2**).[53]

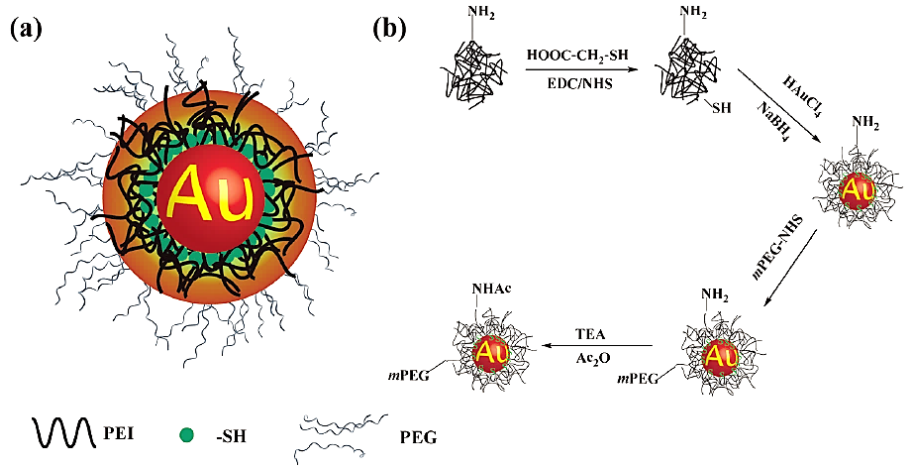

Figure 6.5.2 Synthetic routes of the PEI-PEG-capped GNP. The GNP could be applied for the *in vivo* CT imaging as the contrast reagent.[53] (Copied from RSC Publishing Group)

In addition to polymers, Uthaman et al. applied the mannan for the reduction of M-

GNPs (~9 nm) and subsequent LN CT imaging. This M-GNP shows a high X-ray attenuation of >300 HU and good concentration dependence. Due to the ability of mannan to target antigen-presenting cells, this GNP was internalised through endocytosis and accumulated in the LNs, causing good CT lymphography ability.[54]

6.5.1.2 GNP as a carrier of the radionuclides for ionizing radiation detection

Lymphoscintigraphy is the gold standard for LN imaging and diagnosis. However, due to the short half-life of the radionuclides in blood, they are normally linked with human serum albumin or dextran.[20] As a good carrier, the GNP could significantly alter the *in vivo* pharmacokinetics of the capping molecules. Thus, the radionuclide(^{99m}Tc) could be decorated onto the GNPs for a series of LN detection with ionising radiation emission *in vivo*. Mariquez et al. used the ^{99m}Tc and mannose-labelled GNPs (^{99m}Tc-AuNPs-MAN) for the SPECT/CT imaging of SLN detection. Through tracking the signal, labelling with ^{99m}Tc had no effect on GNP's preferential accumulation within the LNs and behaved like a commercial ^{99m}Tc-Sulfur colloid. They have proved this radiolabeled GNP can serve as the substitute for commercial SPECT/CT reagent.[55]

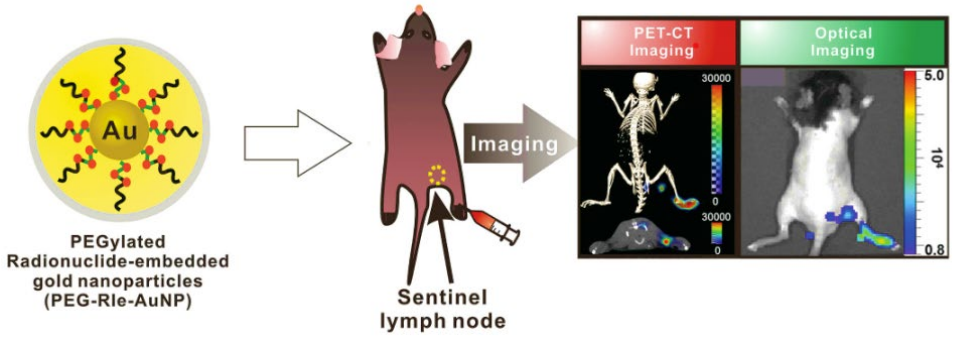

Figure 6.5.3 Synthesis mechanism of radionuclide-embedded PEGylated GNPs for PET-CT and fluorescence SLN imaging.[56] (Copied from Wiley Publishing Group)

Moreover, Lee et al. proposed a novel combination of two radio-lymphatic imaging methods (PET and Cerenkov luminescence imaging (CLI) for the SLN imaging of mice) through one injection of ^{124} I-embedded GNP (RIe-AuNPs). Compared with the

previously reported gold and copper radionuclides, iodine radionuclides are relatively safe for long-term clinical use. After PEGylation, this PEG-Rle-GNP was drained into the SLN after subcutaneous injection. The signal in the SLN was >12-fold that of the control group under low-dose injection, indicating high sensitivity and a non-invasive platform for LN imaging and surgical guidance (**Figure 6.5.3**).[56]

6.5.1.3 GNP as imaging reagent for photoacoustic imaging

Photoacoustic (PA) imaging is a non-invasive method for tissue imaging and disease diagnosis. Under NIR pulse laser irradiation, the receiving system can collect the ultrasound signal generated, and high-contrast images with tissue characteristics could be received.[57] However, due to the low penetration depth limited by light scattering, the detection depth of the PA signal is generally restricted and highly depends on the light absorption efficiency of the contrast agent. Due to the local SPR effect of GNP as well as a high photothermal conversion effect, it has a high absorption of light and could transfer the energy to heat for subsequent acoustic signal generation. Thus, GNP has long been used as the PA contrast agent for blood vessels, tumour tissues, as well as infection foci.[57] Moreover, GNP has also been applied in the imaging of the lymphatic system. As early as 2009, Pan et al. reported the preparation of gold nanobeacons by entrapping octanethiol-capped GNPs within polysorbate or vegan oil to form nano-assemblies. Three different-sized (90/160/290 nm) gold nanobeacons were used for the determination of size influence on their PA imaging ability. It was found that smaller-sized nanobeacons, although with a lower payload of GNPs, had a higher accumulation in LNs and gave better contrast than the bigger ones (**Figure 6.5.4**).[58]

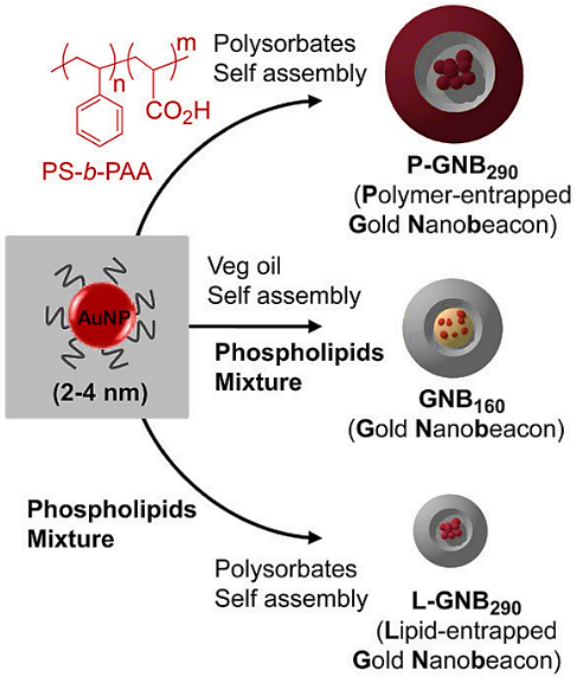

Figure 6.5.4 Synthetic routes of different gold nanobeacons by wrapping 2–4 nm GNPs into polymers or phospholipid layers for the effective photoacoustic imaging of the LN system.[58] (Copied from Elsevier Publishing Group)

Sun et al. applied the glycol chitosan-conjugated GNPs (GC-GNP) for the simultaneous imaging and delivering of antigens to the regional LNs. Through the guidance of ultrasound imaging, cervical LN PA mapping was achieved by the lingual injection, which greatly enhanced the imaging quality of LN mapping in mice. In addition, through linking with OVA, this material was effectively internalised by macrophages *in vitro* to boost the T cell activation in cancer immunotherapy.[59]

6.5.1.4 GNP as the MRI contrast reagent

Although GNPs do not display magnetism, they perform well on contrast-enhanced MRI as well as other imaging modalities. They mainly serve as carriers to enhance the lymphatic targeting ability of materials. Wan et al. applied dysprosium complex ($DyDOTA(amide)_2$) as the GNP coating to prepare the MRI contrast agent. The MRI signal in LN of this complex was significantly enhanced compared with pure DyDOTA NPs and reached 22.9 mM^{-1} s^{-1}, 15-fold that of the Dy complexes alone. In addition, it

also displayed good biocompatibility and adequate body clearance time (**Figure 6.5.5**).[60] Debouttière et al. used the dithiolated diethylenetriaminepentaacetic acid (DTDTPA): Gd for the coating of GNPs and further increased the relaxivity to 585 mM^{-1} s^{-1}.[61]

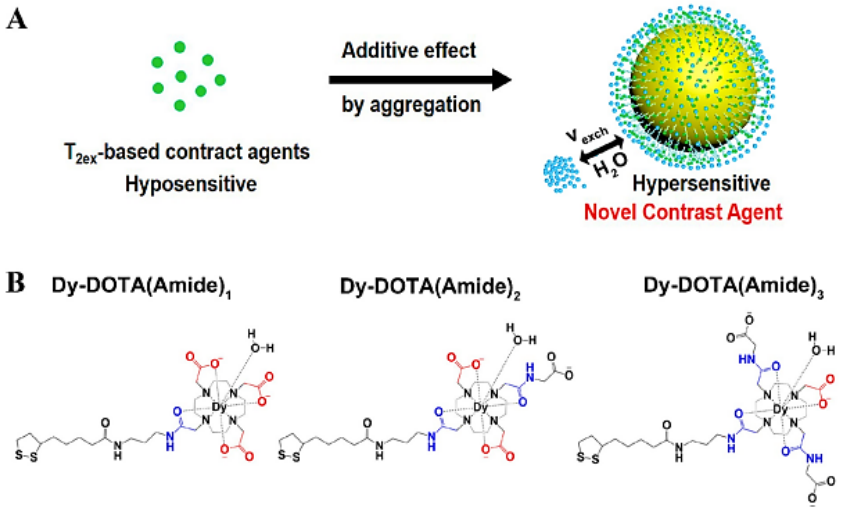

Figure 6.5.5 Dy-containing complexes were applied as the T_{2ex}-contrast reagents for the capping of GNPs. By controlling the amide group number (1,2,3) of the ligand, the GNPs could selectively accumulate in LNs.[60] (Copied from ACS Publishing Group)

6.5.1.5 GNP as dual/multi-modality imaging reagent

As single-modality imaging is always accompanied by disadvantages, dual- or even multi-model imaging for LNs is thus acquired.[62] Due to easy ligand decoration and high stability, GNP-based dual-modality lymphatic imaging agents are common. I have introduced the combination of non-radioactive methods like ultrasound & PA[63] or radioactive methods like PET&CLI.[56] Other combinations could achieve the synergistically enhanced imaging property. To achieve spatiotemporal imaging, Hayashi et al. prepared the Au@SiO_2 for CT/fluorescence dual-modal imaging of LNs and lymphatic vessels. CT was applied for the precise location of LNs, while the NIR fluorescence imaging facilitated the identification and surgical resection (**Figure 6.5.6**).[64]

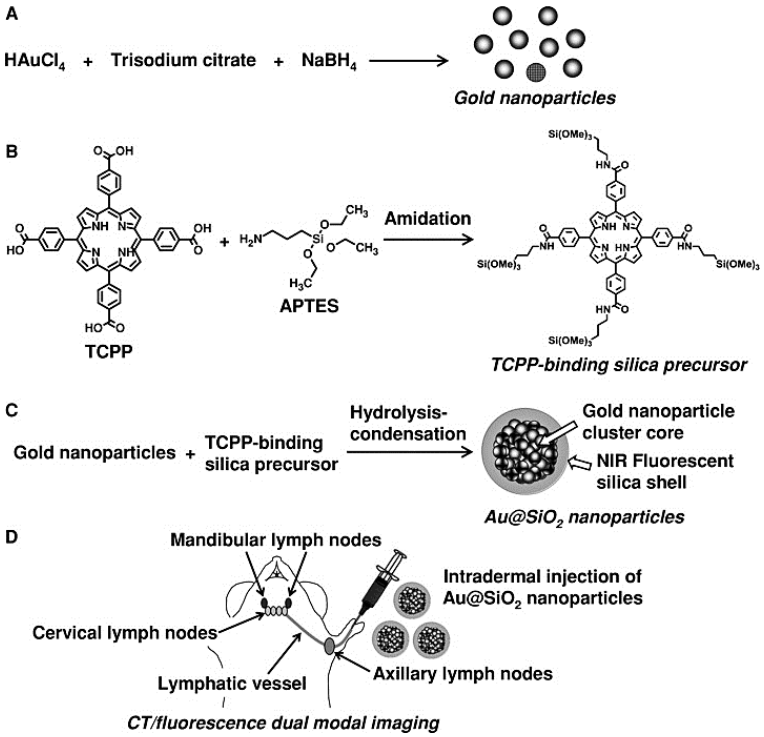

Figure 6.5.6 Preparation scheme of $Au@SiO_2$ NPs for the CT and fluorescence dual-modal imaging of the cervical LN through the intradermal injection and draining into the axillary LNs.[64] (Copied from Wiley Publishing Group)

In addition to imaging, Zhou et al. proved that CpG oligonucleotides and OVA peptide-capped GNPs could stimulate the immune response of dendritic cells and increase the expression of T helper1 cytokines. After tissue homing of these dendritic cells, the GNPs could further increase the CD8+ T cell responses (a type of cytotoxic T lymphocytes).[65] Due to GNP's ability to carry antigens for immune activation, they can be used for simultaneous imaging and immune responsiveness. Therefore, the GNPs have a strong potential as a theranostic platform for clinical applications.

6.5.2 GNCs as potential therapeutic reagents for lymphatic system imaging

6.5.2.1 GNC as NIR imaging probe

Compared with GNPs, the research history of GNCs is shorter, and the research on water-soluble GNCs with high biocompatibility only began in the past decade, but its application in biological imaging is already comparable to GNPs. Different from GNPs,

whose applications are mainly in radiography and PA imaging, the photoluminescent property of GNC is most valued, allowing for efficient spatiotemporal imaging of many tissues, including tumours, bone, and blood vessels, as well as lymphatics and LNs. Other imaging modalities are then combined with GNC fluorescence for dual-modality imaging. Although using GNCs for lymphatic system mapping is still in its infancy, I will provide an overview of their use, including in other parts of the body, to outline their application potential for the lymphatic system.

In the past two decades, NIR fluorescent materials have received unprecedented attention due to their potential application in deep-penetrating bioimaging. The light absorption of water, haemoglobin and oxyhaemoglobin is greatly reduced in the 700-900 nm wavelength range, with much less tissue absorption and signal attenuation. This range is known as the first NIR biological window (NIR-I) (Figure 6.5.7). NIR-I has been considered the requirement for *in vivo* imaging materials. However, with the development of new imaging agents, the restriction of penetration depth was found, which is mainly due to the absorption by other tissues and fluids in the body. In addition, the tissue autofluorescence also influences the signal-to-background ratio.[66] Thus, there is an urgent need to find a more suitable bioimaging window for *in vivo* monitoring and diagnosis. In 2014, the second NIR biological window (NIR-II, 1000–1700 nm) was found.[67] The extremely low absorption and scattering of light by tissue, as well as low autofluorescence in NIR-II, can give high contrast and high-resolution images.

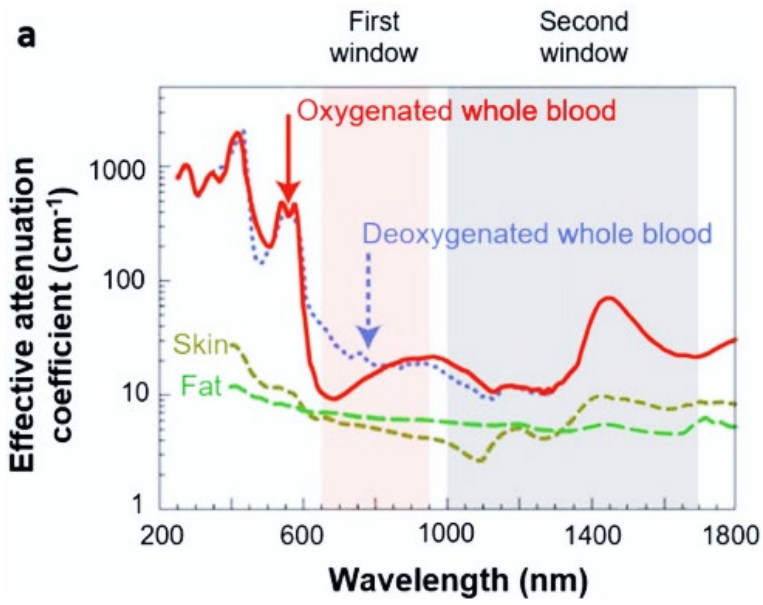

Figure 6.5.7 Diagram showing the absorption of blood, skin, and fat, as well as the ranges of two biological windows. It is obvious that the absorption intensity of all tissues is reduced in the biological windows.[66] (Copied from Wiley Publishing Group)

6.5.2.2 Timeline of GNC in NIR bioimaging

In the beginning, biocompatible fluorescent GNCs are normally prepared with a one-pot hydrothermal synthesis in the presence of peptides, proteins, polymers, or dendrimers. The prepared GNCs are mostly excited by UV light and fluoresce NIR-I to blue-violet lights.[68 69] Although having excellent prospects for detection and *in vitro* imaging, the application of UV excitation is harmful to living organisms, while the emission in the visible light region is also strongly absorbed by haemoglobin, restricting their penetration depth.[70]

However, with the discovery of the NIR fluorescence excitation and emission properties of water-soluble and biocompatible GNCs, these problems are resolved. NIR-II GNCs are efficiently excited by NIR-I light (*e.g.,* 808 nm) and emit in the NIR-II region (*e.g.,* 1100 nm), making them well-suited for *in vivo* imaging.[70] In addition, their atomically precise nature can guarantee druggability and quality control, avoiding batch-to-batch variation. Compared with small organic fluorescent dyes, the advantages of NIR

fluorescent GNC include high photostability, large Stokes shifts, and long photoluminescence lifetime. Although the QY is relatively low and usually around 1%–4%,[71] their high resistance to photobleaching, easy chemical modification, and adequate *in vivo* half-life have gradually gained more attention. Our summary will focus on NIR-II GNCs and their bioimaging applications.

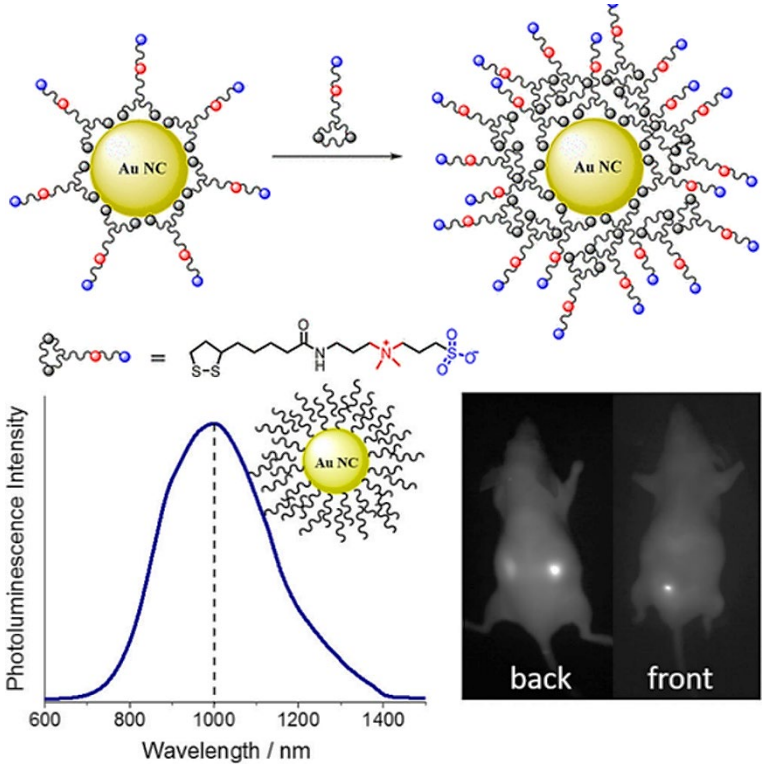

Figure 6.5.8 Schematic showing NIR fluorescent GNCs capped with zwitterion-modified dihydrolipoic acid ligands. It was observed that the *in vivo* metabolism of GNCs is mainly through renal clearance.[72] (Copied from ACS Publishing Group)

The research on NIR-II-emitting GNC began in 2017. Chen et al. reported the short-wave NIR-II imaging ($\lambda_{Em\ max}$=~1000 nm) of mice with GNCs decorated with bidental zwitterionic ligands (lipoic acid-sulfobetaine). Despite a relatively low QY (0.6%) and no clear GNC configuration, this pioneering work has shown a stable NIR fluorescence in the short-wave NIR region (1000-2000 nm). After tail vein injection, the main organs, including the heart, kidneys, and bladder, have demonstrated significant fluorescence, indicating efficient renal clearance (**Figure 6.5.8**).[72] Following this paper, other NIR-II

emitting GNCs for tissue imaging have emerged.[73]

In 2019, Musnier et al. synthesised NIR-emitting, negatively charged GNCs with anisotropic properties. Two ligands, including mercaptohexanoic acid (MHA) and bidentate hexa(ethylene glycol) dithiol (HDT) were applied for the co-capping of the GNC surface. By controlling the capping ratio of HDT to MUA, the formed GNC can further self-assemble into reticulated structures, which further alters their fluorescence properties (Figure 6.5.9).[74]

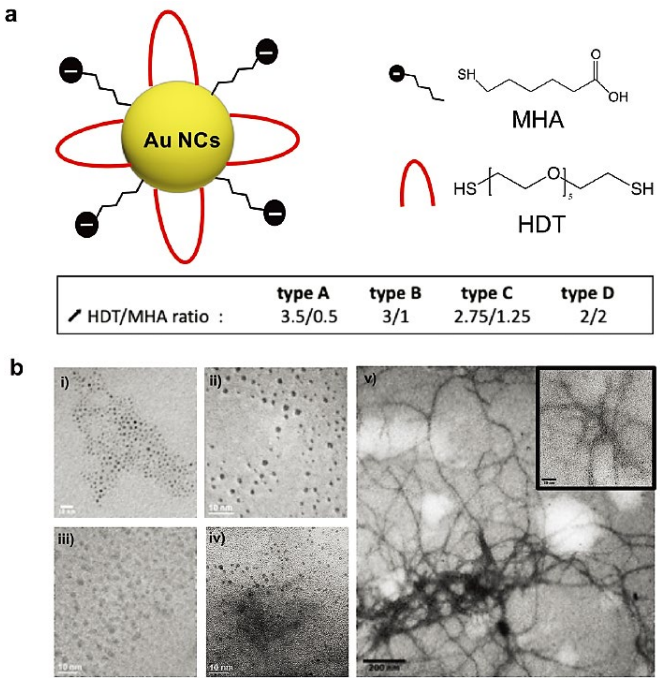

Figure 6.5.9 Synthetic diagram of the NIR-emitting GNC capped with MHA and HDT ligands. By controlling the ligand feed ratio, the GNC could self-assemble into different patterns, thereby controlling their fluorescence characters.[74] (Copied from RSC Publishing Group)

Like the zwitterionic ligand-capped GNC reported above, the maximum emission peak is around 1000 nm. However, through the anisotropic surface modification, the QY was enhanced to 6.1% (10-fold higher). The mechanism was attributed to the influence on the energy transfer processes, leading to new discrete energy levels. Although the chemical formula and *in vivo* experimental results in biosafety studies are lacking, the

potential for the biological applications of this material is high.[74] In addition, Liu et al. did a series of in-depth research on the fluorescence modification and biological application of NIR-emitting GNCs. Based on the $Au_{25}(SR)_{18}$ structure, they tested the influence of different ligand types and heteroatom doping on the QY of the NIR-II fluorescent GNCs. Comparatively, the cysteine-capped GNC with one Cu/Zn atom doping has the highest QY and fluorescent intensity. This optimised GNC was then applied for the imaging of cerebrovascular, mapping of LN, as well as validation of metabolic behaviour. The ability to penetrate skull and skin tissues could provide deep penetration and high-contrast images for disease diagnosis.[75]

In 2020, the research on NIR-II fluorescent GNC was in full swing. Following the previous work, Yu et al. improved the reagents to tetra(ethylene glycol), dithiol (TDT), and mercaptohexanoic acid (MHA) and maintained high fluorescence QY (~6%) based on enhanced compatibility. The fluorescence is detectable across the entire NIR-II range with improved contrast (1 order of magnitude) or spatial resolution (over 59%). Due to its long blood half-life (over 19 h), this dual-ligand GNC was applied for whole-body vascular imaging in mice. Combined with an image-processing program, the observation of vascular abnormalities in transgenic mice was achieved.[50] In addition, Li et al. applied L-glutathione-capped Au_{25} GNCs [$Au_{25}(SG)_{18}$] (QY=0.27%) for the bone imaging of mice. Notably, these GNCs demonstrated a high affinity to hydroxyapatite in all bony tissues, possibly due to the interaction between many carboxyl groups on the surface of GNCs and hydroxyapatite in bones. In addition, such $Au_{25}(SG)_{18}$-type NCs are effectively eliminated through the urinary system without affecting the imaging of ribs and thoracic vertebra. This GNC thus is suitable for whole-body bone imaging (**Figure 6.5.10**).[76]

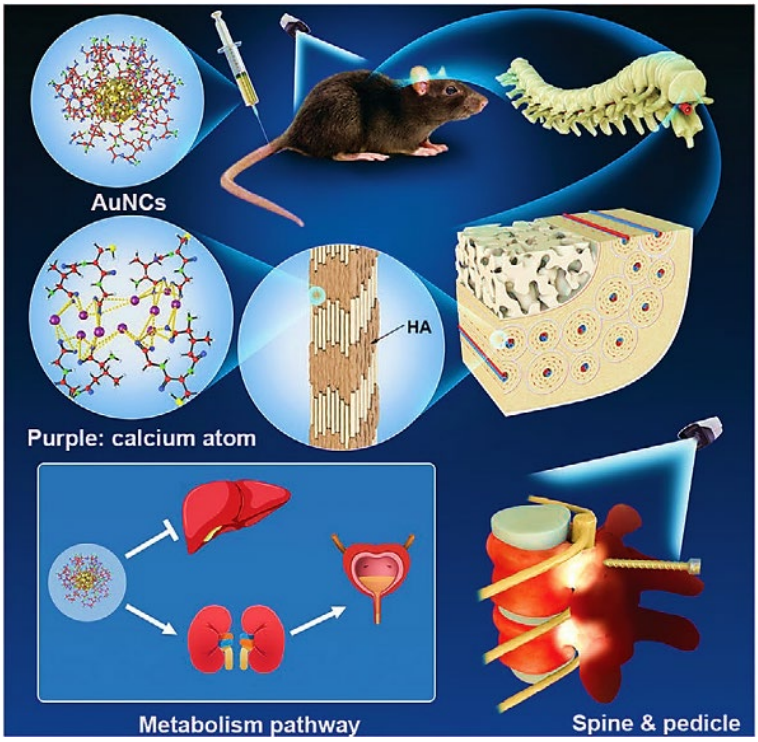

Figure 6.5.10 Applying glutathione as the capping ligand during synthesis, $Au_{25}(SG)_{18}$-type GNC demonstrated high affinity to hydroxyapatite, which could be used for the imaging of spine, ribs or other bone tissues. This GNC is also generally clearable through renal clearance as well as liver metabolism.[76] (Copied from Wiley Publishing Group)

6.5.2.3 NIR fluorescence GNC for tumour imaging and detection

The NIR-II GNC also has an extremely high application value in tumour detection. In another study, Wang et al. prepared the ribonuclease-A (RNase-A)-encapsulated AuNCs for the intestinal imaging and differentiation of the intestinal tumour. This GNC has demonstrated a red-shift of the maximum fluorescence emission to ~1050 nm and demonstrated an >50-fold sensitivity increase after conjugating with proteins. In addition, tumour foci of only 2.5 mm size could be distinguished with this imaging agent.[77] The NIR-II GNCs have been successfully used for image-guided surgery of head and neck tumours on athymic NMRI nude mice. Colombé et al. successfully used the zwitterionic ligand LA-$ZWEt_2$ and LA-PEG_nCOOH (LA: lipoic acid) for the capping of GNCs. Comparatively, the LA-PEG_nCOOH-capped GNC has a relatively higher accumulation rate in the CAL-33 (tongue squamous cell carcinoma) tumour-bearing

mice. Guided by its NIR fluorescence, the operator could conduct the thorough removal of the tumour site, prolonging the survival of mice after surgery (**Figure 6.5.11**).[78]

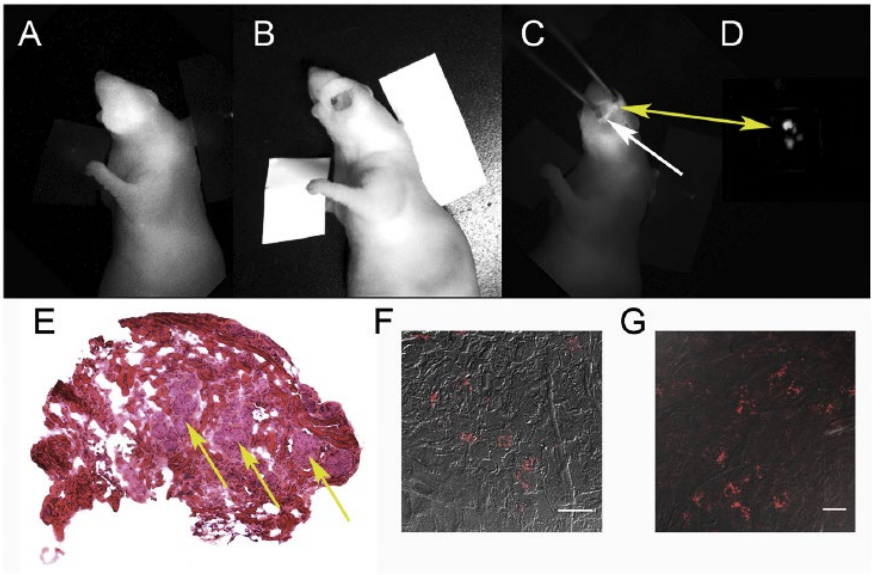

Figure 6.5.11 (A–D) After the administration of dual ligand GNC and taking photos by a NIR animal imager, the tumour location could be clearly located. **(E)** The pathological section clearly shows the lesion location of the tumour. **(F–G)** GNC aggregations at the tumour site can be found by fluorescence co-localization.[78] (Copied from Elsevier Publishing Group)

For tumour imaging, host-guest interaction was also applied for the capping of tumour-targeting GNC. Song et al. reported the application of thiolated β-cyclodextrin (CD) as the capping of GNCs. Through host-guest recognition, the CD host could specifically bind with guest molecule-labelled macromolecules (for example, adamantane, etc.) like antibodies, thus could be used for the target imaging of tumours. Due to the flexibility of the alternative protein modified by the guest molecule, this system can be selected according to the function to be performed without affecting its NIR fluorescence properties.[79] In addition to Au_{25} GNC, the NIR-emitting Au_{22} NC with AIE property was also applied for the bioimaging of living cells. Wei et al. reported the synthesis of BSA-capped Au_{22} NC. The aggregation induced by poly(allylamine hydrochloride) has induced both the increase in photoluminescence intensity and lifetime due to

rigidification of the surface capping.[80]

6.5.2.4 Doping heteroatoms into the NIR-fluorescence GNC

Besides pure GNC, the alloy NIR-II emitting NCs also have good bioimaging prospects. In the paper introduced previously, Cu/Zn/Er/Ag heteroatoms were applied for fluorescence enhancement for GNC. All alloy GNCs demonstrated an enhanced fluorescence intensity and QY compared with the control pure GNCs.[75]

In another study, Yang et al. applied the GSH-capped AuNC-Pt for the scavenging of GSH in the tumour cells to enhance the efficiency of chemotherapy. The $Au_{25}(SG)_{18}$ was applied as the NIR-II probe as well as the carrier to release Pt(IV)-related chemotherapeutic drug. They speculated that the excess GSH in tumour cells could reduce Pt(IV) to Pt(0), causing a decrease in GSH level and perturbation in oxidative stress. In addition, the Au_{25} NC could also bind with GSH to further promote this process. In the in-situ tumour model, this GNC demonstrated excellent imaging and good therapeutic effects (Figure 6.5.12).[81]

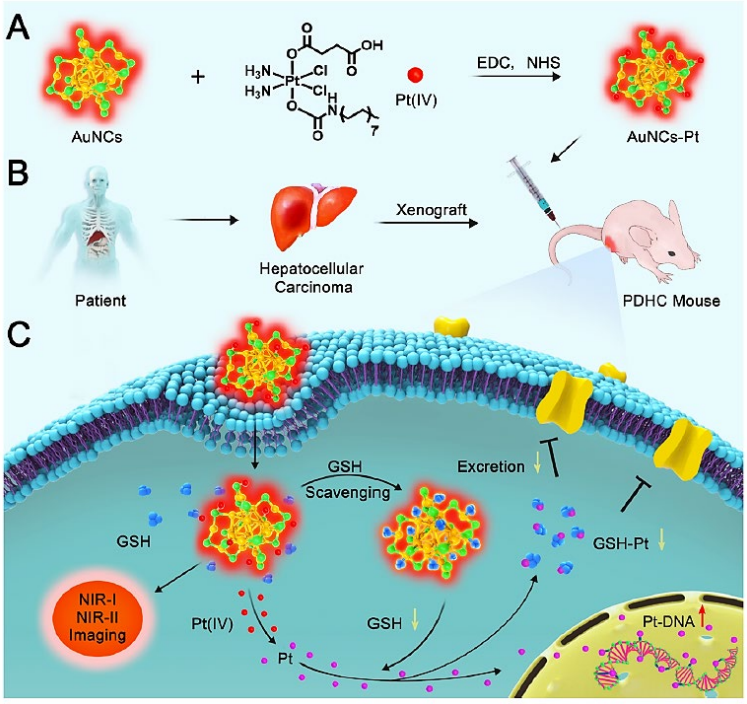

Figure 6.5.12 $Au_{25}(SG)_{18}$ NC was conjugated with Pt-based anticancer drugs. Combining the GSH scavenging ability and the chemotherapeutic ability, this nanomedicine could effectively inhibit the growth of xenografted cancer model.[81] (Copied from ACS Publishing Group)

6.5.2.5 Applying other properties of GNC in bioimaging

GNCs also exhibit a unique two-photon (TP) fluorescence property. Since the absorbed photons are of relatively low energy, they are generally in the NIR region, and if their emission is also in the NIR region, it is extremely beneficial for biological imaging. However, due to the large Stokes shift of GNC, the TPL is normally in the visible light range.[82] [83] Further studies on controlling the Stokes shift by manipulating heteroatom species to alter their TP properties are required.

6.5.2.6 Dual- & multi-modality imaging with GNCs

Based on its outstanding NIR-II fluorescence property, dual-modality imaging and treatment using GNCs is a fascinating method to further increase imaging quality and diagnosis accuracy.[84] Tang et al. reported the NIR fluorescence/PDT dual-modality imaging and treatment of tumour-lymphatic metastasis. Although the GNC chemical

structure in this paper is not well confirmed, it inherits NIR-II fluorescence of Au_{25} NC with maximum emission at ~920 nm under 808 nm laser irradiation, with a QY of 1.1%. In addition, the ROS-induced fluorescence has a good linear relationship with the laser intensity, proving that the use of NIR laser makes the GNCs produce the photodynamic catalytic effect. This PDT could significantly enhance the anti-cancer ability and reduce the tumour cell viability to 20%. With imaging-guided surgery and PDT, the tumour volume was greatly reduced.[85] Similarly, Chen et al. applied the human serum albumin and catalase co-modified GNCs for the NIR fluorescence/PDT dual-modality imaging to relieve the hypoxic tumour environment.[86]

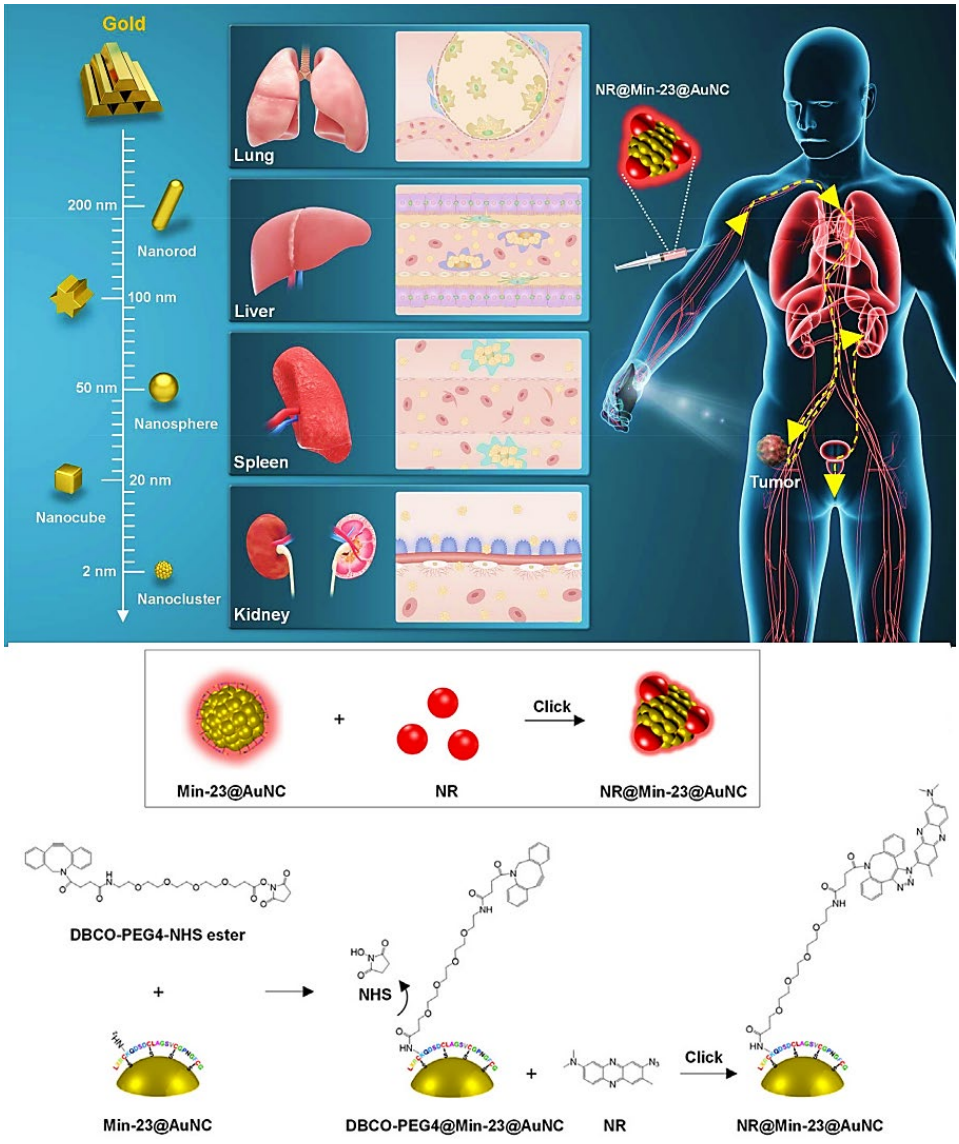

Figure 6.5.13 A NIR fluorescent GNC capped with photosensitive molecule (neutral red) was prepared for simultaneous NIR imaging, photodynamic imaging and tumour

treatment.[87] (Copied from Elsevier Publishing Group)

Kong et al. reported a multifunctional nanoplatform for highly effective PDT imaging and treatment with a smartphone torch last year. The NIR-II emitting GNC was applied as the reporting group as well as the carrier to enhance the tumour accumulation effect. At the same time, a photodynamic dye was covalently linked to the GNC for PDT treatment. The required light energy for PDT can be satisfied with only 8 mW/cm^2 light irradiation (**Figure 6.5.13**).[87] Although the outcome is quite exciting, the observation of NIR-II fluorescence has not been achieved by smartphones. The requirement of two light sources may be where this system needs further optimisation.

In terms of the TP property, He et al. prepared transferrin-capped GNCs and further functionalised the GNC with MnO_2 for the TP-NIR imaging/MRI dual-modal imaging of GSH level in cells. The GSH could react with MnO_2 to generate Mn^{2+} for enhancing the MRI signal, while the release of the transferrin-capped GNCs could recover their NIR-II fluorescence. Through this system, breast cancer cells with high GSH content can be identified (**Figure 6.5.14**).[88]

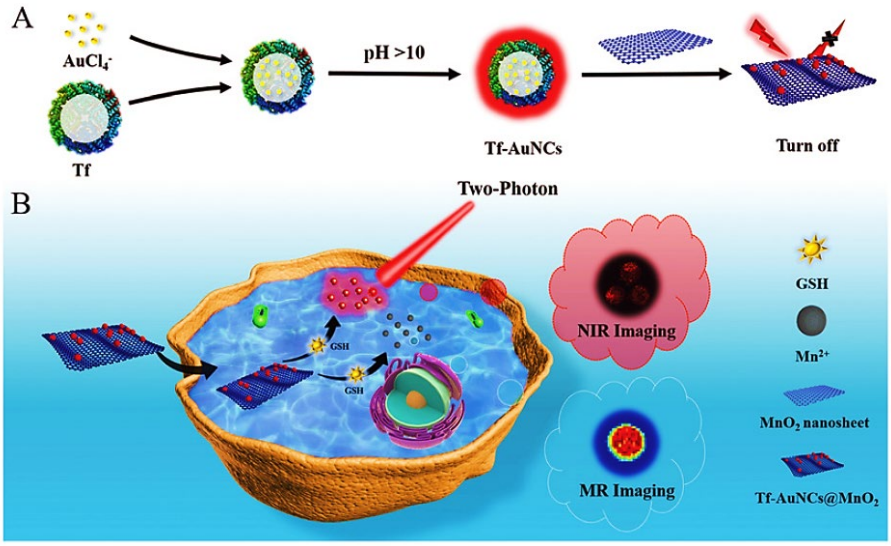

Figure 6.5.14 Schematic diagram of the preparation of Tf-GNCs with two-photon fluorescence and MR dual-modality imaging properties.[88] (Copied from RSC Publishing Group)

In another study, GNC was decorated onto magnetic iron oxide NPs through electrostatic interaction. This highly biocompatible Fe_3O_4@AuNCs was then applied for NIR fluorescence/MRI dual-modal imaging of tumours with high biological imaging potential.[89] Different from GNPs, the CT enhancing ability of GNC itself is usually not ideal and requires a high concentration of the material (up to 50 mg mL^{-1}), which is not suitable for bioimaging.[90] Chen et al. subtly synthesised the NIR-II emitting BSA-capped GNCs and used the iodinated chloramine T to further incorporate I^- into the dual-modal (CT/NIR fluorescence) imaging system. Iodine here was applied to greatly increase the contrast of MRI quality while also as the targeting element that increased the accumulation in the thyroid. The imaging effect for thymoma is out-competing many commercial CT contrast agents. Combined with the NIR fluorescence at ~720 nm, the AuNCs@BSA-I could be used to distinguish thyroid cancer as small as 2 mm^3 (**Figure 6.5.15**).[91]

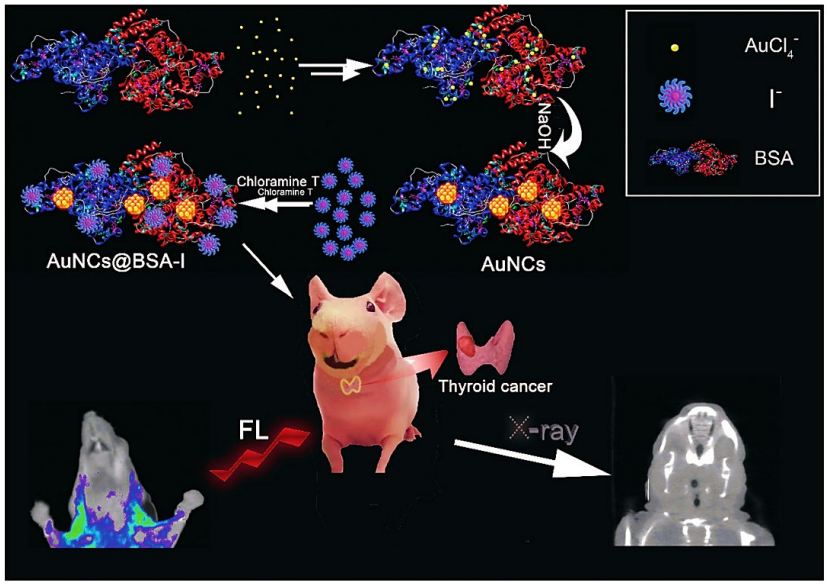

Figure 6.5.15 Iodine was incorporated into BSA-capped GNCs for the tri-modality imaging (Fluorescence/CT/MRI) of thyroid cancer.[91] (Copied from RSC Publishing Group)

In conclusion, the NIR-II emitting GNC provides a good platform for either *in vivo* imaging or surgical guidance.[84] However, limited by their low QY, which is normally less than 5%, the fluorescence is still not comparable to some organic fluorophores (most in

dozens%). In addition, the maximum emission is normally around 1050 nm, which is just at the edge of the NIR-II region. I expect the fluorescence to be more red-shift to further reduce tissue absorption and scattering to enhance the signal-to-noise ratio. Moreover, it is expected to be able to perform heteroatom doping of GNCs to alter their TP properties and achieve NIR-NIR emission. Due to the lower laser energy used in TP, its impact on the organism is relatively small, and the biological application is also more advantageous than ordinary fluorescence imaging. Last but not least, I can observe that most of the as-prepared GNCs are covered with a single type of ligand, lacking fine-tuning of the bi- or multi-ligand ratio on the GNC surface. I hope that by adjusting the ligand ratio on the GNC surface, I could further increase the properties of the NIR-II GNCs and widen their application in the biomedical field (Table 16).

Table 16 Summary of the ligand, atomic number, size, excitation and emission wavelengths, QY, and imaging sites of the GNCs used in the above-mentioned papers

Ligand type	GNC Type	GNC Size (nm)	λ_{ex} (nm)	λ_{em} (nm)	QY (%)	Imaging Site	Ref.
Lipoic acid-based sulfobetaine	Au_{20}-Au_{50}	~1.6	785	1000	0.6	Blood vessels	72
Mercaptohexanoic acid & Hexa (ethylene glycol) dithiol	Au_{25}	1.54/2.46	400/780/980	>1000	3.8	–	74
Glutathione/ Cystine/ Homocysteine	Au_{25}	~1.8	808	1050	0.67	Brain vessels, Lymphatic metastasis	75
Mercaptohexanoic acid & Tetra(ethylene glycol) dithiol	Au_{25}	~2.1	830	930	~6	Blood vessels	50
Glutathione	Au_{25}	~3.3	808	~1000	0.27	Bones	76
Ribonuclease-A	Au_{25}	~3.5	808	1050	~1.9	Intestinal tumour	77
LA-$ZWEt_2$/ LA-PEG_nCOOH	–	3.1/7.2/8.6/10.5	–	~800	5.7/7.1/8.0/9.0	Head and neck	78

						tumours	
β-Cyclodextrin	Au_{25}	~1.85	808	~1050	~0.11	Tumour	79
Glutathione (GSH)	Au_{25}	3.2	808	~1050	0.04-0.05	Tumour	81
6-Aza-2-thio thymine (ATT)	Au-Ag NC	~2.5	360 (720)	695	5.4	Rear paw	83
11-mercaptounde canoic acid (MUA)	–	2–3	365	600–650	–	Tumour	86
Miniprotein-23	Au_{25}	1.81 ± 0.26	808	1050	0.21	Rear leg & Tumour	87
Transferrin	–	~10	365 (920)	681	–	–	88
Glutathione	–	2 ± 0.2	530	650	4.3	–	89
Lysozyme	–	1.29 ± 0.17	550	690	19.61	Tumour	90
BSA	–	6.4	535	690	–	Thyroid tumour	91

6.6 Overview of the project (Part III)

Compared with the high research enthusiasm on the blood cardiocirculatory system, historically, both the knowledge development and depth of research on the lymphatic system are limited.[4] One big reason is that, except for the chyle, most lymph fluid is nearly transparent, which hinders early observation in anatomy.[2] Lymphatic imaging has come a long way, and a variety of radiation (CT/PET/lymphoscintigraphy, etc.) and non-radiation (NMR/NIR fluorescence/PA, etc.) based techniques have been developed. Of all these methods, NIR fluorescence imaging is the least expensive and enables real-time imaging to aid surgery. However, most of the NIR fluorescence contrast agents used clinically are ICG, which has disadvantages, such as limited resistance to photobleaching, instability in water, self-quenching, and a short half-life in the blood.[21] Thus, novel imaging agents are required to overcome these problems. GNP-related imaging materials are widely applied as new nano-contrast agents in lymphatic system imaging.[8] The atomically precise GNCs with NIR-II fluorescence discovered in recent years are more suitable for LN imaging due to their high *in vivo* stability, biocompatibility, and feasible chemical modification of other

therapeutic molecules.[84] [70] However, most Au_{25} GNC-based imaging agents are capped with a single type of ligand, and the precise surface modification with dual or multiple ligands is rare. Thus, I devote myself to surface chemistry to fabricate theranostic GNCs for both imaging and treatment of lymphatic metastasis.

In the following chapter, a dual-ligand-capped NIR-II-emitting Au_{25} NC for the lower body LN imaging of mice will be introduced. Both a mercaptoalkanoic acid ligand and a zwitterionic ligand were co-applied for adjusting the surface negative charge density. By optimising the two-ligand ratio, this GNC could achieve a high accumulation rate in the SLN for imaging and cancer metastasis diagnosis. The high contrast and low latency video could facilitate a live NIR-II surgical resection of metastatic lesions. In addition, a chemotherapeutic drug—methotrexate, was further decorated onto the GNC to achieve an enhanced lymphatic delivery efficiency to reduce its toxicity to other organs (Figure 6.6.1).

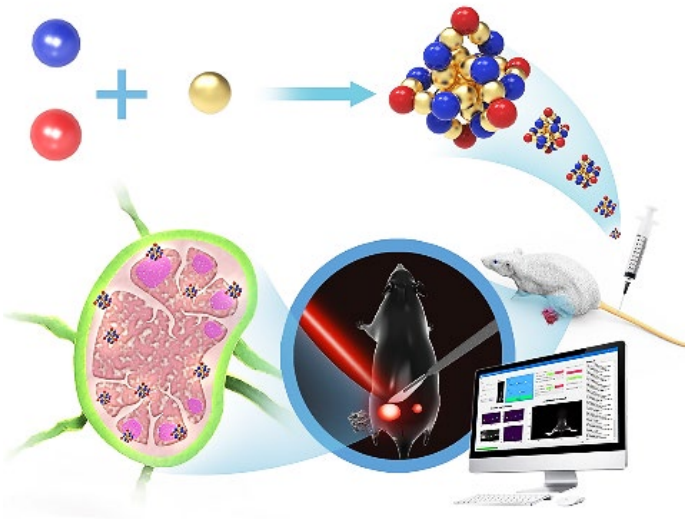

Figure 6.6.1 A NIR-II fluorescent $Au_{25}(SR)_{18}$ nanocluster capped with optimal surface negative charge could effectively accumulate in lymph nodes for imaging-guided surgery and treatment of tumour-lymph node metastasis. After further loading with a chemotherapeutic drug, the GNCs can significantly reduce hepatotoxicity and achieve anti-cancer effects similar to those of the free drug form.

6.7 References

1 M. A. Swartz, *Adv. Drug Deliv. Rev.*, 2001, **50**, 3–20.

2 M. Loukas, S. S. Bellary, M. Kuklinski, J. Ferrauiola, A. Yadav, M. M. Shoja, K. Shaffer and R. S. Tubbs, *Clin. Anat.*, 2011, **24**, 807–816.

3 C. J. van Schaik, L. L. Boer, J. M. T. Draaisma, C. J. M. van der Vleuten, J. J. Janssen, J. J. Fütterer, L. J. Schultze Kool and W. M. Klein, *Clin. Anat.*, 2022, **35**, 701–710.

4 G. Natale, G. Bocci and D. Ribatti, *J. Anat.*, 2017, **231**, 417–429.

5 A. Aspelund, M. R. Robciuc, S. Karaman, T. Makinen and K. Alitalo, *Circ. Res.*, 2016, **118**, 515–530.

6 P. S. Mortimer and S. G. Rockson, *J. Clin. Invest.*, 2014, **124**, 915–921.

7 S. P. Leong, A. Pissas, M. Scarato, F. Gallon, M. H. Pissas, M. Amore, M. Wu, M. B. Faries and A. W. Lund, *Clin. Exp. Metastasis*, 2022, **39**, 139–157.

8 S. Qi, X. Wang, K. Chang, W. Shen, G. Yu and J. Du, *J. Nanobiotechnology*, 2022, **20**, 1–27.

9 A. K. Goswami, M. S. Khaja, T. Downing, N. Kokabi, W. E. Saad and B. S. Majdalany, *Semin. Intervent. Radiol.*, 2020, **37**, 227–236.

10 D. Negrini and A. Moriondo, *J. Physiol.*, 2011, **589**, 2927–2934.

11 W. L. Olszewski, *Lymphat. Res. Biol.*, 2003, **1**, 11–24.

12 M. A. Swartz and M. Skobe, *Microsc. Res. Tech.*, 2001, **55**, 92–99.

13 C. L. Willard-Mack, *Toxicol. Pathol.*, 2006, **34**, 409–424.

14 S. Jalkanen and M. Salmi, *Nat. Rev. Immunol.*, 2020, **20**, 566–578.

15 A. Schudel, D. M. Francis and S. N. Thomas, *Nat. Rev. Mater.*, 2019, **4**, 415–428.

16 N. L. Trevaskis, L. M. Kaminskas and C. J. H. Porter, *Nat. Rev. Drug Discov.*, 2015, **14**, 781–803.

17 D. Olmeda, D. Cerezo-Wallis, E. Castellano-Sanz, S. García-Silva, H. Peinado and M. S. Soengas, *Adv. Drug Deliv. Rev.*, 2021, **175**, 113833.

18 A. K. Polomska and S. T. Proulx, *Adv. Drug Deliv. Rev.*, 2021, **170**, 294–311.

19 D. J. Mariani and A. Renato, *Atlas of Lymphoscintigraphy and Sentinel Node Mapping*, Springer International Publishing, Cham, 2020.

20 S. K. Nune, P. Gunda, B. K. Majeti, P. K. Thallapally and M. L. Forrest, *Adv. Drug*

Deliv. Rev., 2011, **63**, 876–885.

21 C. Egloff-Juras, L. Bezdetnaya, G. Dolivet and H. P. Lassalle, *Int. J. Nanomedicine*, 2019, **14**, 7823–7838.

22 E. P. Porcu, A. Salis, E. Gavini, G. Rassu, M. Maestri and P. Giunchedi, *Biotechnol. Adv.*, 2016, **34**, 768–789.

23 H. Mok, H. Jeong, S. J. Kim and B. Hyun Chung, *Chem. Commun.*, 2012, **48**, 8628–8630.

24 J. C. Kraft and R. J. Y. Ho, *Biochemistry*, 2014, **53**, 1275–1283.

25 S. T. Proulx, P. Luciani, S. Derzsi, M. Rinderknecht, V. Mumprecht, J. C. Leroux and M. Detmar, *Cancer Res.*, 2010, **70**, 7053–7062.

26 M. Fang, M. Chen, L. Liu and Y. Li, *J. Biomed. Nanotechnol.*, 2017, **13**, 1–16.

27 X. Michalet, F. F. Pinaud, L. A. Bentolila, J. M. Tsay, S. Doose, J. J. Li, G. Sundaresan, A. M. Wu, S. S. Gambhir and S. Weiss, *Science*, 2005, **307**, 538–544.

28 S. Kim, Y. T. Lim, E. G. Soltesz, A. M. De Grand, J. Lee, A. Nakayama, J. A. Parker, T. Mihaljevic, R. G. Laurence, D. M. Dor, L. H. Cohn, M. G. Bawendi and J. V. Frangioni, *Nat. Biotechnol.*, 2004, **22**, 93–97.

29 F. Erogbogbo, K. T. Yong, I. Roy, R. Hu, W. C. Law, W. Zhao, H. Ding, F. Wu, R. Kumar, M. T. Swihart and P. N. Prasad, *ACS Nano*, 2011, **5**, 413–423.

30 B. Ballou, L. A. Ernst, S. Andreko, T. Harper, J. A. J. Fitzpatrick, A. S. Waggoner and M. P. Bruchez, *Bioconjug. Chem.*, 2007, **18**, 389–396.

31 S. Wilhelm, *ACS Nano*, 2017, **11**, 10644–10653.

32 A. Xia, Y. Gao, J. Zhou, C. Li, T. Yang, D. Wu, L. Wu and F. Li, *Biomaterials*, 2011, **32**, 7200–7208.

33 S. Qiu, J. Zeng, Y. Hou, L. Chen, J. Ge, L. Wen, C. Liu, Y. Zhang, R. Zhu and M. Gao, *Nanoscale*, 2018, **10**, 21772–21781.

34 Y. Sun, M. Ding, X. Zeng, Y. Xiao, H. Wu, H. Zhou, B. Ding, C. Qu, W. Hou, A. G. A. Er-bu, Y. Zhang, Z. Cheng and X. Hong, *Chem. Sci.*, 2017, **8**, 3489–3493.

35 W. Wu and Z. Li, *Mater. Chem. Front.*, 2021, **5**, 603–626.

36 D. Zhong, W. Chen, Z. Xia, R. Hu, Y. Qi, B. Zhou, W. Li, J. He, Z. Wang, Z. Zhao, D. Ding, M. Tian, B. Z. Tang and M. Zhou, *Nat. Commun.*, 2021, **12**, 1–13.

37 G.-M. Zhang, D. Jiao, S.-C. Nie, Z.-Y. Xu, X. Zhang, Y. Dai, M.-N. Jiao, H. Ou, Y.-B.

Yan and D. Ding, *Biomater. Sci.*, 2022, **10**, 1929–1935.

38 S. N. Thomas and A. Schudel, *Curr. Opin. Chem. Eng.*, 2015, **7**, 65–74.

39 Z. Yang, R. Tian, J. Wu, Q. Fan, B. C. Yung, G. Niu, O. Jacobson, Z. Wang, G. Liu, G. Yu, W. Huang, J. Song and X. Chen, *ACS Nano*, 2017, **11**, 4247–4255.

40 Y. N. Zhang, J. Lazarovits, W. Poon, B. Ouyang, L. N. M. Nguyen, B. R. Kingston and W. C. W. Chan, *Nano Lett.*, 2019, **19**, 7226–7235.

41 T. Nakamura, M. Kawai, Y. Sato, M. Maeki, M. Tokeshi and H. Harashima, *Mol. Pharm.*, 2020, **17**, 944–953.

42 N. A. Rohner and S. N. Thomas, *ACS Biomater. Sci. Eng.*, 2017, **3**, 153–159.

43 X. Ke, G. P. Howard, H. Tang, B. Cheng, M. T. Saung, J. L. Santos and H. Q. Mao, *Adv. Drug Deliv. Rev.*, 2019, **151–152**, 72–93.

44 R. Mammadov, G. Cinar, N. Gunduz, M. Goktas, H. Kayhan, S. Tohumeken, A. E. Topal, I. Orujalipoor, T. Delibasi, A. Dana, S. Ide, A. B. Tekinay and M. O. Guler, *Sci. Rep.*, 2015, **5**, 1–15.

45 R. Agarwal, V. Singh, P. Jurney, L. Shi, S. V. Sreenivasan and K. Roy, *Proc. Natl. Acad. Sci. U. S. A.*, 2013, **110**, 17247–17252.

46 C. A. Fromen, T. B. Rahhal, G. R. Robbins, M. P. Kai, T. W. Shen, J. C. Luft and J. M. DeSimone, *Nanomedicine Nanotechnology, Biol. Med.*, 2016, **12**, 677–687.

47 H. Jiang, Q. Wang and X. Sun, *J. Control. Release*, 2017, **267**, 47–56.

48 J. McCright, C. Skeen, J. Yarmovsky and K. Maisel, *Acta Biomater.*, 2022, **145**, 146–158.

49 A. S. Krishna Kumar and W. L. Tseng, *Anal. Methods*, 2020, **12**, 1809–1826.

50 Z. Yu, B. Musnier, K. D. Wegner, M. Henry, B. Chovelon, A. Desroches-Castan, A. Fertin, U. Resch-Genger, S. Bailly, J. L. Coll, Y. Usson, V. Josserand and X. Le Guével, *ACS Nano*, 2020, **14**, 4973–4981.

51 N. Lee, S. H. Choi and T. Hyeon, *Adv. Mater.*, 2013, **25**, 2641–2660.

52 F. Shi, Y. Yang, J. Chen, Y. Sha, Y. Shu and H. Wu, *Biomed Res. Int.*, 2018, **2018**, 1–6.

53 Y. Zhang, S. Wen, L. Zhao, D. Li, C. Liu, W. Jiang, X. Gao, W. Gu, N. Ma, J. Zhao, X. Shi and Q. Zhao, *Nanoscale*, 2016, **8**, 5567–5577.

54 S. Uthaman, H. S. Kim, V. Revuri, J. J. Min, Y. kyu Lee, K. M. Huh and I. K. Park,

Carbohydr. Polym., 2018, **181**, 27–33.

55 O. J. Estudiante-Mariquez, A. Rodríguez-Galván, D. Ramírez-Hernández, F. F. Contreras-Torres and L. A. Medina, *Molecules*, 2020, **25**, 1982.

56 S. B. Lee, G. S. Yoon, S. W. Lee, S. Y. Jeong, B. C. Ahn, D. K. Lim, J. Lee and Y. H. Jeon, *Small*, 2016, **12**, 4894–4901.

57 Q. Fu, R. Zhu, J. Song, H. Yang and X. Chen, *Adv. Mater.*, 2018, **31**, 1805875.

58 D. Pan, M. Pramanik, A. Senpan, S. Ghosh, S. A. Wickline, L. V. Wang and G. M. Lanza, *Biomaterials*, 2010, **31**, 4088–4093.

59 I. C. Sun, S. Jo, D. Dumani, W. S. Yun, H. Y. Yoon, D. K. Lim, C. H. Ahn, S. Emelianov and K. Kim, *Nanomaterials*, 2021, **11**, 1–13.

60 S. Wan, F. Cui, B. Li, K. Zhao, H. He, Y. Zhang, J. Liu, L. Zhang and K. Liu, *ACS Appl. Nano Mater.*, 2020, **3**, 9433–9439.

61 P. J. Debouttière, S. Roux, F. Vocanson, C. Billotey, O. Beuf, A. Favre-Réguillon, Y. Lin, S. Pellet-Rostaing, R. Lamartine, P. Perriat and O. Tillement, *Adv. Funct. Mater.*, 2006, **16**, 2330–2339.

62 M. A. Kurochkin, S. V. German, A. Abalymov, D. A. Vorontsov, D. A. Gorin and M. V. Novoselova, *J. Biophotonics*, 2022, **15**, e202100149.

63 G. P. Luke, A. Bashyam, K. A. Homan, S. Makhija, Y.-S. Chen and S. Y. Emelianov, *Nanotechnology*, 2013, **24**, 455101.

64 K. Hayashi, M. Nakamura and K. Ishimura, *Adv. Healthc. Mater.*, 2013, **2**, 756–763.

65 Q. Zhou, Y. Zhang, J. Du, Y. Li, Y. Zhou, Q. Fu, J. Zhang, X. Wang and L. Zhan, *ACS Nano*, 2016, **10**, 2678–2692.

66 Kenry, Y. Duan and B. Liu, *Adv. Mater.*, 2018, **30**, 1802394.

67 G. Hong, S. Diao, J. Chang, A. L. Antaris, C. Chen, B. Zhang, S. Zhao, D. N. Atochin, P. L. Huang, K. I. Andreasson, C. J. Kuo and H. Dai, *Nat. Photonics*, 2014, **8**, 723–730.

68 A. Cifuentes-Rius, V. G. Deepagan, J. Xie and N. H. Voelcker, *ACS Appl. Mater. Interfaces*, 2021, **13**, 49581–49588.

69 L. Shang, S. Dong and G. U. Nienhaus, *Nano Today*, 2011, **6**, 401–418.

70 I. M. Khan, S. Niazi, L. Yue, Y. Zhang, I. Pasha, M. K. Iqbal Khan, W. Akhtar, A.

Mohsin, M. F. J. Chughati and Z. Wang, *Talanta*, 2022, **241**, 123228.

71 E. Porret, X. Le Guével and J. L. Coll, *J. Mater. Chem. B*, 2020, **8**, 2216–2232.

72 Y. Chen, D. M. Montana, H. Wei, J. M. Cordero, M. Schneider, X. Le Guével, O. Chen, O. T. Bruns and M. G. Bawendi, *Nano Lett.*, 2017, **17**, 6330–6334.

73 Y. Genji Srinivasulu, Q. Yao, N. Goswami and J. Xie, *Mater. Horizons*, 2020, **7**, 2596–2618.

74 B. Musnier, K. D. Wegner, C. Comby-Zerbino, V. Trouillet, M. Jourdan, I. Häusler, R. Antoine, J. L. Coll, U. Resch-Genger and X. Le Guével, *Nanoscale*, 2019, **11**, 12092–12096.

75 H. Liu, G. Hong, Z. Luo, J. Chen, J. Chang, M. Gong, H. He, J. Yang, X. Yuan, L. Li, X. Mu, J. Wang, W. Mi, J. Luo, J. Xie and X. Zhang, *Adv. Mater.*, 2019, **31**, 1901015.

76 D. Li, Q. Liu, Q. Qi, H. Shi, E. C. Hsu, W. Chen, W. Yuan, Y. Wu, S. Lin, Y. Zeng, Z. Xiao, L. Xu, Y. Zhang, T. Stoyanova, W. Jia and Z. Cheng, *Small*, 2020, **16**, 1–9.

77 W. Wang, Y. Kong, J. Jiang, Q. Xie, Y. Huang, G. Li, D. Wu, H. Zheng, M. Gao, S. Xu, Y. Pan, W. Li, R. Ma, M. X. Wu, X. Li, H. Zuilhof, X. Cai and R. Li, *Angew. Chemie - Int. Ed.*, 2020, **59**, 22431–22435.

78 C. Colombé, X. Le Guével, A. Martin-Serrano, M. Henry, E. Porret, C. Comby-Zerbino, R. Antoine, I. Atallah, B. Busser, J. L. Coll, C. A. Righini and L. Sancey, *Nanomedicine Nanotechnology, Biol. Med.*, 2019, **20**, 102011.

79 X. Song, W. Zhu, X. Ge, R. Li, S. Li, X. X. Chen, J. Song, J. Xie, X. X. Chen and H. Yang, *Angew. Chemie - Int. Ed.*, 2021, **60**, 1306–1312.

80 Y. Wei, W. Luan, F. Gao and X. Hou, *Part. Part. Syst. Charact.*, 2019, **36**, 1900314.

81 Z. Yu, H. Xiao, X. Zhang, Y. Yang, Y. Yu, H. Chen, X. Meng, W. Ma, M. Yu, Z. Li, C. Li and H. Liu, *ACS Nano*, 2020, **14**, 13536–13547.

82 S. M. van de Looij, E. R. Hebels, M. Viola, M. Hembury, S. Oliveira and T. Vermonden, *Bioconjug. Chem.*, 2022, **33**, 4–23.

83 Y. Peng, X. Huang and F. Wang, *Chem. Commun.*, 2021, **57**, 13012–13015.

84 Y. Zheng, J. Wu, H. Jiang and X. Wang, *Coord. Chem. Rev.*, 2020, **431**, 213689.

85 L. Tang, X. Zeng, H. Zhou, C. Gui, Q. Luo, W. Zhou, J. Wu, Q. Li, Y. Li and Y. Xiao, *Chem. Res. Chinese Univ.*, 2021, **37**, 934–942.

86 Q. Chen, J. Chen, Z. Yang, L. Zhang, Z. Dong and Z. Liu, *Nano Res.*, 2018, **11**,

5657–5669.

87 Y. Kong, D. Santos-Carballal, D. Martin, N. N. Sergeeva, W. Wang, G. Liu, B. Johnson, B. Bhayana, Z. Lin, Y. Wang, X. Le Guével, N. H. de Leeuw, D. Zhou and M. X. Wu, *Mater. Today*, 2021, **51**, 96–107.

88 K. He, S. Yu, X. Wang, D. Li, J. Chen, H. Zhong, Q. Xu, Y. X. Wu and N. Gan, *Chem. Commun.*, 2021, **57**, 10391–10394.

89 C. Wang, Y. Yao and Q. Song, *J. Mater. Chem. C*, 2015, **3**, 5910–5917.

90 Y. Liu, G. F. Tian, X. W. He, W. Y. Li and Y. K. Zhang, *J. Mater. Chem. B*, 2016, **4**, 1276–1283.

91 X. Chen, H. Zhu, X. Huang, P. Wang, F. Zhang, W. Li, G. Chen and B. Chen, *Nanoscale*, 2017, **9**, 2219–2231.

Chapter 7
Multifunctional gold nanoclusters for effective targeting, near-infrared fluorescence imaging, diagnosis, and treatment of cancer lymphatic metastasis

7.1 Introduction

Over the past 50 years, tumour metastasis has been the leading cause of mortality in cancer patients,[1] [2] responsible for about 90% of cancer-related death worldwide.[3] [4] Tumor metastasis normally begins from LNs closest to a tumour.[5] [6] Cancer cell diffusion through LNs, especially for highly metastatic cancer types, such as melanoma or breast cancer, is key to cancer metastasis.[7] Thus, lymphatic-based tumour imaging is vital for diagnosing tumour progression[8] and guiding LN removal to control the spread of metastasis.[9] [10] Current clinical LN metastasis imaging materials are limited to preoperative contrast agents, such as ^{99m}Tc complex and small organic dyes (isosulfan blue, indocyanine green (ICG), etc.).[11] However, these agents have several drawbacks, including biosafety issues, non-real-time imaging, short half-life *in vivo,* and being prone to photobleaching. Moreover, the combined application of two imaging reagents does not offer any advantage over each individual agent.[12] Furthermore, decorating drug molecules onto such imaging agents often requires complicated chemical synthesis, which can also compromise the effectiveness of both components. Thus, there is an urgent need for an effective, biocompatible fluorescence platform that can offer stable real-time bioimaging of LNs for diagnosis and imaging-guided surgery of cancer metastasis.[9] [13] [14] Additionally, it would be highly beneficial to integrate imaging-guided diagnosis and treatment of tumour metastasis simultaneously.

Gold nanomaterials have been widely used in biomedical applications owing to their

size tunability, good biocompatibility, and versatile gold-thiol chemistry for easy surface modification and functionalization.[15–19] Recently, GNCs have emerged as a highly attractive, versatile tool for biological and biomedical applications owing to their high stability, low toxicity, and facile preparation.[20–23] Moreover, their highly stable fluorescence in the NIR-II region of the biological window (*e.g.,* 1000–1400 nm) makes it a powerful NIR-II fluorescence bioimaging agent.[24–27] Indeed, NIR-II fluorescent GNCs have been employed for bone imaging,[28] tumour diagnosis,[29 30] angiography,[31] and LN imaging.[32] However, most of such GNCs are capped by a single type of thiolated ligand, which has highly limited their applications. In addition, the physiological environment in organisms is extremely complex, and these single ligand GNCs cannot satisfy the requirement for effective use *in vivo*. Specifically, for LN access, negatively charged GNCs must migrate through the interstitium space, which is filled with intertwined collagen fibres and negatively charged glycosaminoglycan (mainly hyaluronic acid) matrix.[33–35] Therefore, too high or too low a surface charge can lead to either undesirable nonspecific accumulation or rapid elimination through renal clearance.[36–38] Thus, finding the optimal charge density is key to effective LN accumulation, but this is extremely difficult to achieve with GNCs capped with a single type of ligand. Hence, coating GNC with two or multiple functional ligands is necessary to enable suitable surface properties for effective LN bioimaging, surgical guidance and treatment of LN metastasis.

In this study, I synthesized dual-/tri-ligand-capped NIR-II fluorescent $Au_{25}(SR_1)_x(SR_2)_{18-x}$-type GNCs for both LN imaging and treatment of lymphatic metastasis. For LN imaging, I fine-tuned the surface charge density by varying the feed ratio of the anionic (*e.g.,* mercaptoundecanoic (MUA), mercaptoundecylphosphonic (MUP), and mercapto-undecylsulfonic (MUS) acid) to a neutral alkylthiolated zwitterionic ligand (C5) during the GNC synthesis.[39 40] By optimizing the anionic/zwitterionic ligand ratio, I achieved effective accumulation within LNs and produced high-contrast fluorescence images for

LN metastatic diagnosis and surgical guidance without targeting molecules. Based on the imaging result, I synthesized triligand GNC loaded with methotrexate (MTX), a common chemotherapy drug, to investigate the potential of GNC in LN targeted drug delivery to alleviate the side effects of free drugs.[41] Animal experiments confirmed the lymphatic delivery ability of this GNC by offering an excellent therapeutic effect against cancer metastasis with dramatically reduced side effects on the liver and kidneys compared to free MTX.

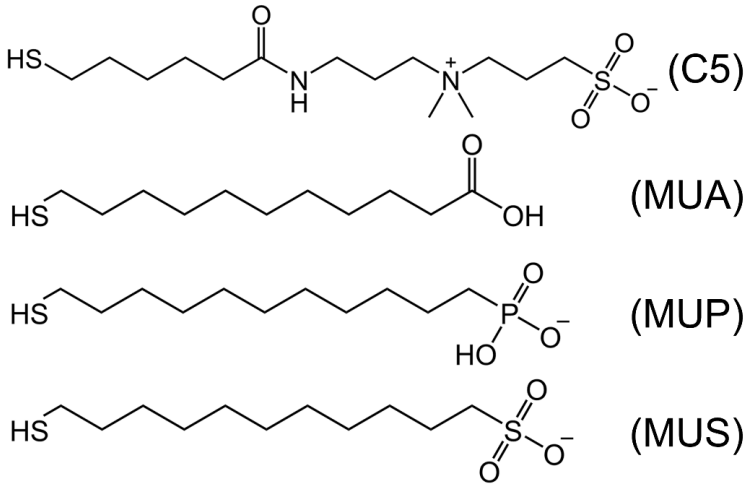

Figure 7.1.1 Chemical structures of all the ligands used in this Chapter.

7.2 Synthesis and characterisation of $Au_{25}(SR_1)_x(SR_2)_{18-x}$-type GNCs

First, I synthesized GNCs capped with single thiolated ligands (MUA, MUP, MUS, or C5) and monitored their ultraviolet-visible (UV–vis) spectra. The mono-ligand-capped GNCs showed prominent characteristic absorption peaks of $Au_{25}(SR)_{18}$-type GNC at ~695 and 790 nm (**Figure 7.2.1**).[42]

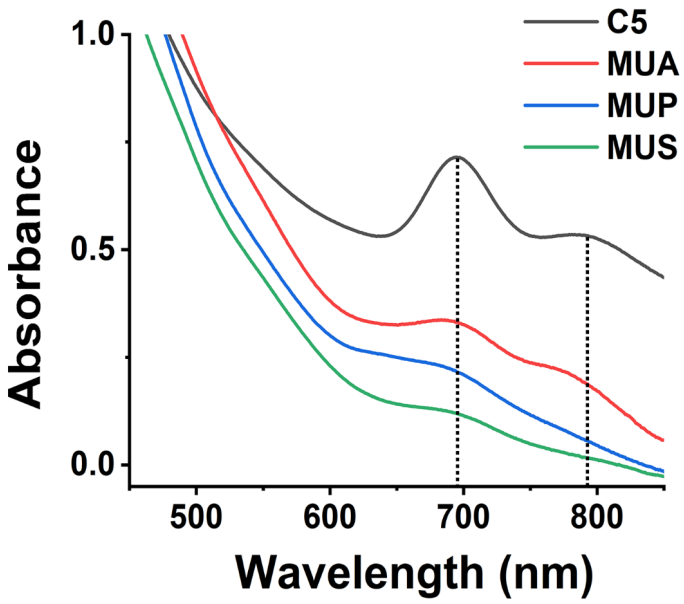

Figure 7.2.1 UV–vis spectra of GNCs prepared with 100% neutral-charge alkylthiolated zwitterionic ligand (C5), mercaptoundecanoic (MUA), mercaptoundecylphosphonic (MUP), and mercaptoundecylsulfonic (MUS) ligands. All samples show characteristic peaks of $Au_{25}(SR)_{18}$ GNC (marked with dotted lines).

We analyzed the molecular weight (MW) of the mono-ligand-capped GNCs by electrospray ionization mass spectrometry (ESI-MS). The clustered MS peaks indicate the presence of $Au_{25}(SR)_{18}$ GNCs, and the calculated mass matches the theoretical MW with charges (**Table 17**).[43]

Table 17 Comparison of the theoretical and observed MWs (plus charge) of fully-C5, MUA, MUP, and MUS capped GNCs

The GNC structure	Theoretical GNC MW (*Da*)	Observed GNC MW (*Da*)
Au_{25} $(C5)_{18}$	11281.88	11380.95 (3 e^-) 11416.94 (4 e^-)
Au_{25} $(MUA^-)_{18}$	8819.48	8853.48 (5 e^-) 8875.50 (4 e^-)
Au_{25} $(MUP^-)_{18}$	9719.12	9732.34 (6 e^-) 9754.32 (5 e^-)
Au_{25} $(MUS^-)_{18}$	9720.56	9853.10 (8 e^-)

The fluorescence spectra of the GNCs were also measured (**Figure 7.2.2**)[26], and they showed a similar shape with a maximum emission peak at 1000–1100 nm, which fell within the NIR-II optical transmission window (1000–1700 nm) of tissue under 808-nm laser excitation.[29]

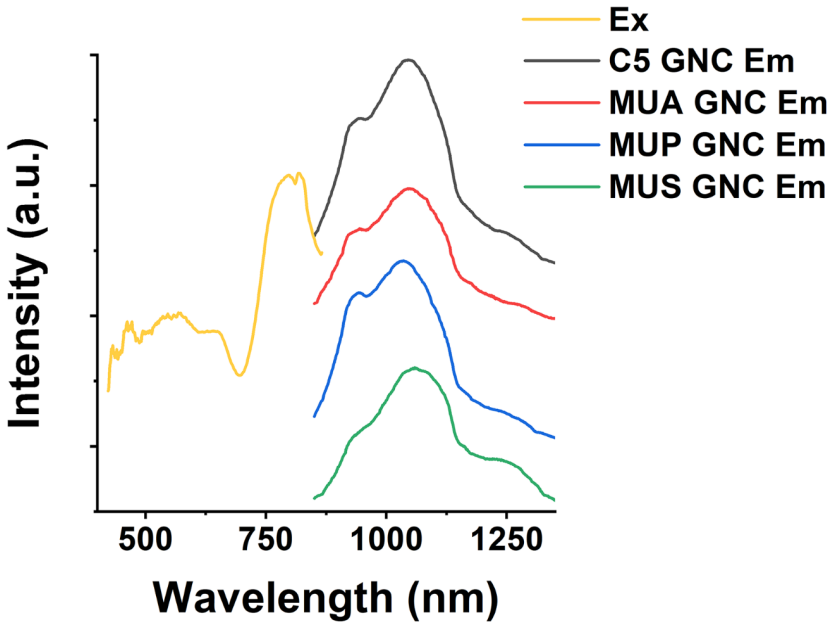

Figure 7.2.2 NIR-II region fluorescence excitation and emission spectra of GNCs capped with 100% C5, MUA, MUP, or MUS ligands. The maximum emission peak for all GNCs is similar and consistent with that of $Au_{25}(SR)_{18}$-type GNC.

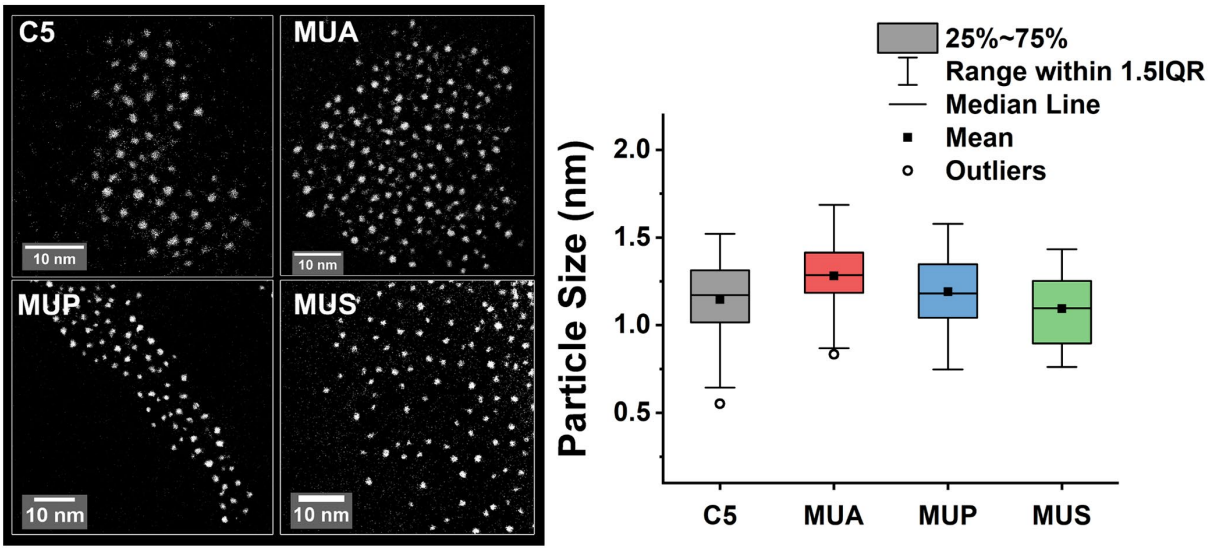

Figure 7.2.3 DSAC-TEM images (left) and box chart (right) of particle sizes for C5-, MUA-

, MUP-, and MUS-capped GNCs. The sizes for the GNCs capped with different ligands are similar, with an average diameter of ~1.2 nm.

DSAC-TEM images with a high-angle ring dark-field detector (HADDF)-STEM mode revealed an average diameter of ~1.2 nm for GNCs capped with different ligands (**Figure 7.2.3**). These results show that $Au_{25}(SR)_{18}$ GNCs capped with 100% of C5, MUA, MUP, or MUS with similar size and optical properties were successfully synthesized, providing a basis for subsequent synthesis of dual-ligand-capped GNCs. I further tuned the feed ratio of MUA, MUP, and MUS to C5 to prepare various dual-ligand-capped GNCs. All mixed-ligand-capped GNCs showed the same characteristic UV–vis absorption peaks as the mono-ligand-capped ones.

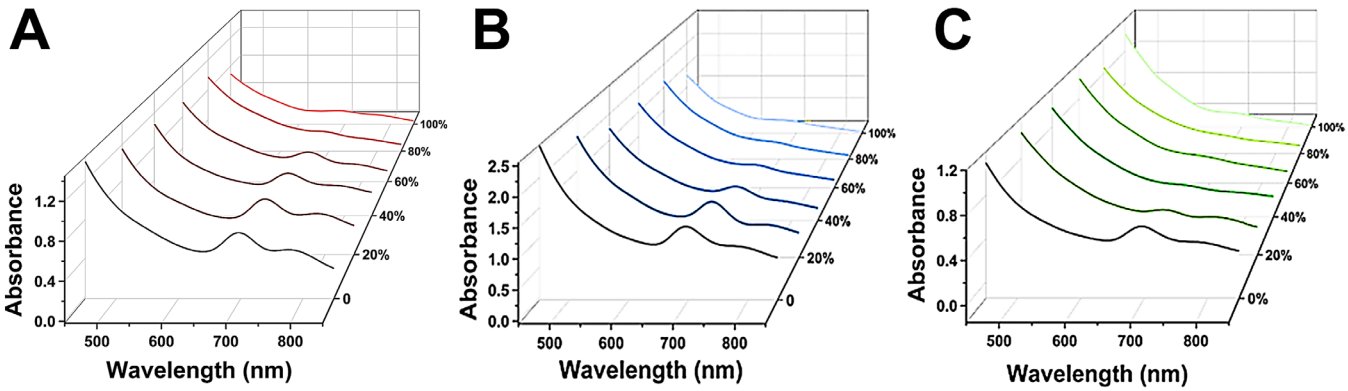

Figure 7.2.4 Representative UV–vis spectra of $Au_{25}(SR_1)_x(SR_2)_{18-x}$ GNCs prepared with an increasing ratio of (A) MUA, (B) MUP, and (C) MUS ligands to C5. The curve gradually becomes smoother with the increasing MUA proportion.

Increasing the feed ratio of the negatively charged ligand reduced the intensity of the UV–vis characteristic peak of the four groups at ~690 nm (**Figure 7.2.4**) and also reduced the GNC NIR fluorescence brightness under the same laser excitation (**Figure 7.2.5**).

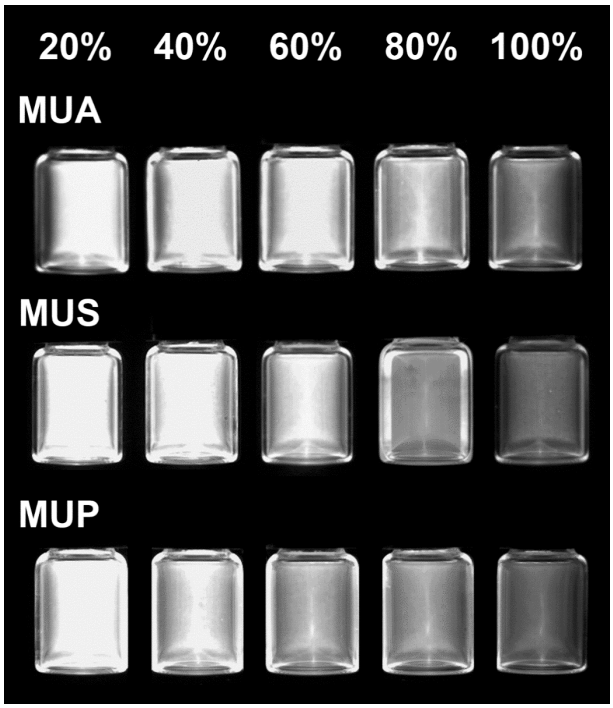

Figure 7.2.5 NIR-II fluorescence images of dual-ligand GNCs prepared with the increasing percentages of the anionic ligands (*e.g.,* MUA, MUS, or MUP) in feeding. It reveals that increasing the negatively charged ligand ratio decreases the fluorescence property of the resulting dual-ligand GNCs. (5 ms, 20 mW cm^{-2})

Table 18 Primary and secondary configurations of GNCs prepared with different MUA feed ratios.

MUA ligand proportion in feeding (%)	**Primary product $[Au_{25}(MUA)_x(C5)_{18-x}]$ (MUA/C5)**	**Secondary product(s) $[Au_{25}(MUA)_x(C5)_{18-x}]$ (MUA/C5)**
0	0/18	–
20	9/9	10/8 & 8/10
40	10/8	11/7 & 9/9
60	13/5	12/6 & 14/4
80	16/2	15/3
100	18/0	–

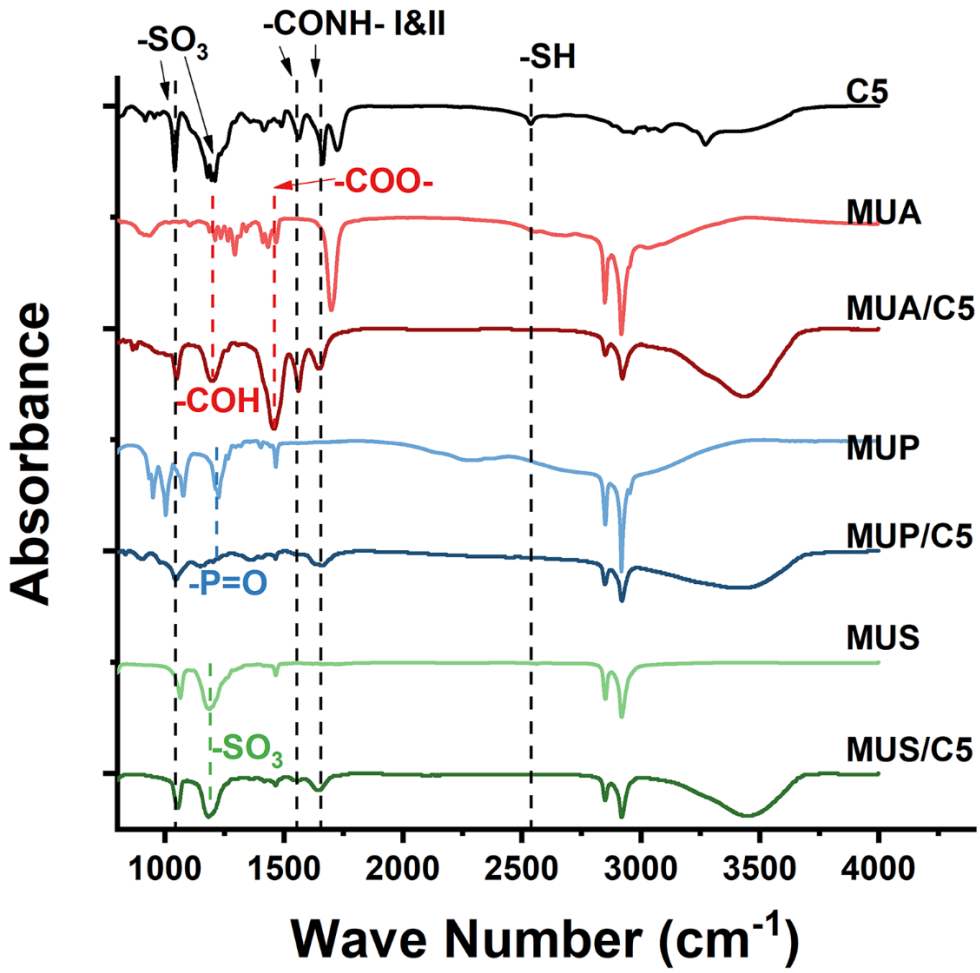

Figure 7.2.6 FTIR spectra of mono-ligand and dual-ligand-capped GNCs. The spectra confirm the coexistence of the corresponding negatively charged ligands and C5 on the GNC surface.

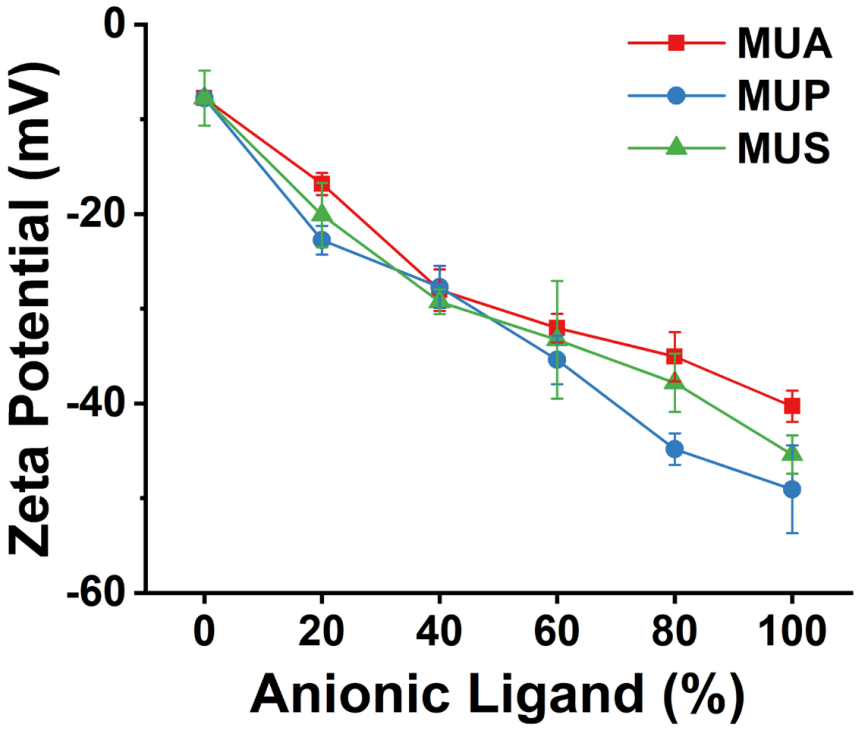

Figure 7.2.7 GNC zeta potential versus anionic ligand feed percentage. The zeta potential of GNCs shifts to more negative as the proportion of the negatively charged ligand increases, confirming that the ligands were effectively capped on the GNC surface (pH = 7).

This phenomenon is similar to that reported by Aldeek et al.[44] Considering this, the fluorescence intensity of each GNC was normalized and adjusted in subsequent experiments to facilitate a direct comparison of GNC content. ESI-MS tests were conducted to confirm the configuration of the $Au_{25}(SR_1)_x(SR_2)_{18-x}$-type GNCs with different feed ratios. MW calculations and analysis showed that MUA has a higher binding affinity to gold kernels than C5, where a 20% feed of MUA has replaced half of the GNC surface C5 ligands (**Table 18**). Fourier transform infrared (FTIR) spectroscopy confirmed that different ligands were successfully incorporated onto the GNCs, and the GNCs showed characteristic infrared absorption peaks of the corresponding MUA, MUP, or MUS peaks of the corresponding free ligands. Meanwhile, the S-H peak at ~2500 nm completely disappeared, confirming the transformation of the free thiol ligand into Au–S bonds (**Figure 7.2.6**).[45] In addition, with an increase in the feed ratio of the anionic

ligands, the zeta potential of the resulting dual-ligand GNCs became progressively more negative, thus providing a charge density gradient for screening the charge-dependent bioaccumulation (Figure 7.2.7).

7.3 Optimizing the ligand feed ratios of the LN targeting ability of GNCs

7.3.1 Intravenous injection results

To study the biodistribution of the anionic- and zwitterionic-ligand-decorated GNCs after parenteral administration, I injected the synthesized GNCs into mice through the tail vein to achieve a fast whole-body distribution. After intravenous injection (I.V.), I anaesthetized the mice and used a NIR-II animal imager to photograph the supine and prone positions of the mice at different time points for 6 h, taking full advantage of the NIR-II fluorescence of the GNCs. I studied the distribution of 100% C5 ligand-capped GNC *in vivo* (Figure 7.3.1). Besides functioning as a charge-neutral ligand in adjusting surface negative charge density, C5 can provide nanomaterials with excellent non-fouling properties owing to the formation of strong hydration layers induced by its zwitterionic sulfobetaine terminal group.[46] [47] Thus, fully zwitterionic-ligand-decorated GNCs should have minimal protein corona formation. Because of their small size, as revealed by transmission electron microscopy (TEM), to be well below the renal clearance threshold (~6.4 nm),[48] [49] they showed rapid renal clearance with a short retention time. Consistent with this, strong NIR-II fluorescence was observed in the bladder shortly after I.V., and the signal faded rapidly in other body parts. One hour after injection, the fluorescence level of the whole body decreased greatly, leaving only faint signals in the liver and kidneys. Subsequently, the biodistribution of GNCs prepared using mixed C5 and MUA ligands with the MUA feed ratio ranging from 0% to 100% was studied (Figure 7.3.1).

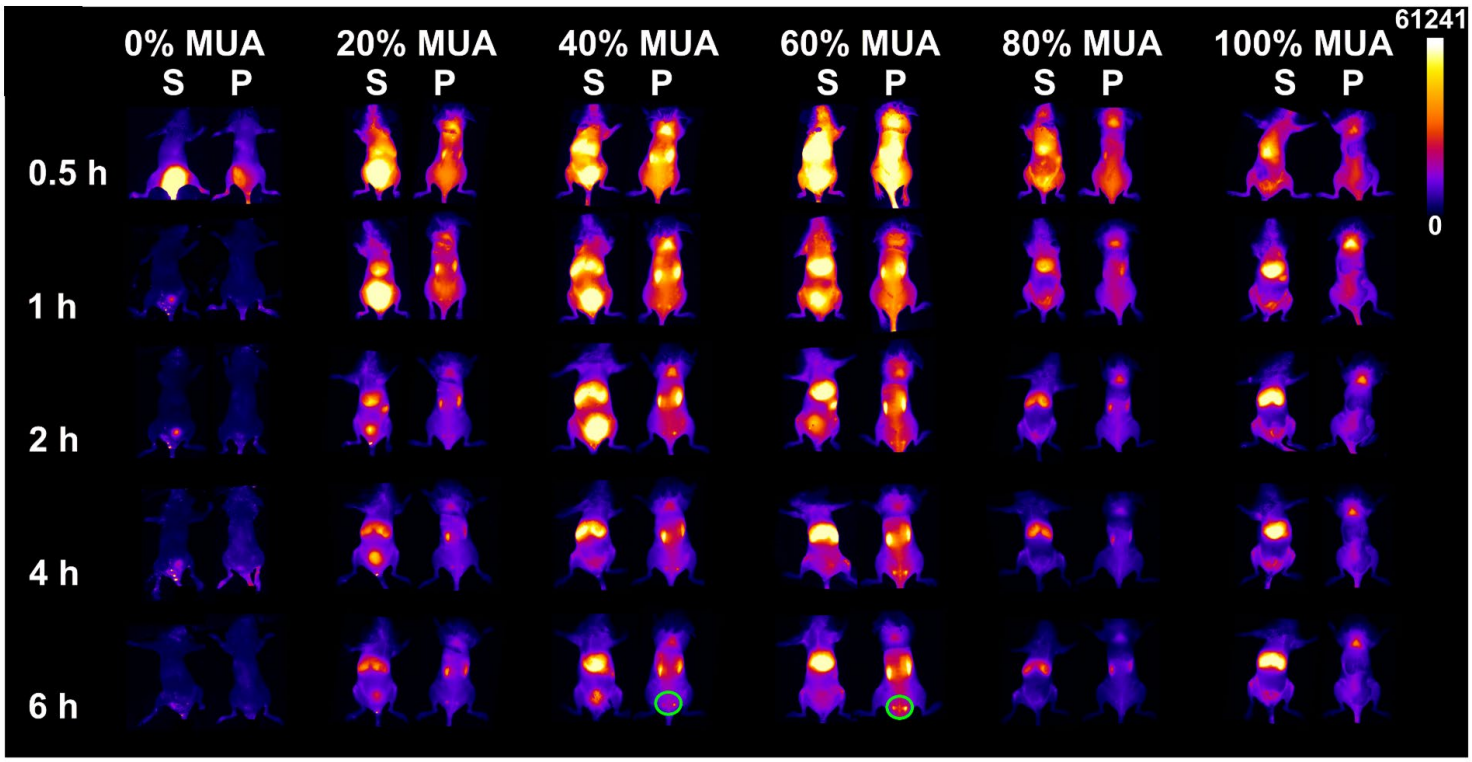

Figure 7.3.1 Time- and MUA-feed-ratio-dependent NIR-II fluorescence image showing *in vivo* distribution of GNCs in mice after intravenous injection of GNC (5 mg kg^{-1}) for 6 h (S: supine position, P: prone position, the same as below). Dual-ligand-capped GNCs with 40%–60% MUA were effectively accumulated in the LNs located in the sciatic area (labelled with green oval, 30 ms, 20 mW cm^{-2}).

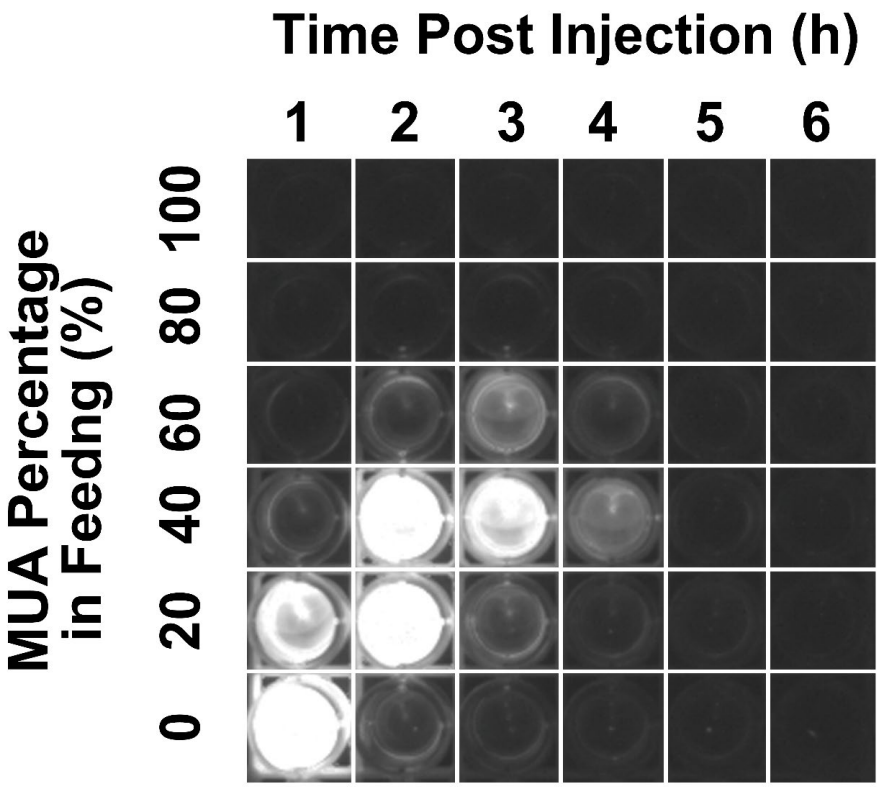

Figure 7.3.2 NIR fluorescence images of urine samples collected at each hour after intravenous administration of 5 mg kg^{-1} MUA-C5-capped GNCs under different MUA percentages in feeding. The renal clearance duration obtained here is consistent with *in vivo* fluorescence imaging shown in Figure 7.3.1 (n = 3).

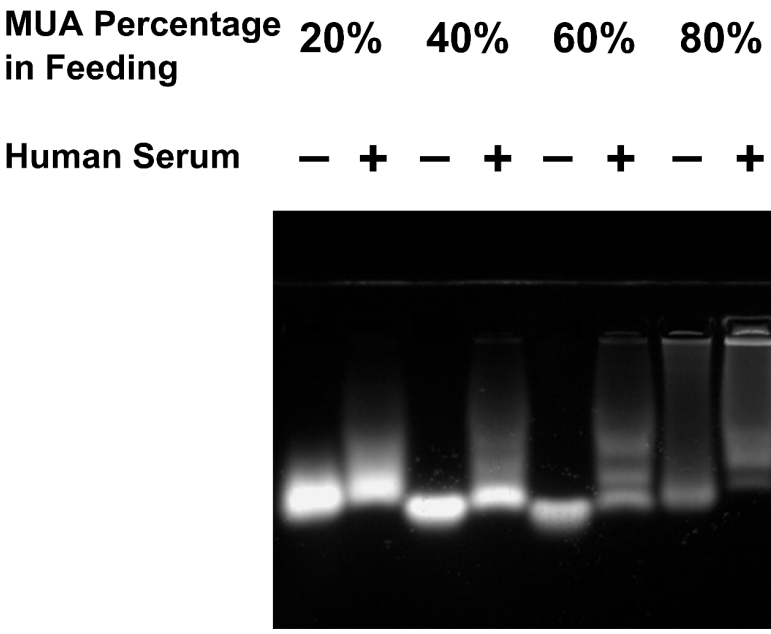

Figure 7.3.3 Agarose gel electrophoresis outcome of GNCs prepared with 20%—80%

MUA ligand in feeding before and after mixing with human serum. The electrophoresis results of serum-mixed samples showed an obvious tailing phenomenon, which also became more pronounced as the MUA ligand percentage increased, indicating significant interactions with serum proteins.

Comparing the results, I could draw a unified relationship between anionic ligand percentage in feeding and the renal clearance time. For example, as the MUA ligand feed ratio increased from 0% to 20%, the retention time of the resulting GNC increased slightly. The renal clearance time increased to approximately 2 h, accompanied by a slightly higher liver and kidney accumulation. However, due to the relatively low MUA content, the behaviour of the GNC was still similar to that of pure C5-capped GNC. Surprisingly, as the MUA ligand feed ratio increased from 40% to 60%, an apparent fluorescence signal appeared in the LN 2 h after injection (indicated by an intense signal in the sacral part of the prone position), confirming the high lymphatic accumulation of GNCs capped with mixed C5 and MUA ligands over a certain ligand ratio range. However, lymphatic accumulation was not observed for GNCs with MUA feed ratios greater than 60%, and the GNCs were mainly retained in the liver and spleen, indicated by prominent fluorescence in these organs. Urine samples collected every hour after the I.V. agree well with the renal clearance results of NIR imaging, which indicate fluorescence in the bladder (Figure 7.3.2). The GNP size *in vivo* is highly related to the negative charge density on the surface, which could be explained by the protein corona formation.[36] Thus, the ability of dual-ligand-capped GNCs with 40%–60% MUA in feeding to accumulate within LNs is attributed to the anionic-charge-induced size change *in vivo*. To illustrate the influence of negative charge density on the size of GNCs, I carried out an electrophoresis study of GNCs with different MUA ratios. Comparing the gel mobility of GNCs with/without human serum, I found that the GNC band gap became wider, and the tailing effect became more obvious with the increase of the MUA ratio. This result indicates that the MUA capping is responsible for the nonspecific interactions of GNCs with serum proteins, most likely due to electrostatic

interactions. The strength of the interaction increased with the increasing MUA feed ratio, leading to extensive protein corona formation on GNCs to increase their overall size (**Figure 7.3.3**). In previous studies, organ distribution tropism was achieved by tuning the overall charge of lipid nanoparticles (NPs).[50] Moreover, the size of lipid NPs was found to significantly affect their LN distribution ability, with smaller (~30 nm) lipid NPs offering higher accumulation efficiency within LNs.[51] In addition, studies on GNC renal clearance have shown that an increase in the size of GNCs drastically affected the renal clearance efficiency due to excess glomerular barriers, which explains the reduction in renal clearance and increased accumulation in LNs observed herein.[52] As the size of the GNC-protein corona complex increased with the increasing anionic charges, the *in vivo* clearance was shifted from the urinary to hepatic pathway, accompanied by reduced distribution within LNs.[53] Thus, a balance of clearance and LN distribution can be achieved by tuning the feed ratio of the anionic and zwitterionic ligands in the GNC preparation.

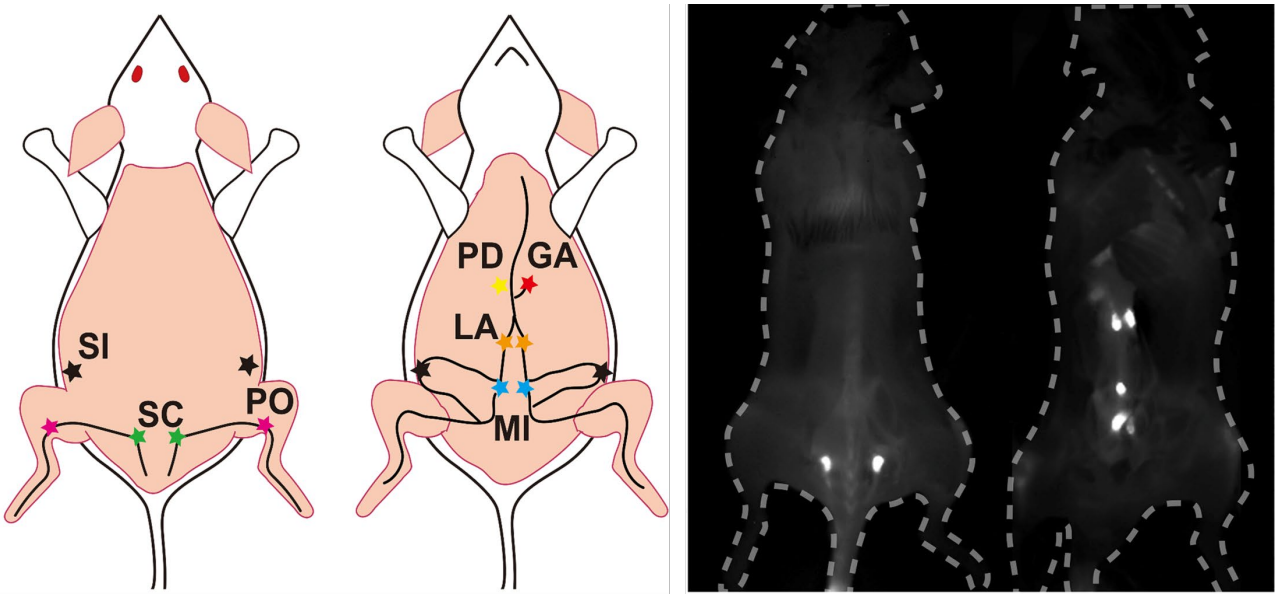

Figure 7.3.4 (Left figure) Diagram of the lower-body LN distribution of mice. Different groups of LNs are marked with different colours. GA: Gastric LN; LA: Lumbar aortic LN; MI: Medial iliac LN; PD: Pancreaticoduodenal LN; PO: Popliteal LN; SC: Sciatic LN; SI: Sub iliac LN. (Right figure) NIR-II fluorescence image demonstrating the accumulation of

GNCs within lower-body LNs of mice. 6-h after I.V. of GNC capped with 50% MUA ligand (and 50% zwitterionic C5 ligands) under 808-nm NIR-laser irradiation, GNCs accumulated in LNs near the spine. Even for gastric LNs far away from the injection site, GNCs still accumulate to give a strong fluorescence contrast that can be used to guide surgical resection (left body: prone position; right body: supine position; 20 ms, 20 mW cm^{-2}).

The hind limbs of the mouse have abundant lymphatics and LNs, including popliteal, sciatic, inguinal, lumbar, gastric, and iliac LNs (**Figure 7.3.4**).[54–57] I conducted anatomy and found that fluorescence signals appeared not only in LNs close to the injection site, such as sciatic LNs (first-draining) but also in remote ones, such as gastric LNs. The absolute QY of GNC prepared with 50% MUA in feeding was 1.48%, which is higher than that of most current NIR-II GNC probes and comparable to that of some NIR emitting small molecular dyes.[28 30 58] Moreover, the average signal-to-background ratio was ~60 in the LN region. This high-contrast fluorescence signal in the lymphatic region is extremely beneficial for noninvasive diagnosis and imaging-guided surgeries. Further, I compared the LN accumulation of MUP- and MUS-incorporated GNCs with varying feed ratios of C5 (**Figure 7.3.5** and **Figure 7.3.6**). However, neither the MUS- nor MUP-capped GNCs showed significant accumulation in LNs, as supported by a much lower fluorescence signal than MUA-GNCs. This result reveals that the LN-accumulating property of GNCs depends not only on the density but also on the type of negatively charged groups decorated on its surface.

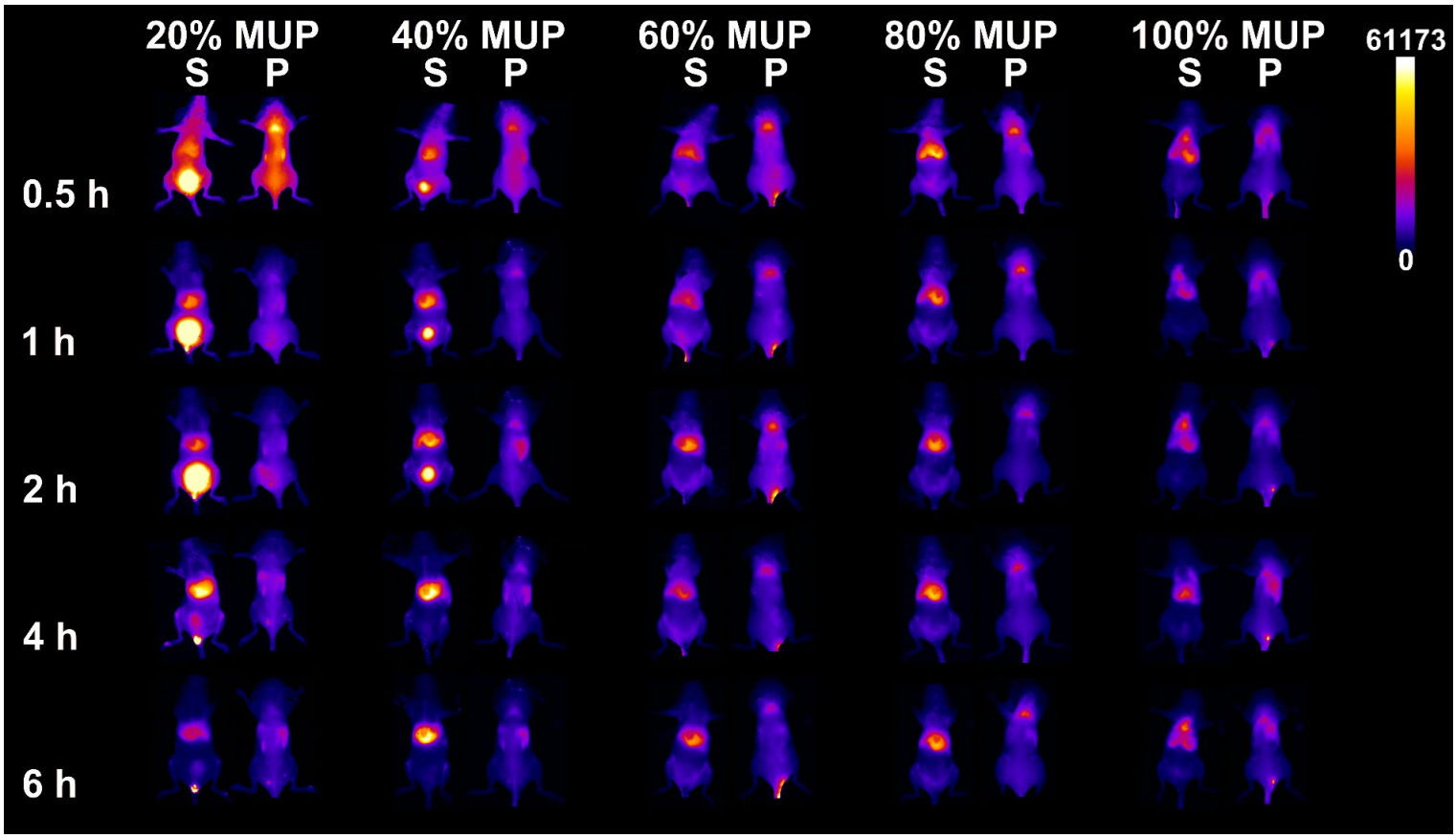

Figure 7.3.5 *In vivo* distribution of MUP-C5 dual-ligand-capped GNCs with different feed ratios after intravenous injection throughout 6 h (left: supine position, right: prone position, same below). No significant accumulation in LNs is observed, a sharp contrast to the result of MUA-GNC (30 ms, 20 mW cm^{-2}).

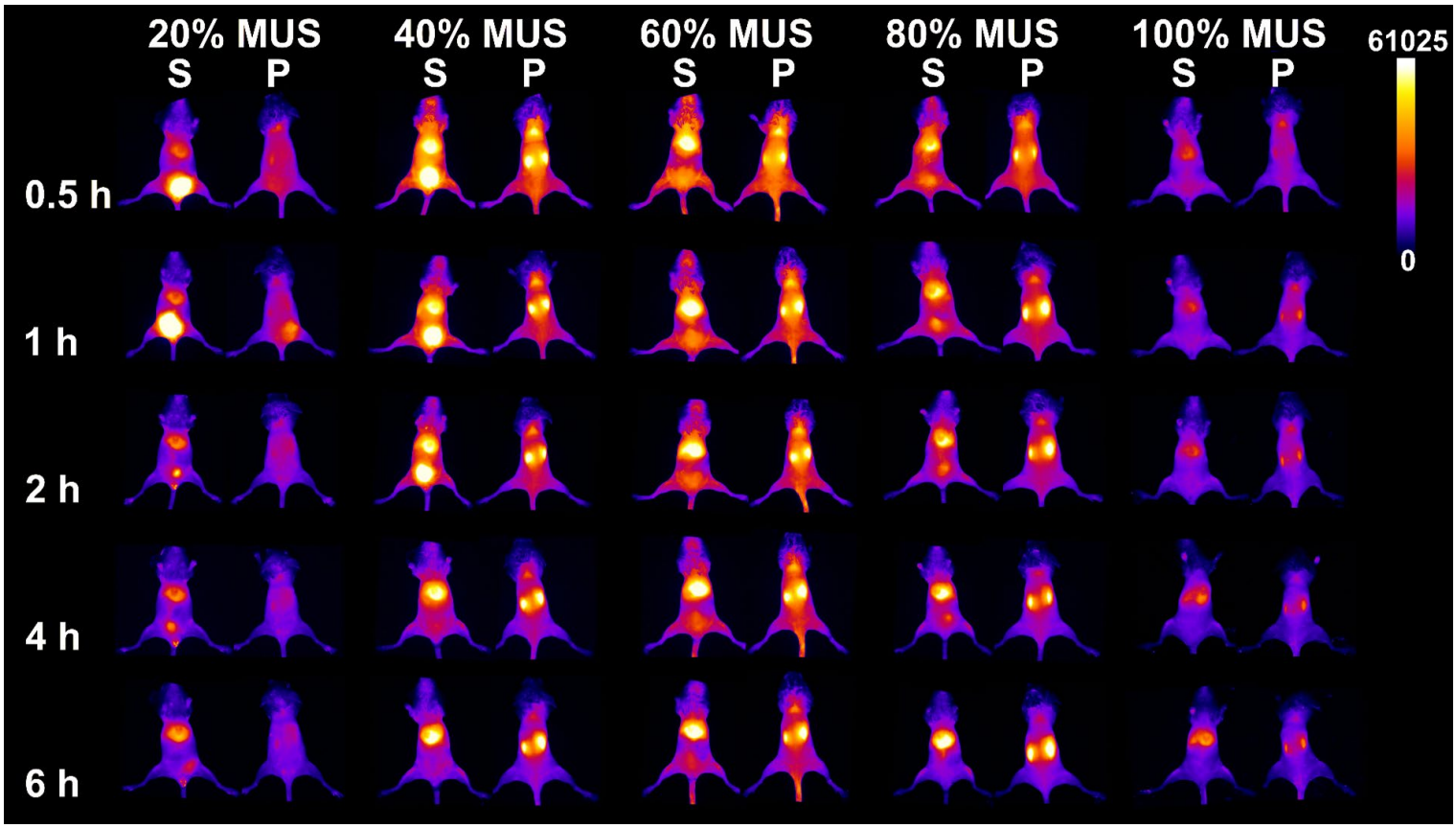

Figure 7.3.6 *In vivo* distribution of MUS-C5 dual-ligand-capped GNCs with different feed ratios after intravenous injection throughout 6 h (left: supine position, right: prone position, same below). No significant accumulation in LNs is observed, a sharp contrast to the result of MUA-GNC (30 ms, 20 mW cm^{-2}).

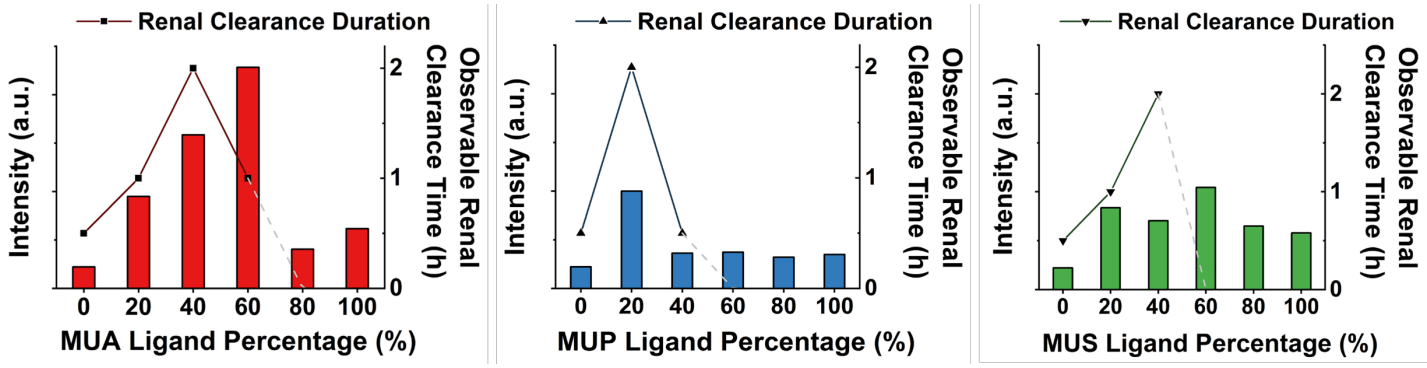

Figure 7.3.7 Plot of the GNC fluorescence intensity in sciatic LNs and renal clearance time against the anionic ligand feed ratio for MUA (red)/MUP (blue)/MUS (green).

We plotted the renal clearance duration and LN fluorescence intensity 6 h after administration against the ligand doping ratio (Figure 7.3.7). There was a tradeoff

between the GNC lymphatic accumulation and its renal clearance time, controlled by the anionic ligand species and feed ratio (*i.e.,* the negative charge density).[17 59] This result implies that fine-tuning the negative charge density of the GNC surface could lead to an effective lymphatic targeting probe. Moreover, ligands carrying a weakly ionizing carboxylic acid group outperformed those carrying strong negative charges, such as MUS and MUP ligands.[60]

7.3.2 Footpad injection results

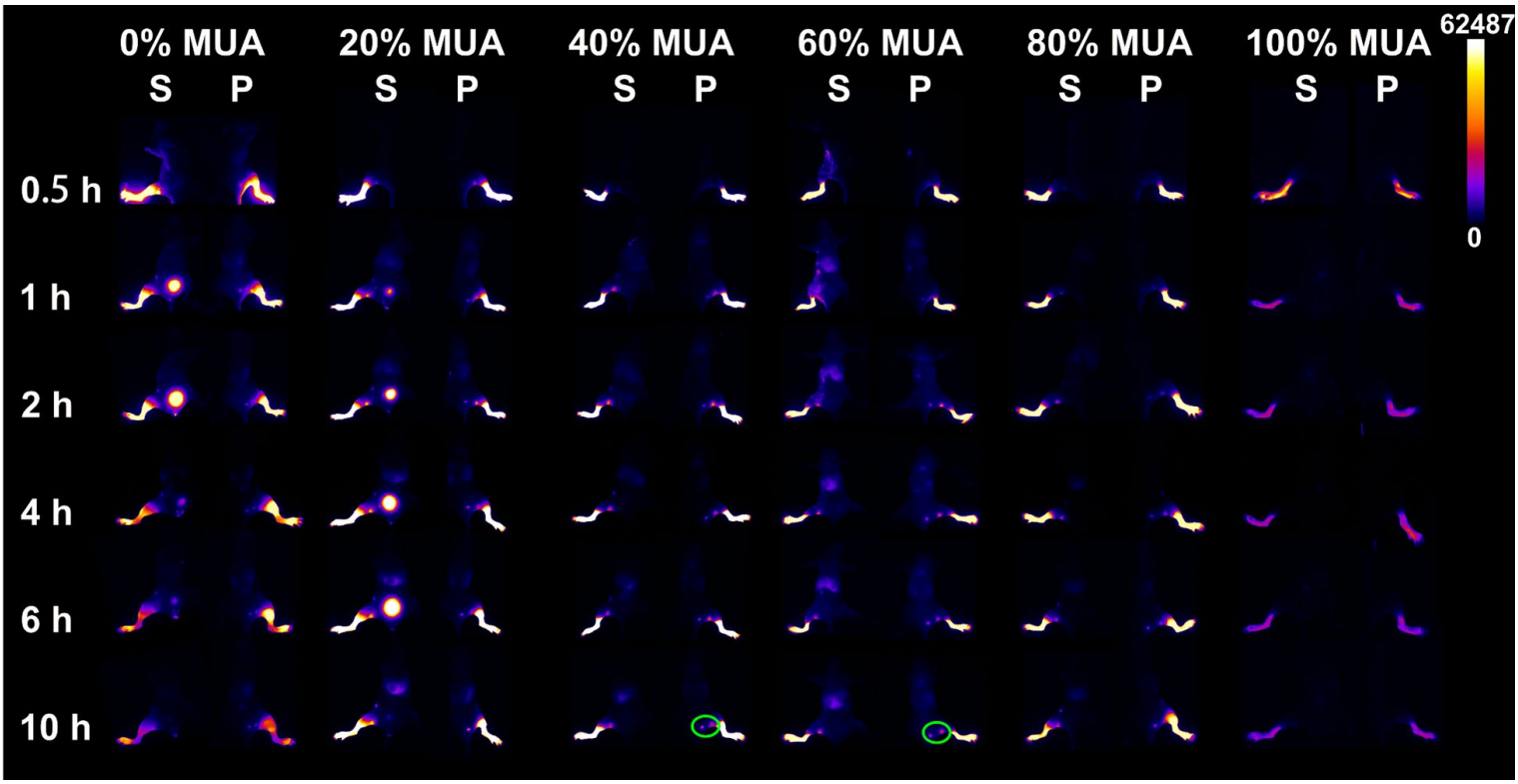

Figure 7.3.8 NIR-II fluorescence images showing the distribution of dual-ligand-capped GNCs with different ratios of MUA after F.P. injection for 10 h. GNCs prepared with less than 20% MUA in feeding showed renal clearance times of up to 6 h. GNCs with 40%–60% MUA in feeding displayed a high retention rate in popliteal and sciatic LNs (labelled with green oval, S: supine position; P: prone position; the same as below. 25 ms, 20 mW cm^{-2}).

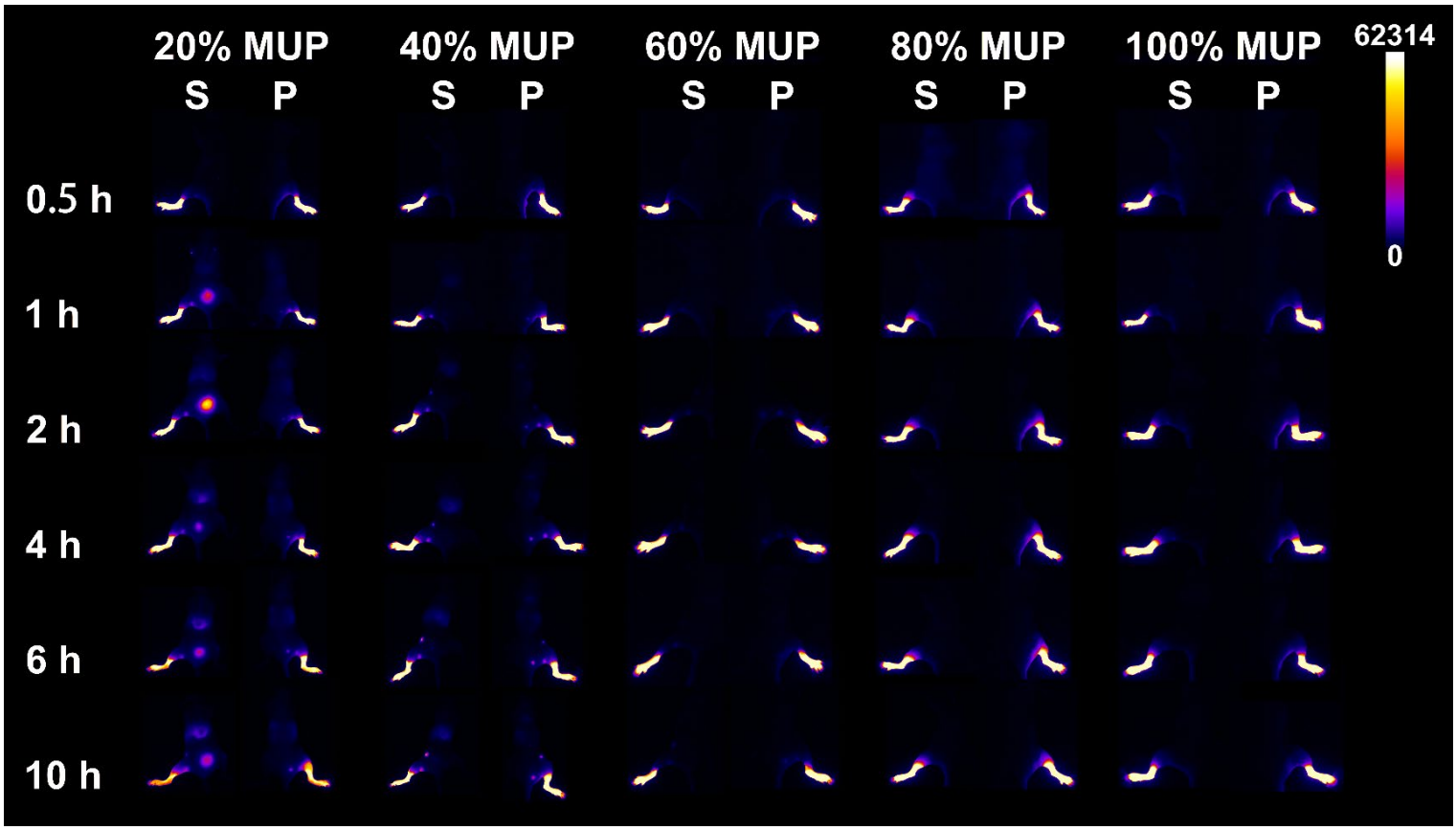

Figure 7.3.9 NIR-II fluorescence image of mice after footpad administration of dual-ligand GNCs prepared under different feed ratios of MUP (25 ms, 20 mW cm^{-2}). The accumulation in popliteal LN is also observed, although the fluorescence intensity is lower than that of MUA-GNCs.

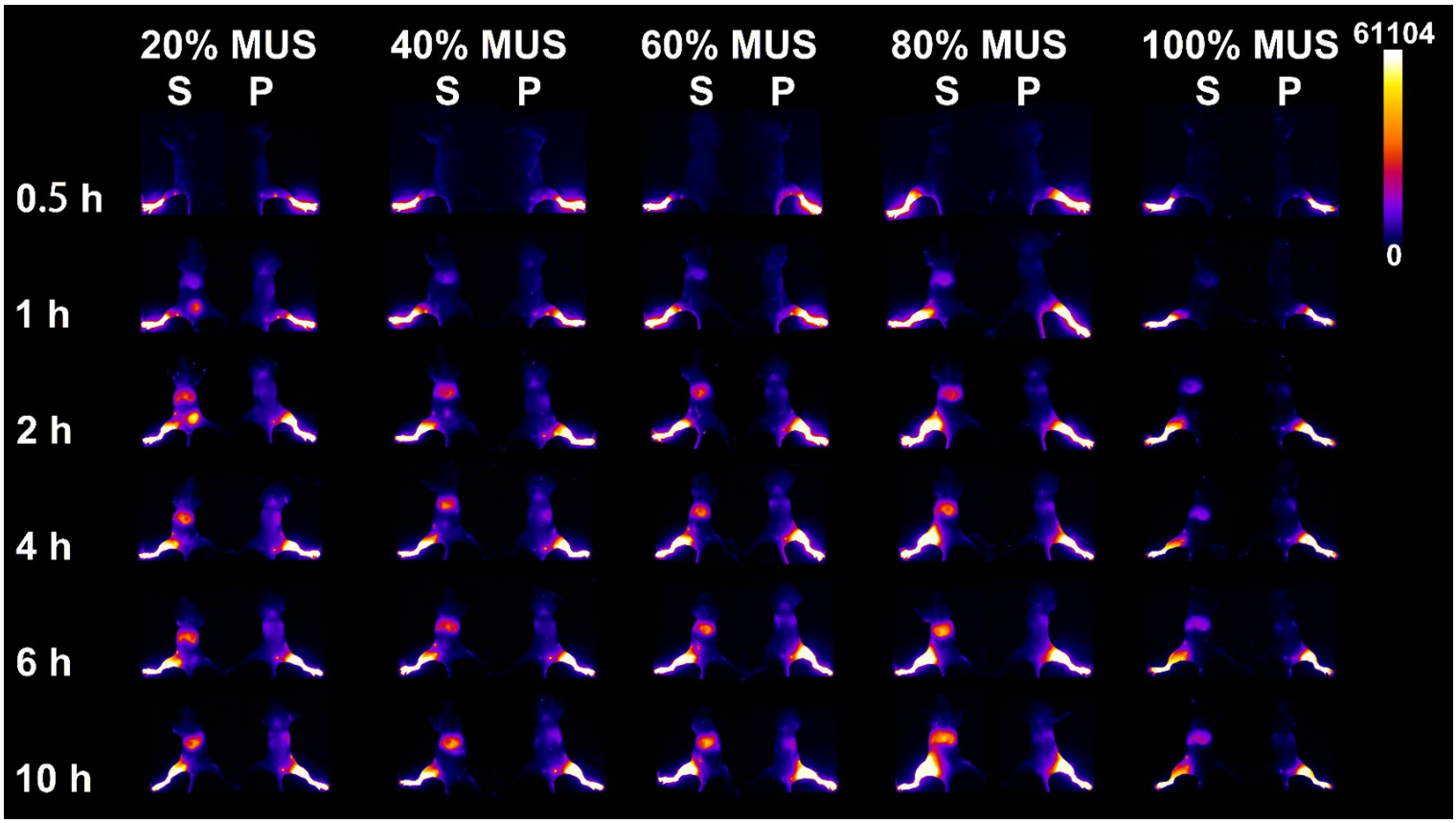

Figure 7.3.10 NIR-II fluorescence image of mice after footpad administration of dual-ligand GNCs prepared under different feed ratios of MUS (25 ms, 20 mW cm^{-2}). The accumulation in popliteal LN is also observed, although the fluorescence intensity is lower than that of MUA-GNCs.

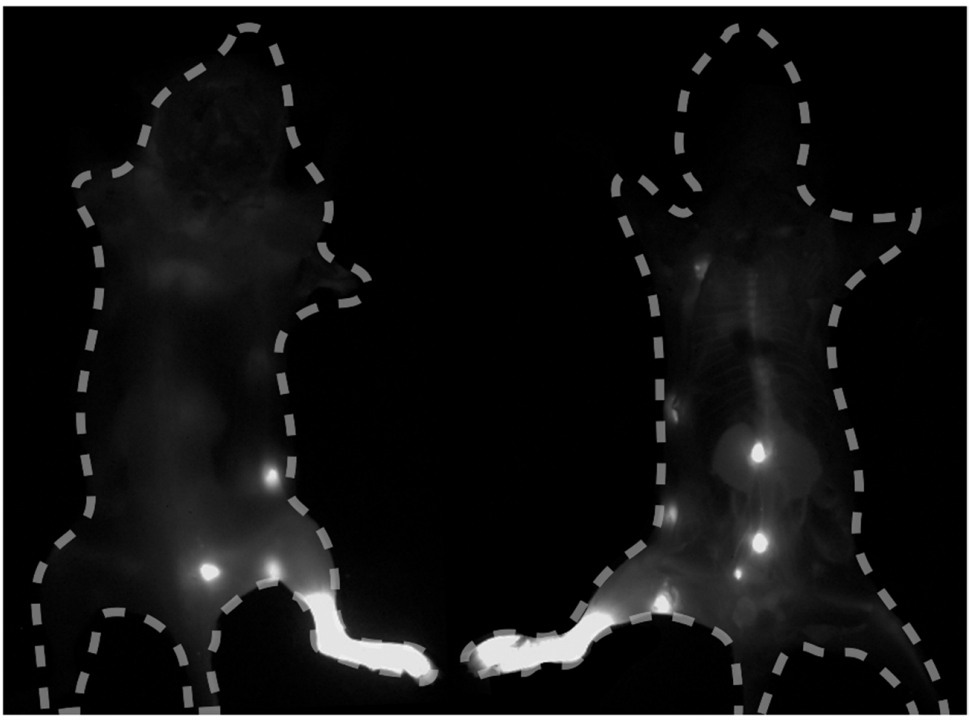

Figure 7.3.11 NIR-II fluorescence image of *in vivo* distribution of GNC with 50% MUA feed under 808-nm laser irradiation 10 h after F.P.. GNCs accumulated in unilateral lower-body LNs, including popliteal and sciatic LNs. Some LNs stained during I.V. were also observable in the F.P. result (left: prone position; right: supine position; 20 ms, 20 mW cm^{-2}).

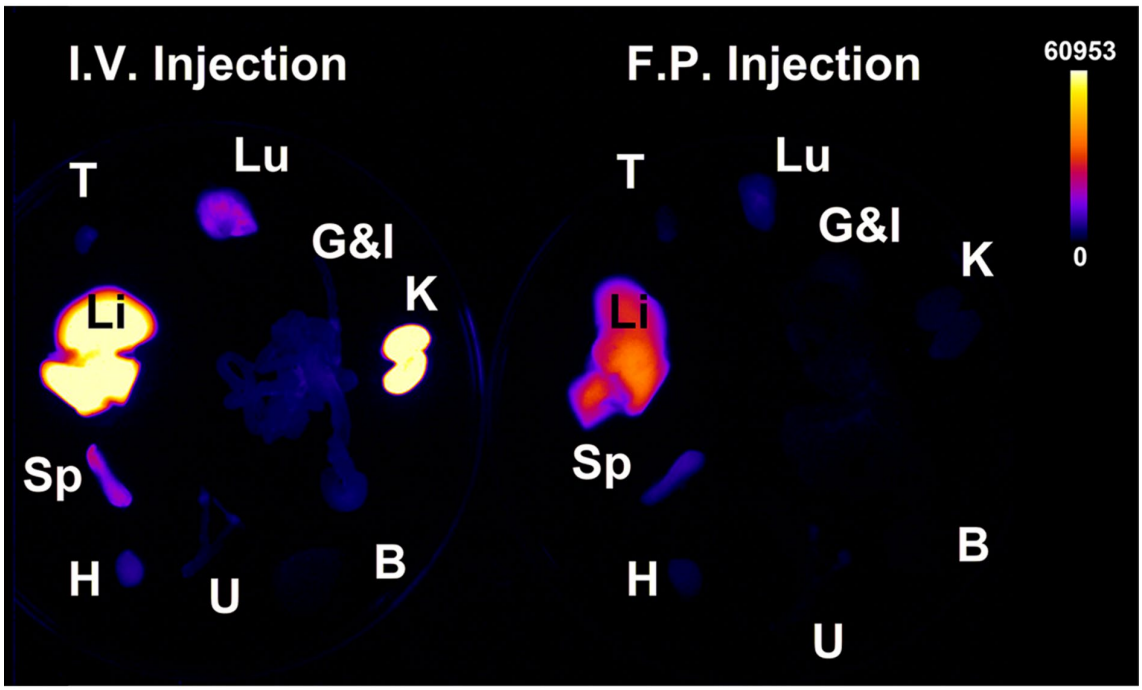

Figure 7.3.12 NIR-II fluorescence images of major organs harvested from mice 10 h

post-administration of dual-ligand-capped GNC with 50% MUA feed *via* different administration methods (B: brain; G&I: gastrointestinal tract; H: heart; K: kidneys; Li: liver; Lu: lungs; Sp: spleen; T: thymus; U: uterus; 20 ms, 20 mW cm^{-2}).

To study how other parenteral administration methods influence the GNC LN-targeting property, I further compared the footpad injection (F.P.) outcome with the I.V. data. F.P. is a common technique for lymphatic dosing because the hind limb region of mice has prosperous lymphatics and LNs.[61] Normally, lymphatic accumulation draining from the blood circulation is poor as the epithelial cell gap of lymphatic vessel capillaries is substantially higher than that of blood vessels.[33] Besides, the blood flow rate is approximately 100–500 times that of lymphatic flows, which can hinder the transportation of GNCs within lymphatics.[62] Comparatively, F.P. could directly drain GNCs to lymphatics through the interstitium and increase contact with the lymphatic system. Thus, F.P. can increase the GNC LN accumulation efficiency while reducing accumulation in other organs.[37] Due to the relatively slow process of crossing the interstitial space, I extended the observation time to 10 h. For example, the fully zwitterionic-ligand-capped GNC gave a relatively quick renal clearance time of ~2 h. As the MUA ligand feed ratio increased to 60%, popliteal and sciatic LNs in the injection site showed intensive fluorescence, which can be easily distinguished from the surrounding tissues. The LN-targeting ability was better than that of the GNCs with MUP or MUS anionic ligand (Figure 7.3.8–Figure 7.3.10). Through comparison, I conclude that for the MUA ligand-capped GNCs, 40%–60% feeding is adequate for lymphatic accumulation. Thus, I used 50% MUA as the optimal ligand feed ratio for GNC preparation in all further experiments (denoted as MUA-GNC hereafter). The distribution of MUA-GNC administered through F.P. was restrained in LNs close to the injection site, including popliteal (first-draining), sciatic, sub-iliac, and medial iliac LNs (Figure 7.3.11). Follow-up pathology analysis confirmed that F.P. resulted in less accumulation of GNCs overall in the organs compared with I.V., especially in the liver and kidneys, which should reduce the potentially toxic side effects caused by non-

desired hepatic and renal accumulation (**Figure 7.3.12**). For all three anionic ligands studied, the relationships between the LN accumulation and ligand feed ratio for the F.P. and I.V. were similar. Moreover, the relationship between the GNC-surface negative charge density and LN accumulation, as shown above, is also applicable to MUP and MUS ligands (**Figure 7.3.13**).

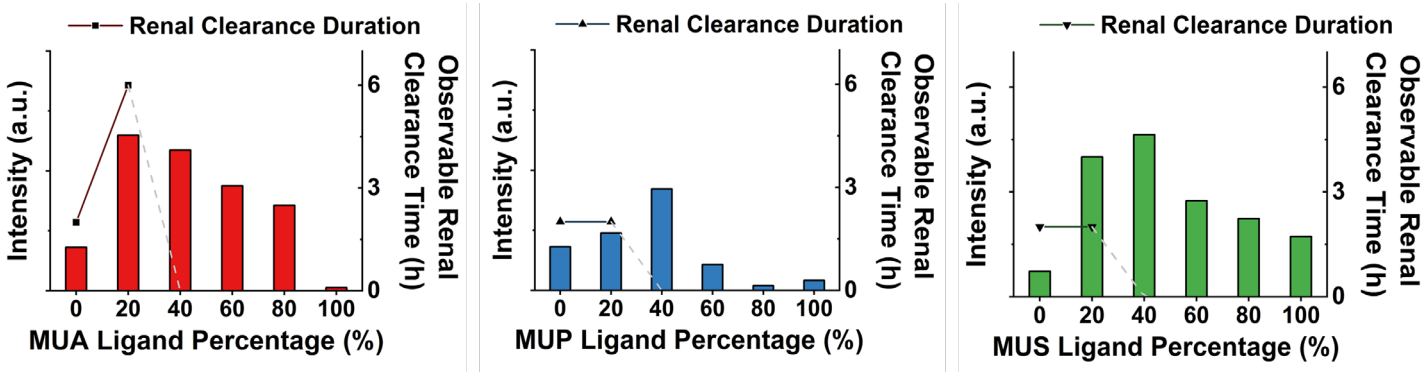

Figure 7.3.13 Plot of the relationship between fluorescence intensity in popliteal LNs and renal clearance time against the anionic ligand ratio of MUA/MUP/MUS ligand.

7.4 Imaging dose optimization and imaging effect comparison with ICG

To find the relationship between the GNC concentration in the lower-body LNs and the exposure time of the NIR imager, I injected an equal volume of serially diluted GNC solution into the mouse footpad and adjusted the fluorescence intensity to be the same to optimize the exposure time (**Figure 7.4.1**). With MUA-GNC as low as 1.2 mg kg^{-1}, I could still acquire a low-latency video with high contrast. However, since the current video uses 30 frames per second as a common frame rate, the shortest delay should be less than 33 ms to avoid inconsistency between the video and the operation. Thus, 5 mg kg^{-1} of MUA-GNC was used as the most suitable concentration for a real-time video with an exposure time as short as 17 ms while avoiding material waste, which is the most suitable for *in vivo* applications. As one of the most widely used NIR bioimaging fluorophores, ICG is widely used for lymphatic imaging and fluorescence-guided surgery.[63] However, as a small organic fluorophore, ICG suffers from several limitations

during *in vivo* applications, including high haemoglobin affinity, short half-life (2–4 min), low hydrophilicity, and difficulty in chemical modification.[64] [65] Moreover, its susceptibility to photobleaching restricts its effective imaging time to 30 min,[66] which is insufficient for deep LN-related surgeries that last for several hours.[58] Besides, the short Stokes shift of ICG requires a necessary matching of the laser source and filter.[67] [68] To overcome these limitations, a biocompatible, highly stable imaging agent that can provide sensitive, long-lasting NIR imaging is urgently needed. I compared the photostability of MUA-GNC and ICG under 808-nm laser radiation (20 mW cm^{-2}) (**Figure 7.4.2**). The fluorescence intensities of MUA-GNC and ICG were adjusted to be similar under a 900-nm long-pass filter before laser irradiation. The fluorescence of ICG rapidly decreased upon exposure to irradiation, losing ~50% of the initial intensity within 30 min, and became almost completely photo-bleached at 2.5 h, indicating poor photostability. In contrast, MUA-GNC showed no observable changes in fluorescence intensity throughout the whole 2.5-h laser radiation, demonstrating highly robust photoluminescence. Further, I compared the fluorescence stability of ICG and MUA-GNC upon exposure to a household incandescent lamp (15 W, ~1125 lm) (**Figure 7.4.3**). Similar to the previous result, the ICG fluorescence decreased continuously, retaining only ~10% of the original intensity at 24 h, indicating poor photostability and aqueous stability.[69] However, the fluorescence of MUA-GNC remained almost constant throughout the 24 h exposure, confirming that the GNC has excellent photostability and stability in a buffer, which is vital for effective, long-term fluorescence imaging. Moreover, the use of GNC for bioimaging does not need strict light-shielding, which can broaden its scope of application. Furthermore, MUA-GNC can be effectively excited by white light from an LED lamp (12 W, ~1200 lm) and emits strong fluorescence, whereas ICG is completely invisible under such conditions (**Figure 7.4.4**). Independence on the type of excitation source is another attractive feature of bioimaging using MUA-GNC. In addition, the NIR fluorescence of GNCs was retained after lyophilization to allow for convenient storage and transportation, which is another highly attractive feature for

practical applications.

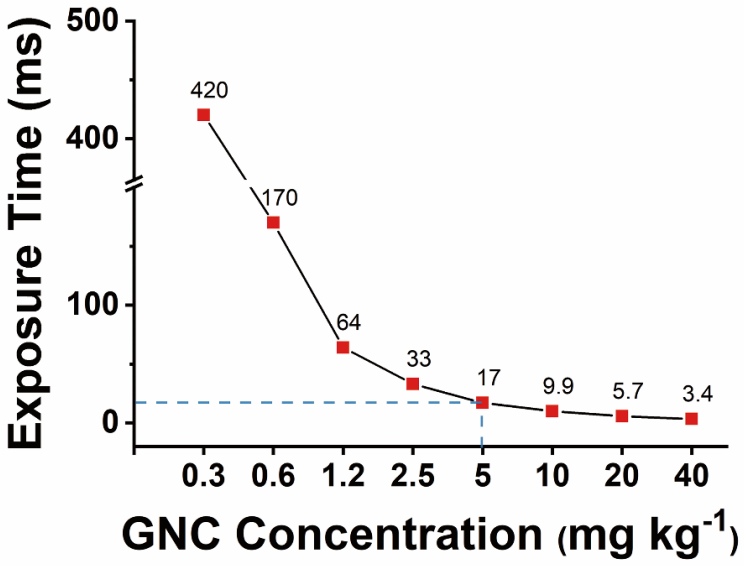

Figure 7.4.1 The relationship between MUA-GNC concentration and the exposure time required to achieve the same fluorescence intensity. Too long an exposure time would cause high imaging latency, while too high a GNC concentration would be wasteful. Here 5 mg kg^{-1} of MUA-GNC is considered optimal due to appropriate concentration and exposure time.

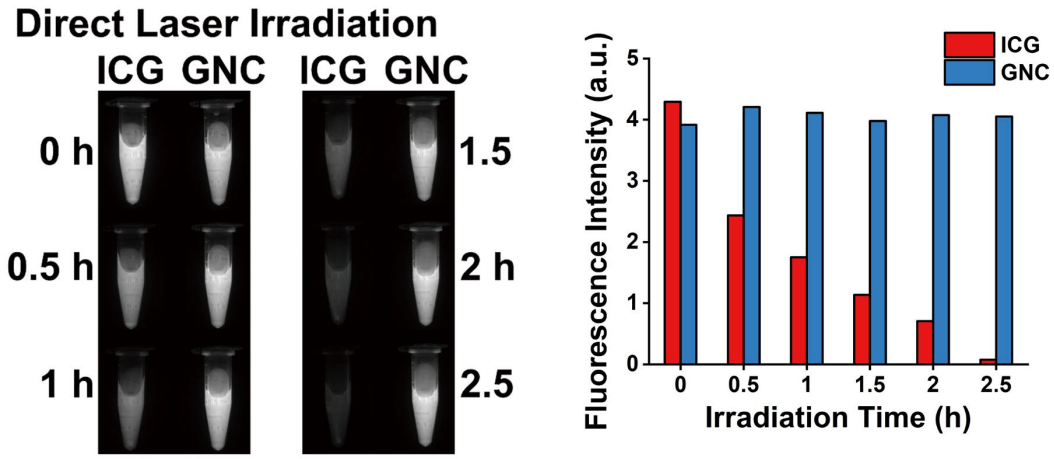

Figure 7.4.2 NIR-II fluorescent images of GNC and ICG on exposure to direct laser irradiation (808 nm, 20 mW cm^{-2}).

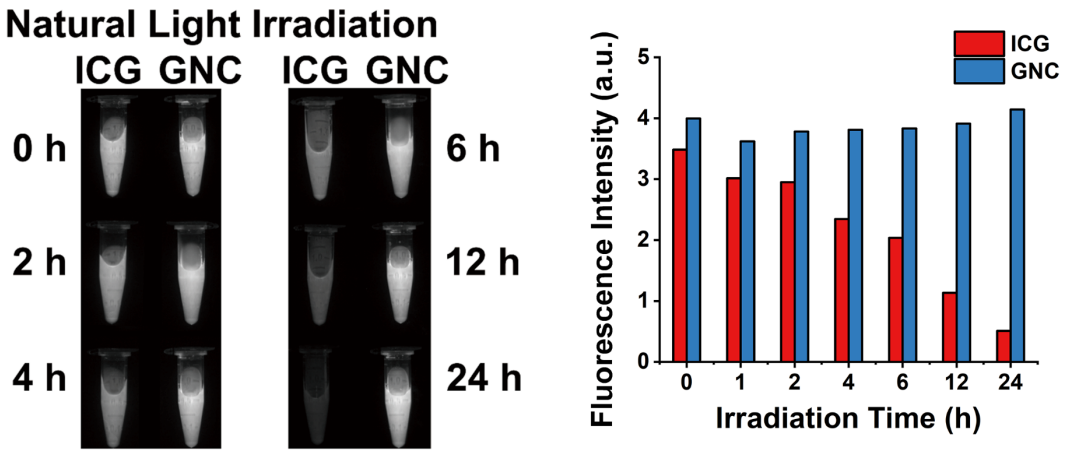

Figure 7.4.3 NIR-II fluorescent images of GNC and ICG on exposure to natural light irradiation, taken with 10 ms exposure, 20 mW cm^{-2}.

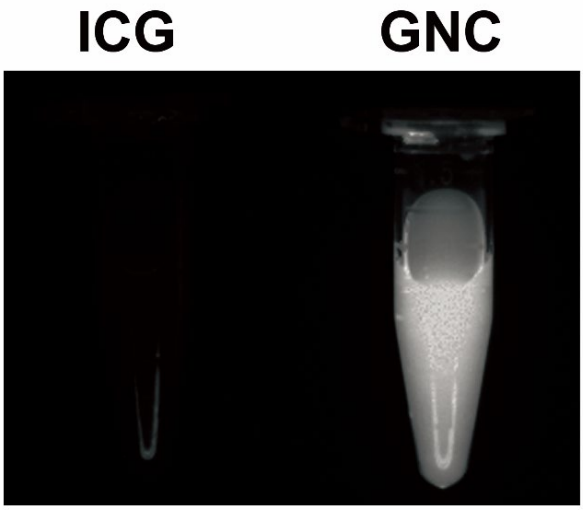

Figure 7.4.4 NIR-II fluorescence images of ICG and GNC upon exposure to an incandescent lamp where GNC is efficiently excited, but ICG is not. The broad absorption of GNC enables a feasible excitation, which is convenient for surgical application (200 ms, 5 mW cm^{-2}).

7.5 MUA-GNC for *in vivo* imaging in tumour-bearing mice

We constructed an *in situ* lymphatic metastasis model by injecting Hep3B human hepatocarcinoma cells into the footpad of mice. After both the I.V. and F.P. of MUA-GNC, I could distinguish between metastatic and normal LNs from the NIR-II fluorescence image generated (**Figure 7.5.1**). After GNC injection, metastatic LNs

showed a significantly increased volume and irregular shapes under NIR fluorescence imaging. After labelling with GNCs, I conducted an imaging-guided surgery to remove sentinel LNs. The stained LNs showed bright NIR-II fluorescence and strong contrast from surrounding tissues, making surgical resection convenient. Even though not professionally trained in surgery, the operator could easily judge the LN location as well as status and perform a resection operation, in which the entire metastatic LN could be completely dissected. After the operation, LNs were stained with hematoxylin and eosin (H&E) to confirm the existence of the metastatic region mixed with normal tissues (Figure 7.5.2). This data was supported by Dr Ning Ren in SUSTech. Heterotopic tumour models, including intraperitoneal and subcutaneous models, were further constructed to demonstrate the potential of the MUA-GNC in imaging-guided surgeries. In the heterotopic models, I.V. of MUA-GNC yielded high NIR-II fluorescence contrast, allowing for feasible diagnosis and surgical removal of LNs (Figure 7.5.3). These results demonstrate the successful use of the mixed-ligand-capped GNCs for the noninvasive diagnosis of tumour LN metastasis and NIR-II fluorescence-guided surgery.

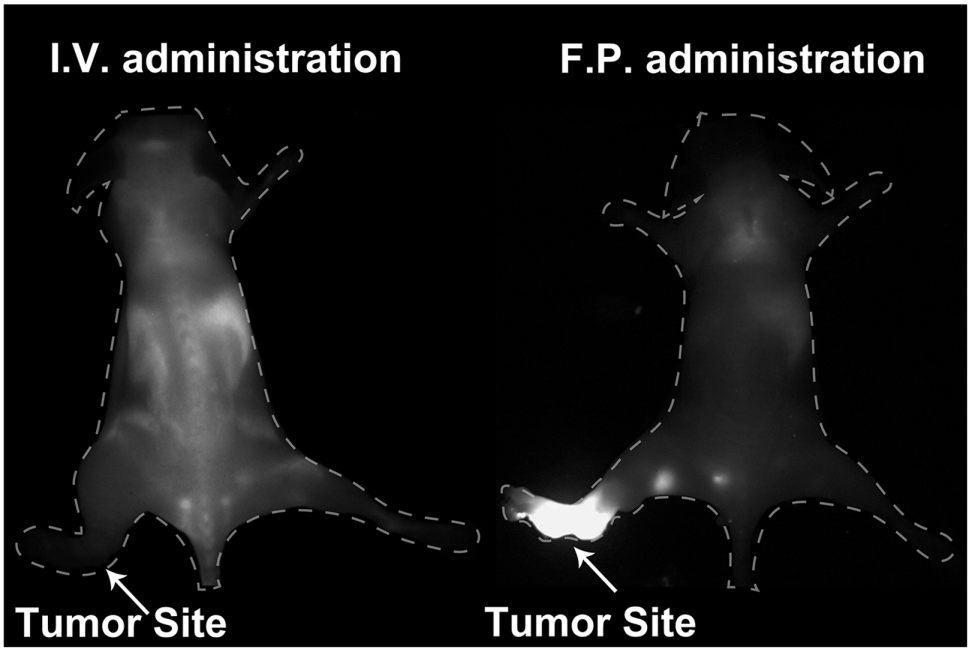

Figure 7.5.1 NIR-II fluorescence image of varied parenteral administration of GNC with 50% MUA in feeding. The GNC was used to directly image LN metastasis in *in situ*

tumour models administered through I.V. (left) and F.P. (right). Both methods could detect the abnormal size of metastatic LNs, although F.P. showed a higher fluorescence contrast in LNs next to the injection site and lower background away from the injection site. (The tumour site is marked with white arrows, 20 ms, 20 mW cm^{-2}).

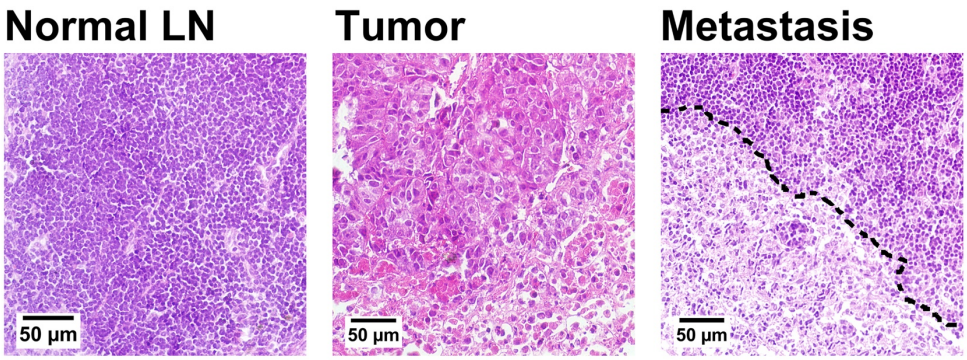

Figure 7.5.2 Hematoxylin and eosin (H&E) staining of the LN section demonstrating the existence of metastasis in the first-draining LNs, which confirms the ability of MUA-GNC in detecting LN metastasis. The dotted line indicates the boundary between the normal LN and tumour tissues.

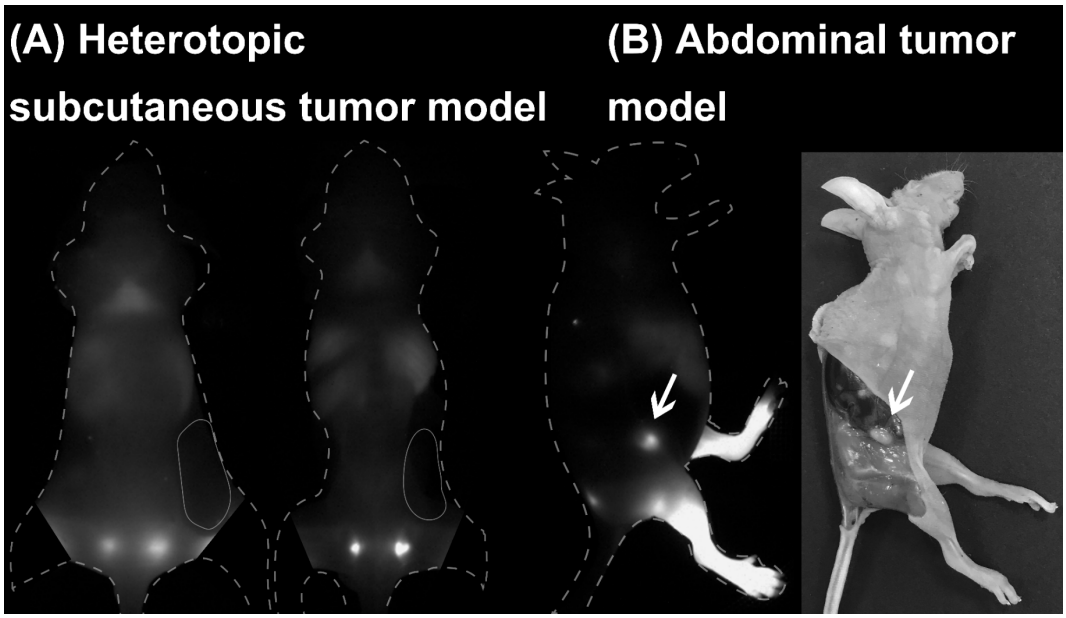

Figure 7.5.3 NIR-II fluorescence image of heterotopic tumour-bearing mice. (A) Heterotopic subcutaneous model of the mouse with metastasis. The tumour site was labelled with a solid line frame. Ipsilateral sciatic LN to the tumour has displayed abnormal size and shape (left: skin retained; right: skin removed). (B) Abdominal

tumour model of mice with metastasis. Metastatic LN was marked with a white arrow in the NIR-II fluorescence image and the corresponding optical photograph. (20 ms, 20 mW cm^{-2})

7.6 Distribution of MUA-GNCs in LNs and their interaction with immune cells

7.6.1 Lymphatic distribution of MUA-GNCs

To examine the penetration depth of MUA-GNC in LNs, I performed frozen sections of normal LN 6 h after the F.P. of MUA-GNC. The 20-μm-thick sections were directly monitored using a NIR microfluorescence imaging system (**Figure 7.6.1**). Compared with the brightfield image, the fluorescence signal appeared either near the afferent lymphatics and lymphatic sinuses or in a deeper cortex region. To further locate the MUA-GNC, I prepared 5-μm-thick LN sections and employed silver staining to amplify the GNC signal to confirm the distribution of GNCs. Consistent with the NIR fluorescence image result, the optical image shows that GNCs accumulated mainly near the afferent lymphatics, subcapsular sinus, and follicular area (**Figure 7.6.2**).[70] TEM characterization of delicate structures after silver staining revealed that GNCs penetrated the lymphatic sinus into the follicles and interacted with B lymphocytes, suggesting a wide distribution and extensive contact of MUA-GNC with several LN-residue immune cells.

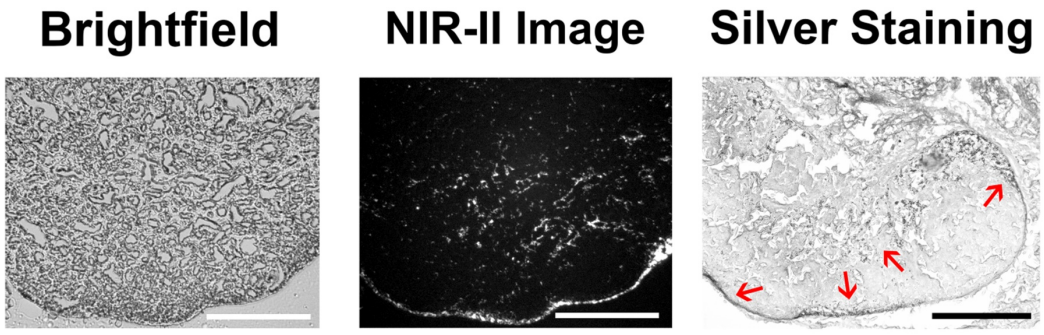

Figure 7.6.1 Brightfield, NIR-II fluorescence, and silver-stained optical images of LN harvested from mice after treatment with MUA-GNC for 10 h. GNC was mainly

distributed in the cortex region around the capsular of LNs. It could also enter the deeper cortex and distribute in the lymphatic follicles (labelled with red arrows; scale bar: 200 µm).

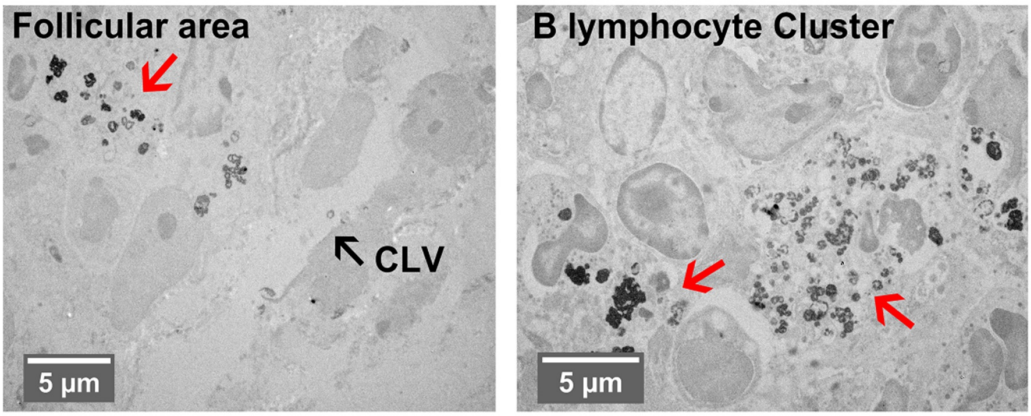

Figure 7.6.2 TEM images of MUA-GNC-treated LN tissue after silver amplification, showing accurate GNC distribution in LNs. The silver staining signals are marked with red arrows. GNC signal was found in follicles and the B cell cluster region, indicating its ability to pass through cortical lymphatic vessels and reach the follicular area (CLV: cortical lymphatic vessel, scale bar: 5 µm).

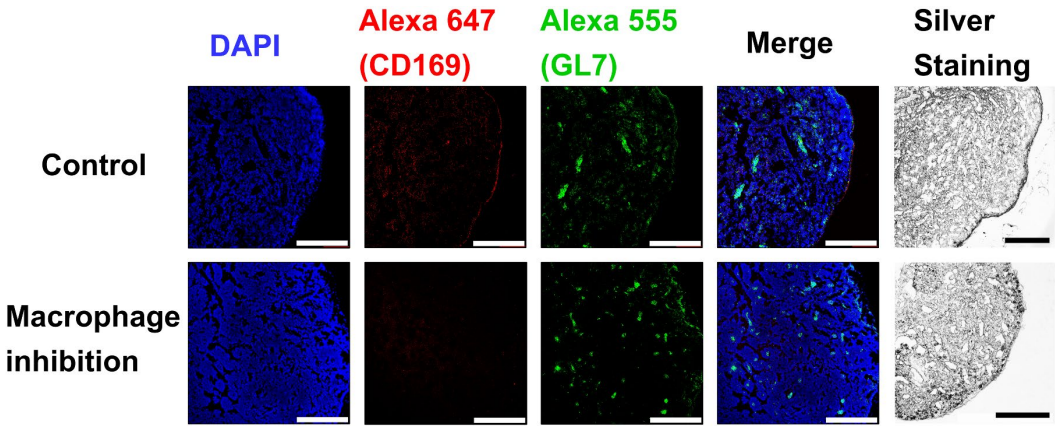

Figure 7.6.3 Confocal images showing the effect of macrophage suppression and the influence on GNC distribution within LNs. The SCS macrophage amount was reduced in the macrophage-inhibited group with significantly enhanced infiltration of MUA-GNC compared with that of the control group. (Alexa 647: CD169-SCS macrophages; Alexa 555: GL7-Geminal centre; scale bar: 200 µm).

7.6.2 Subcapsular sinus macrophage inhibition to further study the distribution of GNCs in LNs

Within LNs, besides dispersed macrophages in lymphatics and antigen-presenting cells in follicles, the subcapsular sinus (SCS) macrophage is responsible for antigen capture and presentation. However, its role in nanomaterial distribution is still unclear.[71] Previous studies have shown that the presence of SCS macrophages obstructs NPs from entering LN follicles by capturing and endocytosing them.[70] To verify the role of SCS macrophages in MUA-GNC distribution within LNs, I used $GdCl_3$ as a macrophage inhibitor three days before GNC application and compared the GNC distribution with that of phosphate buffer saline (PBS) control groups.[72] To confirm the effect of macrophage suppression on the GNC distribution, I prepared 5-μm-thick LN sections and stained the germinal centre (B lymphocyte clusters) and SCS macrophages with anti-GL7 (green) and anti-CD169 (red) antibodies, respectively. The GNC deposition was monitored by silver staining (**Figure 7.6.3**). Comparing the SCS macrophage location with the silver staining result in the control group, I found extensive colocalization of both at subcapsular regions, indicating that SCS plays an important role in the retention of GNCs within LNs.[73]

Macrophage suppression was confirmed by the disappearance of red fluorescence in the SCS area, accompanied by a higher germinal centre formation, possibly resulting from higher retention of MUA-GNC within the follicles without SCS macrophage obstruction. The silver staining result also revealed a different distribution pattern compared to that of the control, with substantially lower retention in the subcapsular area and deeper distribution in the cortex and paracortex layers. Additionally, the GNC NIR-II fluorescence was also different from that of the control, showing reduced surface interception and deepened distribution. This agrees well with the silver staining results, indicating that SCS macrophages hinder GNC LN distribution and accumulation (**Figure 7.6.4**). Together, these results reveal that removing SCS macrophages at the entrance to

the follicles can lead to higher overall accumulation and deeper penetration of GNCs in LNs, as confirmed by a stronger MUA-GNC fluorescence. The function of SCS macrophages in the accumulation of GNCs discovered herein can provide useful guidance for further designs of LN-targeting nanomaterials.

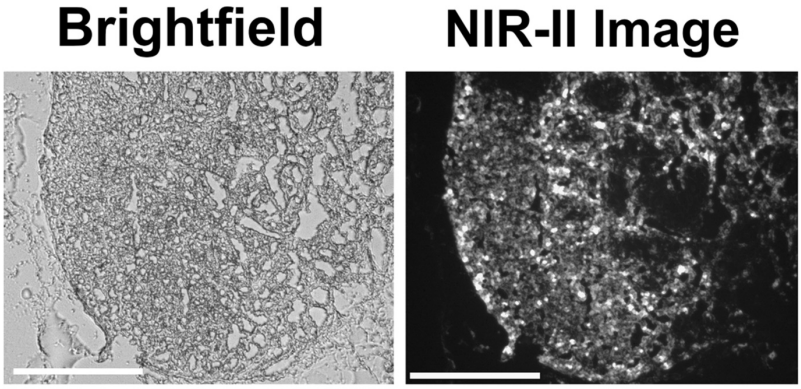

Figure 7.6.4 Brightfield optical and NIR-II fluorescence images of the LN section, showing that GNC was no longer restricted to the subcapsular lymphatic sinuses and penetrated deeply into the paracortex layer for the macrophage-inhibited group (scale bar: 200 μm).

7.7 Biosafety evaluation

The elimination process is a vital indicator for imaging and biosafety of bioimaging agents.[74] Due to the small size and moderately negative surface charge, the body-retention time of MUA-GNC is adequate for *in vivo* imaging: its fluorescence signal in the liver and LNs decayed gradually and became almost invisible 96 h after I.V. administration (**Figure 7.7.1**). Therefore, a single injection of MUA-GNC can satisfy the requirement of imaging-guided surgery, avoiding the need for repeated injections of ICG for the same purpose due to its short *in vivo* half-life and high affinity to haemoglobin.[64] For F.P., the retention within the injection site was prolonged to approximately 144 h. To verify the biosafety of MUA-GNC, I conducted an *in vitro* live-dead staining of human umbilical vein endothelial cells (HUVECs) after treatment with PBS (control) or 100 or 200 μg mL^{-1} GNC (**Figure 7.7.2**). After 24-h incubation, I applied

Calcein-AM and propidium iodide to stain live and dead cells, respectively. There was no obvious difference in the number of dead cells for the control and MUA GNC-treated groups. Together, these results demonstrate that MUA-GNC has high biosafety and can be used in various clinical imaging applications.

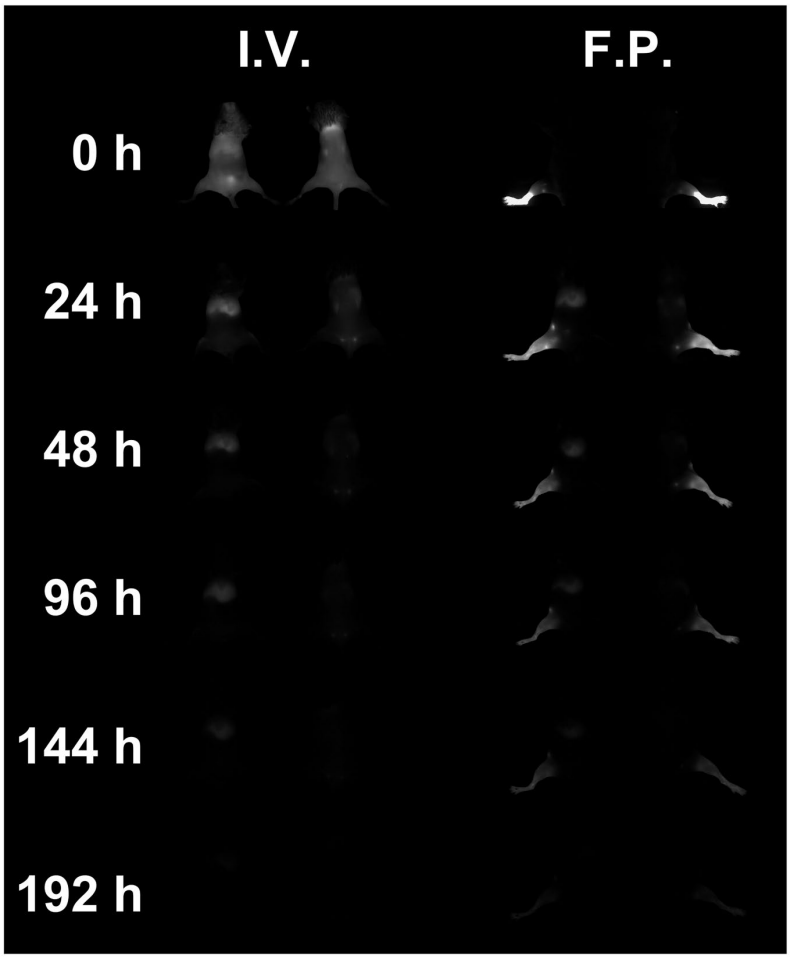

Figure 7.7.1 NIR-II fluorescence image showing the elimination process of GNC in the mouse body with different administration routes (intravenous injection: I.V. and footpad injection: F.P.; 25 ms, 20 mW cm^{-2}).

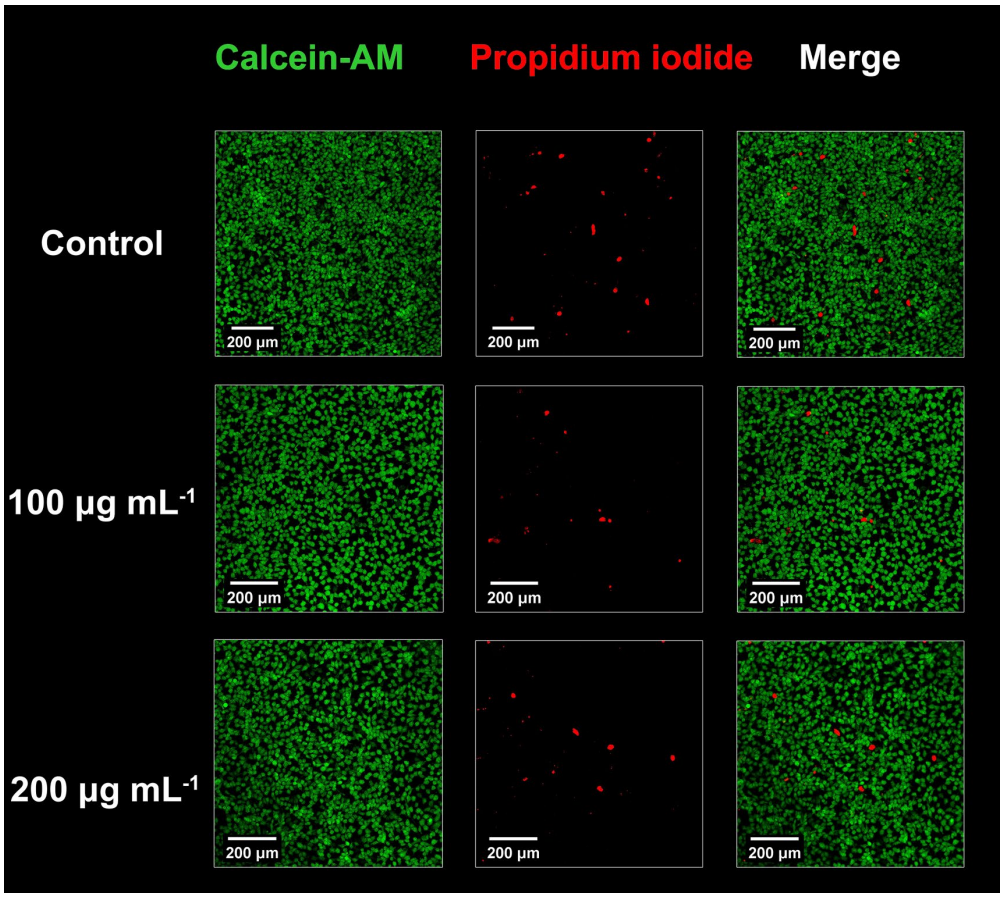

Figure 7.7.2 Live-dead staining result of HUVECs treated with up to 200 μg mL^{-1} GNC for 24 h.

7.8 Characterization of HS-MTX-loaded tri-ligand GNC and analysis of its antiproliferative property

Based on its effective LN accumulation ability, I further explored the use of MUA-GNC in treating cancer metastasis by incorporating methotrexate (MTX), a classic cancer chemotherapeutic drug that inhibits the formation of thymidine, thereby affecting DNA synthesis and cell proliferation.[75] Despite having a high curative effect on the treatment of multiple cancer types, as a small molecular drug, MTX exhibits undesirable whole-body distribution, leading to high hepatotoxicity and nephrotoxicity.[41] In addition, the requirement of frequent doses of MTX due to a short half-life (~1 h) can further worsen its side effects.[76] Based on the good LN targeting ability of MUA-GNC, I hypothesized that using MUA-GNC to deliver MTX specifically into LNs should greatly reduce the toxic side effects of MTX on other tissues. Each MTX molecule has two carboxylic acid groups,

thus can be conveniently coupled with a thiolated tetra(ethylene glycol) amine to give thiolated methotrexate (HS-MTX), which still retains a free carboxylic acid group.[77] After coupling one COOH group to form HS-MTX, there are two ionizable groups, a free COOH (p*Ka* ~2.9) and NH^+ (p*Ka* ~5.7) group in each HS-MTX molecule. Under the physiological pH of 7.4 used in the study, the free COOH group should be fully deprotonated to give a COO^-, while the NH^+ group should also be mostly deprotonated (~98%) to give a neutral N and hence should be mostly charging neutral. Therefore, under the experimental conditions, each GNC-bond HS-MTX molecule should carry one net negative charge and almost the same as a GNC-bond MUA ligand. Indeed, the resulting 30% HS-MTX triligand-capped GNC (abbreviated as **MTX-GNC** hereafter) showed the consistent characteristic UV–vis absorption peaks of the MTX-free counterparts (**Figure 7.8.1**). The size of the MTX-GNC was also similar to that of the MUA-GNC (**Figure 7.8.2**). The *in vitro* anti-cancer effect was measured using HuH-7 cell, a common liver cancer cell line, which revealed a dose-dependent reduction of cell viability with an IC_{50} of ~5.4 μg mL^{-1} (**Figure 7.8.3**).

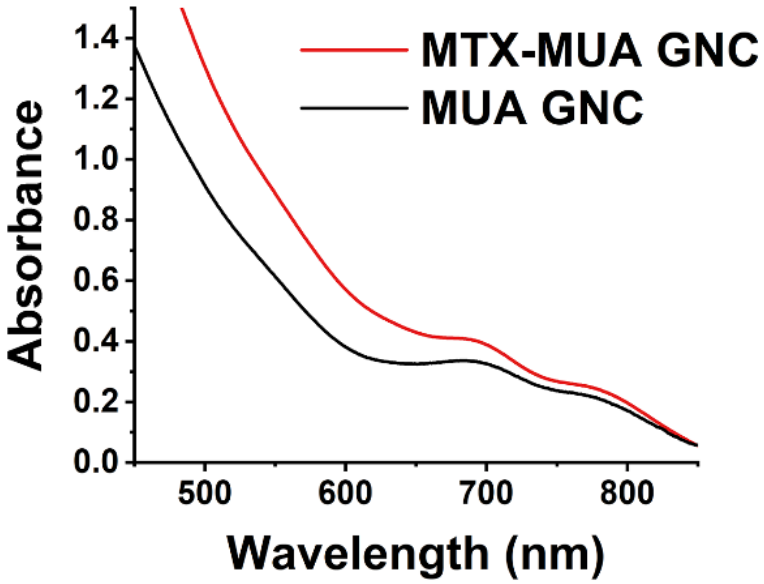

Figure 7.8.1 UV-vis absorption spectra of the MTX-GNC and MUA-GNC. This tri-ligand GNC displays the characteristic UV-vis absorption peaks and uniform size expected for the $Au_{25}(SR)_{18}$ type GNC.

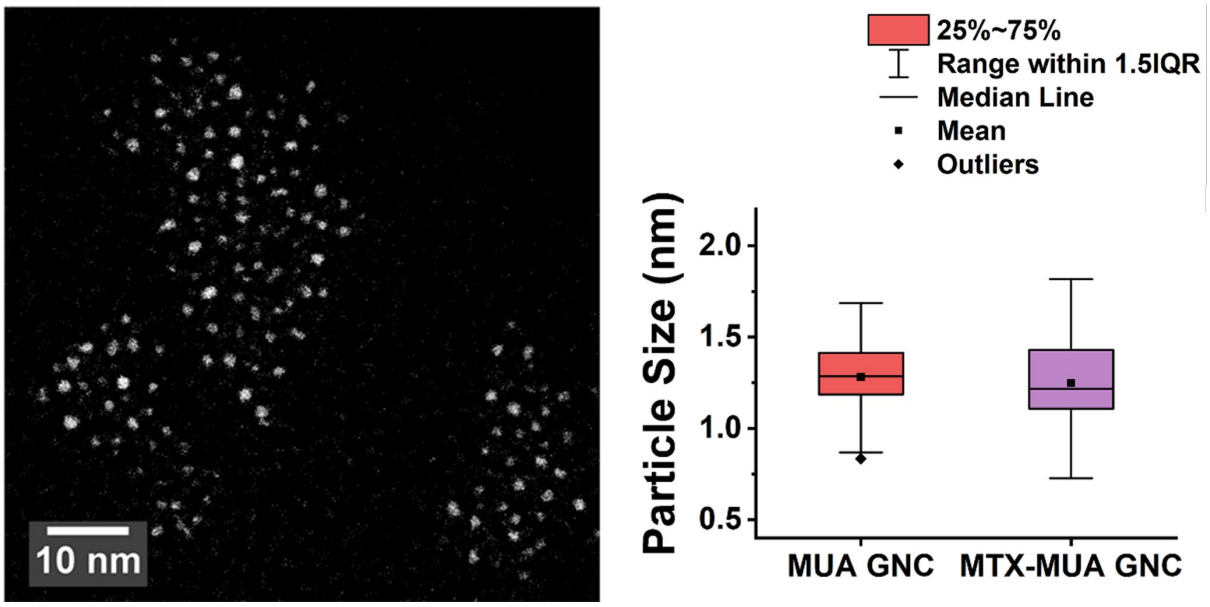

Figure 7.8.2 DSAC-TEM of the MTX-GNC (left) and statistic size comparison of the MTX-GNC and MUA-GNC (right).

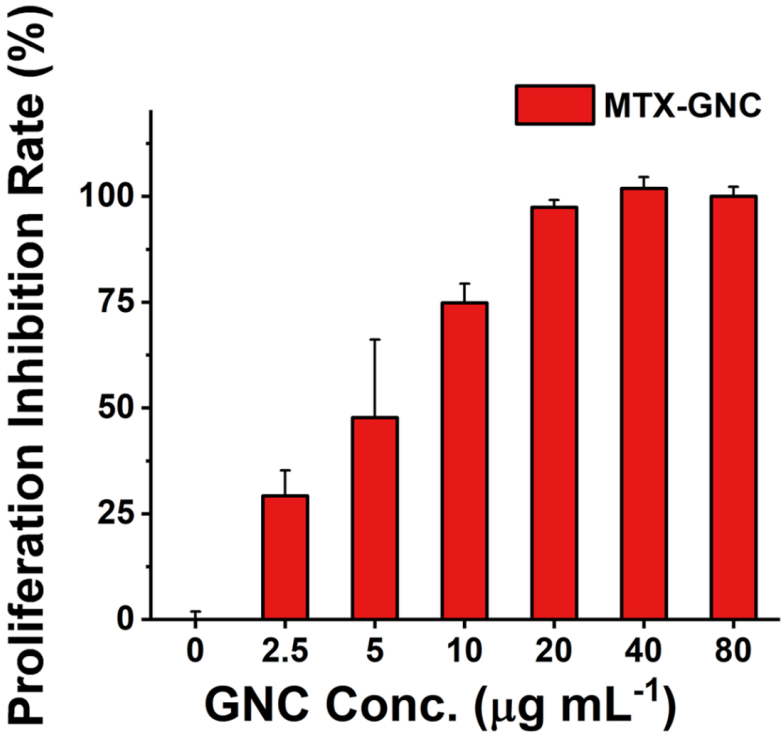

Figure 7.8.3 *In vitro* inhibitory effect of MTX-MUA-C5 GNC to HuH-7 cell line. Complete inhibition of tumour cell growth was achieved at ~20 μg mL^{-1} of GNC.

An *in vitro* wound-healing test was further conducted to visualize the inhibitory effect of MTX-GNC on cell growth and proliferation of HuH-7 cells. Cells treated with ≥5 μg mL^{-1}

MTX-GNC yielded extremely low cell proliferation efficiency compared to the negative control, confirming that HS-MTX maintained its anti-proliferating ability after loading onto the GNC surface (**Figure 7.8.4**). I injected MTX-GNC *via* F.P. (100 µL, 1.6 mg mL^{-1}, the same amount as MUA-GNC described above) into mice and found that its fluorescence intensity and *in vivo* distributions were similar to those treated with MUA-GNC, indicating that partial replacement of MUA with HS-MTX has negligible effects on biophysical properties of MUA-GNC (**Figure 7.8.5**).

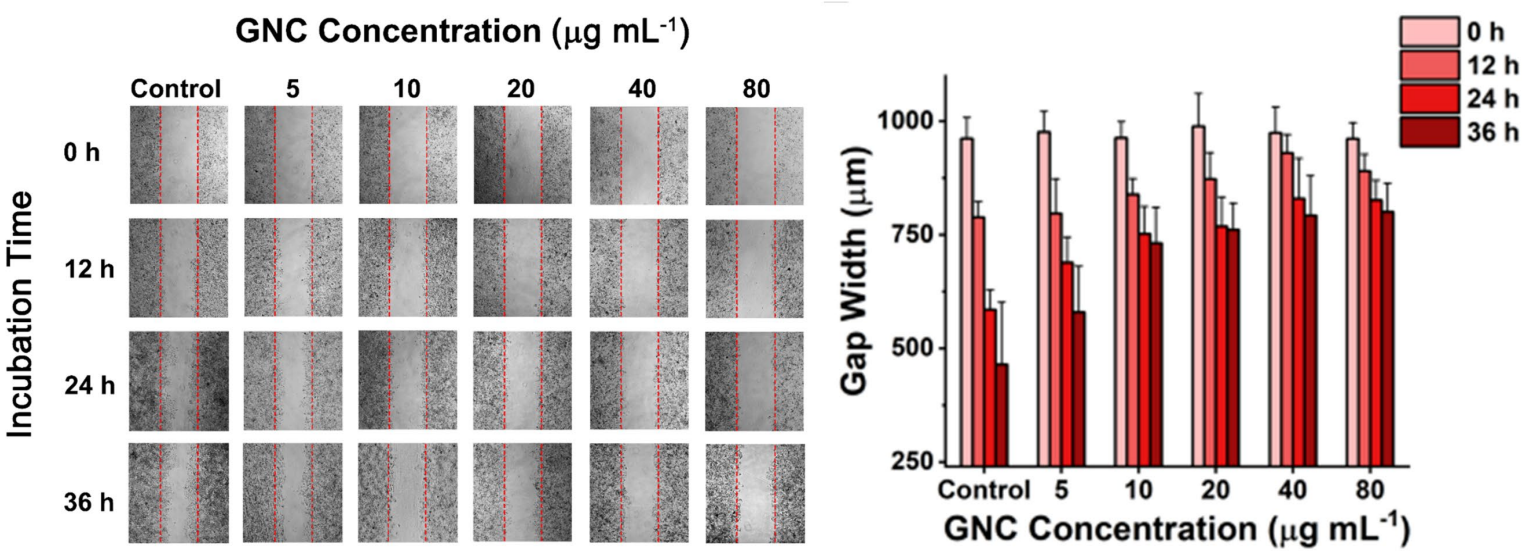

Figure 7.8.4 Optical images showing the effect of MTX-GNC concentration on HuH-7 cell line healing microscale gaps (left) and statistics of scratch-healing results of treatments with different MTX-GNC concentrations displaying similar inhibitory concentrations (right). These results show an excellent inhibitory effect of MTX-GNC on cell proliferation and migration.

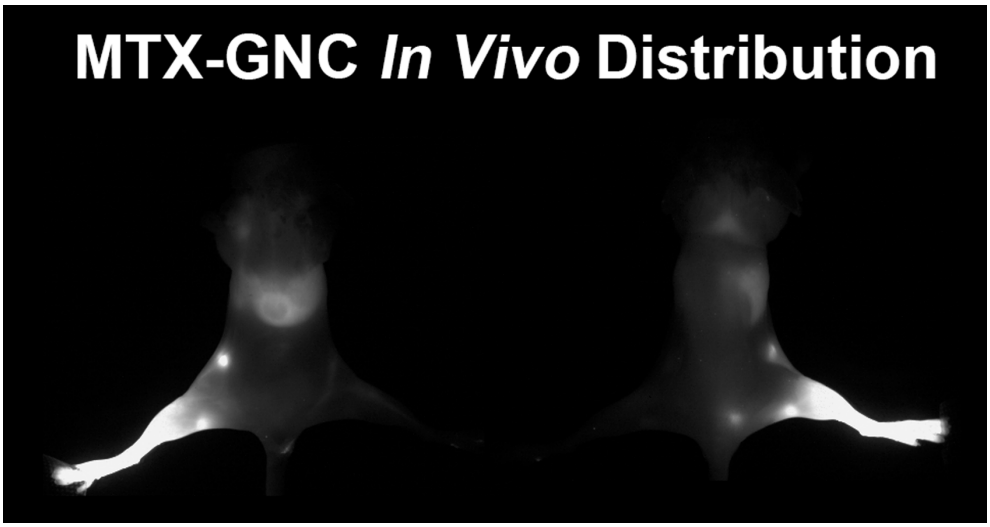

Figure 7.8.5 NIR-II fluorescence image of biodistribution of MTX-GNC after footpad administration. The *in vivo* distribution was not affected by the co-doping of MTX and MUA in MTX-GNC.

7.9 MTX-GNC for the treatment of lymphatic metastasis models and reducing liver and kidney toxicity

Based on such encouraging *in vitro* results, I further extended the study to *in vivo* using lymphatic metastasis models. An LN-metastatic mouse model was constructed by injecting human hepatocarcinoma tumour cell Hep3B into the left hind limb footpad of mice. Four days after injection, the ipsilateral popliteal LN swelled. I then treated the different groups through F.P. of free MTX (5 mg kg^{-1}, equivalent to 15 mg kg^{-1} of MTX-GNC in drug dosage, positive control), MTX-GNC (10 or 20 mg kg^{-1}, 2 × IC_{50} or complete inhibitory dose), MUA-GNC (20 mg kg^{-1}) and PBS (negative control), respectively. The injection was performed once every two days. After 12 days of treatment, the mice were sacrificed, photographed, and their LNs were measured. No abnormal changes in the body weight were found for all the other groups, except for the group treated with free MTX, which showed a sharp decrease (~30%) in body weight (**Figure 7.9.1**).

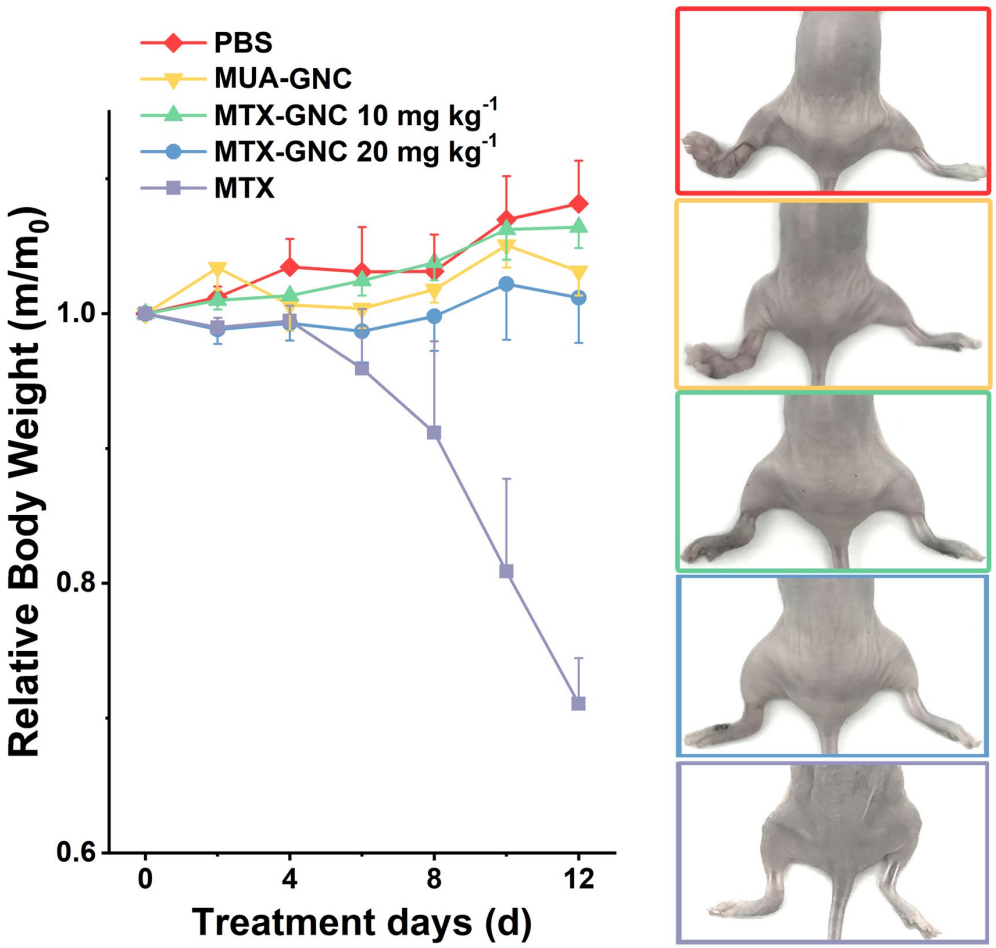

Figure 7.9.1 Left: change in the bodyweight of tumour-bearing mice following different treatment processes; right: pictures of the tumour-bearing body part and skin appearance. After treatment with free MTX, mice were in an unusually emaciated state, accompanied by significantly decreased tumour volume, whereas all other groups showed no significant weight loss or changes in appearance (n = 5).

Moreover, all free-MTX-treated mice were extremely skinny and weak with rough and dull skin, suggesting severe drug-induced injuries and side effects. These results are consistent with the systemic toxicity of the administration of free MTX. In contrast, treatment with a high dosage of MTX-GNC resulted in minimal changes in body weight throughout the treatment, indicating minimal side effects. Laboratory Animal Research Center helped with the analysis of the liver and kidney function indices of different groups. The alanine aminotransferase (ALT), aspartate aminotransferase (AST), and alkaline phosphatase (ALP) levels of the free-MTX group were well-above and about 4,

10, and 1.5 folds higher than the expected normal ranges, whereas those of all other groups were within the normal ranges (**Figure 7.9.2** and **Figure 7.9.3**). Notably, a substantially enlarged AST/ALT ratio indicates severe liver damage and hepatic fibrosis processes. Herein, the AST/ALT ratio was ~10 for the free-MTX group, whereas that for the MTX-GNC-treated group was ~2.5 and comparable to the PBS control group.[78]

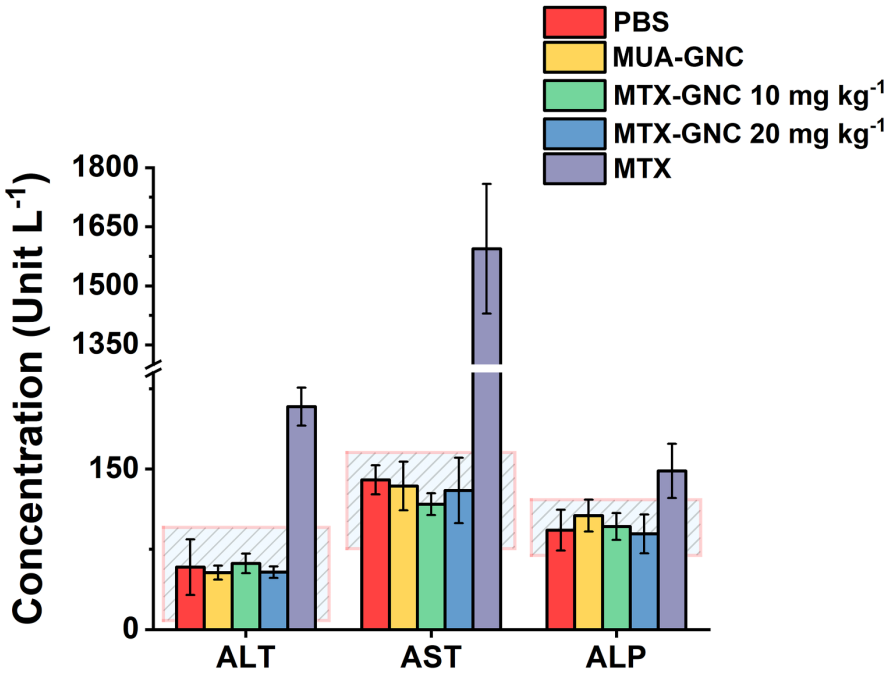

Figure 7.9.2 Comparison of liver biochemical indices for mice taking different treatments. High ALT, AST, and ALP levels were observed in the free-MTX-treated group, indicating acute liver damage. However, the levels of the indicators in all other groups were comparable and within the normal range (n = 4).

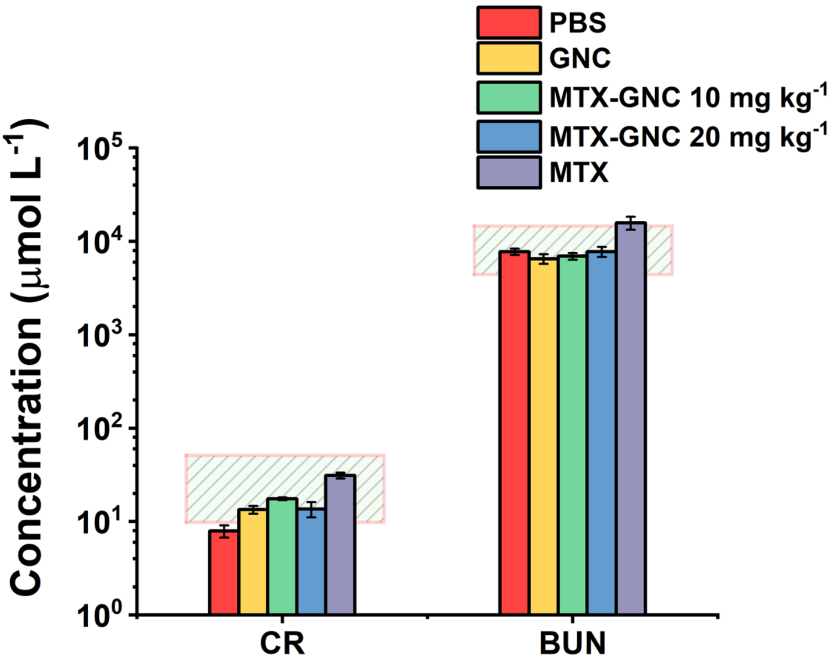

Figure 7.9.3 Comparison of kidney biochemical indexes of different treatment groups. The free MTX group shows a higher CR and BUN level than other groups, indicating partial kidney damage (n = 4).

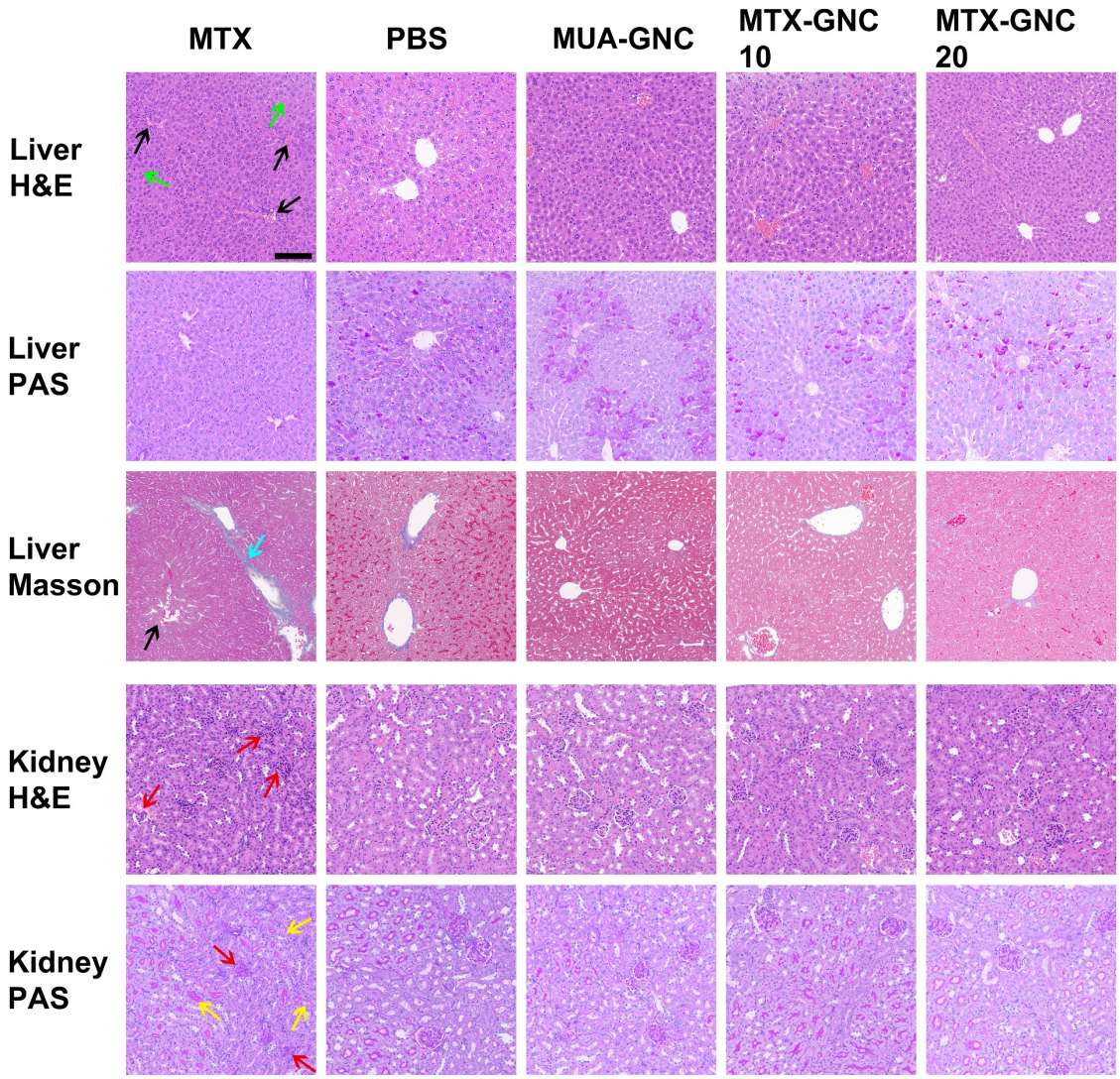

Figure 7.9.4 H&E, PAS, and Masson staining of liver and kidney tissue after different treatment processes. Black arrows: degeneration of liver sinusoids and cords; green arrows: hepatocyte necrosis; azure arrow: hepatic fibre bridging; red arrows: glomerular damage and fibrosis; yellow arrows: brush borders shedding.

Moreover, Dr Ning Ren provided the H&E/PAS/Masson-stained liver and kidney slices. The results revealed that, except for the free-MTX group, all liver cells were arranged radially centred on the central vein, and the liver lobules were orderly structured (**Figure 7.9.4**). The hepatic cords were neatly arranged, and the liver lobules were intact without apparent pathological changes. In contrast, in the free-MTX group, most of the hepatocytes in the liver lobules were swollen, and the sinusoids and hepatic cords disappeared. In addition, the cytoplasm texture was disordered, and local liver cells

appeared in necrosis.[79] Periodic Acid-Schiff (PAS) stain, the most intuitive way to analyze glycogen content, revealed moderate rose-red coarse particles (PAS staining positive) in the cytoplasm and nucleus of hepatocytes in the PBS control group,[80] with the glycogen content abundant and evenly distributed. Glycogen in the GNC-associated groups was mainly distributed in the proximal part of the central vein, and its overall content was relatively high. In contrast, in the free-MTX group, the liver glycogen almost disappeared. This negative PAS stain result indicated that, due to long-term drug damage, the enzyme activity in the liver decreased, reducing glycogen synthesis. Also, the fibrosis process of liver cells accelerated the consumption of glycogen. Under such chronic conditions, glycogen content in the liver cells was gradually depleted. To characterize the degree of fibrosis in the liver, I stained liver sections using the Masson staining method, which stains collagen fibres in blue. In the free-MTX-treated group, severe fibrosis with extensive fibre bridging between portal areas and structural disorders in the liver lobules were observed. These are clear signs of chronic hepatitis fibrosis, but they were not observed in all other groups. For the kidney, except for the free MTX-treated group, H&E staining in all other groups showed a normal renal tissue structure with complete nephrons and no pathological changes in the glomerular or renal interstitium.[81] While for the free-MTX group, the most obvious pathology occurred at glomerular atrophy. There was a significant increase in the mesangial matrix, the proliferation of the mesangial cells, the thickening of the basement membrane, and the accumulation of red staining material in the lumen.[82] PAS results further revealed a structural disorder, brush border loss, and accumulation of disintegrated cell debris in the lumen.[83] Together, these results demonstrated that MTX-GNC retained the therapeutic effect of free MTX but greatly reduced its toxic side effects *in vivo*.

As the tumour tissue was fused with the footpad, separating, and comparing the tumour size in each group was difficult. Alternatively, I measured the cross-sectional

size of the tumour-bearing footpad in each group (**Figure 7.9.5** and **Figure 7.9.6**), and the picture is shown in the insets to the right of **Figure 7.9.1**. MTX-GNC-treated groups showed great tumour volume regression compared with PBS control and MUA-GNC groups. I dissected the ipsilateral popliteal LNs next to the injection site and compared their masses and volumes for all treatment groups; the volume and weight indicate the extent of metastasis (**Figure 7.9.7** and **Figure 7.9.8**). The PBS and MUA-GNC (without MTX loaded) groups showed significantly swollen LNs, indicating serious lymphatic enlargement due to cancer cell proliferation and immune response.[84] However, treatment with MTX-GNC yielded a substantial dose-dependent reduction of the LN size and weight compared to the controls. The LN size and weight for the 20 mg kg^{-1} MTX-GNC group were reduced to ~1/7 and 1/5 of that of the PBS control and MUA-GNC-treated groups, respectively. Despite a slightly larger LN compared to that of the free MTX-treated group, the greatly reduced toxicity and improvement of animal tolerance by MTX-GNC treatment suggest that MTX-GNC is well-suited for treating lymphatic tumour metastasis.

Figure 7.9.5 Optical images of ipsilateral popliteal LN harvested from mice after different treatments. The LN size of MTX-GNC treatment was dose-dependent.

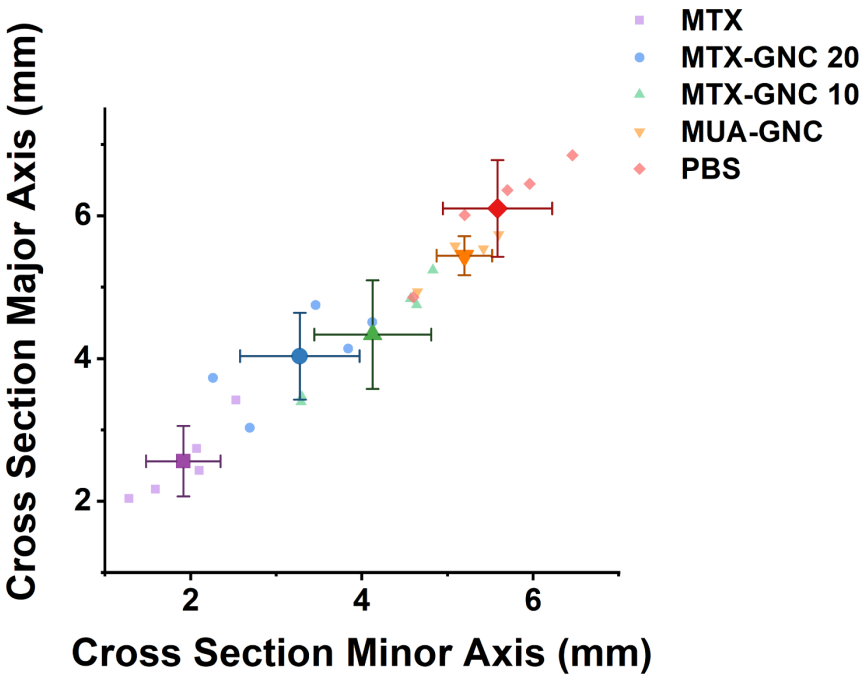

Figure 7.9.6 The major and minor axes of the cross-section of tumour-bearing footpads in different groups reveal the relative tumour size (n = 5).

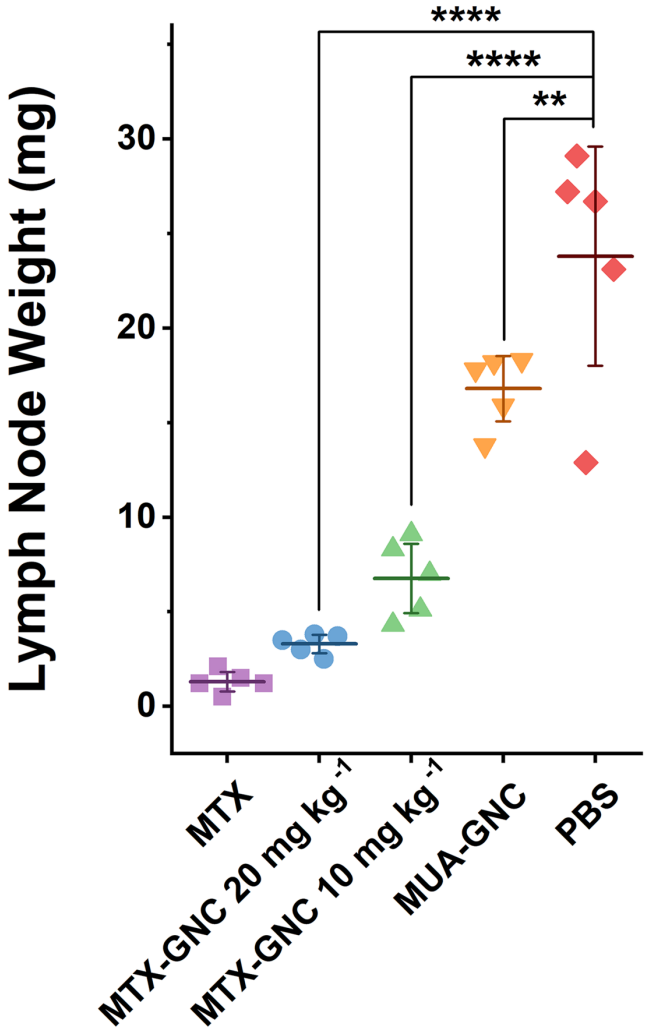

Figure 7.9.7 LN mass statistics of different treatment groups. (n = 5, ****: $P < 0.001$, **: $0.01 < P < 0.05$).

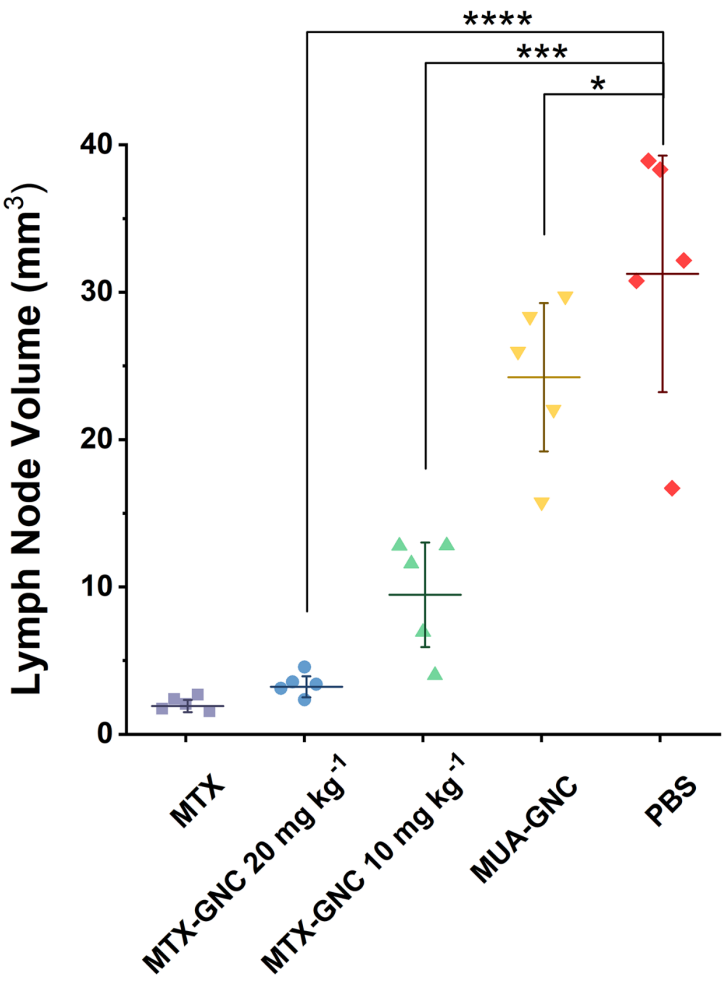

Figure 7.9.8 Comparison of LN volume of different treatment groups (n = 5; ****: $P < 0.001$, ***: $P < 0.01$ and *: $P > 0.05$).

7.10 Conclusions

To conclude, I have successfully prepared novel lymphophilic NIR-II fluorescent GNCs based on the $Au_{25}(SR_1)_x(SR_2)_{18-x}$-type GNC capped with mixed zwitterionic and anionic ligands. By optimizing the anionic ligand type and feed ratio, the optimal GNC exhibits highly effective LN accumulation. Moreover, it displays bright NIR-II fluorescence, which is more photostable and user-friendly than ICG, a widely used commercial LN imaging agent, making it a powerful NIR-II fluorescent probe for LN metastatic diagnosis and surgical guidance. The proposed GNCs show good penetration into the lymphatic follicular area, which can be further enhanced *via* SCS macrophage depletion. Furthermore, I have successfully loaded a hepatotoxic chemotherapeutic drug (MTX)

onto GNC for effective tumour metastasis treatment without onerous chemical synthesis. The MTX-loaded GNC can provide comparable anti-tumour efficacy as free MTX with greatly reduced liver toxicity. Combining advantageous features such as excellent photostability, biocompatibility, ease of ligand decoration, and good therapeutic potency, this GNC can effectively replace the current commercial bioimaging agents in diagnosis, imaging-guided surgery, and treatment of tumour-LN metastasis, and it has a great potential for clinical translation.

7.11 References

1 W. C. Lee, S. Kopetz, I. I. Wistuba and J. Zhang, *Ann. Oncol.*, 2017, **28**, 2045–2047.

2 J. Wang, W. Lu, C. Tang, Y. Liu, J. Sun, X. Mu, L. Zhang, B. Dai, X. Li, H. Zhuo and X. Jiang, *Anal. Chem.*, 2015, **87**, 11893–11900.

3 X. X. Hu, P. P. He, G. Bin Qi, Y. J. Gao, Y. X. Lin, C. Yang, P. P. Yang, H. Hao, L. Wang and H. Wang, *ACS Nano*, 2017, **11**, 4086–4096.

4 C. L. Chaffer and R. A. Weinberg, *Science*, 2011, **331**, 1559–1564.

5 A. S. Heerdt, *JAMA Oncol.*, 2018, **4**, 431.

6 L. F. Sestito and S. N. Thomas, *ACS Pharmacol. Transl. Sci.*, 2019, **2**, 293–310.

7 X.-Y. Zhang and W.-Y. Lu, *Cancer Biol. Med.*, 2014, **11**, 247–254.

8 V. F. Torous and E. Oliva, *Cancer Cytopathol.*, 2021, **129**, 581–582.

9 C. Li, V. C. Torres and K. M. Tichauer, *J. Surg. Oncol.*, 2018, **118**, 301–314.

10 Y. Sun, M. Ding, X. Zeng, Y. Xiao, H. Wu, H. Zhou, B. Ding, C. Qu, W. Hou, A. G. A. Er-bu, Y. Zhang, Z. Cheng and X. Hong, *Chem. Sci.*, 2017, **8**, 3489–3493.

11 H. Lin, Y. Zhou, J. Wang, H. Wang, T. Yao, H. Chen, H. Zheng, Y. Zhang, E. Ren, L. Jiang, C. Chu, X. Chen, J. Mao, F. Wang and G. Liu, *Sci. Adv.*, 2021, **7**, 1–12.

12 P.-S. He, F. Li, G.-H. Li, C. Guo and T.-J. Chen, *BMC Cancer*, 2016, **16**, 107.

13 Z. T. Bennett, Q. Feng, J. A. Bishop, G. Huang, B. D. Sumer and J. Gao, *Theranostics*, 2020, **10**, 3340–3350.

14 S. Qiu, J. Zeng, Y. Hou, L. Chen, J. Ge, L. Wen, C. Liu, Y. Zhang, R. Zhu and M. Gao, *Nanoscale*, 2018, **10**, 21772–21781.

15 X. D. Zhang, J. Chen, Z. Luo, D. Wu, X. Shen, S. S. Song, Y. M. Sun, P. X. Liu, J. Zhao,

S. Huo, S. Fan, F. Fan, X. J. Liang and J. Xie, *Adv. Healthc. Mater.*, 2014, **3**, 133–141.

16 J. P. M. Almeida, A. Y. Lin, E. R. Figueroa, A. E. Foster and R. A. Drezek, *Small*, 2015, **11**, 1453–1459.

17 L. A. Dykman and N. G. Khlebtsov, *Chem. Sci.*, 2017, **8**, 1719–1735.

18 X. Yang, J. Yang, L. Wang, B. Ran, Y. Jia, L. Zhang, G. Yang, H. Shao and X. Jiang, *ACS Nano*, 2017, **11**, 5737–5745.

19 L. Wang, J. Yang, S. Li, Q. Li, S. Liu, W. Zheng and X. Jiang, *Nano Lett.*, 2021, **21**, 1124–1131.

20 Z. Pang, Q. Li, Y. Jia, W. Yan, J. Qi, Y. Guo, F. Hu, D. Zhou and X. Jiang, *Chem. Sci.*, 2021, **12**, 14871–14882.

21 L. Wang, Q. Hou, W. Zheng and X. Jiang, *ACS Nano*, 2021, **15**, 17885–17894.

22 Y. Xie, Y. Liu, J. Yang, Y. Liu, F. Hu, K. Zhu and X. Jiang, *Angew. Chemie - Int. Ed.*, 2018, **57**, 3958–3962.

23 Y. Kong, J. Chen, H. Fang, G. Heath, Y. Wo, W. Wang, Y. Li, Y. Guo, S. D. Evans, S. Chen and D. Zhou, *Chem. Mater.*, 2016, **28**, 3041–3050.

24 Y. Tao, E. Ju, Z. Li, J. Ren and X. Qu, *Adv. Funct. Mater.*, 2014, **24**, 1004–1010.

25 H. Li, H. Li and A. Wan, *Analyst*, 2019, **145**, 348–363.

26 H. Liu, G. Hong, Z. Luo, J. Chen, J. Chang, M. Gong, H. He, J. Yang, X. Yuan, L. Li, X. Mu, J. Wang, W. Mi, J. Luo, J. Xie and X. Zhang, *Adv. Mater.*, 2019, **31**, 1901015.

27 Y. Kong, D. Santos-Carballal, D. Martin, N. N. Sergeeva, W. Wang, G. Liu, B. Johnson, B. Bhayana, Z. Lin, Y. Wang, X. Le Guével, N. H. de Leeuw, D. Zhou and M. X. Wu, *Mater. Today*, 2021, **51**, 96–107.

28 D. Li, Q. Liu, Q. Qi, H. Shi, E. C. Hsu, W. Chen, W. Yuan, Y. Wu, S. Lin, Y. Zeng, Z. Xiao, L. Xu, Y. Zhang, T. Stoyanova, W. Jia and Z. Cheng, *Small*, 2020, **16**, 1–9.

29 W. Wang, Y. Kong, J. Jiang, Q. Xie, Y. Huang, G. Li, D. Wu, H. Zheng, M. Gao, S. Xu, Y. Pan, W. Li, R. Ma, M. X. Wu, X. Li, H. Zuilhof, X. Cai and R. Li, *Angew. Chemie - Int. Ed.*, 2020, **59**, 22431–22435.

30 X. Song, W. Zhu, X. Ge, R. Li, S. Li, X. Chen, J. Song, J. Xie, X. Chen and H. Yang, *Angew. Chemie - Int. Ed.*, 2021, **60**, 1306–1312.

31 Z. Yu, B. Musnier, K. D. Wegner, M. Henry, B. Chovelon, A. Desroches-Castan, A. Fertin, U. Resch-Genger, S. Bailly, J. L. Coll, Y. Usson, V. Josserand and X. Le Guével, *ACS Nano*, 2020, **14**, 4973–4981.

32 L. Tang, X. Zeng, H. Zhou, C. Gui, Q. Luo, W. Zhou, J. Wu, Q. Li, Y. Li and Y. Xiao, *Chem. Res. Chinese Univ.*, 2021, **37**, 934–942.

33 N. L. Trevaskis, L. M. Kaminskas and C. J. H. Porter, *Nat. Rev. Drug Discov.*, 2015, **14**, 781–803.

34 Y. Nishimoto, S. Nagashima, K. Nakajima, T. Ohira, T. Sato, T. Izawa, J. Yamate, K. Higashikawa, Y. Kuge, M. Ogawa and C. Kojima, *Int. J. Pharm.*, 2020, **576**, 119021.

35 Y. Tiantian, Z. Wenji, S. Mingshuang, Y. Rui, S. Shuangshuang, M. Yuling, Y. Jianhua, Y. Xinggang, W. Shujun and P. Weisan, *Int. J. Pharm.*, 2014, **471**, 245–257.

36 A. K. Murthy, R. J. Stover, W. G. Hardin, R. Schramm, G. D. Nie, S. Gourisankar, T. M. Truskett, K. V. Sokolov and K. P. Johnston, *J. Am. Chem. Soc.*, 2013, **135**, 7799–7802.

37 A. Schudel, D. M. Francis and S. N. Thomas, *Nat. Rev. Mater.*, 2019, **4**, 415–428.

38 H. Jiang, Q. Wang and X. Sun, *J. Control. Release*, 2017, **267**, 47–56.

39 B. Li, B. Li, Z. Yuan, Y. He, Y. He, H. C. Hung, S. Jiang and S. Jiang, *Nano Lett.*, 2020, **20**, 4693–4699.

40 J. Shaoyi and C. Zhiqiang, *Adv. Mater.*, 2009, **22**, 920–932.

41 Z. A. Khan, R. Tripathi and B. Mishra, *Expert Opin. Drug Deliv.*, 2012, **9**, 151–169.

42 T. Chen, V. Fung, Q. Yao, Z. Luo, D. E. Jiang and J. Xie, *J. Am. Chem. Soc.*, 2018, **140**, 11370–11377.

43 Z. Luo, V. Nachammai, B. Zhang, N. Yan, D. T. Leong, D. E. Jiang and J. Xie, *J. Am. Chem. Soc.*, 2014, **136**, 10577–10580.

44 F. Aldeek, M. A. H. Muhammed, G. Palui, N. Zhan and H. Mattoussi, *ACS Nano*, 2013, **7**, 2509–2521.

45 P. Pei, W. Shen, H. Zhou, Y. Sun, J. Zhong, T. Liu and K. Yang, *Nano Today*, 2021, **38**, 101144.

46 W. Wang, Y. Guo, C. Tiede, S. Chen, M. Kopytynski, Y. Kong, A. Kulak, D. Tomlinson, R. Chen, M. McPherson and D. Zhou, *ACS Appl. Mater. Interfaces*, 2017, **9**, 15232–15244.

47 Y. Guo, C. Sakonsinsiri, I. Nehlmeier, M. A. Fascione, H. Zhang, W. Wang, S. Pöhlmann, W. B. Turnbull and D. Zhou, *Angew. Chemie*, 2016, **55**, 4738–4742.

48 H. S. Choi, W. Liu, P. Misra, E. Tanaka, J. P. Zimmer, B. Itty Ipe, M. G. Bawendi and J. V Frangioni, *Nat. Biotechnol.*, 2009, **25**, 1165–1170.

49 M. Yu, J. Xu and J. Zheng, *Angew. Chemie*, 2019, **131**, 4156–4172.

50 Q. Cheng, T. Wei, L. Farbiak, L. T. Johnson, S. A. Dilliard and D. J. Siegwart, *Nat. Nanotechnol.*, 2020, **15**, 313–320.

51 T. Nakamura, M. Kawai, Y. Sato, M. Maeki, M. Tokeshi and H. Harashima, *Mol. Pharm.*, 2020, **17**, 944–953.

52 B. Du, X. Jiang, A. Das, Q. Zhou, M. Yu, R. Jin and J. Zheng, *Nat. Nanotechnol.*, 2017, **12**, 1096–1102.

53 E. Porret, X. Le Guével and J. L. Coll, *J. Mater. Chem. B*, 2020, **8**, 2216–2232.

54 Y. Nakajima, K. Asano, K. Mukai, T. Urai, M. Okuwa, J. Sugama and T. Nakatani, *Sci. Rep.*, 2018, **8**, 1–9.

55 W. Van den Broeck, A. Derore and P. Simoens, *J. Immunol. Methods*, 2006, **312**, 12–19.

56 H. Kobayashi, S. Kawamoto, R. A. Star, T. A. Waldmann, Y. Tagaya and M. W. Brechbiel, *Cancer Res.*, 2003, **63**, 271–276.

57 R. Tian, H. Ma, S. Zhu, J. Lau, R. Ma, Y. Liu, L. Lin, S. Chandra, S. Wang, X. Zhu, H. Deng, G. Niu, M. Zhang, A. L. Antaris, K. S. Hettie, B. Yang, Y. Liang and X. Chen, *Adv. Mater.*, 2020, **32**, 1907365.

58 A. L. Antaris, H. Chen, S. Diao, Z. Ma, Z. Zhang, S. Zhu, J. Wang, A. X. Lozano, Q. Fan, L. Chew, M. Zhu, K. Cheng, X. Hong, H. Dai and Z. Cheng, *Nat. Commun.*, 2017, **8**, 1–11.

59 X. Le Guével, M. Henry, V. Motto-Ros, E. Longo, M. I. Montañez, F. Pelascini, O. De La Rochefoucauld, P. Zeitoun, J. L. Coll, V. Josserand and L. Sancey, *Nanoscale*, 2018, **10**, 18657–18664.

60 P. Fiurasek and L. Reven, *Langmuir*, 2007, **23**, 2857–2866.

61 Y. L. Balachandran, X. Li and X. Jiang, *Nano Lett.*, 2021, **21**, 1335–1344.

62 J. A. Yáñez, S. W. J. Wang, I. W. Knemeyer, M. A. Wirth and K. B. Alton, *Adv. Drug Deliv. Rev.*, 2011, **63**, 923–942.

63 S. Zhu, B. C. Yung, S. Chandra, G. Niu, A. L. Antaris and X. Chen, *Theranostics*, 2018, **8**, 4141–4151.

64 E. P. Porcu, A. Salis, E. Gavini, G. Rassu, M. Maestri and P. Giunchedi, *Biotechnol. Adv.*, 2016, **34**, 768–789.

65 X. Peng, J. Wang, F. Zhou, Q. Liu and Z. Zhang, *Cell. Mol. Life Sci.*, 2021, **78**, 5139–5161.

66 H. Mok, H. Jeong, S. J. Kim and B. Hyun Chung, *Chem. Commun.*, 2012, **48**, 8628–8630.

67 J. T. Alander, I. Kaartinen, A. Laakso, T. Pätilä, T. Spillmann, V. V. Tuchin, M. Venermo and P. Välisuo, *Int. J. Biomed. Imaging*, 2012, **2012**, 1–26.

68 Y. Tsujino, K. Mizumoto, Y. Matsuzaka, H. Niihara and E. Morita, *J. Dermatol.*, 2009, **36**, 90–94.

69 C. Egloff-Juras, L. Bezdetnaya, G. Dolivet and H. P. Lassalle, *Int. J. Nanomedicine*, 2019, **14**, 7823–7838.

70 D. A. P. Louie and S. Liao, *Front. Immunol.*, 2019, **10**, 1–9.

71 A. Schudel, A. P. Chapman, M.-K. Yau, C. J. Higginson, D. M. Francis, M. P. Manspeaker, A. R. C. Avecilla, N. A. Rohner, M. G. Finn and S. N. Thomas, *Nat. Nanotechnol.*, 2020, **15**, 491–499.

72 Y.-N. Zhang, W. Poon, E. Sefton and W. C. W. Chan, *ACS Nano*, 2020, **14**, 9478–9490.

73 T. Cai, H. Liu, S. Zhang, J. Hu and L. Zhang, *J. Nanobiotechnology*, 2021, **19**, 1–23.

74 X. D. Zhang, D. Wu, X. Shen, P. X. Liu, F. Y. Fan and S. J. Fan, *Biomaterials*, 2012, **33**, 4628–4638.

75 S. S. Abolmaali, A. M. Tamaddon and R. Dinarvand, *Cancer Chemother. Pharmacol.*, 2013, **71**, 1115–1130.

76 V. Maksimovic, Z. Pavlovic-Popovic, S. Vukmirovic, J. Cvejic, A. Mooranian, H. Al-Salami, M. Mikov and S. Golocorbin-Kon, *Mol. Biol. Rep.*, 2020, **47**, 4699–4708.

77 Y.-H. Chen, C.-Y. Tsai, P.-Y. Huang, M.-Y. Chang, P.-C. Cheng, C.-H. Chou, D.-H. Chen, C.-R. Wang, A.-L. Shiau and C.-L. Wu, *Mol. Pharm.*, 2007, **4**, 713–722.

78 H. Nyblom, E. Björnsson, M. Simrén, F. Aldenborg, S. Almer and R. Olsson, *Liver Int.*, 2006, **26**, 840–845.

79 M. Ettel, G. A. Gonzalez, S. Gera, O. Eze, S. Sigal, J. S. Park and R. Xu, *Hum. Pathol.*, 2017, **68**, 92–98.

80 C. Matté, F. M. Stefanello, V. Mackedanz, C. D. Pederzolli, M. L. Lamers, C. S. Dutra-Filho, M. F. dos Santos and A. T. S. Wyse, *Int. J. Dev. Neurosci.*, 2009, **27**, 337–344.

81 X. L. Wang, T. Zhang, L. H. Hu, S. Q. Sun, W. F. Zhang, Z. Sun, L. H. Shen and B. He, *Oxid. Med. Cell. Longev.*, 2017, **2017**, 6282486.

82 E. Cikler-Dulger and I. Sogut, *Biotech. Histochem.*, 2020, **95**, 186–193.

83 L. J. Stallons, R. M. Whitaker and R. G. Schnellmann, *Toxicol. Lett.*, 2014, **224**, 326–332.

84 M. Matulionyte, D. Dapkute, L. Budenaite, G. Jarockyte and R. Rotomskis, *Int. J. Mol. Sci.*, 2017, **18**, 1–17.

Chapter 8
Overall conclusions and future directions

8.1 Overall conclusions and future directions

This thesis includes **three** parts: **Part I** gives the introduction to GNPs and GNCs (**Chapter 1**) and the summary of experimental materials and methods (**Chapter 2**). **Part II** focuses on a general introduction to antimicrobial GNPs and GNCs (**Chapter 3**), as well as the development of atomically precise antibacterial GNCs for the treatment of Gram-positive MDR bacteria-induced infections in skin infection model (**Chapter 4**) and keratitis model (**Chapter 5**); **Part III** is the introduction of the applications of GNPs and GNCs in lymphatic system imaging (**Chapter 6**), and development of NIR fluorescent atomically precise GNCs for LN imaging-guided surgery and diagnosis and treatment of LN metastases (**Chapter 7**).

In **Part II**, I discovered that control of the feed ratios of the active ligand (P12 or 4MMP) and the zwitterionic (C5) ligand could achieve the optimal balance between the antibacterial ability and the biocompatibility of the GNC.[1] As I mentioned in the introduction part, most of the current antibacterial GNCs or GNPs have focused on the relationship between the ligand type and antibacterial ability. In addition, the ligand used is mainly limited to a single type, lacking the ability to subtly adjust its specific property.[2] In addition, several aspects that need to be urgently resolved for antimicrobial GNC or GNP in future research are summarized below:

1) The synergy of antimicrobial gold nanomaterial with those extensively resisted antibiotics. Since the development of MDR is unstoppable, besides seeking new antibiotics, new methods to resensitise those MDR strains to these “old” antibiotics

and rehabilitate them is a highly valuable approach.[3] In addition, adjuvants that could synergistically slow down the development of MDR are also cherished.[4] Currently, many small molecular β-lactam inhibitors (clavulanic acid, sulbactam, avibactam, etc.) are applied simultaneously as antibiotic cocktails. In terms of gold nanomaterials, the synergy of GNPs with carbapenems, cephalosporins, and quinolones has been discovered.[5] However, the mechanism by which it can produce synergistic effects is still unknown. In Chapter 4, I used a series of experiments to prove that undermining of cell envelope intactness and ROS generation of GNC have an additive effect with imipenem. However, more specific impacts on bacterial transcriptomics and proteomics remain unknown. Therefore, in subsequent studies, more gold nanomaterials should be studied for their synergistic antibacterial effects with frontline antibiotics.

2) The ability of GNPs and GNCs to resensitise non-antimicrobial molecules is highly valuable. This could significantly broaden the scope of discovering new antimicrobial materials.[6] I discovered that volatile mercaptan molecules that have never been applied in antimicrobial applications could serve as new antibacterial capping. The immobilization of these thiol molecules onto Au kernel significantly altered their physicochemical properties and bioactivity.[7] Conceivably, there must be countless undiscovered libraries of compounds with similar antibacterial potentials after conjugation with GNC or GNP to be discovered. At the same time, this methodology should not be limited to the antibacterial application but can be extended to other broad areas in antifungal[8], antiviral[9], antimalarial[10], antiparasitic[11], and anticancer areas.[12]

3) In terms of capping ligands, in addition to the ratio of capping ligands, more attention should be paid to how these affect their underlying properties. For example, the application of different ratios of ligands with different charges will change the overall zeta potential of GNPs, which in turn affects the antibacterial

ability.[13] The relationship between the charge density and the antibacterial ability is still an unassured question. Additionally, applying different ratios of hydrophobic ligands could significantly alter the surface hydrophilicity of the GNP, causing different antibacterial characteristics.[14] For example, by controlling the proportions of both aminophenylboronic acid and mercaptophenylboronic acid, Wang et al. tuned the antibacterial spectrum of GNPs by adjusting the surface capping density.[15] Besides surface charge, hydrophilicity and ligand capping density are the properties that should be studied as a function of the surface ligand ratios.

4) Besides ligand, a study on the relationship between the Au kernel and the antibacterial ability of gold nanomaterial is another important aspect that influences the antibacterial ability. As introduced in Chapter 3, the size-focusing study confirmed that the diameter change of GNPs has a great influence on their antibacterial ability. However, this relationship is extremely unclear, depending on the ligand and bacteria strain. Xie et al. found that DAPT-capped GNP's size is inversely proportional to its antibacterial ability, with the 1.9-nm GNP demonstrating the highest antibacterial ability toward *E. c* and *S. a*.[16] While Zheng et al. found that both the big (5.5 nm) and small (1.8 nm) GNPs are effective against Gram-negative strains.[17] Moreover, for GNCs, there is still lacking a systematic study on the relationship between the Au atomic number of the atomically precise GNCs and their antibacterial ability, which I believe is an attractive direction in future research.

5) Generally, there are more treatments and therapies against MDR Gram-positive bacterial infections than Gram-negative infections.[18] However, the development of MDR in Gram-negative strains is more rapid than in Gram-positive strains.[19] This could be mainly attributed to the structural difference between Gram-positive and Gram-negative strains. The presence of the outer membrane in Gram-negative strains acts as the natural defence that could inhibit the permeation of many

drugs.[20] In addition, many efflux pumps are overexpressed on the outer membrane.[21] In the future, the development of antibiotics or antimicrobial gold nanomaterials should be more focused on Gram-negative bacteria.

6) The antibacterial mechanism of gold nanomaterials is not well studied. Specifically, the mechanistic study is mainly limited to the results shown after bacterial killing or the results obtained with the testing kit. [1] [22] In the study of the mechanism of new antibiotics (like daptomycin), molecular target validation is normally required, which has been often ignored in the nanomaterial antibacterial mechanism research.[23] It is useful to combine transcriptomic and proteomic studies to comprehensively understand the antibacterial effects of nanomaterials.[24]

In Part III, through adjusting the anionic charge density of MUA-GNCs (by controlling the anionic ligand feed ratio), I have successfully controlled the specific accumulation of this NIR fluorescence GNC into the sentinel LNs for the simultaneous diagnosis and treatment of lymphatic metastasis. This concept is derived from previously reported selective organ targeting or SORT, which means adjusting the surface charge density to deliver the NPs into selective organs.[25] I expect that by applying other ligands with different charges, steric hindrance, and hydrophilicity, the GNCs could also achieve selective accumulation into other organs. In addition, due to the lymphophilicity of the MUA-GNC, this gold nanomaterial has a huge potential in other lymphatic system-related applications.[26] As the silver staining result has indicated that the MUA-GNC has entered the follicular (B lymphocyte cluster, cortex) and paracortex regions, which have a wide interaction with antigen-presenting cells (SCS macrophages), B lymphocytes, and T lymphocytes.[27] As the LN is closely related to autoimmunity, this GNC could carry immunosuppressants for the direct and fast treatment of autoimmune diseases by directly inhibiting the proliferation of immune cells and reducing the overall toxicity.[28] Although the selection of additional ligands should be focused on to avoid adverse effects on LN targeting ability. Significantly, the application of SORT can target specific

organs and reduce the side effects of off-target. In addition, this GNC could also be used to deliver immune stimuli or antigen as nano-vaccine to directly evoke antibody secretion and rapidly increases antibody level.[29] Lastly, in addition to LNs, many important immune organs, like the spleen, also participated in taking up this NIR fluorescent GNC (as indicated by NIR fluorescence).[30] However, research on the influence of GNCs on immune organs has rarely been studied. In the current hot period of tumour and coronavirus research, articles related to immunity are also emerging one after another. In combination, it is hoped that this material can play a role in the above-mentioned research areas in the future, thereby improving its clinical application prospects.

8.2 References

1 Z. Pang, Q. Li, Y. Jia, W. Yan, J. Qi, Y. Guo, F. Hu, D. Zhou and X. Jiang, *Chem. Sci.*, 2021, **12**, 14871–14882.

2 K. Zheng, M. I. Setyawati, D. T. Leong and J. Xie, *ACS Nano*, 2017, **11**, 6904–6910.

3 M. Dettweiler, R. J. Melander, G. Porras, C. Risener, L. Marquez, T. Samarakoon, C. Melander and C. L. Quave, *ACS Infect. Dis.*, 2020, **6**, 1667–1673.

4 G. D. Wright, *Trends Microbiol.*, 2016, **24**, 862–871.

5 B. Lee and D. G. Lee, *J. Appl. Microbiol.*, 2019, **127**, 701–712.

6 Y. Cui, Y. Zhao, Y. Tian, W. Zhang, X. Lü and X. Jiang, *Biomaterials*, 2012, **33**, 2327–2333.

7 Y. Zhao, Y. Tian, Y. Cui, W. Liu, W. Ma and X. Jiang, *J. Am. Chem. Soc.*, 2010, **132**, 12349–12356.

8 M. Seong and D. G. Lee, *Microbiol. Res.*, 2018, **207**, 33–40.

9 V. Cagno, P. Andreozzi, M. D'Alicarnasso, P. J. Silva, M. Mueller, M. Galloux, R. Le Goffic, S. T. Jones, M. Vallino, J. Hodek, J. Weber, S. Sen, E. R. Janecek, A. Bekdemir, B. Sanavio, C. Martinelli, M. Donalisio, M. A. R. Welti, J. F. Eleouet, Y. Han, L. Kaiser, L. Vukovic, C. Tapparel, P. Král, S. Krol, D. Lembo and F. Stellacci, *Nat. Mater.*, 2018, **17**, 195–203.

10 S. Varela-Aramburu, C. Ghosh, F. Goerdeler, P. Priegue, O. Moscovitz and P. H. Seeberger, *ACS Appl. Mater. Interfaces*, 2020, **12**, 43380–43387.

11 G. Benelli, *Acta Trop.*, 2018, **178**, 73–80.

12 X. Zhang, X. Chen, Y. W. Jiang, N. Ma, L. Y. Xia, X. Cheng, H. R. Jia, P. Liu, N. Gu, Z. Chen and F. G. Wu, *ACS Appl. Mater. Interfaces*, 2018, **10**, 10601–10606.

13 D. Hu, H. Li, B. Wang, Z. Ye, W. Lei, F. Jia, Q. Jin, K. F. Ren and J. Ji, *ACS Nano*, 2017, **11**, 9330–9339.

14 X. Li, S. M. Robinson, A. Gupta, K. Saha, Z. Jiang, D. F. Moyano, A. Sahar, M. A. Riley and V. M. Rotello, *ACS Nano*, 2014, **8**, 10682–10686.

15 L. Wang, S. Li, J. Yin, J. Yang, Q. Li, W. Zheng, S. Liu and X. Jiang, *Nano Lett.*, 2020, **20**, 5036–5042.

16 Y. Xie, J. Yang, J. Zhang, W. Zheng and X. Jiang, *Angew. Chemie Int. Ed.*, 2020, **59**, 23471–23475.

17 W. Zheng, Y. Jia, Y. Zhao, J. Zhang, Y. Xie, L. Wang, X. Zhao, X. Liu, R. Tang, W. Chen and X. Jiang, *Nano Lett.*, 2021, **21**, 1992–2000.

18 E. Tacconelli, E. Carrara, A. Savoldi, S. Harbarth, M. Mendelson, D. L. Monnet, C. Pulcini, G. Kahlmeter, J. Kluytmans, Y. Carmeli, M. Ouellette, K. Outterson, J. Patel, M. Cavaleri, E. M. Cox, C. R. Houchens, M. L. Grayson, P. Hansen, N. Singh, U. Theuretzbacher, N. Magrini, A. O. Aboderin, S. S. Al-Abri, N. Awang Jalil, N. Benzonana, S. Bhattacharya, A. J. Brink, F. R. Burkert, O. Cars, G. Cornaglia, O. J. Dyar, A. W. Friedrich, A. C. Gales, S. Gandra, C. G. Giske, D. A. Goff, H. Goossens, T. Gottlieb, M. Guzman Blanco, W. Hryniewicz, D. Kattula, T. Jinks, S. S. Kanj, L. Kerr, M. P. Kieny, Y. S. Kim, R. S. Kozlov, J. Labarca, R. Laxminarayan, K. Leder, L. Leibovici, G. Levy-Hara, J. Littman, S. Malhotra-Kumar, V. Manchanda, L. Moja, B. Ndoye, A. Pan, D. L. Paterson, M. Paul, H. Qiu, P. Ramon-Pardo, J. Rodríguez-Baño, M. Sanguinetti, S. Sengupta, M. Sharland, M. Si-Mehand, L. L. Silver, W. Song, M. Steinbakk, J. Thomsen, G. E. Thwaites, J. W. van der Meer, N. Van Kinh, S. Vega, M. V. Villegas, A. Wechsler-Fördös, H. F. L. Wertheim, E. Wesangula, N. Woodford, F. O. Yilmaz and A. Zorzet, *Lancet Infect. Dis.*, 2018, **18**, 318–327.

19 M. I. Hutchings and K. R. Duncan, *Cell Host Microbe*, 2022, **30**, 273–274.

20 P. Nordmann and L. Poirel, *Clin. Infect. Dis.*, 2019, **69**, S521–S528.

21 L. Fernández and R. E. W. Hancock, *Clin. Microbiol. Rev.*, 2012, **25**, 661–681.

22 Y. Xie, Y. Liu, J. Yang, Y. Liu, F. Hu, K. Zhu and X. Jiang, *Angew. Chemie - Int. Ed.*, 2018, **57**, 3958–3962.

23 A. Müller, M. Wenzel, H. Strahl, F. Grein, T. N. V. Saaki, B. Kohl, T. Siersma, J. E.

Bandow, H. G. Sahl, T. Schneider and L. W. Hamoen, *Proc. Natl. Acad. Sci. U. S. A.*, 2016, **113**, E7077–E7086.

24 Z. Huang, Y. Liu, L. Wang, A. Ali, Q. Yao, X. Jiang and Y. Gao, *Biomaterials*, 2020, **253**, 120124.

25 Q. Cheng, T. Wei, L. Farbiak, L. T. Johnson, S. A. Dilliard and D. J. Siegwart, *Nat. Nanotechnol.*, 2020, **15**, 313–320.

26 S. Qi, X. Wang, K. Chang, W. Shen, G. Yu and J. Du, *J. Nanobiotechnology*, 2022, **20**, 1–27.

27 D. A. P. Louie and S. Liao, *Front. Immunol.*, 2019, **10**, 1–9.

28 X. Ke, G. P. Howard, H. Tang, B. Cheng, M. T. Saung, J. L. Santos and H. Q. Mao, *Adv. Drug Deliv. Rev.*, 2019, **151**–**152**, 72–93.

29 S. Kang, S. Ahn, J. Lee, J. Y. Kim, M. Choi, V. Gujrati, H. Kim, J. Kim, E. C. Shin and S. Jon, *J. Control. Release*, 2017, **256**, 56–67.

30 T. Cai, H. Liu, S. Zhang, J. Hu and L. Zhang, *J. Nanobiotechnology*, 2021, **19**, 1–23.